Title
CRITICAL DISCHARGE OF INITIALLY SUBCOOLED WATER THROUGH SLITS

Authors
Anos, C.N.
Schrock, V.E.

Publication Date
1983-06-01

Lawrence Berkeley Laboratory
UNIVERSITY OF CALIFORNIA

Engineering & Technical Services Division

CRITICAL DISCHARGE OF INITIALLY SUBCOOLED WATER THROUGH SLITS

C.N. Amos* and V.E. Schrock
(*Ph.D. Thesis)

June 1983

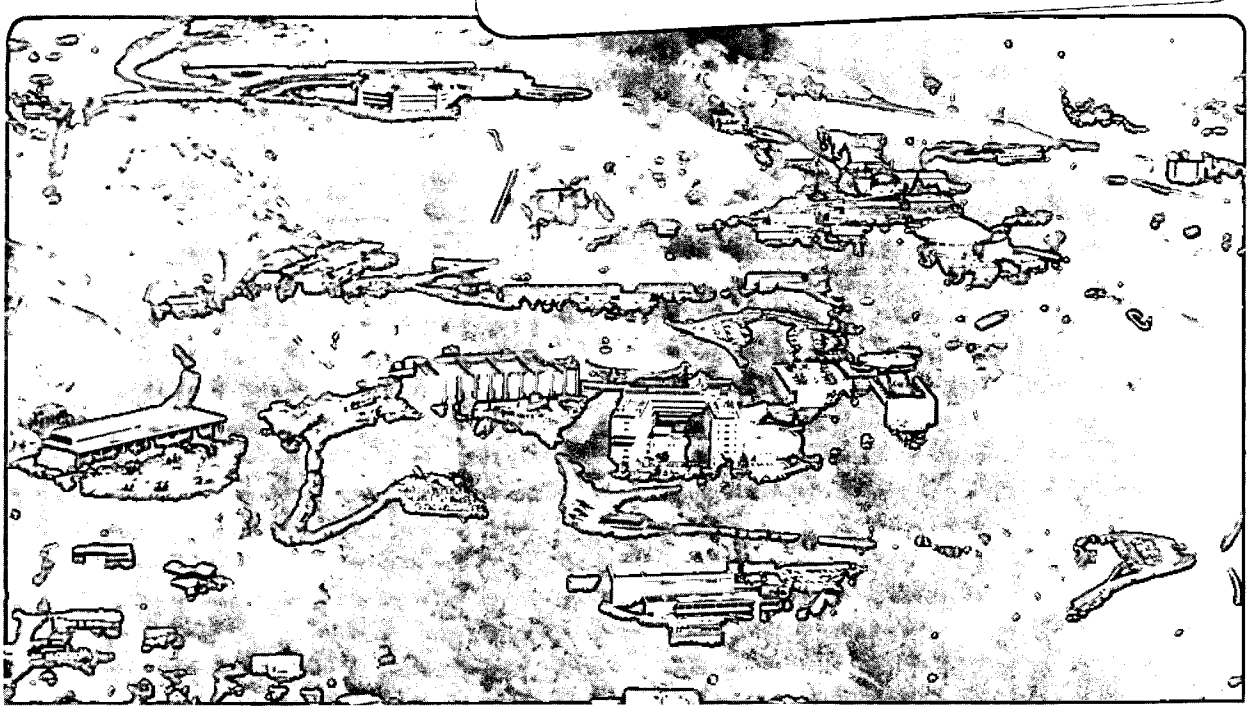

Prepared for the U.S. Department of Energy under Contract DE-AC03-76SF00098

DISCLAIMER

LBL-16363
NUREG/CR-3475

CRITICAL DISCHARGE OF INITIALLY SUBCOOLED WATER THROUGH SLITS

C.N. Amos and V.E. Schrock

Nuclear Engineering Department
Engineering and Technical Services Division
Lawrence Berkeley Laboratory
University of California
Berkeley, California 94720

June 1983

This work was supported by the U.S. Nuclear Regulatory Commission, through NRC Fin No. B 3043 under Interagency Agreement DOE-60-83-208, through U.S. Department of Energy Contract No. DE-AC03-76SF00098.

Table of Contents

CRITICAL DISCHARGE OF INITIALLY SUBCOOLED WATER THROUGH SLITS

C.N. Amos and V.E. Schrock

Nuclear Engineering Department
Engineering and Technical Services Division
Lawrence Berkeley Laboratory
University of California
Berkeley, California 94720

Abstract

This report describes an experimental investigation into the critical flow of initially subcooled water through rectangular slits. The study of such flows is relevant to the prediction of leak flow rates from cracks in piping, or pressure vessels, which contain sufficient enthalpy that vaporization will occur if they are allowed to expand to the ambient pressure. Two new analytical models, which allow for the generation of a metastable liquid phase, are developed. Experimental results are compared with the predictions of both these new models and with a Fanno Homogeneous Equilibrium Model.

Critical flow is a phenomenon of compressible flows which may be defined as the maximum flowrate that can be attained by a fluid flowing from a given stagnation state through a fixed geometry. The study of critical flow in slits is useful in the safety analysis of nuclear power reactor systems. Postulated loss-of-coolant events in these systems include, coolant leakage through cracks in primary system piping and through stuck open safety relief valves. These results are also relevant to the small geometries involved in the latter problem.

To study two-phase critical flow under steady flow conditions a modified blowdown apparatus, which employs a flow of nitrogen gas into the water reservoir to hold the stagnation pressure constant,was designed and constructed. Heating the reservoir to a uniform temperature prior to each experiment kept the fluid stagnation state approximately constant over the course of each run. The test section design was unique in that it allowed a range of slit sizes to be tested using the same hardware. A total of 94 experiments are reported. A parametric study of the effects of stagnation pressure, stagnation subcooling, and length-to-diameter ratio (L/D) of the slit on both the critical mass flux and the pressure profile within the slit was made. Stagnation pressures ranged between 4.1 and 16.2 MPa. Subcoolings were in the range from zero to 65°C. L/D of the slits were between 83 and 400, with the flow direction dimension fixed at 6.35 cm.

It is concluded that frictional effects are predominant in two-phase critical flows for these geometries; which are characterized by large L/D. The critical mass flux was seen to increase with increasing stagnation pressure and/or subcooling. The dependence of the mass flux on the initial subcooling was reduced for subcoolings below 5°C. Measured mass fluxes ranged from 1×10^4 kg/m^2-s, for the smallest fL/D slits, to 7×10^4 kg/m^2-s for the largest fL/D slits with the highest stagnation pressure and subcooling.

The homogeneous nonequilibrium model for two-phase critical flow, developed herein, includes the effects of: channel wall friction, significant reduction of the fluid pressure below saturation prior to the initiation of flashing, and nonequilibrium vapor generation. The model predicts the mass flux data from the present study within 5% with a 64% confidence level. Critical pressure ratios are consistently overpredicted. The extent of this overprediction increases with decreasing stagnation subcooling. The model is also compared to data taken in 20 mm diameter pipes with similar success. Recommendations are made for future modeling efforts.

Acknowledgement

The first author wishes to express his most sincere thanks to those who have made this research possible, and who have contributed to the writing of this report. First, and foremost, to my wife Judy, who's love and patience over the years enabled me to move forward. Her sacrifice is more than I could have asked. My thanks also to Professor Virgil Schrock, his guidance and suggestions were invaluable. I also thank professors L.M. Grossman and C.L. Tien for their reading of the report.

The skill and experience of Dan Winterbauer, John Souza, and the other members of the Nuclear Engineering Department machine shop were vital to the construction of the experiment. Their hard work and support are appreciated. Our thanks also to Al Kropp who's loan of word processing equipment made the production of this document a much easier task. We are grateful for the excellent work of Valerie Kelly, Jean Wolslegal and Shirley Ashley of the LBL Technical Information Department in the preparation of the final manuscript.

We also thank the U.S Nuclear Regulatory Commission for their sponsorship under the direction of Dr. Stan Fabic and Dr. Novak Zuber. This work was supported by the U.S. Nuclear Regulatory Commission, through NRC Fin No. B 3043 under Interagency Agreement DOE-60-83-208, through U.S. Department of Energy Contract No. DE-AC03-76SF00098.

List of Figures

List of Tables

Nomenclature

Symbol	Description	Dimension
A	Cross-sectional area Coefficient matrix	L^2
A_i	Interfacial area	L^2
a	Speed of sound	Lt^{-1}
B	Coefficient matrix	
C	Coefficient for interphase drag or, Integration path, equation (4-8)	
c_p	Specific heat at constant pressure	$L^2t^{-2}T^{-1}$
c_v	Specific heat at constant volume	$L^2t^{-2}T^{-1}$
D	Diameter	L
D_h	Hydraulic diameter	L
D_l	Liquid thermal diffusivity	tL^{-2}
D_s	Thermal diffusivity of steel	tL^{-2}
d	Slit opening dimension	L
d_0	Bubble diameter, Chapter II	L
F	Interphase shear force	MLt^{-2}
f	Friction factor	
f_F	Fanning friction factor	
G	Mass flux	$ML^{-2}t^{-1}$
g	Acceleration of gravity	Lt^{-2}
g_c	Newton constant	
h	Specific enthalpy	Lt^{-2}
h'	Heat transfer coefficient	$MLt^{-2}T^{-1}$
h_{fg}	Latent heat of vaporization	Lt^{-2}

Symbol	Description	Dimension
K	Entry loss coefficient	
k	Slip ratio	
k_s	Boltzmann's constant	$ML^2t^{-2}T^{-1}$
k_l	Liquid thermal conductivity	$MLt^{-3}T^{-1}$
L	Length	L
M	Mass	M
$\dot{m}$	Mass flowrate	Mt^{-1}
N_m	Bubble/Nucleation site density per unit mass	M^{-1}
N_v	Bubble/Nucleation site density per unit volume	L^{-3}
Nu	Nusselt number	
n	Parameter defined by equation (2-12)	
n_s	Nucleation site density	M^{-1}
P	Pressure	$ML^{-1}t^{-2}$
ΔP	Differential pressure	$ML^{-1}t^{-2}$
ΔP_d	Pressure undershoot defined by equation (2-21)	$ML^{-1}t^{-2}$
Q,$\dot{q}$	Heat flowrate	ML^2t^{-3}
$\dot{q}''$	Heat flux	Mt^{-3}
R	Gas constant (specific)	$L^2t^{-2}T^{-1}$
Re	Reynolds number	
R_b	Bubble radius	L
s	Specific entropy	$L^2t^{-2}T^{-1}$
s_{fg}	$s_g - s_f$	$L^2t^{-2}T^{-1}$
T	Temperature	T

Symbol	Description	Dimension
T_c	Thermodynamic critical point temperature	T
T_r	Reduced temperature ($=T/T_c$)	
t	Time	t
u	Velocity	Lt^{-1}
V	Volume	L^3
v	Specific volume	L^3M^{-1}
v_{fg}	$v_g - v_f$	L^3M^{-1}
W	Width	L
x	Vapor mass fraction	
$\bar{Y}$, $\bar{y}$	Column vector of dependent variables	
Z	Compressibility factor (real gas)	
z	Length variable	L

Greek Letters

α	Void fraction	
β	Nonequilibrium rate of change of thermodynamic quality with pressure. Defined by equation (5-34).	$M^{-1}Lt^2$
Γ	Vapor generation rate	Mt^{-1}
γ	Specific heat ratio	
δ	Difference	
Δ	Difference	
ϵ	Constant ($<<1$)	

Symbol	Description	Dimension
η	"Polytropic" exponent, defined by equation (2-13a) or, Fraction of momentum lost to vapor phase. Equation (2-39d), or, Variable, Appendix F	
Θ	Liquid superheat	T
Θ_c	Liquid superheat at flashing inception	T
μ	Viscosity	$ML^{-1}t^{-1}$
ν	Interaction frequency	t^{-1}
ρ	Density	ML^{-3}
Σ'	Depressurization rate	$ML^{-1}t^{-3}$
σ	Surface tension	Mt^{-2}
τ	Shear stress, or,	$ML^{-1}t^{-2}$
	Time constant	t^{-1}
Φ	Heat source	ML^2t^{-3}

Subscripts

b	Bubble
c	Critical
E	Evaluated according to an equilibrium process.
e	Channel entrance
ex	Channel exit or nozzle throat
exit	Channel exit

Symbol	Description	Dimension
exp	Experimental	
f	Saturated liquid, or Final	
fl	Evaluated at the point of flashing.	
g	Saturated vapor	
HE	Homogeneous equilibrium	
HF	Homogeneous, frozen composition	
h	Evaluated at constant enthalpy	
i	Interfacial, or Summation index	
in	Inlet	
j	Summation index	
k	Indicates evaluation for the appropriate phase. k=f,g, or l,or Summation index	
l	Liquid	
P	Evaluated at constant pressure	
s	Evaluated at constant entropy	
sat	Evaluated at saturation condition corresponding to the local pressure.	
t	Nozzle throat	
w	Wall	

Symbol	Description	Dimension
0	Stagnation	

Superscripts

N	Nitrogen	
o	Evaluated at ambient temperature	

CHAPTER I

Introduction

I.1 Critical Flow in Engineered Systems

Critical flow can be defined as the maximum flowrate obtainable for a fluid at a given stagnation state through a given flow channel. A more precise definition is given below.

An understanding of the physical processes involved in critical two-phase flow is important in the modeling of the phenomenon. Prediction of coolant flowrates from postulated breaches in the primary cooling system of a nuclear reactor is an essential part of the safety analysis. Traditionally, this concern has centered around the so called (Large Break) Loss-of-Coolant Accident, LOCA. As Ross [1] has pointed out, one impact of the Three Mile Island accident, in March, 1979, was to focus more attention on the problem of predicting discharge rates from small breaks in the cooling system. The U.S. Nuclear Regulatory Commission (NRC) has required [2] a reevaluation of models for the small break loss-of-coolant accident. This reevaluation included both the break flow model (the subject of this report) and the system response. The response of the system, and thus the development of guidelines for operator actions necessary to mitigate the consequences of such an event, are dependent upon the adequacy of the break flow model.

Problems of two-phase critical flow are not limited to the nuclear power industry. Any application which involves fluids which are either originally two-phase, or will vaporize if allowed to expand to substantially lower pressure, has the potential for critical flow. Critical two-phase flows can occur in fossil fueled power plants and in several chemical process industries; such as paper production. Simoneau [3] has conducted research into the two-phase critical flow of liquid cryogens. This research has been motivated by concern over the safe handling and storage of these materials in the space industry. In an area relevant to public safety, Sallet [4] has investigated the critical flow of Liquefied Natural Gas (LNG) through safety valves on railroad tank cars.

I.2 Definition of Critical Flow

Figure 1-1 shows a prototypic configuration for critical flow. A reservoir, A, contains a compressible fluid at a constant pressure P_0. When the back pressure, P_b, is reduced below P_0, flow begins and a pressure gradient is established in the connecting channel. As P_b is decreased, the flowrate increases until P_b reaches the critical value P_c. The progression of pressure profiles during this process is depicted in the lower portion of Figure 1-1. Once P_b is at or below P_c, further reduction in P_b does not influence either the flowrate, or the pressure distribution in the channel (see profiles 4 & 5 in the figure). The flow is then said to be critical. Thus, the critical flow is the maximum flowrate obtainable for the stagnation state and the flow channel geometry. For an adiabatic flow, both the critical mass flux, G_c, and the critical pressure, P_c, are functions only of the stagnation state and the channel geometry. Heat exchange between the fluid and the channel wall will influence the critical flow. This heat transfer may be influenced by the fluid state within the channel which complicates the problem further.

Dependence of the critical flow parameters, G_c and P_c, on the stagnation state, defined by h_0 and P_0, should be emphasized. Changes in either P_0 or h_0 will change both G_c and P_c. In the case treated in this research, where the stagnation state is a subcooled liquid, the fluid reaches saturation pressure somewhere in the channel. The point at which saturation is reached will influence the thermodynamic state of the fluid downstream. This, in turn, will influence the critical flow.

When the stagnation state is subcooled liquid, and perhaps for a two-phase condition, the evolution of the thermodynamic state of the fluid may be complicated by the formation of a metastable liquid phase. Because of the rapid depressurization rates which are characteristic of critical flows, the fluid may expand in a nonequilibrium manner. Lienhard et al [5] have investigated this phenomenon experimentally and have found that the liquid may depressurize to a point well below the saturation pressure corresponding to its' initial temperature before vaporization begins.

The presence of metastable liquid within the flow will influence the critical flow phenomenon. Vaporization rates within the channel may initially lag behind those for an equilibrium process. This would tend to increase the critical mass flux. The amount of vapor present would be less than for an equilibrium process, decreasing the mixture compressibility. Eventually, the vaporization rate, which is a parameter of many critical flow models, may exceed that of an equilibrium flashing process as the fluid tends to restore equilibrium between the phases. It can be seen that the possibility of nonequilibrium flows complicates the problem of predicting two-phase critical flows.

Critical, or choked, flow is a well known phenomenon in gas dynamics. For a single-phase compressible fluid flow it can be shown that the critical velocity is equal to the local sound propagation speed at the critical location (see Shapiro [6]). This is just the acoustic velocity. By analogy, for the two-phase case, one can say that the critical velocity is equal to the sound speed in the medium. Unfortunately, this is of little help in solving the problem since acoustic propagation in a nonequilibrium two-phase medium is not well understood. One can however, make the identification that a flow is choked when the flow velocity is equal to the local (at the critical plane) sound speed.

As stated above, when the flow is critical, neither the flowrate nor the pressure profile within the channel is affected by changes in the back pressure so long as $P_b \leq P_c$. This result can be expanded to a definition of critical flow: A flow is said to be critical when changes in the flow system downstream of some critical plane do not influence the fluid state or velocity upstream of that plane. The flow is critical, or choked, at that plane.

In fact, this last definition is related to the identification of critical velocity with sound speed. The acoustic velocity is the fastest propagation velocity of a rarefaction wave. If the velocity of the flow is equal that of the fastest pressure disturbance carrying information about a lowering of the back pressure, then this information is not transmitted upstream. That is to say that the flow upstream of the critical section does not "know" that anything has occurred downstream. Similarly, the above definition implies that no information about the state of the fluid or its' velocity is transmitted upstream of the critical location. In Chapter II we discuss two-fluid models for critical flow which generally yield the result that acoustic signals are the fastest moving in a two-phase flow.

To summarize, critical flow in a given channel is the maximum flowrate for a given stagnation state. The fluid velocity at the critical section is analogous to the local sound speed in the fluid. When flow in a channel is critical, the fluid state and flow velocity at any point upstream of the critical section is independent of conditions downstream of that section provided the receiver pressure is not raised above the critical value.

I.3 Objectives

It was the principal purpose of this research program to perform an experimental investigation into the nature of two-phase critical flows through simulated pipe cracks and to develop a model suitable for implementation in Light Water Reactor (LWR) safety analysis codes. The influence of heat transfer from the channel walls on the two-phase critical flow was also investigated. Slit geometries were chosen as an idealization of a circumferential crack in a large diameter pipe. Stagnation conditions investigated were subcooled water at pressures spanning the range which may be expected in nuclear power plants. Pressures covered in the experimental program ranged from 4 MPa to 16 MPa. Subcoolings from zero to 65°C were studied.

Knowledge of discharge rates through pipe cracks and similar geometries is relevant to nuclear reactor safety analysis. For instance, the design basis accident for LWRs is the large break LOCA. This scenario postulates the rupture of a primary cooling system pipe. However, prior to such an event, a crack would have to develop in that pipe and grow to a critical size before rapid crack propagation to a full break could occur. Conceiveably, with an adequate predictive model, combined with a model for crack propagation in the pipe, the entire postulated loss-of-coolant event could be modeled. More importantly, real time simulation of a plant during a small break accident transient could be achieved. Discharge models for small breaks in the cooling system are currently at issue in nuclear power plant licensing. Data from these experiments are useful in testing proposed models. In addition, insight into the physical processes of critical flow from a subcooled stagnation state will aid in the development of future, more accurate models.

Using rectangular slits as an idealization of pipe cracks does not detract from the value of these results. Data from these smooth walled slits will provide an upper bound on flows from cracks. Cracks through the thick walls (typically 6 to 7.5 cm) of primary cooling system pipes would undoubtably have rough walls and may not be straight. Although the slits investigated were only about 20 mm in width, the smallness of the opening dimension, (0.127 to 0.318 mm) means that the observed mass fluxes are independent of the width. Hydraulic diameter was given by:

$$D_h = \frac{2dW}{(d + W)} \qquad (1\text{-}1)$$

and was within 1.9% of the value for infinite parallel planes ($D = 2 \times d$) for all the test section assemblies tested. Extension to circumferential cracks in pipes which may be 60 to 80 cm in length is reasonable.

These experiments have several features, other than the small geometry (D_h), which make them unique in the field. Of primary importance, is the achievement of steady state flows at high pressure and large subcoolings. Pressures as high as 16 MPa were achieved with subcoolings from zero to 65°C. Measurement of pressure profiles within a narrow channel in two-phase flow is also rare. Mass flowrates were measured more accurately than in previous work. This was aided by the fact that the flowrate stayed constant for a minute or more in many instances. Chapter II presents a thorough review of relevant literature.

I.4 Experimental Program

The experimental study which was undertaken as part of this work consisits of 101 tests. (The first seven tests were used to shakedown the equipment, and have not been reported.) Three different slit sizes (0.381, 0.254, and 0.127 mm nominal), five pressure levels (approximately 4.2, 7.1, 9.6, 11.6, and 15.6 MPa), four degrees of subcooling (60, 30, 15, and 3 degrees centigrade) were studied. Several runs were repeated because of equipment failure. Runs have been numbered chronologically. In general, the higher the run number the greater the pressure level and stagnation temperature.

A single test section, capable of being adjusted to the required slit dimension, was used. Because the gaskets used in the test section had a limited life, the test section had to be diassembled after between five and ten runs had been made. At least one cold water calibration of the test section was made for each re-assembly. Run numbers were assigned consecutively with no differentiation between critical flow tests and cold water calibration runs.

Figure 1-1
Prototypical Critical Flow Configuration

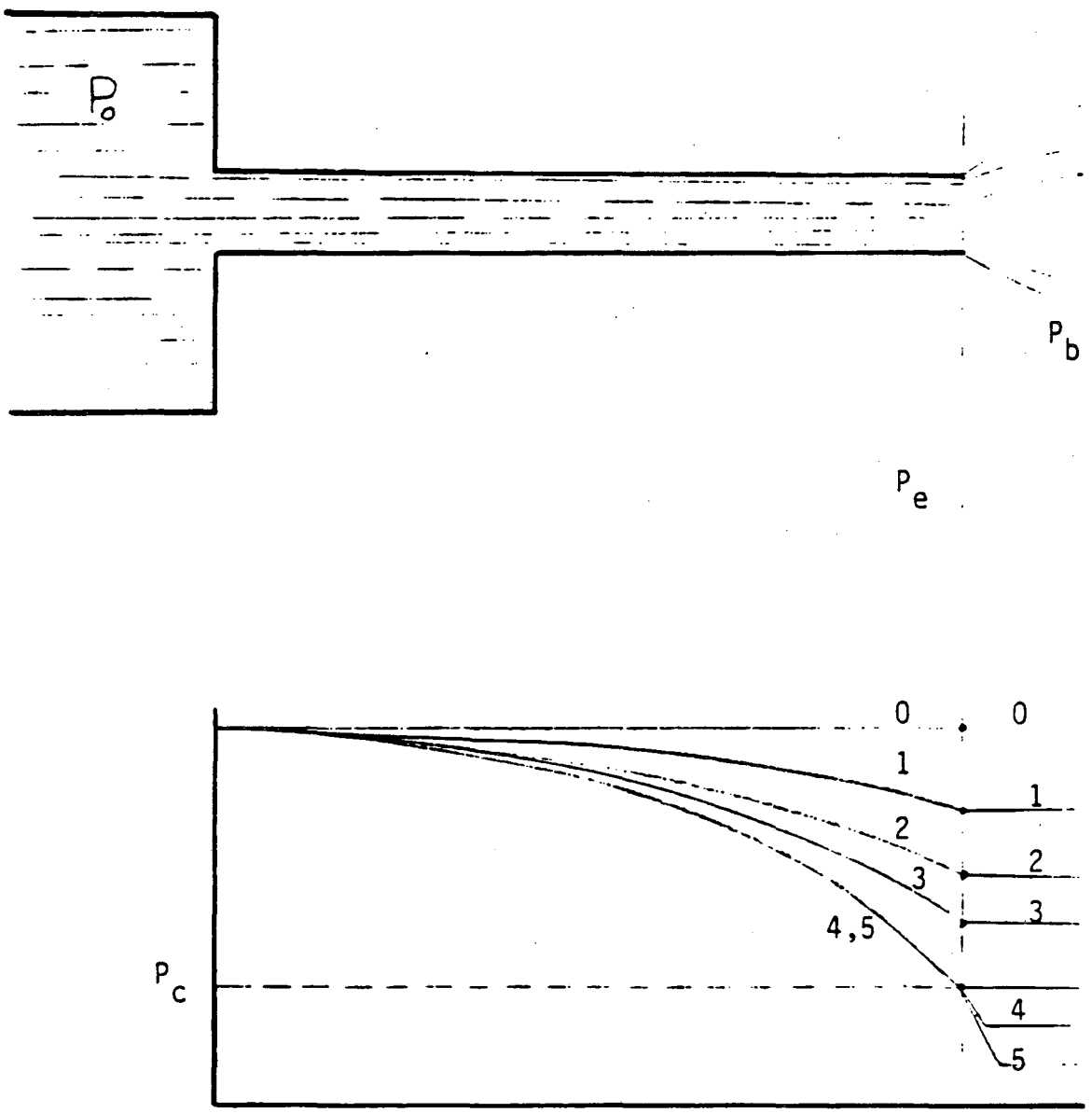

XBL 838-483

CHAPTER II

Literature Survey

In this chapter previous studies of two-phase critical flow are described. The chapter is divided into three sections. In the first section previous experimental studies are discussed. Only those references, which, are either directly relevant to the topic of this experimental study, or are so recent as not to have been included in other surveys, are mentioned. The second section presents a thorough critical evaluation of many of the theoretical models currently available in the literature. The chapter concludes with a general discussion of the application of the definitions of critical flow given in Chapter I to analytical models of the flow.

II.1 Previous Experimental Work

A plethora of experimental studies of two-phase critical flow are available in the literature. Recent summaries by Hall [7] and Abdollahian et al [8,9] outline most of the relevant works. Many have dealt with saturated or two-phase stagnation states. But a few studies with subcooled stagnation states are available. The problem of finding studies which are relevant to a particular flow situation is compounded by the wealth of flow channel geometries which have been investigated. Even when limiting one's self to single component flows, as in this review, the range of available data is large.

A variety of working fluids have been used. Data for water, liquid hydrocarbons (such as Freon), and cryogens (such as liquid nitrogen), are available. Stagnation pressures studied range from subatmospheric to over 200 atmospheres. Critical flow in constant area ducts, nozzles, orifices, and combinations of these have been investigated. Hydraulic diameters of these channels have ranged from 0.1 to 500 mm with lengths up to a few meters. To add to the problem of evaluating the available literature there has been some degree of inconsistency in the nomenclature used for various geometries.

So as to avoid possible confusion from the outset, the terms employed to describe channel geometries in this review are defined below. Ducts are taken to be constant area channels. A pipe is thus a constant area duct with a circular cross-section. Ducts may have either rounded or sharp entrances and may terminate in a diffusing section. (Ducts which terminate in a diffusing section are commonly referred to as "Henry Nozzles" in the literature.) Channels in which the cross-sectional area varies continuously, but not necessarily uniformly, over the length are described as nozzles. Convergent nozzles which terminate in a short constant area section can be indistinguishable from ducts with well-rounded entrances. If a significant amount of frictional pressure loss is present, such geometries should be considered as ducts. Orifices are sudden area reductions in a channel where the length of the reduced area portion is a small fraction of the diameter.

It is beyond the scope of this work to review any but a portion of the available studies. The report by Hall [7] attempts to inventory all of the two-phase critical flow data available. Abdollahian et al [8,9] include in their reference lists citations for much of the available literature.

II.1.1 Effect of Scale

A major issue in this work, and in several recent experimental studies, is the effect of channel size on the critical flow. Extension of two-phase critical flow results, obtained in test sections with diameters on the order of 1 to 10 cm, to reactor safety analysis dealing with pipes as large as 75 cm in diameter, is a subject of concern. In the present study, the extension of previous results to smaller scales has been tested.

Considering diameter effects in nozzles, Sozzi and Sutherland [10] and Morrison [11] have reported an increase in critical mass flux with decreasing diameter. Alleman [12], has reported the opposite result, but his tests show a large amount of scatter in the data which may probably be attributed to dissolved gas effects. Other experimentalists, including Starkman et al [13] saw no diameter influence on mass flux; in the small range of diameters which were studied.

For ducts, very few experiments can be found where the test section length was the same for more than one diameter. James [14] has reported increasing mass flux for increasing diameter. While this is the opposite result to Sozzi and Sutherland's for nozzles, this should be expected when friction is significant. Fauske [15] saw no scale effects.

The Marviken Large Scale Critical Flow Tests [16] were blowdown experiments using short ducts and nozzles. Test section diameters were in the range of hardware used in reactor systems (300 to 500 mm). Unfortunately, no two tests were performed with test sections having differing diameters but the same length. Because these were blowdown experiments which lasted only for a minute or two, and therefore the stagnation state varied rapidly, it is difficult to find data points for which the stagnation condition is the same as for some small scale experiment. Even when such points can be found, there is no way to quantify the effect of the transient nature of the flow in the Marviken system. What comparisons have been made (by Abdollahian et al [9]) reveal no diameter effect.

Test section geometry is a subject of concern when comparing Marviken results with those from small scale experiments. Although the Marviken experimentalists refer to their test sections as "nozzles," they were, in fact, short ducts with rounded entrances. Lengths ranged from 16.6 to 180.9 cm. To further cloud the geometry issue, test sections were mounted on the end of a 5.9m length of pipe having a maximum diameter only 50% larger than that of the largest nozzle. The fluid was accelerated in this pipe to between 16 and 44% of its velocity at the entrance to the "nozzle"; depending on the test section diameter. Pressure losses in the fluid as a result of passage through a ball valve and two instrumentation rings mounted in the pipe changed the state of the fluid from that present in the vessel. Flashing may have occurred within this discharge pipe or the liquid may have become superheated. As a result, the actual stagnation state of the fluid in the Marviken tests is subject to interpretation. While the Marviken data may provide a data base for testing two-phase critical flow models, their usefulness in the identification of parameters relevant to the prediction of such flows is questionable.

II.1.2 Slit Geometries

Experiments which are directly relevant to the problem of flow in slits are rare. Only four such studies have been found in the literature. The earliest of these, reported by Agostinelli et al [17], was done in 1957. Their tests were done in annular, constant area passages with hydraulic diameters in the range of 0.15 to 0.43 mm. Pressures range from 3.50 to 20.51 MPa with water as the working fluid. Results were reported for subcoolings from 9.3°C to 67°C. Most of the data was presented graphically with only a few points tabulated with details of the test parameters.

More recently, Collier et al [18] investigated the critical flow of water in rectangular slits. Preliminary results indicated that flowrates were much smaller than had been anticipated. A few measured pressure profiles were shown but scatter in the pressure data was large. As yet, none of these results have been published in the open literature.

Two other investigations into two-phase critical flow in slits were carried out using liquid nitrogen as the working fluid. Hendricks et al [19] made a qualitative study of radially inward flow through 0.076 mm annular clearance between two glass plates. Flowrate was measured as a function of fluid stagnation state. High speed movies were made through the glass walls of the flow passage. For

inlet conditions with 10K or larger subcooling, flashing was seen to occur near the end of the 0.72 cm (measured along the radius) flow passage. The flashing front appeared to remain uniformly distant from the discharge plane.

Simoneau [20] investigated the flow of subcooled nitrogen through a rectangular slit. The test section used was 2.54 cm in length and width with an opening dimension which was nominally 0.292 mm. This geometry was very similar to that used in the present study. Pressure profiles, in addition to flowrate were measured for steady state flows. A large range of stagnation states were tested. Pressures up to 6.8 MPa were tested with four different subcoolings in the range $0.84 < T_R < 1.03$, $T_R = T_0/T_c$. No presciption for the extension of these results to water is available.

II.1.3 Flow In Long Ducts

Since the test section geometries used in the current work were characterized by high L/D it is worthwhile to mention other studies which share this geometric feature. Many experimentalists have considered L/D as a controlling parameter in two-phase critical flow. Ironically, while L/D is an essential scaling parameter for flows controlled by friction alone, a few workers in the field of two-phase critical flow in ducts have suggested L/D scaling while insisting that friction effects are negligible. The work of Henry [21] is an example of this. L/D scaling is discussed further in Chapter V. In the following discussion, attention has been focused on studies at higher pressures, since these are more relevant to reactor safety issues.

Fauske [15] has measured mass flux and pressure profiles for the two-phase critical flow of saturated steam-water mixtures through pipes. As was common in much of the early work in this field the two-phase stagnation state was created by mixing saturated steam with saturated water. This was believed to be an accurate way of measuring the quality of the fluid entering the test section since steam and liquid flowrates were measured separately. Such a procedure relies heavily on the ability to produce the two fluids in such a way that they are both saturated at the same pressure. They must then be mixed adiabatically to insure that no phase change occurs during the process which would disturb the assumed stagnation state. In general, one has to believe that these attempts led to some error in the determination of the stagnation quality for these experiments. Three of Fauske's test sections were 2.79 m in length and had diameters of 1.227 cm, 0.683 cm and 0.318 cm. A fourth test section was 1.353m long with a 0.318 cm diameter. Inlet pressures ranged from 276 kPa to 2.48 MPa with qualities between 1 and 70%. Fauske reported no observable dependence of flowrate on test section diameter. This is somewhat peculiar since the pressure profiles show evidence of friction effects which should have increased with decreasing diameter.

Henry et al [21] investigated critical flow in ducts. One of their test sections had a rectangular cross section so that measurements of void fraction using a gamma densitometer could be made and interpreted more easily. Stagnation states were two-phase but pressure was not specified. Pressure and void fraction profiles were measured. Flowrates were seen to decrease with increasing L/D. Results for circular and rectangular cross sections were similar.

Henry also noted that pressure measurements near the end of the test section were influenced by the downstream pressure for the test section which had what amounted to a sharp exit (120 degree diffusing angle). The test section with a divergent nozzle (7 degree diffusing angle) attached to the end showed no such effect. On the basis of these observations a so-called two dimensional effect was postulated. (This two-dimensional effect should not be confused with the two-dimensional effect described by Travis et al [23] which has to do with a one-dimensional model not properly accounting for inviscid form losses in complex flow geometries). Henry et al [21] argue that the critical flow plane is convex outward in the flow direction. In this scenario flow is choked at the center of the duct at the exit location. However choking at the wall occurs some distance upstream. Free expansion of the fluid plume leaving the duct at the exit is said to account for this phenomenon. It was

therefore recommended that critical flow test sections be fitted with diffusing nozzles at the exit to obtain accurate pressure profiles at the exit plane of a duct. Hence the proliferation of "Henry nozzles". Such a theory is somewhat at odds with an interpretation of the critical flow phenomenon which says that all features of the flow upstream of the critical section are independent of conditions downstream. Should this not also apply to the presence of a diffuser? It is probably true that understanding of these phenomena is limited by the traditional one-dimensional approach to the problem.

Uchida and Nariai [24] studied the critical flow of saturated and subcooled water through ducts which were 4.0 mm in diameter. Lengths varied from 0 to 2.5 m. Flowrate was seen to decrease with increasing length. Benjamin and Miller [25], Burnell [25], Flinta [27], Isbin and Fauske [28], and Ogasawara [29] have all conducted steady state or slow transient experiments in long ($L/D >$ 100) ducts. All these involved saturated water at the stagnation state. Far less data are available for subcooled water. Borgartz et al [30] conducted a few slow transient experiments in a 4 m duct 32 mm in diameter. These tests were carried out with an initial stagnation pressure of 5.1 MPa. Haubenreich [31] studied a few subcooled cases in ducts 13.9 and 24.3 mm in diameter with $550 < L/D < 570$. Stagnation pressures were as high as 13.6 MPa. Presentation of the data was far from complete. Seynhaeve et al [32] extended the work of Reocreux [33], which was done with stagnation pressures in the range of 150 to 200 kPa, to pressures up to 664 kPa. In addition, test sections with smaller diameters and shorter lengths were used. These experimentalists present excellent documentation of their work. The above list is fairly complete. The dearth of available data for subcooled water stagnation states is apparent.

Several workers (Gallagher [34], Lienhard [5], Necmi and Hancox [35], Riebold and Fritz [36], and Edwards and O'Brien [37]) have studied the rapid depressurization of long pipes which initially contained subcooled water at high pressure. Initial pressures as high as 15 MPa have been used [34]. These fast transient results have shed some light on the nature of flashing flows. However, these results are not directly applicable to the problem at hand.

II.1.4 Flow In Nozzles

Most studies with subcooled water stagnation conditions have been carried out in nozzles or short ducts. A program to study two-phase critical flow in convergent/divergent nozzles, carried out at the University of California, Berkeley, has been reported in two parts. Starkman et al [13] reported the results for two-phase stagnation conditions. Schrock et al [38] reported the results for initially subcooled water. Steady-state flows were investigated and pressure distibutions within the nozzles were measured. Throat diameters were between 4.0 and 6.4 mm. Pressures ranged between 200 and 890 kPa. Higher pressure blowdown studies were conducted by Powell [39] for 11.1 mm diameter nozzles. Although pressures up to 17 MPa and subcoolings between 37 and 148°C were studied, the work focused primarily on the effects of changing the back pressure. Results were presented graphically. Data points were not specifically plotted nor was any estimate of the experimental error stated.

A recent study by Zimmer et al [40] gave detailed information about the flashing flow of subcooled water through convergent/divergent nozzles. Pressure and void profiles were presented. Radial distribution of void was also measured. Nozzle inlet temperatures ranged from 20 to 150°C. Stagnation pressures were 100 to 1000 kPa. Results from 93 runs were reported.

Several studies of high pressure subcooled water discharging through short pipes are worthy of note. Keller et al [41] have experimented with pressures up to the thermodynamic critical point. Test sections were 3.5 mm ducts, 1.75 to 105 mm in length. As with many Soviet works, results are presented graphically and specific comparisons with other experimental studies are difficult. Shiba and Curet [42] investigated flow through large diameter (14.6 to 103 mm) ducts. These experiments were carried out at typical PWR pressures of 15.7 MPa. Zaloudek [43] studied flow in a 12.8 mm diameter pipe 256 mm in length.

Sozzi and Sutherland [10] also studied flow through short pipes. Subcooling was generally low with the initial pressure for the slow blowdown experiments being approximately 6.8 MPa. Data were presented as a function of "universal stagnation quality" which is a non-unique way of specifying the stagnation state of a subcooled fluid on the basis of saturation properties. This presentation implicitly assumes that differences in stagnation pressures between various runs (which were less than 10%) do no influence the flow. True stagnation state can be calculated from the data given by the authors. This must be done in order to compare these results with those of other experimentalists or with an analytical model.

Recent studies by Gros D'Aillon and Jeandey [44] in the French "Super Moby Dick" high pressure flow loop examine flow in a 20 mm diameter test section 363 mm long. The results of these experiments are well documented and include measurements of the radial as well as axial void fraction profile. Their results tend to indicate the presence of inverted annular flow in the test section, at least immediately downstream of the point of flashing inception.

To summarize, while many studies have been done with two-phase stagnation states there is some question as to whether the steam quality was accurately determined. Studies with saturated water stagnation conditions are also fairly numerous but here one must ask how close to the saturated state the fluid was. Small quantities of steam or subcooling may have dramatic impact on the two-phase critical flow. There is a definite lack of data for subcooled stagnation states. A realization of this in recent years has led to further experiments, but there is still a need for high pressure data. The present work deals only with a small rather unique geometry.

II.2 Previous Theoretical Studies

Models for two-phase critical flow are almost as numerous and diverse as experimental studies. Several reviews of these models are already available in the literature. Saha [45] describes many of the more widely known models, concentrating on those which allow thermal nonequilibrium in the flow. Abdollahian et al [8,9] give a brief summary of the key features of most published models. Wallis [46] has made a short critical review of several models but avoids specifics. Henry [47] describes some of the older, simple models, concentrating on those developed by himself and his coworkers. Boure [48] discusses modeling methods in a general and more mathematically precise manner than have other reviewers. A more complete listing of review articles and theoretical analyses of two-phase critical flow may be found in the report by Abdollahian et al [8].

It was the purpose here to provide a more thorough critical review than has been previously available. Insight into the assumptions of the various models often provides clues as to the predictive ability in a given situation. This review was conducted with the objective of defining a model suitable for predicting the results of present experiments. Only a cross section of the available models are discussed in detail. Selected models were compared to other available models where this was appropriate. Emphasis has been laid on the underlying assumptions of the authors and the data base from which they obtained the empiricle parameters of their model.

As a matter of convenience the models to be discussed have been divided into two groups. In the first section models which might be described as simple models are discussed. Generally these models are characterized by their treatment of a two-phase flow as a single-fluid flow. Conservation of mass, momentum, and energy are considered for the two-phase mixture. In the next section two-fluid models are discussed. Two-fluid models are characterized by their treatment of each phase separately. These models usually consider the conservation of mass, momentum and energy separately for both gas and liquid phases. Transfer terms, expressing the interphase transfer of mass, momentum and energy are then required. In many instances, simplifying assumptions are applied which reduce the number of equations to be solved. Sometimes these assumptions have

made categorization by the present scheme somewhat arbitrary. Generally the distinction has been made on the basis of whether the model was derived starting from two-fluid equations or from mixture equations. Because many of the simple models consider the presence of two phases explicitly the term "single-fluid model" is not appropriate.

Simple models have frequently employed an incomplete set of conservation equations. Sometimes this is apparently inadvertent on the part of the authors. In other cases some assumption has been made, either about the phenomenon of critical flow or about the thermodynamic path one of the phases follows, which allows closure of the system of equations without having a conservative model. While models which have an incomplete formulation may have less appeal from a theoretical standpoint, the engineer must consider them for use as a predictive tool. In this endeavor a note of caution must be sounded. When such a model is applied to a situation far removed from those which the author considered in its' design, the model may fail completely. Not to imply that a two-fluid model is always better; these models also contain a certain amount of empiricism in their transfer terms which may make them inaccurate when applied in some situations. The state of the art is such that no model will be accurate in every case. Two-fluid models are more generally applicable and are commonly employed in reactor transient analysis codes as discussed below.

Almost all critical flow models are for one-dimensional flow. The only notable exception is the KFIX code [49] which contains multi-dimensional representation of the two-fluid equations. KFIX does not, however, include a critical flow model. Rather, the flow is allowed to "seek its' own level" meaning that the flow is calculated such that the boundary and initial conditions are satisfied with no attention as to whether the resulting flow prediction matches or exceeds some critical flow criterion. It is presumed that the calculated flow is critical if the pressure difference between stagnation state and receiver is large. While it is certainly possible to employ a multi-dimensional representation of the homogeneous equilibrium model (described below), such an appliction has not been reported in the literature.

II.2.1 Simple Models

Simple models are frequently steady state. Often the results have been applied to transient cases under the presumption that the transient is slow enough for the flow to be considered quasi-steady. In the following discussion, all the models are steady state unless mention is made to the contrary.

II.2.1.1 Homogeneous Equilibrium Model

As the name implies, the homogeneous equilibrium model (HEM) assumes the flow is homogeneous (phases move with equal velocity) and that both phases are in thermodynamic equilibrium (saturated at the local pressure, ie. having the same temperature). Wallis [50] notes that these assumptions are equivalent to treating the mixture as a pseudo-fluid which can be described by a single set of equations as an equivalent single-phase flow.

Critical flow is defined as the maximum attainable flowrate. This is stated mathematically as:

$$\frac{dG}{dP} = 0 \qquad (2\text{-}1)$$

Solution of the conservation equations for the mixture, subject to the constraint (2-1), shows that the flow velocity at the critical section is just the homogeneous equilibrium sound speed. This result is expected in light of the discussion of critical criteria in Chapter I. Thus, one may write for the HEM:

$$u_{ex} = a_{HE} = \left\{ \left(\frac{\partial P}{\partial \rho} \right)_{s,ex} \right\}^{1/2} \tag{2-2}$$

Throughout the ensuing discussion, the subscript "ex" is used to denote evaluation at the critical plane; whether at the exit of a duct, the throat of a nozzle, or some area restriction within the channel (such as an orifice). A full development of the HEM is postponed until Chapter V.

Two points of difficulty concerning the HEM have been noted in the literature. Collins [51] has pointed out that the equality of the mixture velocity at the choking plane with the local sound speed is not a necessary condition for critical flow. If the fluid stagnation state is subcooled liquid, it is possible that at the point of vaporization, the mixture velocity is greater than the homogeneous equilibrium sound speed evaluated at zero quality. This can occur due to the discontinuity in the theoretical equilibrium sound speed at the liquid-vapor saturation line. Note that this is a point at which the single-phase critical flow analogy breaks down. Supersonic flow requires a convergent/divergent nozzle for the single-phase case. For two-phase flow, an analogous phenomenon can occur with a subcooled reservoir condition in any geometry. Collins argued that the propensity for the HEM to under-predict experimentally determined flowrates from subcooled reservoir conditions can be explained in terms of this supersonic choking phenomenon. While it is true that correct application of the HEM requires that one check that supersonic choking cannot occur, it cannot be that this is the principal explanation for the failure of the HEM. It is commonly held that the development of liquid superheat, and perhaps slip, are responsible for the underprediction.

The second point of difficulty appears to arise from a general confusion about irreversible processes. Applications of the HEM are most frequently made with the added assumption that flow in the channel is isentropic. This is a special case of the HEM. It cannot be overemphasized that the Isentropic Homogeneous Equilibrium Model (IHEM) is properly applied *only* to nozzles and orifices.

There exist three physical mechanisms which can drive phase change in a flow channel: area change, friction, and heat addition. Of these only area change can result in an isentropic change in the thermodynamic state of the flowing fluid. Thus, if one is to assume isentropic flow in a duct the fluid state at the entrance plane (after entry pressure loss is accounted for) must be identical to that at the exit plane.

Several authors (eg. Henry [21] and Levy and Abdollahian [52]) have imagined pressure declining along the flow direction in a constant area adiabatic duct in which it has been assumed frictional losses are negligible. Pressure drop is attributed to phase change, but without heat addition or friction to drive it there can be no phase change. While it is true from a pragmatic viewpoint that when frictional effects are small the calculated result assuming an isentropic path is little different from that assuming an isenthalpic one, it is an incorrect approach which has no good justification. When friction is significant the isentropic model will give very different results.

This last point is symptomatic of a problem which plagues many of the simple models. That problem is the confusion between the thermodynamic process involved in the evolution of the fluid state within the channel and the thermodynamic process which is responsible for the choking phenomenon. Taking the HEM as an example, choking occurs isentropically as in the single-phase case of Fanno or Rayleigh Line flow. Friction and heat addition are not thereby excluded from the evolution of the fluid state in the flow channel leading to the point of choking. Only in an ideal nozzle or orifice (frictionless, adiabatic), does the entire process occur isentropically.

Nicolette [53] presents graphical results for a Fanno Line flow using the HEM. This is the same model which was used in this work for comparing experimental results with HEM predictions (see Chapter V). Hancox et al [54] have proposed a transient flow model based on the HEM formulation. Their model does not explicitly include friction, but three unspecified constants in their conservation equations can be taken to represent irreversible losses. Their model uses the method of

characteristics to predict choking. This critical flow criterion is discussed in the last section of this chapter.

The IHEM has been used throughout the two-phase critical flow literature as the standard of comparison for experimental data. Features of this comparison are well known. Critical flowrates are usually underpredicted. One must be careful to distinguish between an IHEM calculation of the critical mass flux based on the local fluid state (ie. P & x), and one based on the stagnation state. Use of the IHEM in calculating the critical mass flux from a given stagnation state is properly restriced for nozzles. For duct flows, or any other situation where the flow path from the stagnation state to the exit state is not isentropic, another model should be used to calculate the evolution of the fluid state. The IHEM is still correctly applied in determining the critical mass flux corresponding to the calculated fluid state at the channel exit. Unfortunately, the IHEM is frequently applied to pipe flows with the IHEM prediction based on the stagnation state of the fluid. These are the comparisons which have been documented in the literature. When applied to long ducts ($L/D > 100$), there has frequently been good agreement between model and experiment for the the mass flowrate. Pressure at the exit of a long duct is always overpredicted. Nicolette [53] notes that the flowrate agreement is fortuitous since the overprediction in exit pressure means that the choking velocity is predicted to be larger than the equilibrium value corresponding to the actual exit pressure. Henry [21] has taken the agreement between measured flowrates and those predicted by the IHEM as an indication that a two-phase mixture flowing in a duct closely approaches an equilibrium state near the exit. In light of the inadequacy of the pressure prediction this is not a valid conclusion.

Underprediction of the mass flowrate by the IHEM in most situations has led to the development of several models which attempt to correct, in a simple way, what their authors interpreted as being deficient in the IHEM assumptions. The attempt of these models to preserve the simple formulation of the conservation equations inherent in treating the two-phase mixture as a single fluid has led to a plethora of models which have an incomplete formulation of the field equations. When the formulation is incomplete, closure has required the introduction of an auxiliary equation. In some cases these auxiliary equations are based on assumptions about the nature of critical flow which cannot be verified experimentally. Indeed, there frequently exists experimental evidence which contradicts these assumptions.

II.2.1.2 Early Slip Models

Three early models for critical two-phase flow were based on their authors' assumption that interphase slip was primarily responsible for the failure of the IHEM. The models due to Moody [55], Fauske [15], and Levy [56] are very similar in their approach. All are incomplete models. Moody's fails to conserve momentum; Fauske and Levy failed to consider conservation of energy. To replace the missing equation an assumption about the nature of the flow was made. Both Moody and Fauske imposed a second criticality condition (in addition to equation 2-1). Moody specified that the mass flux was maximized with respect to the slip ratio (see equation 2-4 below). Fauske assumed that the pressure gradient at the critical plane was maximized with respect to the slip ratio. Levy wrote separate equations for the conservation of mass and momentum in each phase. Critical mass flux was redefined (in a manner analogous to the definition of sound speed, equation 2-2) as the isentropic derivative of the momentum specific volume (which had been defined by Fauske [15]). All three of the models assume that flow is isentropic and should thus be restricted to applications involving nozzles or orifices. The authors compared the predictions of their models to pipe flow data which has led to other workers in the field using these models to predict pipe flows.

Application of the auxiliary equations described above leads to a prediction of the slip ratio. The predictions resulting from each of the three models were:

$$k = \left[\frac{v_g}{v_f}\right]^{\frac{1}{3}} \quad (Moody) \tag{2-3a}$$

$$k = \left[\frac{v_g}{v_f}\right]^{\frac{1}{2}} \quad (Fauske) \tag{2-3b}$$

$$k = \left[\frac{\alpha}{2}\frac{v_g}{v_f}\right]^{\frac{1}{2}} \quad (Levy) \tag{2-3c}$$

These slip ratios are larger than any that have been experimentally observed. Moody's model predicts a slip ratio of 12 at atmospheric pressure. Fauske's prediction was even larger. Levy's model is more appealing, having a dependence on void fraction, but predictions of the slip ratio are still high. Klingebiel [57] attempted to measure slip ratios in steam-water critical flows. His data for pressures between 200 and 500 kPa show slip ratios ranging from approximately 1 to as high as 3. More recent two-phase critical flow models assume slip ratios of unity (see discussion below).

II.2.1.3 Moody Model

Of the three models mentioned above only Moody's is of current interest. It is generally acknowledged that the early slip models have the weaknesses mentioned above. Moody's model is still fairly widely used. There are several reasons for this. Primarily, U.S. law [58] requires that the model be used in the safety analysis of nuclear power plants. The model is also easy to use. Calculations may be done by hand; or charts, provided in Moody's original papers [55,59], may be used. In addition, a few investigators have used the failure of Moody's equilibrium slip model to predict experimental results for pipe flows as justification for the formulation of a thermal nonequilibrium model. Because of these applications Moody's model is described in detail below.

Since equilibrium flow was assumed, fluid properties were taken as saturation values. Moody reasoned that since the critical flowrate is the maximum attainable, it must be a maximum with respect to the slip ratio:

$$\left(\frac{\partial G}{\partial k}\right)_p = 0 \tag{2-4}$$

This equation was required for closure since conservation of momentum was not considered. Since the flow was adiabatic, conservation of energy was written:

$$h_0 = h_f + h_g + \frac{xu_g}{2g_c} + \frac{(1-x)u_f^2}{2g_c} \tag{2-5}$$

Continuity for each phase was expressed:

$$u_g = \frac{xv_g}{\alpha}G \tag{2-6a}$$

$$u_f = \frac{(1-x)v_f}{1-\alpha}G \tag{2-6b}$$

The definition of slip ratio was applied using equations (2-6) to obtain:

$$\alpha = \left[1 - k\left(\frac{1-x}{x}\right)\frac{v_f}{v_g}\right] \tag{2-7}$$

Since the flow was taken to be isentropic, the thermodynamic quality was given by:

$$x = \frac{s_0 - s_f}{s_{fg}} \tag{2-8}$$

Equations (2-5) through (2-8) were solved for G to give:

$$G = \left\{\frac{2g_c\left(h_0 - h_f - \frac{h_{fg}}{s_{fg}}\right)}{\left[\frac{k(s_g - s_0)v_f}{s_{fg}} + \frac{(s_0 - s_f)v_g}{s_{fg}}\right]^2\left[\frac{s_0 - s_f}{s_{fg}} + \frac{s_g - s_0}{k^2 s_{fg}}\right]}\right\}^{1/2} \tag{2-9}$$

Applying (2-4) to equation (2-9) resulted in the slip ratio formulation given in equation (2-3). This result was substituted into equation (2-9). Equation (2-9) was seen to be an expression for the mass flux in terms of quantities which were functions only of the local pressure. An expression for the critical mass flux was obtained by applying the definition, equation (2-1), to equation (2-9).

As noted above this model is correctly applied only to nozzles. Moody has since argued [60], on the basis of the second law of thermodynamics, that slip flow with phase change is intrinsically irreversible. Thus, an isentropic single-component slip model is invalid. This author would agree with such an argument.

Moody [59] also extended his model to two-phase critical flow in ducts. Citing the study by Zivi [61], Moody argued that the slip ratio given in equation (2-3) corresponds to minimum entropy production. Which, he said, characterizes a steady state thermodynamic process. The pipe flow model thus assumed that equation (2-3) would hold at every point in the flow. A momentum equation was written, which, in conjunction with equations (2-5) through (2-7), could be integrated over the flow channel. An average value of the friction factor was assumed for the channel. His method corresponds to a Fanno Line method for his model, similar to that of Nicolette [53] for the HEM. While this model (Moody's) is on sounder theoretical ground than the nozzle flow model the assumption of a slip ratio given by (2-3) is contradicted by the available experimental evidence. Unrealistically high slip ratios probably account for the fact that Moody's model overpredicts critical mass flux results of most experimentalists. As with the HEM, pressure at the critical plane is also overpredicted.

II.2.1.4 Other Simple Slip Flow Models

Moody has more recently [60] proposed a second slip model for two-phase critical flow in ducts. This model was complete in the sense that it employs a full set of conservation equations. The second law was used to determine a stable range of slip ratios. Flow was taken to be adiabatic and frictionless, but not isentropic. As was stated above, it is inconsistent to assume that the fluid state will change in a flow where these conditions hold. Moody states, "homogeneous critical flow is expected to control mass flux in the pipe entrance region." Slip critical flow was imagined to occur at the exit of the duct, accounting for the fact that experiments indicate critical flow behavior at that point. It would be incredibly fortuitous that two fluid states would exist in the same flow path that were critical at the same mass flux. In other words, Moody's second pipe flow model was poorly conceived.

Tentner and Weisman [62] have proposed a simple thermal equilibrium slip model which employs the void fraction correlation of Hughmark [63]. The correlation relates void and quality to mass flux and hydraulic diameter. Equation (2-7) was then solved for the slip ratio. Unlike other simple slip models, this model considered transient flows. The method of characteristics was employed to determine the range of slip ratios for which the three equation model was well posed. (Complex characteristics indicate that a problem is ill-posed mathematically and that the solution does not depend continuously on the initial conditions or is not unique.) Critical flow was predicted on the basis of the smallest characteristic slope being zero.

The model was compared (for the frictionless, adiabatic, case) with Moody's model for nozzle flow. However, predictions were based on the fluid state at the point of choking without consideration of the evolution of the fluid state in a flow channel. Results were similar to those for Moody's model, although the critical mass flux predicted by the Tentner-Weisman model was slightly lower; especially at low quality. Maximum slip ratios were more reasonable in light of experimental evidence (between 1 and 6). While this model represents a sensible formulation of slip flow, it has not been used to predict critical flow from a given stagnation state. This fact, combined with the fact that the authors assumed thermal equilibrium (when many experiments indicate the presence of a metastable liquid phase) accounts for the small amount of attention which the model has received. The approach of using established correlations for void fraction may prove useful if the effects of thermal nonequilibrium are included.

II.2.1.5 Thermal Nonequilibrium Models

Most simple models for two-phase critical flow which have been proposed within the past fifteen years assume that slip is unimportant for single-component critical flows. Results of experiments such as those of Lienhard et al [5] and Reocreux [33], which indicate the presence of liquid superheating, account for the decline in the popularity of equilibrium slip models. Slip has not been completely discounted. Many of the available two-fluid models do allow for slip as well as thermal nonequilibrium. Discussion of these models is postponed until the next section.

II.2.1.6 Henry Model

Probably the most widely used simple model for two-phase critical flow is that due to Henry [21] or Henry et al [22,64,65]. Henry has argued [22] on the basis of his void fraction measurements and a correlation proposed by Fauske [66], which predicts a decrease in slip ratio with thermodynamic quality for two-component systems, that low quality, single-component, two-phase flow is nearly homogeneous. Consequently, his model neglects interphase slip. Discrepancies between HEM predictions and experimental observation were attributed solely to an insufficient rate of vapor generation in the flowing fluid to maintain thermodynamic equilibrium between the phases. Since the vapor present is assumed to be saturated at the local pressure, the liquid becomes superheated.

It is important to note at the outset of this discussion that the Henry model is a correlation of a very limited set of data using the IHEM as a basis. Although the formulation of the conservation equations initially included slip [64], the slip ratio is set equal to unity to obtain the final result. If the presence of interphase slip had affected the results of the experiments which Henry used to determine his correlation parameter, then the parameter evaluated would be influenced. As a result, application of the model to a flow situation where slip is present to a different degree than in those particular experiments, would lead to an inadequate prediction.

Henry derived his model on the basis of equations (2-6), which express continuity for each phase, plus the slip flow momentum equation:

$$\frac{dP}{dz} = \frac{G^2}{g_c}\frac{d}{dz}\left[\frac{(1-x)^2 v_f^2}{(1-\alpha)^2} + \frac{x^2 v_g^2}{\alpha^2}\right] \tag{2-10}$$

Under the assumptions of nonequilibrium flow and that k = k(P), Henry applies the definition of critical flow (2-1) to obtain:

$$G_c^2 = -\left\{k\left[\left[\,1 + x(k-1)\,\right] x \frac{dv_g}{dP} + \left\{v_g\left[\,1 + 2x(k-1)\,\right] + \right.\right.\right.$$

$$\left.\left.\left. kv_l\left[\,2(x-1) + k(1-2x)\,\right]\right\}\frac{dx}{dP} + k\left[\,1 + x(k-2) - x^2(k-1)\,\right]\frac{dv_l}{dP}\right.\right. \tag{2-11}$$

$$\left.\left. + x(1-x)\left(kv_l - \frac{v_g}{k}\right)\frac{dk}{dP}\right]^{-1}\right\}_{ex}$$

The two derivatives, dx/dP and dk/dP, characterize the rates of interphase mass and momentum transfer respectively. To this point the derivation is general to 1-D critical flow provided the derivatives in equation (2-11) are interpreted as total derivatives. Liquid density was assumed constant at the stagnation value, v_{l0}, thus, $dv_l/dP = 0$. Increase in the liquid specific volume due to cooling was neglected. The basic premise of the Henry model is that during the rapid depressurization of a low quality two-phase mixture, mass transfer rate lags behind that of an equilibrium process. Henry correlated the actual quality against the equilibrium quality calculated assuming that the flow is isentropic according to the relation:

$$x = Nx_E \text{ , where } N = \begin{cases} nx_E & x_E \le \dfrac{1}{n} \\ 1.0 & x_E > \dfrac{1}{n} \end{cases} \tag{2-12}$$

Henry suggested n = 7.14 for nozzles [65] based on his analysis of the experiments of Starkman et al [13]; which are for two-phase stagnation conditions. The method which was used for correlating these data was not specified. For ducts, Henry suggested n = 20, based on his own experiments [22]. Recently, Abdollahian [9] has suggested values of n as high as 100. Values which vary with the geometry considered and the stagnation quality were necessary to adequately predict data from the Marviken tests [16].

In this first section, the Henry-Fauske model for nozzles orifices and short ducts [65] is considered. For nozzle flows, Henry and Fauske assumed frozen flow up to the nozzle throat or exit of a short duct (defined as L/D $\le$ 12). To simplify equation (2-11) several assumptions were made. Slip ratio is taken to be unity. The liquid phase was assumed to be incompressible; which is a sufficient assumption for the pressures usually encountered at the critical location. Evaluation of dv_g/dP was somewhat complex. Arguing that equilibrium would not be maintained in the rapid expansion at the throat, it was assumed that the vapor equation of state could be approximated by Pv^n = const. Thus,

$$\left.\frac{dv_g}{dP}\right|_{ex} = \left.\frac{-v_g}{\eta P}\right|_{ex} \tag{2-13}$$

where,

$$\eta = \frac{(1-x)\,\frac{c_{p,l}}{c_{p,g}} + 1}{(1-x)\,\frac{c_{p,l}}{c_{p,g}} + \frac{1}{\gamma_g}} \qquad (2\text{-}13a)$$

Henry states that equation (2-13a) was derived by Tangren et al [67]. In fact, (2-13a) closely approximates Tangren's result with the exception that Henry has assumed that μ ($= M_g/M_l$) used by Tangren is equal to 1-x. The difference is slight when the vapor mass per unit mixture volume is negligible. Tangren derived his result for the passage of a pressure wave through a stagnent two-phase, two-component mixture. The system was assumed adiabatic. Gas and liquid were assumed to maintain equal temperatures, so interphase heat transfer was significant. The relevance of Tangren's studies to the problem of vapor phase expansion in a flashing flow is not clear. It seems that this formulation was chosen for lack of a better choice.

Mass transfer rate at the throat was correlated to the equilibrium value by the relation:

$$\left.\frac{dx}{dP}\right|_{ex} = N \left.\frac{dx_E}{dP}\right|_s \qquad (2\text{-}14)$$

N was given by equation (2-12) but note that (2-14) is not the derivative of (2-12) since N = N(P). x_E and dx_E/dP were calculated on the basis of an isentropic process. This is identical to the method Moody used to evaluate exit quality so equation (2-8) is appropriate for the calculation of Henry's equilibrium quality. s_g, s_{fg}, and their saturation derivatives, were evaluated at the local pressure. Under these assumptions, the general expression for critical mass flux given in equation (2-11) was simplified to:

$$G_c^2 = -\left\{\left[-x_0\,\frac{v_g}{\eta P} + N(v_g - v_{l0})\,\frac{dx_E}{dP}\right]^{-1}\right\}_{ex} \qquad (2\text{-}15)$$

For a two-phase stagnation state the vapor phase was assumed to expand isentropically in the flow channel such that $Pv^\gamma = \text{const}$. In fact, if the vapor were to expand according to that relation it would become supercooled and would tend to condense. At the same time, the liquid, which Henry assumed to expand isothermally, would tend to evaporate. It is difficult to imagine these two processes occurring simultaneously at the same interface. Under these assumptions, the momentum equation (2-10) was integrated over the length of the nozzle (or short duct) to yield an algebraic expression for the throat pressure in terms of the stagnation state. Solving simultaneously with equation (2-15) yielded the critical flow prediction.

The Henry and Fauske claim that their model predicts the data of Starkman et al [13] quite well as far as the flowrate is concerned. Throat pressure was overpredicted. However, the parameter n in equation (2-12) was derived on the basis of this data. As noted above, substantially different values for n may be required to adequately predict flowrates for other geometries or stagnation states. Values of n appropriate for the prediction of nozzle flows from subcooled stagnation states, such as the results of Schrock et al [38] or Sozzi and Sutherland [10] have not been determined.

For the case of long ducts ($12 \le L/D \le 100$), Henry's model formulation [21] was fairly simple but is limited to the case of saturated or subcooled liquid stagnation states. Flashing was assumed to occur a fixed number of diameters downstream of the channel entrance when that entrance was sharp-edged. (A geometry for which Henry claims the model was primarily intended). The thermodynamic quality of the fluid downstream of the flashing location is correlated to that for an isentropic equilibrium process. The pressure drop in the inlet region ($0 \le z/D \le 12$) is taken to be zero once entry loss (single-phase) was accounted for by a head loss coefficient. Frictional losses are neglected and the duct is assumed to be adiabatic. Despite this, Henry conceived pressure loss in

the flow direction. It was also assumed the vapor phase remained saturated at the local pressure. As with the model for flow in nozzles, the liquid density was assumed constant at the stagnation value. Henry assumed that the stagnation state would always be sufficiently close to saturation that entrance pressure losses decompressed the liquid into a superheated state.

Flashing was assumed to occur exactly at L/D = 12 for all cases. This seems very arbitrary but Henry cites various experiments including those of Fauske [15] and those of Uchida and Nariai [24] claiming that experimental evidence points to flashing occurring 12 diameters downstream of the entrance. The basis for this claim is not apparent. Clearly, the flashing location should depend on the degree of stagnation subcooling. From the point of flashing onward thermodynamic quality is assumed to relax exponentially to its' equilibrium value according to the equation:

$$x = x_{LT}\left\{1 - \exp\left[-B\left(\frac{L}{D} - 12\right)\right]\right\} \tag{2-16}$$

where x_{LT} is given by x in equation (2-12). The constant B was chosen such that:

$$x = 0.99x_{LT} \text{ when, } \frac{L}{D} = 100 \tag{2-17}$$

With the assumption that the liquid is incompressible, and that the vapor is always saturated, equation (2-11) was simplified to:

$$G_c^2 = \left[x\frac{dv_g}{dP} - (v_g - v_{l0})N\frac{dx_E}{dP}\right]^{-1}_{ex} \tag{2-18}$$

The momentum equation (2-10) was integrated over the length of the duct to obtain:

$$P_t = P_0 - G_c^2\left[\frac{v_{l0}}{2K^2} + x(v_g - v_{l0})\right]_{ex} \tag{2-19}$$

Equations (2-18) and (2-19) were solved simultaneously to predict the critical flow. Henry claims that his model showed good agreement with flowrate data measured by Fauske [15] and Uchida and Nariai [24]. Critical pressure ratios (P_t/P_0), were consistently overpredicted by 20% or more. The value for n was obtained from Henry et al's data [22]. Critical pressure predictions could not realistically be expected to agree with measured values since the assumptions of the model were not consistent with the basic physics. The model may well be effective for predicting two-phase critical flows under certain conditions. However, the result of such prediction would probably only be valid for flow situations similar to the ones from which Henry derived his correlation.

II.2.1.7 Levy-Abdollahian Model

Recently, Levy and Abdollahian [52] have proposed a model similar, in some respects, to that of Henry. The model is less arbitrary in accounting for the presence of a metastable liquid phase. Rather than specifying a set L/D at which flashing occurs, the correlation of Alamgir and Lienhard [68] was used (Zimmer et al [40] were the first to propose this use of the correlation). Lienhard and his co-workers have developed a correlation for the amount of superheat a liquid will develop before flashing begins during static depressurization. The parameters of the correlation were the thermodynamic state of the liquid phase and the rate at which the liquid was being depressurized. A minimum superheat for vanishing rates of depressurization was predicted by their model. Depressurization rates encountered in most steady state two-phase flows are close to the lower limit of the correlation where a pronounced scatter in the results of Lienhard et al [5] (from which the correlation draws most of the data) was noted.

While the application of an experimental correlation to quantify thermodynamic nonequilibrium in a flashing flow is innovative, this model suffers from many of the deficiencies of Henry's models. Again, these authors have assumed isentropic flow in a duct. This assumption does make the model easy to apply and the authors argue that the assumption of isenthalpic flow would make little difference in the flowrate prediction. Clearly, this cannot be true if a significant frictional loss were present. In addition, the very existence of thermal nonequilibrium precludes an isentropic process. The fluid seeks equilibrium by transferring heat between phases through a finite temperature difference. That is an irreversible process, thus entropy is generated. The model is described in detail below.

Prediction of the pressure undershoot at the point of flashing inception was given by an arbitrary modification (to fit the data of Reocreux [33]) of the Alamgir-Lienhard correlation:

$$\Delta P_d = \frac{0.258\sigma^{1.5}T_r^{13.76}(0.49 + 13.25\Sigma'^{0.8})^{0.5}}{(k_s T_c)^{0.5}\left[1 - \frac{v_l}{v_g}\right]} \tag{2-20}$$

such that:

$$P_{fl} = P_{sat}(T_{l0}) - \Delta P_d \tag{2-21}$$

The modification that was made lowers the pressure undershoot for vanishing depressurization rates, predicted by the original correlation, by 30%. It should be noted that the correlation is invalid in the limit as depressurization rate goes to zero. If depressurization were infinitesimally slow, liquid superheating should be controlled by the availability of nucleation sites, either in the fluid bulk or on the wall. Alamgir and Lienhard [68] gave a lower bound of 405 MPa/sec to the validity of their correlation.

The vapor phase was assumed to remain at saturation. Properties of the liquid phase were taken to be the saturation values at the pressure $P + \Delta P_d$. Thus it was assumed that the flow remained at a pressure ΔP_d below the saturation pressure corresponding to the local liquid temperature. Nonequilibrium quality was evaluated on the basis of an "isentropic process":

$$x = \frac{s_0 - s_l}{s_g - s_l} \tag{2-22}$$

Since the stagnation enthalpy for an isentropic flow is constant, the mixture energy equation could then solved for the mass flux in the case of homogeneous flow. The result was:

$$G^2 = \frac{2}{v^2}\left[h_0 - (1-x)h_l - xh_g\right] \tag{2-23}$$

Depressurization rate, required for the evaluation of equation (2-20) was given by:

$$\Sigma' = \frac{1}{4}(G_t + G_e)\frac{\left[\left(\frac{G}{\rho}\right)_t^2 - \left(\frac{G}{\rho}\right)_e^2\right]}{L} \tag{2-24}$$

This expression was obtained by integrating the momentum equation over the length of the channel to obtain the average depressurization rate.

Critical mass flux was calculated via an iterative process. The value of P_c was guessed and then G_c was calculated by simultaneous solution of equations (2-20) through (2-24). This process was

repeated until G_e was maximized. Iteration could have been avoided by applying the definition (2-1) to equation (2-23) and then solving directly for P_e.

Levy and Abdollahian [52] have made comparisons between the predictions of their model and the flowrates measured in the Marviken experiments [16]. Their comparisons show that the model over-predicts the data for longer ducts when the stagnation state was subcooled liquid. The comparison showed no identifiable trend for two-phase stagnation states. Comparisons made with the flowrate data of Sozzi and Sutherland [10] showed poor agreement.

II.2.1.8 Other Nonequilibrium Models

Simpson and Silver [69], Edwards [70], and Rohatgi and Reshotko [71], have proposed thermal nonequilibrium models which assume homogeneous flow. Restricted to saturated or subcooled liquid stagnation states, these models are characterized by a mechanistic approach to the prediction of vapor generation rates. Essentially, mixture conservation equations were considered. Vapor was taken to be contained in bubbles which were assumed to grow according to the conduction controlled bubble growth model of Plesset and Zwick [72]; which was derived for a constant pressure system.

Edwards' model [70] is limited to ducts with sharp-edged entries. It was assumed that flow separation at the entry produced a constant pressure region in which the bubble growth model of Plesset and Zwick could be correctly applied. (The existence of a constant pressure region following a sharp-edged entry was also argued by Henry [21]). Further downstream, where the pressure was falling, the vapor generation rate was calculated from a one-dimensional, composite slab, heat conduction model. This scenario is not appropriate if the stagnation subcooling is sufficiently high (or the entry loss sufficiently low) that the fluid passage through the entry region does not produce superheating. When flashing occurs, all bubbles were assumed to nucleate instantaneously at a fixed time after saturation pressure was reached. Time delay and the number of bubble nuclei per pound of liquid were parameters of the model. These were determined such that the model gave the best prediction of the flowrate data of Fauske [15] and Zaloudek [43]. Friction effects were neglected in the model.

Simpson and Silver [69] assumed a bubble nucleation rate derived from homogeneous nucleation theory. This is more realistic than the instantaneous nucleation of bubbles at a fixed density assumed by Edwards. Conservation of energy was not considered in this model and again friction was neglected. The model requires two empiracle parameters which describe the nucleation rate and the energy required to activate a bubble nucleus. Results were presented graphically with both ordinate and abscissa functions of the two model parameters. This made the results non-specific in terms of the fluid used and the flow channel configuration, but it also makes the model more difficult to apply. Values of the two parameters for water flow were recommended by the authors. These were derived on the basis of their own experiments. Considerable effort is required to re-cast the model equations in terms of channel geometry, fluid stagnation state, and mass flux as would be required in order to employ the model as a predictive tool.

Rohatgi and Reshotko [71] formulated a model very similar to that of Simpson and Silver. Bubble nucleation and growth were treated in an identical manner. Two enhancements to the previous model were made. First, friction was considered by the introduction of a frictional term with a constant friction factor into the mixture momentum equation. Second, an attempt was made to correct the results of this one-dimensional model for two-dimensional form loss. This was done by subtracting the results of a 2-D potential flow calculation for the pressure field from the 1-D result. The model was presented in a straightforward manner without the dimensionless form of Simpson and Silver. This makes the model far more attractive to use.

The Simpson-Silver and Rohatgi-Reshotko models share a common weakness in their use of the Plesset and Zwick bubble growth formulation which is valid only for constant pressure fields.

Theofanous et al [73], and more recently Jones and Zuber [74] and Cha and Henry [75], have shown that bubble growth rates are much larger when the external pressure is decreasing than is predicted by a constant pressure model. In two-phase critical flow, depressurization rates experienced by the fluid are large as it moves through the steep pressure gradient. It is also questionable whether a bubble can be modeled accurately as being spherical when it is subjected to such large acceleration forces, turbulence and viscous shear.

In all these mechanistic models, critical flow was predicted to occur when the pressure gradient in the flow became arbitrarily large. Rohatgi and Reshotko show that this condition corresponds to the fluid velocity being equal to the isothermal frozen sound speed for their model equations. Frequently the infinite pressure gradient criterion is expedient when models require solution on a digital computer. Integration of the conservation equations along the flow channel becomes more time consuming (and thus more expensive) as the pressure gradient steepens. Terminating the integration when the pressure gradient has attained some arbitrarily large value prevents numerical difficulties and unnecessarily long running times. As is discussed in Chapter V, this criterion is not too ill-chosen.

II.2.2 Two Fluid Models

Two-fluid models are generally derived on the basis of expressions for the conservation of mass, momentum, and energy written separately for each phase. These equations have been formulated in a number of ways depending on the author's choice of dependent variables. Ishii [76] discusses the derivation of one-dimensional transient flow equations at length. Banerjee and Chan [77] have given a more concise discussion giving greater attention to the exact form of the constitutive relations which are required as a result of the integration of the three-dimensional vector equations over a plane transverse to the flow direction.

Boure [78,79] has examined the form of the constitutive relations which govern the interphase transfer of heat, mass, and momentum. He has drawn two important conclusions. 1) Constitutive relations in the available two-fluid models do not reduce to the homogeneous equilibrium model in the limit of increasing rates of interphase heat, mass and momentum transfer. 2) Only when the transfer terms are described as functions of derivatives of the dependent variables is the system of differential equations necessarily well-posed. Ill-posed problems frequently give rise to numerical instability when the equations are integrated on a computer. Boure has presented a general form of the conservation equations which meet these criteria. However, specific methods of evaluating the constitutive terms have not been advanced.

A common representation of the time and space averaged, one-dimensional, conservation equations for phase k (k=1 for liquid, k=2 for gas) is given by:

Mass:

$$\frac{\partial}{\partial t}(\alpha_k \rho_k) + \frac{\partial}{\partial z}(\alpha_k u_k) = \Gamma_k \tag{2-25}$$

Momentum:

$$\alpha_k \rho_k \frac{\partial u_k}{\partial t} + u_k \alpha_k \rho_k \frac{\partial u_k}{\partial z} + \alpha_k \frac{\partial P}{\partial z} = (u_{ki} - u_k) + \tau_{ki} + \tau_{kw} \tag{2-26}$$

Energy:

$$\alpha_k \rho_k \frac{\partial}{\partial t}\left(h_k + \frac{u_k^2}{2}\right) + u_k \alpha_k \rho_k \frac{\partial}{\partial z}\left(h_k + \frac{u_k^2}{2}\right) =$$

$$(h_{0,ki} - h_{0,k})\,\Gamma_k + Q_{wk} + Q_{ki} + \Phi_k \qquad (2\text{-}27)$$

Pdv work has been neglected in (2-27) as is common in the field. It is not clear to which phase this work should be charged, which perhaps accounts for its' frequent neglect. It has been assumed in the above equations that the pressures in each phase are equal: $P = P_1 = P_2$. Boure [78] has argued that this represents too close a coupling between the phases; but this is the assumption of almost every model. Banerjee and Chan [77] have pointed out that the consideration of the difference between the bulk pressure in each phase and the pressure at the interphase boundary allows derivation of the virtual mass effect. This implies that pressure differences between the phases should be considered; at least for bubbly flow. Certainly, when very small bubbles are present the pressure within the bubble is larger than the liquid pressure. This difference should be taken into account in order to correctly model the bubble dynamics.

Equations (2-25) through (2-27) require equations of state for each phase plus evaluation of the constitutive terms. Constitutive terms are described in Table 2-1. Specific representation of the constitutive terms varies widely between models. Simplification of the state equations are also frequently introduced. The liquid phase is often taken to be incompressible. Another common assumption is that the least massive phase (usually the vapor) is saturated at the local pressure. This latter assumption eliminates the need for an expression for the interphase heat transfer since the mass transfer rate determines the energy lost from the metastable phase. In addition, the state equation for the saturated phase is simplified.

A major concern of two-fluid modeling for subcooled or saturated stagnation states, is prediction of the point of flashing inception. Moog [79] has made a thorough survey of the field; his findings will not be repeated here. A typical solution to the problem is that taken by Ardron [80]. Liquid superheat at flashing was a parameter of his model. Other models, such as that of Richter and Minas [81], assume an initial concentration of small bubbles. Growth of the bubbles begins when the liquid superheat is sufficient to activate the nucleation sites. These approaches are nearly equivalent since the superheat at flashing (onset of bubble growth) in the latter model is a function of the assumed initial bubble size; which is a parameter of the model. This approach was originally proposed by Malnes [82], who justified the existence of bubbles in the subcooled liquid on the basis of the presence of dissolved gasses. Giot and Fritte [83] assumed flashing inception at the saturation pressure corresponding to the initial liquid temperature. A mass transfer rate lower that that of an equilibrium process was assumed. Such a model does not allow the flow to approach equilibrium at some point downstream, since the amount of vapor generated always lags behind that for an equilibrium process.

In the following section two of the available two-fluid models are discussed in detail. A discussion of critical flow criteria used in two-fluid modeling has been postponed until the closing section of the chapter.

II.2.2.1 Ardron's Model

Ardron has proposed [80] a steady state, four equation, two-fluid model. Conservation of energy is not considered, rather the liquid superheat was assumed to increase linearly with time:

$$T_l = T_{sat}(P) + \Theta_c + C_1(t - t') \qquad (2\text{-}28)$$

Where Θ_c is the liquid superheat at flashing inception (when t = t') and C_1 (a constant) is a parameter of the model. The vapor was assumed to remain saturated at the local pressure. This assumption, in combination with equation (2-28), eliminates the need for the energy conservation equation (2-27) to obtain closure.

Equations of state were simplified more than was necessary in light of available equations for fluid properties (such as the 1967 ASME Steam Tables). Not only was the liquid phase density assumed constant, but so was the latent heat of vaporization. Vapor was assumed to expand as an ideal gas. A state equation for the saturated vapor was derived under the assumption that the vapor density was negligible compared to that of the liquid. The Clausius-Clapeyron relation was integrated to obtain:

$$\ln P = \frac{-h_{fg}}{R} T^{-1} + C_2 \tag{2-29a}$$

Where C_2 is the constant of integration. Applying the ideal gas law to express T in terms of the vapor density, Ardron obtained:

$$\ln P + h_{fg}\Big|_{T_0} \left[\frac{\rho_g}{P}\right] = C_2 \tag{2-29b}$$

Three constitutive relations were considered. Vapor generation rate was derived in the same manner as that of Rohatgi and Reshotko [71]. The rate of formation of bubble nuclei was taken from the kinetic theory of nucleation in the bulk of a liquid on heterogeneous sites (such as solid particles or bubbles of a non-condensable gas). Density of these nucleation sites, n_s, per unit mass of liquid, was an input parameter of the model. The resulting expression for the rate of formation of bubble nuclei was:

$$\frac{dN}{dt} = n_s \bar{\nu} \exp\left[\frac{-\rho_g h_{fg}^2 (\ln \bar{\nu}) \Theta_c^2}{T_l^2 [P - P_{sat}(T_l)]^2}\right] \tag{2-30}$$

Vapor generation rate was calculated assuming that bubbles nucleated according to equation (2-30) grew according to a heat conduction controlled process. Rather than account for the spherical geometry of the bubbles, as most authors have done, the liquid vapor interface was taken to be planar. Under the linear approximation of liquid superheat given by equation (2-28) the vapor generation rate was given by:

$$\Gamma_g = \frac{\rho_g}{h_{fg}} \int_0^t \left(\frac{dN}{dt}\right)(1-\alpha) \frac{k_l}{[\pi D_l (t-t')]^{1/2}} \left[2\Theta(t) - \Theta(t')\right] \pi R_b \, dt' \tag{2-31}$$

where,

$$R_b = R_b(t,t') + \frac{2k_l (t-t')^{1/2}}{3h_{fg}\rho_g (\pi D_l)^{1/2}} \left[2\Theta(t) - \Theta(t')\right] \tag{2-32}$$

The interphase drag term included two components. Steady state drag corresponds to the Stokes viscous drag, which limits the application to either very small bubbles or practically negligible relative velocities ($Re_b < 0.1$). This term is proportional to the velocity difference between the phases. The second term resulted from consideration of inertial drag on a bubble which is accelerated through the liquid. Frequently referred to as the virtual mass effect, this nomenclature arises from the passage of the bubble accelerating a portion of the liquid mass. Thus the bubble appears to have a virtual mass attached to it. The interphase drag term was given by:

$$\tau_{gi} = -\tau_{li} = \frac{-9\alpha u_l (u_g - u_l)}{2\bar{R}_b^2} - \frac{\rho_l \alpha(1+2\alpha)}{2(1-\alpha)} u_g \left[\frac{\partial u_g}{\partial z} - \frac{\partial u_l}{\partial z} \right] \tag{2-33}$$

The form of the coefficient to the virtual mass term (second term on the right) has a rather obscure origin. It was derived by Zuber [84] for spherical solid particles settling through a liquid under the influence of gravity. Even though this situation is not relevant to the high velocities characteristic of two-phase critical flow, it frequently appears in two-fluid models. Zuber's analysis was based on a calculation of the potential flow field around spherical particles.

As with many of the available two-fluid models, serious limitations are imposed by the assumption that vapor bubbles behave as spherical solid particles. While Ardron avoided this assumption for the interphase mass transfer calculation, it is implicit in his formulation for the interphase drag. Unless the bubbles are very small, surface tension forces would not be adequate to maintain a spherical shape in the face of acceleration and shear forces in the flow. It should be noted that these models, without exception, assume surface tension to be negligible by their neglect of any pressure difference between the phases. Photographs in the reports by Zimmer et al [40] and Reocreux [33] show bubbles which are flattened in the flow direction and which often have irregular interfaces. Drag models which are based on the assumption of spherical geometry are probably inadequate for the correct prediction of interphase slip.

Ardron argued that in bubbly flow the vapor was seldom in contact with the wall. Friction effects were thus restricted to the liquid phase. Wall shear stresses were given by:

$$\tau_{wl} = \frac{-8 f_F \dot{m}^2}{\pi^2 \rho_m D_h^4}$$

$$\tau_{wg} = 0 \tag{2-34}$$

where f_F was the single-phase Fanning friction factor.

Ardron compared his model with the data of Zaloudek [43], Sozzi and Sutherland [10], and Fauske [15]. Superheat at flashing, Θ_c, and the density of nucleation sites, n_s, were determined so as to obtain the best agreement between the flowrate predictions of the model and the data. Predictions agreed well with the data except for the Sozzi and Sutherland data for short pipes with moderate stagnation subcooling. No comparison with measured pressure profiles were made.

II.2.2.2 Richter-Minas Model

Richter and Minas have recently proposed [81] a five equation, steady state model for two-phase critical flow. State equations for both phases were represented more fully than in Ardron's model. The constitutive relations were more simply posed. Such a formulation is more consistent with the current state of the art since interphase transfer phenomena are poorly understood. The only restriction on the state of each phase was that the vapor remains saturated at the local pressure. Only the conservation of energy for the mixture was required under this assumption. An additional result was that the heat lost from the liquid must go to either to the heat of vaporization or kinetic energy of the flow. Separate constitutive relations for interphase heat and mass transfer are therefore not required.

The equations for the model were written:

Mass:

$$\frac{1}{\dot{m}_k}\frac{d\dot{m}_k}{dz} = \frac{1}{\rho_k}\frac{d\rho_k}{dz} + \frac{1}{u_k}\frac{du_k}{dz} + \frac{1}{\alpha_k}\frac{d\alpha_k}{dz} + \frac{1}{A}\frac{dA}{dz} \tag{2-35}$$

Momentum:

$$\rho_k u_k \alpha_k A \frac{du_k}{dz} = -\frac{dP}{dz}\alpha_k A + F_{ki} A_i + F_{kw} A - (u_{ki} - u_k)\dot{m}\frac{dx}{dz} \tag{2-36}$$

Mixture

$$\dot{m}\frac{dx}{dz}\left[(h_g - h_l) + \frac{1}{2}(u_g^2 - u_l^2)\right] + \dot{m}_g\left[\frac{dh_g}{dz} + u_g\frac{du_g}{dz}\right]$$

$$+ \dot{m}_l\left[\frac{dh_l}{dz} + u_l\frac{du_l}{dz}\right] = 0 \tag{2-37}$$

The relationship of these equations to the general formulation can be seen in the expression of the transfer terms as:

$$\Gamma_g = -\Gamma_l = \dot{m}\frac{dx}{xz} \tag{2-38a}$$

$$\dot{m} = \dot{m}_g + \dot{m}_l = u_g\alpha_g\rho_g + u_l\alpha_l\rho_l \tag{2-38b}$$

$$\tau_{ki} = F_{ki} \quad , \quad \tau_{kw} = F_{kw} \tag{2-38c}$$

Following the formulation of Wallis [50], the problem of determining the interface velocity explicitly, was avoided by writing:

$$(u_{li} - u_l) = (1 - \eta)(u_g - u_l)$$

$$(u_{gi} - u_g) = \eta\,(u_g - u_l) \tag{2-39}$$

η is the fraction of the momentum lost by the vapor phase as a result of accelerating the evaporating liquid. Wallis has taken this coefficient to be 0.5 which is equivalent to taking the interface velocity to be the average of that for each phase. Since slip was usually predicted to be small, the value of the constant has little impact on the results of the model.

A simple flow regime map was incorporated into the model. When the void fraction was less that 30%, the flow was assumed to be bubbly. For void fractions greater than 80%, an annular flow pattern was assumed. Intermediate void fractions were taken to constitute a "churn-turbulent" regime. Interphase transfer terms were evaluated depending upon the assumed flow regime. Churn-turbulent regime values were calculated by a linear interpolation between the 30% void and 80% void evaluations.

Virtual mass effects were considered in calculating the interfacial drag in the bubbly regime. The interphase force term was given as:

$$F_{lg}(bubbly) = \frac{3}{4}\frac{C_D(1-\alpha)^{-4.7}}{R_b}(1-\alpha)^3\rho_l(u_g - u_l)|u_g - u_l|$$

$$+ \frac{1}{2}\rho_l u_g \alpha \frac{d}{dz}(u_g - u_l) \qquad (2\text{-}40)$$

for bubbly flow. The single bubble drag coefficient, C_D, was calculated on the basis of bubble Reynolds number according to the recommendation of Rowe and Hernwood [85] for spherical solid particles in a fluidized bed. Abdollahian et al [9] have proposed a modification of the virtual mass term for this model. Their proposal was to multiply the term by Zuber's coefficient as Ardron had done in his model. For the annular flow regime, interphase force was given by the expression recommended by Wallis [50]:

$$F_{lg}(annular) = 0.5C_{fi}A_i\rho_g(u_g - u_l)^2 \qquad (2\text{-}41)$$

where,

$$C_{fi} = 0.005\,[1 + 75(1-\alpha)\,]$$

A_i is the interfacial area given below by equation (2-45). In the churn-turbulent flow regime, the annular form of the interfacial force expression was used (2-41) but the coefficient, C_{fi}, was replaced by a linear interpolation between one appropriate for bubbly flow with 30% void and the coefficient for annular flow at 80% void. The drag coefficient for bubbly flow was evaluated by equating equations (2-40) and (2-41) and solving for C_{fi}; the resulting coefficient was denoted C_{fib}. Denoting the coefficient for annular flow C_{fia}, the value of C_{fi} used in equation (2-41) for churn-turbulent flow was given by:

$$C_{fi} = C_{fib} + 2(\,C_{fib} - C_{fia}\,)(\alpha - 0.8) \qquad (2\text{-}42)$$

Vapor generation was treated by considering the conductive and convective heat transfer from liquid to vapor. Consideration of an energy balance across the liquid-vapor interface gave:

$$\frac{3h'}{R_b}(T_l - T_g)\alpha A_i = \dot{m}\frac{dx}{dz}h_{lg} + \dot{m}_g\frac{dh_g}{dz} \qquad (2\text{-}43)$$

The Nusselt Number for bubbly flow was given by:

$$Nu = \frac{2h'R_b}{k_l} = 2.0 + 0.15R_b^{1/2} \qquad (2\text{-}44)$$

Richter does not specify the source of equation (2-44). Bird et al [86] recommend a similar expression for convective heat transfer to a spherical particle but the coefficient 0.15 was replaced by $0.6Pr^{\frac{2}{3}}$. The constant term, 2.0 can be derived analytically considering conduction heat transfer between a sphere and a surrounding stagnant fluid. Equation (2-44) neglects the fact that the bubble is growing and thus underestimates the heat transfer coefficient. The second term was the convective component and included the relative velocity effects. The interfacial area, A_i, was given by:

$$A_i = \begin{cases} \dfrac{4\alpha^{1/2}}{D_h} & (annular\ flow) \\ 4N_v \pi R_b^2 & (bubbly flow) \end{cases} \tag{2-45}$$

Where N_v was the initial number of bubbles per unit volume which was selected so as to provide agreement between the model and selected data. In the churn-turbulent regime the interfacial area was given by a linear interpolation of the values given by equation (2-45). Heat transfer coefficient in the churn-turbulent and annular regimes was given by a Colburn type analogy to the interfacial drag:

$$h' = 0.25 C_{fi} C_D (1-\alpha)^{-4.7} \rho_l |u_g - u_l| \, Pr^{-\frac{2}{3}} \tag{2-46}$$

It is not clear from the author's description whether N_v is held constant and the bubble radius increased with the calculated void fraction or if the number of bubbles was allowed to increase by way of specifying a maximum bubble size. The former prescription is more likely.

The point of flashing inception was determined in the same manner as for Malnes model [82]. Gas bubbles were assumed to exist in the liquid in the stagnation condition with a density N_v and having an initial diameter d_0. Flashing was taken to begin when the liquid superheat was sufficient to activate a bubble of the assumed size. Richter selected d_0 such that the superheat at flashing was in the range of 1 to 2 degrees centigrade on the basis of values observed by Reocreux [33] in his low pressure experiments. The fluid pressure at the point of flashing inception was given by:

$$P = P_{sat}(T_0) - \frac{4\sigma}{d_0} \tag{2-47}$$

Exact values of N_v and d_0 were determined such that the best agreement between the model predictions of flowrate and the experimental results of Reocreux [33] and Zaloudek [43] were obtained. Richter recommended $N_v = 10^{11}$ m^{-3} and $d_0 = 2.5 \times 10^{-5}$ m.

Richter and Minas found good agreement between the predictions of their model and the measured flowrates of Sozzi and Sutherland [10], Fauske [15], and Zaloudek [43]. Agreement with the pressure profile measured in one of Fauske's experiments was also found to be close. Abdollahian [9] compared Richter's model with flowrates measured during the Marviken tests [16]. Richter's recommendations for the values of the model parameters were used. Results of the comparison were excellent. A slight underprediction of flows through a short duct from subcooled stagnation states was noted. No comparison was made between model predictions and measured test section pressures or void fractions.

Abdollahian et al [9] reported that choking in the churn-turbulent regime was always predicted to occur immediately after the transition to bubbly flow. This corresponds to a critical criterion of $\alpha = 0.3$ which is clearly erroneous. The problem was attributed to large values of C_{fi} (equation 2-42) at $\alpha = 0.3$ resulting in the prediction of very large heat transfer rates (equation 2-46). Acceleration pressure drop thus gives rise to a large pressure gradient which results in the choking criteria ($dP/dz > 2$ bar/mm) being met. While Abdollahian et al suggest that this result was appropriate for the Marviken data, this cannot be true in general. Several experiments, including those of Reocreux [33] and Henry et al [22], indicate void fractions near unity in some instances.

It is probably true that Richter's flow regime map is overly simplistic. Mass flux, as well as void fraction, and possibly other parameters, contribute to the determination of flow regime. As stated above, the models for the interphase transfer terms used in Richter's work are also overly simplistic. The approach of the model is a good one however, and with modification of the transfer terms, probably shows the most promise for the accurate modeling of two-phase critical flow.

II.2.2.3 Drift-Flux Two-Fluid Models

Two fluid models are frequently complex and expensive to apply. Equations must be integrated numerically and the expense involved increases rapidly with the number of equations. This has motivated attempts to model two-phase critical flow with drift-flux models. With the assumption of the vapor phase being saturated at the local pressure a drift-flux formulation requires only four equations. The two momentum equations are replaced by a mixture momentum equation and a correlation of the vapor drift velocity relative to the liquid phase. Kroeger [87] has proposed just such a model. An early version of the Transient Reactor Analysis Code, TRAC-P1A [88], included a five equation drift flux model for one-dimensional two-phase flow. This model allowed for superheating (or supercooling) of the vapor phase.

Drift-flux models have a serious theoretical shortcoming. Zuber and Findlay [89] originally proposed the drift-flux approach for bubbly flow in a vertical channel. The correlation they proposed was based on a model of bubbles rising in a flowing liquid as a result of buoancy forces. Buoancy is unlikely to be important in vertical two-phase critical flow and is almost certainly irrelevant in horizontal flow. Correlations for vapor drift velocity in two-phase critical flow models have generally had a formulation similar to that of Zuber and Findlay. Such an approach implicitly includes assumptions about the void distribution in the channel. Void distribution is unlikely to be similar between the case Zuber and Findlay considered and the case of critical flow. Consequently, it seems improbable that drift-flux models are capable of accurately predicting two-phase critical flows. Indeed, current versions of TRAC [90] employ full six equation models.

Full six equation models for transient two phase flow are employed in recent versions of computer codes used in the transient analysis of LWR's; such as KFIX [49] and TRAC PD2 [90]. RELAP5/MOD1 [91] uses a five equation model which assumes that the least massive phase is saturated at the local pressure. All these codes are written so that constitutive equations may be revised as the understanding of the physics of interphase transport processes is improved. Critical flow prediction is just one application of the two-fluid models within these codes. The same model is applied to analyze other parts of the reactor system. Critical flow criteria, like the constitutive relations, may be improved as understanding of the processes involved increases. In the next section, the criteria which have been used to predict two-phase critical flow will be examined.

II.2.2.4 Critical Flow Criteria

A critical flow criterion will be taken to mean that property of a flow from which it can be judged whether or not that particular flow is critical. There are essentially four criteria which have been proposed in the literature. As one might expect, they are closely related to one another. Depending upon the model, the distinction between criteria may be arbitrary. For instance, in the HEM the maximum mass flux criterion given by equation (2-1) is identical to specifying that the critical velocity is at least the homogeneous equilibrium sound speed. (Should supersonic choking occur, the HEM critical mass flux may be larger than that given by equation 2-1.) If supersonic choking does not occur, the HEM also predicts an infinite pressure gradient at this point.

The maximum mass flux criterion given by equation (2-1) is useful only for simple models which do not require numerical integration of the model equations over the flow channel. Generally this means that the model must neglect friction effects. Solutions for critical flow conditions with such models can be obtained analytically by applying (2-1)

Sound speed criteria are not widely used (other than in the HEM as discussed above). Primarily, this is because models for sound speed in a two phase mixture are not well developed. Development of such models generally depends upon the formulation of expressions for interphase heat, mass, and momentum transfer. As indicated above, these phenomena are not well understood.

To use a sound speed criterion for critical flow prediction the two-phase flow equations must be consistent with the sound speed model. As an example, albeit an extreme one, a sound speed model which assumes the vapor remains at saturation is not consistent with a flow model which allows for the vapor to depart from saturation.

Criteria which depend on the pressure gradient becoming infinite at the critical flow plane have generally not been considered favorably by experimentalists in the field. Certainly it is true that infinite pressure gradients, or discontinuities in the pressure field have not been observed experimentally. Fauske [15] suggested that critical flow could be defined in terms of maximizing the pressure gradient at the critical location. Such an approach cannot be justified in terms of the definitions for critical flow given in Chapter I. This criterion was used by Fauske to obtain closure for what was otherwise an incomplete formulation of the field equations. It is not Fauske's maximization of the pressure gradient which is considered in this section.

First proposed by Simpson and Silver [69], a critical flow criterion which sets some arbitrary high limit on the pressure gradient at the critical plane is the most common among two-phase critical flow models. The advantages of this approach are two-fold. Firstly, when the model equations are integrated numerically, using methods such as those described in Appendix F, computing costs are held down. The reason for this is that the the nodal points required for integration move closer together as the pressure gradient steepens. With a smaller step size, the amount of work required to integrate the equations over a given length of channel increases. Indeed, a point may be reached where the step size has been decreased to less than the machine precision. This results in either an infinite loop or the program being aborted. A second advantage is that it avoids the necessity of computing some auxiliary property of the flow, such as the mixture sound speed, at each node in the integration.

Because a large pressure gradient means large gradients in the other dependent variables the critical flow prediction using this method is frequently little different from a prediction based on a sound speed criterion. Specific examples of this are discussed in Chapter V with reference to the new model that has been developed as part of this research.

Reocreux [92] and Giot and Fritte [83] have proposed a critical criterion based on singularities in the model equations. The model equations can be written symbolically:

$$B\,\bar{y}' = \bar{C} \tag{2-48}$$

the criterion they propose is:

$$\det\left|\,[B]\,\right| = 0 \tag{2-49}$$

This was, in fact, analogous to the infinite pressure gradient criterion with the advantage that the exact point of the singularity was predicted analytically. Because most proposals for the formulation of constitutive terms do not include derivatives of the dependent variables they are represented in the column vector $\bar{C}$. Thus, in such models, the critical criterion is independent of interphase mass and/or momentum transfer.

The last criterion considered is really limited to transient models, but may be imposed as a sound speed criterion (to which it is related) to a steady state model. A two-fluid model for transient two-phase flow may be represented symbolically as:

$$A\,\frac{\partial \bar{y}}{\partial t} + B\,\frac{\partial \bar{y}}{\partial z} = \bar{C} \tag{2-50}$$

The characteristic equation for this system is given by:

$$\det\left| (A\lambda - B) \right| = 0 \qquad (2\text{-}51)$$

where λ is the characteristic velocity. Critical flow is said to occur when the largest real component of λ is at most zero. Physically, this corresponds to an inability of the flow to propagate information upstream of this point. This definition of critical flow was discussed in Chapter I.

Theoretically, the system of equations (2-50) can be transformed into a set of ordinary differential equations along the characteristics. Such a system would have an equivalent criterion for criticality as that given by equation (2-49). In practice, the transformation involves more work than the solution of the partial differential equations (2-50) so few author's have attempted to use this approach.

Boure [48] has pointed out that since constitutive relations are usually included only in the column vector, $\bar{C}$, they are not considered in the critical criterion. He argued for the use of constitutive relations in which include derivatives of the dependent variables. Such formulations have been used by Ardron [80] for interphase momentum transfer and by Richter and Minas [81] for both transfer terms. However, both models employ the infinite pressure gradient criterion.

A critical criterion such as this was used in the RELAP5 code [91]. Ransom et al developed a zero characteristic velocity criterion analytically; on the basis of a four equation two-fluid model (1 mass, 1 energy, and 2 momentum). Roots of the characteristic equations were determined for a wide range of flow conditions. In integrating the five equation two-fluid model used in the code, the zero characteristic velocity criteria developed from the four equation model are used to check if the computed flow at a given node was critical. Clearly, this is not a consistent approach to the prediction of two-phase critical flow. It is, however, the state of the art.

II.2.3 Conclusions

Much work remains to be done in the area of critical flow modeling. It is not clear whether two-fluid models are a better approach to the problem of accurately predicting critical flows than are the simple models. Two-fluid models are more costly to apply and it is not certain that expressions for the constitutive relations will ever be known to degree which warrants the use of two-fluid models. The simpler models are cheaper and are probably more consistent with the amount of empiricism required by the current state of the art. However, details of the flow, such as void or pressure profiles, are incorrectly modeled; even though the flowrate is correctly predicted. Often, there are compensating effects included in the simple models (such as an overprediction of exit pressure leading to a correct flowrate assessment). These effects are not immediately obvious and have led to the belief on the part of some that if a model correctly predicts experimental flowrates, the assumptions of the model are valid.

It would seem that the simple models are more attractive at the present time. While their prediction of details of the flow are often poor, they are more useful as a design tool by virtue of their lower cost. However, two-fluid modeling is useful in understanding the physics of flow situations which are disparate from those for which the simple models were developed. The current problem of two-phase critical flow in small geometries may be an example of an area where two-fluid models may throw some light on the flow processes.

Table 2-1

Constitutive Terms of General Two-Fluid Models

Symbol	Quantity Represented
Γ_k	Rate of interphase mass transfer. $\Gamma_1 = -\Gamma_2$. Γ_2 is the vapor generation rate.
τ_{wk}	Frictional shear stress between the channel wall and phase k.
τ_{ki}	Interphase momentum transfer. Shear stress between phase k and the interface.
Q_{wk}	Heat transfer between channel wall and phase k.
Q_{ki}	Interphase heat transfer. Heat transfer between phases across the interface. $Q_1 = Q_2$.
Φ_k	Rate of enthalpy generation within phase k. Usually due to viscous dissipation; often neqlected.

CHAPTER III

Description of the Experiment

III.1 Description of the Apparatus

The chief objective of the design of the apparatus was to keep the stagnation state of the fluid entering the test section constant. Many previous experiments, such as those of Sozzi and Sutherland [10] and the Marviken tests [16], have been blowdown experiments in which the stagnation pressure has decreased during the course of a test. Interpretation of the results of these experiments is complicated by this feature. With the critical flow constantly changing, along with the stagnation state, determination of the flowrate corresponding to a given stagnation condition is necessarily subject to some error. In addition, the features of a transient flow as compared to a steady state situation are not well known.

A constant pressure blowdown system has been used for these experiments. Nitrogen gas at high pressure was used to push subcooled water through the test section. The nitrogen flowrate was controlled so as to maintain a constant vessel pressure. Prior to starting an experiment, the vessel and the water contained were heated uniformly to the required temperature. Thus, the fluid temperature at the test section was maintained as the water discharged. The test section was also heated so that measurements of the effects of heat transfer from the channel wall to the flowing fluid could be investigated. Pressure and temperature of the fluid immediately upstream of the test section were measured throughout each run so as to assure constancy. Redundant measurements of the mass flowrate were made. Pressures up to 16 MPa with temperatures as high as 350°C were required.

A schematic of the equipment, showing the major components, is presented in Figure 3-1. Nitrogen was supplied to the system from high pressure cylinders. The gas pressure supplied to the vessel was controlled by means of a dome loaded flow controller. A standard pressure regulator was used to supply the dome pressure which, in turn, determined the system pressure. A precision bourdon tube type pressure (Heise) gauge was used to monitor the system set pressure. Gas was fed into the vessel through the top. A cold trap and reflux condenser, which employed running tap water for a heat sink, were used to prevent steam from the vessel penetrating into the gas supply. A shutoff valve in the gas supply line was used to stop the gas flow once the vessel was empty.

Flow through the test section was controlled by a gate valve mounted below it. The two-phase mixture leaving the test section was piped through condensing nozzles into the suppression tank. As one means of determining the mass flowrate, the mass of the tank was recorded using the load cells from which the tank was suspended. Redundant flowrate measurement was provided by measurements of the vessel level using a differential pressure transducer. An automatic data collection system was used to record the data.

Heating of the vessel was accomplished by means of external heaters wrapped around the circumference of the vessel. An additional heater, inside the vessel, was used to boil the water prior to each run to remove dissolved gases. Temperatures within the vessel, and of the vessel wall, were monitored by a system of thermocouples connected to a chart recorder. The test section was heated by strip heaters attached to the outside. All the heaters were controlled by means of variable autotransformers. Photographs of the control panel (Figure 3-2), and of the apparatus itself (Figure 3-3) have been included.

The description of the equipment in the following sections has been divided into component systems: 1) the vessel and associated heaters; 2) the gas pressurization system; 3) the weigh tank/steam suppression system; 4) the test section; 5) the measurement and data collection system. Operational procedures and a discussion of the reliability of the instrumentation compose the final section.

III.1.1 Vessel

The vessel was constructed from a 2.883 m length of 5″ IPS Schedule 160S stainless steel pipe. The inside diameter is nominally 10.73 cm with a wall thickness of 1.7 cm. The top end is capped with a 5″ IPS, Schedule 80S, pipe cap. Two concentric reducers were welded to the lower end. The first being 5″ IPS by 3″ IPS, and the second, 3″ IPS by 1.5″ IPS. Both are Schedule 80S. Type 316 stainless was used for all vessel components for its' corrosion resistance and high temperature strength.

The vessel served as both the reservoir for subcooled water and the container in which the water was heated. Although the long narrow shape of the vessel limited the volume of water available, the advantages of that configuration were two-fold. Firstly, it gave greater accuracy to the to flowrate determinations based on measurements of vessel level. Secondly, the low surface area per unit volume of water decreased the rate at which nitrogen could diffuse into the water.

In order to attach the test section a flange was welded to the bottom of the vessel. A 5 cm length of 1.5″ IPS pipe attaches the flange to the lower reducer. The final inside diameter is 3.81 cm. The flange used is a 1.5″ ANSI 1500# flange. Three modifications were made to the flange before welding it to the vessel. First, a disk with a slot in the center, 3.175 by 0.635 cm, was welded into the sealing face of the flange. This provided a flat surface on which the test section gaskets could seal. Second, a flow transition piece, in the form of a funnel, was made from stainless steel sheet metal. The upstream end was roughly circular; narrowing to the shape of the slot at the downstream end. The funnel was then welded into the slot so as to make the inside surfaces of the slot and the funnel smooth and continuous. A convergent section preceding the slot helped to prevent flow separation at the edges of the slot and to avoid a possible non-uniform flow field at the entrance to the test section. Third, the edge of the flange was cut along two parallel chords so as to accommodate the test section clamping blocks (shown in Figure 3-7).

To facilitate boiling of the water in order to remove dissolved gasses, a heater was installed inside the bottom of the vessel. A 1 kW Calrod tubular heater was selected. The installed heater is shown in Figure 3-4. The heater sheath is 1 cm in diameter and made of Inconel for corrosion resistance. Since the heater is 66 cm long, with a heated length of 30.5 cm, it was necessary to form the heater into an inverted "U" shape. Electrical connections were made by extending the unheated ends of the sheath through the vessel wall. The leads were sealed using Conax packing glands with Grafoil seals. (Grafoil is a graphite based packing material, made by Union Carbide, capable of withstanding temperatures of up to 430°C.) This heater was controlled by a 7.5 amp variable autotransformer.

Thermocouples were installed at 30.5 cm intervals over the length of the vessel. Since radial temperature profiles in the water contained within the vessel were expected to be small, the thermocouples were placed such that the junction (tip) of the probe was approximately at the centerline of the vessel. Iron-constantan (Type J) thermocouples were used. The probes had an outside diameter of 1.6 mm and were fabricated with grounded junctions. Conax midlock fittings, which employ metal compression seals, were used to mount the thermocouples.

Differential pressure measurements between the top and bottom of the constant area portion of the vessel were used to determine the water level. Static pressure taps for this purpose were provided as close to the welds at either end of the pipe section as practicable; about 2.806 m apart. Sense lines, made of 6.4 mm tubing, were mounted in Conax midlock fittings so that the end of the tubing projected approximately 0.25 cm inside the vessel wall.

Stagnation temperature and pressure were measured by the thermocouple and pressure tap located immediately above the flange on the lower end of the vessel. The pressure tap was installed in an identical manner to the taps used in measuring vessel level. The centerline of the tap is approximately 1.9 cm above the top of the flange. A copper-constantan thermocouple (Type T) was used to measure the stagnation temperature. As with the vessel thermocouples, the sheath is 1.6 mm OD made of stainless steel and the junction is grounded. The mounting hole is 3.2 cm above the top of the vessel flange and is separated by 90° from the pressure tap mounting. Bending the probe so that the junction was inside the sheet metal funnel allowed a more accurate determination of the water temperature at the entrance to the test section. Probably because of the extreme environment, the original thermocouple failed about three-quarters of the way through the test program. Failure was evidenced by erratic changes in the temperature reading. It was not possible to bend the replacement probe, which was identical in fabrication to the original, in the same manner. Consequently, the junction was about 3 cm above the entrance to the slit. There is no evidence that the temperature measurement accuracy was affected.

External heaters were installed on the outside surface of the vessel once it had been mounted. These heaters consisted of 10, 1 kW, Calrod tubular heaters, designed to operate on a 220V supply. Each heater has a 6.6 mm diameter incaloy sheath with a heated length of 2.18 m. The manufacturer quotes the maximum allowable sheath temperature as 815°C. The heaters were wrapped in a spiral around the vessel and secured in place with stainless steel hose clamps. To provide control over the heat input range, the heaters were wired in pairs. For fast heating the heater pairs could be connected in parallel to 220V power. In this configuration each pair delivers 2 kW. As the water temperature approached the desired level, the heaters were switched to series wiring connected to 120V autotransformers. This controlled the range of each pair between 0 and 800W. Switching between heater modes was accomplished using a 4-pole double-throw switch for each pair.

Iron-constantan thermocouples were braised to the outside of the vessel at the approximate midpoint of each coiled heater. These thermocouples were constructed from standard thermocouple wire using a heli-arc thermocouple welder to form the junction. Readings from these thermocouples were used during the heat-up phase as a guide for controlling the heater powers so as to bring the vessel wall temperature into equilibrium with water inside.

Excessive heat loss from the vessel was prevented by a 7.5 cm thick layer of insulation applied to the outside of the vessel. Two layers of calcium silicate pipe insulation were used. Since this material is fragile, an aluminium cover was put over the outer layer.

III.1.2 Gas Delivery System

To maintain constant stagnation pressure within the vessel, the gas supply must be at constant pressure. The maximum volumetric flowrate of nitrogen that the system can deliver must be larger than the maximum anticipated volumetric flowrate of water from the vessel. Also, should the water flowrate change, the gas pressure must remain constant.

Nitrogen gas was supplied from six 360 SCF cylinders connected to a common manifold. When fully charged, the gas pressure in the cylinders was 24.8 MPa. The gas flow regulator selected requires approximately 500 kPa differential from supply to downstream side to maintain constant pressure at the flowrates required for these experiments. To maintain a margin for error the supply cylinders were replaced when their pressure fell to within 2 MPa of the stagnation pressure for the next run to be made. Runs were scheduled, to some degree, so as to make best use of the gas supply.

A schematic of the gas delivery system is contained in Figure 3-1. The system has seven components: a hand loaded regulator, a dome loaded regulator, a pressure gauge, a condensate trap, a shutoff valve, a safety relief valve, and a reflux condenser. These components are described in detail below.

The two regulators work as a pair to control the gas pressure. Gas flow was actually regulated by the dome loaded regulator. This regulator, manufactured by Tescom, has a flow capacity of 0.95 cubic meters of gas (at STP) per minute per MPa of inlet pressure (0.23 SCFM/psig inlet). This regulator has an aluminium body and is rated for 41.4 MPa inlet pressure. The regulated pressure is determined by the dome pressure. Dome pressure was set using the hand regulator; which was a standard high pressure regulator (0 to 34.5 MPa) manufactured by Benbow Manufacturing. A bourdon type Heise pressure gauge was used in setting the system pressure. As can be seen from the schematic, the gauge is connected downstream of the regulators and registers the vessel pressure.

Even though the Heise gauge is graduated in 2 psi (13.8 kPa) increments, an accurate setting of the line pressure to a specific value was almost impossible to achieve. There were two reasons for this. First, the hand regulator is not very sensitive in this zero flow application. Second, the dynamic response of the dome regulator is such that it allows the downstream pressure to fall 300 to 400 kPa from the zero flow set point before regulation begins. It took many runs before the author learned the nuances of the system to a degree that allowed reasonably consistent pressure settings. Even though the stagnation pressures were not the exact values originally planned, the regulators held the set pressure extremely constant (0.1 to 0.3% per minute). Set pressures also proved quite repeatable within about 200 kPa.

The condensate trap and reflux condenser served to protect the regulators and pressure gauge from the possible back flow of steam from the vessel. Both pieces of equipment are simple double pipe heat exchangers. The tube side is the gas supply tubing and tap water at about 15°C flows in the annulus side. A needle valve installed at a tee on the bottom end of the cold trap (which is oriented vertically) allows the gas tubing to be purged of condensate. Due to height limitations, the reflux condenser was oriented 75 degrees from vertical. The reflux condenser was designed to remove at least the heat input from the vessel internal heater. This was to allow the contents of the vessel to be boiled with this heater while maintaining the pressure constant.

In order to quickly apply gas pressure, or to stop gas flow, a shutoff valve was incorporated into the supply system. Its' use is detailed in the final section of this chapter in which the operating procedure has been described. To minimize pressure drop, and allow quick actuation, a ball valve was used. Low pressure drop was important since pressure regulation was upstream of the valve. If pressure drop in the gas tubing were significant this would mean that pressure in the vessel would vary with flowrate even though the regulated pressure remained fixed. The valve selected was a Hoke bar stock ball valve which has a design operating pressure of 34.5 MPa. With a 9.5 mm orifice, the Cv factor is 3.4.

Although it was never required, a safety relief valve was included to protect against accidental overpressurization. The valve has a nominal set pressure of 16.5 MPa which is slightly less than 50% of the hydrostatic test pressure which was applied to the vessel after fabrication. With a 1.9 cm diameter outlet line, the valve would provide the maximum possible flowrate for the line from the vessel.

III.1.3 Water Supply

The water supply system is shown to the right of the vessel in Figure 3-1. Water for the apparatus was distilled in a single stage still and stored in 19 liter bottles until needed. A small centrifugal pump was used to pump water from the bottles into the top of the vessel. The pump has a capacity of approximately 2 liters per minute under a 3 m head. The valve on the water fill line was open only for the time necessary to fill the vessel.

III.1.4 Weigh Tank and Steam Suppression System

This section describes all the components downstream of the test section; namely, the main valve, steam suppression piping and nozzles, and the weigh tank. These components are shown in Figure 3-1. The valve controls initiation of the experiment and the effluent steam is piped to the nozzles in the weigh tank were it is condensed. Dynamic measurement of the mass of water in the weigh tank is accomplished with load cells built into the tank support frame.

A flange, similar to the one welded to the vessel, was used to mount the main valve downstream of the test section. Since flow separation is not a concern at the slit exit, a sheet metal funnel was not welded into this flange. The valve was screwed onto a pipe stub, which was welded into the flange, using a 1″ NPT nipple. Downstream pressure measurements were made via a pressure sense line installed inside the pipe stub. So as to avoid impact effects, the end of the sense line was tack welded to the back side of the slotted disk at the face of the flange. The end of the tube was perpendicular to the flow direction and in the area of free expansion for any jet of fluid from the test section. A Conax midlock fitting was used to seal the sense line tube where it penetrates pipe wall. Absolute pressure at this point is measured using a Statham transducer which had a range of 700 kPa.

The downstream pressure transducer had a range corresponding to the expected range of outlet pressures. Since this is far less than the stagnation pressures employed in the experiment, the pressure sense line had a valve arrangement to prevent overpressurization of the transducer. This is shown schematically in Figure 3-1. A ball valve was used to isolate the transducer from the sense line when the main valve was closed. The line between the transducer and the ball valve could be vented to the atmosphere via a needle valve. Venting allows the line to be flushed with water and also provides extra protection for the transducer should the ball valve leak or be inadvertently opened.

Flow through the test section was controlled by the main valve. A 2.5 cm stainless steel gate valve was used. Manufactured by Pacific Valve Company, this valve was rated for operation with 10.5 MPa fluid at 530°C. Performance was satisfactory at 16 MPa and 345°C. Although considerable effort was required to open the valve when subjected to 16 MPa pressures, it required no more than five seconds to open the valve sufficiently so as not to restrict the flow through the test section.

Potential conductive heat loss through the downstream piping was avoided by heating the pipe section above the valve. A tape resistance heater was used. Heater power was controlled between 0 and 160 watts using a variable autotransformer. The fiberglass cover of the heater was rated for operation at 450°C.

The piping downstream of the valve was constructed of 2.5 cm OD brass tubing. Using pipe-to-tube fittings the condensing nozzles were connected to the piping in an H pattern, about 17 cm below the surface of the water in the weigh tank. About 15 cm was allowed between the nozzles and the bottom of the tank.

Steam jet heating nozzles were used for condensing the steam-water mixture leaving the test section. These jet condenser nozzles are manufactured by Pardee Engineering, of Berkeley, California. They are intended for use in the heating of bulk fluids in the process industries. E.G.&G. Idaho Inc. first used nozzles of this type for the purpose of condensing steam in a flow metering application. Many of these nozzles were used successfully in their large scale two-phase blowdown system to condense and measure effluent flows.

A photograph and sketch of one of the condensing nozzles is shown in Figure 3-5. Steam passes through the center of the nozzle and forms a jet. The outer part of the nozzle forms a venturi. With the nozzle submerged, the passage of the jet into the venturi entrained water from the surroundings. The intimate mixture of steam and cold water in this accelerating flow promotes condensation of the steam. Using these nozzles avoided the "bumping" phenomenon usually associated with the condensation of steam in a water pool. Condensation was also much more efficient than if the steam had been allowed to expand freely into the water tank.

It was especially important that all the steam flowing through the test section be condensed in the tank. Escaped steam would have meant a deficit in the mass flowrate assessment. The nozzles performed well and at no time were steam bubbles seen rising from the water surface. Further confirmation of their success is seen in the close agreement between the mass flow calculations based on weigh tank data with those using vessel level data.

The weigh tank consisted of an aluminium tank suspended from load cells which are mounted on a heavy steel frame. Lengths of angle iron, 3.81 cm by 0.64 cm thick, were used to make the frame. Crosspieces for mounting the load cells were constructed by welding to lengths together to form a tube for extra rigidity. The tank is pictured beneath the vessel in Figure 3-3.

Normally, the water level was maintained about 12 cm from the top of the rectangular tank. This was to keep water from being splashed from the tank during a run. A cover for the tank, made of aluminium sheet metal, also helped to keep the water in. About 0.317 cubic meters (317 kg) of cold water were usually in the tank. The tank was lined with plastic sheet to help keep corrosion products out of the water. Because the aluminium sheet, from which the tank was made, was not particularly rigid, the tank was suspended in a steel cradle. The bottom of the cradle, on which the tank rested, has crossmembers (6 mm by 2.5 cm) connecting two pieces of angle iron in which run along the bottom edges of the tank. Vertical members were welded at each corner. The four vertical members were connected along the sides and across the top of the tank. The connecting members were at the level of the top of the tank. Steel cables, attached to turnbuckles which were bolted to the upper crossmembers of the cradle, were used to suspend the tank. The other end of these cables were fastened into clamps designed for this purpose that screwed into the load cells. The turnbuckles were used to level the tank and also to raise it from the ground prior to filling it with water.

III.1.5 Test Section

Four criteria were met in designing the test section: 1) Mounting of the test section was to be conventional (ie. with a flange) so that other test sections could be substituted at a later time. 2) Plastic deformation of the test section should not occur under the conditions of the planned experiments. 3) The size of the slit within the test was to be adjustable. 4) Measurements of fluid pressure and slit wall temperature were to be made within the test section. A drawing of the assembled test section is shown in Figure 3-6.

The slit was formed between two blocks of steel the surfaces of which were ground flat to provide the flow channel with a smooth wall. Strips of shim metal placed between the surfaces hold them the required distance apart. The slit opening dimension is determined by the thickness of shim metal used. The inside edge of each shim formed the sides of the flow channel. In order to seal the edge of the slit against fluid leaks the lower steel block was made "U"-shaped and the other block fit inside the "U". The vertical space between the two blocks is packed with gasket material to prevent leaks. The entire assembly is placed between two thick steel plates connected together by studs. Tightening the nuts on those studs loads the test section to withstand the pressure inside the slit during an experiment. The test section was instrumented with pressure and temperature probes which penetrate up through the lower, "U"-shaped, block. Test section instrumentation is described in the next section of this chapter.

A detailed description of the test section components is given in the this section. Because it is difficult to visualize the test section from drawings, Figures 3-6 and 3-7, a photograph is shown in Figure 3-8. The photograph shows the instrumentation probes used in the experiment. These were excluded from the drawings for clarity. It should be noted that while these figures depict the test section in a vertical orientation it is attached to the vessel with the exit face (front face in figure 3-6) facing toward the floor. The bottom end, with the instrument probes, was on the right side of the vessel as it is shown in Figure 3-3.

Requirements of mounting configuration and strength led to the peculiar shape of the test section. In Figure 3-7, it can be seen that the center part of the test section is roughly square. The corners were cut away so as not to interfere with the studs used to mount the test section to the vessel. These mounting studs run parallel to the slit and connect the vessel flange and the downstream piping flange clamping the test section inbetween them.

The slit is formed between the "U"-shaped block and the insert block. Studs running transverse to the slit, connect the two support plates and keep the two parts together (see Figure 3-6). Fine threads (11 per cm) were used on both ends of the studs in order to minimize the torque necessary to load the test section sufficiently to contain the slit pressures. Support plates are thick, 3.8 cm, to avoid deformation from the bending moment applied when the studs are tightened. Spacer blocks between the center part of the test section and the support plates keep the support plates clear of the flanges. Flattening the edges of the two flanges kept the thickness of the spacer blocks to a minimum.

The lower half of the test section has a "U"-shaped groove, 3.18 cm wide, running the 4.76 cm length of the test section. All the test section instrumentation is mounted in this side of the test section. Grinding the bottom of the groove flat (to within 0.001 mm) provides a smooth wall for the flow channel. The surface of the insert block is also ground flat, this forms the upper wall of the slit. Slit opening dimensions were set by shims, 6.4 mm wide, placed on either side of the bottom of the "U". Three different shim thicknesses were used: 0.127 mm, 0.254 mm, and 0.318 mm. The edges of the shims form the sides of the slit. A piece of shim metal, 0.63 mm thick, was used on top of the insert block to insure that the upper spacer block contacts only the inset block. Thus, all the load exerted by the studs between the support plates is concentrated in the shims. Dowel pins in the upper spacer block fit into holes in the shim metal and insert block to ensure alignment of these parts.

To facilitate the description of the remaining components of the test section, the assembly procedure is described below. Installation of the instrumentation probes is described in Appendix E. For ease of assembly, the test section was welded to form three main components. The lower section consisted of the lower support plate, the lower spacer block, and the "U"-shaped lower half of the test section. The insert block is just a single part. The upper part consisted of the upper support plate and spacer block including the ten cap screws required to pack and hold the gasket material which seals the sides of the slit.

The test section was assembled while being held upright (the instrumentation pointing downward) in a vise. First, the shims were placed on the lower surface of the slit as far to each side as possible. The insert block was then placed on top of the shims. Packing material was put in the wedge-shaped space shown in Figure 3-6. For most of the runs, the packing material used was fiberglass impregnated Teflon which was obtained from Johns-Manville Corporation. This material comes in sheets and was cut to fit the space; the bottom edge was machined into a wedge so as to seal the edge of the slit. The Teflon had a tendency to flow at elevated temperatures and loses all sealing capability at 327°C where it changes phase. Grafoil was used as a packing material for the runs where temperatures exceeded 300°C. Ribbons of Grafoil were placed in the channel between the insert block and the test section. The packing blades, shown in Figure 3-7 were then used to pack the sealant down into the wedge. Once the test section was completely assembled, the cap screws in the upper support plate were tightened to load the material so as to make a seal at the edge of the slit. The Grafoil showed no sign of flowing even at 345°C. The Teflon flowed and tended to obstruct the slit when used above 250°C. This necessitated re-assembly every four or five runs.

Before tightening down the test section, the slit opening was checked with a feeler gauge. If necessary the shims were adjusted. The studs were then inserted between the upper and lower support plates. To insure that the nuts were tightened so as to load the test section evenly, a torque wrench was used. The nuts were tightened in a set pattern in increments of 14 N-m. The slit dimension was checked with a feeler gauge after each increment. An estimate of the amount of torque required

to load the test section sufficiently to hold the fluid pressure was calculated from a force balance. Using tabulated values of the relation between torque and bolt tension, it was calculated that 70 N-m was sufficient loading. In practice, the shims moved in early runs where this torque was applied. It was found that a torque of 110 N-m was necessary to hold the shims and yet not deform the test section.

Gaskets used to seal between the test section and the mounting flanges were made of bonded compressed asbestos. This material is rated for use at 540°C and contains a steel wire mesh for lateral strength. The trade name is Kraolite 1000 and it is manufactured by Johns-Manville. Gaskets were cut from a 1.6 mm thick sheet of the material. A slot matching the slot in the mounting flanges was cut at the center of each gasket for the fluid to pass. Grooves about 0.8 mm deep were cut into the sealing surfaces of the test section and flanges. These grooves help keep the gaskets from being pushed outward by the pressure.

The test section was mounted to the vessel using alloy steel studs 2.54 cm in diameter and 23 cm long. The studs were coarse-threaded on each end. Torquing the nuts to approximately 700 N-m was necessary in order to get the gaskets to seal. Compressed asbestos is quite resilient and it was necessary to deform the gaskets into the grooves cut in the sealing faces to prevent leakage. Because the coefficient of thermal expansion for the alloy steel studs is less than that for the 316 stainless steel test section, it was sometimes necessary to re-tighten the nuts between runs to make up for additional compression of the gaskets.

Normally, one would not expect the gasket configuration used in the test section to seal. The packing material used at the edges of the slit is in contact with the gaskets at each end of the test section. This gasket to gasket interface provides a possible leakage path. Extrusion of the packing material into the asbestos gasket apparently accounts for the success of this design. Undoubtedly, these seals could not have been maintained over long periods of exposure to high pressure and temperature. No assembly was used in more than nine runs; representing a cumulative exposure time for the gaskets of about 35 hours.

To prevent the gaskets from moving during the assembly process, they were attached to the the test section with machine screws. Holes for the screws were tapped into either side of both spacer blocks. Matching holes were punched into each gasket so that the center of the slot in the gasket lined up over the slit in the test section.

The design of the experiment calls for the test section to be heated to the same temperature as the fluid in the vessel. Strip heaters attached to the test section were used for this purpose. The heaters used are Wellman electrical resistance heaters; producing 350 watts at 120 volts. A maximum power of 950 watts was obtained by wiring the heaters in parallel to a 0-140 volt autotransformer. Iron-constantan thermocouples were spot welded to each side of the heaters. These were used in controlling the heaters so that maximum power was obtained while keeping the sheath temperature below 650C; the rated operating temperature for the chrome steel sheaths. Since most of the heat transfer from the heaters to the test section was by radiation, it was desirable to operate the heaters at the maximum safe temperature.

Four iron-constantan thermocouples were spot welded to the test section to monitor the surface temperature. Two thermocouples were placed on opposite sides of the upper and lower spacer blocks. The other two were welded to the sides of the center part of the test section. This distribution allowed some measure of the uniformity of the test section temperature.

Insulating the test section proved to be a difficult proposition. After several different methods had been tried, a cover, filled with calcium silicate insulation, proved satisfactory. This rather ungainly structure is pictured in Figure 3-3. Essentially, a rectangular cavity slightly larger than the test section was carved into two halves of a block of insulation. The interior of the cavity was lined with stainless steel sheet to prevent the insulation from flaking off from contact with the test section.

Semi-round pieces of pipe insulation were placed above and below the block to cover the lower portion of the vessel and flange, and the downstream piping to the main valve. An aluminium cover was fitted over the outside surfaces to keep the material together.

Leads from the thermocouples, attached to the test section and the heaters, were brought out through the joint between the two halves of the insulation cover. Instrumentation probes for the slit were accommodated by a hole cut for this purpose in one end of the cover. Holes were also made for the power leads to the heater and for the stagnation pressure and temperature probes.

III.1.6 Data Collection and Instrumentation

Data collection was performed automatically by an Auto-Data Eight data collection system. Driven by a microcomputer, the system can scan data channels at a maximum rate of 25 channels/sec. On the system used in these experiments, thirty data channels were available. Magnetic tape is used to store the data for later processing by a mainframe computer. Initially, 29 of the thirty available channels were used. Due to the failure of some thermocouples, the number of channels used was reduced to 22 by the time the last run was made. The Auto-Data was operated in a single scan mode. In this mode each connected channel was scanned and this block of channels recorded as a single record on the magnetic tape. It requires 50 msec for the record mark to be recorded on the tape. This means that the time between consecutive scans of a given channel varies with the number of channels connected. Account must be taken of this fact in the data reduction.

Three measurement ranges are available on the Auto-Data: 0-120 mV, 0-1.2 V, and 0-12 V. Only D-C inputs are accepted. The resolution is ± 1 in the least significant bit. For the 120 mV range this is ± 10 microvolts. All measurements, except those from the Validyne transducers and the absolute pressure reading (see below) were in the 0-120 mV range. Reduction of transducer voltage recordings to pressures, temperatures, and weigh tank mass is discussed in Chapter IV.

All temperature measurements were made using thermocouples. Strain gauge type load cells were used to measure the weigh tank mass. Both absolute and differential pressure transducers were of the strain gauge type with the exception of three differential pressure transducers which operate on the variable reluctance principal. Three regulated D-C power supplies powered the strain gauge transducers; voltage regulation was better than 0.01%. The variable reluctance transducers had their own power supply, which is described below.

Pressure taps were made in the lower wall of the slit for use in measuring the axial pressure distribution. Sense lines were connected to these taps through holes drilled into the "U"-shaped block and lower support plate. (Appendix E gives a detailed description of the installation of instrument probes in the test section). Thermocouple probes, embedded in the slit wall within 0.6 mm of the surface, were used to determine the heat transfer between the test section and the flowing fluid. Figure 3-9 is a plan view of the slit showing pressure tap and thermocouple locations. Pressure taps were spaced more closely near the exit of the slit to better determine the pressure profile in this region where the pressure was anticipated to vary rapidly. By staggering the pressure taps transverse to the flow direction, it was hoped to avoid possible effects on the downstream pressure measurements should the taps act as bubble nucleation sites. Thermocouples were placed at regular intervals to aid in the determination of the location of flashing inception.

III.1.6.1 Absolute Pressure Measurements

Three absolute pressure transducers, maunfactured by Gould-Statham, were used in the system. Stagnation pressure was measured using a model PA822-3M transducer which had a range of 0-20.7 MPa. The quoted value of non-linearity plus hysteresis is 0.25% of full scale. The resolution is stated to be infinitesimal. A strain gauge conditioning unit, manufactured by Analog Devices, is used in combination with the stagnation pressure transducer. This unit is a power supply and linear

amplifier combination. With this device, the resolution of the stagnation pressure measurement was ±1.5 kPa. None of the other measurements involved signal conditioning.

Pressure downstream of the test section is also measured using a model PA822 transducer. This transducer had a range of 0-690 kPa. Specifications are identical to those described above. The resolution of this measurement was approximately ±0.2 kPa. With the highest flowrates, this transducer was sometimes overpressurized. The overpressure rating is 200% but some degradation in accuracy may have occurred. Fortunately, this reading is relatively unimportant in interpreting the results.

One of the eight pressure taps within the test section was also instrumented with an absolute pressure transducer. A Statham PA891-3M transducer was used in these measurements. For the first set of runs with each slit size this transducer was used to measure the pressure at the exit plane (tap #8 in Figure 3-9). In the remaining runs it was used for the tap 1.91 cm from the exit (tap #4 in Figure 3-9). (The schedule of experiments is described in Chapter I). This transducer was relocated since it proved less reliable than the others that were used. An older model, Statham quote the non-linearity plus hysteresis as being 1.0% full scale. The resolution is ±9.5 kPa.

III.1.6.2 Differential Pressure Transducers

There were seven differential pressure transducers used to measure the pressure profile within the slit. An eighth differential transducer is used to measure the differential pressure across the constant area portion of the vessel. The latter measurement allows the determination of the vessel liquid inventory. Test section pressure taps will be referred to by the numbers shown in Figure 3-9.

For small pressure differentials within the test section, Validyne, variable reluctance, transducers were used. Manufactured by Validyne Engineering, Inc., these model DP-15 transducers contain only one moving part, the diaphragm. Since the pick-up coils are embedded in the case, the diaphragm can be replaced in the field, thus making it possible to vary the transducer's range. Two of the transducers used in this apparatus had a range of ±2.2 MPa, the third had a ±860 kPa range. These transducers are inherently alternating current devices. A modulator-demodulator (Validyne model CD-15) must be used with each transducer. To cut costs, two of the transducers used in measuring the pressure profile were connected to the same demodulator via an automatic switch which alternated the demodulator between transducers with each Auto-Data scan.

The remaining four test section differential transducers, plus the vessel level transducer were of the strain gauge type. Gould-Statham model PM8142±1000 transducers were used for the test section. These transducers had a range of ±6.89 MPa. The quoted value of non-linearity plus hysteresis is 0.1% of full scale. Resolution is ±1.7 kPa in this application. Vessel level measurements were made with a model PM8142±3.6 transducer. This transducer had a range of ±24.8 kPa. Specifications were as quoted above but with a resolution of ±6 Pa.

Table 3-2 describes the arrangement of the pressure transducers. Two arrangements are shown. The transducers were rearranged after the results of the first experiments had been analyzed so as to take better advantage of the range of each transducer. In addition, only two Validyne transducers were used in the first arrangement. The lower range transducer was fitted with a ±22 kPa diaphragm and used to replace the vessel level transducer which was under repair by the manufacturer.

Provisions were made for flushing all the pressure sensing lines in the equipment with water. For the vessel level measurement, the level determination is made assuming all vertical sections of the line are filled with water. Because the static head due to water in the sense lines was insignificant in comparison to the pressures being measured, the other measurements are not nearly as susceptible to error if the lines were not water filled. To improve the dynamic response it was done anyway. Filling of the lines was accomplished by means of a branch in each sense line which ran to a valve connecting to the water supply line.

III.1.6.3 Load Cells

The mass of the weigh tank was measured by means of load cells which were mounted on the weigh tank frame as described above. Strain gauge type load cells, manufactured by Gould-Statham were used. These were model UC-3 transducers which measure 0 to 60 grams in compression. When used in combination with UC-4-500 adapters, each cell was able to measure 0 to 230 kg in tension. The non-linearity plus hysteresis of the load cells with adapters is 0.5% full scale. Resolution is quoted as being as infinitesimal but practically the resolution was about ±0.03 kg for the present system.

III.1.6.4 Thermocouples

Three different types of thermocouples were used in the apparatus. Temperature measurements required during the heat-up phase of the experiment were made using iron-constantan (ANSI Type J) thermocouples. These included vessel temperature, test section surface temperature, and strip heater sheath temperature. For temperature measurements within the test section, copper-constantan (ANSI Type T) and chromel-constantan (ANSI Type E) thermocouples were used.

A Honeywell, twenty-four channel, print wheel, chart recorder was used to record data from the iron-constantan thermocouples. Temperature measurements required for heater control during the heat-up phase was displayed on this device. A total of thirty-four thermocouples were needed so a switching system was built so that the chart recorder could monitor all of them. The switching system also allowed any single channel to be measured by the Auto-Data should greater accuracy be needed.

Originally, it was intended to use the transient temperature measurements from within the test section to determine the heat flux at the slit wall. This type of analysis proved unfruitful for reasons discussed in Chapter IV. Qualitative information about the temperature profile in the slit wall was obtained by placing the thermocouple junctions as close to the slit wall as possible. Measurement locations are identified in Figure 3-9. Two types of thermocouple were tried for this purpose.

The first type were copper-constantan with exposed junctions. These probes were made from 36 gauge wire in a 1.0 mm diameter stainless steel sheath. Time constants for these thermocouples, as installed, were typically about 2 seconds. The second type used were chromel-constantan, which have a higher Seebeck coefficient than other types of thermocouples, allowing greater resolution. To achieve a faster response time, these thermocouples were obtained with 0.25 mm sheaths; the tip of which forms the measuring junction. The expected time constant is between 0.3 and 0.5 seconds. High temperature epoxy was used to bond most of the thermocouples into the test section (see Appendix E for details on assembly procedures). In many instances the epoxy performed poorly, decreasing the thermal contact between test section and temperature probe, thus increasing the time constant.

The severe thermal environment caused one chromel-constantan and three copper-constantan thermocouples to fail. Three more thermocouples were broken in mounting or removing the test section. The 0.25 mm sheath thermocouples were particularly fragile. Copper-constantan thermocouples are subject to oxidation in air at the equipment operating temperatures, and should probably not have been used.

III.2 Experiment Operating Procedure

In this section the theory and practice of operating the experimental apparatus are discussed. Figure 3-1 identifies the key components of the system which are referred to in this discussion. Most of the procedure was concerned with heating the water and the vessel to a uniform temperature. Pressure

within the vessel had to be controlled during the heating process to ensure that steam was not formed in quantities which could not be condensed by the reflux condenser. In addition, the test section temperature was to be adjusted to approximately that of the water. Prior to initiating flow through the test section the water was boiled for ten to fifteen minutes to remove dissolved gasses. The internal vessel heater was used for this part of the process. Heater power had to be controlled carefully so as to allow the reflux condenser to hold the vessel pressure constant during boiling.

Water for the experiment was supplied by distilling tap water in a single stage still. The water was stored in plastic bottles open to the air. A small centrifugal pump was used to fill the vessel. Air was vented into the room through a vent line connected to the upper vessel level pressure tap penetration. The valve on the water fill line was closed when the vent line began to discharge water. With the pump still running, the valves were then opened which flushed the pressure sense lines with water. A line was considered full once the vent line began to pass water when only the flush valve for that sense line was open.

Having flushed the sense lines, the system was allowed to stand so that the vessel level could drain through the vent line into the weigh tank. When no more water passed through the vent line the level in the vessel was down to the upper tap penetration. The vent line valve was then closed. At this point the electrical bias on all the differential pressure transducers was adjusted to zero. To allow for the expansion of the water during heating, the vessel level was then lowered to a point which was appropriate for the initial conditions of the experiment to be performed. This level was calculated on the basis of a ratio of the saturated water density at the planned temperature and the density at room temperature. Water was drained through the test section by opening the main valve. Vessel level transducer readings were used to determine when the correct amount of water had been drained.

Prior to the application of pressure to the system, the block valve for the outlet pressure transducer was closed. At this point, the correct operation of all the instrumentation, and the Auto-Data was verified. Readings for each channel to be used in the run were recorded in the experimental checklist. At this point all differential pressures should have read zero, absolute pressures should have read atmospheric pressure plus the head of water in the vessel which was read by the level transducer. Thermocouples should all have shown room temperature. Instrument readings were written down to provide verification of the instrument's operation in the case that some anomaly was found in the data.

Before the heaters were turned on, flow of cooling water through the reflux condenser and cold trap was started. Tap water at approximately 18°C was used. Flow was controlled by valves connecting to the building water supply. Gas pressure was then applied to the vessel. Typically heating was begun under about 1.4 MPa of nitrogen pressure. This limited the amount of boiling in the vessel prior to reaching the desired pressure.

The vessel was heated from the bottom up. This was necessary since the test section was not insulated as well as the vessel and even with the strip heaters the rate at which the test section could be heated was lower than that for the vessel. At the start of heating, all the heaters except the upper three pairs on the vessel were turned to full power. The upper heaters were operated at about 10% power (200 watts per pair) to prevent an excessive gradient in the vessel temperature. The upper part of the vessel tended to be heated by natural circulation of the water anyway. Keeping the upper elevations of the vessel cooler helped avoid flooding of the reflux condenser by condensing steam created from subcooled boiling on the internal heater and lower vessel walls.

As heating progressed, power to the test section heaters was reduced to maintain the temperature of the heater sheaths below the recommended limit. Water temperature within the vessel was

monitored on the chart recorder via the vessel's internal thermocouples. Vessel pressure was increased as the water temperature rose so as to keep the water subcooled. Typically the pressure within the vessel was maintained approximately 1 MPa above the saturation pressure corresponding to the highest measured water temperature.

This heating procedure usually resulted in the water temperature at the top of the vessel being 30°C cooler than at the bottom. As the test section reached within 5 degrees of the required temperature, the test section heaters were cut back to 30% power, and the lower vessel heaters were reduced to 25%. The upper three pairs were raised to 25%. Power to the vessel internal heater was cut to prevent excessive boiling as the water approaches saturation.

Power to the heaters was then adjusted to bring the vessel and the water to an isothermal state. To avoid overloading the reflux condenser, the water was heated in a subcooled state. This resulted in the nitrogen pressure being to high to boil the water once the required initial temperature was reached. Pressure was reduced by slowly bleeding nitrogen off through the purge valve on the bottom of the cold trap. This must be done carefully so as not to pull steam into the gas line. The gas was bled in short, slow releases of approximately 1 second duration. During this process, the pressure in the vessel was seen to drop as the valve was opened and then slowly recover after the valve was closed. This recovery is due to two mechanisms. First, nitrogen gas comes out of solution with the water. Second, when the gas and water vapor mixture are bled into the condenser, the total pressure above the gas-liquid interface drops. Since the partial pressure of water vapor also drops, liquid must evaporate to restore equilibrium. Fortunately, after a few releases the pressure did not rise back to the original value and the bursts began to reduce the pressure.

Once the saturation point was reached, the gas block valve was closed; isolating the gas supply form the vessel. Saturation was characterized by an inability to further reduce the vessel pressure as well as the agreement between the pressure shown on the Heise gauge and the saturation pressure corresponding to the measured temperature. Boiling was begun by turning the vessel internal heater back on. The external heaters' power was reduced to almost zero. Evidence of boiling in the vessel could be seen in fluctuations in the vessel level reading. These fluctuations were associated with level swell. During boiling, the vessel temperature and pressure remained roughly constant: the heater power was adjusted if necessary. External and test section heater powers were also adjusted so as to bring the vessel wall and test section temperatures close to that of the water. Two to three minutes after boiling was begun, the Auto-Data was started. This provided a pre-run data set, allowed verification that the Auto-Data was functioning properly, and put a leader on the data tape to be used during the data reduction to determine the scan rate. The chart recorder was set to monitor the vessel internal and test section external thermocouples. This provided a visualization of the temperature profile within the vessel. Once the profile was uniform at the required temperature, power to the heaters was cut.

The Auto-Data had to run at least 11 minutes before the run was started so as to have sufficient data to determine the scan rate. Approximately 10 minutes after the Auto-Data was started, provided the vessel temperature was uniform at the correct level, the gas supply pressure was set. When the 11 minute period was over, the gas block valve was opened and the outlet transducer vent line valve was closed. The water in the vessel was now at the required condition of subcooling. Opening the main valve, started the test.

Immediately after flow started, the output trace from the differential pressure transducer at the exit plane at the test section was photographed on the oscilloscope. Since this transducer was the variable reluctance type, with a frequency response of 5 kHz, it was capable of recording pressure rapid fluctuations present at the exit plane. As the picture was taken, the outlet transducer block valve was opened so measurements of the outlet pressure could be recorded.

The gas block valve was closed before the vessel became empty. This was to reduce the pressure behind the nitrogen being blown into the weigh tank once the vessel was empty. Usually, this was

done when the level reached about 10% of it's original value. The main valve was closed immediately when nitrogen started to escape into the tank. The Auto-Data was then stopped; terminating the run.

Table 3-1

Key to Figure 3-1

Component Number	Description
1	Nitrogen cylinder
2	Hand loaded regulator
3	Gas flow contoller
4	Heise pressure gauge
5	Cold trap
6	Gas line purge valve
7	Gas block valve
8	Safety relief valve
9	Reflux condenser
10	Vessel vent valve
11	Vessel level transducer
12	Test section
13	Outlet transducer block valve
14	Outlet transducer vent valve
15	Main valve
16	Weigh tank
17	Jet condenser nozzle (4)
18	Water block valve
19	Pump
20	Water supply

Table 3-2

Pressure Transducer Connections

Runs #1 through #30

Measurement Location (Tap #)*	Upstream Connection (Tap #)*	Transducer Used
1	Stagnation	Statham PM8142±1000 (s/n 649)
2	Stagnation	Statham PM8142±1000 (s/n 650)
3	Stagnation	Statham PM8142±1000 (s/n 651)
4	Stagnation	Statham PM8142±1000 (s/n 652)
5	1	Validyne CD-15 (s/n 50139)
7	1	Validyne CD-15 (s/n 50140)
8	None (absolute)	Statham PA891-3M

Runs #31 through #101

Measurement Location (Tap #)*	Upstream Connection (Tap #)*	Transducer Used
1	Stagnation	Statham PM8142±1000 (s/n 649)
2	1	Validyne CD-15 (s/n 50141)
3	1	Validyne CD-15 (s/n 50139)
4	None (absolute)	Statham PA891-3M
5	Stagnation	Statham PM8142±1000 (s/n 650)
6	Stagnation	Statham PM8142±1000 (s/n 651)
7	Stagnation	Statham PM8142±1000 (s/n 652)
8	7	Validyne CD-15 (s/n 50140)

* *Refer to Figure* 3-9 for *pressure tap locations*

NB: Calibration data for pressure transducers given in appendix C.

Figure 3-1
Schematic of Experimental Equipment

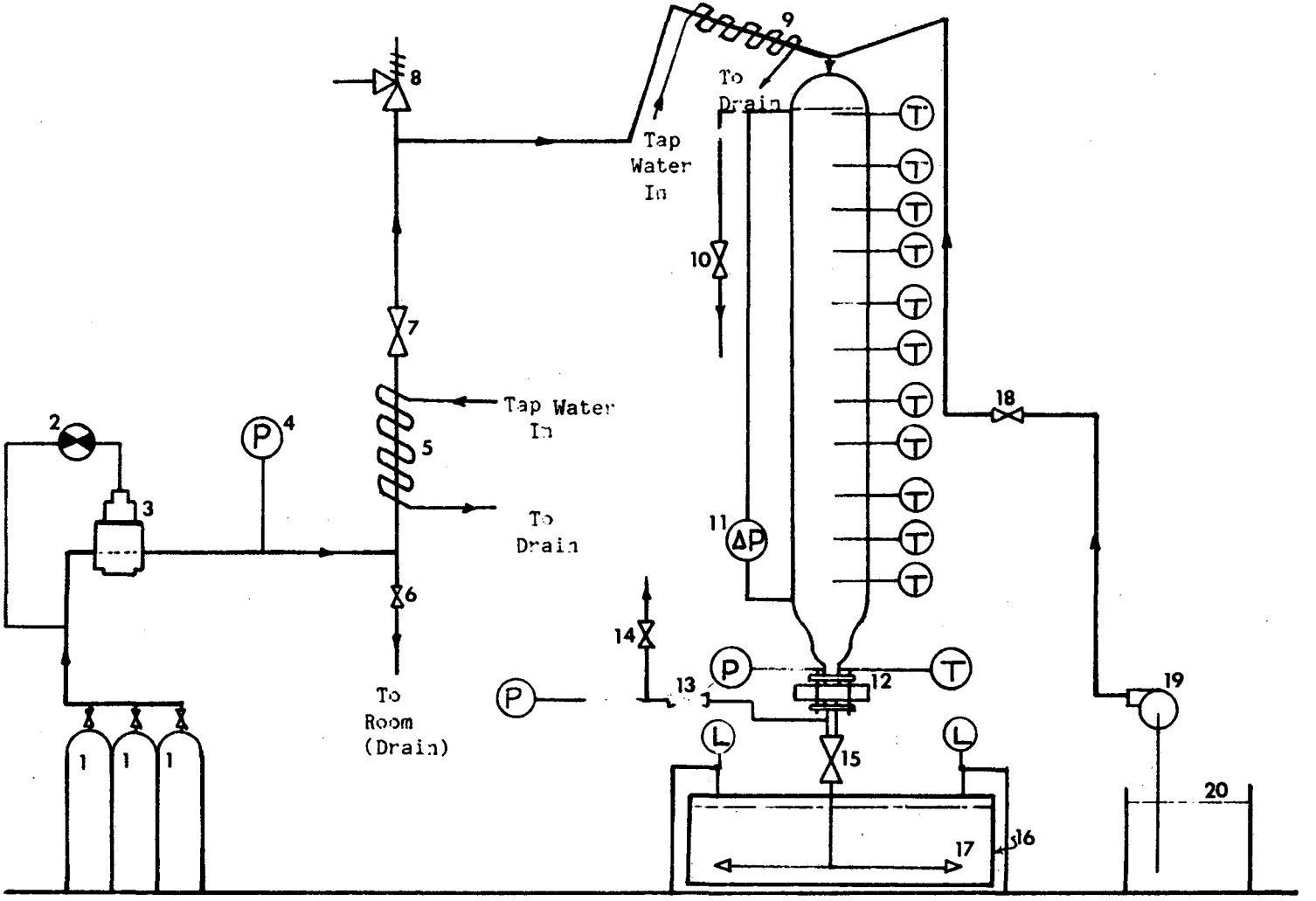

XBL 838-484

Figure 3-2
Experiment Control Panel

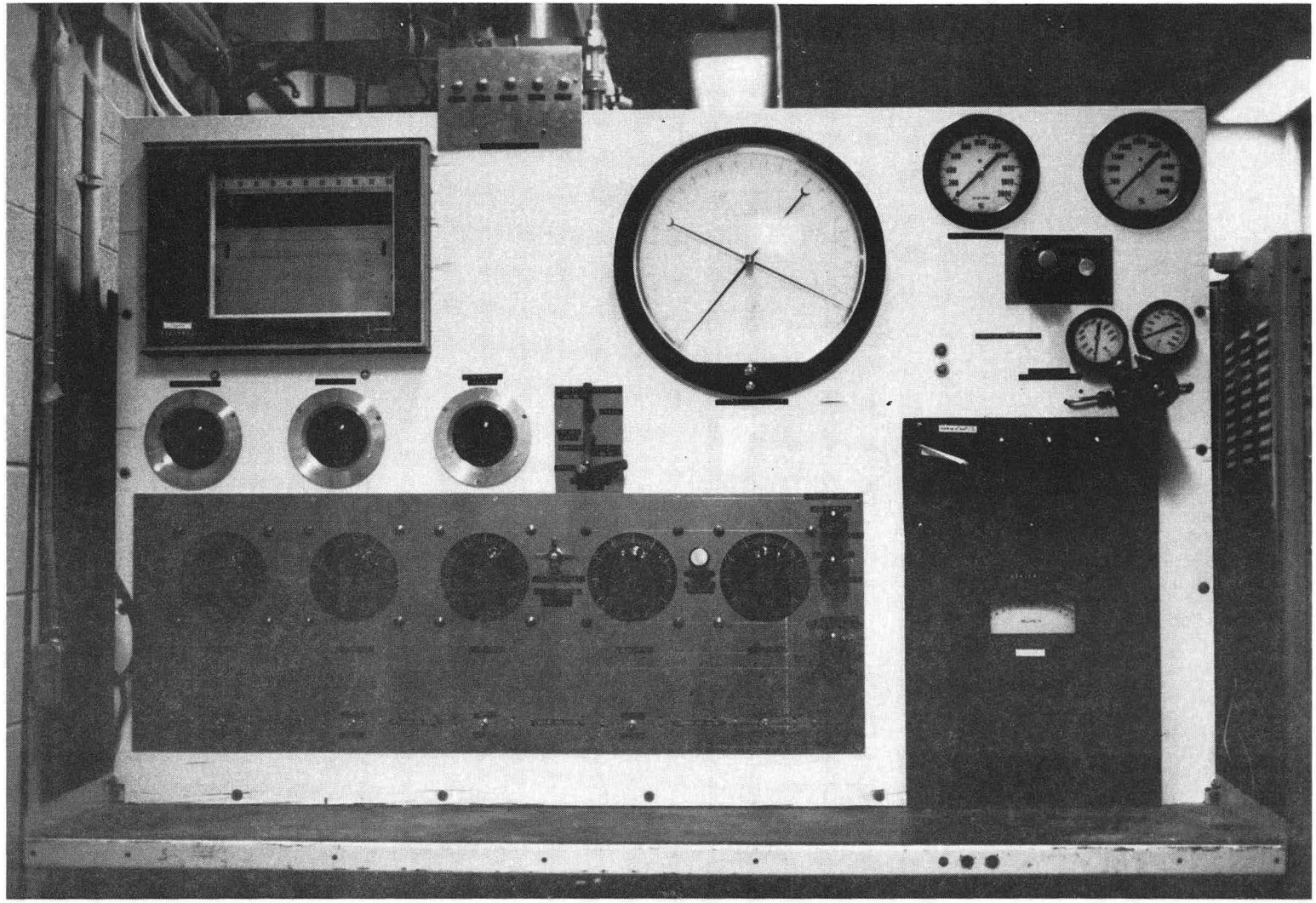

XBB 838-6753

Figure 3-3
Overview of Apparatus

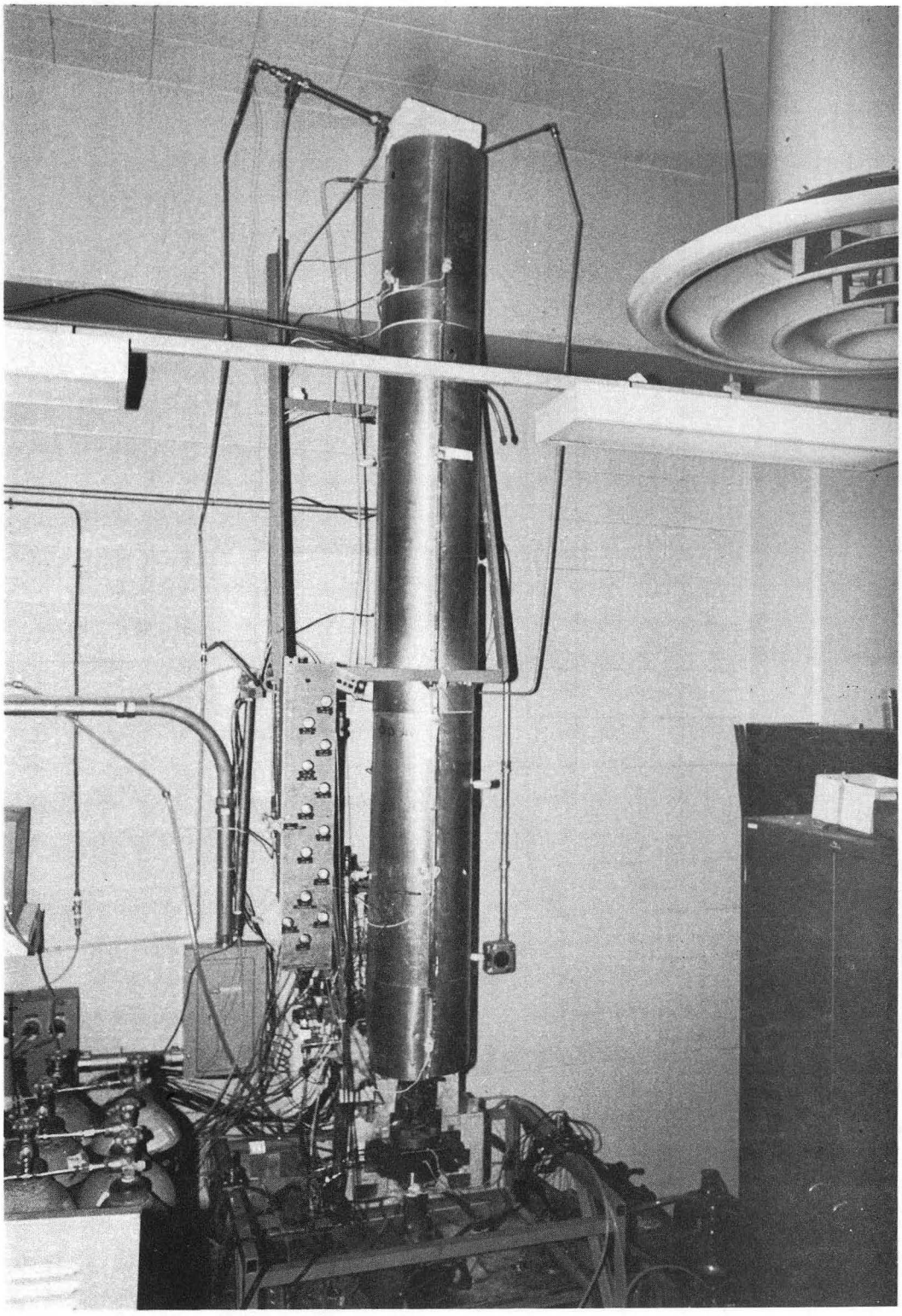

XBB 838-6754

Figure 3-4
Vessel Internal Heater Inslallation

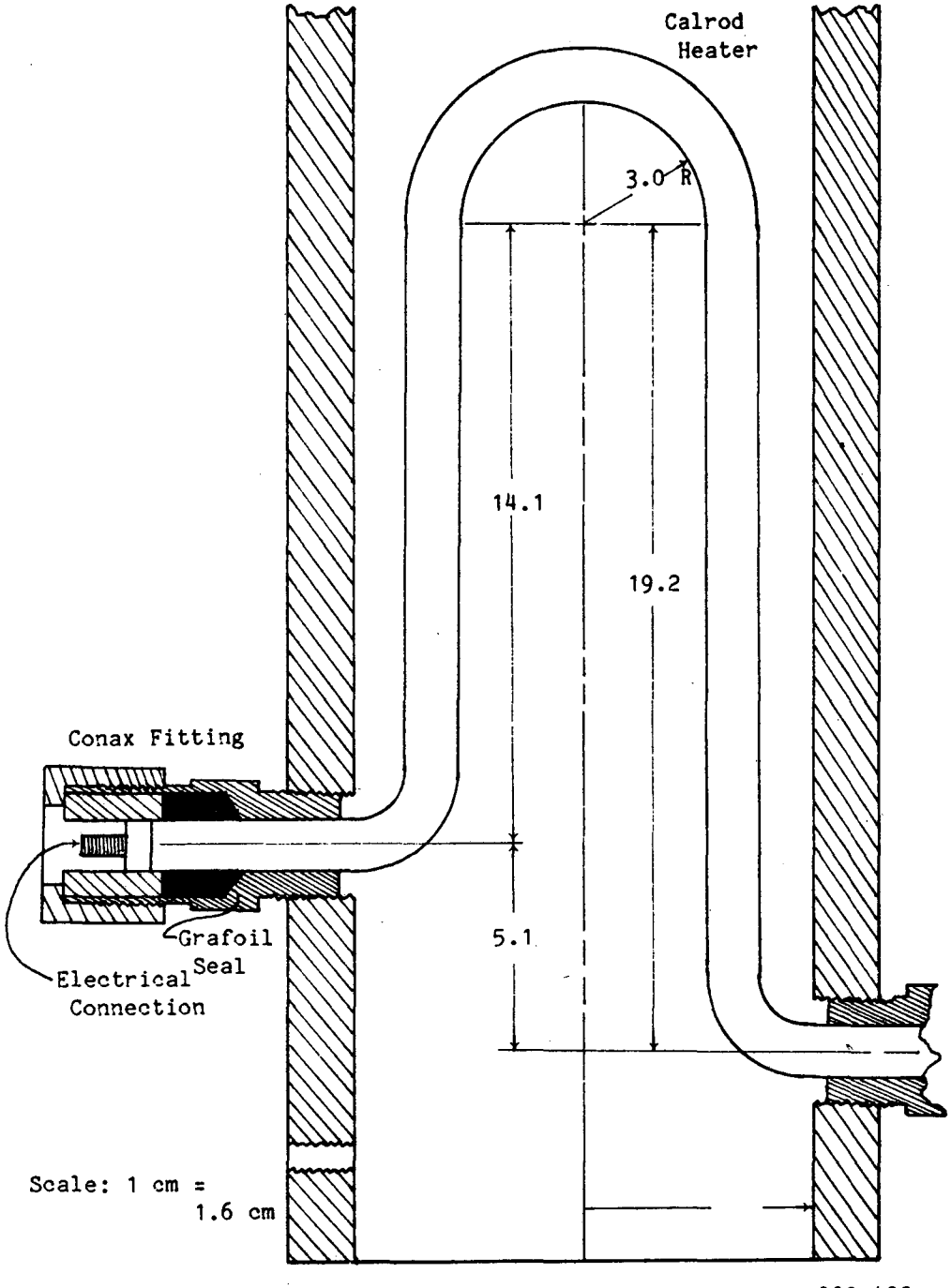

XBL 838-485

Figure 3-5
Jet Condensing Nozzle

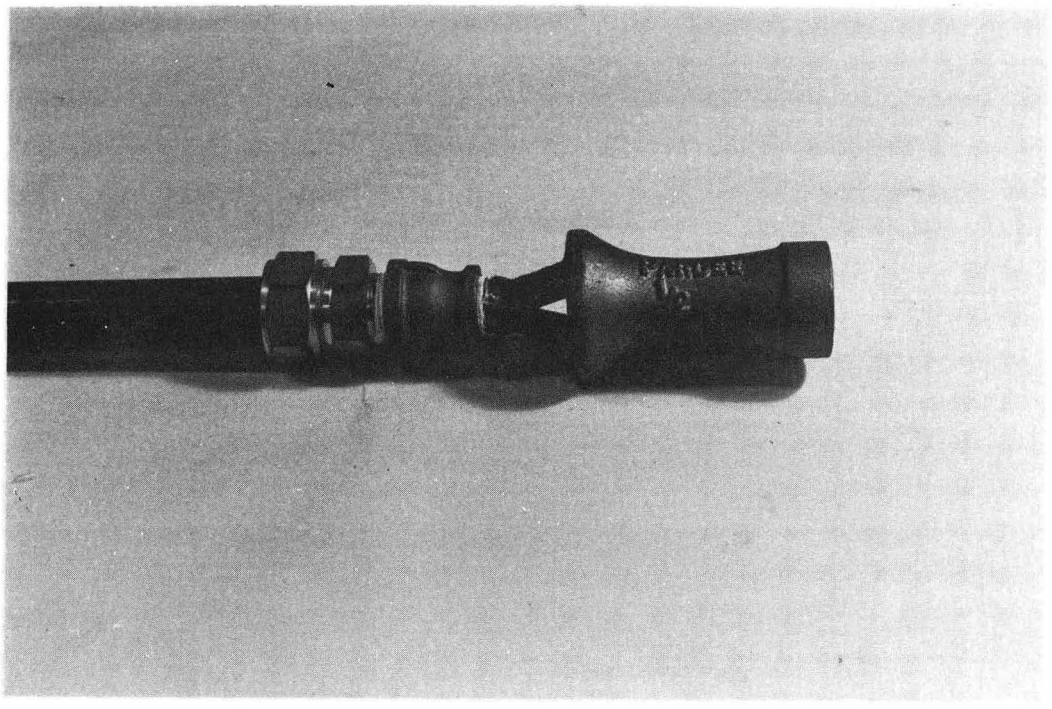

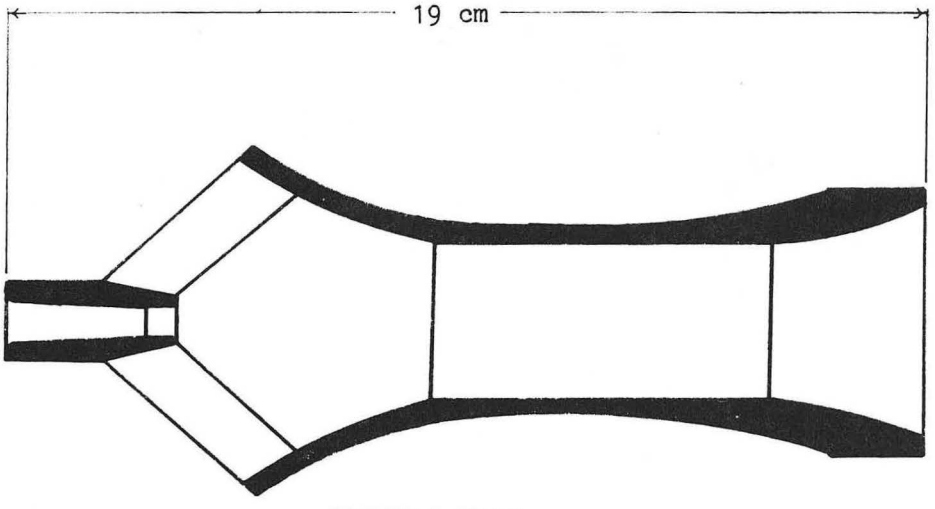

SECTION VIEW

XBB 838-6755

Figure 3-6

Test Section Assembly View

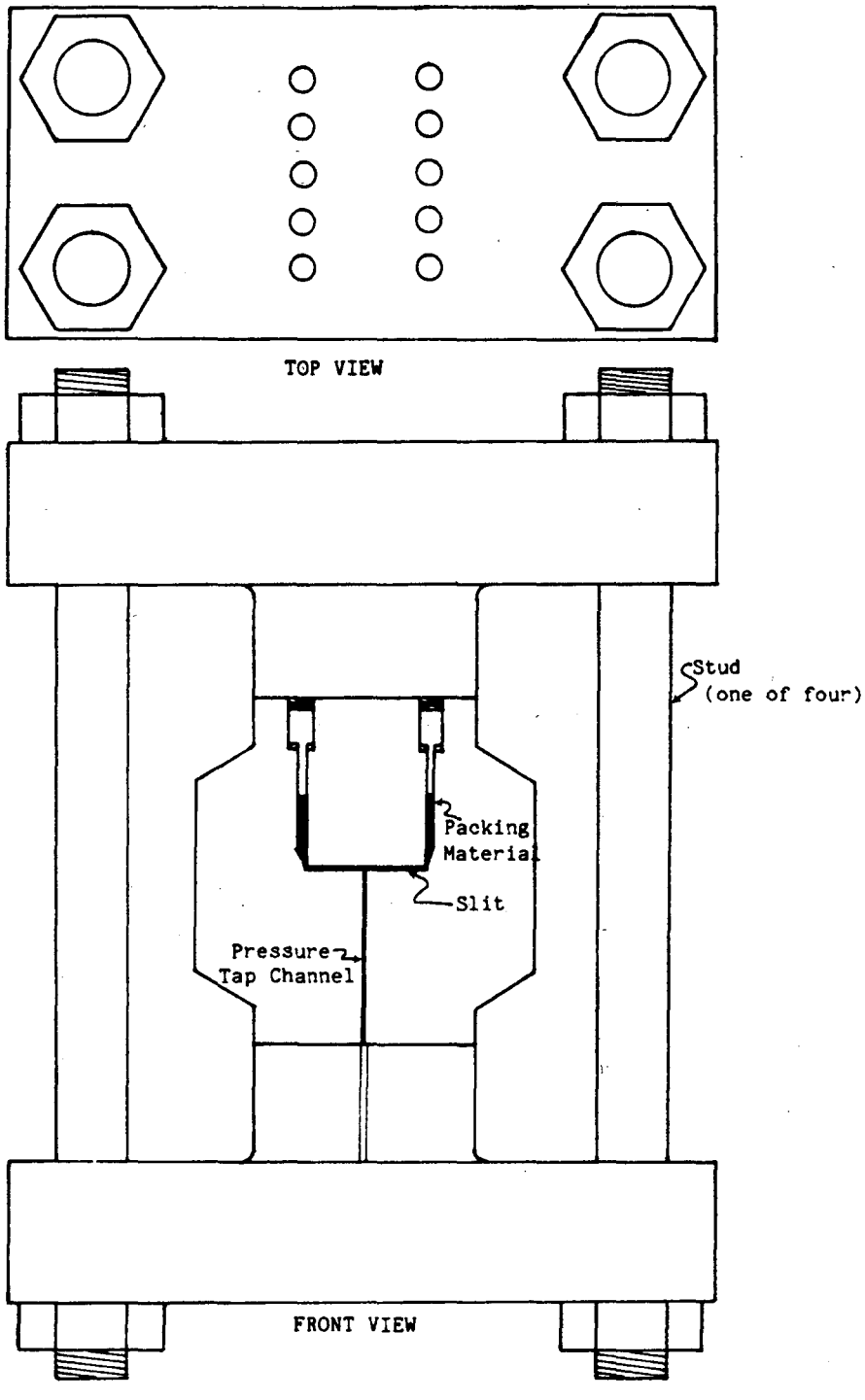

XBL 838-486

Figure 3-7
Test Section Exploded View

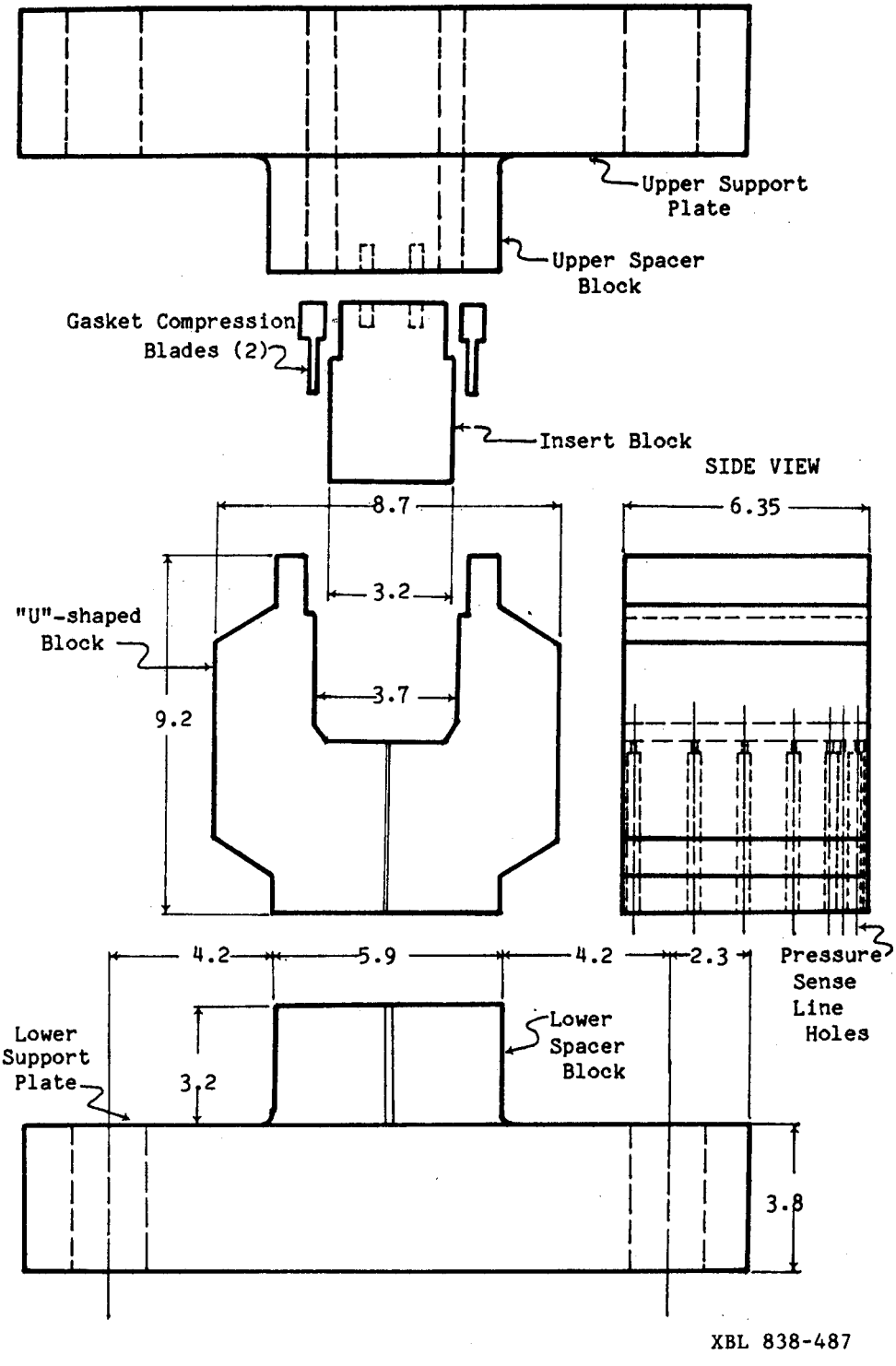

Figure 3-8
Completed Test Section

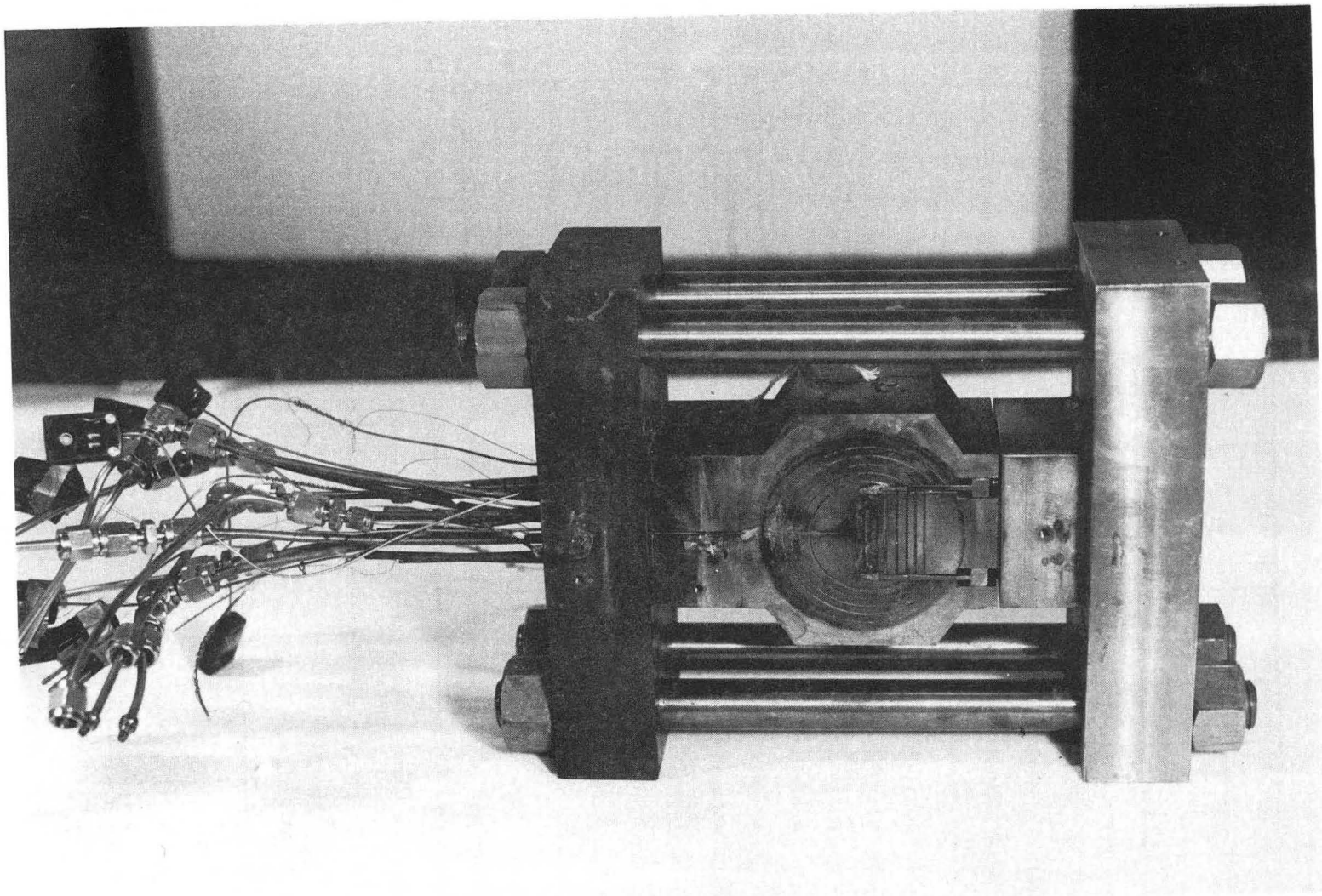

XBB 838-6756

Figure 3-9
Test Section Instrumentation, Plan View

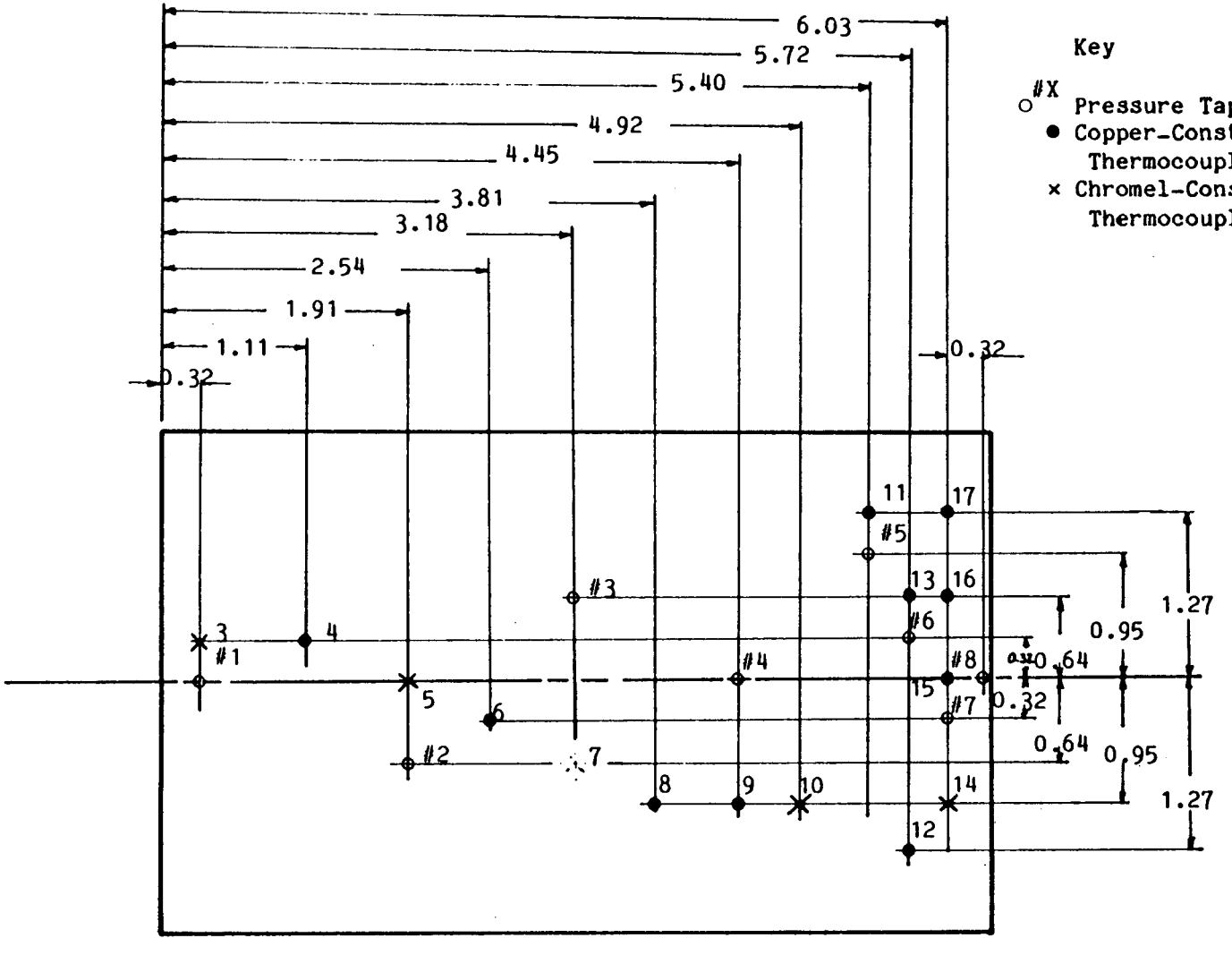

XBL 838-488

CHAPTER IV

Data Reduction and Results

In this chapter the results of the experimental program are presented. Methods applied for the reduction of raw data, obtained by the data collection system, are described in the first section. It was apparent, both from examination of the test section, and the results of the data reduction, that deformation of the test section had occurred during the early part of the experimental program. This deformation resulted in slit sizes which were somewhat smaller than intended. After the problem was discovered, the test section was repaired. Runs made when the test section had a smaller opening dimension than the thickness of the shims used, required calculation of a correction factor for the mass flux. Calculation of this correction is described in the second section. The chapter concludes with a discussion of the experimental results. Comparisons between the data and two-phase critical flow models are discussed in Chapter V. These comparisons shed additional light on the interpretation of experimental results. Discussion of these, more speculative, observations has been postponed until after the models used have been described in Chapter V.

IV.1 Reduction Program

Data reduction was done on a CDC 7600 computer in two sequential steps. Two steps were used to facilitate storage of the data. In the first step, data was rewritten in a more convenient form than that produced by the Auto-Data Eight data collection system (described in Chapter III). Actual reduction of the data was done as a separate step as a matter of convenience. Reduction involved the conversion of raw data, in volts or millivolts, to pressures, temperatures, and weigh tank mass. Stagnation state (density and enthalpy), test section pressure profile, and mass flowrate were also calculated by this program.

The Auto-Data writes voltage data (in millivolts) on 7 track magnetic tape. Formatting is IBM compatible with a density of 556 bits per inch (bpi). More efficient storage and handling of the data was accomplished by running a program on the CDC 7600 which read the Auto-Data tape and stored the information on a data tape in CDC compatible format with a density of 6250 bpi. In this manner, the 20 reels of tape that were produced by the Auto-Data in the course of these experiments have been reduced to less than 60 percent of a single reel. Each data file was assigned an address on the tape so that data from any given experiment may be accessed at random. The program also wrote the raw data onto microfiche for manual inspection.

Another function of the first program was the determination of the elapsed time between consecutive readings of the same channel. As was mentioned in Chapter III, this information was derived from data taken by the Auto-Data prior to initiating flow through the test section. The program scanned this section of the data until the first change in the Auto-Data clock reading was detected. Clock readings, in hours and minutes, are recorded at the beginning of each scan of the channels in use. This change in the minutes reading was taken as the arbitrary zero. The data were then scanned until ten minutes was seen to have elapsed on the clock. Intervening scans were counted. Dividing the scan count into ten minutes gave the time between scans which was then recorded at the beginning of each data file. Since the change in clock reading was only detected to the nearest scan, there is a maximum error in the calculation of one scan in the interval. Thus the calculated time between scans has an associated maximum error of ± 1.7 msec.

The data reduction program has five main sections. Results calculated by the program were printed and also stored on magnetic tape so that printed output could be reproduced without re-running the program. Reduced data was also made available for computer plotting in this manner.

IV.1.1 Reduction of Basic Measurements

The first section of the data reduction program reads the data as formatted by the first program. Millivolt readings for each channel at each time step were then converted to temperature, pressure, differential pressure, weigh tank mass, or equivalent volume discharged from the vessel; as was appropriate. Equations used for this conversion are detailed in Appendix C. Reduction of the data proceeded stepwise, with the results printed at each time step. Stagnation pressure and temperature, pressure measurements within the test section, and other measurements required for the determination of the mass flowrate, were stored in arrays as a function of time for processing by subsequent sections.

Stagnation state was determined in the second section of the program. Readings from the stagnation pressure transducer and thermocouple were input into a subroutine which employs the state equations for subcooled water as given in the 1967 ASME Steam Tables. Specific enthalpy and density of the fluid entering the test section were thus calculated. Density results were required for the mass flowrate calculation.

Pressure profile within the test section was calculated for each time step. The calculation was made by adding the measured pressure at the upstream tap location to the pressure measured by each differential transducer. For some of the measurements, this was the stagnation pressure, for others, the pressure at some location within the slit, calculated from a differential pressure reading. Table 3-2 shows the upstream bias of each transducer. Pressure tap locations are shown in Figure 3-9.

IV.1.2 Nitrogen Density Determination

Nitrogen density within the vessel could not be measured during an experiment. An estimate of the density at each time step was required in order to calculate the mass flowrate. Details of the mass flowrate calculation are given below along with estimates of the impact that errors in estimating the nitrogen density had on the calculated flowrates.

Since the pressure in the vessel was known, as was the state equation for nitrogen, the problem of estimating the density was reduced to that of estimating the temperature of the nitrogen in the vessel. A very simplistic model has been used to estimate the nitrogen temperature. It has been assumed that the portion of the vessel not filled with water contains only pure nitrogen at the measured stagnation pressure. Neglecting the partial pressure of water vapor lead to an overestimate of the nitrogen density or no more than 36% (assuming an ideal gas) even if water vapor fills the available volume. Further, it has been assumed that nitrogen entered the vessel at room temperature and is heated only by contact with the walls. The vessel walls are insulated and have a large heat capacity relative to the gas, so it was assumed that the walls remained isothermal at the water stagnation temperature.

Under these assumptions, the temperature of the nitrogen could be calculated once the heat transfer coefficient between the wall and the gas was known. The procedure used was to calculate the specific enthalpy from an energy balance and then apply the equation of state to calculate the temperature. Specific enthalpy was given by the equation,

$$h^N(t) = \frac{\int_0^t \dot{m}_{in}^N h_{in}^N dt + \int_0^t \dot{q}''_w A_w dt + M_0^N h_0^N}{M_0^N + \int_0^t \dot{m}_{in}^N dt} \qquad (4\text{-}1)$$

M_0^N, the original mass of nitrogen in the vessel was calculated assuming that the available volume is that above the upper pressure tap. $\dot{m}_{in}^N$, the inlet mass flowrate of nitrogen was determined from a

mass balance on the vessel. Account was taken for the expansion of gas in the vessel due to heating. The resulting equation was:

$$\dot{m}_{in}^{N} = \rho_{in}^{N} \left[\frac{\dot{m}}{\rho_0} - M^N \frac{dv^N}{dt} \right] \tag{4-2}$$

Where dv^N/dt is the time rate of change of the nitrogen specific volume due to heating.

To estimate the heat transfer coefficient, two further assumptions were made. First it was assumed that the water mass flowrate was constant. Second, it was assumed that the gas temperature decreased linearly from the stagnation condition to the final value T_f. The method used to calculate T_f is described below. Clearly, the latter assumption was incorrect. With this as a first approximation, one could then proceed to make successively better estimates. One iteration was found sufficient to obtain accuracy consistent with the remainder of the calculation

Heat transfer from the vessel walls into the gas was assumed to be by free convection. The bulk velocity of the gas was small (approximately the liquid-gas interface velocity) and does not exceed 5 cm/sec in any run. It was usually more on the order of 1 cm/sec. Using the model of natural convection in a long (L/D $\leq$ 40) vertical slot given by Raithby and Hollands [93] it is assumed that:

$$Nu \propto (Gr\ Pr)^{\frac{1}{3}} \tag{4-3}$$

The heat flux to the gas is then written as:

$$\dot{q} = \pi h' D L_g (T_w - T^N) \tag{4-4}$$

where,

$$L_g = (L - L_w)$$

h' is some proportionality constant which would include any forced convection effects which may have been present. L_g is the height of the gas filled portion of the vessel; D the vessel diameter. The data reduction program calculated h' for each run in the manner outlined below. Equation (4-1) was then applied to estimate the nitrogen temperature at each time step.

The temperature of nitrogen in the vessel at the end of each run, T_f, was calculated from the data. Differential pressure measurements, taken immediately after all the liquid had discharged from the vessel, allowed the determination of the density of the gas remaining. Combined with the stagnation pressure data, this allowed the calculation of T_f.

Mass flowrate of gas into the vessel was obtained from equation (4-2) until the gas block valve was closed. That time, t_s, could be identified from the data. After that time, the inlet gas flow was taken to be zero. With the assumption that the nitrogen temperature varies linearly with time, one writes:

$$T^N(t) = T_0 + \frac{T_f - T_0}{t_f - t_0} (t - t_0) \tag{4-5}$$

Where t_f is the time at which T_f was determined. T_0 is the fluid stagnation temperature at the time flow through the test section was initiated, t_0.

Using equations (4-2), (4-4), and (4-5) in equation (4-1) one obtains:

$$h^N(t_f) = \frac{3h'V}{2Dt_f} a^{\frac{4}{3}} \left[t^{\frac{8}{3}} - t_s^{\frac{8}{3}} \right] + h^N(t_s) \tag{4-6a}$$

where,

$$a = \frac{T_f - T_0}{t_f - t_0} \tag{4-6b}$$

and,

$$h^N(t_s) = \left\{ h_{in}^N \rho_{in}^N \frac{V}{t_f} \left[t_s - \left(\frac{T_0}{a} + \frac{V_0}{V} t_f \right) \ln \left(1 - \frac{a_0}{T_0} \right) \right] \right.$$

$$\left. + \frac{3h'}{2D} \frac{V}{t_f} a^{\frac{4}{3}} t^{\frac{8}{3}} + M_0^N h_0^N \right\} \div \left\{ \rho_{in}^N \frac{V}{t_f} \left[t_s - \right. \right. \tag{4-6c}$$

$$\left. \left. \left(\frac{T_0}{a} + \frac{V_0}{V} t_f \right) \ln \left(1 - \frac{a}{T_0} t_s \right) \right] + M_0^N \right\}$$

V is the volume of the vessel above the lower pressure tap and V_0 is the volume available above the upper tap. Solution of (4-6a,c) for h' is straight forward. The resulting value was used to evaluate $h^N(t)$ at each time step using equation (4-1). Integrals were approximated as sums over previous time steps.

It is important to note that the simple form of equations (4-6) results from assuming ideal gas behavior for N_2 in calculating dv^N/dt in equation (4-2). Such a restriction was not imposed in evaluating $h^N(t)$ at each time step. Rather the state equation,

$$V^N = \frac{Z^N(P,T)\, R^N T}{P} \tag{4-7}$$

was employed. Data for the compressibility, Z, was interpolated from tabulated data. The same formulation was used to evaluate the density at each time step once (4-1) had been solved for all times.

IV.1.3 Mass Flowrate Calculation

Initially, three methods were used to calculate the mass flowrate for each experiment. Two of the methods relied on the same data, namely that from the vessel level transducer. Both of these calculations required the nitrogen density information which was calculated as described above. The third method relied on direct measurement of the mass of water in the condensate tank. This method was completely independent of the other two. and served as a check on the other methods. Due to considerations which are described below, the discharge volume method, which relied on vessel level data was the most reliable. In all cases the flowrate was calculated by numerical differentiation of the vessel mass history.

IV.1.3.1 Differential Pressure Method

This method involved a traditional evaluation of mass effluence based on transient measurements of the reservoir level. Referring to Figure 4-1 it is seen that the differential pressure, P, measured by the transducer is given by:

$$\Delta P = -\int_C \rho(y)\,\frac{\bar{g}}{g_c}\cdot d\bar{y} \tag{4-8}$$

since the integral over the closed path, including the transducer, must be zero; otherwise fluid in the sense lines would accelerate. Referring to the dimensions given in the figure, and assuming that the nitrogen density could be approximated as being constant in space, the integral in (4-8) can be evaluated as:

$$\Delta P = L\rho_w^0 - \int_0^{L_w} \rho(z)dz - \rho^N(L - L_w) \tag{4-9}$$

Where ρ_w^0 is the density of the water in the sense lines; with the superscript zero indicating evaluation at room temperature. Dimensions are shown in Figure 4-1. The first term on the right hand side of equation (4-9) arises from the differential pressure contribution from water in the sense lines. Vertical portions of the sense lines were kept at least 30 cm from the outer cover of the vessel insulation. This ensured that fluid in those portions of the sense lines had a uniform density. Sections of the sense lines protruding from the insulation supported a temperature (and therefore density) gradient. These sections were maintained horizontal so as to contribute nothing to the integral (4-8).

As can be seen from the data, water in the vessel invariably cooled as the run progressed. Traces from the vessel internal thermocouples showed that the water cooled from the top downward. In some of the longer runs (eg. #15, #49) this cooling was as much as 10°C over the ten minute duration of the run. More typically, the drop in temperature was 4°C during a run. Since there was some error in the nitrogen density determination and in the measurement of vessel diameter, D, accounting for variations in water density, which were at most 1.5%, seemed unwarranted. Thus the mass of water in the vessel at each time step was given by:

$$M(t) = \rho(t)\,\frac{\pi D^2}{4}\left[\frac{\Delta P - L\left(\rho_w^N - \rho^N(t)\right)}{\rho(t) - \rho^N(t)}\right] \tag{4-10}$$

IV.1.3.2 Discharge Volume Method

While related to the method described above in that it relied upon the same data, this method is more direct. As described in Appendix C, the level transducer was calibrated by two different procedures. The first, using a water manometer, provided the calibration curve used to reduce data for the previous method. The second, based on a measurement of the volume of water contained in the vessel, is the basis for the method described below.

Input data for this method is the equivalent volume of water (at 20.5°C) that had been discharged from the vessel at the end of each time step. This data is represented symbolically as VD(t). Recall from Chapter III that the level transducer was balanced to read zero with the vessel full at the start of each run. Prior to starting flow through the test section, the water in the vessel is hot and thus less dense; therefore, $VD(t_0) \neq 0$. Once flow began, account was taken of the fact that fluid leaving the vessel was replaced by nitrogen. Assuming the gas density to be uniform, a mass balance on the

vessel gave:

$$M(t) = \left[V - VD(t_0) \frac{\rho_w^0}{\rho_0 - \rho_0^N} \right] - \int_{t_0}^{t} \frac{dVD}{dt} \left(\frac{\rho_w^0}{\rho - \rho^N} \right) dt \qquad (4\text{-}11)$$

Where the first term on the right hand side of (4-11) is the mass of water in the vessel at t_0. The second term is the evaluation of the mass discharged up until time t. d(VD)/dt was taken to be the slope of the best fit line (in the least-squares sense) to five data points centered at the time of interest. Integration in (4-11) was performed using the trapezoidal rule with each data point forming the end point of an interval.

IV.1.3.3 Weigh Tank Method

This method was the most straightforward. Reduction of the load cell data provided weigh tank mass at each time step. The mass discharged up to time t was simply:

$$M(t) = W(t) - W(t_0) \qquad (4\text{-}12)$$

where W is the measured weigh tank mass.

Because the weigh tank was suspended from only two points, it was subject to sway. Motion of the water in the tank induced by the jet nozzles caused the tank to oscillate with an amplitude and period which depended on the flowrate. This resulted in considerable scatter in the weigh tank data. Data tables in Appendix A quantify this scatter.

IV.1.4 Calculation of the Mass Flux

Each of the procedures described above resulted in a history of the vessel mass inventory. Mass flowrates were calculated by numerical differentiation of these data. The mass flux was then calculated by simply dividing the calculated flowrate at each time step by the slit cross-sectional area.

Two methods for differentiating the data were employed. In the first method, a cubic spline was fitted to the data. The spline was chosen in such a way that the rms error of the spline was equal to some specified parameter. Essentially the choice of this parameter controlled the degree of data smoothing. The data reduction program attempted to adjust the smoothing parameter so that the rms error in the spline was equal to the rms error between the data and a straight line interpolating twenty points taken during an interval when the mass flowrate should have been roughly constant. This choice of the parameter proved satisfactory in most instances. Mass flowrate was calculated as the derivative of the spline at each data point.

The second method used was straight linear interpolation of the points using a least-squares algorithm. Fits to three, nine, and twenty-nine points, centered at each data point, were calculated. Only the twenty-nine point fits have been reported in Appendix A since they proved to be the most stable and agreed more closely with the spline calculation. Weigh tank data was particularly difficult to deal with. Because of the large, and rapid, oscillations in the mass reading with a frequency larger than the scan frequency of the Auto-Data, the linear interpolation technique tended to introduce data aliasing. Aliasing is the phenomenon in which a high frequency signal appears as a lower frequency in averaged data. As a result, the weigh tank mass flux calculation tended to fall first above and then below the calculations based on the other two methods. This phenomenon is seen in the data tables (Appendix A). Spline data showed the same effect when the smoothing parameter was large. A small smoothing parameter could sometimes be used, but more often than

not this resulted in insufficient smoothing so that the calculated mass flux oscillated two hundred percent or more.

Mass flux data reported in Appendix A are eleven point averages of either the spline or linear interpolation data. The method which showed the least rms error in the average was selected. Usually this was the interpolation. Variations in flowrate which may have occurred at the beginning of each test were more readily revealed by the spline calculation. Over most of the runs, the two calculations agree within the calculated error. Generally, the linear interpolation varies least over the course of a run. In several cases the spline failed to produce reasonable results because the smoothing parameter was chosen too small. Weigh tank data was usually subject to this problem.

IV.2 Corrections to Slit Opening Dimensions

Table 4-1 shows the pseudo-discharge coefficients calculated for each cold water calibration run. Mass flux was calculated assuming nominal slit dimensions. These coefficients are essentially the equivalent head loss coefficient for the test section calculated from the formula:

$$C_{PD} = \frac{G}{\left[2\rho(P_0 - P_{ex}) \right]^{1/2}} \tag{4-13}$$

As can be seen from the table, there was some variation in the flow characteristics of each slit assembly. Ideally these pseudo-discharge coefficients would be identical for each nominal slit size. Variations which are present were due, for the most part, to some assemblies having a narrower opening dimension than intended. Examination of the test section surfaces after run #55 (runs were numbered chronologically; as described in Chapter I) showed indentations in the metal where the shims had been. Prior to run #56 the lower face of the test section insert block was re-ground flat. Shims were repositioned inward in future assemblies so as to maintain the intended slit opening dimension. Runs prior to #56, which had smaller opening dimensions, required corrections to the mass flux calculations which had been based on the nominal opening dimension. Correction factors were calculated by the procedure outlined below. Data given in Appendix A has been corrected.

IV.2.1 Correction Procedure

An initial, crude, comparison of the assembly dimensions based on the cold water calibration runs was made via the pseudo-discharge coefficient. This renders a qualitative comparison of the assemblies. The comparison was not useful for quantitative correction since both entry loss and friction effects are lumped into this parameter. Because of the low measured pressure differential between the exit plane of the test section and the downstream pipe section (see pressure profiles in Appendix B) exit losses were neglected.

Definitive comparison between various assemblies was made under the basic assumption that friction losses in assemblies that had roughly comparable opening dimensions were equal. Specifically, the Blasius friction factor was assumed:

$$f = CRe^{-0.25} \tag{4-14}$$

This expression is valid for $2300 < Re < 30{,}000$. Reynolds numbers for the cold water calibration runs ranged between 4×10^3 and 3×10^4. The value of C was taken to be constant between assemblies with the same nominal opening dimension (ie. assemblies which used the same shim thickness). Since C describes the relative roughness of the channel wall, and characteristics of the wall were not drastically changed in the course of the experimental program, this assumption was probably valid.

A value for C was calculated on the basis of early runs with the test section. It seems likely that the test section was deformed during run #31, perhaps as a result of the yield strength of the steel decreasing during the heating involved in vacuum braising the pressure tap sense lines (described in Appendix E). C was determined for a particular assembly on the basis of the measured gradient in static pressure. The momentum equation for single-phase incompressible flow in a constant area duct with friction is:

$$\frac{P_{in} - P_{ex}}{L} = \frac{f}{D_h}\frac{G^2}{2\rho} \tag{4-15}$$

D_h is the actual hydraulic diameter of the slit. Test section inlet pressure was found by extrapolation of the static pressure profile within the slit to the entrance location (z=0). These profiles are shown in Section IV of Appendix B. Substituting the definition of Reynolds Number in terms of mass flowrate and hydraulic diameter and using equation (1-1) one obtains the following expression for C in terms of measured quantities:

$$C = \frac{2\rho\,(P_e - P_{ex})\,D_h^{1.25}}{G^{1.75}L\mu^{0.25}} \tag{4-16}$$

Equation (4-16) was rearranged to solve for d, the actual opening dimension, for runs where this dimension was uncertain:

$$\frac{(W+d)^{1.25}}{Wd} = \frac{4.757\rho(P_e - P_{ex})}{CL\mu^{0.25}\dot{m}^{1.75}} \tag{4-17}$$

Equation (4-17) is transcendental in d and was solved by an iterative procedure.

IV.2.2 Sample Calculation

In order to demonstrate the procedure described above, a sample calculation is presented below using the data from run #31. The run selected as a standard for comparison was #14. There were three reasons for this selection: First, being an early run, the test section had not been subjected to high temperatures or stresses and was almost certainly not deformed. Second, the pseudo-discharge coefficients for runs #62, #83, and #90, which were made after the insert block surface had been re-ground, agree within 5%. Third, this was the first assembly having pressure taps; thus great care had been taken in the assembly process, with all dimensions checked carefully both before and after the run.

Table 4-2 shows the pertinent data for run #14. Substitution of these values into equation (4-16) yields C = 0.4637. This value of C corresponds to only one of the averaging periods for run #14 listed in Appendix A. Data from the remaining periods (there are four of them) were also used to obtain estimates of C; again using equation (5-16). The average value of C from these five calculations was 0.47725. This value was combined with data from run #31 which is also shown Table 4-2 in equation (4-17) to give the result d = 1.054×10^{-4} m. This is a reduction of 0.02 mm (17%) which is consistent with the measurements of the indentation in the test section which were made in preparation for re-grinding the surface. The largest depression measured was 0.03 mm.

Opening dimensions were estimated for each of the assemblies which showed pseudo-discharge coefficients which were inconsistent with other assemblies of the same nominal opening dimension. Results are summarized in Table 4-4. Table 4-4 also shows the assembly code which has been assigned to each test section assembly used. The code consists of a number and a letter. Numbers refer to the nominal slit opening dimension: 1 = 0.127 mm, 2 = 0.254 mm, and 3 = 0.381 mm. The letter is a sequence designation; A for the first used, B for the second. Only those assemblies instrumented with pressure taps have been considered. No calibration runs were made for

assemblies 1B, 2A, or 3A. It was originally intended to make calibration runs after a series of test with a given assembly was completed. For these particular assemblies, the pressure taps leaked so badly after the last run that a calibration run was not practicable. For subsequent tests, the calibration runs were made early in the series. The selection of the assembly to provide the standard value for C is discussed in the following section.

IV.2.3 Corrections To 0.254 mm and 0.318 mm Slit Assembly Dimensions

The 0.254 mm nominal assemblies suffered most from deformation of the test section. Several of the runs were repeated after the problem had been corrected so as to gain confidence in the results. The assemblies used for runs #35 and #53 had similar deformations to those used for #31 and #46 respectively. Run #73 was made after the insert block had been re-ground but the shims apparently slipped into the indentations in the "U"-shaped block, a problem which was not discovered until after disassembly. Runs #91 and #101 were chosen as being made with assemblies with well known dimensions. It was noted that the pseudo-discharge coefficient for these runs was within 5% of that for run #10 which was made prior to cutting the pressure taps when the test section was new.

For the 0.381 mm nominal assemblies, runs #56 and #77 have pseudo-discharge coefficients which agree closely with each other and with that for run #12, which again, was made without pressure taps when the test section was new.

Data used for making the corrections are shown in Table 4-3. The calculated opening dimension for affected assemblies are shown in Table 4-4 along with the correction factor which was applied to the mass flux calculated by the data reduction program for runs which used those assemblies. Support for this correction technique was lent by the fact that reductions in the opening dimension from the nominal value are seen to increase with consecutive assemblies. For example, runs #31, #35 and #40 all showed reductions of approximately 0.021 mm. Runs #46 and #53 show reductions of 0.047 and 0.038 mm respectively which is a reasonable comparison. In Chapter V, it was noted that mass flux trends are reasonably predicted by critical flow models applied, indicating the validity of the correction.

IV.3 Presentation of Results

A summary of the results for each run is presented in Appendix A. Graphical presentations of the measured pressure profiles are included in Appendix B, in addition to the tabulated data in A. In this section data trends will be analyzed based on these results. The method of presentation is described in the introductory section to each appendix.

Tables 4-5 through 4-7 show the test matrix for the 0.381 mm, 0.254 mm, and 0.127 mm nominal slit dimensions respectively. Runs which for one reason or another are deemed to have poor data reliability have been deleted from this tabulation but may be found in the appendices. Run numbers are chronological and are indicated only for reference.

Because of the problems encountered with the dimensional stability of the test section, the data for the larger slit sizes are generally more reliable than those for the smaller slit: First, the smaller size assemblies were harder to put together and were more subject to dimensional distortion. Second, the largest measured distortion of the test section surfaces was 0.03 mm. This is 24% of the smallest slit opening but only 8% of the largest. In analyzing the data trends, greater weight has been given to measurements taken with the largest slits.

Results from a few of the runs have been discounted because of their lack of consistency with the other data. Comparison of the results of these runs with the prediction of two-phase critical flow models in Chapter V serves to confirm this lack of consistency. The runs for which the calculated flowrate was substantially lower than might be expected on the basis of the remaining runs are listed

in Table 4-8. Lower flowrates could be explained by particles from within the vessel (eg. metal shavings, or accumulated scale) becoming lodged within the slit. Even though the inside of the vessel was thoroughly cleaned, the possibility of some particles remaining still exists.

The remaining runs are self-consistent once the impact of the variation in frictional pressure loss due to differing hydraulic diameters has been taken into account. As noted in Appendix D, results for runs where a correction factor has been applied to the mass flux to account for variations in slit dimension are subject to greater uncertainty.

It is noted that the pressure taps leaked during runs #24 through #30. Leaks were worst for runs #26 and #30. The leaks were repaired after each of these runs. The second repair was permanent (described in Appendix E). Flowrate through the leaks around the pressure tap tubes were probably not large enough to influence the flowrate. If they had been, flowrate calculated from the weigh tank data should have been noticably less than that calculated from vessel level measurements. Fluid leaking from the taps did not condense in the tank. No appreciable difference was noted between the results of these calculations. that the measured exit pressure was low.

Measured slit exit pressure, prior to run #31, was probably too low. In the earlier runs (#14 through #30) the sense line for the exit pressure tap was fastened into the groove in the downstream face of the test section (Figure 3-6) using high-temperature epoxy. (Appendix E details the installation of instrumentation probes). The epoxy did not tolerate the steam-water environment well, and rapidly dissolved. As a result, the exit pressure tap was not secured to the test section for runs #17 through #30. This freedom of movement may have allowed the tap to be pushed downstream of the critical section in these runs. It is particularly evident in runs #24 through #26 that the measured exit pressure was low. In all probability this is due to the biasing of this measurement toward the downstream pressure because all or part of the tap was downstream of the critical location.

IV.4 Discussion of Results

In this section results of the experimental program are discussed in terms of parametric effects. The parameters studied in this work were stagnation pressure, stagnation subcooling, and slit opening dimension. In addition, the possible effects of heat transfer between the slit wall and the fluid are discussed. Since the comparison between these experimental results and two-phase critical flow models gives additional insight into the phenomenon, further discussion of the results is given in Chapter V. However, those observations tend to be more speculative than those given below since they are inferred from comparison of the data to models which may not take into account all the factors involved in this complex phenomenon.

IV.4.1 Effect of Stagnation Pressure

As would be expected, it is the general trend of the data that mass flux increases as the stagnation pressure increases; for a fixed stagnation subcooling and channel geometry. This trend is obscured, to some degree, by competing factors such as varying hydraulic diameters between assemblies, the amount of initial subcooling, and apparently, changing frictional effects.

Tables 4-5 through 4-7 give both the hydraulic diameter and the pressure loss at the entrance to the slit for each of the runs considered. These parameters are required for proper analysis of the data trends. The effect of channel hydraulic diameter on the mass flux is discussed below.

Entry head loss coefficient (in terms of equivalent fL/D) varied considerably between runs, which has complicated interpretation of the data. This loss has been estimated from the measured pressure profiles by the method outlined in Chapter V. Tables 5-1 through 5-3 give the entry loss coefficient, K, for each run defined by:

$$K = \frac{2(P_0 - P_e)}{G_{exp}^2 v_{l0}} \tag{4-18}$$

For the 0.381 mm nominal slits, this coefficient is fairly uniform, ranging from 0.996 to 1.3. The range is somewhat larger for the 0.254 mm slits; from approximately 0.9 to 1.7 (neglecting the result for run #23). Another indication of the problems encountered with the 0.127 mm slits is the large disparity in entry loss coefficients; which range from 0.466 to 5.142.

Ideally the entry loss coefficient should be 2.69, independent of slit size. This result can be determined analytically from 1-D potential flow theory for rectangular channel with a sharp entrance considering zero approach velocity. The lower values encountered for the majority of the runs considered here is probably due to rounding of the entrance. On the scale of slits tested in this work, even a slight rounding of the edge of the test section would probably cause a significant reduction in the entry loss. While every effort was made during the fabrication of the test section to maintain sharp edges on the pieces forming the slit, a slight bevel may have been produced in removing the burr which was generated in grinding the slit walls (described in Chapter III). Even if this were not the case, the erosive action of high velocity water would soon round the edge.

Comparisons between runs made using the same assembly are the most reliable. Unfortunately, each assembly was generally used at only one pressure level. There are a few exceptions, which appear to reveal somewhat surprising results. Runs #43 and #45 were made with the same assembly and with similar amounts of initial subcooling. Stagnation pressure in run #43 was 21% higher yet the mass fluxes differ by only 1.2%. A comparison between runs #41 and #42 shows a similar result. Previous experiments reported in the literature have not demonstrated this phenomenon. It should be noted, however, that there are no previous results for duct flows at this pressure level with high initial subcoolings. The analysis of the single-phase pressure gradient, which is made in Chapter V, reveals that the single-phase friction factor is 10% larger for the higher pressure runs. This increase in friction is not accounted for by the increase in the Reynolds number due to a lower liquid viscosity at elevated temperature. Since these four runs are the only instances of this occurrence, the most reasonable conclusion is that there is some error in the data for runs #41 and #43 (which have friction factors lower than the average). The assembly with which these runs were made (3B) had a less than nominal opening dimension and the mass flowrates were corrected. This would seem to increase the liklihood of this explanation.

IV.4.2 Effect of Subcooling

Previous experimentalists who have studied the two-phase critical flow of initially subcooled liquid (discussed in Chapter II) have reported an increase in critical mass flux with increasing stagnation subcooling. This trend is reproduced in the current data. Dependence of results on stagnation subcooling is more easily analyzed than is the effect of pressure since, in several instances, runs made with the same assembly can be compared.

Figure 4-2 is a graphical presentation of mass flux vs subcooling using the most reliable data. The curves shown are for the same nominal test section L/D (=85, the 0.381 mm nominal assemblies). Data points have been labeled with the run number. Actual stagnation pressure may vary among points on a given curve. Correspondence between stagnation pressures was generally close enough that the data points fall along a smooth curve. In general, the use of a single parameter, such as subcooling or "universal stagnation quality", (discussed in Chapter II) to analyze data trends, is not recommended. Two independent fluid properties are required to define the thermodynamic state. However, for the purpose of this comparison, the use of subcooling as a single parameter is convenient.

The dependence of mass flux on stagnation subcooling approaches a linear relationship for high subcooling. Below 15°C, some of the data indicate that the mass flux becomes less dependent on

stagnation subcooling. As a consequence, a point of inflection in curves B and C has been shown. Such an inflection is not without precedent. Graphical presentations of the Sozzi and Sutherland data [10] show a similar trend for critical flow in ducts. The effect was more pronounced for their test section with a sharp-edged entrance.

Figure 4-3 shows the influence of the stagnation subcooling on the measured critical pressure ratio. All the available data points were plotted in the figure and labeled by run number. The large amount of scatter in the data is apparent. Causes of this scatter are discussed in the next section. No clear dependence of the critical pressure ratio on the stagnation pressure was observed. Sozzi and Sutherland [10] reported that their data, taken in a convergent/divergent nozzle, also showed no influence of the stagnation pressure. However, their data was obtained over a limited range of stagnation pressures: between 4.14 and 6.89 MPa (600 to 1000 psia). Their data show a scatter of $\pm 5\%$ even though all points were taken in the same channel.

Two-phase frictional pressure drop is generally much greater than that for a single-phase flow with the same mass flux. As subcooling decreases, the point of flashing inception should move closer to the inlet. In addition, the quantity of vapor generated should be larger. Both these influences should lead to an increase in the total pressure drop across the test section as subcooling decreases for the same mass flux. This leads to a marked decline in mass flux as subcooling decreases for a fixed stagnation pressure. While this trend was noted in the previous section, the decline is not as evident as would be expected. Most of the runs made with low subcooling show a much higher mass flux than might be expected from extrapolation from runs with higher subcooling.

There are two possible explanations for the results obtained in these experiments. First, that a greater degree of nonequilibrium is present in the runs with low subcooling; which leads to an increase in the critical mass flux. The opposite phenomena is generally agreed to be present. Nonequilibrium has previously been seen to increase with stagnation subcooling. Second, that flow regime is such that the frictional portion of the total two-phase pressure loss is much less than would be expected, perhaps less than the single-phase loss. This may occur should the vapor blanket a large portion of the channel wall. This latter hypothesis is supported by the comparison of the data with two-phase critical flow models. A full discussion is therefore postponed until the closing section of Chapter V.

The effect of initial subcooling on the critical pressure ratio is evident from Figure 4-3. Curves shown in the figure represent the best fit (in a least-squares sense) second order polynomial to the critical pressure ratio data for each nominal slit size. These curves are not intended to represent an interpolation of the data, but are merely an aid to identifying trends. A maximum in the critical pressure ratio with respect to subcooling is evident. The approximate locus of these maxima, as a function of slit size, is indicated by the dashed curve in the figure. The data of Schrock et al [38] indicate what may be a similar trend for nozzles. These data showed a peak between 2 and 3°C subcooling. Too few data points were taken for subcoolings below this for the authors to be able to make this observation. It seems that Sozzi and Sutherland's data were not extended to sufficiently high subcooling to see this phenomenon. In Chapter V it is seen that critical flow models employed in the present study reproduce this trend toward a maximum in the critical pressure ratio with respect to initial subcooling.

IV.4.3 Effect of Slit Opening Dimension

More data on the effect of variations in the slit opening dimension on the critical flow were collected than had originally been intended. This was due to the fact that several of the test section assemblies has a smaller slit opening dimension than planned. As expected, the critical mass flux is seen to decrease with increasing length-to-diameter ratio (L/D) of the channel. Critical pressure ratio also decreases. In this section, the experimental results are discussed in terms of L/D. It is apparent from the results that channel friction has an important influence on the critical mass flux.

For frictional flows, fL/D is the controlling parameter. Nominal values of L/D_h in these experiments were 85, 126, and 252 for the 0.381, 0.254, and 0.127 mm nominal slit openings, respectively. Actual values appear to have ranged from 85 to 399; calculated from the corrected dimensions given in Table 4-4.

In Chapter II, observations of the effect of test section diameter on the critical mass flux, made by previous investigators, were discussed. As yet, no definitive study has been made which examines the influence of the scale of the channel on the critical mass flux. Sozzi and Sutherland [10] reported a 20% higher mass flux for a nozzle with a 1.27 cm throat diameter than for a nozzle with a 1.9 cm throat. It is noted, however, that the shapes of the nozzles used in this comparison were not the same. Schrock et al [13, 38] saw no diameter effect. For ducts with significant friction, such as the slits in the present study, a decrease in the channel hydraulic diameter for a fixed length leads to a reduction in the mass flux. This result is a consequence of the increase in fL/D. It is this effect which is seen in the present results. The influence of the scale of an experiment on the critical mass flux cannot be determined from these results. When friction is significant, fL/D should be held constant between test sections in order to determine the scale effect, if any. Such was not the case for the present experiments.

The effect of the length-to-diameter ratio of the slit on the critical mass flux measured in these experiments can be seen in Figure 4-4. For single phase flow with a fixed stagnation state, exit pressure, and channel friction factor, the mass flux is inversely proportional to the square root of L/D. A similar dependence of mass flux on L/D is evident in the figure. This indicates the importance of frictional effects in determining the critical mass flux in these experiments. The curves shown in Figure 4-4 show the critical mass flux to be approximately proportional to $(L/D)^{-0.7}$. A stronger dependence on L/D, than for the single-phase case, is expected due to the variation in the flashing location. The location of flashing inception varies with the channel geometry, for a fixed stagnation state, due to changes in the single-phase pressure drop. These features are discussed more thoroughly in the next section.

Dependence of the critical pressure ratio on the hydraulic diameter of the channel has been mentioned in the previous section. Figure 4-3 shows a decline in the critical pressure with increasing L/D. The effect of stagnation subcooling is also evident; as discussed above. Curve C in Figure 4-3, which is representative of the smallest nominal slit size, shows a much weaker dependence of the critical pressure ratio on the stagnation subcooling than do the other curves. Indeed, a maximization of the critical pressure ratio is barely noticable. It appears to be the case that the initial subcooling for which the pressure ratio is maximized decreases with increasing L/D. Since data in Figure 4-3 has been presented on the basis of nominal slit dimension, the variation between actual slit sizes intended to have the same opening dimension accounts for much of the scatter. The influence of channel geometry on the observed effects of changes in the stagnation subcooling are discussed below. The pressure profiles in Appendix B indicate that the location of flashing inception moves upstream as the hydraulic diameter of the channel is decreased for a given stagnation condition.

Figure 4-5 shows the combined influences of the length-to-diameter ratio of the channel, and stagnation subcooling, on the critical mass flux. Critical mass flux is plotted as a function of stagnation subcooling on the same scale as Figure 4-3. (Curves C and E in Figure 4-3 are duplicated as E and F in Figure 4-5). Stagnation pressure and L/D of the channel are approximately constant along each curve. The slope of the curves, at subcoolings larger than 10°C, is seen to decrease as L/D increases for fixed stagnation pressure. This indicates that the effect of an increase in the stagnation subcooling, for a fixed stagnation pressure, is diminished for channels with larger L/D. As discussed above, the critical pressure ratio was less dependent on the stagnation subcooling for higher L/D.

IV.4.4 Location of Flashing Inception

In the absence of void fraction measurements, the approximate location of flashing inception must be inferred from the pressure profile data. Measured pressure profiles are presented graphically in Appendix B. Single-phase flow is characterized by a linear pressure profile. Flashing in the flow is indicated by the deviation of the pressure profile from a straight line. A graphical technique is therefore available for estimating the location of flashing inception. Using graphs of the pressure data (shown in Appendix B), a straight line is drawn through those data points which lie above the saturation pressure corresponding to the liquid stagnation temperature (shown by the horizontal dashed line in each graph in the appendix). Points above the saturation pressure must correspond to single-phase flow. The point of tangency between this line and a curve drawn through the data points starting from the exit and moving upstream, indicates the approximate location of flashing inception. This point has been indicated on the graphs in Appendix B. The accuracy of this technique is dependent upon how closely spaced pressure measurements are. Because the determination of the point at which flashing begins is only approximate, the discussion of parametric trends in these data is mainly qualitative. The data do not reveal anything unexpected.

Two problems arise in the determination of the location of flashing inception by the technique described above. First, when the stagnation subcooling is low, flashing occurs sufficiently close to the slit entrance that the pressure gradient in the single-phase region cannot be established. Practically, this means that when flashing occurred upstream of pressure tap #2 (1.91 cm from the entrance), the location of flashing inception cannot be determined. The second problem results from the anomalous pressure data obtained from pressure taps near the exit for runs with substantial inlet subcooling. This anomally takes the form of a rise in the measured pressure, within the channel, along the flow direction. Possible explanations for this phenomenon are discussed in a later section of this chapter. The cause of this problem may have been a systematic problem with the instrumentation. Alternatively, this may be an actual physical phenomenon. Whatever the cause, the relation of this "hump" in the pressure profile to the saturation pressure indicates that it is associated with the point of flashing inception. It seems reasonable to take the location at which this pressure rise begins as the approximate point at which flashing was initiated. This allows the determination of the point within a few millimeters (the separation between pressure taps near the exit). This is probably greater accuracy than is allowed by the graphical technique applied further upstream where the taps are more widely spaced.

Dependence of the location of flashing inception on stagnation subcooling and the hydraulic diameter of the channel was as expected. Pressure effects were less easily determined from the available data. This was especially true since the scale of the graphs in Appendix B varies with the stagnation pressure. It is clear, however, that the pressure undershoot at the point where flashing begins tends to increase with the stagnation pressure. This result is predicted by the Alamgir-Lienhard correlation [68], which was described in Chapter II.

The point of flashing inception moves closer to the slit entrance as the stagnation subcooling is decreased. This occurs because less depressurization is required to initiate flashing. The reduction in critical mass flux due to larger exit quality does not sufficiently decrease the pressure gradient to keep the location of flashing inception from moving. It also appears that the amount of pressure undershoot required to start the generation of vapor decreases with the subcooling. This result is also predicted by the Alamgir-Lienhard correlation. Decreasing the hydraulic diameter also moves the flashing location closer to the entrance. The latter result is explained in terms of the increased pressure gradient due to friction. No effect of the channel size on the undershoot at flashing was apparent.

In some instances, it appears that flashing occurred at, or slightly below, the saturation pressure. This was probably due to the presence of deterministic nucleation sites on the slit wall. These may result from pitting of the surface; which was observed. The pressure taps themselves may be possible nucleation sites. In Chapter V, the influence of wall nucleation sites on the pressure undershoot at the point of flashing is discussed in more detail.

IV.4.5 Exit Pressure Oscillations

As described in Chapter III, the output signal from the pressure transducer connected to the exit pressure tap (#8 in Figure 3-9) was recorded on an oscilloscope as well as the Auto-Data Eight data collection system. Photographs of the oscilloscope trace were taken manually at various times during each run. Principally, pictures were taken when the output trace from the transducer was observed to change. For runs subsequent to run #30, the exit pressure was measured by a Validyne DP-15 transducer with a ± 2.41 MPa range. This transducer has a frequency response of 5 kHz; a much higher frequency than the observed pressure oscillations. Prior to run #31, a Gould-Statham strain gauge transducer was used to measure the exit pressure. The latter transducer had an inadequate frequency response to measure pressure oscillations.

Figures 4-6 through 4-9 show photographs of exit pressure traces for four representative runs. Each photograph shows a time span of 2 seconds. These results are for a range of pressures and subcoolings, as indicated in the figures. It was noted that the magnitude of the oscillations tended to be slightly larger for the smaller slit sizes. Observed fluctuations in the exit pressure did not exceed 100 kPa. Usually, these fluctuation were limited to approximately 30 kPa.

Pressure fluctuations at the exit pressure tap were largest as flow in the slit was established. The upper photograph in each of the figures (labeled a) was taken as soon as possible after the main valve started to open. Usually, the valve was not yet fully open when the photograph was taken. However, the valve was open sufficiently so as not to restrict the flow. Large fluctuations in the exit pressure were associated with the establishment of steady flow through the slit. As discussed in the next section, this was probably a result of wall heat transfer effects. The time span over which these large fluctuations were observed corresponds to the period over which the heat flux from the slit wall to the fluid was largest.

The magnitude of the observed pressure fluctuations were dependent on the stagnation subcooling. When the subcooling was low (Figures 4-6 and 4-9) the pressure fluctuations during the initial period were largest. For the highest subcoolings (Figures 4-7 and 4-8), pressure fluctuations were minimal and reduced only slightly later in the run. The absence of large fluctuations during the initial period was associated with flashing occurring at the exit of the slit. Pressure level at the exit was not observed to influence the magnitude of the fluctuations.

The exact mechanism which gives rise to oscillations in the exit pressure is not known. The dependence on subcooling suggests that they are a result of the flashing phenomenon. Most likely, variations in the location at which flashing begins as critical flow is being established in the slit cause the large, lower frequency, variations early in the run. The stochastic nature of the nucleation process might be expected to give rise to the higher frequency oscillations which appear to persist throughout the run. The rapid growth of bubbles in the early stage of growth may give rise to pressure disturbances which are propagated downstream. Thus the dependence of pressure fluctuations on subcooling could be explained in terms of the rapidity of bubble growth, which depends on the amount of the liquid superheat at flashing inception.

IV.4.6 Effect of Wall Heat Transfer

Previous experimentalists in the field of two-phase critical flow have generally ignored the possible influence of wall heat transfer on the critical flow phenomenon. The majority of two-phase critical flow models (including those used in this study) assume the flow channel to be adiabatic. Exceptions to this are the two-fluid transient reactor analysis codes such as KFIX [49], TRAC [90] and RELAP5 [91]. These codes include models for convective heat transfer between the flowing fluid and the duct wall. Small scale critical flow experiments have previously been carried out either with test sections covered with thermal insulation or with no attention paid to heat losses to the environment. Little, if any, mention is made about the temperature of the test section prior to the initiation

of flow. In steady state experiments one presumes that heat loss from the fluid to the environment has achieved an equilibrium level or is negligible.

It was the original intent of this experimental program to analyze the effects of wall heat transfer on two-phase critical flow in slits. To this end, care was taken in each experiment to heat the test section to approximately the fluid stagnation temperature prior to starting each run. The initial test section temperature has been recorded for each run in the upper right hand corner of the data tables in Appendix A. In the case of flow from a crack in a large diameter pipe, of which these experiments are an idealization, the pipe wall would be expected to have an initial temperature close to that of the fluid within the pipe. This is the situation which was approximated by heating the test section to the fluid temperature. Wall heat transfer effects were expected to be significant in this geometry where the wetted perimeter of the flow channel is large compared to the cross section. This implies that the surface area available for heat transfer is large relative to the fluid mass flowrate. Under these circumstances, the increase in the enthalpy of the flowing fluid due to wall heat flux may be expected to influence the critical flow.

Heat flow from the wall to the fluid increases the static enthalpy, which would be expected to decrease the critical mass flux. The effect of wall heat transfer would not necessarily be identical to that of increasing the stagnation enthalpy (lowering the initial subcooling) by a quantity equal to the amount of heat transferred from the wall. Development of the flow regime in the flow channel would be influenced by the influx of heat from the wall. This may result in a change in the frictional pressure drop and interphase slip. While the anticipated influence of heat addition from the wall was a reduction in the critical mass flux, the magnitude of this effect, and the influence on the pressure profile within the channel, were not known.

No influence of wall heat transfer could be determined from these experimental results. The presence of heat transfer from the test section to the fluid is evidenced by the temperature measurements from the thermocouples embedded in the slit wall. Figures 4-10 through 4-15 show sample thermocouple data as a function of time. Each temperature trace has been labeled with the thermocouple number. Thermocouples were numbered consecutively from inlet to outlet. The exact location of each thermocouple is shown in Figure 3-9. Stagnation temperature for each run is indicated by the dashed line running across the top of each graph. The time at which flow through the test section was initiated is indicated by the vertical broken line on the right labeled "start". It can be seen that the test section temperature was constant and roughly uniform prior to the start of each test. Once flow began, the temperature within the wall changed rapidly toward the fluid temperature at that axial position. Between 60 and 90 percent of the change in temperature recorded by a thermocouple occurred within the first 5 seconds after flow began. The fact that this time interval corresponds with that for the large fluctuations in exit pressure, discussed in the previous section, is probably not coincidental.

In this section an upper bound on the magnitude of the heat flux from the wall to the flowing fluid is established. It is shown that the magnitude of heat flow into the fluid indicates that wall heat transfer effects are negligible throughout most of the run. For the purposes of this analysis it is assumed that the slit walls behave as a semi-infinite medium as far a conduction heat transfer is concerned. Axial conduction is also neglected. Since the test section is massive (~22 kg), and well insulated, this idealization is appropriate. In addition, the largest time for which this approximation is valid may be estimated from the model.

The temperature profile in a semi-infinite medium with convective heat transfer to a fluid at the surface (which undergoes a stepwise decrease in temperature a time zero) is given by the expression:

$$\frac{T_s(t,y) - T_f}{T_0 - T_f} = \text{erf}\left(\frac{y}{2(D_s t)^{1/2}}\right) + \exp\left(h^* y - h^{*2} D_s t\right) \times \text{erfc}\left(\frac{y}{2(D_s t)^{1/2}} + h^*(D_s t)^{1/2}\right) \tag{4-19}$$

$$h^* = \frac{h'}{k_s} \tag{4-19a}$$

which was derived by Carslaw and Jaeger [94]. D_s and k_s are, respectively, the thermal diffusivity and conductivity of the medium. T_f is the fluid temperature (assumed constant) and T_0 is the initial temperature of the medium (assumed uniform) and the temperature of the fluid for times less than zero. T_s is the temperature of the medium at a depth y from the surface at time t after the fluid came in contact with the surface. Since the heat transfer coefficient between the slit wall and the flashing fluid is unknown, the limiting case of the expression is considered to obtain an upper bound on the heat flux. As the heat transfer coefficient, h', becomes indefinitely large, the expression for the temperature profile in the slit wall can be approximated as:

$$\frac{T_s(y,t) - T_f}{T_0 - T_f} = erf\left(\frac{y}{2(D_s t)^{1/2}}\right) \tag{4-20}$$

which is the solution to the heat conduction problem in a semi-infinite medium assuming that the surface temperature is lowered instantaneously to the fluid temperature at the time t=0. Heat flux at the slit wall is given by differentiating equation (4-20) with respect to y and evaluating the derivative at y=0. The resulting expression for the maximum heat flux to the fluid from each side of the channel is:

$$\dot{q}''_w = \frac{k_s(T_0 - T_f)}{(\pi D_s t)^{1/2}} \tag{4-21}$$

Equation (4-21) can be employed to give an upper bound on the heat flow rate from the test section to the fluid. The maximum enthalpy rise in the flowing fluid is given by:

$$\Delta h_{\max} = 2\int_{z_{fl}}^{z_{ex}} \frac{\dot{q}''_w(z)dz}{Gd} \tag{4-22}$$

where the integral is over the length of the two-phase region. The factor of two is required to account for the contribution from each wall. Evaluation of equation (4-22) requires knowledge of the fluid temperature as a function of axial location within the slit. Fluid temperature will be bounded below by the saturation temperature corresponding to the local pressure. Since the pressure decreases in the flow direction there is an axial temperature gradient in the slit wall. Axial conduction has been neglected in this analysis. To simplify the integral of equation (4-22) the fluid temperature will be assumed to vary linearly from the stagnation temperature to the saturation temperature corresponding to the exit pressure. This approximation consistently underestimates the fluid temperature. Under these assumptions, the average enthalpy rise of the fluid between times t_1 and t_2 ($t_2 > t_1 > 0$) is given by:

$$\overline{\Delta h}_{\max} = \frac{2k_s(\pi D_s)^{-1/2}}{(t_2 - t_1)Gd} \frac{[T_0 - T_{sat}(P_{ex})]}{z_{ex} - z_{fl}} \times (z_{ex}^2 - z_{fl}^2)(t_2^{1/2} - t_1^{1/2}) \tag{4-23}$$

The average enthalpy rise in the fluid due to wall heat transfer is maximized for runs with maximum pressure and minimum subcooling. This situation corresponds to the largest temperature drop across the test section ; the key parameter in equation (4-23). Run #100 was used in a sample calculation. Flashing was taken to occur at the entrance (z_{fl}=0). The average enthalpy rise for the first five seconds after flow was initiated was calculated to be 238 J/kg, which corresponds to an increase in the exit quality of approximately 0.014%, assuming all the energy is used in vaporizing the liquid. For the five second period beginning 30 seconds after flow begins, the predicted average enthalpy rise is only 46 J/kg; a reduction of 80% over that calculated for the initial five second period.

The predicted enthalpy rises for other runs are similar in magnitude. Because the possible change in exit quality due to this effect is so small, it seems unlikely that this would give rise to the observed oscillations in the measured exit pressure. However, the heat transfer coefficient between the wall and the fluid is actually finite. This means that the slit walls retain some superheat. In the first few seconds of flow this superheating of the wall may effect the nucleation characteristics, altering the location of flashing inception. This mechanism seems a more likely possibility than the increase in the fluid enthalpy.

IV.4.7 Dissolved Gas Effects

Many experiments which have been performed to investigate two-phase critical flow, including the present ones, have employed de-gassed water as the working fluid. Noncondensable gasses are removed so as to free the experimental results from whatever influence these gasses may have. Some experimentalists, including the Marviken workers [16] and Alamgir et al [95], have attempted to study the effect of dissolved gasses on the critical flow and flashing phenomena by including at least one run in which no attempt was made remove dissolved gasses from the fluid. These workers have not demonstrated an influence of dissolved gasses. However, their observations depend on their ability to duplicate stagnation conditions between runs with and without dissolved gasses.

Quantifying the influence of dissolved gasses on the critical flow phenomenon is important in the application of experimental results to the analysis of critical flow in nuclear power reactor systems. Water used in reactor systems is almost certainly saturated with noncondensable radiolytic gasses in solution. However, many experiments have been performed using degassed water. Even though previous experimentalists have not observed an effect of dissolved gasses, a theoretical study of nucleation and bubble growth phenomena indicate that one should be present. Forest and Ward [96] have shown that the presence of nitrogen dissolved in ethyl ether raised the pressure at which nucleation occurred. The extent of the increase corresponded closely with the predictions a theoretical model. This same theory predicts a similar influence for water.

The present experimental program did not intentionally include a study of dissolved gas effects. However the reduction in the measured critical mass flux which was observed in many of the experimental runs can best be explained in terms of an increase in the dissolved gas content of the water. In the data tables in Appendix A, it is observed that, in many of the runs, the measured mass flux decreases while the stagnation subcooling actually increases slightly. In many instances, the stagnation pressure also increased. This effect is more pronounced when the stagnation subcooling is highest.

These observations are consistent with the assumption that dissolved nitrogen, which diffuses into the initially degassed water from the top, causes a reduction in the critical mass flux. The larger effect in runs with higher subcoolings would be expected since the saturation quantity of gas which may be dissolved in the water increases with increasing subcooling. Runs with the shortest duration (highest mass flux) were completed in one to two minutes which allows little time for gas to diffuse into the water. The reduction in the mass flux for runs with longer duration is more pronounced. These runs lasted for as long as ten minutes, so higher gas content in the water at the end of the run would be expected. Reduction in mass flux is typically on the order of 5%. Critical pressure ratio decreases as well.

IV.4.8 Pressure Profile Anomalies

As mentioned above, measured pressure profiles show anomalous behavior in the vicinity of the exit plane. Pressure within the slit appears to increase in the flow direction for many of the experimental runs. In this section three possible explanations for this phenomenon are proposed.

The most simple explanation is that the pressure measurements are inaccurate. Inaccuracies may be due to failure of the pressure transducers. Alternatively a burr on the pressure tap could cause a faulty reading. Pressure transducers were tested, and the calibration checked, after the experimental program was completed. This examination revealed the pressure transducers functioned properly and were calibrated by the original calibration curves within the error of that determination (see Appendix C). The Statham pressure transducer, PA-891-3M, which for a majority of the runs (#31 through #101) was connected to tap #4 (shown in Figure 3-9), consistently read low. Measured pressure profiles, shown in Appendix B, clearly show this. In Appendix A, the drift in transducer calibration over the course of a run is indicated. The difference between the stagnation pressure and that indicated by a transducer connected to a test section pressure tap, under the zero flow condition at the end of each run, has been termed the calibration drift. This transducer consistently appeared to drift 100 kPa or more low; a much larger amount than the other transducers, which consistently show approximately zero drift. During the calibration check of the transducers, which was performed at the end of the experimental program, it was noted that this transducer frequently required two to three minutes for the reading to stabilize after a change in the applied pressure. This deficiency was not evident in the original calibration. Clearly the transducer was damaged during the experimental program and the readings are unreliable. These readings were not involved in the apparent pressure rise.

Problems with the pressure taps would be expected to show the same trend in the cold calibration runs and when flashing occurred upstream and flow at the tap was clearly two-phase. Such is not the case. Pressure data from the downstream taps (#6, #7) fall on or below the straight line extrapolated from upstream data in the cold water calibration runs. For runs with low subcooling the data show no unexpected features, but for the most part show a monotonic decrease in the flow direction.

The second explanation is that the observed phenomenon is a result of flashing inception from a highly metastable condition. In static depressurization experiments, such a those of Alamgir et al [95], such a pressure recovery is observed. Fluid pressure is seen to recover almost to the saturation pressure before flow begins. This pressure recovery is attributed to the inertia of the fluid constraining the expansion of the fluid necessary to accommodate the vapor formed. If flow in a duct is viewed in a Lagrangian sense, it may appear that this mechanism could account for the pressure rise. Following a "packet" of fluid as it moves down the duct, the pressure declines until the undershoot is sufficient for flashing to occur. Vapor is formed rapidly and the packet expands. Just as in static depressurization, the liquid inertia may be imagined to constrain the expanding bubbles. This constraint causes the kinetic energy of the expanding bubbles to be converted into static pressure. Viewing the flow in a Eulerian sense this explanation is less reasonable. For the pressure to rise in a constant area duct the fluid density must increase. This implies that the vapor must condense. Since the liquid is superheated, condensation cannot occur on the liquid-vapor interface. No other sites are available for condensation. Thus, this explanation for the pressure rise is also unlikely to be the correct one.

A third alternative is suggested by the pressure data from the cold water calibration runs. Graphs of these data are included in Section IV of Appendix B. Were the slits uniform in cross section, and the surface characteristics of the wall sufficiently uniform that the friction factor remains constant, the pressure data should fall on a straight line between the entrance pressure and that at the exit. As shown in the appendix, downstream pressure data fall below that line. This suggests that the slits were not uniform in cross section. A reduction in the cross-sectional area explains the cold water calibration data. It also explains the pressure rise. If an area restriction is present because the slit walls are not smooth, the fluid will depressurize as it flows into the zone of reduced area and

accelerates. This pressure reduction may well cause flashing to occur. If the slit again widens, the fluid expansion in this "divergent" section may cause the observed pressure recovery. This postulated widening is supported by the calibration data which shows a zone where the pressure gradient is reduced in the last centimeter before the exit.

It is also noted that a few of the runs show pressure profiles which diverge from the linear reduction in the flow direction, which is characteristic of single-phase flow with friction, while the pressure is still greater than the saturation pressure. This may be explained in terms of variations in the channel dimension over the length of the slit. However, the effect is not present in all the runs made with the same assembly. A more likely explanation is a problem with the pressure transducers, their power supply, or the sense lines.

Before accepting the explanation of nonuniform slit cross section for the observed pressure rise, it is noted that the data of Jeandey et al [97] show the same phenomenon in one of their runs. These experiments were carried out in a 20 mm diameter duct. The constant area section was 35.8 cm long and was preceded by a conical convergent section. A nozzle with a 7 degree diffusing angle was attached at the exit. The run in question was designated 20B148C. Stagnation pressure was 2 MPa, with a subcooling of 63.9°C. A rise in the pressure of 6 kPa in 6 mm is seen starting 114 mm from the exit of the constant area section. The authors do not mention this result. Descriptions of the test section indicate that the interior wall was smooth and uniform. It is possible that this measurement was erroneous; none of the other runs, which number 66 for subcooled stagnation states, reveal this phenomenon. However, this particular run has the highest subcooling.

IV.5 Future Work

The data reported herein are clearly influenced by uncertainties in the dimensions of the flow channel. While it is true that actual cracks would be characterized by non-uniform cross section, it was the intent of this program to remove these uncertainties. In spite of the problems, the data reveal important characteristics of the critical flow of highly subcooled water through ducts. The need for additional studies in small geometries is underscored. Data for flow through tubes, in which the channel geometry is better determined will prove useful in confirming the parametric trends identified in this study. this is especially true for the pressure profile data. Void fraction data could also be obtained in tubes.

Wall heat transfer effects are best studied in tubes. Heating the tubes externally would provide a known heat flux to the fluid. The effect of heat transfer could then be studied systematically.

Table 4-1

Pseudo-Discharge Coefficients For Cold Water Calibration Runs

Run (#)	Nominal Slit Size (mm)	Stagnation Pressure (MPa)	Mass Flux (kg/m^2-s)	Pseudo-Discharge Coefficient
8	0.127	2.588	1.693×10^4	0.241
14	0.127	2.796	1.794×10^4	0.243
31	0.127	2.704	1.495×10^4	0.172
46	0.127	2.706	1.340×10^4	0.117
62	0.127	2.621	1.641×10^4	0.233
83	0.127	2.584	1.710×10^4	0.245
90	0.127	2.565	1.640×10^4	0.235
10	0.254	2.565	2.921×10^4	0.418
35	0.254	2.509	2.620×10^4	0.342
53	0.254	2.491	2.598×10^4	0.314
73	0.254	2.629	2.630×10^4	0.346
91	0.254	2.530	2.828×10^4	0.407
101	0.254	2.581	2.744×10^4	0.393
12	0.381	2.628	3.738×10^4	0.528
40	0.381	2.469	3.474×10^4	0.482
56	0.381	2.469	3.588×10^4	0.524
73	0.381	2.469	3.657×10^4	0.534

Table 4-2

Data For Sample Calculation of Slit Dimension Comparison

Parameter	Symbol	Data		Units
		Run #14	Run #31	
Channel Length	L	6.35	6.35	cm
Width of Slit	W	2.024	2.065	cm
Inlet Pressure	P_e	2433	2286	kPa
Exit Pressure	P_{ex}	124	117	kPa
Inlet Density	ρ	999.1	999.4	kg/m^3
Inlet Viscosity	μ	1.029×10^{-3}	1.029×10^{-3}	$N\cdot s/m^2$
Mass Flowrate	$\dot{m}$	4.655×10^{-2}	3.226×10^{-2}	kg/s
Mass Flux (uncorrected)	G	1.795×10^4	1.230×10^4	kg/m^2-s
Coefficient of Eqn.(4-14)	C	0.4637	0.4773*	
Hydraulic Diameter	D_h	0.252	0.209+	mm

*Assumed

+Calculated Result

Table 4-3

Summary of Test Section Calibration Data Used For Correction of Mass Flux Results

Run	Inlet State		Exit Pressure	Mass Flowrate	Slit Width	Friction Coefficient
	P_e	T_0				C
(#)	(MPa)	(°C)	(kPa)	(kg/s)	(cm)	
14*	2.493	22.6	124	0.0465	2.024	0.4773
31	2.335	20.4	117	0.0324	2.065	0.4773
46	2.538	29.2	122	0.0215	2.042	0.4773
101*	1.872	25.4	125	0.1280	1.836	0.3999
35	2.036	19.5	117	0.1218	2.029	0.3999
53	2.110	29.2	114	0.1125	2.050	0.3999
73	1.923	27.8	115	0.1209	1.946	0.3999
56*	1.727	23.6	124	0.2629	1.923	0.3748
40	1.768	22.8	127	0.2552	2.040	0.3748

*Reference Case

Table 4-4

Results of Dimensional Correction Calculation

Run (#)	Assembly Code	Pseudo-Discharge Coefficient	Calculated Opening Dimension (mm)	Mass Flux Correction	Affected Runs (#)
14	1A	0.243	0.1270	1.000	14/-22
31	1C	0.172	0.1048	1.212	31/-34
46	1D	0.117	0.0794	1.599	46/-50
62	1E	0.233	0.1270	1.000	61/-67
83	1F	0.245	0.1270	1.000	80/-90
90	1F	0.235	0.1270	1.000	80/-90
35	2B	0.342	0.2290	1.109	35/-39
53	2C	0.314	0.2107	1.206	51/-55
73	2D	0.346	0.2351	1.081	68/-72
91	2E	0.407	0.2540	1.000	91/-101
101	2E	0.393	0.2540	1.000	91/-101
40	3B	0.482	0.3591	1.061	40/-45
56	3C	0.524	0.3810	1.000	56/-60
77	3D	0.534	0.3810	1.000	74/-79

Table 4-5

Test Matrix
0.381 mm Nominal Slit Opening Dimension

Nominal Stagnation Pressure	Test Parameters	Nominal Stagnation Subcooling			
		60°C	30°C	15°C	3°C
4.2 MPa	Run #	59	57	58	60
	Pressure (MPa)	4.270	4.216	4.180	4.123
	Subcooling (°C)	59.1	27.7	13.9	2.7
	D_h (m)	7.472E-4	7.472E-4	7.472E-4	7.472E-4
	G($\frac{kg}{m^2 \cdot s}$)	4.095E+4	3.250E+4	2.540E+4	1.434E+4
	Entry Loss (kPa)	1311	692	428	-na-
7.2 MPa	Run #	30	27	28	29
	Pressure (MPa)	7.101	7.071	7.077	7.090
	Subcooling (°C)	62.8	29.3	15.6	5.9
	D_h (m)	7.481E-4	7.481E-4	7.481E-4	7.481E-4
	G($\frac{kg}{m^2 \cdot s}$)	5.790E+4	4.416E+4	3.399E+4	2.511E+4
	Entry Loss (kPa)	2188	1339	815	-na-
9.6 MPa	Run #	41	43	44	75
	Pressure (MPa)	9.595	9.585	9.623	9.546
	Subcooling (°C)	59.4	29.8	14.8	0.0
	D_h (m)	7.075E-4	7.075E-4	7.075E-4	7.474E-4
	G($\frac{kg}{m^2 \cdot s}$)	5.792E+4	4.433E+4	3.313E+4	2.624E+4
	Entry Loss (kPa)	2268	1454	855	-na-
11.6 MPa	Run #	42	45	76	79
	Pressure (MPa)	11.592	11.604	11.682	11.672
	Subcooling (°C)	54.6	29.7	11.9	2.0
	D_h (m)	7.075E-4	7.075E-4	7.474E-4	7.474E-4
	G($\frac{kg}{m^2 \cdot s}$)	5.805E+4	4.446E+4	3.860E+4	3.055E+4
	Entry Loss (kPa)	2576	1632	1069	-na-
15.6 MPa	Run #	74	78		
	Pressure (MPa)	15.369	15.453		
	Subcooling (°C)	54.3	26.0		
	D_h (m)	7.474E-4	7.474E-4		
	G($\frac{kg}{m^2 \cdot s}$)	6.955E+4	5.284E+4		
	Entry Loss (kPa)	3610	2508		

Table 4-6

Test Matrix
0.254 mm Nominal Slit Opening Dimension

Nominal Stagnation Pressure	Test Parameters	Nominal Stagnation Subcooling			
		60°C	30°C	15°C	3°C
4.2 MPa	Run #	68	70	69	71
	Pressure (MPa)	4.289	4.321	4.282	4.276
	Subcooling (°C)	59.5	30.7	15.0	5.6
	D_h (m)	4.644E-4	4.644E-4	4.644E-4	4.644E-4
	G($\frac{kg}{m^2 \cdot s}$)	3.498E+4	2.848E+4	2.158E+4	1.689E+4
	Entry Loss (kPa)	736	522	306	184
7.2 MPa	Run #	51	24	25	26
	Pressure (MPa)	7.055	7.055	7.055	6.999
	Subcooling (°C)	60.7	29.0	18.0	3.1
	D_h (m)	4.181E-4	5.017E-4	5.017E-4	5.017E-4
	G($\frac{kg}{m^2 \cdot s}$)	4.099E+4	3.642E+4	3.143E+4	2.025E+4
	Entry Loss (kPa)	1041	893	534	-na-
9.6 MPa	Run #	98	37	38	99
	Pressure (MPa)	9.785	9.603	9.667	9.611
	Subcooling (°C)	58.4	27.8	22.2	0.0
	D_h (m)	5.012E-4	4.533E-4	4.533E-4	5.012E-4
	G($\frac{kg}{m^2 \cdot s}$)	4.900E+4	3.249E+4	2.748E+4	2.250E+4
	Entry Loss (kPa)	1821	928	776	-na-
11.6 MPa	Run #	95	96	93	94
	Pressure (MPa)	12.423	11.641	11.837	11.674
	Subcooling (°C)	61.1	26.3	12.8	2.0
	D_h (m)	5.012E-4	5.012E-4	5.012E-4	5.012E-4
	G($\frac{kg}{m^2 \cdot s}$)	5.118E+4	3.892E+4	3.216E+4	2.052E+4
	Entry Loss (kPa)	2806	1367	904	-na-
15.6 MPa	Run #	72		97	100
	Pressure (MPa)	15.600		15.748	15.705
	Subcooling (°C)	54.0		11.7	2.1
	D_h (m)	4.644E-4		5.012E-4	5.0012E-4
	G($\frac{kg}{m^2 \cdot s}$)	5.015E+4		3.685E+4	3.284E+4
	Entry Loss (kPa)	2340		1143	-na-

Table 4-7

Test Matrix
0.127 mm Nominal Slit Opening Dimension

Nominal Stagnation Pressure	Test Parameters	Nominal Stagnation Subcooling			
		60°C	30°C	15°C	3°C
4.2 MPa	Run #	61	64	63	65
	Pressure (MPa)	4.217	4.260	4.231	4.382
	Subcooling (°C)	60.8	30.2	15.0	5.6
	D_h (m)	2.524E-4	2.524E-4	2.524E-4	2.524E-4
	G($\frac{kg}{m^2 \cdot s}$)	2.216E+4	1.670E+4	1.306E+4	1.305E+4
	Entry Loss (kPa)	1294	558	410	-na-
7.2 MPa	Run #	50	67	85	86
	Pressure (MPa)	7.205	7.203	7.189	7.179
	Subcooling (°C)	63.5	29.8	14.2	3.8
	D_h (m)	1.588E-4	2.524E-4	2.523E-4	2.523E-4
	G($\frac{kg}{m^2 \cdot s}$)	1.927E+4	1.670E+4	1.544E+4	1.472E+4
	Entry Loss (kPa)	674	756	541	-na-
9.6 MPa	Run #	84	48	49	82
	Pressure (MPa)	9.684	9.645	9.661	9.660
	Subcooling (°C)	56.8	30.5	14.6	0.0
	D_h (m)	2.523E-4	1.588E-4	1.588E-4	2.523E-4
	G($\frac{kg}{m^2 \cdot s}$)	3.009E+4	1.899E+4	1.538E+4	1.681E+4
	Entry Loss (kPa)	460	523	135	-na-
11.6 MPa	Run #	88	66	80	81
	Pressure (MPa)	11.860	12.078	11.796	11.537
	Subcooling (°C)	57.9	30.0	13.1	0.2
	D_h (m)	2.523E-4	2.524E-4	2.523E-4	2.523E-4
	G($\frac{kg}{m^2 \cdot s}$)	3.254E+4	3.161E+4	2.234E+4	2.126E+4
	Entry Loss (kPa)	441	961	251	-na-
15.6 MPa	Run #	87	89		
	Pressure (MPa)	15.927	16.122		
	Subcooling (°C)	56.7	27.8		
	D_h (m)	2.523E-4	2.523E-4		
	G($\frac{kg}{m^2 \cdot s}$)	3.759E+4	3.030E+4		
	Entry Loss (kPa)	784	506		

Table 4-8

Runs For Which Results Are Inconsistent With
The Body of Data

Discounted Run (#)	Run(s) for Comparison (#)	Explanation
21	34,85	Mass flux 20% lower than run #34 which has smaller D_h.
22	86	Mass flux compares well with run #86, but entry pressure loss is too large (3.1 MPa). (see pressure profile, Appendix B)
23	51	Mass flux 4.2% larger than for run #51 even though D_h is smaller. Also, Chapter V model comparison.
94	93,97 and 100	Reduction in mass flux between runs #93 and #94 is much larger than would be expected from comparing runs #97 and #100. Also, Chapter V model comparison. Run #93 may have had two-phase stagnation state.

Figure 4-1
Vessel Level Determination

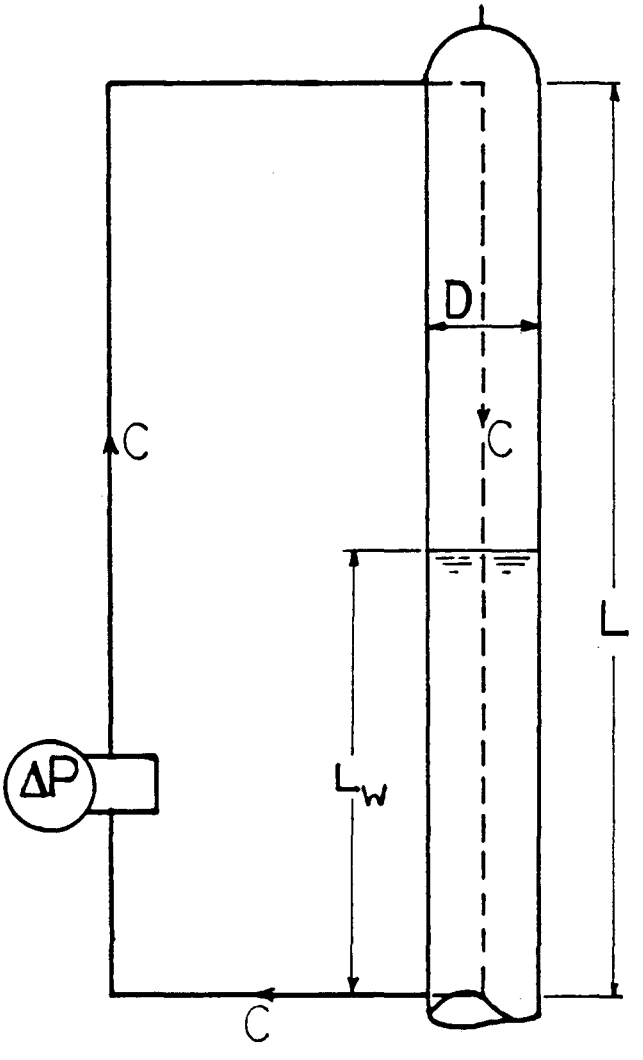

XBL 838-489

Figure 4-2
Mass Flux Versus Stagnation Subcooling

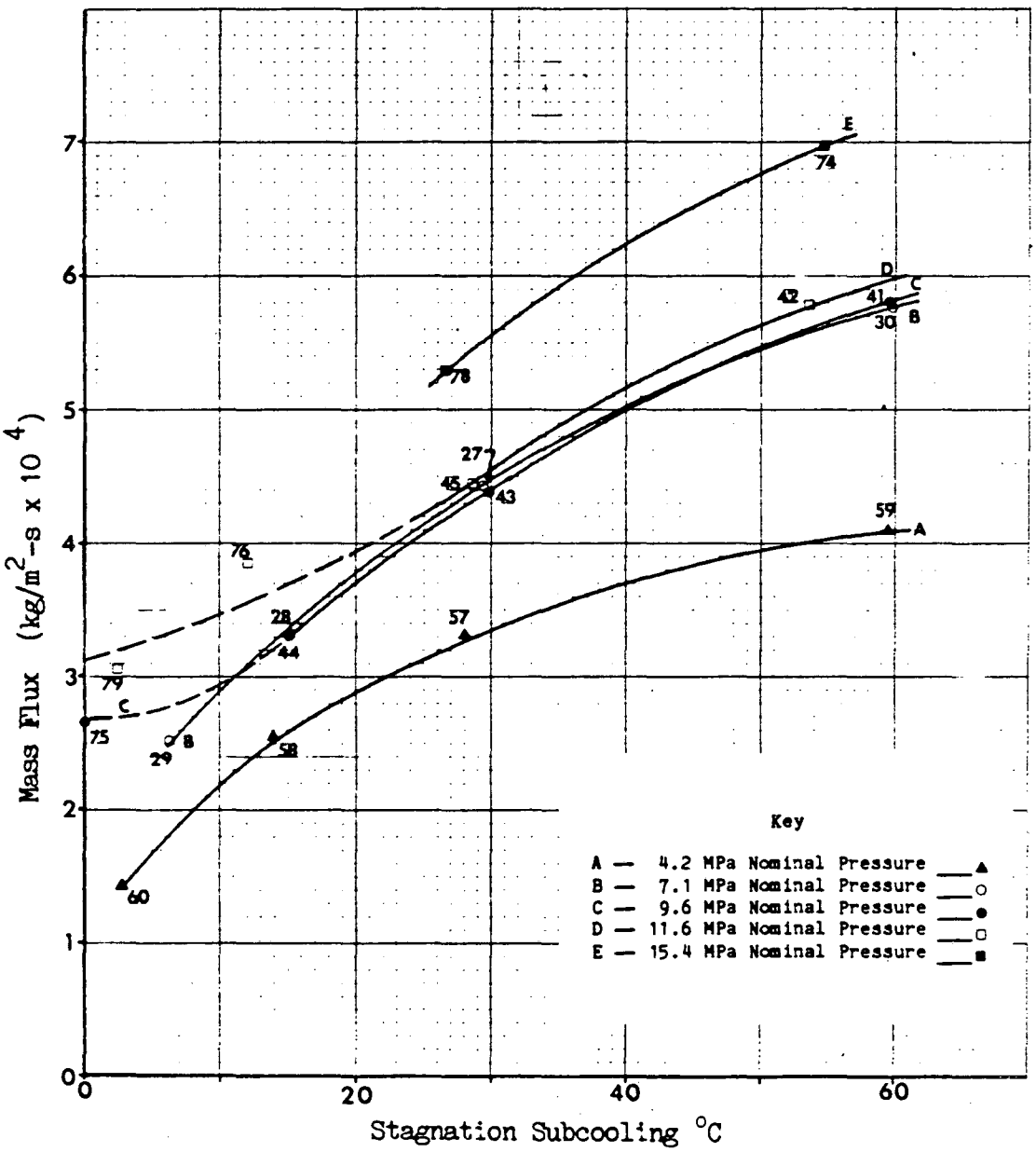

XBL 838-490

Figure 4-3
Critical Pressure Ratio Versus Subcooling

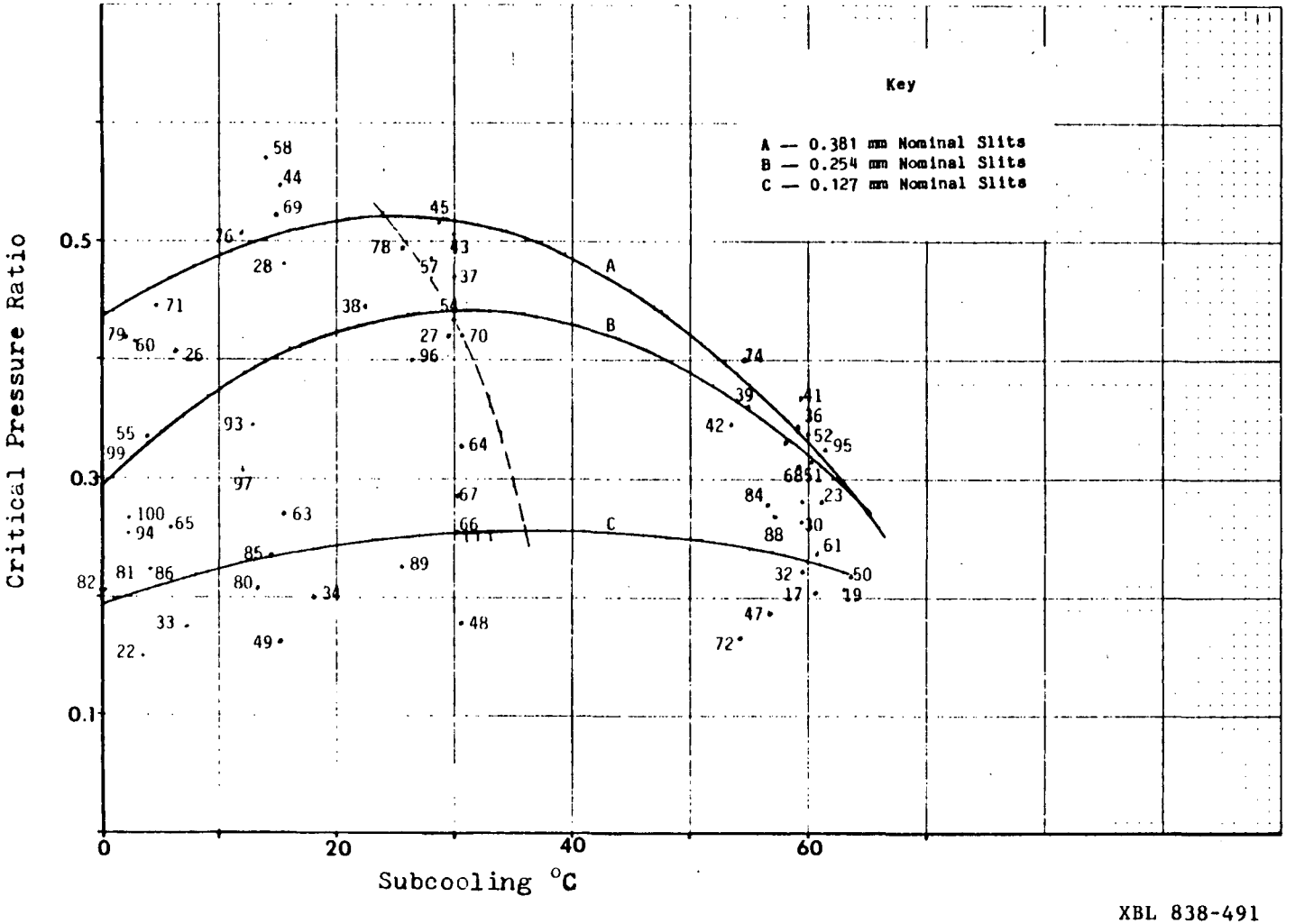

XBL 838-491

Figure 4-4
Mass Flux Versus L/D

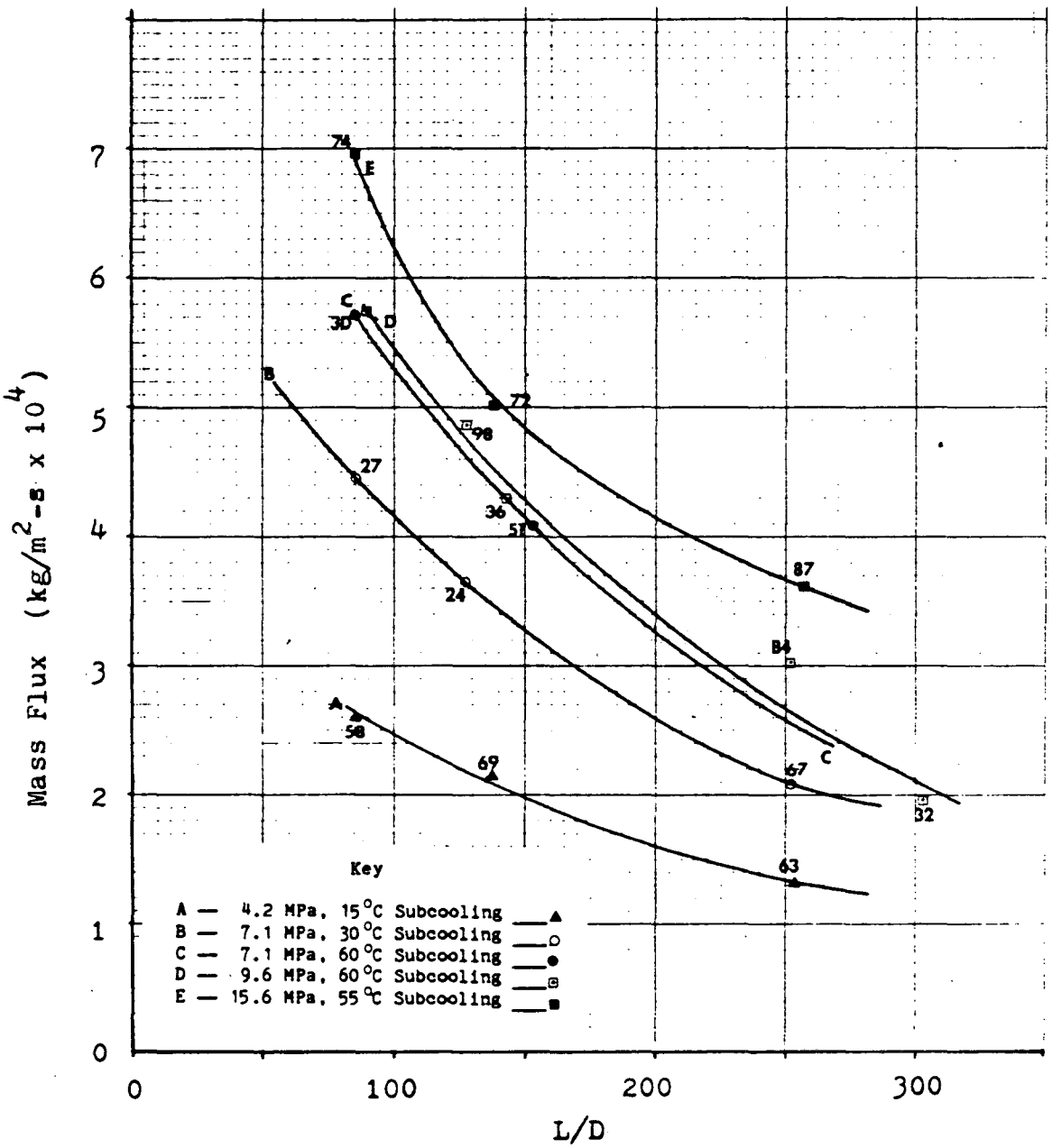

XBL 838-492

Figure 4-5
Mass Flux Versus Stagnation Subcooling

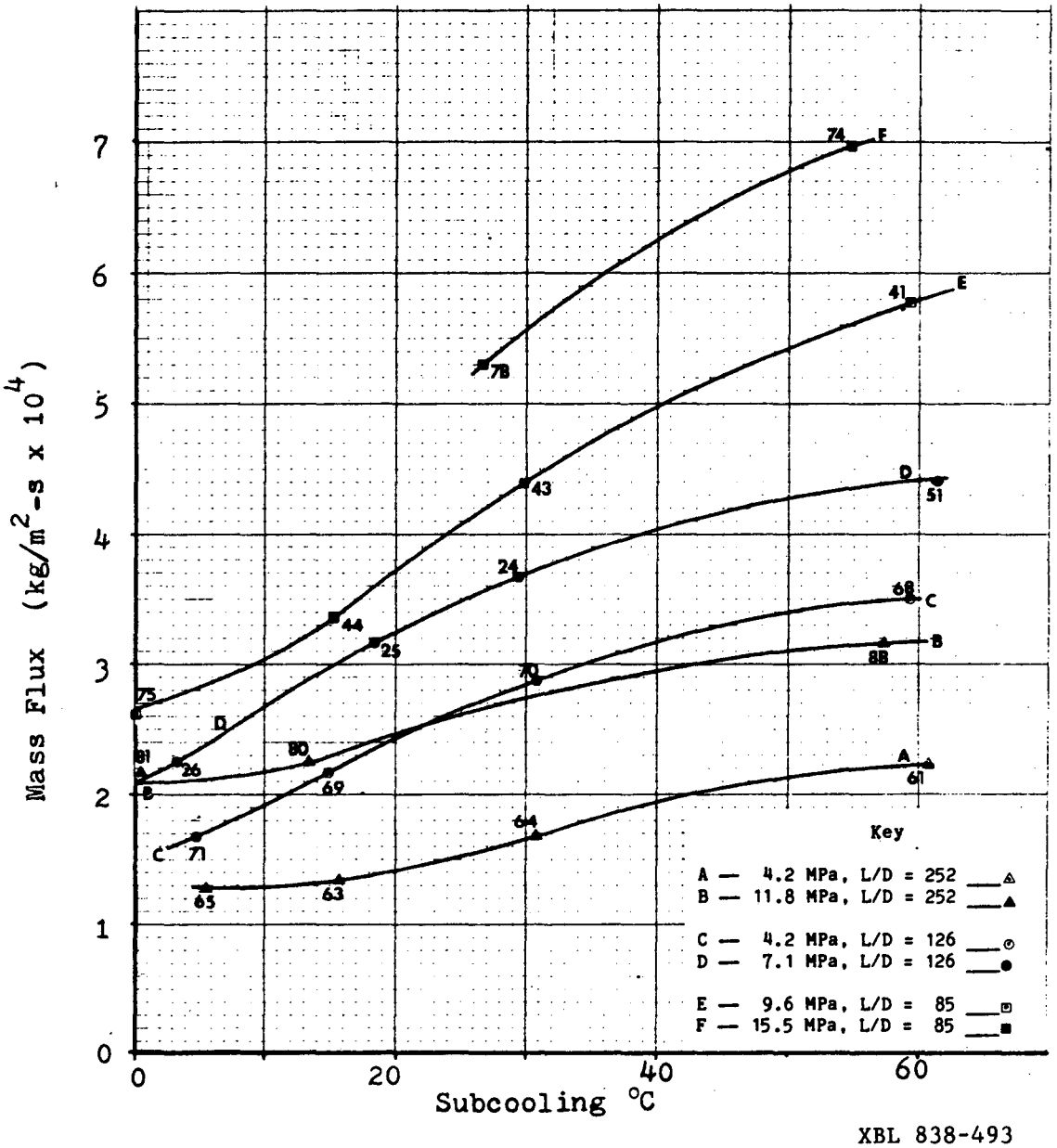

Figure 4-6
Run #60, Exit Pressure Trace

P = 4.1 MPa, Θ_o = 3 °C
Vertical Scale: 40 kPa/cm, Horizontal Scale: 5 cm = 1 sec.

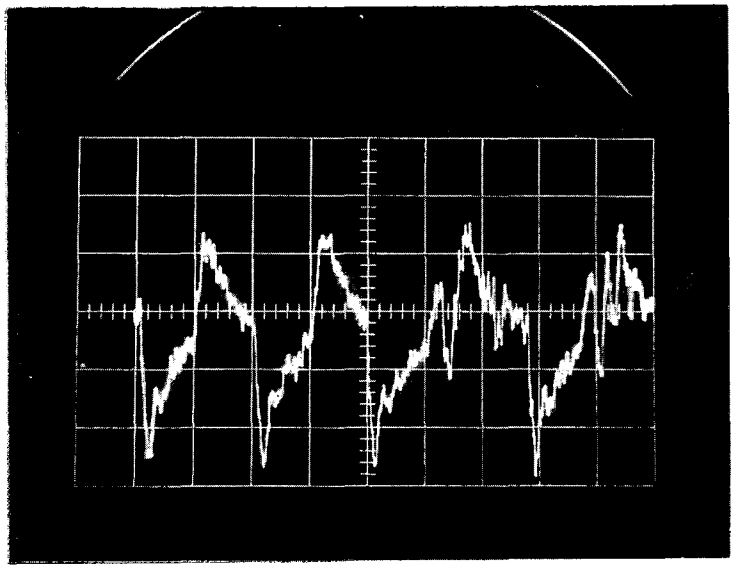

a) Begins 10 sec. after flow initiated, t ≈ 50 sec.

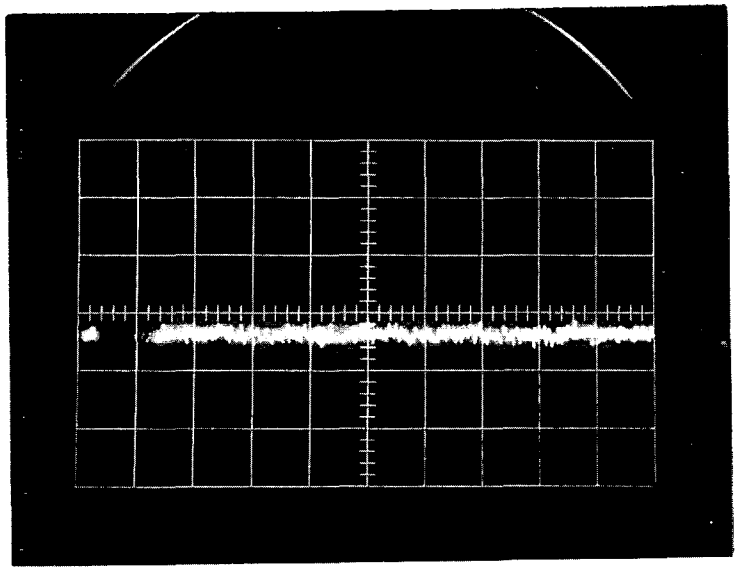

b) Begins 85 sec. after flow initiated, t ≈ 125 sec.

XBB 838-6757

Figure 4-7
Run #51, Exit Pressure Trace

P = 7.2 MPa, Θ_o= 60°C
Vertical Scale: 40 kPa/cm, Horizontal Scale: 5 cm = 1 sec.

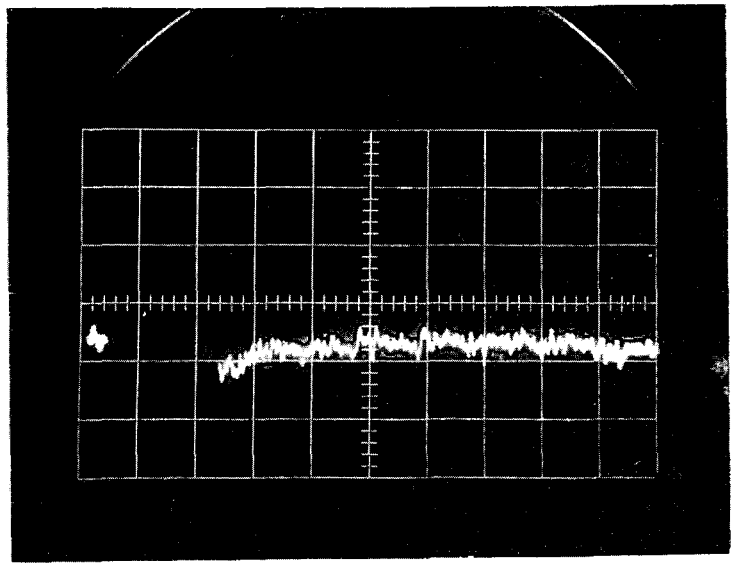

a) Begins 10 sec. after flow initiated, t ≃ 50 sec.

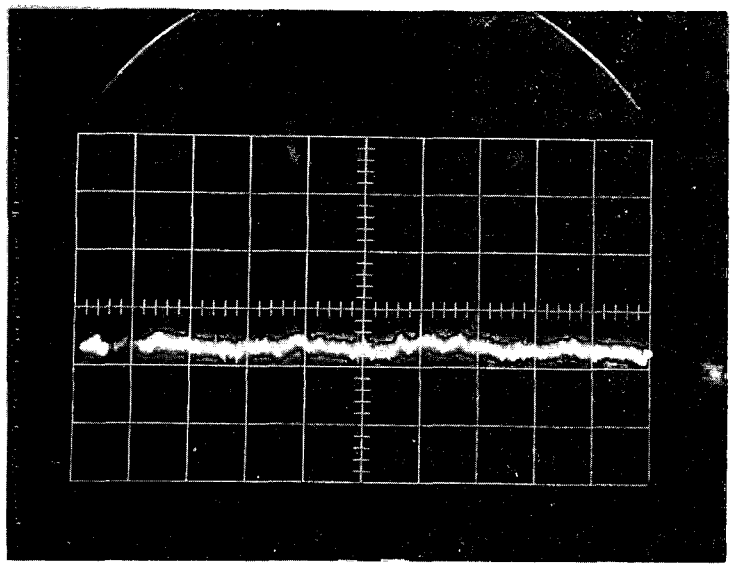

b) Begins 60 sec. after flow initiated, t ≃ 100 sec.

XBB 838-6758

Figure 4-8
Run #42, Exit Pressure Trace

P = 11.6 MPa, Θ_o = 53°C
Vertical Scale: 40 kPa/cm, Horizontal Scale: 5 cm = 1 sec.

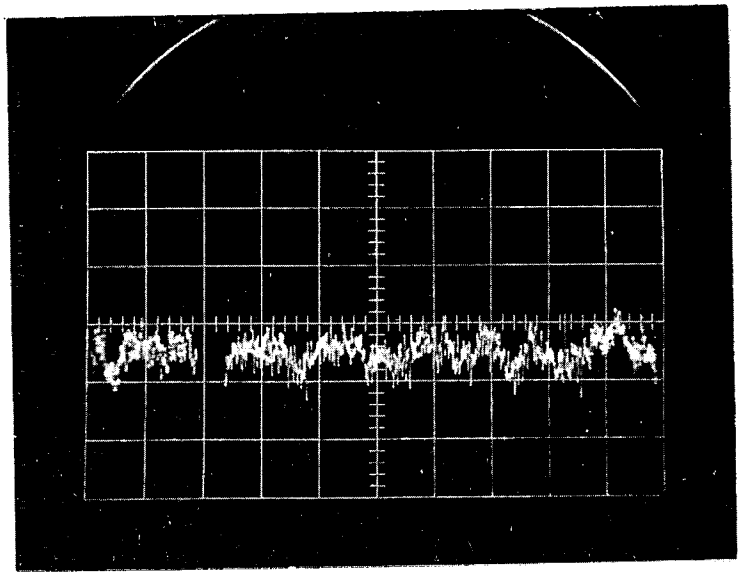

a) Begins 10 sec. after flow initiated, t ≈ 85 sec.

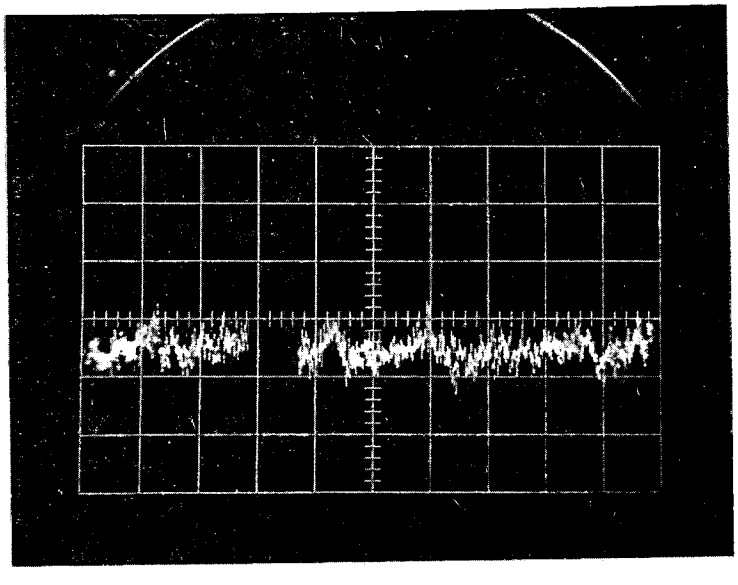

b) Begins 25 sec. after flow initiated, t ≈ 100 sec.

XBB 838-6759

Figure 4-9
Run #99, Exit Pressure Trace

P = 9.6 MPa, Θ_o = 0 °C
Vertical Scale: 40 kPa/cm, Horizontal Scale: 5 cm = 1 sec.

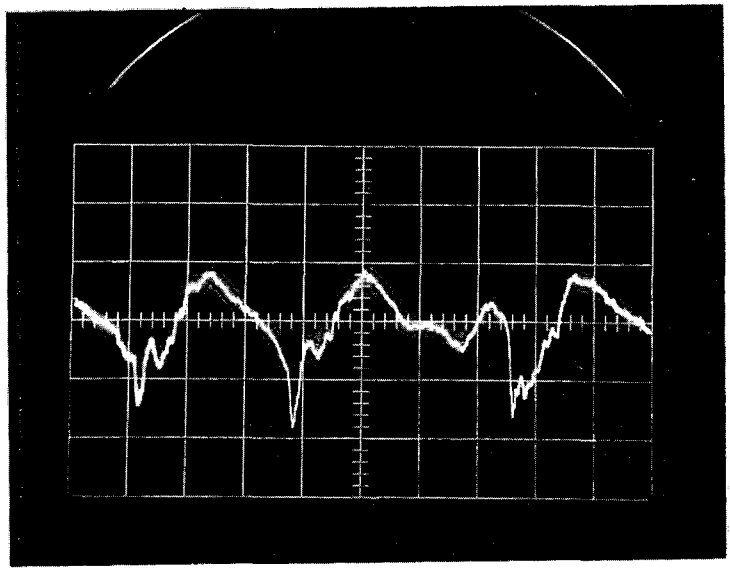

a) Begins 20 sec. after flow initiated, t ≃ 55 sec.

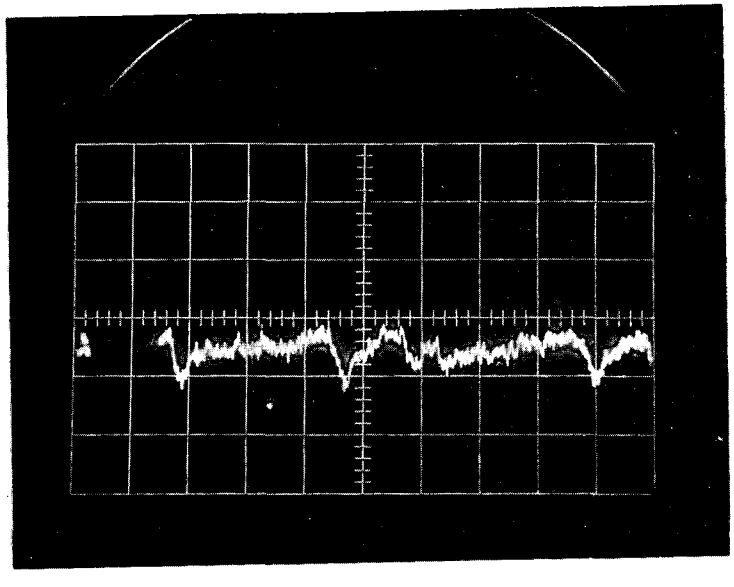

b) Begins 85 sec. after flow initiated, t ≃ 120 sec.

XBB 838-6760

Figure 4-10

Run #30: D_h=0.748 P_o = 7.1 MPa θ_o=60 °C

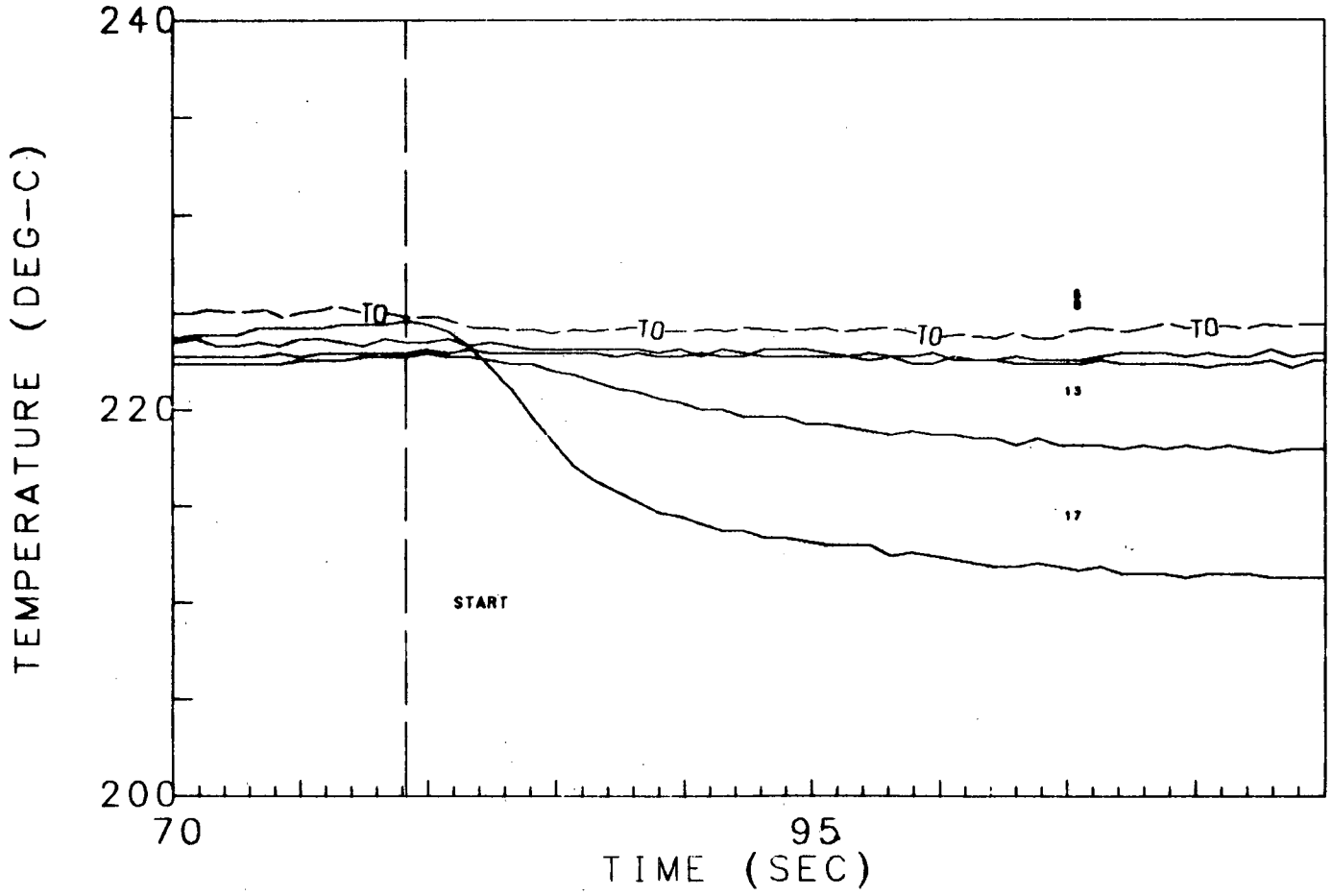

THERMOCOUPLE TRACES FOR NOS. 2, 6, 8, 13, 17

XBL 838-494

Figure 4-11
Run #59: D_h=0.747 mm P_o =4.3 MPa Θ_o=59 °C

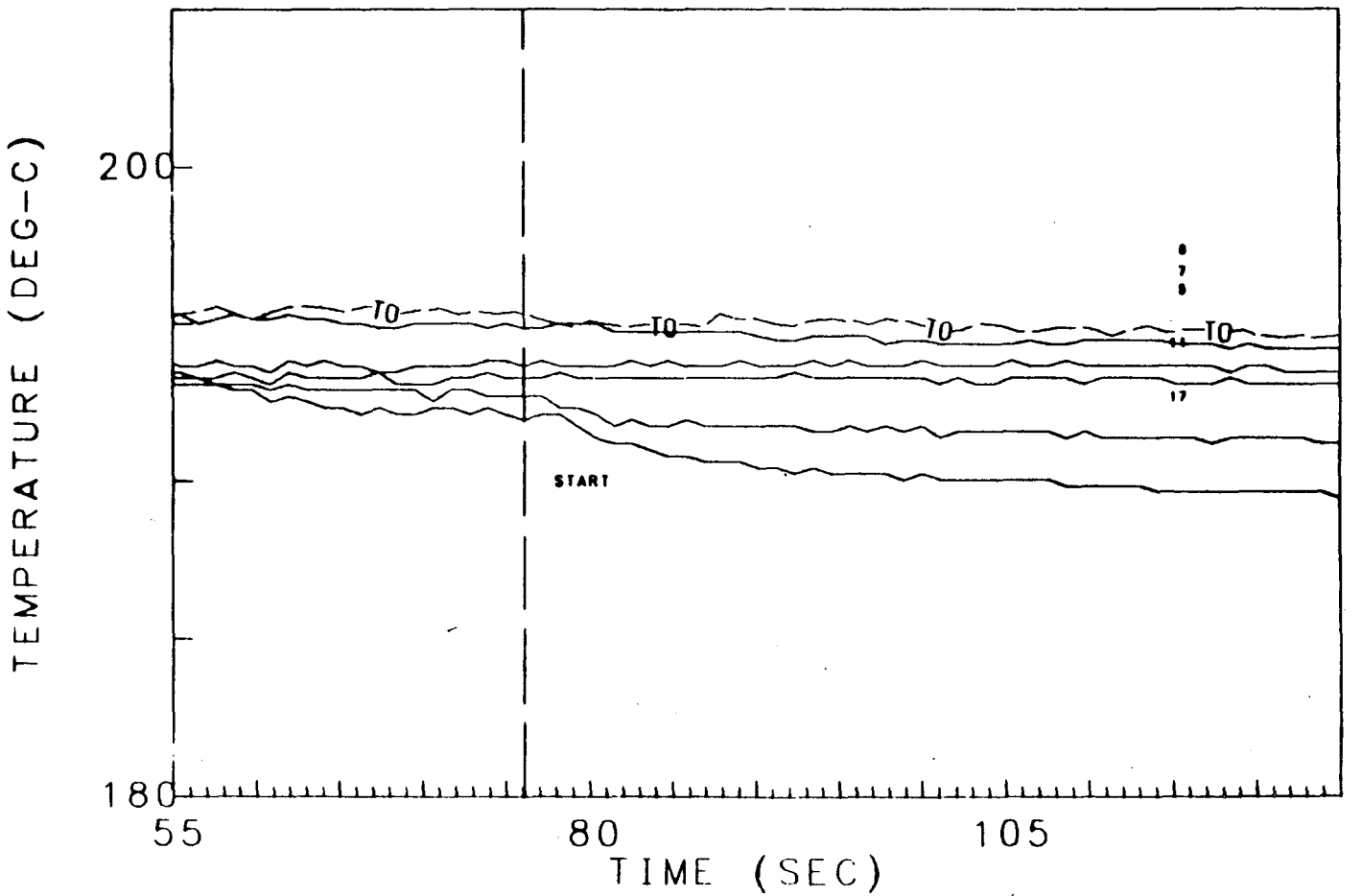

THERMOCOUPLE TRACES FOR NOS. 2, 5, 6, 7, 11, 17

XBL 838-495

Figure 4-12
Run #24: D_h=0.502 mm P_o =7.1 MPa Θ_o=29 °C

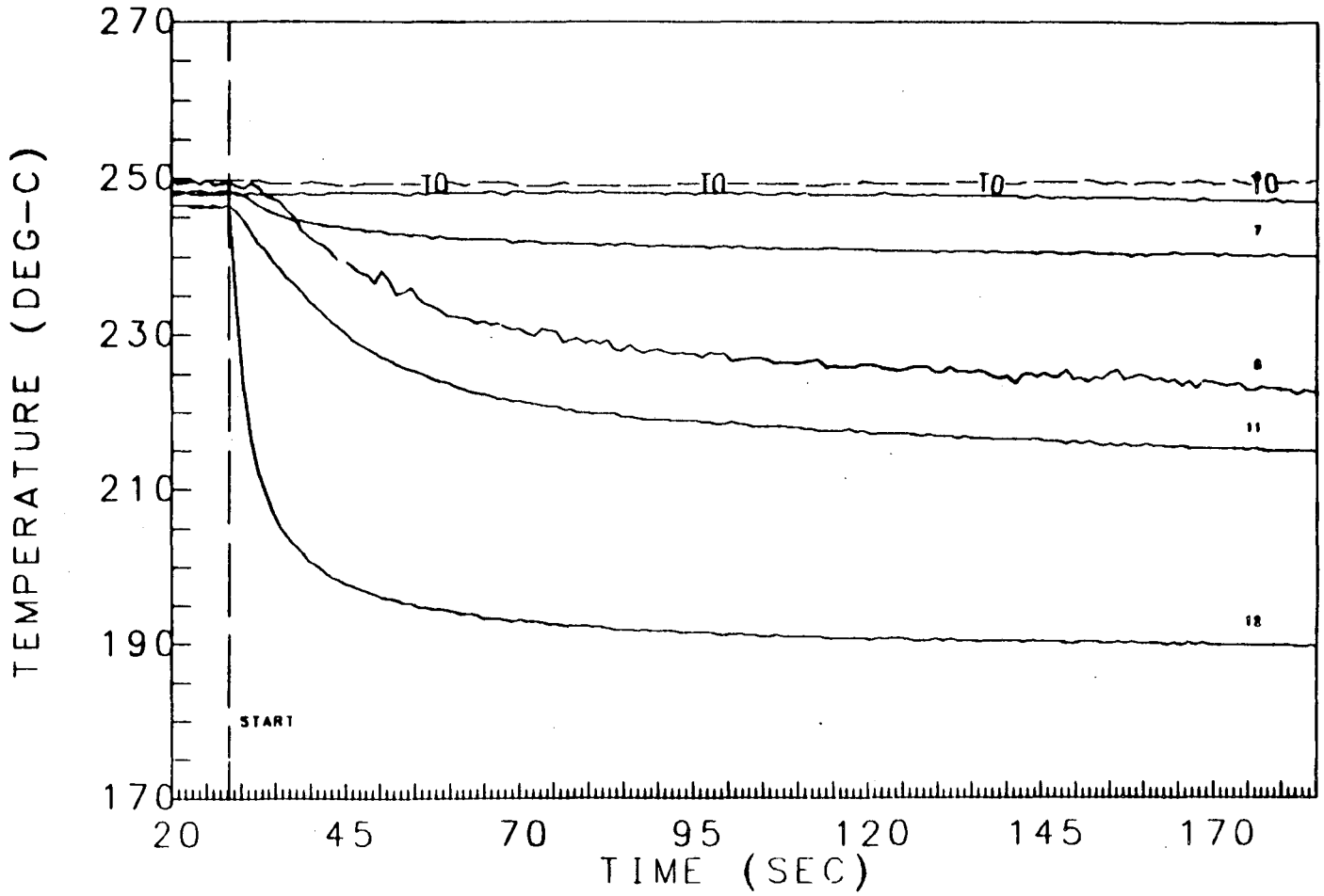

THERMOCOUPLE TRACES FOR NOS. 2, 3, 7, 8, 11, 12

XBL 838-496

Figure 4-13
Run #54: D_h=0.418 mm P_o =11.7 MPa θ_o=30 °C

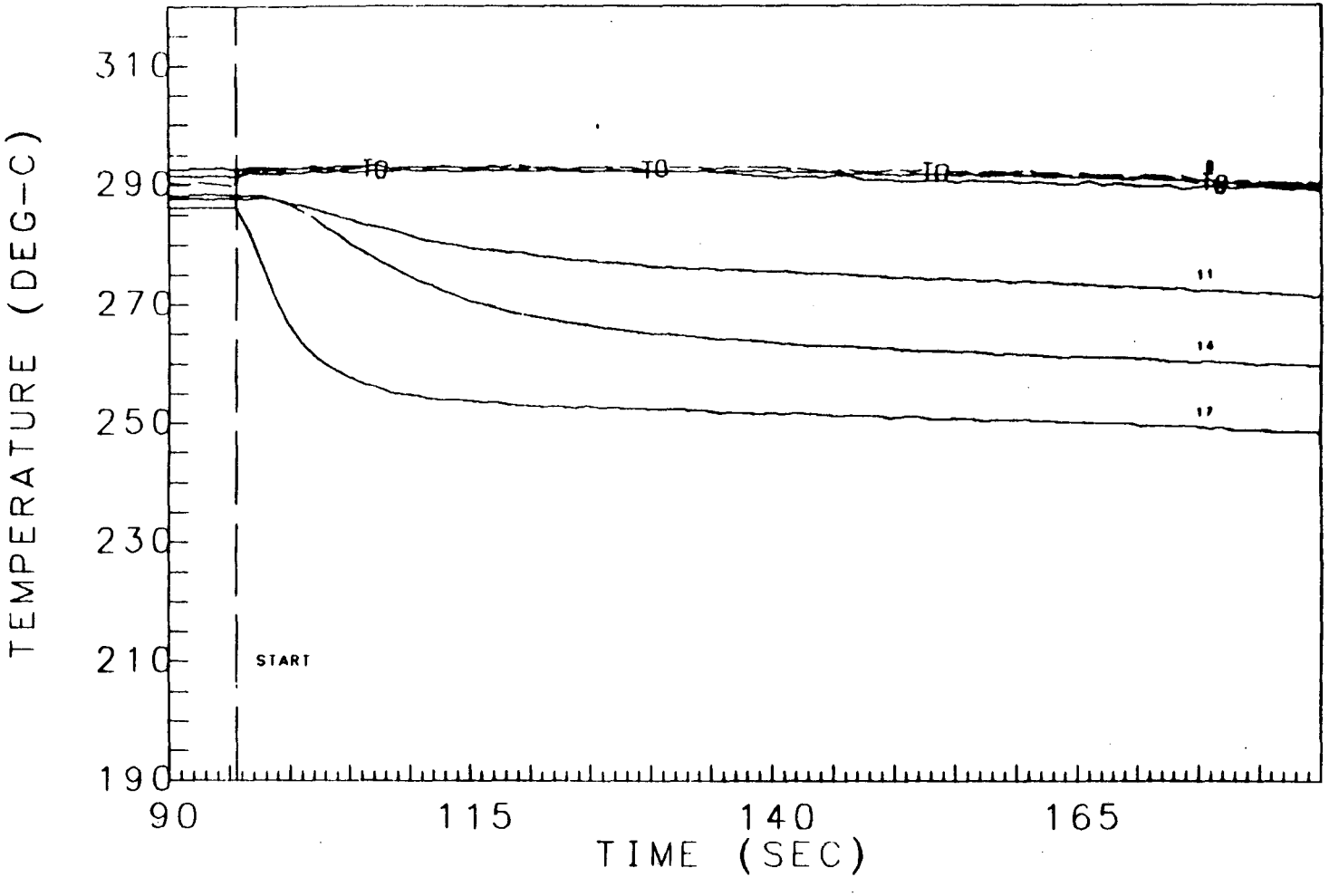

THERMOCOUPLE TRACES FOR NOS. 2, 7, 8, 11, 14, 17

XBL 838-497

Figure 4-14
Run #65: D_h=0.252 mm P_o=4.3 MPa θ_o=6 °C

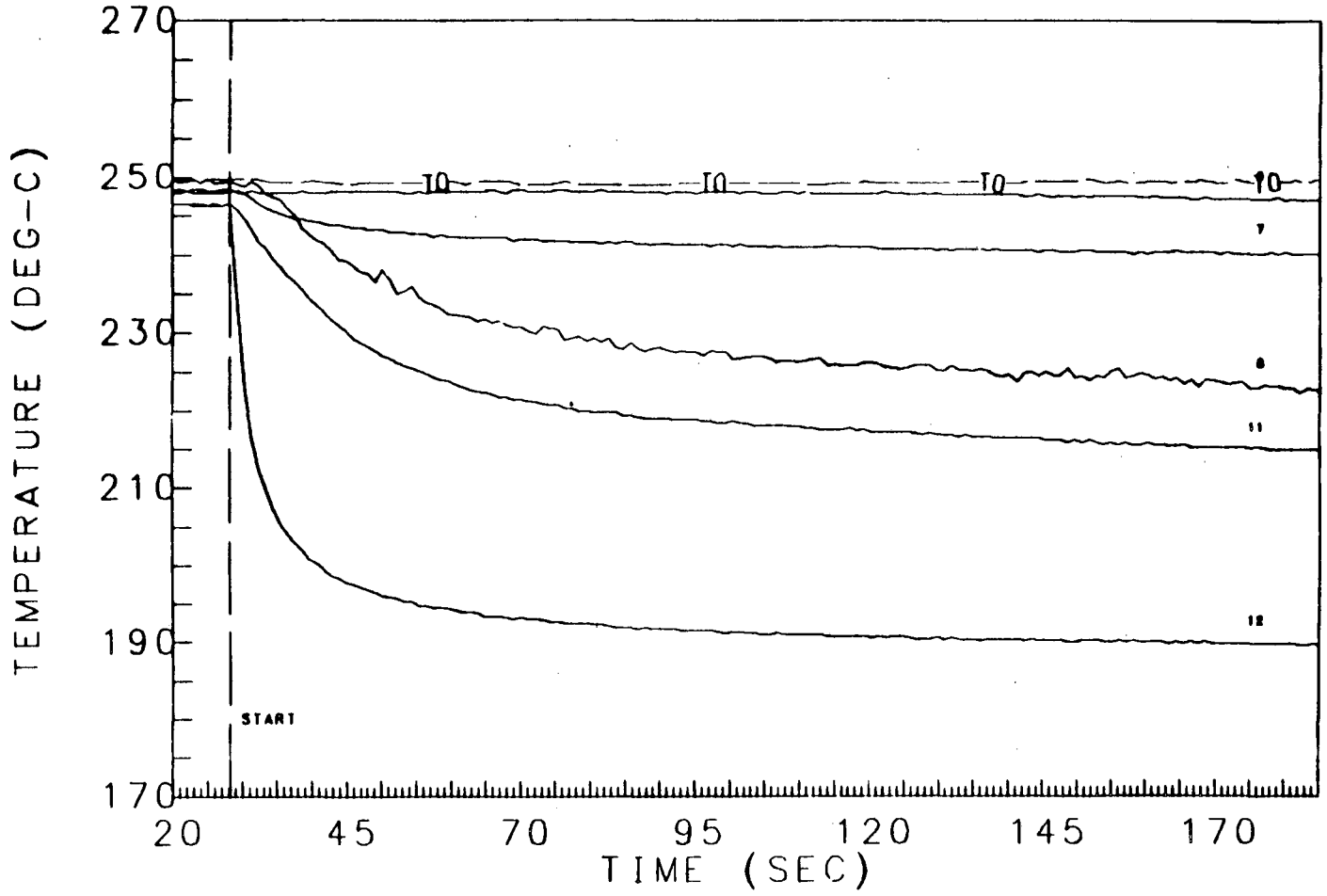

THERMOCOUPLE TRACES FOR NOS. 2, 3, 7, 8, 11, 12

XBL 838-498

Figure 4-15
Run #94: D_h=0.502 mm P_o=11.7 MPa θ_o=2 °C

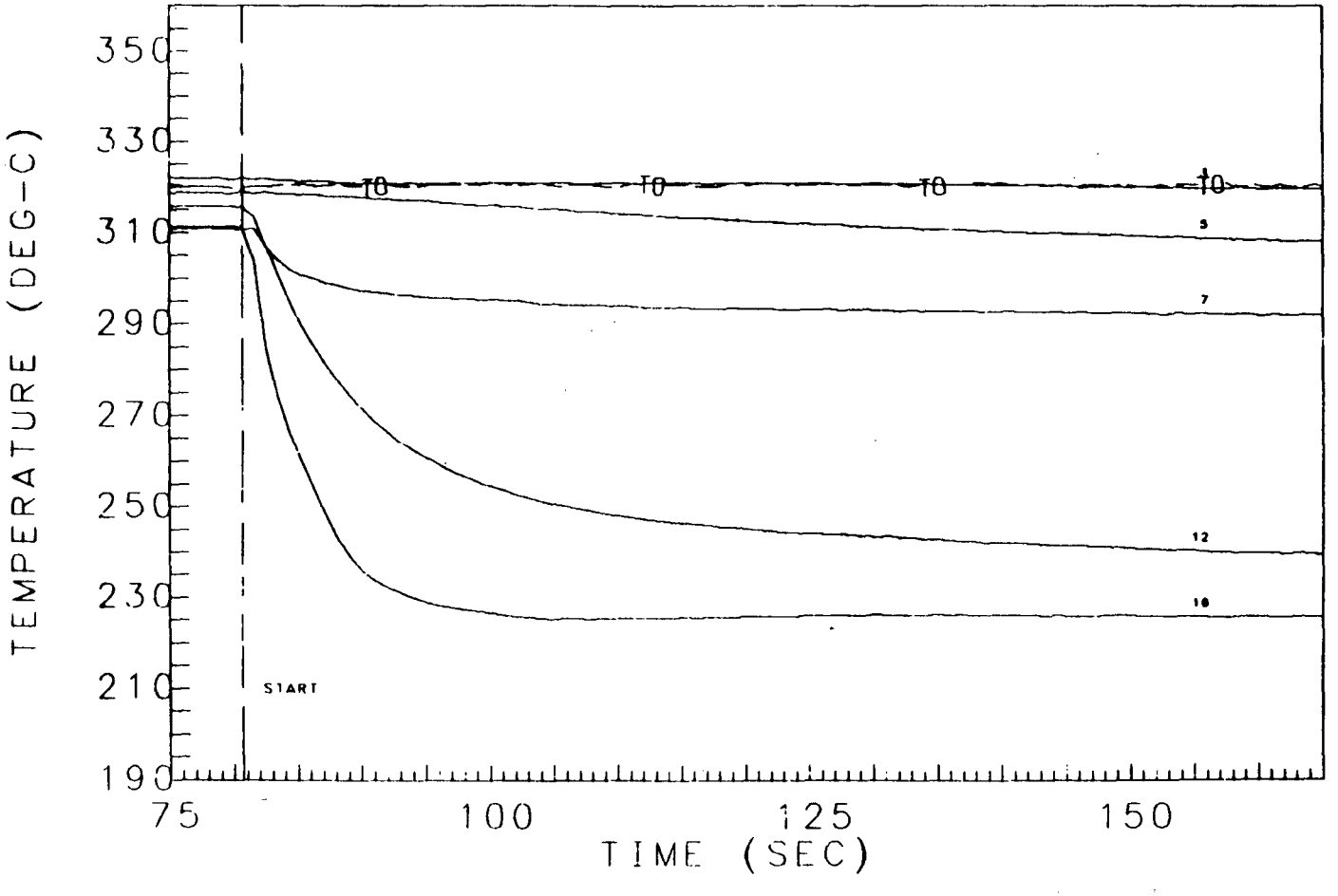

THERMOCOUPLE TRACES FOR NOS. 2, 3, 5, 7, 12, 16

XBL 838-499

Chapter V

Modeling

In this chapter the experimental results are compared to theoretical models for two-phase critical flow. Only simple models have been considered. There are several reasons for not using a two-fluid model. First, as was stated in Chapter II, given the current state of the art, there is no clear advantage in using two-fluid models. Second, two-fluid models are more costly to apply. Third, transfer terms used in two-fluid models have been developed assuming flow in a channel of a much larger size than has been considered in this work. It is unlikely that interphase transfer models, developed under the assumptions which have been made about flows in channels studied in previous experiments, are appropriate to this geometry. For instance, models such as that of Richter and Minas [81] which model the vapor generation rate assuming conduction controlled bubble growth, are clearly invalid when the channel is smaller than the assumed bubble diameter. Both of the two-fluid models which were discussed in Chapter II assumed spherical bubbles in modeling the interphase drag.

Almost all the available simple models neglect friction, and/or model vapor generation rate in terms of the conduction controlled growth of a single bubble. Nicolette's [53] proposal of Fanno line flow using the HEM, and Moody's extension of his slip flow model for nozzles to pipe flows [59], are the only simple models in literature which are suitable for the case at hand. A Fanno Homogeneous Equlibrium Model, identical in formulation to that proposed by Nicolette, has been used for comparison with the experimental data. The deficiencies of Moody's model were discussed in Chapter II. Two new simple models have been developed and are presented in this chapter. The first of these is based on Henry's Model [21]. The original model has been modified to include friction but the technique of correlating the actual thermodynamic quality against the equilibrium quality has been preserved. As justification for the development of this model, the results of predictions made with the original Henry model have been presented.

The second model which has been developed borrows from several previous proposals. The criterion for flashing inception was based on the Alamgir-Lienhard correlation [68]; as has been proposed by Abuaf et al [98]. The metastable liquid phase has been assumed to relax toward equilibrium in an exponential manner analogous to that proposed by Bauer, et al, [99]. Finally, the critical flow criterion was taken from Kroeger's formulation [87] of the nonequilibrium sound speed for homogeneous flow. His derivation was based on a method of characteristics analysis of a four equation drift-flux formulation.

V.1 Criteria for a Two-Phase Critical Flow Model

Frequently two-phase critical flow models have been judged on the basis of their ability to predict experimentally determined flowrates. Success in the prediction of flowrates have led some to claim that the agreement between model and experiment proves (or at least justifies) the assumptions inherent in the model. Clearly, this is not a sound conclusion. As was pointed out in Chapter II, there may be compensating errors.

Three criteria have been used to judge the usefulness of the models proposed herein: 1) Agreement between measured flowrate and model prediction. 2) Agreement between measured pressure at the exit of the flow channel and the critical pressure predicted by the model. 3) Agreement between the location of flashing inception determined from the pressure profile data and the location predicted by the model. The determination of the point of flashing inception from the data was somewhat subjective. In the absence of void profile measurements, the best available information was obtained from the pressure profiles, as was outlined in Chapter IV. Results are presented graphically in Appendix B.

V.2 Development of Models

The Homogeneous Equilibrium Model (HEM) and the Modified Henry Model (MHM) were developed on the basis of mixture conservation equations. They differ only in their expression for the vapor generation rate. It should be pointed out that, like Henry's original model, the modified version developed here does not conserve energy correctly. The Homogeneous Non-Equilibrium (HNEM) model proposed here was derived on the basis of the two-fluid equations. Mass, momentum, and energy are correctly conserved.

V.2.1 Single-Phase Liquid Flow

Because the stagnation conditions considered in this work were in most instances highly subcooled, flashing did not occur in many of the runs until very close to the test section exit. This feature required that an accurate model for the single-phase liquid flow be incorporated into all three of the models used to predict the results. Because of the high pressures involved in these experiments the compressibility of the liquid phase was taken into account.

For the steady state, vertically downward, flow of a single-phase fluid in a adiabatic channel with friction, the following simple expressions for the conservation of mass, momentum, and energy are valid:

Mass:

$$\rho UA = \text{const.} \tag{5-1}$$

Momentum:

$$\rho u \frac{du}{dz} = -\frac{dP}{dz} - \left(\frac{dP}{dz}\right)_f + \rho g z \tag{5-2}$$

Energy:

$$h_0 = h + \frac{u^2}{2} = \text{const.} \tag{5-3}$$

Solution for flow of the liquid phase was obtained by taking d/dz of equations (5-1) and (5-3) to obtain:

Mass:

$$\frac{1}{\rho}\frac{d\rho}{dz} + \frac{1}{u}\frac{du}{dz} + \frac{1}{A}\frac{dA}{dz} = 0 \tag{5-4}$$

Energy:

$$\frac{dh}{dz} + u\frac{du}{dz} = 0 \tag{5-5}$$

State equations for the subcooled liquid were taken from the 1967 ASME Steam Tables. State equations may be represented symbolically as:

$$v_l = v_l(T,P) \tag{5-6a}$$

$$h_l = h_l(T,P) \tag{5-6b}$$

Thus, the dependent variables of the system were P, T, and u. Expanding the total derivatives in equations (5-4) and (5-5) the system to be integrated was:

$$\frac{-1}{v_l}\left(\frac{\partial v_l}{\partial P}\right)_T \frac{dP}{dz} + \frac{1}{u}\frac{du}{dz} - \frac{1}{v_l}\left(\frac{\partial v_l}{\partial T}\right)_P \frac{dT}{dz} = \frac{-1}{A}\frac{dA}{dz} \tag{5-7}$$

$$\frac{dP}{dz} + \frac{u}{v_l}\frac{du}{dz} = -\left(\frac{dP}{dz}\right)_f + \frac{g}{v_l} \tag{5-8}$$

$$\left(\frac{\partial h_l}{\partial P}\right)_T \frac{dP}{dz} + u\frac{du}{dz} + c_{pl}\frac{dT}{dz} = 0 \tag{5-9}$$

Entry losses were accounted for assuming a pressure loss given by:

$$\Delta P_e = K\frac{u^2}{2v_l} \tag{5-10}$$

where K is the entry loss coefficient calculated from the data. Normally, the pressure loss at the entrance was taken to occur isothermally. When the stagnation state was close to saturation, the entry loss was sometimes predicted to be sufficiently high that the flashing criterion was met. For the HEM it was assumed that flashing occurred when pressure inside the entrance was lower than the saturation pressure corresponding to the liquid temperature. In this case the entry loss was assumed to occur isentropically. Quality at the channel entry (z=0) was then evaluated by:

$$x(z_0) = \frac{s_0 - s_f\left(P_0(z_0)\right)}{s_{fg}\left(P_0(z_0)\right)} \tag{5-11}$$

In this case there is no single-phase flow region and only the two-phase equations are required. For the MHM, when the entry loss brought the fluid pressure below saturation flashing was taken to occur at exactly $z = 12D_h$; independent of the amount of superheating present at this location. This is exactly the assumption of Henry's original model. For the nonequilibrium model, if the entry pressure was less than that required for flashing by the Alamgir-Lienhard correlation, flashing was taken to occur at this lower entry pressure. This was done on the basis of the assumption that depressurization in the entry region was so rapid that flashing could not occur. In the modeling of the present data there are only two instances where entry loss was sufficiently high to make use of this assumption.

The boundary condition for the integration of equations (5-6) through (5-7) was related to the stagnation state by:

$$\left.\begin{aligned} P(z_0) &= P_0 - \Delta P_e \\ T(z_0) &= T_0 \end{aligned}\right\} \tag{5-12}$$

The critical flow prediction of a model was obtained by an iterative process. Successive estimations of the critical mass flux were made until the value which caused the choking criterion to be met at the exit of the given channel was found. The solution strategy is discussed in detail below. The downstream boundary condition for single-phase flow was determined by the flashing inception criteria which have been mentioned above but are discussed separately below for each of the three models employed.

V.2.2 Homogeneous Equilibrium Model

As was stated in Chapter II, Wallis [50] has noted that the HEM is essentially a representation of the two-phase flow as an equivalent single-phase flow. The two-phase mixture is treated as a quasi-fluid, the state equations for which are given by the mixture properties:

$$v = (1-x)v_f(P) + xv_g(P)$$

$$h = (1-x)h_f(P) + xh_g(p) \tag{5-13}$$

Since the mixture is assumed to be in thermodynamic equilibrium, the necessary dependent variables are P, u and x. Again, the 1967 ASME Steam Tables were used to obtain the saturated fluid properties. The single-fluid equations (5-4), (5-2) and (5-5) were re-written for the HEM as:

$$\frac{-1}{v}\left[(1-x)\frac{dv_f}{dP} + x\,\frac{dv_g}{dP}\right]\frac{dP}{dz} + \frac{1}{u}\,\frac{du}{dz} - \frac{v_{fg}}{v}\,\frac{dx}{dz} = 0 \tag{5-14}$$

$$\frac{dP}{dz} + \frac{u}{v}\,\frac{du}{dz} = -\left(\frac{dP}{dz}\right)_f + \frac{g}{v} \tag{5-15}$$

$$\left[(1-x)\,\frac{dh_f}{dP} + x\,\frac{dh_g}{dP}\right]\frac{dP}{dz} + u\,\frac{du}{dz} + h_{fg}\,\frac{dx}{dz} = 0 \tag{5-16}$$

V.2.2.1 Flashing Criteria

Upstream boundary conditions were given by the solution of the liquid flow equations at the point where the flashing criteria were met. For the HEM this criterion was straight forward:

$$P_{fl} = P_{sat}(T) \tag{5-17}$$

The boundary conditions for the HEM equations were thus:

$$P(z_{fl}) = P_{sat}(T)$$

$$u(z_{fl}) = u(z_{fl}) \qquad \text{from liquid equations}$$

$$x(z_{fl}) = 0 \tag{5-18}$$

V.2.2.2 Critical Flow Criteria

A sound speed criterion was used to determine when the flow was critical. This was given by equation (2-2). Expanding this equation in terms of properties required in the integration of equations (5-14) through (5-16) gave:

$$u_c = a_{HE} = \left[\frac{1}{v} \left((1-x) \frac{dv_f}{dP} + x \frac{dv_g}{dP} + v_{fg} \left(\frac{dx}{dP} \right)_s \right) \right]^{-1/2} \tag{5-19}$$

The equilibrium mass transfer rate for an isentropic process was given by taking the saturation derivative of equation (5-11) with respect to pressure:

$$\left(\frac{dx}{dP} \right)_s = \frac{(1-x) \frac{ds_f}{dP} + x \frac{ds_g}{dP}}{s_{fg}} \tag{5-20}$$

Integration of the model equations was terminated once the mixture velocity was equal to the critical velocity given by equation (5-19). Supersonic choking was presumed to occur if the liquid velocity was larger than the zero quality sound speed. In this instance, flashing and choking coincide at the exit plane. The zero quality sound speed is evaluated by taking x=0 in equations (5-20) and (5-19).

V.2.3 Modified Henry Model

Henry's model for two-phase critical flow in long ducts is described in detail in Chapter II. Frictional effects were not considered in Henry's proposal. Henry's model is thus inadequate for the prediction of the results of the present experiments. A comparison between Henry's model and these results has been included below as part of the section on the application of models in this research program.

Just as Henry's model was a correlation to the IHEM, the modified version is a correlation to the Fanno Line HEM, described in the preceding section. There are three advantages to this approach. First, the formulation is simple and, in fact, is more simply solved than the HEM. This is because the energy equation is replaced by a simple correlation. Second, the model includes the most important facets of two-phase critical flow from subcooled stagnation conditions. Flashing is assumed to occur after the liquid has become superheated. The quantity of vapor generated is assumed to be less than that corresponding to an equilibrium flow. Vapor generation rate is taken to increase to the equilibrium rate as the thermodynamic quality of the flowing mixture increases. These are features of all thermodynamic nonequilibrium models. However, other models do not predict equilibrium vapor generation rates in the limit of high quality, as does Henry's. Third, critical flow is a natural result of the model equations, just as in the HEM. As with the HEM, the critical velocity is the two-phase sound speed predicted by the model equations.

The equations for the Modified Henry Model (MHM) are developed below. Conservation of mixture mass and momentum are expressed exactly as for the HEM. Equations (5-14) and (5-15) are employed. Mixture energy conservation is replaced by an expression which correlates the vapor generation rate to the equilibrium rate. The proposed correlation is:

$$\frac{dx}{dz} = N \frac{dx_E}{dP} \frac{dP}{dz} \left\{ 1 - \exp\left[-B \left(\frac{z - z_{fl}}{D_h} \right) \right] \right\} +$$

$$\left(\frac{B}{D_h} \right) N x_E \exp\left[-B \left(\frac{z - z_{fl}}{D_h} \right) \right] \qquad (5\text{-}21)$$

The value of B was taken to be 0.0523 as proposed by Henry.

Equation (5-21) was derived from Henry's original correlation by taking the derivative of equation (2-16) with respect to pressure. (In Henry's original paper [21] equation (2-16) was derived erroneously; despite this, the above form has been employed in the current model.) Energy is not conserved in the proposed model. For the thermodynamic quality of the mixture to be lower than that assuming equilibrium vapor production, one or both of the phases must have a temperature larger than the saturation temperature corresponding to the local pressure. Usually the liquid is assumed to be superheated. This model takes both phases to have saturation properties. Henry's original formulation assumed the liquid to be isothermal and incompressible. That assumption also fails to conserve energy rigorously but should be closer to the actual situation, provided the quality is not sufficiently high that equilibrium is approached.

V.2.3.1 Flashing Criterion

Flashing is assumed to occur 12 hydraulic diameters downstream of the point at which the liquid pressure reaches the saturation value corresponding to it's temperature. This criterion is only slightly less arbitrary than Henry's original proposal that flashing occurs 12 diameters downstream of a sharp entrance. With the present criterion, flashing location is dependent on the initial subcooling. Boundary conditions for the model equations are specified by equation (5-18), with the exception that the pressure is taken to be that predicted by the liquid flow equations at the flashing location. The model allows a discontinuity in liquid temperature at the point of flashing inception since the liquid is taken to be saturated at the local pressure in the two-phase region.

The proposed modification to Henry's model, described above, could be improved by making the flashing criterion a function of the stagnation state and local fluid velocity. Even with the essentially arbitrary selection of model parameters, taken directly from Henry's original proposal, the model is fairly successful in predicting the experimentally determined critical mass flux. Because the nonequilibrium model described in the next section includes more rigorous conservation of energy, and includes an explicit calculation of the liquid temperature, it was more attractive than the MHM. Development efforts were therefore concentrated on the nonequilibrium model.

V.2.3.2 Critical Flow Criterion

The choking condition is given by the same expression as for the HEM, given by equation (5-19). This result is obtained by applying the critical criterion, equation (2-1), to the model equations. However, the quality x is interpreted as the nonequilibrium thermodynamic quality predicted by the model. The mass transfer term (the last term on the right hand side of equation 5-19) is given by:

$$\left(\frac{dx}{dP} \right)_s = N \frac{dx_E}{dP} \qquad (5\text{-}22)$$

The mixture compressibility is predicted to be lower than that for an equilibrium process since the vapor generation rate is lower. Choking is predicted to occur at a higher velocity for a given thermodynamic quality than for the HEM. The result is that choking is predicted to occur at a lower

pressure. As noted above, the HEM tends to overpredict exit pressure. The Modified Henry Model should be expected to be an improvement on this situation.

V.2.4 Homogeneous Nonequilibrium Model

A new model has been developed to predict the critical flow of initially subcooled water in ducts. The proposed model incorporates some of the more recent proposals for two-phase critical flow modeling. A criterion for flashing inception based on the Alamgir-Lienhard correlation [68] is included. Critical flow is predicted on the basis of a nonequilibrium sound speed model developed by Kroeger [87]. His derivation was based on a method of characteristics analysis of a set of nonequilibrium homogeneous flow equations. In keeping with the current perception that interphase slip is unimportant, the model assumes homogeneous flow.

The selected dependent variables for the model are pressure (P), liquid temperature (T_l), mixture velocity (u), and thermodynamic quality (x). Three mixture conservation equations are considered. Vapor is assumed to be saturated at the local pressure. The liquid is assumed to be superheated. Phasic properties were calculated from the 1967 ASME Steam Tables. For lack of better information, properties for the metastable liquid were calculated by extrapolating subcooled liquid properties into the metastable region.

Conservation equations were derived by summing the two-fluid conservation equations for each phase. The resulting mixture equations have no interphase transfer terms. Mass transfer terms sum to zero. Momentum transfer is not a factor for homogeneous flow. Interphase heat transfer is included in the superheat correlation since the vapor phase is assumed saturated. The conservation equations employed are:

Mass:

$$-\frac{1}{v}\left[(1-x)\left(\frac{\partial v_l}{\partial P}\right)_T + x\left(\frac{dv_g}{dP}\right)_{sat}\right]\frac{dP}{dz} + \frac{1}{u}\frac{du}{dz} + \frac{v_g - v_l}{v}\frac{dx}{dz} + (1-x)\left(\frac{\partial v_l}{\partial T}\right)_P \frac{dT_l}{dz} = 0 \qquad (5\text{-}23)$$

Momentum:

$$\frac{dP}{dz} + \frac{u}{v}\frac{du}{dz} = -\left(\frac{dP}{dz}\right)_f + \frac{g}{v} \qquad (5\text{-}24)$$

Energy:

$$\left[(1-x)\left(\frac{\partial h_l}{\partial P}\right)_{T_l} + x\left(\frac{dh_g}{dP}\right)_{sat}\right]\frac{dP}{dz} + u\frac{du}{dz} + (h_g - h_l)\frac{dx}{dz} = 0 \qquad (5\text{-}25)$$

A correlation for the liquid superheat is given by the equation:

$$\frac{dP}{dz} - \left(\frac{dP}{dT}\right)_{sat} \frac{dT}{dz} = \Delta P_{fl} e^{\frac{-t_r}{\tau'}} \tag{5-26}$$

Where t_r is the residence time of the two-phase mixture in the duct. Residence time is given by:

$$t_r(z) = \int_{z_{fl}}^{z} \frac{dz'}{u(z')} \tag{5-27}$$

The integral in equation (5-27) was approximated by replacing u(z') with a quadratic polynomial denoted U(z'). The polynomial has the following properties:

$$\begin{aligned} U(z_{fl}) &= u(z_{fl}) \\ U(z) &= u(z) \\ \left.\frac{dU}{dz}\right|_z &= \frac{du}{dz} \end{aligned} \tag{5-28}$$

Polynomial coefficients were recalculated at each step in the integration. τ' is a parameter of the model and describes the rate at which the two-phase mixture relaxes to equilibrium. ΔP_{fl} is the pressure undershoot at flashing given by:

$$\Delta P_{fl} = \Delta P_d = P_{sat}\left(T_l(z_{fl})\right) - P(z_{fl}) \tag{5-29}$$

The exponential relaxation to equilibrium was first proposed by Bauer et al [99] and is consistent with Kroeger's proposal for the sound speed (described below). In light of the lack of better information about vapor generation in an adiabatic two-phase flow, an exponential relaxation model is a simple formulation which characterizes known features of such flows. A discussion of the selection of the time constant τ' has been postponed for inclusion in the section on the comparison between model prediction and experiment results.

V.2.4.1 Flashing Criterion

Recent proposals for models of the two-phase critical flow of initially subcooled water in nozzles, made by Levy and Abdollahian [52] and Abuaf et al [98], have employed the flashing correlation of Alamgir and Lienhard [68]. These models have been fairly successful in predicting experimentally measured mass flowrates. The Alamgir-Lienhard correlation was developed from the static depressurization data of Lienhard et al [5]. Wall nucleation was assumed to be responsible for the flashing phenomenon. Previous models for flashing inception(such as Simpson and Silver [69] and Edwards [70]), which rely on heterogeneous nucleation theory, require that one assume the presence of bubble nuclei in the subcooled liquid. Assumptions made about the density of nuclei in the liquid are unsubstantiated, experimentally. The density assumed in these models was that which resulted in good prediction of the flow. Such models for flashing inception have only been employed in conjunction with mechanistic models for vapor generation, which are more complex than the present proposal.

The Alamgir-Lienhard correlation has been used as a basis for the flashing inception criterion in the present model. Use of the correlation is consistent with the simplicity of the vapor generation model proposed by equation (5-26). The correlation is founded in direct experimental evidence rather than evidence implied by the success of a critical flow model. However, it was necessary to modify the

correlation in order to predict the experimentally determined critical mass flux. Pressure undershoot at flashing predicted by the correlation was multiplied by a factor, S, between 0.1 and 0.9, given by the expression:

$$S = a + bu \tag{5-30}$$

The constants a and b were selected so as to give the best comparison between the mass flux predictions of the HNEM and the data obtained in the present experimental program. An alternative approach would have been to correlate S such that the flashing location inferred from the pressure profile data was predicted by the model. Had this been done, the experimental mass flux would have been underpredicted by the model; if the assumption of homogeneous flow had been preserved along with the application of accepted models for two-phase frictional pressure drop.

The values of the parameters used in the Alamgir-Lienhard correlation multiplier, S, were: a=0.533 and b=-0.0034 s/m, for runs with a 0.381 mm nominal slit opening dimension. A negative coefficient for the velocity (b) was somewhat surprising. This indicates a decrease in the predicted pressure undershoot with increasing velocity. The opposite trend is predicted by the Alamgir-Lienhard correlation. The effect of the correction factor, S, is thus to make the predicted pressure undershoot at flashing more nearly constant; independent of the liquid properties. It is noted that the observed dependence of the correction factor S on the fluid velocity does not necessarily indicate that the liquid superheat at the point of flashing inception is dependent on the velocity in the same manner. The constants in the correlation of S were determined so that a good prediction of the critical mass flux was obtained. The location of flashing inception is poorly predicted (discussed below).

For the smaller slit sizes (0.252mm and below) the values of the parameters were: a=0.286 and b=0.00927s/m. Two characteristics of the multiplier S should be noted. First, for the lowest velocities encountered (15-20 m/s) S is virtually independent of slit size (S=0.47). This corresponds to the runs with the lowest pressures and subcoolings. S ranges between a minimum of 0.26 for runs with the highest velocity in the large slits (80 m/s) and a maximum of 0.95 for the highest velocity in the small slits. The predicted range of the pressure undershoot at the point of flashing inception was from 0.25 MPa to 0.8 MPa. This parameter increased monotonically, although not linearly, with the predicted liquid velocity.

Reduction of the pressure undershoot predicted by the Alamgir-Lienhard correlation by the factor S can be justified by considering the origins of the correlation. The stated range of validity for the correlation is for depressurization rates in the range from 400 MPa/s to 182 GPa/s (0.004 Matm/s to 1.803 Matm/s). Within that range the authors quote a probable error (1 standard deviation) of ±10.4%. In the present experiments depressurization rates prior to flashing inception are between 16 MPa/s and 8700 MPa/s. The majority of cases being outside the range of the correlation. Alamgir and Lienhard show scatter in the available data for depressurization rates below 400 MPa/s. Clearly, if depressurization of a liquid below it's saturation pressure is sufficiently slow, equilibrium will be more closely maintained and vaporization will begin when the superheating is sufficient to activate the available sites. Equation (5-30) proposes a simple modification to the Alamgir-Lienhard correlation which attempts to extend the correlation to lower rates of depressurization. Since the fluid velocity influences the viscous shear at the wall, the modification may also account for wall nucleation characteristics, should these be important. Indeed, the Reynolds number may have proven to be a more useful correlation parameter, in equation (5-30), than the velocity.

In some instances, entry loss is sufficiently large that the undershoot predicted by the modified Alamgir-Lienhard correlation is exceeded at the channel entrance (z=0). When this occurs, it is assumed that flashing begins immediately inside the entry. This is reasonable since the depressurization rate of the liquid during passage through a sharp entrance is very large. Insufficient time for vaporization is allowed during this process. Flashing should thus begin at the lower pressure, after passage through the entrance. Entry pressure loss is calculated for pure liquid flow.

V.2.4.2 Critical Flow Criterion

As with other models proposed for comparison with the data obtained in this work, a sound speed criterion for critical flow is used in this model. Kroeger has proposed [87] a formulation for the sound speed in a metastable flow. A method of characteristic analysis for a five equation drift-flux model, in which the vapor phase was assumed saturated at the local pressure, was used. The resulting expression for sound speed in the mixture for the special case of zero drift velocity (no slip) was given by:

$$a = a_{HF}\left[\frac{1}{1 - R\beta\rho a_{HF}^2}\right] \tag{5-31}$$

where a_{HF} is the homogeneous frozen sound speed given by:

$$a_{HF} = v\left\{\frac{1}{c_{pl}}\left(\frac{\partial v_l}{\partial T_l}\right)_P\left[x\left(\frac{dh_g}{dP}\right)_{sat} - v\right] - x\left(\frac{dv_g}{dP}\right)_{sat} - (1-x)\left(\frac{\partial v_l}{\partial P}\right)_T\right\}^{-1/2} \tag{5-32}$$

R is the non-dimensional mixture compressibility given by:

$$R = \frac{1}{v}\left\{(v_g - v_l) + \frac{h_g - h_l}{c_{pl}}\left(\frac{\partial v_l}{\partial P}\right)_P\right\} \tag{5-33}$$

The factor β accounts for nonequilibrium mass transfer:

$$\beta = \frac{dx_E}{dP}\left(1 + \frac{x_E - x}{\tau'}\right) \tag{5-34}$$

where x_E is the equilibrium thermodynamic quality corresponding to the local mixture enthalpy:

$$x_E = \frac{h - h_l}{h_g - h_l} \tag{5-35a}$$

$$\frac{dx_E}{dP} = \frac{(1-x)\left(\frac{dh_f}{dP}\right)_{sat} + x\left(\frac{dh_g}{dP}\right)_{sat}}{h_{fg}} \tag{5-35b}$$

Note that the conversion of thermal energy into kinetic has been neglected in (5-35b) and the static mixture enthalpy is taken as constant. In light of the fact that equation (5-35) is only a correlation for the vapor generation rate, this approximation does not detract from the accuracy of the final result. τ^* is a dimensionless parameter of the model which characterizes the rate at which the metastable liquid relaxes to equilibrium during the choking process (or during the passage of a rarefaction wave). This relaxation should occur more slowly than in the flow channel because less time is allowed for a given change in pressure. (The pressure gradient and the flow velocity are highest at the exit plane.)

The results of the model were not sensitive to the value of τ^* for $\tau^* \geq 1$. For $\tau^* \geq 1$ the pressure gradient, as well as gradients of the other dependent variables, are very large at the exit plane. This means that the choking location is insensitive to the exact value of sound speed used since the velocity increases rapidly in the flow direction while the sound speed decreases. Typically, pressure gradients at the exit were predicted to be on the order of 10^{11} Pa/m and velocity gradients approximately 10^7 (m/s)/m. For $\tau^* > 10$ the model equations cannot be successfully integrated because the pressure gradient grows to exceed 10^{13} Pa/m before the choking criterion is met. When gradients of the dependent variables are too large, the step size necessary to integrate the equations become so small as to be effectively zero for the computer used. (Numerical methods employed are described in the next section.) To avoid this problem when larger values of τ^* are used, a secondary critical criterion is employed. The flow is deemed critical when $dP/dz > 1 \times 10^{12}$ Pa/m. This value of the gradient is far larger than that used in the Richter-Minas model, of 2×10^8 Pa/m (2 bars/mm), for the determination of critical flow. τ^* is taken as 2.5 in this work since this corresponds to pressure gradients below 10^{13} Pa/m for all cases tested. Using $\tau^* < 1$ results in nearly identical prediction of the critical mass flux (critical velocity within 0.1%) provided the predicted pressure gradient is above 10^9 Pa/m. Smaller values of τ^* indicate larger mass transfer rates and the pressure gradient at the critical plane is predicted to be lower that those assumed by previous workers such as Rohatgi and Reshotko [71], Ardron [80], or Richter and Minas [81].

For $x = x_E$ equation (5-31) reduces to the homogeneous equilibrium sound speed as would be expected. When $x < x_E$ the sound speed is less than the equilibrium value at the same pressure and thermodynamic quality. This is the opposite result to Henry's model which predicts sound speed to be greater than the equilibrium value. Figure 5-1 shows the comparison between the frozen sound speed, the equilibrium sound speed and the prediction of Henry's and Kroeger's models as a function of void fraction for a given liquid superheat.

Supersonic choking is predicted by the model when the liquid velocity at the point of flashing inception is greater than the sound speed predicted by equation 5-31 for $x=0$. This interpretation is consistent with the model equations, (5-23) through (5-26), which yield a positive pressure gradient when $a>u$ and $x=0$. The pressure gradient is indefinite ($dP/dz \rightarrow \infty$) when $a=u$ with $x=0$; which is the result used as a critical criterion by Rohatgi and Reshotko [71] and Reocreux [92] in their models.

V.3 Numerical Solution of the Model Equations

A computer program has been developed which performs numerical integration of the model equations described in the preceeding sections. Fluid stagnation state, channel geometry, and single phase friction factor are input quantities. The critical flow model to be used is selected by an input parameter of the program. The method to be used in calculating two-phase frictional pressure drop is selected in a like manner. An iterative solution technique is employed. Two initial guesses for the critical mass flux are supplied to the program. The channel length corresponding to critical flow at each mass flux for the model selected is then calculated. Using a combination of bisection and interpolation algorithms, the program searches for the mass flux for which the flow is predicted to be critical at the exit of the channel.

V.3.1 Integration of the Model Equations

The computer program was run on the CDC 7600 computer at Lawrence Berkeley Laboratory. Mathematical subroutines available in the machine's library were used extensively in the program as a means of optimizing the solution procedure. Integration of the model equations was performed by ordinary differential equation solvers which are part of the subroutine library developed by the Numerical Algorithms Group (NAG) at Oxford University in England. The numerical methods used by these routines are described in Appendix F.

These particular routines were selected because they incorporate an option which allows termination of the integration of a system of ODE'S when some user input function of the solution is zero. This feature is ideally suited to the work at hand. The equations for single-phase liquid flow were integrated using a fourth order Runge-Kutta scheme. Termination of the integration at the flashing location was achieved by posing the flashing criteria as functions of the solution, FLC(Y,z). For the Homogeneous Equilibrium Model the function was given by:

$$\mathrm{FLC}(\bar{Y},z) = P - P_{sat}(T) \tag{5-36}$$

For the Modified Henry Model:

$$\mathrm{FLC}(\bar{Y},z) = 12 - \frac{z_{sat} - z}{D_h} \tag{5-37}$$

where z_{sat} is the value of z at which FLC in equation (5-36) is zero. For the Homogeneous Nonequilibrium Model, FLC was given by:

$$\mathrm{FLC}(\bar{Y},z) = P + \Delta P_{fl} - P_{sat}(T) \tag{5-38}$$

where ΔP_d was given by the modified Alamgir-Lienhard correlation as a function of P, T_l, and u.

Integration of the two-phase flow equations was terminated when the critical flow criterion was met. The critical criterion for each model was posed in the form:

$$\mathrm{G}(\bar{Y},z) = G_c(\bar{Y}) - u\,\rho(\bar{Y}) \tag{5-39}$$

The critical mass flux corresponding to the local state, $G_c(\bar{Y})$, was calculated according to the particular model being used. Supersonic choking was assumed to occur if $\mathrm{GC}(\bar{Y},z_{fl}) < 0$ at $z = z_{fl}$. In a few instances, integration was terminated when the pressure gradient was excessively high. When the calculated pressure gradient exceeded 10 MPa/m $\mathrm{GC}(\bar{Y},z)$ was set to zero to terminate integration. The difference between the mass flux and the critical mass flux at the location where integration was terminated was then printed out. Typically the difference was 0.01% or less, and never exceeded 0.1%.

V.3.2 Running Time

Computer running time required for the HNEM predictions varied by an order of magnitude depending on the case considered. Typically, when the stagnation subcooling was sufficiently high that flashing occurred at or near the exit, approximately 15 CP seconds were required for the calculation. This varied little between the three models. In the worst case, which was low stagnation pressure and subcooling with flashing occurring at, or near, the entrance, running time for the HNEM was approximately 140 CP seconds. In comparison, the HEM required approximately 70 CP seconds for similar cases; the MHM required approximately 65 CP seconds. Running time could be reduced by supplying more accurate initial guesses for the critical mass flux. The times stated here were for initial guesses 60% above and below the experimental mass flux.

V.4 Friction Models

Single phase friction factor was calculated from the familiar equation

$$f = C'' \, \mathrm{Re}^{-0.2} \tag{5-40}$$

The coefficient, C″, was determined from the data as described in the next section.

For two phase flow, three options for calculating the frictional pressure drop were available. The simplest of these is the formulation proposed by Owens [100]. In this approach, the two-phase friction factor is assumed to be equal to that for single phase flow. Thus,

$$\left(\frac{dP}{dz}\right)_f = f\,\frac{G^2 v}{2D_h} \tag{5-41}$$

Where f is given by equation (5-40) with the Reynolds number evaluated for the liquid flowing alone in the duct.

Another simple approach, proposed by Levy [101], was also available. Levy showed that the Lockhart-Martinelli correlation [102] for two-phase friction pressure drop was closely approximated by the expression:

$$\left(\frac{dP}{dz}\right)_f = \frac{1}{(1-\alpha)^2}\,f\,\frac{[G(1-x)]^2 v_l}{2D_h} \tag{5-42}$$

Where f is again the single-phase value. Levy showed that equation (5-42) agreed with the Lockhart-Martinelli correlation within a few percent for pressures greater than 700 kPa. The computer program is also capable of implementing the Martinelli-Nelson [103] correlation. This formulation was not used. The possible gain in accuracy by using the Martinelli-Nelson correlation was negated by the addition computation required.

V.5 Pressure Profile Calculation

Calculation of the pressure profile within the slit was required to evaluate the performance of each model. To calculate this, the model equations were integrated using a different differential equation solving package with the critical mass flux assumed to be that calculated by the NAG routine. Apart from the need to calculate the pressure profile, integration using a second numerical algorithm verified the results of the first calculation.

The computer subroutine, LSODI, developed at Lawrence Livermore Laboratory was selected for this task. (A description of this routine is given in Appendix F.) Unlike the NAG routines, employed to find the critical mass flux, this program solves an implicit set of ordinary differential equations. The NAG Library routines required a separate Gaussian elimination algorithm to put the equation is the form $y'=f(x)$. Since LSODI solves an implicit system (such as shown in equations 5-14 through 5-16) such a computation is not required. The solution procedure is thus more accurate, and more efficient, than that used in the NAG routines. LSODI was used in both the single and two-phase regions. Being a more conventional routine than the NAG routines, LSODI integrates the system of ODE's between a beginning and ending value of the independent variable. In the single-phase region, integration limits were from the entry, $z=0$, to the point of flashing inception previously determined by the NAG routine. For the two-phase region, integration was between the flashing location and the exit of the channel. Differences between the results of the two routines were negligible. For single-phase flow, the calculated pressure, velocity and water temperature were the same to five significant figures. In the integration of the two-phase case, calculated exit pressures were always within 0.5%. In some cases LSODI failed to carry the integration out to the end of the channel because the pressure gradient was calculated so large as to reduce the mesh size to effectively zero; thus terminating integration. In other words, LSODI predicted choking to occur further upstream. The distance between the location where this occurred and the slit exit was on the order of 0.05 mm, and was therefore considered negligible.

V.6 Determination of Input Data

Stagnation conditions, flow channel geometry, entry loss coefficient, and single phase friction factor were required input to the model program. This information was taken from the summary information for each experimental run. These summaries are presented in tabular form in Appendix A.

As is discussed in Chapter IV, data from each run has been presented in terms of averages of the measured quantities over approximately 10 readings. The models were applied to only one interval from each run since there is little variation between the intervals for any given run. Parameters for the model were selected to correspond with those from an interval during which the flowrate and stagnation conditions were constant. The first interval for any given run which met these conditions was selected. Data from early in a run was preferred since there is reason to suspect that later results may be affected by an increased amount of nitrogen dissolved in the water.

Stagnation pressure and temperature were taken to be the average values for the interval. The measured width of the channel and the corrected opening dimension were supplied for the assembly used in that particular run. Friction factor and entry loss coefficient were determined from the pressure profile data.

In order to determine the single-phase friction factor and the entry loss coefficient, single-phase pressure gradient was determined separately for each run. The gradient was taken to be the slope of the best fit line through the pressure measurements obtained from taps #1 through #4 (see Figure 3-9). Measured pressures which were below the saturation pressure corresponding to the stagnation temperature were excluded. Thus, for example, if tap #4 showed a pressure less than saturation, 3 measurements were used. For runs where tap #2 showed a pressure less than saturation the single-phase region was too short for the pressure gradient to be determined. The friction factor and entry loss were determined from similar runs as outlined below.

Once the single-phase pressure gradient was determined the friction factor was calculated from:

$$f = \frac{2D_h}{G_{exp}^2 v_l} \left(\frac{dP}{dz}\right)_l \tag{5-43}$$

where the specific volume of the liquid was evaluated at the stagnation state. The program actually requires C″ in equation (5-40) in order to calculate the friction factor as the fluid accelerates. Thus, the liquid Reynolds number in the single phase region was calculated by the program using the experimental mass flux data. C″ was calculated from:

$$C'' = f \left(\frac{G_{exp} D_h}{\mu_l}\right)^{0.2} \tag{5-44}$$

Entry loss coefficient was calculated by extrapolating the best fit line through the pressure tap readings back to z=0. The loss coefficient was then calculated from the expression:

$$K = \frac{2}{G_{exp} v_l} [P_0 - P_e] \tag{5-45}$$

Where P_e is the pressure inside the entrance to the slit calculated by extrapolation of the pressure data.

For runs where the inlet subcooling was sufficiently low that no single-phase pressure gradient could be determined, friction factor and entry loss coefficient were calculated from the data taken in other runs using the same assembly. The coefficient used in calculating single phase friction, C″, was assumed constant between assemblies. Thus for a run where the single-phase flow region was too short to determine the pressure gradient, friction factor was calculated from:

$$f_2 = f_1 \left[\frac{G_{exp,1}}{G_{exp,2}} \frac{\mu_{l,2}}{\mu_{l,1}} \right]^{0.2} \tag{5-46}$$

where the subscript "l" denotes parameters of the run for which f could be determined. Usually this run was the run which chronologically preceded the one in question. Entry loss coefficients were assumed to be equal, independent of mass flux, for the same assembly. Since the data reveals that this was not always the case, engineering judgment has been exercised. In some cases the entry loss coefficient was adjusted after the initial run of the modeling program so that the predicted entry pressure agreed with the measured value when the model flowrate was equal to the observed value. Friction and entry loss parameters for each run which was modeled are given in Tables 5-1 through 5-3. A summary of stagnation conditions used as input to the model program and the experimentally determined mass fluxes are given along with the model results in Tables 5-4 through 5-12.

V.7 Error Control

Before presenting the results of the model calculations, it is appropriate to discuss the error in the solution to the model equations which results from the application of finite difference techniques. The equations which were solved by the subroutines discussed above were not the equations written above, but rather finite difference approximations to these equations. Only in the limit of an infinitesimal finite difference mesh are an equation and its' finite difference approximation identical. As a result the calculated solution is not the same as the "exact" solution. The amount of the error introduced into the finite difference solution is controlled by user input error tolerances. Use of the tolerance parameters within the subroutine is discussed in Appendix F. Optimum values for the error parameters were different for each model. Parameters were selected so as to be the largest value for which a reduction in the magnitude did not change the computed solution for a test case. The test case was run #60 which has low pressure and low subcooling; such cases required a smaller error tolerance since the system of equations to be solved had a greater tendency toward stiffness (discussed in Appendix F). A large tolerance is preferable since it reduces the amount of computer time required for solution.

V.8 Presentation of Results

The comparison between the measured critical mass flux and that predicted by each of the models is shown in Figures 5-2 through 5-4. Tables 5-4 through 5-12 summarize the results of the model calculations. Each table presents results for a given nominal slit size. Tables 5-4 through 5-6 are the Homogeneous Equilibrium Model results. Table 5-7 through 5-9 are the Modified Henry Model results. The Homogeneous Nonequilibrium Model results are given in Tables 5-10 through 5-12. Each table entry shows the stagnation state of the fluid and the corrected value of the assembly hydraulic diameter as calculated in Chapter IV. Measured and calculated pressure at the exit plane of the slit are also presented. A comparison between the mass flux calculated by the model and the measured value is given by the parameter ΔG_c which is defined by:

$$\Delta G_c = \frac{G_c - G_{exp}}{G_{exp}} \times 100\% \tag{5-47}$$

where G_{exp} is the experimentally determined critical mass flux and G_c is the value predicted by the model. Positive values of ΔG_c indicate over prediction of the data by the model; negative values underprediction. The tables also show the location of flashing (in cm from the entrance) predicted by the model. When the word "Exit" appears in this column it indicates that supersonic choking

was predicted to occur at the exit. In other words the flow was critical at the location of flashing inception. Graphs of the pressure profiles calculated by the HNEM are shown in Appendix B along with the measured pressure data. The comparison between the predicted location of flashing and that inferred from the data is also shown in these graphs.

Results for the 0.381 mm nominal slit size are generally more reliable than for the other slit sizes. The reasons for this have been discussed in Chapter IV. Conclusions regarding the applicability of these models have been based primarily on the comparisons between model and data for these largest slit sizes.

V.8.1 Homogeneous Equilibrium Model Results

Previous authors, including Fauske [15], Henry [21] and Moody [55], have noted that the assumption of homogeneous equilibrium flow has led to the underprediction of experimentally determined critical mass flux data. These comparisons have been made using the Isentropic Homogeneous Equilibrium Model (IHEM). Such a comparison is inappropriate for flow in ducts since isentropic flow is precluded when the fluid pressure declines along a constant area duct. Nicolette [53] compared the results of his Fanno flow homogeneous equilibrium model to Fauske's data [15]. Critical mass flux tended to be underpredicted by Nicolette's model. Critical pressure was overpredicted in every instance. All the comparisons made by Nicolette were for two-phase stagnation states. Starkman et al [13] reported that their flowrate data for the critical flow of water through nozzles were underpredicted by the IHEM for stagnation qualities below 10%. Schrock et al [38] showed that this trend extended to the data for subcooled stagnation conditions.

Tables 5-4 through 5-6 show results of the HEM predictions. Figure 5-2 presents the comparison with critical mass flux data graphically. As was expected, on the basis of these previously comparisons, mass flux tended to be underpredicted by the HEM and the exit pressure was overpredicted. In general, the smaller the slit size, the greater the discrepancy between model and data.

One feature of the comparison which was not expected is the decline in predictive accuracy with decreasing subcooling. Comparing runs with the same geometry, and stagnation pressures that were roughly equal, the underprediction of the experimental mass flowrate increases as the stagnation subcooling decreases. Examples of this trend can be seen in Runs #27 through #30 and #41, #43, #44, and #75 in Table 5-4. Prediction of the critical pressure may improve slightly as the subcooling decreases. Contrary to these results, Nicolette [53] reported an improvement in the accuracy of his model's prediction of Fauske's data for higher stagnation enthalpy. Schrock et al [38] reported the same trend for their data.

In Chapter IV, it was noted that the pressure profiles shown in Appendix B indicate that in most instances there was appreciable superheating of the water before flashing occurred. It has been proposed by Henry [21] that for a long tube ($L/D>100$) there is sufficient time for the two-phase mixture, which was initially metastable, to relax to an equilibrium condition. Henry thus anticipated that flow in ducts would be more closely approximated by the HEM as L/D approached 100. Under the premise that given sufficient length of duct a flow will tend toward homogeneous equilibrium, one would anticipate that flow from a stagnation state characterized by low subcooling would be better modeled by the HEM than flow from a highly subcooled state. Since flashing occurs further from the exit for small amounts of subcooling, more time is allowed for this relaxation to equilibrium. These suppositions about the relaxation of a metastable state are not substantiated by the present data. It may be that there is a lag in the vaporization caused by the steep pressure gradient as the plane of choking is approached. This effect could be important even in very long ducts.

The most probable explanation of the discrepancy between these results and those of previous experimentalists lies in the size of the flow channel. Bubble sizes are restricted to the minimum channel dimension and must deform before they have grown to that dimension. Once they have reached this

size they are no longer bubbles and the area of liquid-vapor interface available for mass and momentum transfer is restricted. As a result the flow may not be able to relax to equilibrium, and interphase slip may be generated. This discussion of interphase mass and momentum transfer is continued in the last section of this chapter as part of the discussion of the results for the Homogeneous Nonequilibrium Model.

On the basis of the results presented in tables 5-4 through 5-6 it is clear that the HEM is inadequate for the prediction of critical flow in slits. It has also been shown that the previous suppositions, by Henry et al, regarding the dependence of the accuracy of an HEM prediction on the length-to-diameter ratio of the channel are not supported. The range of geometries and stagnation states for which this assumption can be made needs to be investigated.

V.8.2 Modified Henry Model Results

In presenting these results for the Modified Henry Model it is not intended to recommend this approach as a model for two-phase critical flow. The model is at best a technique for correlating experimental results. In specifying flashing to occur a fixed number of diameters downstream of the point where the saturation pressure was reached, the stagnation state, upon which this location should certainly depend, is not considered. This deficiency is propagated into the vapor generation model which assumes relaxation of the superheat at flashing (which has been arbitrarily specified) at a rate which has been correlated to the equilibrium rate. The critical criterion contains this same relaxation parameter, nx_E, even though the vaporization rate at the critical plane, where the pressure gradient is large, may be very different from that encountered in the flow channel.

Despite the shortcomings of this approach, the comparison between model and experiment indicates that this may be an effective way to correlate the data. Agreement between this model and the experimental results is better than for the HEM. The comparison between the measured and predicted critical mass flux is shown graphically in Figure 5-3. As with the HEM and the original Henry Model (described in Chapter II), the exit pressure is overpredicted.

It was originally hoped that adjustment of the model parameters n, B, and L/D at flashing, would result in a correlation for the results which would predict both the critical mass flux and the critical pressure. However, examination of the results shown in Tables 5-7 through 5-9, which were calculated using the values of the parameters Henry recommended for his simple correlation to the IHEM, (n=20, B=0.0523, and L/D at flashing =12) tend to indicate that this was not feasible with any simple correlation of the parameters.

For the HEM, it was noted that the amount of underprediction by the model increased with decreasing subcooling. This trend was evident for each set of data with the same nominal pressure and slit size. (There are exceptions where the mass flowrate data was clearly inconsistent with the other results; these have been mentioned above.) The MHM results show no clear trend.

Once again the data for 0.381mm nominal slit size are considered. Runs #27 through #30 show a tendency toward overprediction with decreasing stagnation subcooling. The set of runs consisting of #42, #45, #76, and #79 show the opposite trend. Critical pressure prediction does not follow the same trend as the data. The data show the critical pressure increasing as the subcooling decreases until some limit is reached; which is apparently dependent on slit size. Below that limit of subcooling, the critical pressure decreases as the subcooling decreases. This feature of the results was discussed more fully in Chapter IV. It should be noted that while the HEM predicts this trend in the data, the MHM does not.

Because of the lack of clear trends in the MHM prediction it was decided to concentrate model development efforts toward the development of a true nonequilibrium model. The model discussed below is more consistent with the physics of the flow. The flashing inception criterion is more based

on direct experimental measurements of the amount of pressure undershoot required for flashing inception. In addition, the model includes explicit conservation of energy.

For a majority of the experiments performed as part of this research, where the stagnation subcooling was 15C or higher, the MHM predicts the measure flowrate within 5%. It must be emphasized that this correspondence is highly fortuitous. In the first place, critical pressure in incorrectly predicted. Secondly, the parameters for the model were selected essentially arbitrarily.

V.8.3 Henry Model For Long Ducts

Since the MHM, described above, was developed on the basis of the Henry model for long ducts [21], the results of a prediction of the experimental results using Henry's original model has been included for completeness. The theoretical development of the model has been discussed in Chapter II. In this section the section the equations to be solved to obtain the model prediction are presented. Tables 5-13 through 5-15 show the results of this calculation.

A prediction for two-phase critical flow according to the Henry model is obtained by simultaneous solution of the two equations:

$$G_c^2 = \left[x \frac{dh_g}{dP} - (v_g - v_{l0}) N \frac{dx_E}{dP} \right]_{ex}^{-1} \tag{5-48}$$

$$P_{ex} = P_0 - G_c^2 \left[\frac{v_{l0}}{2K} + x(v_g - v_{l0}) \right]_{ex} \tag{5-49}$$

These equations were given above as (2-18) and (2-19) respectively. The parameter N was given by equation (2-12) with n=20. The quality, x, was calculated from equation (2-16) with B=0.0523. Values of the constants n and B were those recommended by Henry. Equilibrium vapor generation rate was calculated according to an "isentropic" process:

$$\frac{dx_E}{dP} = -\left[\frac{(1-x)\frac{ds_f}{dP} + x\frac{ds_g}{dP}}{s_{fg}} \right] \tag{5-50}$$

Fluid properties were calculated from the canonical and derived equations for the properties of steam and water given in the 1967 ASME Steam Tables. Derivatives of the properties were calculated by numerical differentiation of these equations.

Since the Henry model neglects frictional effects, the critical mass flux is greatly overpredicted. As would be expected, the extent of the overprediction decreases for larger slit sizes, where frictional effects are less important. Critical pressure is also overpredicted. These results indicate that Henry's assertion that his model is valid in the range $100 \leq L/D \leq 12$ requires qualification. (The 0.381mm slit have an L/D of approximately 85.) The actual range of validity of Henry's correlation has not been determined.

V.8.4 Homogeneous Nonequilibrium Model Results

The parameters a and b in equation (5-30) were determined so as to give the best correspondence between the model prediction and the mass flux data. Values were determined separately for each nominal slit size. Values for the 0.127 mm slits and 0.254 mm slits were sufficiently close that an average value for each parameter was used in modeling both. The results of the parametric study

carried out to determine the best values of a and b indicated that the values of the multiplying factor S increased with decreasing slit size. Numerical values for the constants have been given above in connection with the discussion of the introduction of the Alamgir-Lienhard correction factor (Equation 5-30). It was not possible to match the experimental pressure profiles. The reasons for this lack of agreement are discussed below. Pressure profiles predicted by the model are compared with the data in Appendix B.

One further model parameter remains to be discussed. The parameter τ' in equation (5-26) describes the rate at which the metastable liquid phase relaxes to equilibrium. The Levy-Abdollahian model [52] which has been described in Chapter II assumes that the pressure undershoot remains constant along the flow channel, ie. :

$$P(z) = P_{sat}\left(T_l(z)\right) + \Delta P_{fl} \tag{5-51}$$

In the current model this assumption is approximated by setting τ' equal to some large number (τ' = 100 sec. was used). However, the overprediction of the critical pressure ratio by the model increases as τ' increases. It was decided to select τ' as the lowest value (fastest relaxation of the metastable phase) which resulted in the curvature of the predicted pressure profile in the channel remaining positive. A negative curvature was predicted for τ' sufficiently small. Since such a phenomenon was not observed experimentally, τ' was selected accordingly. The final value was $\tau' = 1.1 \times 10^{-3}$ sec. Critical mass flux predicted by the model decreased no more than 10% as τ' varied from 100 to 1×10^{-5} sec with S fixed.

Comparisons between the prediction of the HNEM and the data from the experimental work presented herein are shown in tables 5-10 through 5-12. Agreement between the model prediction and the measured critical flowrate is within 12.3% for the largest slit size. The comparison for the smaller slits is similar except in the case of the run #65 which was underpredicted by 20.5%. The other runs which show poor agreement (#21 and #22) were noted as being of dubious validity in Chapter IV (Table 4-8).

The model tends to underpredict the mass flux data. Underprediction is worst at the lowest subcoolings. While it is possible to improve the mass flux prediction by increasing the amount of pressure undershoot required for flashing inception (increase S) this results in the model predicting flashing at the channel exit in every case but the lowest subcoolings. The model already predicts flashing to occur further downstream than is evidenced by the measured pressure profiles. Values of S selected seem to be a good compromise between underprediction and the mass flux and overprediction of the superheat at flashing.

In addition to predicting flashing to occur too far downstream, the model underpredicts the pressure drop in the slit in the two-phase region. Even when the mass flux is correctly predicted, (or overpredicted) this can be seen. Runs #55 and #60 are excellent examples but the problem is evident for every prediction of the data for runs where two-phase flow was evidenced. For some of the runs with high subcooling, flashing appears to have occurred at, or very near, the exit of the slit. In these cases the critical pressure ratio and the pressure profile within the slit are adequately predicted (eg. runs #59, #41, #68, #36). This merely validates the single-phase liquid flow model. Flashing was predicted to occur at the exit in many runs where the pressure profiles clearly indicate flashing at some point upstream (eg. runs #58, #28, #69, #25).

An effort was made to correct the predicted frictional pressure drop by replacing the friction term in equation (5-24) by an expression of the form:

$$\left(\frac{dP}{dz}\right)_f = C(1-\alpha)^n f \frac{G^2 v}{2D_h} \tag{5-52}$$

A parametric study was carried out using runs #60 and #44. The data from these runs was reliable and the two-phase region evidenced in the experimental pressure profiles was sufficiently long that some significance could be attached to being able to model them numerically. In this study the flashing location was fixed at the approximate location inferred from the measured pressure profiles (indicated in Appendix B). This was accomplished by adjustment of the factor S. Vaporization rate was adjusted by changing τ' so as to keep G_c within 5% of the experimental value. The constant, C, was varied from 0 to 10 for values of n ranging from -5 to +5. A total of ten combinations were tried for each of the two runs. For C greater than 2 and n less than zero the frictional loss was so large that the experimental mass flux could not be matched. It was not possible to match the experimentally measured pressure profile via this procedure.

A further study was suggested by the results of this numerical experiment. The frictional pressure drop required to match the data may be studied by using the proposed two-phase flow model equations (5-23) through (5-25). Measured pressure data could be used as a forcing function; replacing equation (5-26). The model equations could be integrated from the point of flashing inception, inferred from the data, to the channel exit. The value of $(dP/dz)_f$ could thus be determined at every point in the flow. In this scheme, the vapor generation rate is determined by the initial superheat, indicated by the assumed point of flashing inception, and the measured pressure data. It is not known whether the frictional pressure drop predicted by this procedure would be reasonable.

It must be concluded that the HNEM fails to account for significant characteristics of two-phase critical flow. In particular, the momentum loss from the flow due to two-phase friction is too large. In order to obtain a reasonable prediction of the critical mass flux, the amount of pressure undershoot at the point of flashing inception was overpredicted. While the method represents an adequate method of correlating the critical mass flux data it does not accurately model two-phase critical flow through rectangular slit. Recommendations for improving the model are made below.

V.8.5 Comparison of the HNEM with Super Moby Dick Data

Since the small slits tested in the current experimental program are a unique geometry and data from similar experiments are not available, it was deemed necessary to compare the HNEM with other available data. The French Super Moby Dick experiments were selected for this comparison. Several factors influenced this choice. The requirement that the data be for flow in ducts from initially subcooled stagnation states was the most limiting. Sozzi and Sutherland's data [10] was taken at moderately high pressure but stagnation subcooling was significantly lower than in the present work. In addition pressure profiles were not measured, so the single-phase friction factor could not be determined. The results French Super Moby Dick experiment, reported by Jeandey et al [97], proved to be the best choice. These experiments were carried out in a 20 mm diameter duct. The constant area section was 35.8 cm long and was preceded by a conical convergent section. A nozzle with a 7 degree diffusing angle was attached to the exit. Table 5-13 shows the comparison between the HNEM and their data. Single phase friction factor and the entry loss coefficient were determined from the reported pressure profiles [97]. These calculations were done in the same manner as those for the data in Appendix A; Table 5-14 shows the results. Model predictions were obtained using the same values of the parameters (a, b, and τ') as were used for 0.381 mm slits. The mass flux data is slightly overpredicted. Unlike the slit data, the overprediction increases with subcooling. Critical pressure ratio is also overpredicted when the experimental data reveal void fractions at the exit of the duct greater than 5%. The success of the model in predicting mass flux data from an experiment with very different geometry is encouraging. However, the model still fails to correctly predict the pressure loss in the two-phase flow region.

V.9 Conclusions

Several conclusions may be drawn on the basis of the preceeding analysis. Parametric trends of the data were examined in Chapter IV. These results may be summarized as follows:

1) Critical mass flux for a fixed geometry and stagnation subcooling generally increases with increasing stagnation pressure. The data indicate a reduction of this effect at higher stagnation pressure levels. This reduction was related to an apparent increase in the single-phase friction factor at higher pressures. Because of the variations in geometry between test section assemblies, there are little data to support a conclusion that this reduction of the pressure effect was actually present.

2) Critical mass flux, for a fixed geometry and stagnation pressure, increases with increasing stagnation subcooling. The dependence is reduced for initial subcoolings below 5C.

3) Critical mass flux for a fixed stagnation state decreases with increasing length-to-diameter ratio of the channel. Frictional effects predominate and fL/D appears to be the appropriate scaling parameter. Since the effects of test section scale (hydraulic diameter) were not studied as part of this program, the extension of these results to larger diameter flow passages on the basis of simple fL/D scaling is not recommended.

4) Critical pressure ratios were observed to be independent of stagnation pressure. Measured critical pressure ratios exhibit a maximum with respect to stagnation subcooling. The magnitude of the critical pressure ratio, and the value of stagnation subcooling for which it is maximized, are dependent on L/D of the channel.

5) Heat transfer from the slit wall to the flowing fluid was shown to have a negligible influence on the critical mass flux.

6) Reduction of the measured critical mass flux toward the end of each run, despite an increase in the stagnation subcooling which was usually present, was attributed to the effect of dissolved gasses.

Drawing conclusions on the basis of the results of a model which inadequately describes the physics of the flow is frequently ill-advised. Such a procedure applied to the IHEM led some investigators to conclude that interphase slip was of greater importance in the determination of two-phase critical flow than thermodynamic nonequilibrium. This conclusion was probably falacious. Errors such as this occur because a model may have a number of shortcomings, not all of which are recognized by the investigator. The following conclusions may be drawn with respect to the application of the HNEM in the prediction of the present data:

7) The Homogeneous Nonequilibrium Model is fairly successful in predicting the two-phase critical mass flux through slits. Agreement is typically within 5% (1σ), for all slit sizes. The model is more successful for larger slits, possibly due to the more reliable determination of the channel geometery used in calculating the mass flux from flowrate data. The model exhibits a tendency to underpredict the data; as shown by Figure 5-3.

8) Prediction of the experimentally measured mass fluxes by the HNEM improves with increasing stagnation subcooling. The model shows a tendency toward greater underprediction of the measured flowrates when the stagnation subcooling was less than 10C.

9) Mass flux predictions by the HNEM compare favorably (within a maximum error of 4.2%) with experimental results measured in a test section with a hydraulic diameter 27 times larger than the largest slit tested in the present program. (The data taken by Jeandey et al [97]). L/D in these experiments was one fifth that of the largest slits. This comparison indicated that the model is applicable over a wide range of flow channel geometries.

10) The location of flashing inception predicted by the HNEM is further downstream than that which is evident from the measured pressure profiles. Such was not the case when the pressure profile indicated flashing at the exit of the slit or the model predicted flashing at the profiles. Such was not the case when the pressure profile indicated entrance.

11) The Alamgir-Lienhard correlation overpredicts the pressure undershoot at flashing inception for steady state critical flow in slits. This conclusion may be drawn by inferrence from the previous conclusion since the A-L correlation was multiplied by a factor less than unity in the present model.

12) Critical pressure ratio predicted by the HNEM is larger than the measured value with the exception of a few instances with high subcooling when flashing occurred at the channel exit. Observed trends in the dependence of critical pressure ratio on stagnation subcooling (described in 4). above) were predicted by the model.

13) Total two-phase pressure drop predicted by the HNEM was always lower than the measured value. This indicated that standard models for pressure drop in boiling two-phase flows are inadequate for flashing flows in the present geometry. Further research into this feature of the comparison between model and experiment is required.

14) The proposed model (HNEM) is useful for predicting the critical mass flux for water from initially subcooled stagnation states. The model predicts the present data within the experimental accuracy. One may expect the prediction to be slightly less reliable when the stagnation state is close to the saturation condition. Predictions for low subcooling usually underestimate the mass flux. The model is apparently valid over a wide range of geometries. fL/D of the channel must be known.

V.10 Recommendations for Future Modeling Efforts

As stated above, comparison of the predicted pressure profiles with the experimental data, (shown in Appendix B) reveal that the model predicts flashing to occur further downstream than the data indicates. The apparent decrease in the flashing superheat with increasing velocity for larger channels (indicated by the constant b in equation 5-30 being less than zero) is probably due to inadequate modeling of the flow in the two-phase region. The model inaccurately models the two-phased pressure drop. It is the nature of these data that the lower velocities correspond to a greater length of the two-phase region. A higher flashing superheat is required to compensate for the overprediction of the two-phase frictional pressure loss by the model in order to achieve a correct prediction of the mass flux.

The failure of the Alamgir-Lienhard correlation is not surprising. Recall that it was derived on the basis of static depressurization and assumes that the principal mechanism for the inception of flashing is wall nucleation. For flow in a channel, depressurization rates are generally below the range of validity for the correlation. In addition, flow in the channel and the presence of viscous shear in the fluid adjacent to the wall may alter the wall nucleation characteristics. Alamgir et al [95,68] noted scatter in the data at low depressurization rates (below 0.004 Mbar/s). They attributed this scatter to "the presence of deterministic nucleation sites." Classical heterogeneous nucleation theory predicts the superheat necessary for flashing inception to be given by:

$$\theta_{fl} = \frac{2T_{sat}\sigma}{h_{fg}\rho_g r_c} \tag{5-53}$$

where r_c is the radius of the largest available cavity. The validity of this expression was verified by Griffith and Wallis [104] who immersed a plate, with artificial nucleation sites on the surface, in a saturated liquid which was then slowly decompressed. It seems probable that the superheat at flashing, for flow in a duct where depressurization rates are low, may be dependent on the size of defects in the duct wall. Such sites were certainly available in the present experiments. Exposure to high temperature water caused pitting of the surface which was visible upon close inspection.

While it is still not certain that wall nucleation is the mechanism for flashing inception, this is apparently the assumption of many recent workers in the field. The data of Jeandey et al [97] the show void fraction to be higher adjacent to the pipe wall, which suggests vapor formation at the wall. Since superheat at flashing is not observed to be large enough for homogeneous nucleation in the bulk to occur "deterministic sites" must still be responsible. These sites may be bubbles of a noncondensable gas, as suggested by Malnes [82], or small particles of some foreign material entrained in the flow.

There is no direct experimental evidence of interphase slip in the present study. Slip between the phases is suggested as a possible explanation for the failure of the homogeneous models to correctly predict the two-phase pressure drop. Model results suggest that while the total pressure drop was underpredicted, the frictional pressure loss was overpredicted. This is evidenced by the necessity of overpredicting the pressure undershoot at flashing in order to match the experimentally determined mass flux.

Interphase slip would result in a decrease in the static pressure while preserving the flow momentum. Frictional loss, has the effect of reducing the fluid momentum. Energy lost goes into heating the flow (this effect is neglected by the models). Introduction of slip decreases the mixture void fraction for a given local thermodynamic state. A reduction in the void fraction is predicted to reduce the frictional pressure drop by both the Levy [101] and the Martinelli-Nelson [103] correlations. It has been argued by Henry et al [64], and others, that slip is unlikely in a bubbly flow because of the large interfacial drag. The virtual mass effect would also tend to eliminate slip in bubbly flows. The tendency of the vapor to accelerate relative to the liquid phase is reduced by the virtual mass effect. However, it would seem that bubbly flow is unlikely to be present in small slit geometries for void fractions larger than a few percent.

Assuming that bubbles nucleate preferentially on defects in the channel wall, bubbles would tend to "stream" from these points. Bubbles nucleated in the viscous sublayer would be expected to be detached from the wall once they grew sufficiently to extend into the turbulent zone. Bubbles would grow rapidly under the combined influence of liquid superheat and rapidly falling pressure. Provided the nucleation site density were sufficiently low, the bubbles would reach a diameter equal to the slit opening dimension before the void fraction exceeded a few percent. Once this occurred, streams of vapor would be formed which would fill the channel. These "channels" of vapor would run parallel to the liquid. The interfacial surface area would be reduced considerably from that for bubbly flow and the virtual mass effect would be eliminated. Reduction in the interphase drag would increase the tendency toward slip. Wall friction would be reduced since friction between the wall and the vapor is negligible compared to that between the wall and the liquid. The flow pattern conceived is similar to that postulated by Wallis and Richter [105] in their "isentropic streamtube" model. In this model the vapor formed is assumed to flow isentropically in streamtubes that are physically separate from the liquid. A new streamtube is created upon each incremental loss in fluid pressure. Flow in the streamtubes, and in the liquid, is assumed isentropic. While the authors state that they do not visualize this flow pattern actually occurring in a nozzle (the channel geometry for which the model is intended) their method of modeling the flow may be useful for this geometry. The model would also have to be adapted to include frictional effects, the occurrence of flashing below the saturation pressure, and slip.

It is recognized that the above scenario is speculative but it does explain the observed comparison between model and data. Modeling of such a flow regime requires a two-fluid model to include both thermal nonequilibrium and interphase slip effects. A modified version of the Richter-Minas model [81] is probably best suited for this purpose. Correlation for interphase mass and momentum transfer would require modification. In addition, the flashing inception criterion should account for depressurization rate as well as local superheat.

An alternative explanation for the inability of accepted models for two-phase pressure drop to predict the measured data is suggested by the pressure profiles measured during the cold water calibration

runs. These profiles show a deviation of the pressure data from the straight line which should characterize single-phase flow in a constant area duct. The data suggest a reduction in the slit flow area roughly 3 cm from the entrance. This is indicated by pressure data which fall below a line drawn through the upstream data. Reduction in the measured single-phase pressure gradient farther downstream may indicate a subsequent increase in the channel area. However, careful checks of the slit opening with a feeler gauge during the assembly of the test section did not reveal such a geometry. In addition, several runs with high subcooling are predicted accurately by the constant area model.

Further basic research, such as that carried out by Alamgir et al [5,95], is required to study the proper formulation of the transfer terms in two-phase critical flow models. While terms in two-phase critical flow models. While critical flow experiments are useful in assessing models the interaction of various physical mechanisms, such as slip and thermal nonequilibrium, make determination of the individual effects of each of the effects difficult or impossible. In addition, the effects of wall heat transfer require study. This work could be carried out in externally heated small tubes so that the wall heat flux is known. Comparison of the data from tubes will the present data would reveal the effect, if any, of the rectangular geometry.

Table 5-1

Single-Phase Pressure Loss Summary
0.381 mm Nominal Slit Size

Run (#)	Assembly Code	Pressure Gradient (MPa/m)	Reynolds Number	Friction Factor	Entry Loss Coefficient*
59	3C	-29.8	2.219×10^5	0.0232	1.362
57	3C	-19.1	2.048×10^5	0.0225	1.090
58	3C	-12.8	1.685×10^5	0.0244	1.097
60*	3C	-na-	9.979×10^4	0.0275	1.3
30	3A	-38.7	3.589×10^5	0.0145	1.102
27	3A	-23.0	3.152×10^5	0.0140	1.088
28	3A	-14.9	2.557×10^5	0.0148	1.085
29*	3A	-na-	1.965×10^5	0.0158	1.1
41	3B	-58.3	3.759×10^5	0.0199	1.092
43	3B	-37.3	3.188×10^5	0.0207	1.147
44	3B	-23.7	2.541×10^5	0.0222	1.131
75*	3D	-na-	2.276×10^5	0.0242	1.1
42	3B	-66.8	3.968×10^5	0.0222	1.211
45	3B	-43.0	3.389×10^5	0.0226	1.209
76	3D	-31.7	3.289×10^5	0.0221	0.996
79*	3D	-na-	2.689×10^5	0.0232	1.0
74	3D	-88.5	5.479×10^5	0.0204	1.112
78	3D	-46.1	4.570×10^5	0.0169	1.227

*Friction Factor and Entry Loss Coefficient Estimated

Table 5-2

Single-Phase Pressure Loss Summary
0.254 mm Nominal Slit Size

Run (#)	Assembly Code	Pressure Gradient (MPa/m)	Reynolds Number	Friction Factor	Entry Loss Coefficient*
68	2D	-37.2	1.173×10^5	0.0248	1.057
70	2D	-26.0	1.106×10^5	0.0249	1.076
69	2D	-15.5	8.972×10^4	0.0251	1.070
71	2D	-9.5	7.301×10^4	0.0249	1.041
23	2A	-7.2	1.795×10^5	0.0033	3.135
51	2C	-58.9	1.435×10^5	0.0246	1.041
24	2A	-30.0	1.733×10^5	0.0182	1.076
25	2A	-22.5	1.580×10^5	0.0181	0.886
26*	2A	-na-	1.067×10^5	0.0199	0.9
36	2B	-74.4	1.827×10^5	0.0281	1.250
37	2B	-45.1	1.520×10^5	0.0293	1.331
38	2B	-30.6	1.314×10^5	0.0274	1.530
55*	2C	-na-	1.038×10^5	0.0272	1.1
98	2E	-76.0	2.270×10^5	0.0257	1.216
99*	2E	-na-	1.285×10^5	0.0296	1.2
52	2C	-88.9	1.987×10^5	0.0242	1.134
39	2B	-102.3	2.020×10^5	0.0372	1.085
54	2C	-57.3	1.786×10^5	0.0237	1.040
95	2E	-82.6	2.581×10^5	0.0247	1.680
96	2E	-52.4	2.122×10^5	0.0251	1.308
93	2E	-37.5	1.897×10^5	0.0254	1.223
94*	2E	-na-	1.214×10^5	0.0284	1.2
72*	2D	-na-	2.463×10^5	0.0206	1.4
92	2E	-72.4	2.575×10^5	0.0259	1.028
97	2E	-65.0	2.252×10^5	0.0304	1.067
100*	2E	-na-	2.063×10^5	0.0249	1.2

*Friction Factor and Entry Loss Coefficient Estimated

Table 5-3

Single-Phase Pressure Loss Summary
0.127 mm Nominal Slit Size

Run (#)	Assembly Code	Pressure Gradient (MPa/m)	Reynolds Number g	Friction Factor	Entry Loss Coefficient*
15*	1A	-na-	1.557×10^4	0.0431	1.2
61	1E	-32.0	4.009×10^4	0.0287	4.599
64	1E	-29.6	3.506×10^4	0.0450	3.328
63	1E	-18.3	2.920×10^4	0.0446	3.955
65*	1E	-na-	2.954×10^4	0.0442	4.0
17	1A	-60.0	7.344×10^4	0.0210	1.031
19	1B	-51.1	8.414×10^4	0.0134	1.676
50	1D	-63.3	2.548×10^4	0.0453	3.038
67	1E	-44.9	5.014×10^4	0.0415	2.772
20	1B	-39.7	7.040×10^4	0.0165	1.667
22*	1B	-na-	3.704×10^4	0.0194	1.7
21*	1B	-na-	2.478×10^4	0.0214	1.7
34	1C	-37.4	2.625×10^4	0.0761	4.522
33*	1C	-na-	2.388×10^4	0.0779	5.0
85	1F	-25.1	3.944×10^4	0.0408	3.483
86*	1F	-na-	3.801×10^4	0.0412	3.5
32	1C	-88.9	3.727×10^4	0.0791	5.142
84	1F	-81.2	7.058×10^4	0.0363	0.815
82*	1F	-na-	4.832×10^4	0.0380	0.8
48	1D	-58.0	3.086×10^4	0.0389	2.057
49	1D	-47.9	2.604×10^4	0.0482	0.837
47	1D	-123.2	4.489×10^4	0.0364	0.466
88	1F	-114.4	7.878×10^4	0.0444	0.615
66	1E	-75.0	8.627×10^4	0.0277	1.406
80	1F	-50.2	6.352×10^4	0.0360	0.668
81*	1F	-na-	6.472×10^4	0.0350	0.7
87	1F	-151.1	9.714×10^4	0.0314	0.876
89	1F	-79.9	8.525×10^4	0.0324	0.722

*Friction Factor and Entry Loss Coefficient Estimated

Table 5-4
Model Comparison

Homogeneous Equilibrium Model

3.81E-4 m Nominal Slit Opening

Run	Stagnation		Experiment			Theory		
	Pressure	Subcooling	D_h	G_c	P_{ex}	Flashing Location	ΔG_c	P_{ex}
(#)	(MPa)	(°C)	(mm)	(kg/m^2-s)	(kPa)	(cm)	(%)	(kPa)
59	4.271	59.3	0.747	4.099E+4	1313	Exit	-5.98	1404
57	4.220	28.0	0.747	3.256E+4	2047	Exit	-7.95	2581
58	4.187	13.9	0.747	2.526E+4	2387	Exit	-16.79	3302
60	4.134	2.9	0.747	1.433E+4	1791	1.709	-7.24	2509
30	7.093	59.6	0.748	5.781E+4	1878	Exit	-0.75	2499
27	7.073	29.6	0.748	4.416E+4	2970	Exit	-3.97	4467
28	7.077	15.6	0.748	3.398E+4	3400	Exit	-8.62	5587
29	7.091	6.2	0.748	2.522E+4	2886	3.055	-8.87	4752
41	9.595	59.4	0.708	5.792E+4	3552	Exit	-2.73	3885
43	9.584	29.9	0.708	4.394E+4	4820	Exit	-6.88	6219
44	9.619	15.1	0.708	3.323E+4	5264	5.580	-8.59	6460
75	9.542	0.0	0.747	2.663E+4	4191	0.0	-23.23	4801
42	11.580	53.3	0.708	5.783E+4	4478	Exit	-2.41	5017
45	11.608	28.6	0.708	4.448E+4	5997	Exit	-7.51	7798
76	11.672	11.8	0.747	3.860E+4	5905	4.666	-17.90	7279
79	11.672	2.1	0.747	3.058E+4	4887	0.0	-19.31	6030
74	15.398	54.6	0.747	6.969E+4	6135	Exit	-7.82	7338
78	15.452	26.5	0.747	5.296E+4	7613	Exit	-9.61	10860

Table 5-5
Model Comparison
Homogeneous Equilibrium Model
2.54E-4 m Nominal Slit Opening

Run	Stagnation		Experiment			Theory		
	Pressure	Subcooling	D_h	G_c	P_{ex}	Flashing Location	ΔG_c	P_{ex}
(#)	(MPa)	(°C)	(mm)	(kg/m^2-s)	(kPa)	(cm)	(%)	(kPa)
68	4.289	59.6	0.464	3.500E+4	1210	Exit	-4.24	1405
70	4.320	30.7	0.464	2.849E+4	1820	Exit	-9.69	2511
69	4.281	14.9	0.464	2.160E+4	2229	6.289	-14.88	3166
71	4.272	4.8	0.464	1.687E+4	1909	3.346	-20.82	2520
23	7.117	61.2	0.502	4.271E+4	2016	Exit	+8.09	2590
51	7.050	60.3	0.418	4.091E+4	2214	Exit	-4.17	2611
24	7.055	29.2	0.502	3.641E+4	1007	Exit	-5.04	4481
25	7.055	18.2	0.502	3.131E+4	748	Exit	-8.04	5346
26	7.000	3.3	0.502	2.027E+4	595	1.367	-9.87	3896
36	9.553	59.1	0.453	4.405E+4	3309	Exit	-5.43	3885
37	9.600	28.1	0.453	3.247E+4	4446	6.273	-8.60	5936
38	9.667	22.4	0.453	2.748E+4	4301	5.877	+1.31	5784
55	9.602	3.9	0.418	2.198E+4	3098	1.337	-13.93	4406
98	9.774	58.0	0.502	4.883E+4	3239	Exit	-8.74	4071
99	9.609	0.0	0.502	2.254E+4	2972	0.0	-24.47	4054
52	11.728	59.9	0.418	4.924E+4	3994	Exit	-4.85	4920
39	11.601	54.9	0.453	4.413E+4	4187	Exit	-11.79	5255
54	11.696	30.0	0.418	3.852E+4	5065	6.314	-8.84	7322
95	12.420	61.5	0.502	5.137E+4	4039	Exit	-5.83	5143
96	11.642	26.4	0.502	3.901E+4	4636	6.166	-13.14	7209
93	11.838	12.9	0.502	3.224E+4	4070	4.230	-14.33	6420
94	11.675	2.2	0.502	2.058E+4	2940	0.0	+1.28	5150
72	15.601	54.2	0.464	5.019E+4	2605	Exit	6.80	7490
92	15.798	12.0	0.502	4.231E+4	-	3.705	-27.11	7855
97	15.747	12.0	0.502	3.703E+4	4838	3.632	-20.63	7503
100	15.703	2.2	0.502	3.292E+4	4184	1.254	-24.96	6644

Table 5-6
Model Comparison

Homogeneous Equilibrium Model

1.27E-4 m Nominal Slit Opening

Run	Stagnation		Experiment			Theory		
	Pressure	Subcooling	D_h	G_c	P_{ex}	Flashing Location	ΔG_c	P_{ex}
(#)	(MPa)	(°C)	(mm)	(kg/m^2-s)	(kPa)	(cm)	(%)	(kPa)
15	2.734	2.0	0.254	7.267E+3	686	1.777	-19.33	1072
61	4.216	60.8	0.252	2.219E+4	1005	Exit	-7.53	1336
64	4.248	30.9	0.252	1.667E+4	1398	6.295	-15.93	2286
63	4.231	15.7	0.252	1.298E+4	1142	5.118	-16.84	1974
65	4.334	5.9	0.252	1.257E+4	1115	2.766	-33.97	1633
17	7.608	60.6	0.252	3.471E+4	1552	Exit	-1.13	2602
19	7.099	63.0	0.252	4.017E+4	1669	Exit	-3.00	2501
50	7.208	63.7	0.159	1.930E+4	1563	Exit	-0.22	2522
67	7.206	30.1	0.252	2.076E+4	2068	5.962	-12.81	3441
20	7.086	48.3	0.252	3.152E+4	2233	Exit	+4.48	3259
22	7.030	3.7	0.252	1.402E+4	1049	1.114	+4.39	3176
21	6.957	18.2	0.252	9.895E+3	803	5.720	+116.44	4186
34	7.208	18.2	0.209	1.258E+4	1444	4.726	-13.14	2296
33	7.113	7.2	0.209	1.103E+4	1240	2.640	-24.58	1852
85	7.189	14.3	0.252	1.541E+4	1696	4.306	-8.13	2963
86	7.196	4.1	0.252	1.419E+4	1601	1.078	-25.16	2366
32	9.666	59.5	0.209	1.945E+4	2147	6.235	-8.82	3233
82	9.661	0.0	0.252	1.682E+4	1985	0.0	-27.86	2929
84	9.672	56.6	0.252	3.010E+4	2694	Exit	-0.78	4112
48	9.645	30.6	0.159	1.897E+4	1719	5.640	-4.69	3773
49	9.640	15.4	0.159	1.518E+4	1583	5.400	-9.22	3130
47	11.611	57.0	0.159	2.903E+4	2184	6.339	-11.55	4849
88	11.886	57.2	0.252	3.191E+4	3214	Exit	-7.89	5210
66	12.073	30.2	0.252	3.161E+4	3059	5.823	-13.76	5911
80	11.798	13.4	0.252	2.219E+4	2453	4.155	-9.01	4787
81	11.535	0.3	0.252	2.173E+4	2348	0.0	-35.51	3550
87	15.917	56.8	0.252	3.659E+4	-	Exit	+4.27	7357
89	15.579	25.7	0.252	2.914E+4	3537	5.332	-3.04	6778

Table 5-7
Model Comparison

Modified Henry Model

3.81E-4 m Nominal Slit Opening

Run	Stagnation		Experiment			Theory		
	Pressure	Subcooling	D_h	G_c	P_{ex}	Flashing Location	ΔG_c	P_{ex}
(#)	(MPa)	(°C)	(mm)	(kg/m^2-s)	(kPa)	(cm)	(%)	(kPa)
59	4.271	59.3	0.747	4.099E+4	1313	Exit	-1.43	1141
57	4.220	28.0	0.747	3.256E+4	2047	6.211	-2.28	2374
58	4.187	13.9	0.747	2.526E+4	2387	4.864	-2.95	2830
60	4.134	2.9	0.747	1.433E+4	1791	0.897	+23.36	3012
30	7.093	59.6	0.748	5.781E+4	1878	Exit	+3.45	2129
27	7.073	29.6	0.748	4.416E+4	2970	6.033	+1.58	4128
28	7.077	15.6	0.748	3.398E+4	3400	4.622	+4.40	4892
29	7.091	6.2	0.748	2.522E+4	2886	1.374	+10.36	5280
41	9.595	59.4	0.708	5.792E+4	3552	Exit	+1.93	3366
43	9.584	29.9	0.708	4.394E+4	4820	5.877	+0.31	5595
44	9.619	15.1	0.708	3.323E+4	5264	5.400	+4.21	6548
75	9.542	0.0	0.747	2.663E+4	4191	0.897	-12.50	5504
42	11.580	53.3	0.708	5.783E+4	4478	Exit	+2.27	4419
45	11.608	28.6	0.708	4.448E+4	5997	5.692	+0.85	6913
76	11.672	11.8	0.747	3.860E+4	5905	3.824	-7.74	8108
79	11.672	2.1	0.747	3.058E+4	4887	0.897	-9.67	6795
74	15.398	54.6	0.747	6.969E+4	6135	Exit	-3.24	6570
78	15.452	26.5	0.747	5.296E+4	7613	5.720	-1.03	9686

Table 5-8
Model Comparison
Modified Henry Model
2.54E-4 m Nominal Slit Opening

Run	Stagnation		Experiment			Theory		
	Pressure	Subcooling	D_h	G_c	P_{ex}	Flashing Location	ΔG_c	P_{ex}
(#)	(MPa)	(°C)	(mm)	(kg/m^2-s)	(kPa)	(cm)	(%)	(kPa)
68	4.289	59.6	0.464	3.500E+4	1210	Exit	-0.49	1198
70	4.320	30.7	0.464	2.849E+4	1820	6.078	-4.30	2261
69	4.281	14.9	0.464	2.160E+4	2229	4.863	-0.95	2759
71	4.272	4.8	0.464	1.687E+4	1909	2.018	+0.58	2969
23	7.117	61.2	0.502	4.271E+4	2016	Exit	+8.69	2539
51	7.050	60.3	0.418	4.091E+4	2214	Exit	-0.72	2318
24	7.055	29.2	0.502	3.641E+4	1007	5.876	+1.55	4025
25	7.055	18.2	0.502	3.131E+4	748	5.182	+4.18	4619
26	7.000	3.3	0.502	2.027E+4	595	0.763	+10.67	4778
36	9.553	59.1	0.453	4.405E+4	3309	Exit	-1.86	3490
37	9.600	28.1	0.453	3.247E+4	4446	5.524	+0.27	5403
38	9.667	22.4	0.453	2.748E+4	4301	5.036	11.64	5792
55	9.602	3.9	0.418	2.198E+4	3098	1.089	+0.22	5167
98	9.774	58.0	0.502	4.883E+4	3239	Exit	-5.11	3650
99	9.609	0.0	0.502	2.254E+4	2972	0.601	-12.62	4727
52	11.728	59.9	0.418	4.924E+4	3994	Exit	-1.53	4480
39	11.601	54.9	0.453	4.413E+4	4187	6.317	-7.84	4715
54	11.696	30.0	0.418	3.852E+4	5065	5.648	-0.72	6632
95	12.420	61.5	0.502	5.137E+4	4039	Exit	-2.50	4660
96	11.642	26.4	0.502	3.901E+4	4636	5.401	-4.73	6875
93	11.838	12.9	0.502	3.224E+4	4070	3.754	-5.70	7070
94	11.675	2.2	0.502	2.058E+4	2940	0.601	-14.03	5861
72	15.601	54.2	0.464	5.019E+4	2605	6.271	+10.86	6869
92	15.798	12.0	0.502	4.231E+4	-	3.577	-21.53	8474
97	15.747	12.0	0.502	3.703E+4	4838	3.546	-14.63	8085
100	15.703	2.2	0.502	3.292E+4	4184	-na-	-	-

Table 5-9
Model Comparison
Modified Henry Model
1.27E-4 m Nominal Slit Opening

Run	Stagnation		Experiment			Theory		
	Pressure	Subcooling	D_h	G_e	P_{ex}	Flashing Location	ΔG_e	P_{ex}
(#)	(MPa)	(°C)	(mm)	(kg/m^2-s)	(kPa)	(cm)	(%)	(kPa)
15	2.734	2.0	0.254	7.267E+3	686	0.861	+15.57	1512
61	4.216	60.8	0.252	2.219E+4	1005	6.311	-5.83	1230
64	4.248	30.9	0.252	1.667E+4	1398	5.543	-9.20	1958
63	4.231	15.7	0.252	1.298E+4	1142	3.925	-5.75	2245
65	4.334	5.9	0.252	1.257E+4	1115	1.467	-18.46	2017
17	7.608	60.6	0.252	3.471E+4	1552	Exit	+1.14	2417
19	7.099	63.0	0.252	4.017E+4	1669	Exit	-1.26	2349
50	7.208	63.7	0.159	1.930E+4	1563	6.146	+2.88	2127
67	7.206	30.1	0.252	2.076E+4	2068	5.318	-6.16	3470
20	7.086	48.3	0.252	3.152E+4	2233	6.163	+7.76	2970
22	7.030	3.7	0.252	1.402E+4	1049	0.316	+27.19	3879
21	6.957	18.2	0.252	9.895E+3	803	4.523	+141.36	4226
34	7.208	18.2	0.209	1.258E+4	1444	4.027	-4.36	2554
33	7.113	7.2	0.209	1.103E+4	1240	1.890	-11.55	2193
85	7.189	14.3	0.252	1.541E+4	1696	3.408	+2.72	3339
86	7.196	4.1	0.252	1.419E+4	1601	0.408	-9.63	2877
32	9.666	59.5	0.209	1.945E+4	2147	5.952	-4.90	3002
82	9.661	0.0	0.252	1.682E+4	1985	0.303	-12.80	3575
84	9.672	56.6	0.252	3.010E+4	2694	6.185	+3.21	3597
48	9.645	30.6	0.159	1.897E+4	1719	5.161	+1.31	4047
49	9.640	15.4	0.159	1.518E+4	1583	3.880	+0.25	3483
47	11.611	57.0	0.159	2.903E+4	2184	6.045	-7.58	4201
88	11.886	57.2	0.252	3.191E+4	3214	6.125	-3.50	4428
66	12.073	30.2	0.252	3.161E+4	3059	5.360	-8.11	6291
80	11.798	13.4	0.252	2.219E+4	2453	3.805	-0.91	5274
81	11.535	0.3	0.252	2.173E+4	2348	0.303	-25.01	4183
87	15.917	56.8	0.252	3.659E+4	-	6.118	+8.96	6405
89	15.579	25.7	0.252	2.914E+4	3537	5.093	+2.33	7165

Table 5-10
Model Comparison

Homogeneous Nonequilibrium Model

3.81E-4 m Nominal Slit Opening

Run	Stagnation			Experiment		Theory		
	Pressure	Subcooling	D_h	G_c	P_{ex}	Flashing Location	ΔG_c	P_{ex}
(#)	(MPa)	(°C)	(mm)	(kg/m^2-s)	(kPa)	(cm)	(%)	(kPa)
59	4.271	59.3	0.747	4.099E+4	1313	Exit	-3.92	1286
57	4.220	28.0	0.747	3.256E+4	2047	Exit	-3.21	2423
58	4.187	13.9	0.747	2.526E+4	2387	Exit	-9.21	3148
60	4.134	2.9	0.747	1.433E+4	1791	2.721	+0.91	2693
30	7.093	59.6	0.748	5.781E+4	1878	Exit	+1.92	2265
27	7.073	29.6	0.748	4.416E+4	2970	Exit	+1.22	4197
28	7.077	15.6	0.748	3.398E+4	3400	Exit	-0.84	5342
29	7.091	6.2	0.748	2.522E+4	2886	4.453	-1.81	5039
41	9.595	59.4	0.708	5.792E+4	3552	Exit	+1.83	3377
43	9.584	29.9	0.708	4.394E+4	4820	Exit	+0.19	5730
44	9.619	15.1	0.708	3.323E+4	5264	6.146	-1.94	6756
75	9.542	0.0	0.747	2.663E+4	4191	0.125	-11.54	5446
42	11.580	53.3	0.708	5.783E+4	4478	Exit	+3.11	4310
45	11.608	28.6	0.708	4.448E+4	5997	Exit	+0.10	7196
76	11.672	11.8	0.747	3.860E+4	5905	5.209	-12.30	7634
79	11.672	2.1	0.747	3.058E+4	4887	0.286	-9.74	6696
74	15.398	54.6	0.747	6.969E+4	6135	Exit	-2.38	6423
78	15.452	26.5	0.747	5.296E+4	7613	Exit	-4.16	10350

Table 5-11
Model Comparison

Homogeneous Nonequilibrium Model

2.54E-4 m Nominal Slit Opening

Run	Stagnation		Experiment			Theory		
	Pressure	Subcooling	D_h	G_c	P_{ex}	Flashing Location	ΔG_c	P_{ex}
(#)	(MPa)	(°C)	(mm)	(kg/m^2-s)	(kPa)	(cm)	(%)	(kPa)
68	4.289	59.6	0.464	3.500E+4	1210	Exit	-2.25	1296
70	4.320	30.7	0.464	2.849E+4	1820	Exit	-4.96	2336
69	4.281	14.9	0.464	2.160E+4	2229	Exit	-5.45	3116
71	4.272	4.8	0.464	1.687E+4	1909	4.905	-8.31	2834
23	7.117	61.2	0.502	4.271E+4	2016	Exit	+10.31	2404
51	7.050	60.3	0.418	4.091E+4	2214	Exit	-1.52	2387
24	7.055	29.2	0.502	3.641E+4	1007	Exit	+1.19	4163
25	7.055	18.2	0.502	3.131E+4	748	Exit	+1.54	5008
26	7.000	3.3	0.502	2.027E+4	595	3.373	+4.32	4406
36	9.553	59.1	0.453	4.405E+4	3309	Exit	-2.34	3544
37	9.600	28.1	0.453	3.247E+4	4446	Exit	-2.92	5991
38	9.667	22.4	0.453	2.748E+4	4301	6.181	+7.38	5970
55	9.602	3.9	0.418	2.198E+4	3098	2.325	+0.46	5062
98	9.774	58.0	0.502	4.883E+4	3239	Exit	-5.63	3711
99	9.609	0.0	0.502	2.254E+4	2972	0.125	-8.85	4814
52	11.728	59.9	0.418	4.924E+4	3994	Exit	-1.47	4472
39	11.601	54.9	0.453	4.413E+4	4187	Exit	-8.44	4814
54	11.696	30.0	0.418	3.852E+4	5065	Exit	-3.22	7219
95	12.420	61.5	0.502	5.137E+4	4039	Exit	-2.67	4684
96	11.642	26.4	0.502	3.901E+4	4636	6.337	-8.13	7413
93	11.838	12.9	0.502	3.224E+4	4070	4.693	-7.79	6783
94	11.675	2.2	0.502	2.058E+4	2940	0.606	+18.13	5948
72	15.601	54.2	0.464	5.019E+4	2605	Exit	+11.08	6875
92	15.798	12.0	0.502	4.231E+4	-	5.932	-4.21	7914
97	15.747	12.0	0.502	3.703E+4	4838	5.521	+2.37	7001
100	15.703	2.2	0.502	3.292E+4	4184	1.013	-10.15	6713

Table 5-12
Model Comparison

Homogeneous Nonequilibrium Model

1.27E-4 m Nominal Slit Opening

Run	Stagnation		Experiment			Theory		
	Pressure	Subcooling	D_h	G_e	P_{ex}	Flashing Location	ΔG_e	P_{ex}
(#)	(MPa)	(°C)	(mm)	(kg/m^2-s)	(kPa)	(cm)	(%)	(kPa)
15	2.734	2.0	0.254	7.267E+3	686	3.320	+6.65	1373
61	4.216	60.8	0.252	2.219E+4	1005	Exit	-5.94	1244
64	4.248	30.9	0.252	1.667E+4	1398	Exit	-12.16	2322
63	4.231	15.7	0.252	1.298E+4	1142	5.289	-9.08	2109
65	4.334	5.9	0.252	1.257E+4	1115	3.263	-20.49	1929
17	7.608	60.6	0.252	3.471E+4	1552	Exit	+1.52	2385
19	7.099	63.0	0.252	4.017E+4	1669	Exit	-0.61	2291
50	7.208	63.7	0.159	1.930E+4	1563	Exit	+1.97	2337
67	7.206	30.1	0.252	2.076E+4	2068	6.087	-8.60	4239
20	7.086	48.3	0.252	3.152E+4	2233	Exit	+8.19	3006
22	7.030	3.7	0.252	1.402E+4	1049	Exit	+24.13	3703
21	6.957	18.2	0.252	9.895E+3	803	6.086	+131.80	4360
34	7.208	18.2	0.209	1.258E+4	1444	4.538	-3.28	2518
33	7.113	7.2	0.209	1.103E+4	1240	2.627	-7.54	2250
85	7.189	14.3	0.252	1.541E+4	1696	4.408	+1.93	3227
86	7.196	4.1	0.252	1.419E+4	1601	1.718	-7.29	2889
32	9.666	59.5	0.209	1.945E+4	2147	6.288	-6.64	3239
82	9.661	0.0	0.252	1.682E+4	1985	0.845	-5.40	3794
84	9.672	56.6	0.252	3.010E+4	2694	Exit	+2.52	3780
48	9.645	30.6	0.159	1.897E+4	1719	5.652	+0.79	3904
49	9.640	15.4	0.159	1.518E+4	1583	4.267	+2.61	3487
47	11.611	57.0	0.159	2.903E+4	2184	Exit	-8.67	4693
88	11.886	57.2	0.252	3.191E+4	3214	Exit	-4.71	4797
66	12.073	30.2	0.252	3.161E+4	3059	5.982	-9.67	6047
80	11.798	13.4	0.252	2.219E+4	2453	4.198	+1.11	5242
81	11.535	0.3	0.252	2.173E+4	2348	0.624	-16.91	4532
87	15.917	56.8	0.252	3.659E+4	-	Exit	+8.15	6777
89	15.579	25.7	0.252	2.914E+4	3537	5.377	+2.30	7043

Table 5-13
Model Comparison

Henry Model: Long Ducts

3.81E-4 m Nominal Slit Opening

Run	Stagnation		Experiment			Theory		
	Pressure	Subcooling	D_h	G_c	P_{ex}	Flashing Location	ΔG_c	P_{ex}
(#)	(MPa)	(°C)	(mm)	(kg/m^2-s)	(kPa)	(cm)	(%)	(kPa)
59	4.271	59.3	0.747	4.099E+4	1313	-	412.3	1354
57	4.220	28.0	0.747	3.256E+4	2047	-	380.1	2368
58	4.187	13.9	0.747	2.526E+4	2387	-	365.4	2800
60	4.134	2.9	0.747	1.433E+4	1791	-	463.0	2861
30	7.093	59.6	0.748	5.781E+4	1878	-	352.1	2379
27	7.073	29.6	0.748	4.416E+4	2970	-	337.2	4027
28	7.077	15.6	0.748	3.398E+4	3400	-	338.1	4673
29	7.091	6.2	0.748	2.522E+4	2886	-	360.4	4704
41	9.595	59.4	0.708	5.792E+4	3552	-	394.9	3645
43	9.584	29.9	0.708	4.394E+4	4820	-	391.1	5543
44	9.619	15.1	0.708	3.323E+4	5264	-	391.7	6384
75	9.542	0.0	0.747	2.663E+4	4191	-	-na-	-na-
42	11.580	53.3	0.708	5.783E+4	4478	-	425.4	4665
45	11.608	28.6	0.708	4.448E+4	5997	-	409.3	6881
76	11.672	11.8	0.747	3.860E+4	5905	-	327.9	7331
79	11.672	2.1	0.747	3.058E+4	4887	-	371.9	6246
74	15.398	54.6	0.747	6.969E+4	6135	-	418.4	6782
78	15.452	26.5	0.747	5.296E+4	7613	-	357.8	9482

Table 5-14
Model Comparison
Henry Model: Long Ducts
2.54E-4 m Nominal Slit Opening

Run	Stagnation		Experiment			Theory		
	Pressure	Subcooling	D_h	G_c	P_{ex}	Flashing Location	ΔG_c	P_{ex}
(#)	(MPa)	(°C)	(mm)	(kg/m^2-s)	(kPa)	(cm)	(%)	(kPa)
68	4.289	59.6	0.464	3.500E+4	1210	-	501.8	1354
70	4.320	30.7	0.464	2.849E+4	1820	-	-na-	-na-
69	4.281	14.9	0.464	2.160E+4	2229	-	460.5	2838
71	4.272	4.8	0.464	1.687E+4	1909	-	418.4	2956
23	7.117	61.2	0.502	4.271E+4	2016	-	506.3	2466
51	7.050	60.3	0.418	4.091E+4	2214	-	527.1	2479
24	7.055	29.2	0.502	3.641E+4	1007	-	426.2	4035
25	7.055	18.2	0.502	3.131E+4	748	-	402.5	4559
26	7.000	3.3	0.502	2.027E+4	595	-	439.3	4425
36	9.553	59.1	0.453	4.405E+4	3309	-	548.2	3644
37	9.600	28.1	0.453	3.247E+4	4446	-	546.7	5668
38	9.667	22.4	0.453	2.748E+4	4301	-	595.4	6061
55	9.602	3.9	0.418	2.198E+4	3098	-	500.9	5622
98	9.774	58.0	0.502	4.883E+4	3239	-	485.4	3812
99	9.609	0.0	0.502	2.254E+4	2972	-	-na-	-na-
52	11.728	59.9	0.418	4.924E+4	3994	-	528.9	4583
39	11.601	54.9	0.453	4.413E+4	4187	-	589.9	4886
54	11.696	30.0	0.418	3.852E+4	5065	-	500.9	6830
95	12.420	61.5	0.502	5.137E+4	4039	-	522.2	4783
96	11.642	26.4	0.502	3.901E+4	4636	-	461.0	7062
93	11.838	12.9	0.502	3.224E+4	4070	-	421.9	7510
94	11.675	2.2	0.502	2.058E+4	2940	-	596.0	6210
72	15.601	54.2	0.464	5.019E+4	2605	-	558.3	6865
92	15.798	12.0	0.502	4.231E+4	-	-	347.0	8688
97	15.747	12.0	0.502	3.703E+4	4838	-	410.3	8681
100	15.703	2.2	0.502	3.292E+4	4184	-	396.3	7102

Table 5-15
Model Comparison
Henry Model: Long Ducts
1.27E-4 m Nominal Slit Opening

Run	Stagnation		Experiment				Theory	
	Pressure	Subcooling	D_h	G_c	P_{ex}	Flashing Location	ΔG_c	P_{ex}
(#)	(MPa)	(°C)	(mm)	(kg/m^2-s)	(kPa)	(cm)	(%)	(kPa)
15	2.734	2.0	0.254	7.267E+3	686	-	770.2	1914
61	4.216	60.8	0.252	2.219E+4	1005	-	849.6	1219
64	4.248	30.9	0.252	1.667E+4	1398	-	872.9	2294
63	4.231	15.7	0.252	1.298E+4	1142	-	833.1	2800
65	4.334	5.9	0.252	1.257E+4	1115	-	628.2	2999
17	7.608	60.6	0.252	3.471E+4	1552	-	641.5	2470
19	7.099	63.0	0.252	4.017E+4	1669	-	550.9	2379
50	7.208	63.7	0.159	1.930E+4	1563	-	1268.0	2397
67	7.206	30.1	0.252	2.076E+4	2068	-	841.0	4082
20	7.086	48.3	0.252	3.152E+4	2233	-	649.3	3056
22	7.030	3.7	0.252	1.402E+4	1049	-	685.7	4463
21	6.957	18.2	0.252	9.895E+3	803	-	1480.0	4496
34	7.208	18.2	0.209	1.258E+4	1444	-	1158.0	4661
33	7.113	7.2	0.209	1.103E+4	1240	-	965.9	4770
85	7.189	14.3	0.252	1.541E+4	1696	-	835.1	4785
86	7.196	4.1	0.252	1.419E+4	1601	-	691.8	4571
32	9.666	59.5	0.209	1.945E+4	2147	-	1378.0	3674
82	9.661	0.0	0.252	1.682E+4	1985	-	-na-	-na-
84	9.672	56.6	0.252	3.010E+4	2694	-	837.2	3847
48	9.645	30.6	0.159	1.897E+4	1719	-	1051.0	5529
49	9.640	15.4	0.159	1.518E+4	1583	-	979.9	6383
47	11.611	57.0	0.159	2.903E+4	2184	-	942.4	4728
88	11.886	57.2	0.252	3.191E+4	3214	-	857.8	4844
66	12.073	30.2	0.252	3.161E+4	3059	-	640.6	7060
80	11.798	13.4	0.252	2.219E+4	2453	-	662.1	7552
81	11.535	0.3	0.252	2.173E+4	2348	-	539.3	5988
87	15.917	56.8	0.252	3.659E+4	-	-	827.5	6775
89	15.579	25.7	0.252	2.914E+4	3537	-	720.8	9639

Table 5-16
Data of Jeandey and Gros D'Aillon [97]
Comparison With Homogeneous Nonequilibrium Model

Run	Stagnation Pressure	Stagnation Subcooling	Experimental		Theory	
			G_c	P_{ex}	ΔG_c	P_{ex}
(#)	(MPa)	(°C)	(kg/m^2-s)	(kPa)	(%)	(kPa)
20B148C	2.003	63.9	4.88×10^4	428	-0.55	424
20B151C	2.000	61.3	4.82×10^4	451	-0.60	454
20B165C	2.001	46.9	4.48×10^4	625	-0.32	656
20B167C	2.004	45.3	4.41×10^4	647	-0.27	682
20B193C	2.006	19.3	3.27×10^4	1103	+0.16	1228
60B248C	6.004	27.2	5.59×10^4	3111	+4.16	3672
60B255C	6.001	20.5	5.00×10^4	3428	-0.75	4078
60B257C	6.009	17.8	4.75×10^4	3558	-0.68	4257
48B234C	4.820	27.6	5.21×10^4	2441	+0.55	2824
42B234C	4.292	20.5	4.45×10^4	2419	+0.90	2802
62B252C	6.255	26.3	5.60×10^4	3285	+3.92	3904
58B252C	5.812	21.5	5.01×10^4	3280	-0.45	3869
83B280C	8.385	18.2	5.36×10^4	4962	+1.74	6148
40B227C	4.003	22.9	4.52×10^4	2160	-0.38	2485

Table 5-17
Data of Jeandey and Gros D'Aillon [97]
Single-Phase Pressure Loss Summary

Run (#)	Pressure Gradient (kPa/m)	Reynolds Number	Friction Factor	Entry Loss Coefficient*
20B148C	-770.1	5.322×10^6	0.0119	0.986
20B151C	-745.1	5.355×10^6	0.0118	0.990
20B165C	-646.6	5.483×10^6	0.0116	0.978
20B167C	-639.6	5.453×10^6	0.0119	0.986
20B193C	-412.4	4.708×10^6	0.0135	0.990
60B248C	-1040.8	1.033×10^7	0.0107	0.986
60B255C	-964.4	9.241×10^6	0.0122	0.986
60B257C	-873.5	9.112×10^6	0.0122	0.988
48B234C	-861.5	9.090×10^6	0.0104	0.982
42B234C	-674.4	7.772×10^6	0.0112	0.985
62B252C	-1037.3	1.049×10^7	0.0106	0.990
58B252C	-954.8	9.398×10^6	0.0121	0.994
83B280C	-na-	1.111×10^7	0.0105	0.996
40B227C	-760.7	7.676×10^6	0.0124	0.988

*Calculated for entire convergent entry section

Figure 5-1
Theoretical Sound Speed Versus Void Fraction

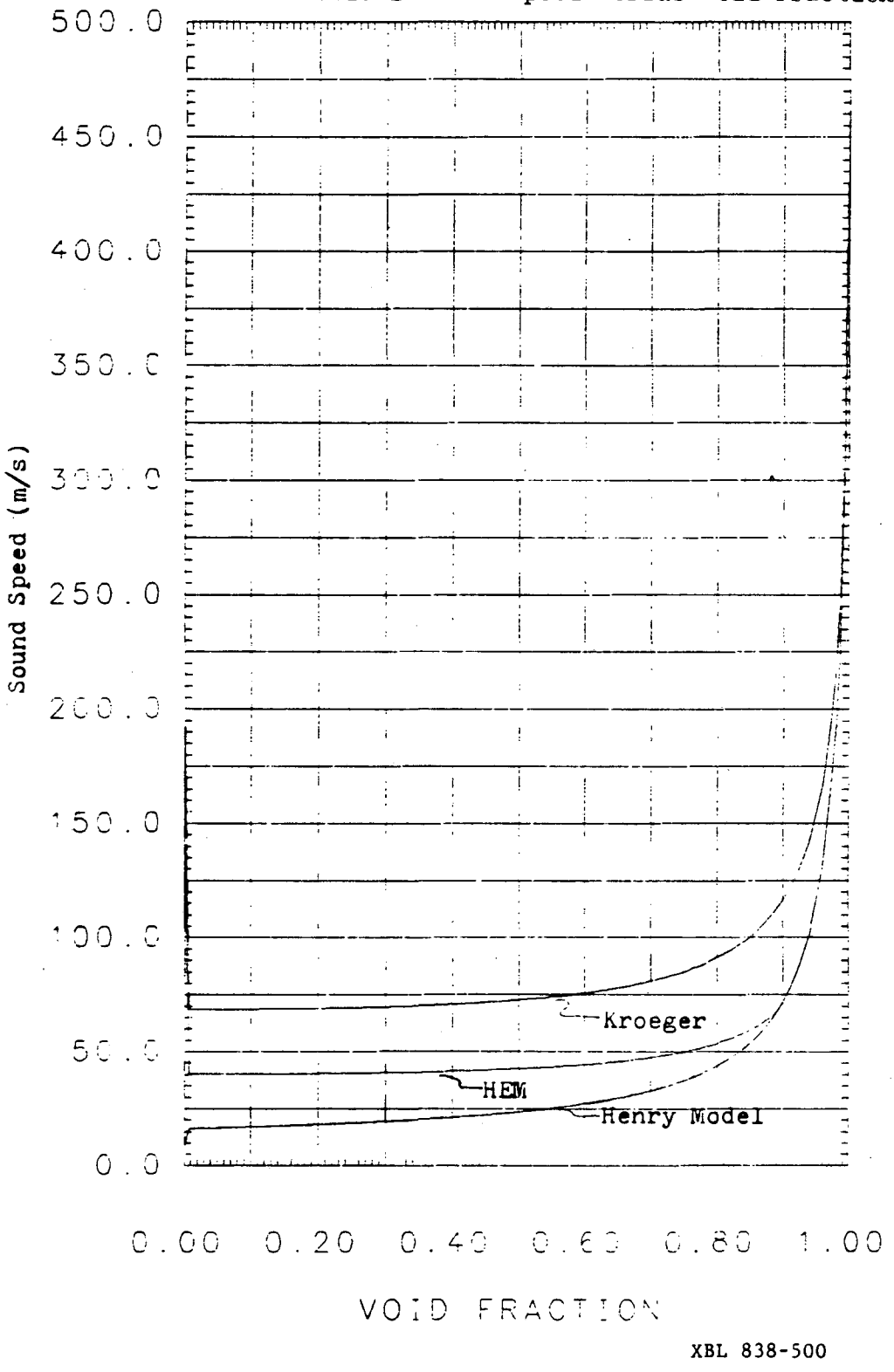

XBL 838-500

Figure 5-2

Homogeneous Equilibrium Model
G_{th} versus G_{exp}

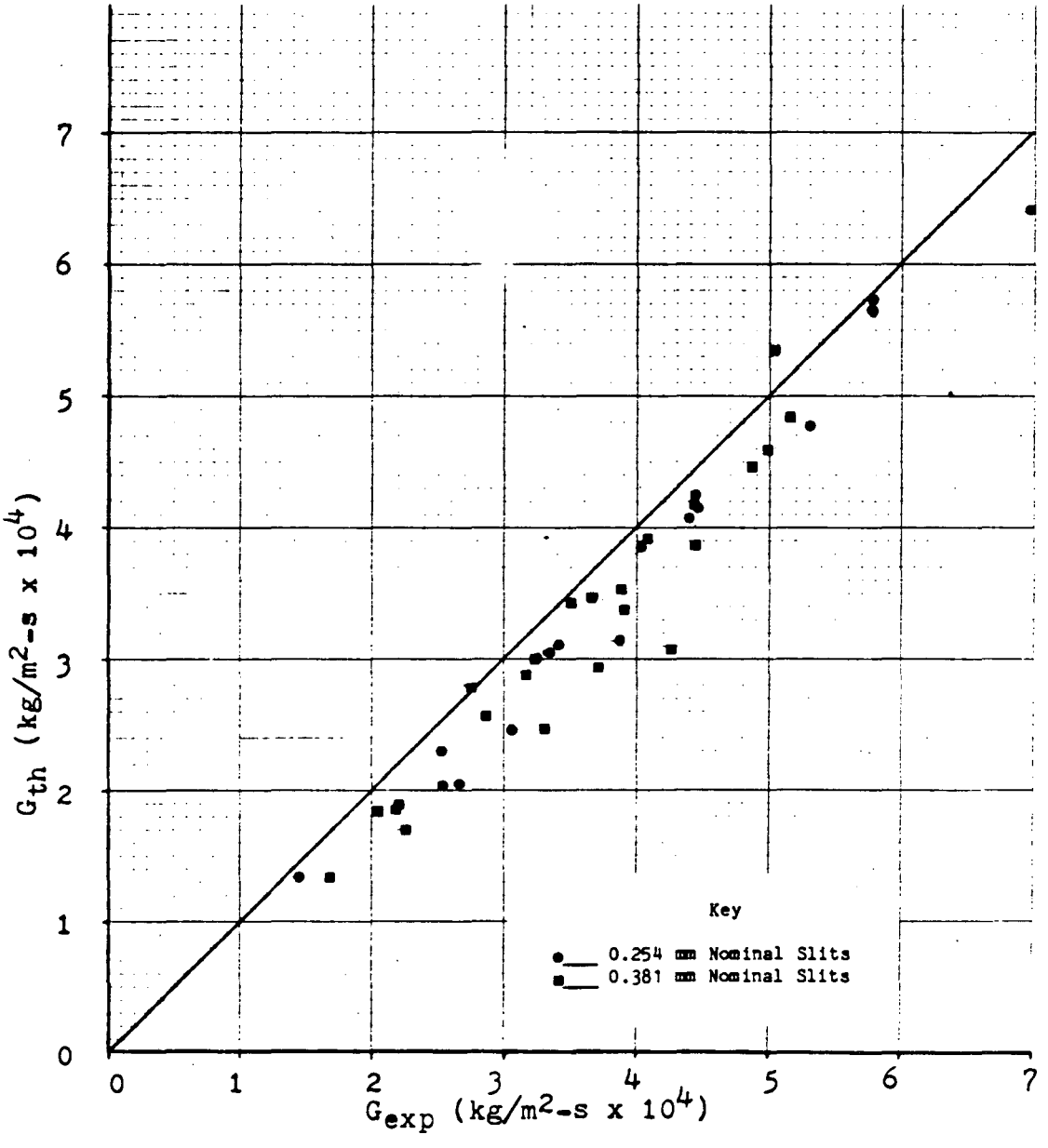

XBL 838-501

Figure 5-3

Modified Henry Model

G_{th} versus G_{exp}

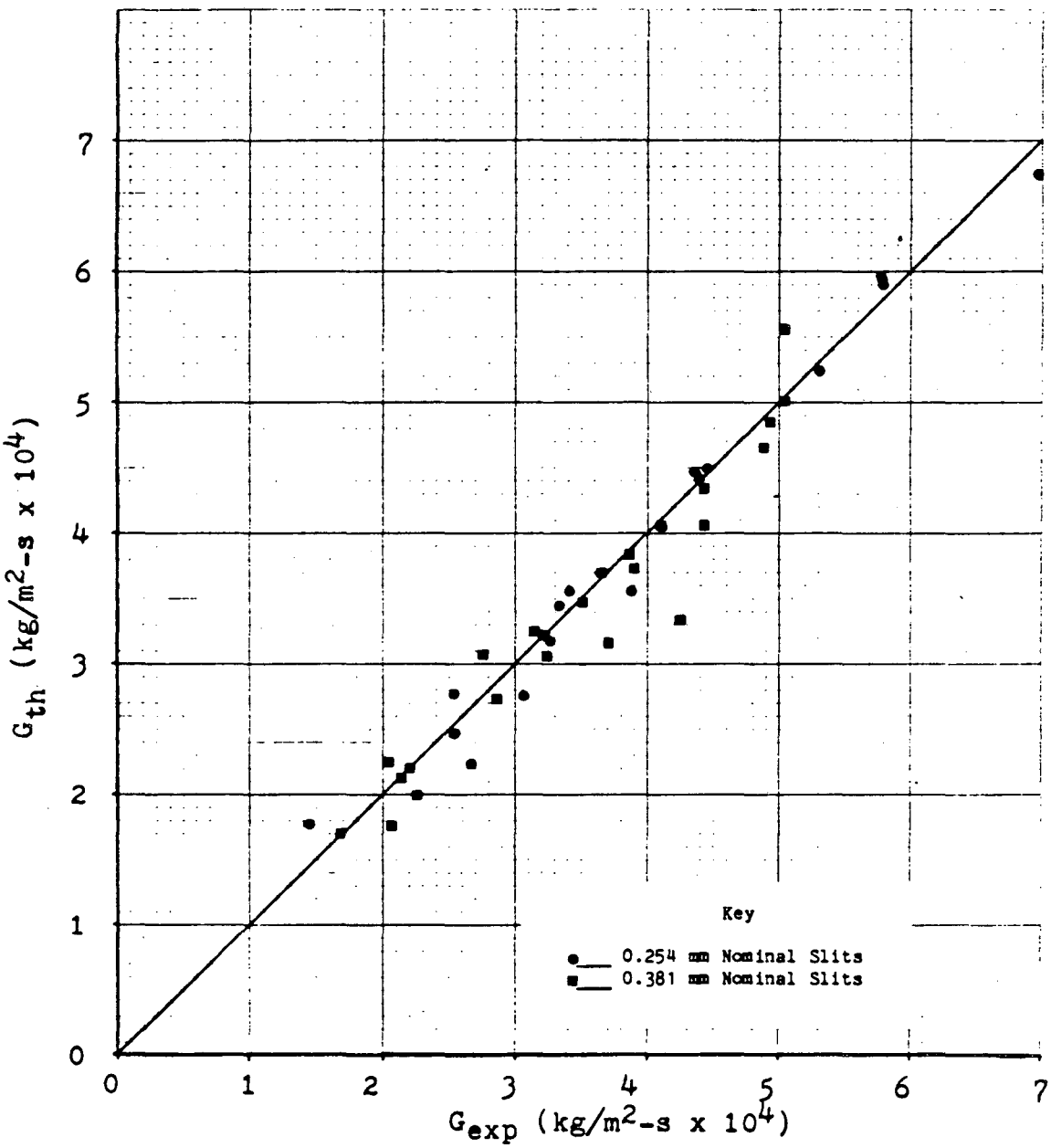

XBL 838-502

Figure 5-4

Homogeneous Nonequilibrium Model

G_{th} versus G_{exp}

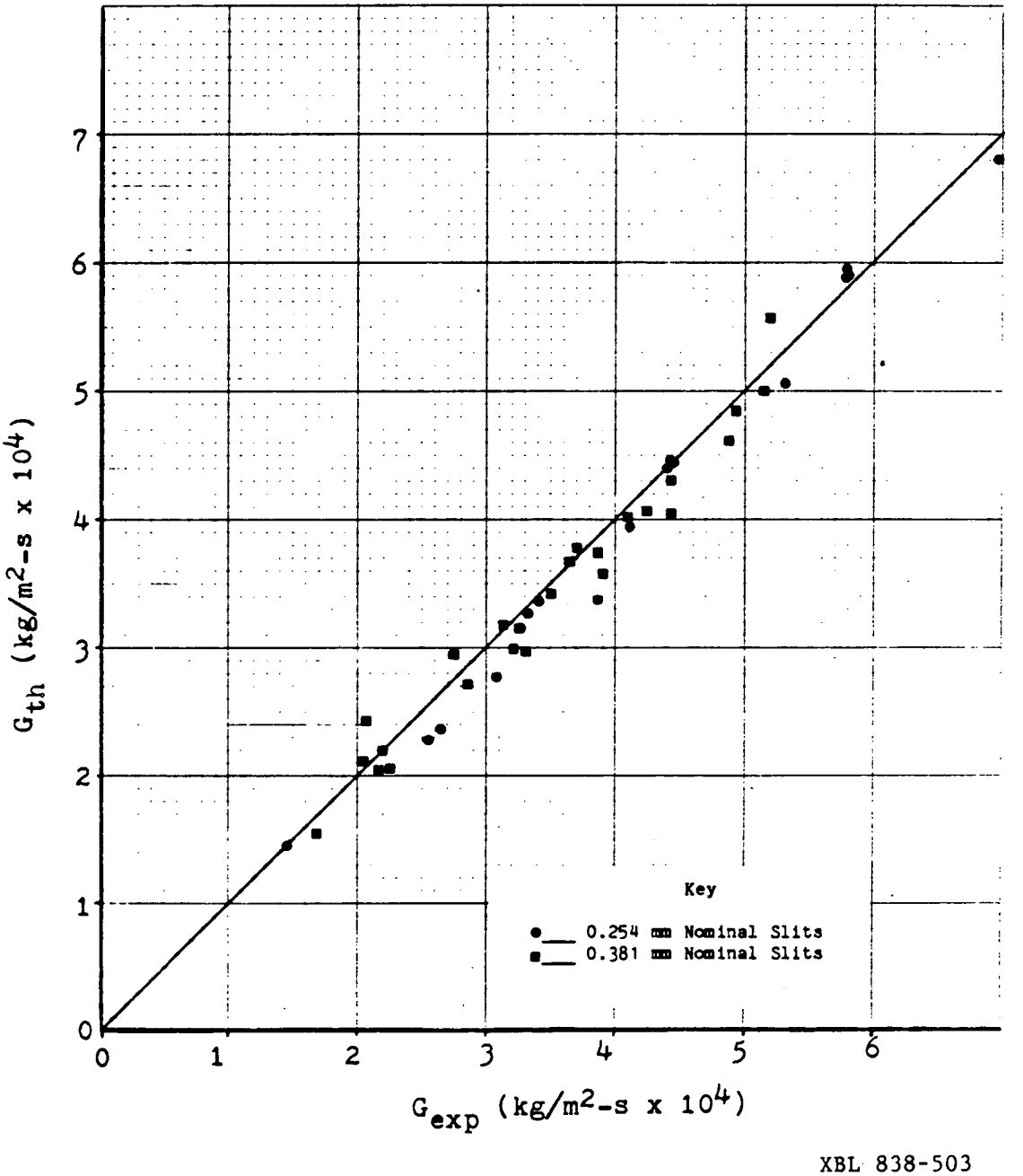

XBL 838-503

APPENDIX A

Data Tables

This appendix contains summaries of the data collected in this experimental program. Runs #8 through #101 (94 runs in all) are reported. The first 8 runs were shakedown tests and are not reported. Data tables are in order of increasing run number (chronological). Tables are identified by run number only.

The heading of each table gives the channel geometry, and initial test section temperature. Channel dimensions are those estimated by the procedure described in Chapter IV. Initial test section temperatures are the maximum and minimum recorded prior to the initiation of flow through the test section. The difference between the two readings is usually indicative of the axial temperature gradient in the test section at that time. Lower temperatures at the outlet of the test section resulted from heat loss through the downstream piping, which exceeded the capacity of the guard heater (described in Chapter III).

The tables presented in this section contain data abstracted from the reduced data (the computation of which is described in Chapter III) by computer. Table entries were calculated from the reduced data as an average of eleven measurements centered around the time indicated. The time span over which the average was taken varies from 6.6 sec to 14.3 sec, depending upon how many data channels were connected during that run. For a majority of the runs, the averaging period was approximately 12 seconds. The zero reference for the times indicated is the time at which the reduced data record begins. This time is approximately 11 minutes after data collection was initiated. The period over which the data was not reduced, is that period required to determine the scanning frequency of the Auto-Data Eight (described in Chapter IV). These times have been indicated in order to establish the elapsed time between reported data for a given run. In addition, this information allows the retrieval of the data, which is represented by an average in these tables, from the data tapes.

The rms error between the data and the reported average is indicated in each table. For stagnation state data, the rms error is indicated on the line below the average; in the same units. Error in the calculated mass flowrates is reported as a percentage of the average. The difference between the result of the Volume Discharge Method and that of the Weigh Tank Method for determining the critical mass flux, is reported on the last line of that section of the table as a percentage of the Volume Discharge Method calculation. (Methods used to calculate the mass flowrate are described in Chapter IV.)

For the pressure profile data, the rms error in each entry is given in parentheses. Since the averages were calculated from reduced data, the effect of variations in the measured upstream pressure is included in the error calculation for those measurements made with differential pressure transducers (identified in Figure 3-9). An additional indication of the error associated with the pressure profile measurements is given in the last column of the pressure profile summaries. Labeled "Drift", this column shows the mean difference between the stagnation pressure measurement and the pressure measured at that location within the slit after the main valve had been closed. Ideally, this entry should be zero. With no flow through the test section pressure upstream of the main valve should be uniform. The entry represents the maximum possible drift in the transducer zero over the course of a run. In those instances where there was insufficient data collected after flow was terminated (fewer than three points) a "-" appears in this column. For some runs, a transducer may have been subjected to a pressure greater than its' range, malfunctioned, or have been disconnected. When this was the case, the table entry is given as "-na-".

RUN # 8 SUMMARY

Test Section Dimensions

.1270 mm Opening
20.98 mm Width
2.6645e-06 m^2 Area
.2525 mm Hydraulic Diameter

Initial Test Section Temperatures

21.2 °C Maximum
20.3 °C Minimum

Stagnation State					
Calculated Value	Time(sec)				
	116.17	186.56	271.30	368.34	622.55
Pressure(kPa)	2481.	2487.	2492.	2498.	2509.
Error (kpa)	1.	1.	1.	1.	1.
Temperature (°C)	19.8	19.7	19.7	19.6	20.1
Error (°C)	.1	.1	.1	.2	.1
Subcooling (°C)	204.	204.	204.	204.	204.

Corrected Mass Flux ($kg/m^2 x sec$)					
Calculated Value	Time(sec)				
	116.17	186.56	271.30	368.34	622.55
Volume Method	1.715e+04	1.695e+04	1.692e+04	1.696e+04	1.703e+04
Error (%)	.0	0.	.0	.0	.0
Weigh Tank	1.576e+04	1.576e+04	1.576e+04	1.576e+04	1.576e+04
Error (%)	0.	0.	0.	0.	0.
% Difference	8.1	7.0	6.9	7.1	7.5

RUN # 9 SUMMARY

Test Section Dimensions

.1270 mm Opening
20.98 mm Width
2.6645e-06 m^2 Area
.2525 mm Hydraulic Diameter

Initial Test Section Temperatures

263.7 °C Maximum
258.4 °C Minimum

Stagnation State					
Calculated Value	Time(sec)				
	53.99	103.19	196.81	306.15	421.64
Pressure(kPa)	6817.	6811.	6801.	6786.	6779.
Error (kpa)	1.	2.	2.	2.	1.
Temperature (°C)	272.5	274.3	274.2	272.8	270.4
Error (°C)	.2	.1	.1	.1	.1
Subcooling (°C)	11.5	9.6	9.7	10.9	13.3

Corrected Mass Flux ($kg/m^2 x sec$)					
Calculated Value	Time(sec)				
	53.99	103.19	196.81	306.15	421.64
Volume Method	1.677e+04	1.616e+04	1.608e+04	1.603e+04	1.600e+04
Error (%)	.0	.0	.0	.0	.0
Weigh Tank	1.407e+04	1.373e+04	1.346e+04	1.373e+04	1.375e+04
Error (%)	.3	.2	.3	.3	.3
% Difference	16.1	15.0	16.3	14.4	14.1

RUN # 10 SUMMARY

Test Section Dimensions
.2540 mm Opening
20.98 mm Width
5.3289e-06 m^2 Area
.5019 mm Hydraulic Diameter

Initial Test Section Temperatures
21.7 °C Maximum
21.2 °C Minimum

Stagnation State				
Calculated Value	Time(sec)			
	114.81	150.34	180.41	236.45
Pressure(kPa)	2502.	2502.	2503.	2501.
Error (kpa)	0.	1.	1.	1.
Temperature (°C)	21.9	22.6	22.8	23.0
Error (°C)	.2	.2	.1	.1
Subcooling (°C)	202.	201.	201.	201.

Corrected Mass Flux ($kg/m^2 x sec$)				
Calculated Value	Time(sec)			
	114.81	150.34	180.41	236.45
Volume Method	2.924e+04	2.901e+04	2.903e+04	2.866e+04
Error (%)	.0	.0	.0	.0
Weigh Tank	-na-	2.657e+04	2.716e+04	2.749e+04
Error (%)	-	.0	.0	.0
% Difference	-na-	8.4	6.5	4.1

RUN # 11 SUMMARY

Test Section Dimensions
.2540 mm Opening
20.31 mm Width
5.1587e-06 m^2 Area
.5017 mm Hydraulic Diameter

Initial Test Section Temperatures
219.3 °C Maximum
210.7 °C Minimum

Stagnation State			
Calculated Value	Time(sec)		
	230.72	253.24	281.91
Pressure(kPa)	6939.	6940.	6925.
Error (kpa)	1.	3.	2.
Temperature (°C)	219.4	219.6	220.2
Error (°C)	.2	.1	.2
Subcooling (°C)	65.8	65.6	64.9

Corrected Mass Flux ($kg/m^2 x sec$)			
Calculated Value	Time(sec)		
	230.72	253.24	281.91
Volume Method	4.877e+04	4.869e+04	4.828e+04
Error (%)	.0	.0	.0
Weigh Tank	3.172e+04	4.423e+04	3.612e+04
Error (%)	1.1	.6	.8
% Difference	35.0	9.2	25.2

RUN # 12 SUMMARY

Test Section Dimensions		Initial Test Section Temperatures	
.3810	mm Opening	21.7	°C Maximum
19.92	mm Width	21.5	°C Minimum

7.5895e-06 m^2 Area
.7477 mm Hydraulic Diameter

Stagnation State			
Calculated Value	Time(sec)		
	103.19	140.77	166.74
Pressure(kPa)	2637.	2624.	2615.
Error (kpa)	1.	1.	1.
Temperature (°C)	21.4	21.3	21.5
Error (°C)	.1	.1	.1
Subcooling (°C)	205.	205.	205.

Corrected Mass Flux ($kg/m^2 x sec$)			
Calculated Value	Time(sec)		
	103.19	140.77	166.74
Volume Method	3.737e+04	3.712e+04	3.678e+04
Error (%)	.0	.0	.0
Weigh Tank	3.659e+04	3.684e+04	3.658e+04
Error (%)	.0	.0	.0
% Difference	2.1	.8	.5

RUN # 13 SUMMARY

(Test Section Reversed on This Run)

Test Section Dimensions		Initial Test Section Temperatures	
.3810	mm Opening	22.5	°C Maximum
19.92	mm Width	22.2	°C Minimum

7.5895e-06 m^2 Area
.7477 mm Hydraulic Diameter

Stagnation State			
Calculated Value	Time(sec)		
	100.46	126.42	173.58
Pressure(kPa)	2518.	2512.	2500.
Error (kpa)	1.	1.	1.
Temperature (°C)	22.4	22.5	23.2
Error (°C)	.1	.2	.1
Subcooling (°C)	202.	202.	201.

Corrected Mass Flux ($kg/m^2 x sec$)			
Calculated Value	Time(sec)		
	100.46	126.42	173.58
Volume Method	3.609e+04	3.585e+04	3.607e+04
Error (%)	.0	.0	.0
Weigh Tank	3.533e+04	3.644e+04	3.629e+04
Error (%)	.0	.0	.0
% Difference	2.1	-1.6	-.6

RUN # 14 SUMMARY

Test Section Dimensions
.1270 mm Opening
20.24 mm Width
2.5705e-06 m^2 Area
.2524 mm Hydraulic Diameter

Initial Test Section Temperatures
22.2 °C Maximum
22.0 °C Minimum

Stagnation State

Calculated Value	Time(sec) 124.27	242.72	296.12	380.58	499.03
Pressure(kPa)	2736.	2786.	2805.	2831.	2860.
Error (kpa)	2.	2.	1.	1.	1.
Temperature (°C)	22.1	22.5	22.6	22.7	22.6
Error (°C)	.1	.2	.2	.2	.1
Subcooling (°C)	207.	207.	208.	208.	209.

Corrected Mass Flux ($kg/m^2 x sec$)

Calculated Value	Time(sec) 124.27	242.72	296.12	380.58	499.03
Volume Method	6.980e+09	6.958e+09	6.973e+09	6.990e+09	6.971e+09
Error (%)	.0	.0	.0	.0	.0
Weigh Tank	5.742e+09	6.134e+09	6.084e+09	6.043e+09	6.035e+09
Error (%)	.0	.0	.0	.0	.0
% Difference	17.7	11.8	12.7	13.5	13.4

Pressure Profile Summary (in kPa)

Distance from Entrance (cm)	Time(sec) 124.27	242.72	296.12	380.58	499.03	Drift (kPa)
.318	2316(2)	2362(2)	2378(1)	2402(2)	2427(2)	0
1.91	1806(2)	1836(2)	1849(1)	1851(2)	1868(1)	0
3.18	1313(2)	1335(2)	1345(1)	1348(2)	1360(1)	0
4.45	822(2)	836(2)	843(1)	845(1)	852(1)	0
5.40	630(3)	642(1)	648(1)	616(1)	617(2)	3
5.72	-na-	-na-	-na-	-na-	-na-	-
6.03	1501(2)	1530(2)	1540(1)	1555(1)	1571(2)	843
exit	194(8)	192(9)	196(8)	196(7)	191(9)	13
outlet	123(0)	123(0)	123(0)	123(0)	123(0)	

RUN # 15 SUMMARY

Test Section Dimensions
.1270 mm Opening
20.24 mm Width
2.5705e-06 m^2 Area
.2524 mm Hydraulic Diameter

Initial Test Section Temperatures
216.3 °C Maximum
99.6 °C Minimum

Stagnation State

Calculated Value	Time(sec) 112.44	232.63	379.00	593.21	883.60
Pressure(kPa)	2734.	2738.	2741.	2739.	2744.
Error (kpa)	1.	1.	1.	1.	1.
Temperature (°C)	226.9	225.8	223.5	221.1	217.6
Error (°C)	.1	.1	.1	.1	.1
Subcooling (°C)	1.9	3.0	5.4	7.7	11.3

Corrected Mass Flux ($kg/m^2 x sec$)

Calculated Value	Time(sec) 112.44	232.63	379.00	593.21	883.60
Volume Method	7.210e+03	7.023e+03	8.381e+03	8.824e+03	9.374e+03
Error (%)	.0	.0	.0	.0	.0
Weigh Tank	6.751e+03	6.919e+03	7.312e+03	8.012e+03	8.565e+03
Error (%)	.0	.0	.0	.0	.0
% Difference	6.4	1.5	12.8	9.2	8.6

Pressure Profile Summary (in kPa)

Distance from Entrance (cm)	Time(sec) 112.44	232.63	379.00	593.21	883.60	Drift (kPa)
.318	2602(2)	2594(2)	2571(3)	2543(1)	2518(2)	-
1.91	2477(1)	2478(2)	2467(3)	2427(2)	2381(2)	-
3.18	2308(3)	2323(5)	2362(2)	2320(2)	2265(3)	-
4.45	1983(3)	1860(10)	1975(12)	2040(9)	2014(3)	-
5.40	1626(3)	1666(49)	1742(2)	1795(2)	1856(2)	-
5.72	-na-	-na-	-na-	-na-	-na-	-
6.03	1193(3)	1201(7)	1291(4)	1342(2)	1383(2)	-
exit	693(5)	703(7)	766(4)	802(5)	830(7)	-0
outlet	126(3)	125(0)	127(0)	128(0)	129(0)	

RUN # 16 SUMMARY

(The Test Section Was Reversed For This Run)

Test Section Dimensions
.1270 mm Opening
20.24 mm Width
2.5705e-06 m^2 Area
.2524 mm Hydraulic Diameter

Initial Test Section Temperatures
21.0 °C Maximum
20.5 °C Minimum

Stagnation State

Calculated Value	Time(sec) 94.93	132.54	216.72	418.21	598.21
Pressure(kPa)	2767.	2774.	2787.	2811.	2733.
Error (kpa)	1.	1.	1.	1.	16.
Temperature (°C)	20.9	21.0	21.2	21.3	21.5
Error (°C)	.1	.1	.1	.1	.1
Subcooling (°C)	208.	209.	209.	209.	207.

Corrected Mass Flux ($kg/m^2 x sec$)

Calculated Value	Time(sec) 94.93	132.54	216.72	418.21	598.21
Volume Method	1.763e+04	1.753e+04	1.746e+04	1.744e+04	1.700e+04
Error (%)	.0	.0	.0	.0	.0
Weigh Tank	1.444e+04	1.457e+04	1.489e+04	1.529e+04	1.532e+04
Error (%)	.0	.0	.0	.0	0.
% Difference	18.1	16.8	14.7	12.3	9.9

Pressure Profile Summary (in kPa)

Distance from Entrance (cm)	Time(sec) 94.93	132.54	216.72	418.21	598.21	Drift (kPa)
.318	268(2)	268(1)	267(1)	266(2)	268(2)	-
1.59	940(1)	942(3)	943(3)	949(4)	927(6)	-
2.86	1432(2)	1437(4)	1439(2)	1451(2)	1411(15)	-
4.13	1879(1)	1887(2)	1893(3)	1909(3)	1853(13)	-
5.40	2344(4)	2250(98)	2255(21)	2375(1)	2301(12)	-
5.72	-na-	-na-	-na-	-na-	-na-	-
6.03	2571(2)	2578(3)	2591(5)	2616(2)	2550(37)	-
exit	2780(6)	2790(8)	2805(7)	2827(11)	2742(20)	1.
outlet	124(0)	124(0)	124(0)	124(0)	125(0)	

RUN # 17 SUMMARY

Test Section Dimensions
.1270 mm Opening
20.24 mm Width
2.5705e-06 m^2 Area
.2524 mm Hydraulic Diameter

Initial Test Section Temperatures
216.9 °C Maximum
22.9 °C Minimum

Stagnation State

Calculated Value	Time(sec) 69.88	108.07	223.60	339.13	454.66
Pressure(kPa)	7070.	5884.	3667.	3121.	2890.
Error (kpa)	2.	148.	22.	9.	6.
Temperature (°C)	221.3	218.1	225.8	224.3	222.2
Error (°C)	6.5	4.9	.1	.1	.1
Subcooling (°C)	65.2	56.1	19.5	11.7	9.5

Corrected Mass Flux ($kg/m^2 x sec$)

Calculated Value	Time(sec) 69.88	108.07	223.60	339.13	454.66
Volume Method	3.491e+04	2.486e+04	1.639e+04	1.122e+04	1.068e+04
Error (%)	.0	.0	.0	.0	.0
Weigh Tank	-na-	-na-	5.674e+03	7.854e+03	9.337e+03
Error (%)	-	-	.0	.0	.0
% Difference	-na-	-na-	65.4	30.0	12.6

Pressure Profile Summary (in kPa)

Distance from Entrance (cm)	Time(sec) 69.88	108.07	223.60	339.13	454.66	Drift (kPa)
.318	6122(2)	5195(119)	3409(18)	2976(7)	2771(6)	-
1.91	5212(2)	4522(94)	3126(14)	2804(5)	2635(5)	-
3.18	4402(2)	3906(72)	2870(10)	2649(4)	2498(5)	-
4.45	-na-	-na-	-na-	-na-	-na-	-na-
5.40	-na-	5002(732)	2397(5)	2230(8)	2016(7)	-
5.72	-na-	-na-	-na-	-na-	-na-	-
6.03	-na-	-na-	2205(7)	1790(10)	1582(5)	-
exit	1449(6)	1450(10)	1204(8)	887(7)	805(6)	91
outlet	125(0)	124(0)	144(5)	136(0)	134(0)	

RUN # 18 SUMMARY

Test Section Dimensions
.1270 mm Opening
20.33 mm Width
2.5819e-06 m^2 Area
.2524 mm Hydraulic Diameter

Initial Test Section Temperatures
23.7 °C Maximum
23.5 °C Minimum

Stagnation State					
Calculated Value	Time(sec)				
	80.37	236.45	431.78	537.38	603.74
Pressure(kPa)	2623.	2645.	2660.	2666.	2669.
Error (kpa)	1.	1.	1.	1.	1.
Temperature (°C)	22.7	22.8	22.8	22.9	22.9
Error (°C)	.1	.2	.0	.1	.2
Subcooling (°C)	204.	204.	204.	205.	205.

Corrected Mass Flux ($kg/m^2 \times sec$)					
Calculated Value	Time(sec)				
	80.37	236.45	431.78	537.38	603.74
Volume Method	1.697e+04	1.674e+04	1.671e+04	1.659e+04	1.682e+04
Error (%)	.0	.0	.0	.0	.0
Weigh Tank	1.464e+04	1.479e+04	1.494e+04	1.498e+04	1.498e+04
Error (%)	.0	.0	.0	0.	0.
% Difference	13.7	11.7	10.5	9.7	11.0

Pressure Profile Summary (in kPa)						
Distance from Entrance (cm)	Time(sec)					Drift (kPa)
	80.37	236.45	431.78	537.38	603.74	
.318	2166(1)	2184(1)	2197(1)	2202(1)	2205(1)	0
1.91	1526(1)	1536(1)	1545(1)	1549(1)	1551(1)	6
3.18	1057(1)	1063(1)	1069(2)	1072(1)	1075(1)	0
4.45	766(1)	772(1)	778(1)	782(1)	785(1)	0
5.40	341(1)	341(1)	343(1)	345(1)	346(1)	0
5.72	-na-	-na-	-na-	-na-	-na-	-
6.03	203(1)	200(1)	201(1)	202(2)	204(2)	0
exit	184(8)	188(5)	186(6)	189(6)	182(14)	15
outlet	122(0)	122(0)	122(0)	123(0)	124(0)	

RUN # 19 SUMMARY

Test Section Dimensions
.1270 mm Opening
20.33 mm Width
2.5819e-06 m^2 Area
.2524 mm Hydraulic Diameter

Initial Test Section Temperatures
227.3 °C Maximum
224.4 °C Minimum

Stagnation State			
Calculated Value	Time(sec)		
	70.70	127.44	223.26
Pressure(kPa)	7088.	7100.	7095.
Error (kpa)	1.	1.	2.
Temperature (°C)	224.6	223.8	222.3
Error (°C)	.2	.1	.1
Subcooling (°C)	62.1	62.9	64.4

Corrected Mass Flux ($kg/m^2 \times sec$)			
Calculated Value	Time(sec)		
	70.70	127.44	223.26
Volume Method	3.818e+04	4.013e+04	4.143e+04
Error (%)	.0	.0	.0
Weigh Tank	3.392e+04	3.559e+04	3.872e+04
Error (%)	.0	.0	.0
% Difference	11.2	11.3	6.5

Pressure Profile Summary (in kPa)				
Distance from Entrance (cm)	Time(sec)			Drift (kPa)
	70.70	127.44	223.26	
.318	5328(2)	5305(5)	5227(2)	2
1.91	4584(2)	4582(2)	4535(3)	8
3.18	3850(2)	3834(3)	3795(5)	4
4.45	3178(3)	3152(3)	3142(7)	6
5.40	-na-	-na-	-na-	-
5.72	-na-	-na-	-na-	-
6.03	-na-	-na-	-na-	-
exit	1612(6)	1628(6)	1643(9)	-108
outlet	218(45)	249(0)	261(1)	

RUN # 20 SUMMARY

Test Section Dimensions		Initial Test Section Temperatures	
.1270	mm Opening	227.3	°C Maximum
20.33	mm Width	224.4	°C Minimum
2.5819e-06	m^2 Area		
.2524	mm Hydraulic Diameter		

Stagnation State

Calculated Value	Time(sec) 91.16	131.16	194.42	215.81
Pressure(kPa)	7098.	7100.	7095.	7098.
Error (kpa)	1.	1.	1.	1.
Temperature (°C)	224.5	223.8	223.1	222.6
Error (°C)	.2	.1	.1	.3
Subcooling (°C)	62.3	63.0	63.6	64.1

Corrected Mass Flux ($kg/m^2 x sec$)

Calculated Value	Time(sec) 91.16	131.16	194.42	215.81
Volume Method	3.912e+04	4.016e+04	4.154e+04	4.152e+04
Error (%)	.0	.0	.0	.0
Weigh Tank	3.533e+04	3.580e+04	3.872e+04	3.879e+04
Error (%)	.0	.0	.0	.0
% Difference	9.7	10.9	6.8	6.6

Pressure Profile Summary (in kPa)

Distance from Entrance (cm)	Time(sec) 91.16	131.16	194.42	215.81	Drift (kPa)
.318	5318(9)	5300(5)	5234(2)	5231(2)	2
1.91	4594(6)	4579(3)	4531(2)	4534(2)	8
3.18	3853(4)	3830(3)	3779(2)	3789(3)	4
4.45	3175(2)	3148(3)	3112(2)	3131(3)	6
5.40	-na-	-na-	-na-	-na-	-
5.72	-na-	-na-	-na-	-na-	-
6.03	-na-	-na-	-na-	-na-	-
exit	1628(8)	1644(8)	1651(7)	1645(5)	-96
outlet	243(2)	249(1)	258(2)	261(1)	

RUN # 21 SUMMARY

Test Section Dimensions		Initial Test Section Temperatures	
.1270	mm Opening	264.0	°C Maximum
20.33	mm Width	252.1	°C Minimum
2.5819e-06	m^2 Area		
.2524	mm Hydraulic Diameter		

Stagnation State

Calculated Value	Time(sec) 60.38	188.05	305.37	562.43	712.52
Pressure(kPa)	6945.	6951.	6958.	6967.	6969.
Error (kpa)	1.	2.	1.	1.	1.
Temperature (°C)	270.1	269.2	267.4	264.6	262.0
Error (°C)	.1	.2	.1	.1	.2
Subcooling (°C)	15.1	16.1	18.0	20.9	23.5

Corrected Mass Flux ($kg/m^2 x sec$)

Calculated Value	Time(sec) 60.38	188.05	305.37	562.43	712.52
Volume Method	9.746e+03	9.839e+03	9.864e+03	9.648e+03	9.594e+03
Error (%)	.0	.0	.0	.0	.0
Weigh Tank	9.010e+03	9.010e+03	9.010e+03	9.010e+03	9.010e+03
Error (%)	0.	0.	0.	0.	0.
% Difference	7.5	8.4	8.7	6.6	6.1

Pressure Profile Summary (in kPa)

Distance from Entrance (cm)	Time(sec) 60.38	188.05	305.37	562.43	712.52	Drift (kPa)
.318	2934(14)	2878(4)	2910(2)	3004(3)	3076(4)	-
1.91	2668(11)	2615(5)	2638(5)	2738(4)	2836(8)	-
3.18	2500(10)	2443(3)	2457(2)	2543(3)	2629(5)	-
4.45	2166(11)	2103(3)	2106(3)	2172(4)	2246(4)	-
5.40	1399(15)	1323(4)	1298(4)	1341(5)	1392(5)	-
5.72	-na-	-na-	-na-	-na-	-na-	-
6.03	2418(12)	2364(4)	2378(2)	2443(4)	2500(4)	-
exit	662(9)	650(25)	636(6)	634(12)	646(15)	-1
outlet	140(0)	138(0)	138(0)	138(0)	138(0)	

RUN # 22 SUMMARY

Test Section Dimensions
.1270 mm Opening
14.83 mm Width
1.8834e-06 m^2 Area
.2518 mm Hydraulic Diameter

Initial Test Section Temperatures
277.6 °C Maximum
274.3 °C Minimum

Stagnation State			
Calculated Value	Time(sec)		
	95.74	138.65	206.33
Pressure(kPa)	7050.	7043.	7032.
Error (kpa)	6.	2.	2.
Temperature (°C)	284.2	281.9	282.5
Error (°C)	.1	2.9	.1
Subcooling (°C)	2.1	4.3	3.6

Corrected Mass Flux ($kg/m^2 \times sec$)			
Calculated Value	Time(sec)		
	95.74	138.65	206.33
Volume Method	1.883e+04	1.911e+04	1.913e+04
Error (%)	.0	.0	.0
Weigh Tank	1.677e+04	1.677e+04	1.677e+04
Error (%)	0.	0.	0.
% Difference	11.0	12.3	12.3

Pressure Profile Summary (in kPa)				
Distance from Entrance (cm)	Time(sec)			Drift (kPa)
	95.74	138.65	206.33	
.318	3783(9)	3838(6)	3925(6)	4
1.91	3304(9)	3358(13)	3434(10)	4
3.18	2945(8)	2989(9)	3058(5)	1007
4.45	2479(7)	2508(7)	2553(4)	7
5.40	2212(7)	2229(20)	2248(7)	-135
5.72	-na-	-na-	-na-	-
6.03	1285(5)	1289(8)	1308(6)	0
exit	888(9)	891(6)	899(6)	-147
outlet	154(0)	154(0)	155(0)	

RUN # 23 SUMMARY

Test Section Dimensions
.2540 mm Opening
20.46 mm Width
5.1968e-06 m^2 Area
.5018 mm Hydraulic Diameter

Initial Test Section Temperatures
227.0 °C Maximum
223.3 °C Minimum

Stagnation State			
Calculated Value	Time(sec)		
	89.84	123.63	154.95
Pressure(kPa)	7108.	7119.	7118.
Error (kpa)	2.	1.	1.
Temperature (°C)	223.8	225.8	225.7
Error (°C)	.1	.2	.2
Subcooling (°C)	63.0	61.1	61.2

Corrected Mass Flux ($kg/m^2 \times sec$)			
Calculated Value	Time(sec)		
	89.84	123.63	154.95
Volume Method	4.287e+04	4.271e+04	4.197e+04
Error (%)	.0	.0	.0
Weigh Tank	3.772e+04	3.769e+04	4.188e+04
Error (%)	.0	.1	.1
% Difference	12.0	11.8	.2

Pressure Profile Summary (in kPa)				
Distance from Entrance (cm)	Time(sec)			Drift (kPa)
	89.84	123.63	154.95	
.318	3659(3)	3691(2)	3750(14)	4
1.91	3507(3)	3548(2)	3611(14)	8
3.18	3441(3)	3486(4)	3549(15)	4
4.45	3016(3)	3064(2)	3134(14)	6
5.40	2685(6)	2752(2)	2824(15)	0
5.72	-na-	-na-	-na-	-
6.03	2525(5)	2592(2)	2651(12)	0
exit	1933(7)	1981(8)	2027(12)	-87
outlet	286(198)	538(2)	539(2)	

RUN # 24 SUMMARY

Test Section Dimensions
.2540 mm Opening
20.45 mm Width
5.1943e-06 m^2 Area
.5018 mm Hydraulic Diameter

Initial Test Section Temperatures
257.3 °C Maximum
256.2 °C Minimum

Stagnation State

Calculated Value	Time(sec) 95.60	118.68	146.70
Pressure(kPa)	7049.	7055.	7046.
Error (kpa)	2.	2.	2.
Temperature (°C)	257.5	257.4	256.9
Error (°C)	.2	.2	.2
Subcooling (°C)	28.7	29.0	29.4

Corrected Mass Flux ($kg/m^2 x sec$)

Calculated Value	Time(sec) 95.60	118.68	146.70
Volume Method	3.609e+04	3.642e+04	3.612e+04
Error (%)	.0	.0	.0
Weigh Tank	3.029e+04	3.483e+04	3.421e+04
Error (%)	.0	.1	.1
% Difference	16.1	4.4	5.3

Pressure Profile Summary (in kPa)

Distance from Entrance (cm)	Time(sec) 95.60	118.68	146.70	Drift (kPa)
.318	6069(2)	6071(2)	6059(2)	1
1.91	5579(2)	5575(2)	5558(1)	0
3.18	5214(2)	5203(2)	5182(2)	0
4.45	4766(2)	4752(2)	4726(2)	0
5.40	4427(17)	4396(8)	4379(17)	97
5.72	-na-	-na-	-na-	-
6.03	4310(2)	4298(3)	4274(3)	0
exit	864(10)	879(12)	886(9)	-
outlet	440(7)	545(4)	551(4)	

RUN # 25 SUMMARY

Test Section Dimensions
.2540 mm Opening
20.35 mm Width
5.1689e-06 m^2 Area
.5017 mm Hydraulic Diameter

Initial Test Section Temperatures
269.4 °C Maximum
267.6 °C Minimum

Stagnation State

Calculated Value	Time(sec) 74.18	106.32	138.46
Pressure(kPa)	7050.	7055.	7057.
Error (kpa)	3.	2.	1.
Temperature (°C)	268.8	268.3	266.4
Error (°C)	.1	.1	.1
Subcooling (°C)	17.5	18.0	19.9

Corrected Mass Flux ($kg/m^2 x sec$)

Calculated Value	Time(sec) 74.18	106.32	138.46
Volume Method	3.097e+04	3.143e+04	3.070e+04
Error (%)	.0	.0	.0
Weigh Tank	2.771e+04	2.935e+04	2.831e+04
Error (%)	.1	.1	.1
% Difference	10.5	6.6	7.8

Pressure Profile Summary (in kPa)

Distance from Entrance (cm)	Time(sec) 74.18	106.32	138.46	Drift (kPa)
.318	6429(3)	6432(2)	6444(2)	0
1.91	6062(2)	6058(2)	6073(2)	0
3.18	5786(2)	5775(2)	5791(2)	0
4.45	5448(2)	5433(2)	5451(2)	0
5.40	5225(3)	5204(2)	5175(6)	-432
5.72	-na-	-na-	-na-	-
6.03	4720(3)	4701(2)	4632(2)	-14
exit	-na-	-na-	-na-	-na-
outlet	614(7)	615(6)	604(4)	

RUN # 26 SUMMARY

Test Section Dimensions		Initial Test Section Temperatures	
.2540	mm Opening	249.1	°C Maximum
20.35	mm Width	243.3	°C Minimum
5.1689e-06	m^2 Area		
.5017	mm Hydraulic Diameter		

Stagnation State

Calculated Value	Time(sec) 52.67	82.30	133.33	164.61
Pressure(kPa)	7003.	6999.	6985.	6979.
Error (kpa)	2.	1.	1.	2.
Temperature (°C)	282.7	282.7	281.8	280.5
Error (°C)	.1	.1	.3	.1
Subcooling (°C)	3.1	3.1	3.8	5.1

Corrected Mass Flux ($kg/m^2 x sec$)

Calculated Value	Time(sec) 52.67	82.30	133.33	164.61
Volume Method	2.007e+04	2.025e+04	2.033e+04	2.041e+04
Error (%)	.0	.0	.0	.0
Weigh Tank	1.916e+04	1.835e+04	2.028e+04	1.987e+04
Error (%)	.2	.1	.1	.1
% Difference	4.5	9.4	.2	2.6

Pressure Profile Summary (in kPa)

Distance from Entrance (cm)	Time(sec) 52.67	82.30	133.33	164.61	Drift (kPa)
.318	6703(2)	6704(1)	6686(2)	6670(2)	3
1.91	6456(2)	6455(3)	6437(3)	6417(3)	0
3.18	6096(2)	6090(4)	6089(3)	6098(2)	11
4.45	5458(3)	5446(5)	5459(4)	5499(5)	15
5.40	4650(9)	4623(2)	4645(6)	4701(14)	69
5.72	-na-	-na-	-na-	-na-	-
6.03	6548(2)	6549(1)	6531(2)	3907(8)	-82
exit	-na-	-na-	-na-	-na-	-na-
outlet	318(130)	404(5)	405(5)	409(5)	

RUN # 27 SUMMARY

Test Section Dimensions		Initial Test Section Temperatures	
.3810	mm Opening	257.8	°C Maximum
20.45	mm Width	254.8	°C Minimum
7.7915e-06	m^2 Area		
.7481	mm Hydraulic Diameter		

Stagnation State

Calculated Value	Time(sec) 36.26	52.75	67.58
Pressure(kPa)	7071.	7075.	7053.
Error (kpa)	3.	3.	53.
Temperature (°C)	257.2	257.0	256.6
Error (°C)	.2	.1	.4
Subcooling (°C)	29.3	29.6	29.7

Corrected Mass Flux ($kg/m^2 x sec$)

Calculated Value	Time(sec) 36.26	52.75	67.58
Volume Method	4.416e+04	4.381e+04	4.194e+04
Error (%)	.0	.0	.1
Weigh Tank	3.989e+04	4.239e+04	3.413e+04
Error (%)	.1	.1	.5
% Difference	9.7	3.2	18.6

Pressure Profile Summary (in kPa)

Distance from Entrance (cm)	Time(sec) 36.26	52.75	67.58	Drift (kPa)
.318	5669(5)	5668(4)	5720(19)	0
1.91	5294(7)	5293(5)	5363(13)	0
3.18	5013(7)	5011(6)	5097(13)	0
4.45	4683(9)	4680(7)	4782(20)	0
5.40	4495(7)	4486(4)	4581(17)	-7
5.72	-na-	-na-	-na-	-
6.03	4301(6)	4296(4)	4341(10)	0
exit	2834(7)	2832(6)	2902(11)	-105
outlet	995(375)	1155(4)	1146(7)	

RUN # 28 SUMMARY

Test Section Dimensions		Initial Test Section Temperatures	
.3810	mm Opening	267.2	°C Maximum
20.45	mm Width	265.3	°C Minimum
7.7915e-06	m^2 Area		
.7481	mm Hydraulic Diameter		

Stagnation State

Calculated Value	Time(sec)		
	36.26	52.75	67.58
Pressure(kPa)	7066.	7077.	7082.
Error (kpa)	4.	2.	1.
Temperature (°C)	271.2	271.0	270.9
Error (°C)	.2	.1	.2
Subcooling (°C)	15.2	15.6	15.7

Corrected Mass Flux ($kg/m^2 x sec$)

Calculated Value	Time(sec)		
	36.26	52.75	67.58
Volume Method	3.338e+04	3.399e+04	3.413e+04
Error (%)	.0	.0	.0
Weigh Tank	3.211e+04	3.393e+04	3.097e+04
Error (%)	.1	.1	.1
% Difference	3.8	.2	9.3

Pressure Profile Summary (in kPa)

Distance from Entrance (cm)	Time(sec)			Drift (kPa)
	36.26	52.75	67.58	
.318	6221(3)	6221(3)	6225(1)	0
1.91	5970(4)	5966(3)	5967(2)	-3
3.18	5804(4)	5797(2)	5799(1)	0
4.45	5581(4)	5570(3)	5571(2)	2
5.40	5379(3)	5370(4)	5367(5)	-7
5.72	-na-	-na-	-na-	-
6.03	4899(1)	4891(3)	4890(3)	5
exit	3262(6)	3261(9)	3260(7)	-107
outlet	795(431)	1076(5)	1074(8)	

RUN # 29 SUMMARY

Test Section Dimensions		Initial Test Section Temperatures	
.3810	mm Opening	275.2	°C Maximum
20.45	mm Width	268.6	°C Minimum
7.7915e-06	m^2 Area		
.7481	mm Hydraulic Diameter		

Stagnation State

Calculated Value	Time(sec)			
	67.58	87.36	108.89	125.27
Pressure(kPa)	7079.	7090.	7098.	7103.
Error (kpa)	4.	3.	2.	2.
Temperature (°C)	281.1	280.7	280.6	279.5
Error (°C)	.1	.2	.1	.2
Subcooling (°C)	5.5	5.9	6.2	7.2

Corrected Mass Flux ($kg/m^2 x sec$)

Calculated Value	Time(sec)			
	67.58	87.36	108.89	125.27
Volume Method	2.436e+04	2.511e+04	2.537e+04	2.575e+04
Error (%)	.0	.0	.0	.0
Weigh Tank	2.651e+04	2.696e+04	2.463e+04	2.541e+04
Error (%)	.1	.1	.1	.1
% Difference	-8.8	-7.4	2.9	1.3

Pressure Profile Summary (in kPa)

Distance from Entrance (cm)	Time(sec)				Drift (kPa)
	67.58	87.36	108.89	125.27	
.318	6617(3)	6614(3)	6614(2)	6606(3)	0
1.91	6441(3)	6445(2)	6448(3)	6430(4)	-3
3.18	6148(4)	6170(4)	6187(3)	6168(3)	0
4.45	5705(4)	5729(4)	5748(4)	5740(5)	0
5.40	5170(5)	5193(14)	5227(4)	5231(6)	-16
5.72	-na-	-na-	-na-	-na-	-
6.03	4496(6)	4520(3)	4552(5)	4572(14)	-6
exit	2711(10)	2740(7)	2757(8)	2783(7)	-87
outlet	681(286)	819(18)	826(19)	835(17)	

RUN # 30 SUMMARY

Test Section Dimensions	Initial Test Section Temperatures
.3810 mm Opening	224.2 °C Maximum
20.45 mm Width	222.8 °C Minimum
7.7915e-06 m^2 Area	
.7481 mm Hydraulic Diameter	

Stagnation State		
Calculated Value	Time(sec)	
	96.43	104.67
Pressure(kPa)	7092.	7101.
Error (kpa)	4.	3.
Temperature (°C)	224.0	224.0
Error (°C)	.1	.3
Subcooling (°C)	62.6	62.8

Corrected Mass Flux ($kg/m^2 x sec$)		
Calculated Value	Time(sec)	
	96.43	104.67
Volume Method	5.776e+04	5.790e+04
Error (%)	.0	.0
Weigh Tank	6.016e+04	5.367e+04
Error (%)	.1	.1
% Difference	-4.2	7.3

Pressure Profile Summary (in kPa)			
Distance from Entrance (cm)	Time(sec)		Drift (kPa)
	96.43	104.67	
.318	4785(3)	4789(5)	0
1.91	4154(5)	4156(6)	0
3.18	3691(14)	3683(5)	0
4.45	3152(6)	3150(5)	0
5.40	2796(5)	2794(5)	-8
5.72	-na-	-na-	-
6.03	2640(7)	2633(5)	7
exit	1850(14)	1851(8)	-77
outlet	1147(5)	1147(4)	

RUN # 31 SUMMARY

Test Section Dimensions	Initial Test Section Temperatures
.1048 mm Opening	19.8 °C Maximum
20.65 mm Width	19.3 °C Minimum
2.1641e-06 m^2 Area	
.2085 mm Hydraulic Diameter	

Stagnation State					
Calculated Value	Time(sec)				
	134.62	278.53	422.44	566.34	710.25
Pressure(kPa)	2642.	2677.	2707.	2734.	2759.
Error (kpa)	1.	1.	1.	1.	1.
Temperature (°C)	20.2	20.5	20.6	20.5	20.6
Error (°C)	.2	.2	.1	.1	.2
Subcooling (°C)	207.	207.	208.	208.	209.

Corrected Mass Flux ($kg/m^2 x sec$)					
Calculated Value	Time(sec)				
	134.62	278.53	422.44	566.34	710.25
Volume Method	1.492e+04	1.497e+04	1.497e+04	1.490e+04	1.498e+04
Error (%)	.0	.0	.0	.0	.0
Weigh Tank	1.493e+04	1.493e+04	1.493e+04	1.493e+04	1.493e+04
Error (%)	0.	0.	0.	0.	0.
% Difference	-.1	.3	.3	-.2	.4

Pressure Profile Summary (in kPa)						
Distance from Entrance (cm)	Time(sec)					Drift (kPa)
	134.62	278.53	422.44	566.34	710.25	
.318	2175(1)	2202(1)	2225(1)	2238(2)	2259(1)	-
1.91	1587(1)	1609(1)	1626(1)	1637(2)	1652(1)	-
3.18	1138(1)	1152(2)	1163(1)	1167(3)	1179(1)	-
4.45	465(5)	472(5)	477(4)	481(6)	483(6)	-2
5.40	334(1)	338(1)	338(1)	339(1)	340(1)	-
5.72	321(2)	325(1)	326(1)	325(1)	327(1)	-
6.03	253(2)	255(1)	254(1)	253(1)	253(2)	-
exit	211(2)	212(1)	211(1)	210(1)	210(1)	-
outlet	117(0)	117(0)	117(0)	117(0)	117(0)	

RUN # 32 SUMMARY

Test Section Dimensions
.1048 mm Opening
20.65 mm Width
2.1641e-06 m^2 Area
.2085 mm Hydraulic Diameter

Initial Test Section Temperatures
235.4 °C Maximum
225.3 °C Minimum

Stagnation State					
Calculated Value	Time(sec) 122.78	162.16	277.99	467.95	565.25
Pressure(kPa)	9676.	9668.	9641.	9596.	9573.
Error (kpa)	1.	2.	2.	1.	1.
Temperature (°C)	248.5	249.1	248.9	246.4	244.6
Error (°C)	.1	.2	.2	.2	.2
Subcooling (°C)	60.1	59.4	59.4	61.6	63.2

Corrected Mass Flux ($kg/m^2 x sec$)					
Calculated Value	Time(sec) 122.78	162.16	277.99	467.95	565.25
Volume Method	1.932e+04	1.941e+04	1.905e+04	1.809e+04	1.824e+04
Error (%)	.0	.0	.0	.0	.0
Weigh Tank	2.002e+04	1.914e+04	1.939e+04	1.818e+04	1.787e+04
Error (%)	.0	.0	.0	.0	.0
% Difference	-3.7	1.4	-1.8	-.5	2.0

Pressure Profile Summary (in kPa)						
Distance from Entrance (cm)	Time(sec) 122.78	162.16	277.99	467.95	565.25	Drift (kPa)
.318	8113(5)	8166(4)	8218(2)	8235(2)	8245(1)	-
1.91	7928(5)	7982(4)	8034(2)	8051(2)	8060(1)	-
3.18	5582(6)	5627(4)	5675(5)	5810(4)	5863(3)	-
4.45	4589(6)	4615(5)	4657(7)	4834(6)	4873(7)	3
5.40	3866(5)	3891(3)	3929(6)	3957(5)	3852(5)	-
5.72	3696(3)	3713(2)	3717(3)	3490(5)	3381(3)	-
6.03	3259(7)	3246(5)	3163(9)	2919(5)	2852(3)	-
exit	2154(8)	2126(4)	2084(6)	1992(4)	1949(2)	-
outlet	170(2)	171(1)	170(2)	165(2)	163(1)	

RUN # 33 SUMMARY

Test Section Dimensions
.1048 mm Opening
20.65 mm Width
2.1641e-06 m^2 Area
.2085 mm Hydraulic Diameter

Initial Test Section Temperatures
280.1 °C Maximum
212.0 °C Minimum

Stagnation State					
Calculated Value	Time(sec) 31.33	96.32	206.58	500.19	716.05
Pressure(kPa)	7076.	7110.	7146.	7213.	7242.
Error (kpa)	2.	2.	1.	3.	1.
Temperature (°C)	280.2	279.9	278.6	275.0	271.6
Error (°C)	.1	.1	.1	.1	.2
Subcooling (°C)	6.4	7.0	8.6	12.8	16.5

Corrected Mass Flux ($kg/m^2 x sec$)					
Calculated Value	Time(sec) 31.33	96.32	206.58	500.19	716.05
Volume Method	9.154e+03	9.431e+03	9.676e+03	9.956e+03	9.922e+03
Error (%)	.0	.0	.0	.0	.0
Weigh Tank	9.743e+03	9.743e+03	9.743e+03	9.743e+03	9.743e+03
Error (%)	0.	0.	0.	0.	0.
% Difference	-6.4	-3.3	-.7	2.1	1.8

Pressure Profile Summary (in kPa)						
Distance from Entrance (cm)	Time(sec) 31.33	96.32	206.58	500.19	716.05	Drift (kPa)
.318	6552(6)	6589(3)	6633(2)	6640(2)	6621(1)	-
1.91	6118(9)	6188(4)	6219(2)	6184(2)	6189(77)	-
3.18	5384(11)	5489(7)	5601(3)	5656(2)	5608(3)	-
4.45	3991(10)	4062(9)	4157(5)	4223(5)	4235(6)	-4
5.40	3052(12)	3085(11)	3141(3)	3185(1)	3200(2)	-
5.72	2536(17)	2541(9)	2581(2)	2609(2)	2622(2)	-
6.03	1985(33)	1983(29)	2008(2)	2025(2)	2037(1)	-
exit	1239(50)	1241(36)	1246(2)	1260(2)	1268(2)	-
outlet	136(0)	136(0)	136(0)	137(0)	137(0)	

RUN # 34 SUMMARY

Test Section Dimensions
.1048 mm Opening
20.65 mm Width
2.1641e-06 m^2 Area
.2085 mm Hydraulic Diameter

Initial Test Section Temperatures
271.5 °C Maximum
265.6 °C Minimum

Stagnation State					
Calculated Value	Time(sec)				
	110.25	161.32	257.64	480.46	742.75
Pressure(kPa)	7153.	7204.	7260.	7330.	7373.
Error (kpa)	6.	4.	3.	1.	1.
Temperature (°C)	270.3	269.8	268.6	265.8	261.1
Error (°C)	.1	.1	.2	.1	.2
Subcooling (°C)	16.9	18.0	19.7	23.1	28.2

Corrected Mass Flux ($kg/m^2 x sec$)					
Calculated Value	Time(sec)				
	110.25	161.32	257.64	480.46	742.75
Volume Method	1.080e+04	1.357e+04	1.169e+04	1.206e+04	1.220e+04
Error (%)	.0	.1	.0	.1	.0
Weigh Tank	1.071e+04	1.104e+04	1.168e+04	1.263e+04	1.211e+04
Error (%)	.0	.0	.0	.0	.0
% Difference	.8	18.6	.1	-4.7	.7

Pressure Profile Summary (in kPa)						
Distance from Entrance (cm)	Time(sec)					Drift (kPa)
	110.25	161.32	257.64	480.46	742.75	
.318	6600(9)	6619(4)	6650(2)	6687(2)	6704(2)	-
1.91	6011(8)	6033(5)	6047(3)	6044(2)	6034(2)	-
3.18	5545(5)	5550(3)	5538(3)	5494(2)	5457(3)	-
4.45	4855(11)	4881(8)	4923(5)	4895(5)	4761(4)	-5
5.40	3468(16)	3455(9)	3478(3)	3488(2)	3496(2)	-
5.72	2906(17)	2880(3)	2891(2)	2893(2)	2873(2)	-
6.03	2318(43)	2312(9)	2301(2)	2306(2)	2300(2)	-
exit	1446(64)	1466(24)	1437(2)	1449(2)	1457(2)	-
outlet	145(0)	143(0)	143(0)	144(0)	143(0)	

RUN # 35 SUMMARY

Test Section Dimensions
.2292 mm Opening
20.29 mm Width
4.6505e-06 m^2 Area
.4533 mm Hydraulic Diameter

Initial Test Section Temperatures
24.2 °C Maximum
23.7 °C Minimum

Stagnation State			
Calculated Value	Time(sec)		
	48.74	96.32	186.85
Pressure(kPa)	2492.	2506.	2526.
Error (kpa)	1.	1.	0.
Temperature (°C)	19.4	19.4	19.6
Error (°C)	.2	.2	.1
Subcooling (°C)	204.	205.	205.

Corrected Mass Flux ($kg/m^2 x sec$)			
Calculated Value	Time(sec)		
	48.74	96.32	186.85
Volume Method	2.610e+04	2.619e+04	2.622e+04
Error (%)	.0	.0	.0
Weigh Tank	2.517e+04	2.603e+04	2.609e+04
Error (%)	.0	.0	.0
% Difference	3.6	.6	.5

Pressure Profile Summary (in kPa)				
Distance from Entrance (cm)	Time(sec)			Drift (kPa)
	48.74	96.32	186.85	
.318	1907(1)	1916(1)	1927(1)	-
1.91	1513(1)	1521(1)	1533(1)	-
3.18	1051(2)	1058(1)	1069(1)	-
4.45	609(7)	610(8)	615(5)	-1
5.40	317(1)	317(1)	317(1)	-
5.72	250(1)	249(1)	249(2)	-
6.03	208(1)	206(1)	206(1)	-
exit	163(1)	162(1)	162(1)	-
outlet	118(0)	117(0)	117(0)	

RUN # 36 SUMMARY

Test Section Dimensions
.2292 mm Opening
20.29 mm Width
4.6505e-06 m^2 Area
.4533 mm Hydraulic Diameter

Initial Test Section Temperatures
247.8 °C Maximum
242.8 °C Minimum

Stagnation State

Calculated Value	Time(sec) 82.40	104.45	124.18
Pressure(kPa)	9557.	9542.	9525.
Error (kpa)	4.	5.	4.
Temperature (°C)	244.6	247.6	246.9
Error (°C)	8.6	1.2	.1
Subcooling (°C)	63.1	59.9	60.5

Corrected Mass Flux ($kg/m^2 \times sec$)

Calculated Value	Time(sec) 82.40	104.45	124.18
Volume Method	4.394e+04	4.412e+04	4.377e+04
Error (%)	.0	.0	.0
Weigh Tank	4.284e+04	4.369e+04	4.567e+04
Error (%)	.0	.0	.0
% Difference	2.5	1.0	-4.3

Pressure Profile Summary (in kPa)

Distance from Entrance (cm)	Time(sec) 82.40	104.45	124.18	Drift (kPa)
.318	7812(4)	7804(3)	7815(2)	0
1.91	6609(5)	6597(4)	6966(552)	33
3.18	5688(5)	5674(6)	5721(5)	18
4.45	4888(6)	4879(11)	4944(12)	57
5.40	4096(7)	4093(9)	4167(9)	0
5.72	3971(6)	3969(8)	4042(10)	0
6.03	3946(4)	3943(11)	3999(4)	0
exit	3311(7)	3317(14)	3360(3)	-6
outlet	638(4)	627(5)	616(4)	

RUN # 37 SUMMARY

Test Section Dimensions
.2292 mm Opening
20.29 mm Width
4.6505e-06 m^2 Area
.4533 mm Hydraulic Diameter

Initial Test Section Temperatures
279.5 °C Maximum
275.0 °C Minimum

Stagnation State

Calculated Value	Time(sec) 51.06	64.99	104.45	123.02
Pressure(kPa)	9618.	9625.	9603.	9593.
Error (kpa)	3.	2.	2.	2.
Temperature (°C)	280.9	280.9	280.2	279.1
Error (°C)	.1	.1	.1	.3
Subcooling (°C)	27.2	27.2	27.8	28.8

Corrected Mass Flux ($kg/m^2 \times sec$)

Calculated Value	Time(sec) 51.06	64.99	104.45	123.02
Volume Method	3.198e+04	3.215e+04	3.249e+04	3.232e+04
Error (%)	.0	.0	.0	.0
Weigh Tank	3.464e+04	3.288e+04	3.250e+04	3.240e+04
Error (%)	.0	.0	.0	.0
% Difference	-8.3	-2.3	-.0	-.2

Pressure Profile Summary (in kPa)

Distance from Entrance (cm)	Time(sec) 51.06	64.99	104.45	123.02	Drift (kPa)
.318	8551(4)	8557(2)	8530(2)	8532(3)	-2
1.91	7842(3)	7843(3)	7808(2)	7817(3)	0
3.18	7289(3)	7284(6)	7239(3)	7253(4)	2
4.45	6834(0)	6825(9)	6777(6)	6803(6)	70
5.40	6310(4)	6298(9)	6243(5)	6248(4)	0
5.72	6083(9)	6066(7)	6020(4)	5971(6)	0
6.03	5633(10)	5612(6)	5571(5)	5513(5)	0
exit	4494(10)	4478(6)	4451(3)	4406(7)	-41
outlet	675(5)	671(4)	663(3)	660(8)	

RUN # 38 SUMMARY

Test Section Dimensions		Initial Test Section Temperatures	
.2292	mm Opening	295.6	°C Maximum
20.29	mm Width	286.5	°C Minimum
4.6505e-06	m^2 Area		
.4533	mm Hydraulic Diameter		

Stagnation State

Calculated Value	Time(sec) 47.58	74.44	114.89	147.39
Pressure(kPa)	9679.	9678.	9667.	9663.
Error (kpa)	2.	6.	1.	1.
Temperature (°C)	287.0	286.7	286.3	284.5
Error (°C)	.2	.2	.2	.1
Subcooling (°C)	21.6	21.9	22.2	23.9

Corrected Mass Flux ($kg/m^2 x sec$)

Calculated Value	Time(sec) 47.58	74.44	114.89	147.39
Volume Method	2.699e+04	2.722e+04	2.748e+04	2.741e+04
Error (%)	.0	.0	.0	.0
Weigh Tank	2.733e+04	2.878e+04	2.744e+04	2.746e+04
Error (%)	.0	.0	.0	.0
% Difference	-1.3	-5.7	.2	-.2

Pressure Profile Summary (in kPa)

Distance from Entrance (cm)	Time(sec) 47.58	74.44	114.89	147.39	Drift (kPa)
.318	-na-	8799(5)	8789(2)	8783(2)	0
1.91	-na-	8325(5)	8312(2)	8308(2)	466
3.18	-na-	7931(5)	7914(2)	7908(3)	2
4.45	-na-	7709(9)	7692(9)	7677(7)	78
5.40	-na-	6822(10)	6775(20)	6632(11)	21
5.72	-na-	6397(9)	6348(20)	6201(14)	0
6.03	-na-	5725(21)	5686(15)	5548(18)	0
exit	-na-	4342(40)	4310(9)	4253(8)	-43
outlet	128(0)	1122(7)	1111(8)	1112(5)	

RUN # 39 SUMMARY

Test Section Dimensions		Initial Test Section Temperatures	
.2292	mm Opening	204.0	°C Maximum
20.29	mm Width	165.2	°C Minimum
4.6505e-06	m^2 Area		
.4533	mm Hydraulic Diameter		

Stagnation State

Calculated Value	Time(sec) 89.36	107.93	128.82
Pressure(kPa)	11599.	11603.	11599.
Error (kpa)	2.	2.	2.
Temperature (°C)	266.9	267.2	267.4
Error (°C)	.3	.1	.2
Subcooling (°C)	55.1	54.8	54.6

Corrected Mass Flux ($kg/m^2 x sec$)

Calculated Value	Time(sec) 89.36	107.93	128.82
Volume Method	4.396e+04	4.412e+04	4.388e+04
Error (%)	.0	.0	.0
Weigh Tank	4.556e+04	4.484e+04	4.390e+04
Error (%)	.0	.0	.0
% Difference	-3.6	-1.6	-.0

Pressure Profile Summary (in kPa)

Distance from Entrance (cm)	Time(sec) 89.36	107.93	128.82	Drift (kPa)
.318	9920(8)	9929(3)	9932(8)	0
1.91	9719(8)	9729(3)	9731(8)	66
3.18	6987(11)	7000(4)	7026(24)	16
4.45	6058(19)	6075(5)	6120(32)	112
5.40	5220(21)	5252(4)	5300(36)	0
5.72	5171(19)	5200(4)	5241(28)	0
6.03	5081(19)	5105(8)	5109(6)	0
exit	4158(18)	4186(7)	4199(10)	0
outlet	1115(6)	1107(3)	1091(7)	

RUN # 40 SUMMARY

Test Section Dimensions		Initial Test Section Temperatures	
.3600	mm Opening	25.7	°C Maximum
20.40	mm Width	25.2	°C Minimum
7.3440e-06	m^2 Area		
.7075	mm Hydraulic Diameter		

Stagnation State			
Calculated Value	Time(sec)		
	68.60	90.70	123.26
Pressure(kPa)	2479.	2472.	2462.
Error (kpa)	1.	2.	1.
Temperature (°C)	22.7	22.9	23.3
Error (°C)	.2	.2	.4
Subcooling (°C)	201.	200.	200.

Corrected Mass Flux ($kg/m^2 x sec$)			
Calculated Value	Time(sec)		
	68.60	90.70	123.26
Volume Method	3.494e+04	3.484e+04	3.456e+04
Error (%)	.0	.0	.0
Weigh Tank	3.394e+04	3.489e+04	3.337e+04
Error (%)	.0	.0	.0
% Difference	2.9	-.1	3.4

Pressure Profile Summary (in kPa)				
Distance from Entrance (cm)	Time(sec)			Drift (kPa)
	68.60	90.70	123.26	
.318	1677(1)	1673(1)	1666(2)	-
1.91	1252(1)	1248(1)	1243(2)	-
3.18	868(1)	865(1)	861(2)	-
4.45	518(5)	515(4)	516(7)	0
5.40	253(1)	253(1)	251(1)	-
5.72	209(1)	207(1)	207(1)	-
6.03	177(1)	176(1)	176(1)	-
e it	91(1)	91(1)	92(1)	-
outlet	127(0)	127(0)	127(0)	

RUN # 41 SUMMARY

Test Section Dimensions		Initial Test Section Temperatures	
.3600	mm Opening	247.5	°C Maximum
20.40	mm Width	243.3	°C Minimum
7.3440e-06	m^2 Area		
.7075	mm Hydraulic Diameter		

Stagnation State		
Calculated Value	Time(sec)	
	75.44	87.04
Pressure(kPa)	9585.	9595.
Error (kpa)	6.	2.
Temperature (°C)	246.4	247.7
Error (°C)	4.2	3.3
Subcooling (°C)	61.4	60.3

Corrected Mass Flux ($kg/m^2 x sec$)		
Calculated Value	Time(sec)	
	75.44	87.04
Volume Method	5.756e+04	5.791e+04
Error (%)	.0	.0
Weigh Tank	5.240e+04	5.443e+04
Error (%)	.1	.0
% Difference	9.0	6.0

Pressure Profile Summary (in kPa)			
Distance from Entrance (cm)	Time(sec)		Drift (kPa)
	75.44	87.04	
.318	7100(3)	7117(16)	0
1.91	6142(4)	6159(20)	0
3.18	5412(6)	5431(27)	3
4.45	4791(6)	4816(37)	96
5.40	4171(7)	4195(34)	0
5.72	4077(8)	4100(32)	0
6.03	4135(9)	4161(30)	0
exit	3491(6)	3512(22)	-6
outlet	558(541)	1041(421)	

RUN # 42 SUMMARY

Test Section Dimensions		Initial Test Section Temperatures	
.3600	mm Opening	267.6	°C Maximum
20.40	mm Width	257.6	°C Minimum
7.3440e-06	m^2 Area		
.7075	mm Hydraulic Diameter		

Stagnation State		
Calculated Value	Time(sec)	
	104.25	115.83
Pressure(kPa)	11574.	11592.
Error (kpa)	7.	5.
Temperature (°C)	264.5	267.4
Error (°C)	1.6	1.9
Subcooling (°C)	57.4	54.6

Corrected Mass Flux ($kg/m^2 x sec$)		
Calculated Value	Time(sec)	
	104.25	115.83
Volume Method	5.772e+04	5.805e+04
Error (%)	.0	.0
Weigh Tank	5.502e+04	4.991e+04
Error (%)	.1	.0
% Difference	4.7	14.0

Pressure Profile Summary (in kPa)			
Distance from Entrance (cm)	Time(sec)		Drift (kPa)
	104.25	115.83	
.318	8798(5)	8841(28)	1
1.91	7713(4)	7760(32)	14
3.18	6890(5)	6942(42)	8
4.45	6212(9)	6286(56)	88
5.40	5443(7)	5510(53)	7
5.72	5335(7)	5394(50)	0
6.03	5385(6)	5451(40)	0
exit	4478(8)	4536(51)	-4
outlet	960(448)	1220(1)	

RUN # 43 SUMMARY

Test Section Dimensions		Initial Test Section Temperatures	
.3600	mm Opening	280.1	°C Maximum
20.40	mm Width	276.6	°C Minimum
7.3440e-06	m^2 Area		
.7075	mm Hydraulic Diameter		

Stagnation State		
Calculated Value	Time(sec)	
	67.31	82.40
Pressure(kPa)	9582.	9585.
Error (kpa)	4.	4.
Temperature (°C)	278.2	278.0
Error (°C)	.1	.2
Subcooling (°C)	29.6	29.8

Corrected Mass Flux ($kg/m^2 x sec$)		
Calculated Value	Time(sec)	
	67.31	82.40
Volume Method	4.369e+04	4.433e+04
Error (%)	.0	.0
Weigh Tank	3.776e+04	3.956e+04
Error (%)	.1	.0
% Difference	13.6	10.8

Pressure Profile Summary (in kPa)			
Distance from Entrance (cm)	Time(sec)		Drift (kPa)
	67.31	82.40	
.318	8020(2)	8018(5)	0
1.91	7398(3)	7394(6)	0
3.18	6960(5)	6952(6)	0
4.45	6666(9)	6663(9)	132
5.40	6169(7)	6160(8)	0
5.72	6062(7)	6056(7)	0
6.03	5820(3)	5817(5)	0
exit	4822(5)	4823(6)	-23
outlet	1248(2)	1246(1)	

RUN # 44 SUMMARY

Test Section Dimensions
.3600 mm Opening
20.40 mm Width
7.3440e-06 m^2 Area
.7075 mm Hydraulic Diameter

Initial Test Section Temperatures
293.6 °C Maximum
290.3 °C Minimum

Stagnation State

Calculated Value	Time(sec) 74.13	88.03	108.88
Pressure(kPa)	9629.	9633.	9623.
Error (kpa)	3.	3.	3.
Temperature (°C)	294.3	294.1	293.4
Error (°C)	.1	.3	.8
Subcooling (°C)	13.9	14.2	14.8

Corrected Mass Flux ($kg/m^2 x sec$)

Calculated Value	Time(sec) 74.13	88.03	108.88
Volume Method	3.265e+04	3.289e+04	3.313e+04
Error (%)	.0	.0	.0
Weigh Tank	3.276e+04	3.176e+04	3.055e+04
Error (%)	.1	.1	.0
% Difference	-.3	3.4	7.8

Pressure Profile Summary (in kPa)

Distance from Entrance (cm)	Time(sec) 74.13	88.03	108.88	Drift (kPa)
.318	8710(2)	8709(3)	8703(5)	0
1.91	8309(2)	8307(3)	8302(5)	0
3.18	8041(2)	8035(3)	8032(6)	1
4.45	7967(4)	7961(7)	7955(8)	76
5.40	7187(3)	7182(5)	7147(16)	23
5.72	6916(3)	6909(4)	6871(16)	0
6.03	6502(8)	6488(5)	6447(15)	1
exit	5303(4)	5303(5)	5273(10)	-26
outlet	1231(1)	1231(1)	1232(1)	

RUN # 45 SUMMARY

Test Section Dimensions
.3600 mm Opening
20.40 mm Width
7.3440e-06 m^2 Area
.7075 mm Hydraulic Diameter

Initial Test Section Temperatures
292.0 °C Maximum
289.5 °C Minimum

Stagnation State

Calculated Value	Time(sec) 128.57	140.15
Pressure(kPa)	11604.	11609.
Error (kpa)	4.	3.
Temperature (°C)	292.4	293.5
Error (°C)	2.3	.3
Subcooling (°C)	29.7	28.6

Corrected Mass Flux ($kg/m^2 x sec$)

Calculated Value	Time(sec) 128.57	140.15
Volume Method	4.446e+04	4.441e+04
Error (%)	.0	.0
Weigh Tank	4.113e+04	4.475e+04
Error (%)	.0	.0
% Difference	7.5	-.8

Pressure Profile Summary (in kPa)

Distance from Entrance (cm)	Time(sec) 128.57	140.15	Drift (kPa)
.318	9859(3)	9874(17)	0
1.91	9114(4)	9133(22)	0
3.18	8636(6)	8653(24)	2
4.45	8322(6)	8349(42)	88
5.40	7668(8)	7689(25)	0
5.72	7550(10)	7555(8)	0
6.03	7187(5)	7182(10)	0
exit	5995(4)	5997(10)	-25
outlet	644(541)	1211(2)	

RUN # 46 SUMMARY

Test Section Dimensions		Initial Test Section Temperatures	
.1270	mm Opening	26.4	°C Maximum
20.42	mm Width	23.1	°C Minimum
2.5933e-06	m^2 Area		
.2524	mm Hydraulic Diameter		

Stagnation State

Calculated Value	Time(sec) 95.16	188.01	304.06	447.97	594.20
Pressure(kPa)	2604.	2626.	2648.	2673.	2698.
Error (kpa)	1.	2.	1.	0.	1.
Temperature (°C)	26.9	28.2	29.2	29.7	29.7
Error (°C)	.3	.2	.2	.2	.1
Subcooling (°C)	199.	198.	198.	198.	198.

Corrected Mass Flux ($kg/m^2 x sec$)

Calculated Value	Time(sec) 95.16	188.01	304.06	447.97	594.20
Volume Method	7.951e+03	8.172e+03	8.264e+03	8.380e+03	8.411e+03
Error (%)	.0	.0	.0	.0	.0
Weigh Tank	7.676e+03	7.704e+03	7.753e+03	7.814e+03	7.859e+03
Error (%)	.0	.0	.0	.0	.0
% Difference	3.5	5.7	6.2	6.8	6.6

Pressure Profile Summary (in kPa)

Distance from Entrance (cm)	Time(sec) 95.16	188.01	304.06	447.97	594.20	Drift (kPa)
.318	2351(1)	2371(1)	2388(1)	2407(2)	2430(1)	-
1.91	1783(1)	1800(1)	1813(2)	1828(2)	1845(1)	-
3.18	1265(1)	1277(1)	1283(2)	1295(1)	1305(1)	-
4.45	609(4)	612(5)	612(4)	616(4)	620(4)	-2
5.40	349(2)	350(1)	349(2)	350(1)	353(2)	-
5.72	258(1)	259(1)	257(1)	258(2)	260(1)	-
6.03	217(1)	216(1)	214(1)	215(1)	216(2)	-
exit	197(1)	197(1)	194(1)	194(1)	195(2)	-
outlet	122(0)	122(0)	122(0)	122(0)	123(0)	

RUN # 47 SUMMARY

Test Section Dimensions		Initial Test Section Temperatures	
.0797	mm Opening	270.8	°C Maximum
20.42	mm Width	253.2	°C Minimum
1.6271e-06	m^2 Area		
.1587	mm Hydraulic Diameter		

Stagnation State

Calculated Value	Time(sec) 164.80	206.58	263.44	350.48	504.84
Pressure(kPa)	11632.	11614.	11585.	11544.	11478.
Error (kpa)	2.	2.	2.	1.	1.
Temperature (°C)	263.3	265.1	265.2	264.4	261.7
Error (°C)	.8	.1	.1	.1	.2
Subcooling (°C)	59.0	57.1	56.8	57.3	59.6

Corrected Mass Flux ($kg/m^2 x sec$)

Calculated Value	Time(sec) 164.80	206.58	263.44	350.48	504.84
Volume Method	2.897e+04	2.903e+04	2.881e+04	2.839e+04	2.772e+04
Error (%)	.0	.0	.0	.0	.0
Weigh Tank	2.229e+04	2.908e+04	2.984e+04	2.882e+04	2.736e+04
Error (%)	.1	.0	.0	.0	.0
% Difference	23.1	-.2	-3.6	-1.5	1.3

Pressure Profile Summary (in kPa)

Distance from Entrance (cm)	Time(sec) 164.80	206.58	263.44	350.48	504.84	Drift (kPa)
.318	10947(9)	10969(2)	10966(2)	10943(1)	10913(1)	-
1.91	10748(9)	10770(2)	10767(2)	10744(1)	10714(1)	-
3.18	10666(9)	10688(2)	8045(2)	8079(1)	8206(2)	-
4.45	6268(18)	6309(5)	6340(7)	6397(6)	6621(5)	4
5.40	4981(30)	5050(3)	5076(3)	5167(2)	5196(2)	-
5.72	4663(27)	4718(2)	4738(4)	4731(2)	4388(4)	-
6.03	4188(9)	4147(5)	4101(5)	3901(7)	3579(2)	-
exit	2275(20)	2188(7)	2163(6)	2128(3)	2110(2)	-
outlet	151(30)	189(2)	187(2)	184(2)	180(2)	

RUN # 48 SUMMARY

Test Section Dimensions
.0797 mm Opening
20.42 mm Width
1.6271e-06 m^2 Area
.1587 mm Hydraulic Diameter

Initial Test Section Temperatures
284.6 °C Maximum
272.9 °C Minimum

Stagnation State

Calculated Value	Time(sec) 112.36	188.80	277.99	506.18	691.51
Pressure(kPa)	9655.	9645.	9633.	9609.	9593.
Error (kpa)	2.	2.	1.	1.	1.
Temperature (°C)	278.1	277.8	277.6	275.2	272.0
Error (°C)	.1	.1	.1	.1	.1
Subcooling (°C)	30.3	30.5	30.7	32.8	35.9

Corrected Mass Flux ($kg/m^2 x sec$)

Calculated Value	Time(sec) 112.36	188.80	277.99	506.18	691.51
Volume Method	1.882e+04	1.899e+04	1.860e+04	1.784e+04	1.756e+04
Error (%)	.0	.0	.0	.0	.0
Weigh Tank	1.594e+04	1.888e+04	1.868e+04	1.762e+04	1.738e+04
Error (%)	.0	.0	.0	.0	.0
% Difference	15.3	.6	-.4	1.2	1.0

Pressure Profile Summary (in kPa)

Distance from Entrance (cm)	Time(sec) 112.36	188.80	277.99	506.18	691.51	Drift (kPa)
.318	8924(8)	8954(3)	8960(2)	8952(2)	8938(2)	-
1.91	8059(4)	8093(2)	8105(2)	8117(1)	8110(2)	-
3.18	7266(5)	7287(3)	7298(1)	7324(2)	7321(1)	-
4.45	6345(9)	6330(7)	6333(5)	6349(6)	6264(7)	2
5.40	4703(29)	4634(3)	4601(2)	4467(1)	4427(2)	-
5.72	3635(19)	3562(2)	3538(2)	3468(1)	3418(3)	-
6.03	2892(50)	2827(2)	2799(1)	2734(1)	2696(1)	-
exit	1720(55)	1721(1)	1713(1)	1682(1)	1662(1)	-
outlet	145(25)	171(1)	169(1)	164(1)	162(1)	

RUN # 49 SUMMARY

Test Section Dimensions
.0797 mm Opening
20.42 mm Width
1.6271e-06 m^2 Area
.1587 mm Hydraulic Diameter

Initial Test Section Temperatures
294.1 °C Maximum
285.8 °C Minimum

Stagnation State

Calculated Value	Time(sec) 108.50	162.75	249.55	529.48	755.15
Pressure(kPa)	9671.	9661.	9642.	9590.	9556.
Error (kpa)	2.	2.	2.	2.	1.
Temperature (°C)	294.2	293.8	292.9	289.0	285.4
Error (°C)	.1	.1	.1	.1	.2
Subcooling (°C)	14.4	14.6	15.4	18.9	22.3

Corrected Mass Flux ($kg/m^2 x sec$)

Calculated Value	Time(sec) 108.50	162.75	249.55	529.48	755.15
Volume Method	1.539e+04	1.538e+04	1.522e+04	1.487e+04	1.471e+04
Error (%)	.1	.0	.0	.0	.0
Weigh Tank	1.440e+04	1.542e+04	1.498e+04	1.456e+04	1.464e+04
Error (%)	.0	.0	.0	.0	.0
% Difference	6.4	-.3	1.6	2.1	.5

Pressure Profile Summary (in kPa)

Distance from Entrance (cm)	Time(sec) 108.50	162.75	249.55	529.48	755.15	Drift (kPa)
.318	9377(2)	9372(17)	9339(2)	9303(1)	9270(2)	-
1.91	8645(2)	8657(10)	8635(1)	8576(1)	8530(2)	-
3.18	7993(2)	7993(15)	7964(3)	7873(1)	7808(3)	-
4.45	6707(9)	6699(4)	6689(8)	6623(7)	6542(5)	3
5.40	4586(27)	4515(15)	4483(2)	4408(3)	4361(2)	-
5.72	3591(14)	3516(7)	3463(2)	3389(2)	3351(1)	-
6.03	2828(28)	2742(29)	2692(2)	2634(2)	2609(1)	-
exit	1643(29)	1601(36)	1584(2)	1561(2)	1554(1)	-
outlet	152(1)	149(1)	147(1)	145(1)	144(1)	

RUN # 50 SUMMARY

Test Section Dimensions		Initial Test Section Temperatures	
.0797	mm Opening	232.3	°C Maximum
20.42	mm Width	222.8	°C Minimum
1.6271e-06	m^2 Area		
.1587	mm Hydraulic Diameter		

Stagnation State

Calculated Value	Time(sec) 115.22	166.30	289.13	542.39	635.67
Pressure(kPa)	7205.	7252.	7322.	7396.	7410.
Error (kpa)	4.	3.	3.	1.	1.
Temperature (°C)	224.2	224.0	223.4	221.1	219.9
Error (°C)	.1	.1	.1	.1	.1
Subcooling (°C)	63.5	64.2	65.5	68.4	69.8

Corrected Mass Flux ($kg/m^2 x sec$)

Calculated Value	Time(sec) 115.22	166.30	289.13	542.39	635.67
Volume Method	1.927e+04	1.919e+04	1.892e+04	1.823e+04	1.801e+04
Error (%)	.0	.0	.0	.0	.0
Weigh Tank	2.015e+04	1.939e+04	1.789e+04	1.904e+04	1.907e+04
Error (%)	.1	.0	.0	.1	.1
% Difference	-4.6	-1.0	5.4	-4.4	-5.9

Pressure Profile Summary (in kPa)

Distance from Entrance (cm)	Time(sec) 115.22	166.30	289.13	542.39	635.67	Drift (kPa)
.318	6289(11)	6347(3)	6417(2)	6519(1)	6547(1)	-
1.91	5416(6)	5475(3)	5531(2)	5642(2)	5676(1)	-
3.18	4472(14)	4518(4)	4558(2)	4678(2)	4715(2)	-
4.45	3331(4)	3345(7)	3353(6)	3470(5)	3514(7)	-5
5.40	2591(14)	2584(9)	2590(1)	2723(3)	2752(2)	-
5.72	2393(2)	2396(5)	2399(1)	2502(2)	2482(2)	-
6.03	2276(3)	2281(8)	2273(1)	2250(2)	2198(2)	-
exit	1567(12)	1505(8)	1570(3)	1421(3)	1398(2)	-
outlet	140(2)	139(1)	138(1)	137(1)	136(1)	

RUN # 51 SUMMARY

Test Section Dimensions		Initial Test Section Temperatures	
.2112	mm Opening	227.5	°C Maximum
20.50	mm Width	222.9	°C Minimum
4.3296e-06	m^2 Area		
.4181	mm Hydraulic Diameter		

Stagnation State

Calculated Value	Time(sec) 90.05	103.07	129.11
Pressure(kPa)	7041.	7048.	7055.
Error (kpa)	1.	2.	1.
Temperature (°C)	226.1	226.1	225.6
Error (°C)	.1	.1	.1
Subcooling (°C)	60.0	60.2	60.7

Corrected Mass Flux ($kg/m^2 x sec$)

Calculated Value	Time(sec) 90.05	103.07	129.11
Volume Method	4.053e+04	4.080e+04	4.099e+04
Error (%)	.0	.0	.0
Weigh Tank	4.080e+04	4.090e+04	3.988e+04
Error (%)	.0	.0	.0
% Difference	-.7	-.3	2.7

Pressure Profile Summary (in kPa)

Distance from Entrance (cm)	Time(sec) 90.05	103.07	129.11	Drift (kPa)
.318	5809(1)	5814(2)	5816(1)	0
1.91	4903(2)	4902(1)	4898(1)	18
3.18	4135(2)	4131(1)	4123(2)	0
4.45	3366(4)	3364(8)	3350(9)	-1634
5.40	2800(2)	2795(2)	2781(2)	0
5.72	2677(3)	2670(3)	2657(2)	0
6.03	2715(3)	2711(2)	2695(2)	0
exit	2215(3)	2214(2)	2208(2)	-13
outlet	857(9)	847(7)	831(6)	

RUN # 52 SUMMARY

Test Section Dimensions		Initial Test Section Temperatures	
.2112	mm Opening	262.8	°C Maximum
20.50	mm Width	255.7	°C Minimum
4.3296e-06	m^2 Area		
.4181	mm Hydraulic Diameter		

Stagnation State			
Calculated Value	Time(sec)		
	113.04	127.17	150.00
Pressure(kPa)	11708.	11726.	11737.
Error (kpa)	5.	4.	4.
Temperature (°C)	263.3	263.1	262.6
Error (°C)	.1	.1	.1
Subcooling (°C)	59.5	59.8	60.3

Corrected Mass Flux ($kg/m^2 x sec$)			
Calculated Value	Time(sec)		
	113.04	127.17	150.00
Volume Method	4.849e+04	4.914e+04	4.936e+04
Error (%)	.0	.0	.0
Weigh Tank	5.153e+04	5.091e+04	4.940e+04
Error (%)	.1	.1	.0
% Difference	-6.3	-3.6	-.1

Pressure Profile Summary (in kPa)				
Distance from Entrance (cm)	Time(sec)			Drift (kPa)
	113.04	127.17	150.00	
.318	9693(5)	9702(3)	9708(5)	0
1.91	9514(5)	9523(3)	9529(5)	0
3.18	7178(6)	7164(7)	7151(5)	3
4.45	6128(5)	6107(9)	6094(8)	-2850
5.40	5140(8)	5121(8)	5104(8)	28
5.72	4972(6)	4953(8)	4937(8)	0
6.03	5005(6)	4983(8)	4974(6)	0
exit	4042(15)	4001(17)	4011(22)	-8
outlet	1196(5)	1195(4)	1189(5)	

RUN # 53 SUMMARY

Test Section Dimensions		Initial Test Section Temperatures	
.2112	mm Opening	30.3	°C Maximum
20.50	mm Width	29.7	°C Minimum
4.3296e-06	m^2 Area		
.4181	mm Hydraulic Diameter		

Stagnation State			
Calculated Value	Time(sec)		
	158.41	217.00	296.20
Pressure(kPa)	2505.	2493.	2477.
Error (kpa)	1.	1.	1.
Temperature (°C)	28.8	29.4	29.3
Error (°C)	.2	.2	.1
Subcooling (°C)	195.	194.	194.

Corrected Mass Flux ($kg/m^2 x sec$)			
Calculated Value	Time(sec)		
	158.41	217.00	296.20
Volume Method	2.620e+04	2.604e+04	2.579e+04
Error (%)	.0	.0	.0
Weigh Tank	2.447e+04	2.552e+04	2.523e+04
Error (%)	.0	.0	.0
% Difference	6.6	2.0	2.2

Pressure Profile Summary (in kPa)				
Distance from Entrance (cm)	Time(sec)			Drift (kPa)
	158.41	217.00	296.20	
.318	2003(2)	1994(1)	1982(1)	-
1.91	1624(2)	1613(1)	1603(1)	-
3.18	1162(2)	1152(1)	1147(1)	-
4.45	535(6)	531(6)	527(5)	0
5.40	340(2)	335(1)	333(1)	-
5.72	265(1)	261(1)	259(1)	-
6.03	223(2)	220(1)	218(1)	-
exit	156(2)	155(1)	153(1)	-
outlet	116(0)	114(0)	114(0)	

RUN # 54 SUMMARY

Test Section Dimensions		Initial Test Section Temperatures	
.2112	mm Opening	295.0	°C Maximum
20.50	mm Width	286.0	°C Minimum
4.3296e-06	m^2 Area		
.4181	mm Hydraulic Diameter		

Stagnation State				
Calculated Value	Time(sec)			
	110.67	125.86	144.30	182.28
Pressure(kPa)	11692.	11697.	11690.	11671.
Error (kpa)	3.	2.	2.	3.
Temperature (°C)	292.9	292.8	292.4	290.0
Error (°C)	.1	.1	.3	.2
Subcooling (°C)	29.8	29.9	30.2	32.5

Corrected Mass Flux ($kg/m^2 x sec$)				
Calculated Value	Time(sec)			
	110.67	125.86	144.30	182.28
Volume Method	3.809e+04	3.844e+04	3.849e+04	3.775e+04
Error (%)	.0	.0	.0	.0
Weigh Tank	3.742e+04	3.907e+04	3.822e+04	3.642e+04
Error (%)	.0	.0	.0	.0
% Difference	1.8	-1.6	.7	3.5

Pressure Profile Summary (in kPa)					
Distance from Entrance (cm)	Time(sec)				Drift (kPa)
	110.67	125.86	144.30	182.28	
.318	10476(5)	10483(2)	10485(3)	10513(2)	0
1.91	9508(5)	9507(2)	9510(5)	9567(6)	0
3.18	8858(4)	8852(3)	8857(8)	8941(7)	0
4.45	8126(7)	8118(8)	8120(8)	8236(12)	-
5.40	7522(4)	7513(4)	7518(7)	7468(17)	22
5.72	7290(3)	7277(3)	7248(10)	7041(26)	0
6.03	6710(6)	6693(3)	6665(11)	6468(25)	0
exit	5055(10)	5061(8)	5050(9)	4863(19)	-25
outlet	1047(389)	1223(4)	1212(7)	1199(7)	

RUN # 55 SUMMARY

Test Section Dimensions		Initial Test Section Temperatures	
.2112	mm Opening	306.5	°C Maximum
20.50	mm Width	297.6	°C Minimum
4.3296e-06	m^2 Area		
.4181	mm Hydraulic Diameter		

Stagnation State				
Calculated Value	Time(sec)			
	74.86	88.97	135.62	181.19
Pressure(kPa)	9636.	9631.	9605.	9578.
Error (kpa)	4.	4.	2.	3.
Temperature (°C)	304.5	304.6	304.3	303.2
Error (°C)	.1	.1	.1	.3
Subcooling (°C)	3.8	3.6	3.7	4.6

Corrected Mass Flux ($kg/m^2 x sec$)				
Calculated Value	Time(sec)			
	74.86	88.97	135.62	181.19
Volume Method	2.205e+04	2.206e+04	2.200e+04	2.212e+04
Error (%)	.0	.0	.0	.0
Weigh Tank	2.195e+04	2.256e+04	2.101e+04	2.231e+04
Error (%)	.0	.0	.0	.0
% Difference	.4	-2.3	4.5	-.9

Pressure Profile Summary (in kPa)					
Distance from Entrance (cm)	Time(sec)				Drift (kPa)
	74.86	88.97	135.62	181.19	
.318	-na-	9164(3)	9147(2)	9119(4)	12
1.91	-na-	8626(3)	8616(2)	8601(3)	29
3.18	-na-	8010(6)	7999(4)	7995(4)	15
4.45	-na-	8227(11)	8228(4)	8245(7)	1320
5.40	-na-	5453(20)	5441(10)	5456(8)	71
5.72	-na-	4843(18)	4829(1)	4836(6)	50
6.03	-na-	4273(7)	4249(2)	4249(5)	52
exit	-na-	3102(5)	3090(2)	3095(4)	-54
outlet	-na-	593(18)	573(12)	564(11)	

RUN # 56 SUMMARY

Test Section Dimensions		Initial Test Section Temperatures	
.3810	mm Opening	24.5	°C Maximum
19.23	mm Width	23.9	°C Minimum

7.3266e-06 m^2 Area
.7472 mm Hydraulic Diameter

Stagnation State		
Calculated Value	Time(sec)	
	66.30	100.00
Pressure(kPa)	2477.	2465.
Error (kpa)	1.	1.
Temperature (°C)	23.6	23.5
Error (°C)	.2	.2
Subcooling (°C)	200.	200.

Corrected Mass Flux ($kg/m^2 x sec$)		
Calculated Value	Time(sec)	
	66.30	100.00
Volume Method	3.597e+04	3.581e+04
Error (%)	.0	.0
Weigh Tank	3.493e+04	3.401e+04
Error (%)	.0	.0
% Difference	2.9	5.0

Pressure Profile Summary (in kPa)			
Distance from Entrance (cm)	Time(sec)		Drift (kPa)
	66.30	100.00	
.318	1642(2)	1633(1)	0
1.91	1193(2)	1185(1)	0
3.18	827(2)	820(1)	0
4.45	384(5)	380(4)	-76
5.40	241(5)	225(1)	0
5.72	644(50)	441(7)	82
6.03	208(6)	197(1)	-4
exit	221(1)	221(1)	-
outlet	124(0)	124(0)	

RUN # 57 SUMMARY

Test Section Dimensions		Initial Test Section Temperatures	
.3810	mm Opening	223.3	°C Maximum
19.23	mm Width	220.2	°C Minimum

7.3266e-06 m^2 Area
.7472 mm Hydraulic Diameter

Stagnation State			
Calculated Value	Time(sec)		
	67.27	88.97	104.16
Pressure(kPa)	4221.	4216.	4210.
Error (kpa)	2.	2.	3.
Temperature (°C)	225.7	225.8	225.4
Error (°C)	.1	.1	.1
Subcooling (°C)	27.9	27.7	27.9

Corrected Mass Flux ($kg/m^2 x sec$)			
Calculated Value	Time(sec)		
	67.27	88.97	104.16
Volume Method	3.280e+04	3.250e+04	3.242e+04
Error (%)	.0	.0	.0
Weigh Tank	3.380e+04	3.148e+04	3.104e+04
Error (%)	.0	.0	.0
% Difference	-3.0	3.1	4.3

Pressure Profile Summary (in kPa)				
Distance from Entrance (cm)	Time(sec)			Drift (kPa)
	67.27	88.97	104.16	
.318	3471(2)	3471(1)	3467(2)	-
1.91	3154(1)	3154(1)	3152(2)	-
3.18	2925(2)	2925(1)	2923(1)	-
4.45	2742(4)	2745(6)	2744(6)	0
5.40	2540(1)	2541(2)	2540(2)	-
5.72	2538(1)	2538(2)	2537(2)	-
6.03	2463(1)	2469(2)	2468(2)	-
exit	2046(2)	2058(4)	2063(3)	-
outlet	725(181)	786(10)	776(11)	

RUN # 58 SUMMARY

Test Section Dimensions
.3810 mm Opening
19.23 mm Width
7.3266e-06 m^2 Area
.7472 mm Hydraulic Diameter

Initial Test Section Temperatures
239.6 °C Maximum
236.3 °C Minimum

Stagnation State				
Calculated Value	Time(sec)			
	60.87	82.61	106.52	128.26
Pressure(kPa)	4186.	4180.	4173.	4166.
Error (kpa)	3.	1.	2.	2.
Temperature (°C)	239.2	239.0	238.5	237.5
Error (°C)	.1	.1	.2	.2
Subcooling (°C)	13.9	13.9	14.3	15.3

Corrected Mass Flux (kg/m^2xsec)				
Calculated Value	Time(sec)			
	60.87	82.61	106.52	128.26
Volume Method	2.502e+04	2.540e+04	2.545e+04	2.546e+04
Error (%)	.0	.0	.0	.0
Weigh Tank	2.597e+04	2.391e+04	2.544e+04	2.440e+04
Error (%)	.0	.0	.0	.0
% Difference	-3.8	5.9	.0	4.2

Pressure Profile Summary (in kPa)					
Distance from Entrance (cm)	Time(sec)				Drift (kPa)
	60.87	82.61	106.52	128.26	
.318	3715(4)	3711(2)	3702(2)	3695(2)	0
1.91	3515(4)	3512(2)	3501(3)	3495(2)	0
3.18	3368(4)	3366(2)	3354(3)	3348(2)	234
4.45	3193(6)	3184(6)	3170(7)	3168(6)	30
5.40	3092(3)	3088(2)	3080(2)	3068(4)	0
5.72	3043(3)	3041(1)	3027(2)	3015(4)	0
6.03	2904(3)	2900(2)	2891(3)	2864(6)	0
exit	2387(3)	2384(1)	2377(2)	2364(4)	-6
outlet	1145(5)	1141(4)	1129(6)	1120(6)	

RUN # 59 SUMMARY

Test Section Dimensions
.3810 mm Opening
19.23 mm Width
7.3266e-06 m^2 Area
.7472 mm Hydraulic Diameter

Initial Test Section Temperatures
195.6 °C Maximum
192.3 °C Minimum

Stagnation State		
Calculated Value	Time(sec)	
	92.39	108.70
Pressure(kPa)	4270.	4270.
Error (kpa)	2.	3.
Temperature (°C)	195.1	194.8
Error (°C)	.1	.1
Subcooling (°C)	59.1	59.4

Corrected Mass Flux (kg/m^2xsec)		
Calculated Value	Time(sec)	
	92.39	108.70
Volume Method	4.095e+04	4.093e+04
Error (%)	.0	.0
Weigh Tank	4.172e+04	4.063e+04
Error (%)	.0	.0
% Difference	-1.9	.7

Pressure Profile Summary (in kPa)			
Distance from Entrance (cm)	Time(sec)		Drift (kPa)
	92.39	108.70	
.318	2864(17)	2843(3)	1
1.91	2403(12)	2399(3)	0
3.18	2055(14)	2056(2)	-5
4.45	1618(5)	1613(4)	-703
5.40	1480(2)	1476(2)	0
5.72	1476(2)	1472(2)	0
6.03	1485(2)	1480(2)	0
exit	1315(3)	1310(2)	-4
outlet	1042(9)	1039(8)	

RUN # 60 SUMMARY

Test Section Dimensions		Initial Test Section Temperatures	
.3810	mm Opening	249.9	°C Maximum
19.23	mm Width	242.8	°C Minimum
7.3266e-06	m^2 Area		
.7472	mm Hydraulic Diameter		

Stagnation State				
Calculated Value	Time(sec)			
	81.37	101.99	125.86	156.24
Pressure(kPa)	4150.	4137.	4123.	4104.
Error (kpa)	4.	2.	3.	3.
Temperature (°C)	249.4	249.5	249.4	249.2
Error (°C)	.1	.1	.1	.1
Subcooling (°C)	3.1	2.8	2.7	2.6

Corrected Mass Flux ($kg/m^2 \times sec$)				
Calculated Value	Time(sec)			
	81.37	101.99	125.86	156.24
Volume Method	1.460e+04	1.436e+04	1.434e+04	1.400e+04
Error (%)	.0	.0	.0	.0
Weigh Tank	1.509e+04	1.450e+04	1.379e+04	1.343e+04
Error (%)	.0	.0	.0	.0
% Difference	-3.3	-1.0	3.8	4.1

Pressure Profile Summary (in kPa)					
Distance from Entrance (cm)	Time(sec)				Drift (kPa)
	81.37	101.99	125.86	156.24	
.318	3919(4)	3909(2)	3898(3)	3879(2)	0
1.91	3780(5)	3766(2)	3750(4)	3730(3)	0
3.18	3585(5)	3564(4)	3548(4)	3528(2)	3
4.45	3285(7)	3262(5)	3242(9)	3219(6)	-793
5.40	2820(8)	2787(3)	2769(8)	2745(5)	0
5.72	2616(8)	2591(3)	2569(4)	2548(3)	0
6.03	2373(14)	2345(12)	2332(2)	2312(3)	0
exit	1821(24)	1792(18)	1779(2)	1765(2)	-9
outlet	666(23)	650(7)	632(7)	617(6)	

RUN # 61 SUMMARY

Test Section Dimensions		Initial Test Section Temperatures	
.1270	mm Opening	205.1	°C Maximum
19.43	mm Width	192.5	°C Minimum
2.4676e-06	m^2 Area		
.2524	mm Hydraulic Diameter		

Stagnation State					
Calculated Value	Time(sec)				
	58.74	74.48	151.05	316.78	360.74
Pressure(kPa)	4217.	4217.	4207.	4182.	4175.
Error (kpa)	1.	1.	1.	1.	1.
Temperature (°C)	192.7	192.5	192.4	191.4	191.0
Error (°C)	.1	.1	.1	.1	.1
Subcooling (°C)	60.8	61.0	60.9	61.6	61.9

Corrected Mass Flux ($kg/m^2 \times sec$)					
Calculated Value	Time(sec)				
	58.74	74.48	151.05	316.78	360.74
Volume Method	2.216e+04	2.194e+04	2.137e+04	2.027e+04	1.995e+04
Error (%)	.0	.0	.0	.0	.0
Weigh Tank	2.166e+04	2.276e+04	2.109e+04	2.023e+04	1.971e+04
Error (%)	.0	.0	.0	.0	.0
% Difference	2.3	-3.8	1.3	.2	1.2

Pressure Profile Summary (in kPa)						
Distance from Entrance (cm)	Time(sec)					Drift (kPa)
	58.74	74.48	151.05	316.78	360.74	
.318	2836(9)	2782(6)	2809(1)	2825(2)	2826(1)	4
1.91	2313(9)	2280(6)	2302(3)	2332(2)	2337(1)	0
3.18	1919(8)	1897(7)	1904(1)	1944(2)	1950(1)	-4
4.45	1451(5)	1442(5)	1445(10)	1497(4)	1507(4)	-na-
5.40	1321(4)	1312(2)	1311(4)	1364(1)	1373(1)	11
5.72	1289(2)	1289(3)	1293(3)	1346(1)	1351(1)	0
6.03	1225(4)	1225(1)	1224(3)	1289(1)	1288(1)	0
exit	1006(5)	1001(2)	1000(4)	1031(2)	1029(2)	-1
outlet	133(14)	151(8)	151(1)	145(1)	144(1)	

RUN # 62 SUMMARY

Test Section Dimensions
.1270 mm Opening
19.43 mm Width
2.4676e-06 m^2 Area
.2524 mm Hydraulic Diameter

Initial Test Section Temperatures
28.1 °C Maximum
27.5 °C Minimum

Stagnation State					
Calculated Value	Time(sec)				
	97.38	150.79	301.57	546.60	678.53
Pressure(kPa)	2574.	2588.	2614.	2650.	2667.
Error (kpa)	1.	1.	1.	1.	1.
Temperature (°C)	27.7	28.1	28.6	28.7	29.2
Error (°C)	.1	.2	.1	.2	.1
Subcooling (°C)	198.	198.	198.	198.	198.

Corrected Mass Flux ($kg/m^2 x sec$)					
Calculated Value	Time(sec)				
	97.38	150.79	301.57	546.60	678.53
Volume Method	1.630e+04	1.633e+04	1.637e+04	1.631e+04	1.652e+04
Error (%)	.0	.0	.0	.0	.0
Weigh Tank	1.605e+04	1.615e+04	1.641e+04	1.630e+04	1.630e+04
Error (%)	.0	.0	.0	.0	.0
% Difference	1.5	1.1	-.2	.1	1.3

Pressure Profile Summary (in kPa)						
Distance from Entrance (cm)	Time(sec)					Drift (kPa)
	97.38	150.79	301.57	546.60	678.53	
.318	1980(2)	1991(1)	2010(1)	2035(2)	2049(2)	4
1.91	1424(1)	1430(1)	1445(11)	1459(2)	1469(2)	0
3.18	970(1)	973(1)	980(2)	991(2)	998(2)	-na-
4.45	469(8)	471(6)	468(4)	474(9)	479(7)	-na-
5.40	284(3)	259(2)	244(1)	241(1)	240(1)	-na-
5.72	263(1)	262(2)	262(1)	263(1)	265(1)	-5
6.03	232(1)	231(1)	231(1)	232(1)	233(1)	-7
exit	186(1)	185(1)	185(1)	185(1)	186(1)	0
outlet	124(0)	124(0)	124(0)	119(0)	120(0)	

RUN # 63 SUMMARY

Test Section Dimensions
.1270 mm Opening
19.43 mm Width
2.4676e-06 m^2 Area
.2524 mm Hydraulic Diameter

Initial Test Section Temperatures
238.4 °C Maximum
235.4 °C Minimum

Stagnation State					
Calculated Value	Time(sec)				
	104.71	121.47	157.07	397.91	640.84
Pressure(kPa)	4232.	4231.	4225.	4207.	4186.
Error (kpa)	2.	2.	1.	1.	1.
Temperature (°C)	238.8	238.7	238.5	237.3	234.2
Error (°C)	.1	.1	.1	.1	.1
Subcooling (°C)	14.9	15.0	15.1	16.1	18.9

Corrected Mass Flux ($kg/m^2 x sec$)					
Calculated Value	Time(sec)				
	104.71	121.47	157.07	397.91	640.84
Volume Method	1.293e+04	1.306e+04	1.299e+04	1.290e+04	1.282e+04
Error (%)	.0	.0	.0	.0	.0
Weigh Tank	1.191e+04	1.192e+04	1.169e+04	1.217e+04	1.289e+04
Error (%)	.1	.4	.3	.0	.0
% Difference	7.9	8.7	10.0	5.6	-.5

Pressure Profile Summary (in kPa)						
Distance from Entrance (cm)	Time(sec)					Drift (kPa)
	104.71	121.47	157.07	397.91	640.84	
.318	3764(3)	3761(2)	3753(2)	3719(1)	3696(1)	0
1.91	3483(3)	3480(2)	3474(2)	3435(1)	3408(2)	267
3.18	3242(3)	3238(2)	3230(2)	3186(1)	3157(2)	14
4.45	3058(4)	3056(3)	3048(4)	3004(5)	2950(3)	-1042
5.40	2226(16)	2201(12)	2169(8)	2131(1)	2050(1)	0
5.72	2115(5)	2097(2)	2083(2)	2075(1)	2041(1)	0
6.03	1769(15)	1765(15)	1747(2)	1725(1)	1707(1)	0
exit	1136(15)	1151(17)	1141(1)	1141(1)	1132(1)	-17
outlet	159(0)	159(1)	157(0)	156(0)	155(0)	

RUN # 64 SUMMARY

Test Section Dimensions		Initial Test Section Temperatures	
.1270	mm Opening	225.7	°C Maximum
19.43	mm Width	222.4	°C Minimum
2.4676e-06	m^2 Area		
.2524	mm Hydraulic Diameter		

Stagnation State

Calculated Value	Time(sec) 58.64	79.58	186.39	477.49	534.03
Pressure(kPa)	4242.	4247.	4260.	4287.	4291.
Error (kpa)	1.	3.	2.	1.	1.
Temperature (°C)	223.4	223.5	223.9	223.3	222.8
Error (°C)	.1	.1	.1	.1	.1
Subcooling (°C)	30.5	30.4	30.2	31.2	31.7

Corrected Mass Flux ($kg/m^2 \times sec$)

Calculated Value	Time(sec) 58.64	79.58	186.39	477.49	534.03
Volume Method	1.663e+04	1.667e+04	1.670e+04	1.599e+04	1.593e+04
Error (%)	.0	.0	.0	.0	.0
Weigh Tank	1.739e+04	1.576e+04	1.655e+04	1.574e+04	1.631e+04
Error (%)	.0	.0	.0	.0	.0
% Difference	-4.5	5.5	.9	1.6	-2.3

Pressure Profile Summary (in kPa)

Distance from Entrance (cm)	Time(sec) 58.64	79.58	186.39	477.49	534.03	Drift (kPa)
.318	3590(9)	3596(7)	3621(2)	3680(2)	3691(1)	0
1.91	3119(7)	3129(7)	3150(2)	3250(42)	3246(2)	8
3.18	2749(8)	2755(4)	2775(2)	2867(3)	2885(2)	0
4.45	2470(5)	2477(5)	2489(7)	2591(6)	2611(7)	29
5.40	2025(4)	2027(5)	2033(2)	2068(1)	2049(2)	36
5.72	2134(8)	2144(3)	2162(2)	2200(2)	2172(3)	0
6.03	2002(7)	2017(3)	2027(2)	1970(2)	1941(2)	0
exit	1373(7)	1391(9)	1405(5)	1296(1)	1282(1)	-4
outlet	136(9)	143(0)	142(0)	140(0)	139(0)	

RUN # 65 SUMMARY

Test Section Dimensions		Initial Test Section Temperatures	
.1270	mm Opening	249.9	°C Maximum
19.43	mm Width	245.1	°C Minimum
2.4676e-06	m^2 Area		
.2524	mm Hydraulic Diameter		

Stagnation State

Calculated Value	Time(sec) 46.07	69.11	144.50	320.42	546.60
Pressure(kPa)	4325.	4333.	4349.	4382.	4407.
Error (kpa)	2.	3.	1.	1.	1.
Temperature (°C)	249.4	249.4	249.5	250.2	250.5
Error (°C)	.1	.1	.1	.1	.1
Subcooling (°C)	5.6	5.7	5.8	5.6	5.6

Corrected Mass Flux ($kg/m^2 \times sec$)

Calculated Value	Time(sec) 46.07	69.11	144.50	320.42	546.60
Volume Method	1.229e+04	1.253e+04	1.269e+04	1.305e+04	1.269e+04
Error (%)	.0	.0	.0	.0	.0
Weigh Tank	1.264e+04	1.264e+04	1.264e+04	1.264e+04	1.264e+04
Error (%)	0.	0.	0.	0.	0.
% Difference	-2.9	-.9	.4	3.1	.4

Pressure Profile Summary (in kPa)

Distance from Entrance (cm)	Time(sec) 46.07	69.11	144.50	320.42	546.60	Drift (kPa)
.318	4130(2)	4137(2)	4153(2)	4187(1)	4219(1)	0
1.91	3880(3)	3884(2)	3897(1)	3931(1)	3974(1)	0
3.18	3684(2)	3684(2)	3696(1)	3730(2)	3756(1)	11
4.45	3294(8)	3293(5)	3307(6)	3284(5)	3157(6)	-1100
5.40	2245(11)	2241(12)	2259(2)	2259(3)	2219(2)	28
5.72	2039(10)	2026(9)	2031(2)	2020(2)	1976(2)	0
6.03	1710(30)	1714(23)	1715(2)	1705(2)	1662(3)	0
exit	1091(44)	1112(34)	1130(2)	1134(2)	1111(2)	-17
outlet	133(1)	132(1)	132(1)	133(1)	126(2)	

RUN # 66 SUMMARY

Test Section Dimensions
.1270 mm Opening
19.43 mm Width
2.4676e-06 m^2 Area
.2524 mm Hydraulic Diameter

Initial Test Section Temperatures
293.7 °C Maximum
290.0 °C Minimum

Stagnation State

Calculated Value	Time(sec) 46.07	62.83	98.43	136.13	209.42
Pressure(kPa)	12105.	12097.	12078.	12055.	12019.
Error (kpa)	3.	2.	3.	1.	3.
Temperature (°C)	295.3	295.3	295.2	294.7	292.7
Error (°C)	.1	.1	.1	.1	.2
Subcooling (°C)	30.0	30.0	30.0	30.3	32.1

Corrected Mass Flux ($kg/m^2 x sec$)

Calculated Value	Time(sec) 46.07	62.83	98.43	136.13	209.42
Volume Method	3.109e+04	3.142e+04	3.161e+04	3.131e+04	3.101e+04
Error (%)	.0	.0	.0	.0	.0
Weigh Tank	3.448e+04	3.177e+04	3.194e+04	3.199e+04	3.047e+04
Error (%)	.1	.0	.0	.0	.0
% Difference	-10.9	-1.1	-1.0	-2.2	1.7

Pressure Profile Summary (in kPa)

Distance from Entrance (cm)	Time(sec) 46.07	62.83	98.43	136.13	209.42	Drift (kPa)
.318	10941(2)	10943(2)	10932(4)	10916(2)	10922(2)	0
1.91	9581(5)	9570(3)	9556(4)	9543(2)	9602(3)	0
3.18	8841(16)	8810(3)	8800(5)	8792(3)	8893(7)	-4
4.45	6193(11)	6161(6)	6148(6)	6150(6)	6258(11)	-na-
5.40	6662(26)	6608(5)	6617(3)	6573(4)	6249(21)	39
5.72	5866(48)	5779(9)	5789(2)	5725(4)	5357(17)	0
6.03	4770(76)	4690(2)	4708(15)	4672(4)	4512(7)	0
exit	3089(96)	3051(4)	3062(4)	3053(3)	3013(3)	-41
outlet	279(45)	290(2)	288(1)	286(4)	282(4)	

RUN # 67 SUMMARY

Test Section Dimensions
.1270 mm Opening
19.43 mm Width
2.4676e-06 m^2 Area
.2524 mm Hydraulic Diameter

Initial Test Section Temperatures
257.5 °C Maximum
252.5 °C Minimum

Stagnation State

Calculated Value	Time(sec) 86.01	104.90	157.34	352.45	425.87
Pressure(kPa)	7203.	7215.	7240.	7294.	7307.
Error (kpa)	4.	2.	2.	1.	2.
Temperature (°C)	257.9	257.7	257.4	254.4	252.6
Error (°C)	.1	.1	.1	.1	.3
Subcooling (°C)	29.8	30.2	30.7	34.2	36.1

Corrected Mass Flux ($kg/m^2 x sec$)

Calculated Value	Time(sec) 86.01	104.90	157.34	352.45	425.87
Volume Method	2.071e+04	2.073e+04	2.090e+04	2.045e+04	2.010e+04
Error (%)	.0	.0	.0	.0	.0
Weigh Tank	2.052e+04	2.079e+04	2.079e+04	2.068e+04	2.091e+04
Error (%)	.0	.0	.0	.0	.0
% Difference	.9	-.3	.5	-1.1	-4.0

Pressure Profile Summary (in kPa)

Distance from Entrance (cm)	Time(sec) 86.01	104.90	157.34	352.45	425.87	Drift (kPa)
.318	6301(3)	6333(20)	6369(2)	6433(2)	6447(3)	0
1.91	5613(2)	5634(13)	5652(1)	5714(2)	5728(4)	0
3.18	5020(2)	5036(16)	5045(1)	5096(2)	5108(4)	781
4.45	4573(3)	4576(7)	4564(6)	4599(4)	4596(5)	24
5.40	3764(6)	3727(8)	3687(3)	3469(3)	3365(13)	14
5.72	3818(2)	3783(26)	3748(2)	3573(3)	3460(19)	0
6.03	3313(5)	3299(8)	3295(2)	3054(2)	2981(8)	0
exit	2064(6)	2070(7)	2076(3)	2010(2)	1987(2)	-19
outlet	297(3)	293(2)	288(2)	160(0)	159(0)	

RUN # 68 SUMMARY

Test Section Dimensions		Initial Test Section Temperatures	
.2350	mm Opening	194.6	°C Maximum
19.46	mm Width	190.2	°C Minimum
4.5731e-06	m^2 Area		
.4644	mm Hydraulic Diameter		

Stagnation State

Calculated Value	Time(sec) 72.25	94.24	131.94	175.92
Pressure(kPa)	4279.	4289.	4291.	4293.
Error (kpa)	1.	1.	2.	1.
Temperature (°C)	195.1	195.0	194.7	194.1
Error (°C)	.1	.1	.1	.2
Subcooling (°C)	59.3	59.5	59.8	60.5

Corrected Mass Flux ($kg/m^2 x sec$)

Calculated Value	Time(sec) 72.25	94.24	131.94	175.92
Volume Method	3.479e+04	3.498e+04	3.496e+04	3.471e+04
Error (%)	.0	.0	.0	.0
Weigh Tank	3.441e+04	3.570e+04	3.488e+04	3.476e+04
Error (%)	.0	.0	.0	.0
% Difference	1.1	-2.1	.2	-.1

Pressure Profile Summary (in kPa)

Distance from Entrance (cm)	Time(sec) 72.25	94.24	131.94	175.92	Drift (kPa)
.318	3418(2)	3427(2)	3431(2)	3437(3)	0
1.91	2849(2)	2856(2)	2857(2)	2863(4)	-6
3.18	2355(2)	2358(1)	2357(2)	2364(5)	0
4.45	1855(5)	1856(5)	1852(5)	1863(8)	32
5.40	1495(1)	1492(1)	1486(2)	1499(5)	6
5.72	1434(2)	1434(1)	1429(2)	1441(4)	0
6.03	1390(3)	1394(4)	1402(1)	1427(7)	0
exit	1200(5)	1211(2)	1207(1)	1219(9)	1
outlet	338(1)	290(1)	291(1)	292(1)	

RUN # 69 SUMMARY

Test Section Dimensions		Initial Test Section Temperatures	
.2350	mm Opening	242.1	°C Maximum
19.46	mm Width	236.5	°C Minimum
4.5731e-06	m^2 Area		
.4644	mm Hydraulic Diameter		

Stagnation State

Calculated Value	Time(sec) 75.39	94.24	163.35	224.08
Pressure(kPa)	4280.	4282.	4273.	4270.
Error (kpa)	1.	1.	2.	1.
Temperature (°C)	239.6	239.7	239.2	237.8
Error (°C)	.2	.1	.1	.1
Subcooling (°C)	14.8	14.7	15.1	16.5

Corrected Mass Flux ($kg/m^2 x sec$)

Calculated Value	Time(sec) 75.39	94.24	163.35	224.08
Volume Method	2.138e+04	2.158e+04	2.163e+04	2.158e+04
Error (%)	.0	.0	.0	.0
Weigh Tank	2.134e+04	2.175e+04	2.125e+04	2.104e+04
Error (%)	.0	.0	.0	.0
% Difference	.2	-.8	1.8	2.5

Pressure Profile Summary (in kPa)

Distance from Entrance (cm)	Time(sec) 75.39	94.24	163.35	224.08	Drift (kPa)
.318	3921(3)	3926(1)	3914(2)	3907(1)	0
1.91	3683(3)	3686(1)	3670(2)	3660(1)	8
3.18	3478(2)	3481(1)	3460(2)	3446(1)	0
4.45	3328(4)	3332(5)	3307(5)	3290(7)	58
5.40	3082(3)	3085(1)	3058(1)	3037(2)	0
5.72	3013(2)	3017(2)	2993(2)	2965(2)	-2
6.03	2849(3)	2852(1)	2829(2)	2791(3)	-2
exit	2229(2)	2233(2)	2232(3)	2204(4)	-5
outlet	376(168)	479(36)	225(1)	227(1)	

RUN # 70 SUMMARY

Test Section Dimensions
.2350 mm Opening
19.46 mm Width
4.5731e-06 m^2 Area
.4644 mm Hydraulic Diameter

Initial Test Section Temperatures
227.5 °C Maximum
222.8 °C Minimum

Stagnation State				
Calculated Value	Time(sec)			
	72.25	92.15	140.31	186.39
Pressure(kPa)	4318.	4321.	4322.	4322.
Error (kpa)	2.	2.	1.	1.
Temperature (°C)	224.1	224.3	224.0	223.1
Error (°C)	.1	.1	.1	.2
Subcooling (°C)	30.8	30.7	31.0	31.9

Corrected Mass Flux ($kg/m^2 x sec$)				
Calculated Value	Time(sec)			
	72.25	92.15	140.31	186.39
Volume Method	2.824e+04	2.848e+04	2.847e+04	2.832e+04
Error (%)	.0	.0	.0	.0
Weigh Tank	2.817e+04	2.851e+04	2.889e+04	2.819e+04
Error (%)	.0	.0	.0	.0
% Difference	.2	-.1	-1.5	.5

Pressure Profile Summary (in kPa)					
Distance from Entrance (cm)	Time(sec)				Drift (kPa)
	72.25	92.15	140.31	186.39	
.318	3704(3)	3713(2)	3714(2)	3716(2)	0
1.91	3294(2)	3304(2)	3303(2)	3305(2)	8
3.18	2961(2)	2971(2)	2968(2)	2970(1)	1
4.45	2675(7)	2680(7)	2675(4)	2681(8)	-715
5.40	2372(3)	2380(2)	2373(2)	2377(2)	0
5.72	2331(3)	2343(2)	2338(2)	2336(2)	0
6.03	2257(3)	2270(2)	2267(2)	2276(3)	0
exit	1814(3)	1820(3)	1829(3)	1857(4)	-3
outlet	352(1)	350(1)	349(1)	346(1)	

RUN # 71 SUMMARY

Test Section Dimensions
.2350 mm Opening
19.46 mm Width
4.5731e-06 m^2 Area
.4644 mm Hydraulic Diameter

Initial Test Section Temperatures
253.4 °C Maximum
248.4 °C Minimum

Stagnation State				
Calculated Value	Time(sec)			
	70.16	92.15	144.50	209.42
Pressure(kPa)	4270.	4273.	4276.	4281.
Error (kpa)	2.	2.	1.	2.
Temperature (°C)	249.4	249.5	249.3	248.7
Error (°C)	.1	.1	.1	.1
Subcooling (°C)	4.9	4.8	5.1	5.7

Corrected Mass Flux ($kg/m^2 x sec$)				
Calculated Value	Time(sec)			
	70.16	92.15	144.50	209.42
Volume Method	1.685e+04	1.683e+04	1.689e+04	1.707e+04
Error (%)	.0	.0	.0	.0
Weigh Tank	1.682e+04	1.669e+04	1.655e+04	1.688e+04
Error (%)	.0	.0	.0	.0
% Difference	.2	.8	2.1	1.1

Pressure Profile Summary (in kPa)					
Distance from Entrance (cm)	Time(sec)				Drift (kPa)
	70.16	92.15	144.50	209.42	
.318	4056(2)	4060(2)	4062(2)	4061(1)	0
1.91	3904(2)	3908(3)	3908(2)	3903(1)	7
3.18	3773(2)	3774(2)	3772(2)	3763(1)	3
4.45	3674(5)	3671(6)	3669(3)	3657(5)	-571
5.40	3319(3)	3313(1)	3318(1)	3320(2)	19
5.72	3147(4)	3134(3)	3143(2)	3159(2)	0
6.03	2706(18)	2698(10)	2718(3)	2752(4)	0
exit	1910(21)	1903(8)	1922(3)	1952(4)	-14
outlet	200(60)	211(23)	194(0)	195(0)	

RUN # 72 SUMMARY

Test Section Dimensions
.2350 mm Opening
19.46 mm Width
4.5731e-06 m^2 Area
.4644 mm Hydraulic Diameter

Initial Test Section Temperatures
192.7 °C Maximum
144.6 °C Minimum

Stagnation State			
Calculated Value	Time(sec)		
	104.90	121.68	132.17
Pressure(kPa)	15588.	15600.	15604.
Error (kpa)	3.	3.	6.
Temperature (°C)	291.4	291.3	291.0
Error (°C)	.1	.1	.1
Subcooling (°C)	53.8	54.0	54.3

Corrected Mass Flux ($kg/m^2 x sec$)			
Calculated Value	Time(sec)		
	104.90	121.68	132.17
Volume Method	4.985e+04	5.015e+04	5.017e+04
Error (%)	.0	.0	.0
Weigh Tank	4.805e+04	5.633e+04	5.005e+04
Error (%)	.0	.0	.1
% Difference	3.6	-12.3	.2

Pressure Profile Summary (in kPa)				
Distance from Entrance (cm)	Time(sec)			Drift (kPa)
	104.90	121.68	132.17	
.318	12861(3)	12859(7)	12847(3)	1
1.91	12572(122)	12477(7)	12466(3)	-110
3.18	12570(3)	12568(7)	12557(3)	0
4.45	5913(12)	5879(10)	5876(9)	-
5.40	7735(24)	7658(14)	7633(5)	54
5.72	7049(4)	7037(5)	7031(4)	8
6.03	6836(13)	6824(4)	6822(5)	4
exit	5597(6)	5604(4)	5604(6)	-19
outlet	349(411)	1101(3)	1099(4)	

RUN # 73 SUMMARY

Test Section Dimensions
.2350 mm Opening
19.46 mm Width
4.5731e-06 m^2 Area
.4644 mm Hydraulic Diameter

Initial Test Section Temperatures
27.9 °C Maximum
27.4 °C Minimum

Stagnation State			
Calculated Value	Time(sec)		
	56.64	92.31	140.56
Pressure(kPa)	2641.	2632.	2619.
Error (kpa)	2.	1.	1.
Temperature (°C)	27.6	27.9	28.0
Error (°C)	.2	.1	.1
Subcooling (°C)	199.	199.	198.

Corrected Mass Flux ($kg/m^2 x sec$)			
Calculated Value	Time(sec)		
	56.64	92.31	140.56
Volume Method	2.651e+04	2.647e+04	2.633e+04
Error (%)	.0	.0	.0
Weigh Tank	2.526e+04	2.614e+04	2.607e+04
Error (%)	.0	.0	.0
% Difference	4.7	1.2	1.0

Pressure Profile Summary (in kPa)				
Distance from Entrance (cm)	Time(sec)			Drift (kPa)
	56.64	92.31	140.56	
.318	1832(2)	1824(1)	1815(1)	0
1.91	1382(2)	1374(1)	1367(1)	0
3.18	982(2)	976(1)	971(1)	0
4.45	514(5)	513(7)	508(9)	-232
5.40	287(2)	284(2)	282(2)	0
5.72	236(2)	232(2)	230(1)	0
6.03	198(1)	197(2)	195(1)	-5
exit	131(1)	130(2)	128(2)	0
outlet	118(0)	116(0)	116(0)	

RUN # 74 SUMMARY

Test Section Dimensions		Initial Test Section Temperatures	
.3810	mm Opening	285.2	°C Maximum
19.30	mm Width	279.0	°C Minimum
7.3533e-06	m^2 Area		
.7472	mm Hydraulic Diameter		

Stagnation State		
Calculated Value	Time(sec)	
	89.01	99.48
Pressure(kPa)	15369.	15457.
Error (kpa)	18.	49.
Temperature (°C)	289.8	288.9
Error (°C)	.2	.7
Subcooling (°C)	54.3	55.6

Corrected Mass Flux ($kg/m^2 x sec$)		
Calculated Value	Time(sec)	
	89.01	99.48
Volume Method	6.955e+04	6.996e+04
Error (%)	.0	.0
Weigh Tank	7.440e+04	6.590e+04
Error (%)	.1	.1
% Difference	-7.0	5.8

Pressure Profile Summary (in kPa)			
Distance from Entrance (cm)	Time(sec)		Drift (kPa)
	89.01	99.48	
.318	11476(7)	11574(73)	0
1.91	11068(7)	11166(73)	0
3.18	9056(13)	9136(79)	-na-
4.45	6085(18)	6190(93)	-na-
5.40	7265(14)	7331(76)	14
5.72	7200(16)	7263(61)	-2
6.03	7250(16)	7261(18)	0
exit	6133(6)	6146(8)	-24
outlet	1239(6)	1244(1)	

RUN # 75 SUMMARY

Test Section Dimensions		Initial Test Section Temperatures	
.3810	mm Opening	316.1	°C Maximum
19.30	mm Width	306.0	°C Minimum
7.3533e-06	m^2 Area		
.7472	mm Hydraulic Diameter		

Stagnation State		
Calculated Value	Time(sec)	
	84.97	98.60
Pressure(kPa)	9546.	9544.
Error (kpa)	3.	3.
Temperature (°C)	311.9	311.7
Error (°C)	3.2	2.0
Subcooling (°C)	0.	0.

Corrected Mass Flux ($kg/m^2 x sec$)		
Calculated Value	Time(sec)	
	84.97	98.60
Volume Method	2.624e+04	2.654e+04
Error (%)	.0	.0
Weigh Tank	2.594e+04	2.785e+04
Error (%)	.0	.1
% Difference	1.1	-4.9

Pressure Profile Summary (in kPa)			
Distance from Entrance (cm)	Time(sec)		Drift (kPa)
	84.97	98.60	
.318	8920(3)	8919(3)	1
1.91	8397(3)	8396(3)	79
3.18	7992(6)	7991(5)	0
4.45	7391(7)	7395(8)	139
5.40	6202(16)	6196(3)	30
5.72	5791(7)	5788(6)	0
6.03	5314(13)	5303(28)	0
exit	4200(27)	4189(39)	-49
outlet	1085(547)	1059(417)	

RUN # 76 SUMMARY

Test Section Dimensions		Initial Test Section Temperatures	
.3810	mm Opening	307.2	°C Maximum
19.30	mm Width	193.9	°C Minimum
7.3533e-06	m^2 Area		
.7472	mm Hydraulic Diameter		

Stagnation State		
Calculated Value	Time(sec) 77.49	92.15
Pressure(kPa)	11666.	11682.
Error (kpa)	6.	3.
Temperature (°C)	310.8	310.7
Error (°C)	.1	.1
Subcooling (°C)	11.7	11.9

Corrected Mass Flux ($kg/m^2 x sec$)		
Calculated Value	Time(sec) 77.49	92.15
Volume Method	3.859e+04	3.860e+04
Error (%)	.0	.0
Weigh Tank	3.625e+04	3.441e+04
Error (%)	.1	.1
% Difference	6.1	10.8

Pressure Profile Summary (in kPa)			
Distance from Entrance (cm)	Time(sec) 77.49	92.15	Drift (kPa)
.318	10498(5)	10510(3)	0
1.91	9996(3)	10002(3)	0
3.18	9766(3)	9768(3)	0
4.45	9663(5)	9659(5)	166
5.40	8444(4)	8447(3)	36
5.72	8074(5)	8075(3)	0
6.03	7506(3)	7508(3)	0
exit	5905(4)	5911(3)	-41
outlet	982(427)	1194(6)	

RUN # 77 SUMMARY

Test Section Dimensions		Initial Test Section Temperatures	
.3810	mm Opening	30.8	°C Maximum
19.30	mm Width	30.1	°C Minimum
7.3533e-06	m^2 Area		
.7472	mm Hydraulic Diameter		

Stagnation State		
Calculated Value	Time(sec) 56.64	90.21
Pressure(kPa)	2476.	2465.
Error (kpa)	1.	1.
Temperature (°C)	29.3	29.5
Error (°C)	.1	.2
Subcooling (°C)	194.	194.

Corrected Mass Flux ($kg/m^2 x sec$)		
Calculated Value	Time(sec) 56.64	90.21
Volume Method	3.669e+04	3.648e+04
Error (%)	.0	.0
Weigh Tank	3.628e+04	3.624e+04
Error (%)	.0	.0
% Difference	1.1	.7

Pressure Profile Summary (in kPa)			
Distance from Entrance (cm)	Time(sec) 56.64	90.21	Drift (kPa)
.318	1453(2)	1446(2)	2
1.91	1054(2)	1047(1)	0
3.18	759(2)	752(2)	-6
4.45	449(3)	446(5)	14
5.40	265(20)	195(2)	0
5.72	160(2)	157(2)	0
6.03	146(3)	141(1)	0
exit	87(2)	87(1)	4
outlet	123(0)	121(1)	

RUN # 78 SUMMARY

Test Section Dimensions		Initial Test Section Temperatures	
.3810	mm Opening	318.0	°C Maximum
19.30	mm Width	308.9	°C Minimum
7.3533e-06	m^2 Area		
.7472	mm Hydraulic Diameter		

Stagnation State

Calculated Value	Time(sec) 58.64	64.92	71.20
Pressure(kPa)	15435.	15446.	15453.
Error (kpa)	4.	8.	3.
Temperature (°C)	319.1	318.9	318.5
Error (°C)	.1	.1	.3
Subcooling (°C)	25.3	25.6	26.0

Corrected Mass Flux ($kg/m^2 x sec$)

Calculated Value	Time(sec) 58.64	64.92	71.20
Volume Method	5.139e+04	5.202e+04	5.284e+04
Error (%)	.0	.0	.0
Weigh Tank	4.828e+04	4.399e+04	3.973e+04
Error (%)	.0	.1	.0
% Difference	6.1	15.4	24.8

Pressure Profile Summary (in kPa)

Distance from Entrance (cm)	Time(sec) 58.64	64.92	71.20	Drift (kPa)
.318	12819(4)	12828(16)	12870(16)	-2
1.91	11784(7)	11788(16)	11836(23)	252
3.18	11515(9)	11516(16)	11564(24)	2
4.45	-na-	-na-	-na-	-na-
5.40	10167(9)	10158(5)	10157(6)	39
5.72	9923(6)	9913(7)	9882(20)	0
6.03	9329(7)	9316(10)	9270(25)	21
exit	7707(3)	7700(13)	7648(26)	-57
outlet	1245(0)	1246(1)	1247(0)	

RUN # 79 SUMMARY

Test Section Dimensions		Initial Test Section Temperatures	
.3810	mm Opening	322.7	°C Maximum
19.30	mm Width	315.4	°C Minimum
7.3533e-06	m^2 Area		
.7472	mm Hydraulic Diameter		

Stagnation State

Calculated Value	Time(sec) 105.76	115.18	137.17	153.93
Pressure(kPa)	11686.	11691.	11689.	11672.
Error (kpa)	3.	3.	4.	1.
Temperature (°C)	323.4	323.3	322.9	320.6
Error (°C)	.1	.1	.3	.1
Subcooling (°C)	0.	0.	0.	2.0

Corrected Mass Flux ($kg/m^2 x sec$)

Calculated Value	Time(sec) 105.76	115.18	137.17	153.93
Volume Method	2.889e+04	2.894e+04	2.892e+04	3.055e+04
Error (%)	.0	.0	.0	.0
Weigh Tank	-na-	-na-	-na-	-na-

Pressure Profile Summary (in kPa)

Distance from Entrance (cm)	Time(sec) 105.76	115.18	137.17	153.93	Drift (kPa)
.318	10879(4)	10885(3)	10884(5)	10854(1)	-1
1.91	10122(5)	10129(4)	10132(3)	10137(1)	472
3.18	9626(8)	9638(5)	9644(5)	9672(1)	-1
4.45	-na-	-na-	-na-	-na-	-na-
5.40	7353(9)	7365(10)	7364(9)	7454(4)	21
5.72	6806(12)	6813(3)	6825(10)	6919(3)	0
6.03	6205(36)	6209(14)	6193(20)	6280(5)	25
exit	4865(49)	4827(39)	4829(9)	4890(4)	-65
outlet	1126(10)	1095(19)	1089(19)	1099(2)	

RUN # 80 SUMMARY

Test Section Dimensions		Initial Test Section Temperatures	
.1270	mm Opening	307.9	°C Maximum
18.67	mm Width	290.2	°C Minimum
2.3711e-06	m^2 Area		
.2523	mm Hydraulic Diameter		

Stagnation State

Calculated Value	Time(sec)				
	52.68	71.22	113.17	185.37	243.90
Pressure(kPa)	11787.	11796.	11800.	11793.	11793.
Error (kpa)	3.	3.	3.	2.	2.
Temperature (°C)	310.0	310.3	310.3	308.6	307.3
Error (°C)	.1	.2	.2	.1	.2
Subcooling (°C)	13.3	13.1	13.1	14.7	16.1

Corrected Mass Flux ($kg/m^2 x sec$)

Calculated Value	Time(sec)				
	52.68	71.22	113.17	185.37	243.90
Volume Method	2.218e+04	2.234e+04	2.227e+04	2.196e+04	2.200e+04
Error (%)	.0	.0	.0	.0	.0
Weigh Tank	2.252e+04	2.216e+04	2.219e+04	2.228e+04	2.189e+04
Error (%)	.1	.0	.0	.0	.0
% Difference	-1.6	.8	.4	-1.5	.5

Pressure Profile Summary (in kPa)

Distance from Entrance (cm)	Time(sec)					Drift (kPa)
	52.68	71.22	113.17	185.37	243.90	
.318	11368(4)	11386(4)	11406(2)	11408(3)	11409(2)	0
1.91	10556(2)	10572(5)	10601(2)	10598(3)	10594(3)	0
3.18	9940(4)	9945(5)	9972(3)	9960(3)	9948(3)	0
4.45	8369(22)	8310(7)	8289(7)	8264(12)	8175(7)	-3289
5.40	6206(30)	6143(18)	6134(2)	6157(4)	6161(2)	30
5.72	5170(35)	5139(10)	5122(3)	5113(2)	5102(3)	0
6.03	4356(81)	4323(30)	4279(3)	4264(2)	4254(2)	0
exit	2471(87)	2477(38)	2453(2)	2453(2)	2452(2)	-19
outlet	235(2)	230(2)	226(1)	217(1)	215(1)	

RUN # 81 SUMMARY

Test Section Dimensions		Initial Test Section Temperatures	
.1270	mm Opening	322.7	°C Maximum
18.67	mm Width	296.2	°C Minimum
2.3711e-06	m^2 Area		
.2523	mm Hydraulic Diameter		

Stagnation State

Calculated Value	Time(sec)			
	125.20	125.20	124.90	124.90
Pressure(kPa)	11574.	11565.	11546.	11537.
Error (kpa)	2.	2.	1.	2.
Temperature (°C)	323.5	323.6	322.2	321.4
Error (°C)	.1	.0	.1	.1
Subcooling (°C)	0.	0.	0.	.2

Corrected Mass Flux ($kg/m^2 x sec$)

Calculated Value	Time(sec)			
	125.20	125.20	124.90	124.90
Volume Method	2.011e+04	2.028e+04	2.058e+04	2.126e+04
Error (%)	.0	.0	.0	.0
Weigh Tank	1.577e+04	2.110e+04	2.116e+04	2.115e+04
Error (%)	.0	.0	.0	.0
% Difference	21.6	-4.0	-2.9	.5

Pressure Profile Summary (in kPa)

Distance from Entrance (cm)	Time(sec)				Drift (kPa)
	125.20	125.20	124.90	124.90	
.318	7290(4)	7303(1)	7293(2)	7285(1)	0
1.91	6707(10)	6727(10)	6753(2)	6758(1)	144
3.18	-na-	-na-	-na-	-na-	-na-
4.45	5063(16)	5093(16)	5123(6)	5123(5)	-3619
5.40	5458(18)	5494(3)	5520(3)	5531(1)	86
5.72	4491(17)	4528(2)	4565(2)	4585(2)	0
6.03	4950(18)	4966(15)	5032(3)	5064(2)	0
exit	4572(32)	4637(27)	4737(3)	4775(2)	125
outlet	125(0)	125(0)	125(0)	125(0)	

RUN # 82 SUMMARY

Test Section Dimensions
.1270 mm Opening
18.67 mm Width
2.3711e-06 m^2 Area
.2523 mm Hydraulic Diameter

Initial Test Section Temperatures
309.4 °C Maximum
264.0 °C Minimum

Stagnation State

Calculated Value	Time(sec) 39.02	56.59	113.17	308.29	384.39
Pressure(kPa)	9661.	9660.	9651.	9629.	9627.
Error (kpa)	3.	1.	3.	1.	1.
Temperature (°C)	308.8	308.7	308.4	306.7	305.4
Error (°C)	.1	.1	.2	.1	.2
Subcooling (°C)	0.	0.	0.	1.5	2.7

Corrected Mass Flux ($kg/m^2 x sec$)

Calculated Value	Time(sec) 39.02	56.59	113.17	308.29	384.39
Volume Method	1.693e+04	1.681e+04	1.642e+04	1.612e+04	1.613e+04
Error (%)	.0	.0	.0	.0	.0
Weigh Tank	1.625e+04	1.625e+04	1.625e+04	1.625e+04	1.625e+04
Error (%)	0.	0.	0.	0.	0.
% Difference	4.0	3.3	1.0	-.8	-.7

Pressure Profile Summary (in kPa)

Distance from Entrance (cm)	Time(sec) 39.02	56.59	113.17	308.29	384.39	Drift (kPa)
.318	9417(3)	9418(2)	9420(2)	9406(2)	9400(2)	0
1.91	8953(3)	8949(6)	8965(2)	8956(2)	8942(1)	0
3.18	8230(20)	8210(3)	8242(3)	8291(2)	8316(3)	13
4.45	6353(21)	6329(15)	6361(6)	6392(6)	6415(5)	-283
5.40	4938(31)	4922(4)	4931(1)	4944(2)	4961(2)	38
5.72	4145(38)	4136(10)	4125(3)	4115(2)	4129(2)	13
6.03	3394(37)	3376(20)	3338(22)	3323(2)	3339(3)	13
exit	1985(39)	1994(28)	1982(33)	1980(2)	1993(2)	-17
outlet	173(12)	171(2)	169(2)	168(2)	169(2)	

RUN # 83 SUMMARY

Test Section Dimensions
.1270 mm Opening
18.67 mm Width
2.3711e-06 m^2 Area
.2523 mm Hydraulic Diameter

Initial Test Section Temperatures
46.4 °C Maximum
31.1 °C Minimum

Stagnation State

Calculated Value	Time(sec) 52.68	138.54	258.54	505.37	624.39
Pressure(kPa)	2543.	2562.	2579.	2607.	2618.
Error (kpa)	1.	1.	1.	1.	1.
Temperature (°C)	31.1	31.2	31.2	31.1	31.5
Error (°C)	.2	.2	.1	.2	.2
Subcooling (°C)	194.	194.	194.	195.	195.

Corrected Mass Flux ($kg/m^2 x sec$)

Calculated Value	Time(sec) 52.68	138.54	258.54	505.37	624.39
Volume Method	1.702e+04	1.709e+04	1.717e+04	1.687e+04	1.729e+04
Error (%)	.0	.0	.0	.0	.0
Weigh Tank	1.667e+04	1.667e+04	1.667e+04	1.667e+04	1.667e+04
Error (%)	0.	0.	0.	0.	0.
% Difference	2.1	2.5	2.9	1.2	3.6

Pressure Profile Summary (in kPa)

Distance from Entrance (cm)	Time(sec) 52.68	138.54	258.54	505.37	624.39	Drift (kPa)
.318	2273(1)	2291(2)	2307(1)	2335(1)	2345(1)	0
1.91	1894(1)	1909(2)	1926(1)	1948(1)	1956(1)	8
3.18	1451(1)	1455(1)	1476(2)	1468(1)	1473(1)	0
4.45	721(3)	728(4)	738(5)	736(4)	740(4)	-86
5.40	358(1)	358(1)	362(1)	364(1)	367(2)	0
5.72	256(2)	257(2)	259(1)	260(1)	263(3)	0
6.03	202(2)	200(1)	202(1)	197(3)	197(2)	0
exit	106(2)	104(1)	106(2)	104(3)	108(2)	0
outlet	123(0)	114(0)	114(0)	115(0)	115(0)	

RUN # 84 SUMMARY

Test Section Dimensions		Initial Test Section Temperatures	
.1270	mm Opening	250.7	°C Maximum
18.67	mm Width	236.8	°C Minimum
2.3711e-06	m^2 Area		
.2523	mm Hydraulic Diameter		

Stagnation State

Calculated Value	Time(sec) 82.93	99.51	140.49	238.05	318.05
Pressure(kPa)	9562.	9667.	9684.	9687.	9688.
Error (kpa)	1.	6.	2.	2.	1.
Temperature (°C)	252.0	252.1	251.8	250.8	248.7
Error (°C)	.1	.1	.1	.1	.1
Subcooling (°C)	55.7	56.4	56.8	57.8	59.9

Corrected Mass Flux ($kg/m^2 x sec$)

Calculated Value	Time(sec) 82.93	99.51	140.49	238.05	318.05
Volume Method	2.996e+04	3.004e+04	3.009e+04	2.990e+04	2.903e+04
Error (%)	.0	.0	.0	.0	.0
Weigh Tank	3.000e+04	2.948e+04	3.088e+04	2.949e+04	2.856e+04
Error (%)	.0	.0	.0	.0	.0
% Difference	-.1	1.9	-2.6	1.4	1.6

Pressure Profile Summary (in kPa)

Distance from Entrance (cm)	Time(sec) 82.93	99.51	140.49	238.05	318.05	Drift (kPa)
.318	8803(4)	8907(8)	8937(3)	8962(2)	9005(3)	0
1.91	7651(5)	7743(8)	7777(3)	7823(4)	7922(5)	-52
3.18	6508(4)	6576(6)	6603(3)	6654(7)	6816(12)	7
4.45	4696(5)	4723(4)	4727(4)	4783(10)	5012(18)	-2411
5.40	4057(5)	4070(5)	4061(3)	4097(11)	4367(17)	0
5.72	3860(4)	3864(6)	3847(5)	3909(11)	4086(4)	0
6.03	3766(2)	3787(8)	3782(3)	3808(10)	3802(6)	0
exit	2690(6)	2659(10)	2665(3)	2674(16)	2582(9)	0
outlet	240(1)	238(1)	238(1)	233(3)	225(2)	

RUN # 85 SUMMARY

Test Section Dimensions		Initial Test Section Temperatures	
.1270	mm Opening	276.9	°C Maximum
18.67	mm Width	269.9	°C Minimum
2.3711e-06	m^2 Area		
.2523	mm Hydraulic Diameter		

Stagnation State

Calculated Value	Time(sec) 110.63	131.25	230.63	466.88	540.00
Pressure(kPa)	7189.	7197.	7219.	7246.	7249.
Error (kpa)	1.	2.	2.	1.	1.
Temperature (°C)	273.4	273.3	272.8	270.2	268.6
Error (°C)	.1	.1	.1	.1	.1
Subcooling (°C)	14.2	14.4	15.1	17.9	19.6

Corrected Mass Flux ($kg/m^2 x sec$)

Calculated Value	Time(sec) 110.63	131.25	230.63	466.88	540.00
Volume Method	1.544e+04	1.540e+04	1.528e+04	1.524e+04	1.533e+04
Error (%)	.0	.0	.0	.0	.0
Weigh Tank	1.211e+04	1.478e+04	1.551e+04	1.519e+04	1.475e+04
Error (%)	.0	.0	.0	.0	.0
% Difference	21.6	4.0	-1.5	.3	3.8

Pressure Profile Summary (in kPa)

Distance from Entrance (cm)	Time(sec) 110.63	131.25	230.63	466.88	540.00	Drift (kPa)
.318	6557(4)	6574(7)	6604(1)	6616(1)	6609(2)	0
1.91	6187(3)	6198(6)	6224(1)	6226(1)	6214(2)	0
3.18	5840(3)	5846(4)	5863(1)	5847(2)	5827(2)	0
4.45	5447(6)	5452(7)	5464(6)	5402(5)	5374(5)	-
5.40	4026(20)	4009(8)	4025(3)	4027(1)	4023(2)	42
5.72	3402(15)	3389(9)	3385(2)	3392(1)	3399(1)	0
6.03	2867(28)	2826(29)	2817(1)	2822(1)	2829(1)	0
exit	1689(32)	1684(25)	1711(1)	1720(2)	1724(1)	-17
outlet	160(3)	160(2)	158(1)	158(2)	158(2)	

RUN # 86 SUMMARY

Test Section Dimensions
.1270 mm Opening
18.67 mm Width
2.3711e-06 m^2 Area
.2523 mm Hydraulic Diameter

Initial Test Section Temperatures
288.4 °C Maximum
279.7 °C Minimum

Stagnation State

Calculated Value	Time(sec) 94.69	118.13	200.63	419.06	534.38
Pressure(kPa)	7179.	7194.	7231.	7280.	7290.
Error (kpa)	4.	2.	2.	2.	1.
Temperature (°C)	283.8	283.8	283.3	280.7	278.3
Error (°C)	.1	.1	.1	.2	.2
Subcooling (°C)	3.8	3.9	4.7	7.7	10.2

Corrected Mass Flux ($kg/m^2 x sec$)

Calculated Value	Time(sec) 94.69	118.13	200.63	419.06	534.38
Volume Method	1.472e+04	1.405e+04	1.429e+04	1.466e+04	1.500e+04
Error (%)	.0	.0	.0	.0	.0
Weigh Tank	1.246e+04	1.362e+04	1.417e+04	1.427e+04	1.476e+04
Error (%)	.0	.0	.0	.0	.0
% Difference	15.4	3.1	.9	2.7	1.6

Pressure Profile Summary (in kPa)

Distance from Entrance (cm)	Time(sec) 94.69	118.13	200.63	419.06	534.38	Drift (kPa)
.318	7003(4)	7020(2)	7059(2)	7098(2)	7100(2)	0
1.91	6695(4)	6715(10)	6747(3)	6762(1)	6747(3)	0
3.18	6392(4)	6403(3)	6433(2)	6423(1)	6387(2)	0
4.45	5462(11)	5472(6)	5551(5)	5699(4)	5764(6)	17
5.40	3940(21)	3923(3)	3967(3)	4038(4)	4091(2)	38
5.72	3354(10)	3348(8)	3367(2)	3412(4)	3457(2)	0
6.03	2768(19)	2766(2)	2771(2)	2803(3)	2845(2)	0
exit	1586(24)	1601(2)	1616(2)	1650(3)	1685(2)	0
outlet	151(1)	149(1)	150(1)	133(1)	133(1)	

RUN # 87 SUMMARY

Test Section Dimensions
.1270 mm Opening
18.67 mm Width
2.3711e-06 m^2 Area
.2523 mm Hydraulic Diameter

Initial Test Section Temperatures
288.9 °C Maximum
282.5 °C Minimum

Stagnation State

Calculated Value	Time(sec) 27.19	41.25	88.13	138.75	187.50
Pressure(kPa)	15927.	15924.	15901.	15883.	15868.
Error (kpa)	2.	2.	3.	2.	2.
Temperature (°C)	290.3	290.3	289.7	288.4	285.9
Error (°C)	.1	.1	.1	.1	.2
Subcooling (°C)	56.7	56.6	57.1	58.3	60.8

Corrected Mass Flux ($kg/m^2 x sec$)

Calculated Value	Time(sec) 27.19	41.25	88.13	138.75	187.50
Volume Method	3.759e+04	3.583e+04	3.653e+04	3.497e+04	3.389e+04
Error (%)	.0	.0	.0	.0	.0
Weigh Tank	3.635e+04	3.707e+04	3.699e+04	3.425e+04	3.439e+04
Error (%)	.0	.0	.0	.0	.0
% Difference	3.3	-3.5	-1.3	2.1	-1.5

Pressure Profile Summary (in kPa)

Distance from Entrance (cm)	Time(sec) 27.19	41.25	88.13	138.75	187.50	Drift (kPa)
.318	14659(4)	14673(3)	14686(2)	14729(5)	14783(2)	0
1.91	13916(4)	13929(3)	13942(2)	13985(5)	14040(2)	500
3.18	14360(4)	14374(3)	14387(2)	14430(5)	14484(2)	10
4.45	-na-	-na-	-na-	-na-	-na-	-na-.
5.40	8149(12)	8110(9)	8018(5)	7958(5)	7801(11)	69
5.72	6938(3)	6937(3)	6926(4)	6948(9)	6648(9)	30
6.03	6397(6)	6393(4)	6363(5)	6193(20)	5805(13)	64
exit	6444(6)	6441(4)	6411(5)	6240(20)	3465(8)	7
outlet	253(103)	335(2)	329(1)	321(3)	312(3)	

RUN # 88 SUMMARY

Test Section Dimensions
.1270 mm Opening
18.67 mm Width
2.3711e-06 m^2 Area
.2523 mm Hydraulic Diameter

Initial Test Section Temperatures
270.4 °C Maximum
263.2 °C Minimum

Stagnation State

Calculated Value	Time(sec) 88.13	108.75	124.69	230.63	320.63
Pressure(kPa)	11860.	11875.	11883.	11911.	11933.
Error (kpa)	3.	2.	2.	3.	1.
Temperature (°C)	265.8	266.5	266.8	266.2	264.2
Error (°C)	.1	.2	.2	.2	.1
Subcooling (°C)	57.9	57.4	57.1	57.9	60.1

Corrected Mass Flux ($kg/m^2 x sec$)

Calculated Value	Time(sec) 88.13	108.75	124.69	230.63	320.63
Volume Method	3.245e+04	3.177e+04	3.183e+04	3.128e+04	3.032e+04
Error (%)	.0	.0	.0	.0	.0
Weigh Tank	3.241e+04	3.155e+04	3.201e+04	3.075e+04	3.017e+04
Error (%)	.1	.0	.0	.0	.0
% Difference	.1	.7	-.6	1.7	.5

Pressure Profile Summary (in kPa)

Distance from Entrance (cm)	Time(sec) 88.13	108.75	124.69	230.63	320.63	Drift (kPa)
.318	10936(8)	10976(6)	10999(3)	11071(2)	11148(5)	0
1.91	10746(8)	10785(6)	10808(3)	10880(2)	10958(5)	0
3.18	8130(7)	8182(10)	8217(5)	8336(5)	8570(14)	10
4.45	5979(5)	6026(9)	6052(4)	6166(6)	6500(28)	-111
5.40	5075(10)	5130(11)	5157(5)	5248(4)	5587(20)	55
5.72	4885(7)	4938(11)	4966(5)	5071(5)	5153(6)	0
6.03	4753(5)	4791(6)	4804(4)	4830(7)	4633(13)	19
exit	3197(9)	3202(7)	3211(5)	3149(7)	2981(13)	2
outlet	192(73)	277(2)	274(2)	267(1)	257(2)	

RUN # 89 SUMMARY

Test Section Dimensions
.1270 mm Opening
18.67 mm Width
2.3711e-06 m^2 Area
.2523 mm Hydraulic Diameter

Initial Test Section Temperatures
318.6 °C Maximum
308.9 °C Minimum

Stagnation State

Calculated Value	Time(sec) 41.25	60.00	88.13	168.75	198.75
Pressure(kPa)	16140.	16122.	15577.	15761.	15745.
Error (kpa)	2.	5.	4.	2.	2.
Temperature (°C)	320.2	320.1	319.7	317.5	316.5
Error (°C)	.1	.1	.1	.3	.1
Subcooling (°C)	27.9	27.8	25.5	28.6	29.5

Corrected Mass Flux ($kg/m^2 x sec$)

Calculated Value	Time(sec) 41.25	60.00	88.13	168.75	198.75
Volume Method	3.018e+04	3.030e+04	2.892e+04	2.858e+04	2.829e+04
Error (%)	.0	.0	.0	.0	.0
Weigh Tank	3.199e+04	2.946e+04	3.022e+04	2.930e+04	2.900e+04
Error (%)	.0	.0	.0	.0	.0
% Difference	-6.0	2.8	-4.5	-2.5	-2.5

Pressure Profile Summary (in kPa)

Distance from Entrance (cm)	Time(sec) 41.25	60.00	88.13	168.75	198.75	Drift (kPa)
.318	15340(2)	15338(3)	14873(4)	15066(2)	15060(2)	0
1.91	15086(2)	15084(3)	14618(4)	14811(2)	14805(2)	0
3.18	12874(20)	12857(4)	12584(5)	12777(8)	12797(3)	104
4.45	10757(21)	10747(5)	10585(6)	10721(8)	10732(8)	-116
5.40	8873(83)	8775(5)	8331(3)	8281(41)	8165(13)	59
5.72	7015(74)	6954(6)	6607(4)	6655(16)	6608(6)	15
6.03	6367(11)	6343(7)	5776(5)	5944(3)	5921(3)	20
exit	4027(93)	4028(77)	3532(49)	3698(5)	3687(2)	16
outlet	297(49)	312(2)	294(1)	293(1)	290(1)	

RUN # 90 SUMMARY

Test Section Dimensions		Initial Test Section Temperatures	
.1270	mm Opening	33.2	°C Maximum
18.67	mm Width	32.8	°C Minimum
2.3711e-06	m^2 Area		
.2523	mm Hydraulic Diameter		

Stagnation State

Calculated Value	Time(sec) 65.63	187.50	303.75	574.50	663.75
Pressure(kPa)	2534.	2546.	2558.	2584.	2592.
Error (kpa)	1.	1.	1.	1.	1.
Temperature (°C)	31.5	31.7	31.8	31.8	32.0
Error (°C)	.1	.1	.1	.1	.2
Subcooling (°C)	193.	193.	193.	194.	194.

Corrected Mass Flux ($kg/m^2 x sec$)

Calculated Value	Time(sec) 65.63	187.50	303.75	574.50	663.75
Volume Method	1.645e+04	1.644e+04	1.641e+04	1.631e+04	1.636e+04
Error (%)	.0	.0	.0	.0	.0
Weigh Tank	1.443e+04	1.551e+04	1.603e+04	1.613e+04	1.618e+04
Error (%)	.0	.0	.0	0.	0.
% Difference	12.3	5.6	2.3	1.1	1.1

Pressure Profile Summary (in kPa)

Distance from Entrance (cm)	Time(sec) 65.63	187.50	303.75	574.50	663.75	Drift (kPa)
.318	2283(2)	2293(2)	2304(1)	2328(1)	2336(1)	0
1.91	1929(1)	1938(1)	1946(1)	1963(1)	1969(1)	0
3.18	1450(2)	1455(1)	1462(1)	1475(1)	1481(1)	2
4.45	626(6)	629(4)	631(5)	636(4)	638(6)	-60
5.40	380(2)	381(1)	383(1)	387(2)	388(1)	2
5.72	287(2)	287(2)	289(2)	290(1)	292(1)	0
6.03	226(2)	226(1)	228(1)	229(2)	230(1)	0
exit	146(2)	147(2)	150(2)	150(2)	151(2)	0
outlet	124(0)	121(0)	121(0)	121(0)	121(0)	

RUN # 91 SUMMARY

Test Section Dimensions		Initial Test Section Temperatures	
.2540	mm Opening	25.2	°C Maximum
18.36	mm Width	24.9	°C Minimum
4.6634e-06	m^2 Area		
.5011	mm Hydraulic Diameter		

Stagnation State

Calculated Value	Time(sec) 99.53	120.19	170.89
Pressure(kPa)	2536.	2532.	2522.
Error (kpa)	1.	1.	1.
Temperature (°C)	25.2	25.5	25.6
Error (°C)	.1	.2	.1
Subcooling (°C)	200.	199.	199.

Corrected Mass Flux ($kg/m^2 x sec$)

Calculated Value	Time(sec) 99.53	120.19	170.89
Volume Method	2.829e+04	2.825e+04	2.813e+04
Error (%)	.0	.0	.0
Weigh Tank	2.616e+04	2.754e+04	2.822e+04
Error (%)	.0	.0	.0
% Difference	7.6	2.5	-.3

Pressure Profile Summary (in kPa)

Distance from Entrance (cm)	Time(sec) 99.53	120.19	170.89	Drift (kPa)
.318	1935(1)	1930(1)	1922(1)	0
1.91	1387(1)	1384(1)	1382(1)	0
3.18	964(2)	958(1)	955(1)	3
4.45	445(5)	443(4)	443(3)	-34
5.40	392(2)	384(1)	369(1)	-
5.72	213(2)	208(1)	207(2)	0
6.03	191(7)	183(1)	181(1)	-4
exit	121(1)	120(1)	118(1)	6
outlet	124(0)	118(0)	117(0)	

RUN # 92 SUMMARY

Test Section Dimensions
.2540 mm Opening
18.36 mm Width
4.6634e-06 m^2 Area
.5011 mm Hydraulic Diameter

Initial Test Section Temperatures
328.0 °C Maximum
308.3 °C Minimum

Stagnation State				
Calculated Value	Time(sec)			
	55.31	64.69	74.06	95.63
Pressure(kPa)	15798.	15802.	15803.	15787.
Error (kpa)	3.	2.	2.	4.
Temperature (°C)	334.4	334.9	334.9	334.2
Error (°C)	.6	.1	.2	.1
Subcooling (°C)	11.9	11.4	11.4	12.1

Corrected Mass Flux ($kg/m^2 x sec$)				
Calculated Value	Time(sec)			
	55.31	64.69	74.06	95.63
Volume Method	4.210e+04	4.099e+04	4.000e+04	3.881e+04
Error (%)	.0	.0	.0	.0
Weigh Tank	3.950e+04	4.392e+04	4.505e+04	3.933e+04
Error (%)	.0	.1	.1	.1
% Difference	6.2	-7.2	-12.6	-1.4

Pressure Profile Summary (in kPa)					
Distance from Entrance (cm)	Time(sec)				Drift (kPa)
	55.31	64.69	74.06	95.63	
.318	14134(36)	14255(31)	14328(20)	14401(3)	0
1.91	13889(36)	14010(31)	14083(20)	14155(3)	24
3.18	12058(22)	12128(18)	12169(12)	12260(9)	-2
4.45	10869(8)	10884(8)	10890(5)	10977(5)	-104
5.40	9074(60)	8922(50)	8809(41)	8522(33)	61
5.72	9281(49)	9116(48)	8992(40)	8633(44)	0
6.03	8367(76)	8143(62)	7986(47)	7625(38)	0
exit	8448(76)	8224(62)	8067(47)	7707(38)	0
outlet	124(0)	124(0)	124(0)	124(0)	

RUN # 93 SUMMARY

Test Section Dimensions
.2540 mm Opening
18.36 mm Width
4.6634e-06 m^2 Area
.5011 mm Hydraulic Diameter

Initial Test Section Temperatures
315.6 °C Maximum
306.9 °C Minimum

Stagnation State			
Calculated Value	Time(sec)		
	75.82	89.86	114.20
Pressure(kPa)	11831.	11837.	11835.
Error (kpa)	2.	2.	1.
Temperature (°C)	310.9	310.8	310.4
Error (°C)	.1	.1	.1
Subcooling (°C)	12.7	12.8	13.2

Corrected Mass Flux ($kg/m^2 x sec$)			
Calculated Value	Time(sec)		
	75.82	89.86	114.20
Volume Method	3.192e+04	3.216e+04	3.212e+04
Error (%)	.0	.0	.0
Weigh Tank	3.496e+04	3.434e+04	3.282e+04
Error (%)	.0	.0	.1
% Difference	-9.5	-6.8	-2.2

Pressure Profile Summary (in kPa)				
Distance from Entrance (cm)	Time(sec)			Drift (kPa)
	75.82	89.86	114.20	
.318	10832(3)	10837(3)	10843(2)	0
1.91	10151(4)	10153(2)	10159(2)	38
3.18	9767(2)	9763(3)	9765(2)	1
4.45	8969(3)	8961(5)	8932(13)	-95
5.40	-na-	-na-	-na-	-na-
5.72	7016(15)	7008(4)	6979(15)	0
6.03	6131(34)	6128(3)	6110(11)	0
exit	4073(55)	4072(3)	4056(7)	-12
outlet	260(237)	673(216)	762(16)	

RUN # 94 SUMMARY

Test Section Dimensions
.2540 mm Opening
18.36 mm Width
4.6634e-06 m^2 Area
.5011 mm Hydraulic Diameter

Initial Test Section Temperatures
322.0 °C Maximum
311.3 °C Minimum

Stagnation State				
Calculated Value	Time(sec)			
	99.38	108.75	129.38	180.94
Pressure(kPa)	11672.	11674.	11670.	11660.
Error (kpa)	3.	3.	3.	2.
Temperature (°C)	320.6	320.5	320.6	319.8
Error (°C)	.1	.1	.1	.1
Subcooling (°C)	1.9	2.0	1.9	2.7

Corrected Mass Flux ($kg/m^2 x sec$)				
Calculated Value	Time(sec)			
	99.38	108.75	129.38	180.94
Volume Method	1.981e+04	2.052e+04	2.032e+04	2.037e+04
Error (%)	.0	.0	.0	.0
Weigh Tank	2.078e+04	2.122e+04	2.082e+04	2.013e+04
Error (%)	.1	.0	.0	.0
% Difference	-4.9	-3.4	-2.5	1.2

Pressure Profile Summary (in kPa)					
Distance from Entrance (cm)	Time(sec)				Drift (kPa)
	99.38	108.75	129.38	180.94	
.318	8892(23)	8905(4)	8922(9)	8918(3)	0
1.91	8223(25)	8231(6)	8249(11)	8253(6)	0
3.18	7588(19)	7594(7)	7619(10)	7627(4)	0
4.45	6316(18)	6322(10)	6334(9)	6345(6)	-85
5.40	4781(11)	4753(11)	4716(12)	4596(6)	54
5.72	4717(14)	4721(5)	4727(7)	4721(3)	0
6.03	4170(18)	4194(24)	4189(27)	4189(26)	0
exit	2960(38)	2961(52)	2913(32)	2907(48)	0
outlet	335(180)	451(115)	491(17)	484(18)	

RUN # 95 SUMMARY

Test Section Dimensions
.2540 mm Opening
18.36 mm Width
4.6634e-06 m^2 Area
.5011 mm Hydraulic Diameter

Initial Test Section Temperatures
275.0 °C Maximum
263.3 °C Minimum

Stagnation State			
Calculated Value	Time(sec)		
	45.94	55.31	81.56
Pressure(kPa)	12429.	12423.	12239.
Error (kpa)	3.	3.	8.
Temperature (°C)	266.4	266.2	265.2
Error (°C)	.1	.2	.3
Subcooling (°C)	61.0	61.1	61.0

Corrected Mass Flux ($kg/m^2 x sec$)			
Calculated Value	Time(sec)		
	45.94	55.31	81.56
Volume Method	5.086e+04	5.118e+04	5.089e+04
Error (%)	.0	.0	.0
Weigh Tank	5.177e+04	4.955e+04	5.381e+04
Error (%)	.0	.0	.1
% Difference	-1.8	3.2	-5.7

Pressure Profile Summary (in kPa)				
Distance from Entrance (cm)	Time(sec)			Drift (kPa)
	45.94	55.31	81.56	
.318	9353(3)	9351(3)	9288(10)	0
1.91	9137(3)	9135(3)	9072(10)	105
3.18	6991(5)	6982(4)	6998(23)	24
4.45	5531(6)	5517(7)	5564(32)	-105
5.40	-na-	-na-	-na-	-na-
5.72	5037(6)	5025(5)	5076(21)	0
6.03	5083(5)	5069(6)	5081(14)	0
exit	4066(15)	4042(7)	4042(12)	4
outlet	317(350)	935(196)	957(21)	

RUN # 96 SUMMARY

Test Section Dimensions
.2540 mm Opening
18.36 mm Width
4.6634e-06 m^2 Area
.5011 mm Hydraulic Diameter

Initial Test Section Temperatures
306.4 °C Maximum
294.0 °C Minimum

Stagnation State				
Calculated Value	Time(sec)			
	85.31	103.13	129.38	157.50
Pressure(kPa)	11638.	11641.	11634.	11623.
Error (kpa)	2.	2.	3.	3.
Temperature (°C)	296.2	296.0	295.4	293.0
Error (°C)	.1	.1	.2	.3
Subcooling (°C)	26.1	26.3	26.9	29.2

Corrected Mass Flux (kg/m^2xsec)				
Calculated Value	Time(sec)			
	85.31	103.13	129.38	157.50
Volume Method	3.842e+04	3.892e+04	3.873e+04	3.833e+04
Error (%)	.0	.0	.0	.0
Weigh Tank	4.107e+04	3.775e+04	4.163e+04	3.299e+04
Error (%)	.0	.1	.1	.1
% Difference	-6.9	3.0	-7.5	13.9

Pressure Profile Summary (in kPa)					
Distance from Entrance (cm)	Time(sec)				Drift (kPa)
	85.31	103.13	129.38	157.50	
.318	10124(2)	10130(3)	10154(7)	10193(4)	0
1.91	9222(2)	9221(2)	9255(9)	9321(7)	-21
3.18	8645(3)	8638(3)	8678(11)	8766(10)	3
4.45	7790(5)	7774(4)	7828(15)	7925(10)	-98
5.40	-na-	-na-	-na-	-na-	-na-
5.72	7194(5)	7188(2)	7120(21)	6908(29)	0
6.03	6671(11)	6652(5)	6580(18)	6377(30)	0
exit	4648(15)	4640(6)	4547(14)	4401(20)	4
outlet	758(248)	868(34)	855(24)	821(21)	

RUN # 97 SUMMARY

Test Section Dimensions
.2540 mm Opening
18.36 mm Width
4.6634e-06 m^2 Area
.5011 mm Hydraulic Diameter

Initial Test Section Temperatures
338.0 °C Maximum
325.3 °C Minimum

Stagnation State			
Calculated Value	Time(sec)		
	55.23	71.14	96.41
Pressure(kPa)	15753.	15748.	15721.
Error (kpa)	2.	3.	3.
Temperature (°C)	334.5	334.4	333.5
Error (°C)	.1	.1	.2
Subcooling (°C)	11.6	11.7	12.4

Corrected Mass Flux (kg/m^2xsec)			
Calculated Value	Time(sec)		
	55.23	71.14	96.41
Volume Method	3.646e+04	3.685e+04	3.674e+04
Error (%)	.0	.0	.0
Weigh Tank	3.928e+04	4.248e+04	4.015e+04
Error (%)	.1	.0	.1
% Difference	-7.7	-15.3	-9.3

Pressure Profile Summary (in kPa)				
Distance from Entrance (cm)	Time(sec)			Drift (kPa)
	55.23	71.14	96.41	
.318	14405(2)	14398(3)	14388(5)	0
1.91	13385(4)	13364(4)	13360(5)	0
3.18	13016(8)	12988(6)	12975(3)	0
4.45	11299(31)	11266(6)	11147(28)	-93
5.40	8811(71)	8700(10)	8712(38)	52
5.72	8216(43)	8194(10)	8152(14)	0
6.03	7253(76)	7206(48)	7188(34)	0
exit	4904(65)	4823(67)	4774(57)	93
outlet	1025(21)	1014(22)	1003(16)	

RUN # 98 SUMMARY

Test Section Dimensions
.2540 mm Opening
18.36 mm Width
4.6634e-06 m^2 Area
.5011 mm Hydraulic Diameter

Initial Test Section Temperatures
262.8 °C Maximum
249.1 °C Minimum

Stagnation State

Calculated Value	Time(sec) 75.94	88.13	114.38
Pressure(kPa)	9769.	9782.	9785.
Error (kpa)	4.	3.	2.
Temperature (°C)	251.4	251.3	250.9
Error (°C)	.1	.2	.1
Subcooling (°C)	57.8	58.0	58.4

Corrected Mass Flux ($kg/m^2 x sec$)

Calculated Value	Time(sec) 75.94	88.13	114.38
Volume Method	4.850e+04	4.883e+04	4.900e+04
Error (%)	.0	.0	.0
Weigh Tank	5.184e+04	4.592e+04	5.185e+04
Error (%)	.0	.0	.1
% Difference	-6.9	6.0	-5.8

Pressure Profile Summary (in kPa)

Distance from Entrance (cm)	Time(sec) 75.94	88.13	114.38	Drift (kPa)
.318	7706(5)	7719(2)	7725(2)	0
1.91	6461(4)	7538(2)	7544(2)	0
3.18	5536(3)	5534(3)	5529(3)	3
4.45	4406(4)	4400(5)	4391(5)	-72
5.40	-na-	-na-	-na-	-na-
5.72	3974(3)	3959(7)	3958(5)	0
6.03	3993(4)	3990(4)	3981(3)	0
exit	3237(10)	3232(5)	3211(5)	0
outlet	802(112)	794(160)	834(8)	

RUN # 99 SUMMARY

Test Section Dimensions
.2540 mm Opening
18.36 mm Width
4.6634e-06 m^2 Area
.5011 mm Hydraulic Diameter

Initial Test Section Temperatures
308.2 °C Maximum
301.6 °C Minimum

Stagnation State

Calculated Value	Time(sec) 59.06	68.44	120.94	151.88
Pressure(kPa)	9614.	9611.	9576.	9559.
Error (kpa)	1.	3.	3.	2.
Temperature (°C)	308.2	308.2	307.9	306.8
Error (°C)	.1	.1	.1	.2
Subcooling (°C)	0.	0.	0.	.9

Corrected Mass Flux ($kg/m^2 x sec$)

Calculated Value	Time(sec) 59.06	68.44	120.94	151.88
Volume Method	2.222e+04	2.250e+04	2.240e+04	2.237e+04
Error (%)	.0	.0	.0	.0
Weigh Tank	2.286e+04	2.160e+04	2.079e+04	2.175e+04
Error (%)	.0	.0	.0	.0
% Difference	-2.9	4.0	7.2	2.8

Pressure Profile Summary (in kPa)

Distance from Entrance (cm)	Time(sec) 59.06	68.44	120.94	151.88	Drift (kPa)
.318	9117(1)	9115(3)	9087(3)	9068(3)	0
1.91	8477(3)	8469(4)	8445(2)	8437(2)	22
3.18	7825(4)	7818(6)	7801(5)	7814(3)	-0
4.45	6583(12)	6579(8)	6567(7)	6596(5)	-67
5.40	-na-	-na-	-na-	-na-	-na-
5.72	4850(14)	4846(7)	4828(3)	4848(5)	0
6.03	4334(4)	4328(14)	4312(2)	4330(4)	0
exit	2982(8)	2967(40)	2917(6)	2930(5)	-15
outlet	425(129)	489(10)	466(18)	478(28)	

RUN #100 SUMMARY

Test Section Dimensions
.2540 mm Opening
18.36 mm Width
4.6634e-06 m^2 Area
.5011 mm Hydraulic Diameter

Initial Test Section Temperatures
345.9 °C Maximum
333.5 °C Minimum

Stagnation State				
Calculated Value	Time(sec)			
	111.56	123.75	157.50	186.56
Pressure(kPa)	15736.	15738.	15720.	15705.
Error (kpa)	3.	4.	4.	2.
Temperature (°C)	345.7	345.7	344.9	343.7
Error (°C)	.1	.1	.2	.1
Subcooling (°C)	.3	.3	1.0	2.1

Corrected Mass Flux ($kg/m^2 x sec$)				
Calculated Value	Time(sec)			
	111.56	123.75	157.50	186.56
Volume Method	2.985e+04	3.051e+04	3.076e+04	3.284e+04
Error (%)	.0	.0	.0	.0
Weigh Tank	3.106e+04	3.330e+04	3.527e+04	3.355e+04
Error (%)	.0	.1	.1	.1
% Difference	-4.1	-9.1	-14.7	-2.2

Pressure Profile Summary (in kPa)					
Distance from Entrance (cm)	Time(sec)				Drift (kPa)
	111.56	123.75	157.50	186.56	
.318	14620(3)	14620(4)	14610(4)	14599(1)	0
1.91	14359(3)	14358(4)	14348(4)	14338(1)	0
3.18	12129(25)	12088(10)	12090(5)	12114(1)	0
4.45	9916(35)	9871(9)	9891(6)	9916(4)	-95
5.40	-na-	-na-	-na-	-na-	-na-
5.72	7144(39)	7117(12)	7135(13)	7117(6)	0
6.03	6302(40)	6286(7)	6288(4)	6249(1)	0
exit	4358(15)	4335(17)	4245(8)	4147(7)	0
outlet	136(19)	714(306)	889(28)	717(5)	

RUN #101 SUMMARY

Test Section Dimensions
.2540 mm Opening
18.36 mm Width
4.6634e-06 m^2 Area
.5011 mm Hydraulic Diameter

Initial Test Section Temperatures
26.2 °C Maximum
25.6 °C Minimum

Stagnation State			
Calculated Value	Time(sec)		
	86.25	118.13	179.06
Pressure(kPa)	2569.	2577.	2591.
Error (kpa)	1.	1.	1.
Temperature (°C)	25.5	25.5	25.4
Error (°C)	.1	.1	.1
Subcooling (°C)	200.	200.	200.

Corrected Mass Flux ($kg/m^2 x sec$)			
Calculated Value	Time(sec)		
	86.25	118.13	179.06
Volume Method	2.740e+04	2.745e+04	2.739e+04
Error (%)	.0	.0	.0
Weigh Tank	2.687e+04	2.717e+04	2.731e+04
Error (%)	.0	.0	.0
% Difference	1.9	1.0	.3

Pressure Profile Summary (in kPa)				
Distance from Entrance (cm)	Time(sec)			Drift (kPa)
	86.25	118.13	179.06	
.318	1760(1)	1765(1)	1770(1)	0
1.91	1325(1)	1329(1)	1333(1)	0
3.18	905(1)	907(1)	911(1)	2
4.45	456(8)	456(9)	454(4)	-21
5.40	-na-	-na-	-na-	-na-
5.72	191(1)	190(1)	191(1)	0
6.03	162(2)	161(1)	161(2)	-5
exit	111(2)	111(1)	111(2)	7
outlet	125(0)	125(0)	125(0)	

APPENDIX B

Pressure Profiles

This appendix contains graphs of the pressure profile data for those runs which were used for comparison with the theoretical model described in Chapter V. Missing runs exhibited features which shed serious doubt on the validity of the data. The plotted data points were obtained from the data summaries given in Appendix A. A dashed line has been faired through the data. Pressure profiles, for each run, predicted by the Homogeneous Nonequilibrium Model (described in Chapter V), are also shown (as solid lines) for comparison with the data. The appendix is divided into four sections. The first three sections present data for critical flow; each section contains graphs for a particular nominal slit size. Cold water calibration data are presented in the last section. Within each of the first three sections, the graphs are ordered by increasing pressure and then decreasing subcooling within each nominal pressure level. This is the same ordering as has been used for Tables 5-4 through 5-15. Each graph includes a legend, showing run number, stagnation state, and other pertinent information.

Data points were plotted with a confidence bar showing the uncertainty interval. The height of the bar is three times (3X) the rms error indicated in Appendix A. A factor of three was used to roughly correspond to a confidence level of 99%. In most instances, the confidence bars are smaller that the data point and cannot be seen in the scale of these graphs.

The location of flashing inception which may be inferred from the measured pressure profile has also been indicated on each graph by a vertical line and a circle on the abscissa. The procedure by which this estimate was made is described in Chapter IV. When flashing occurred at the channel exit, the pressure profile is linear and no flashing location is indicated. A pressure profile which shows no linear portion indicates flashing at the entrance; in these cases the location of flashing inception has also not been marked. In a few instances, the pressure profiles show extremely anaomalous behavior and it was not possible to locate the point where flashing began.

Pressure profile predictions generally lie above the data points. This reflects the tendency of the HNEM to underpredict the critical mass flux. Underprediction of the mass flux results in an underprediction of both the entry loss and the frictional pressure pressure drop. Thus, pressures within the slit are overpredicted. The predicted point of flashing inception is indicated by the sudden increase in the slope of the predicted pressure profile.

SECTION I

0.381 mm Nominal Slit Opening

PRESSURE PROFILE, 59

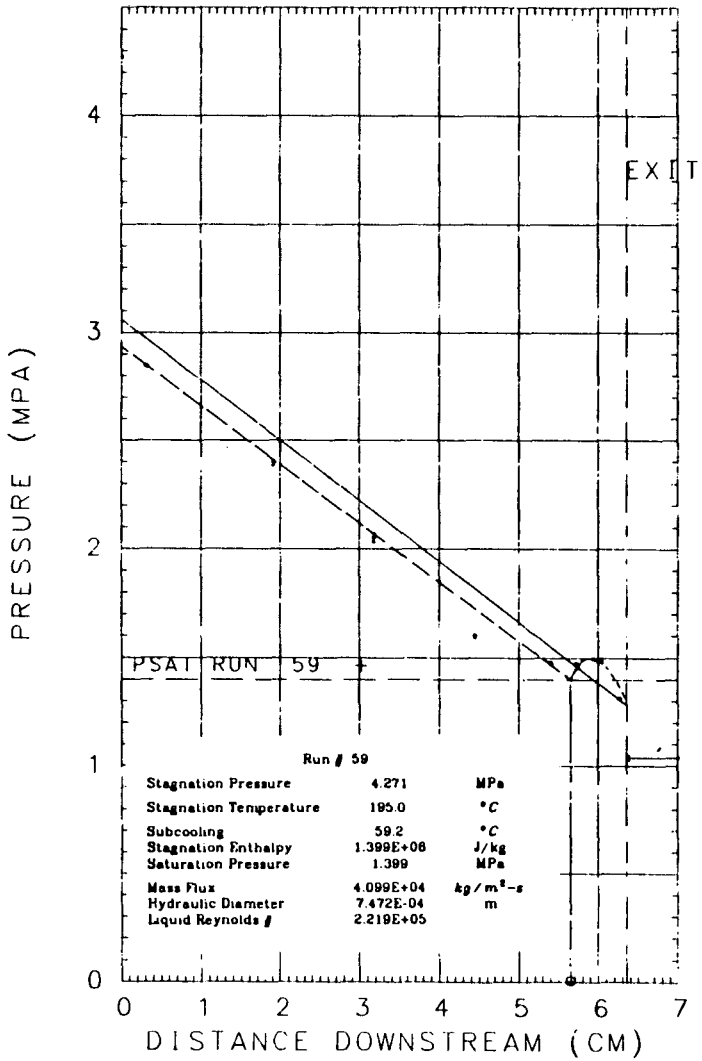

PRESSURE PROFILE, 57

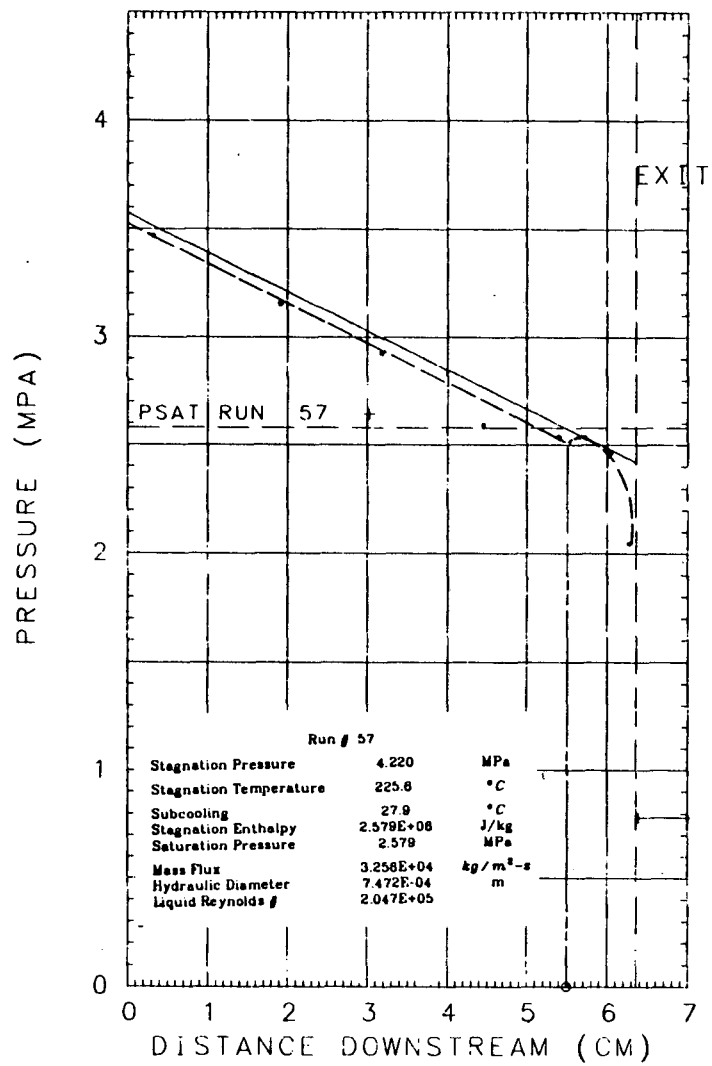

XBL 838-11053

PRESSURE PROFILE, 58

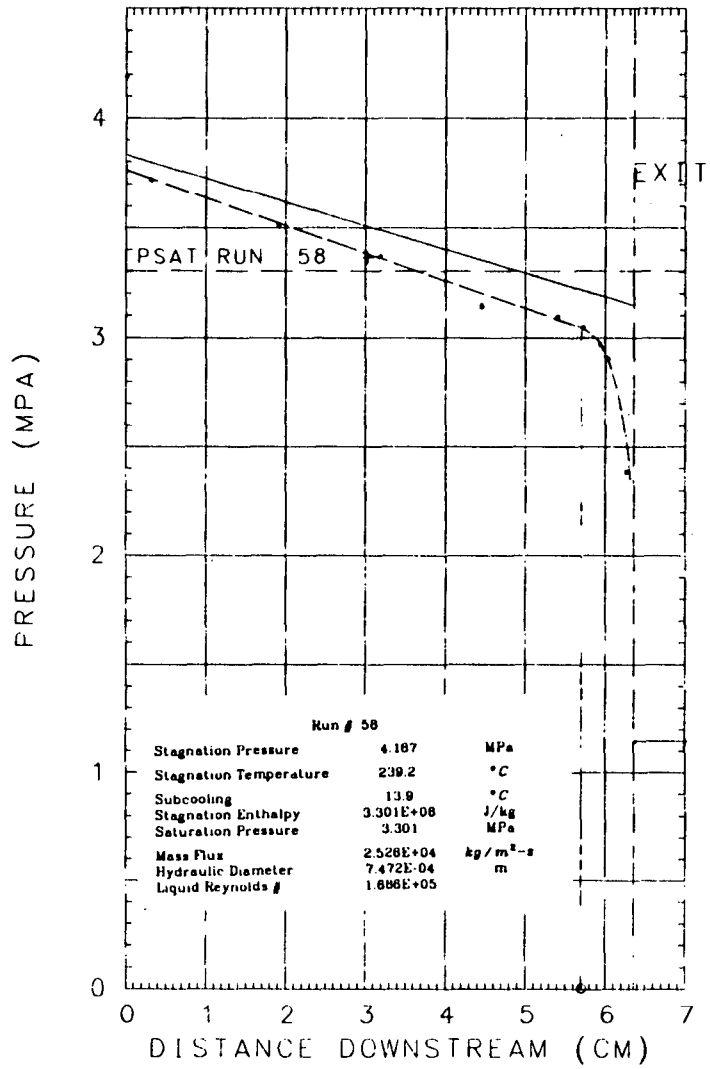

PRESSURE PROFILE, 60

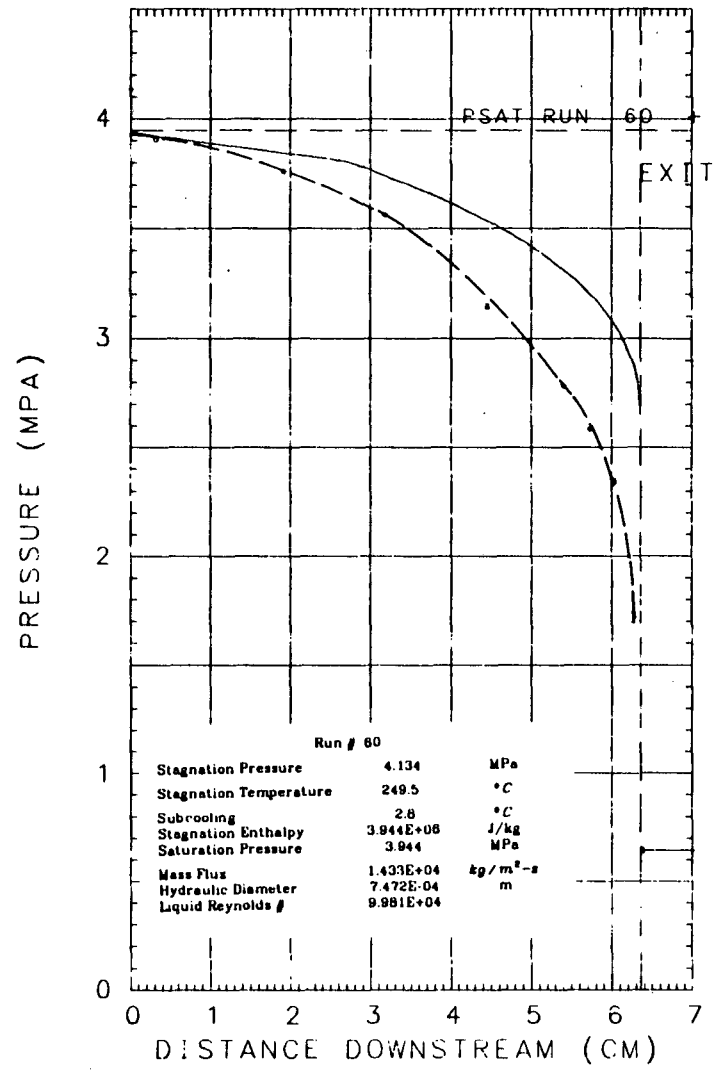

XBL 838-11052

PRESSURE PROFILE, 30

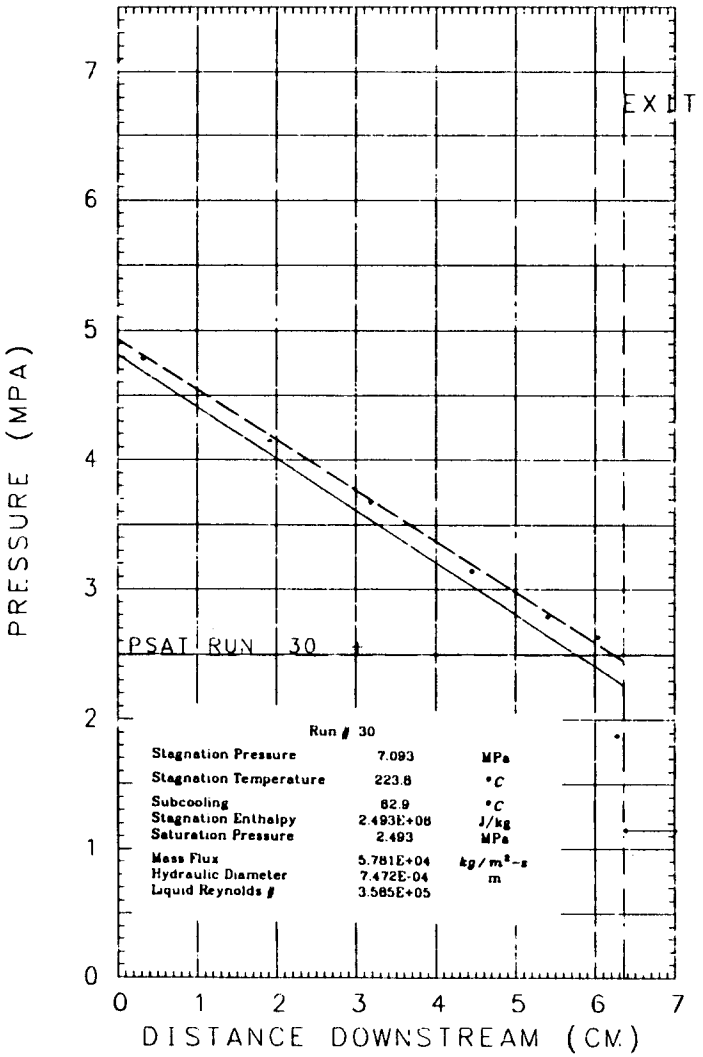

PRESSURE PROFILE, 27

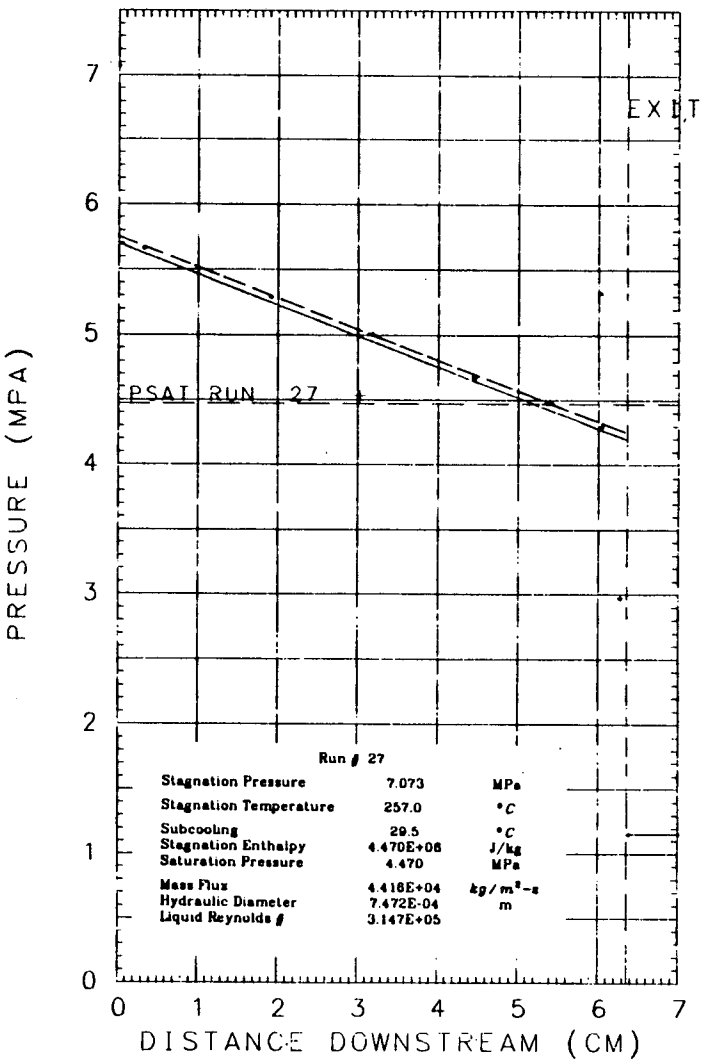

-- XBL 838-11032 --

PRESSURE PROFILE, 28

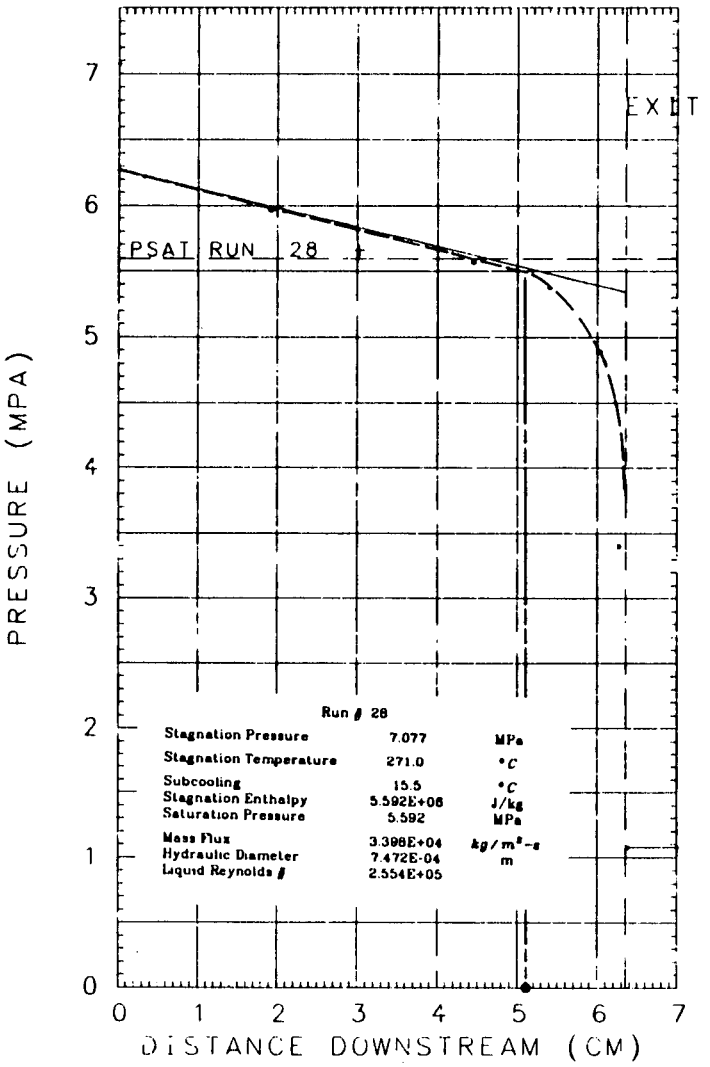

PRESSURE PROFILE, 29

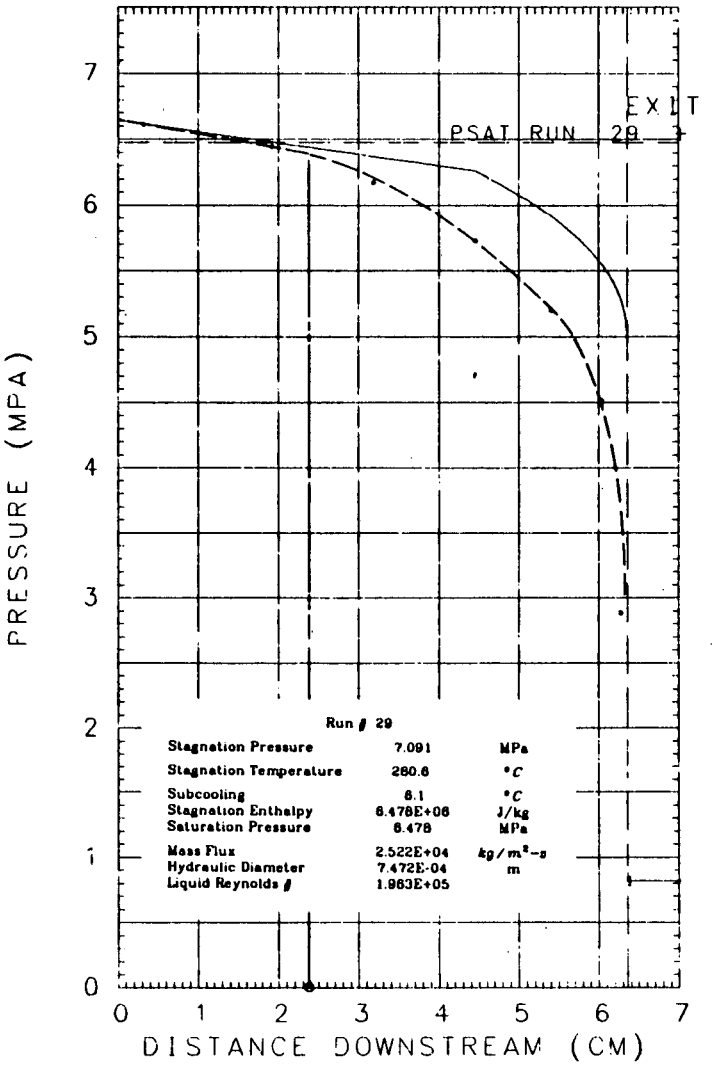

XBL 838-11031

PRESSURE PROFILE, 41

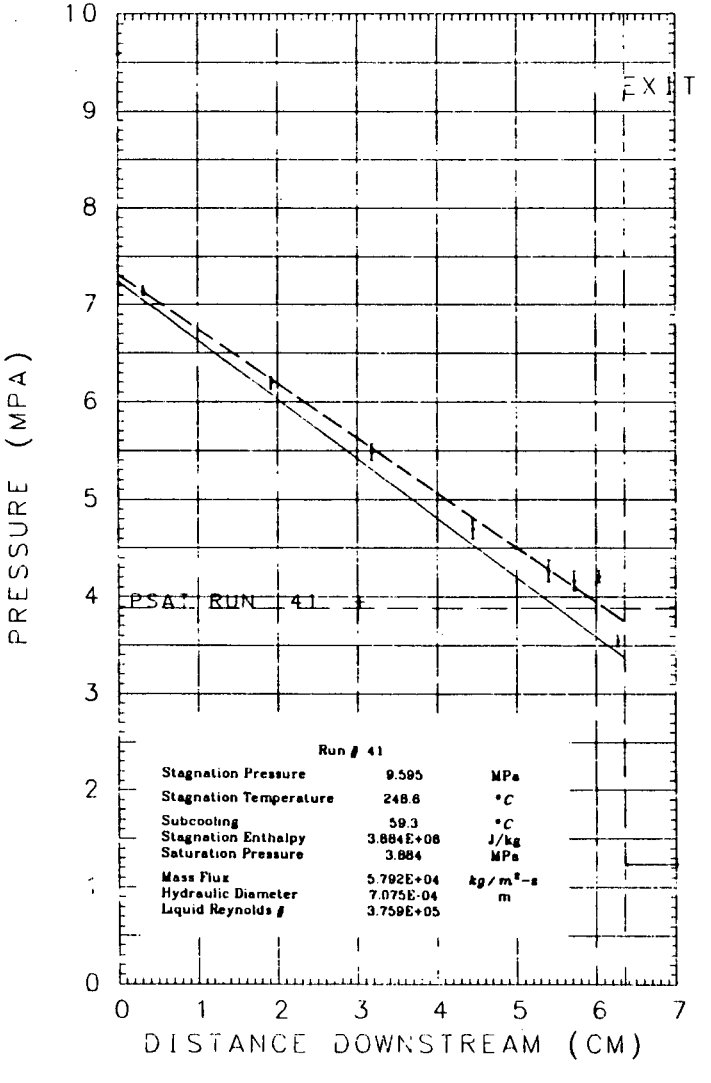

PRESSURE PROFILE, 43

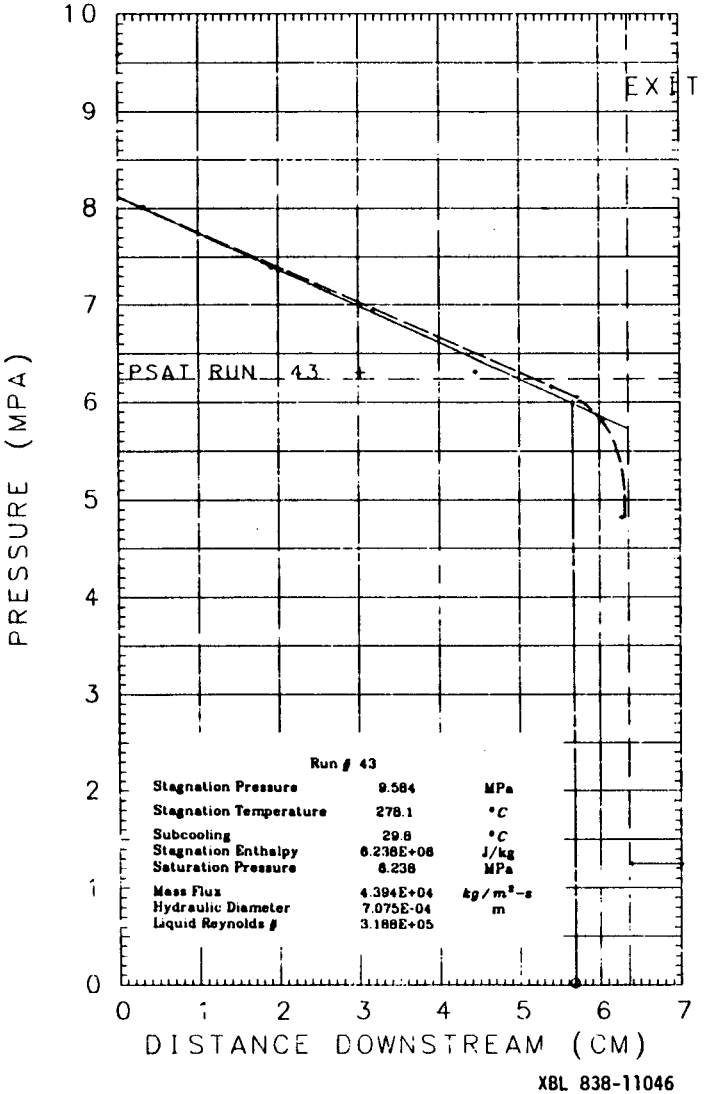

XBL 838-11046

PRESSURE PROFILE, 44

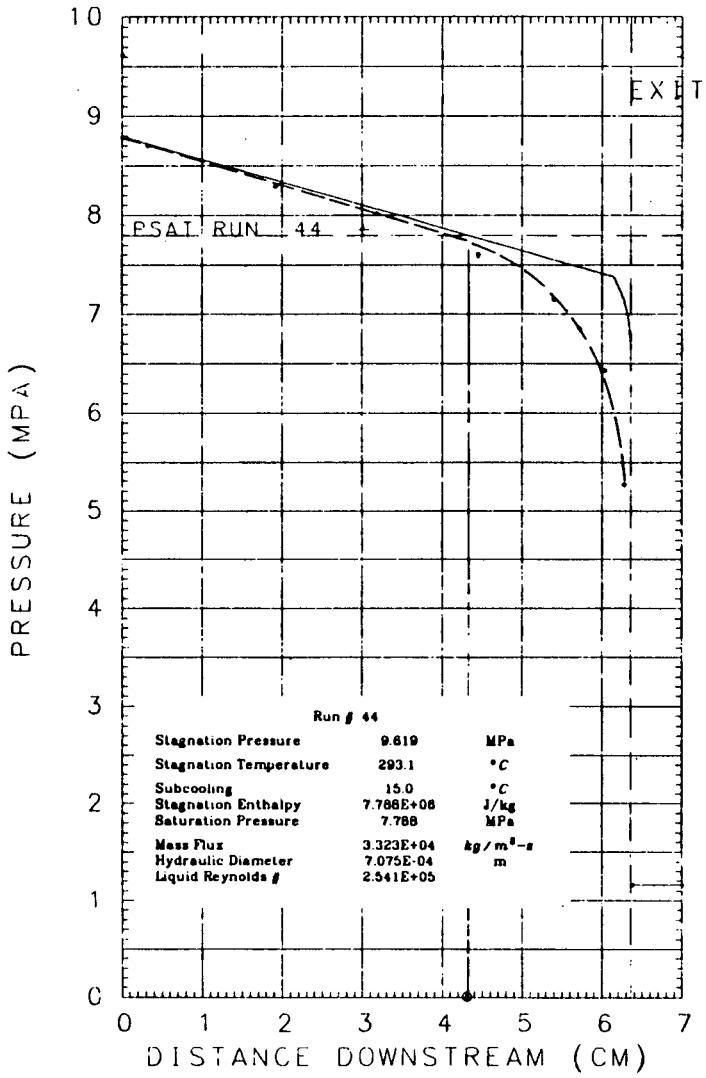

PRESSURE PROFILE, 75

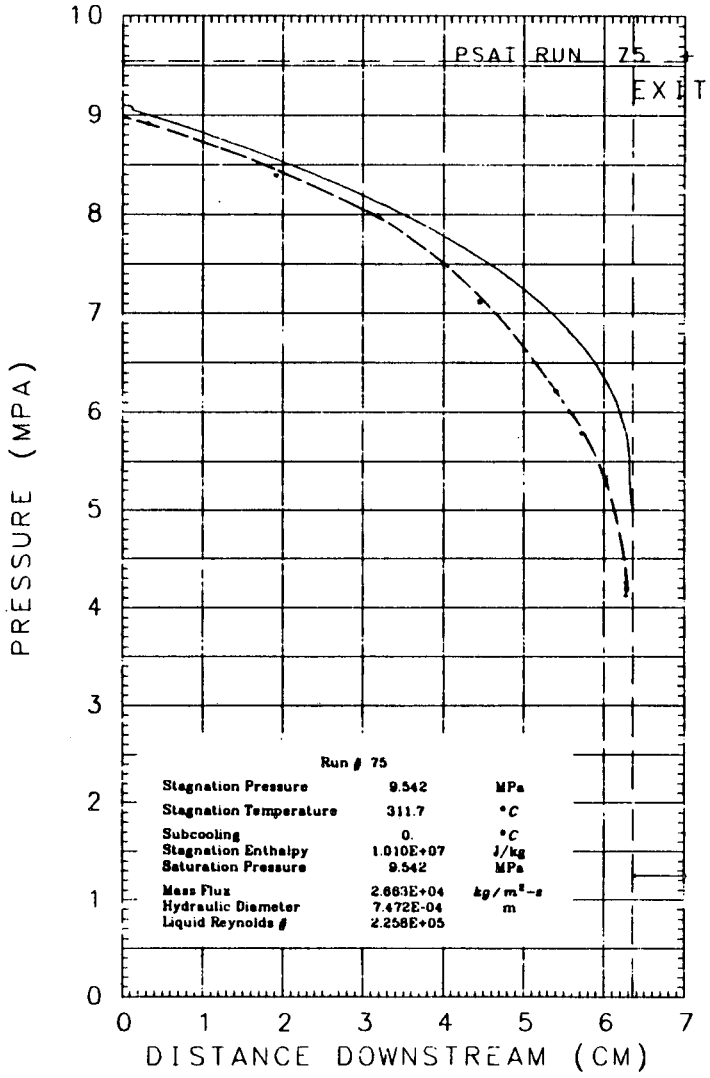

XBL 838-11047

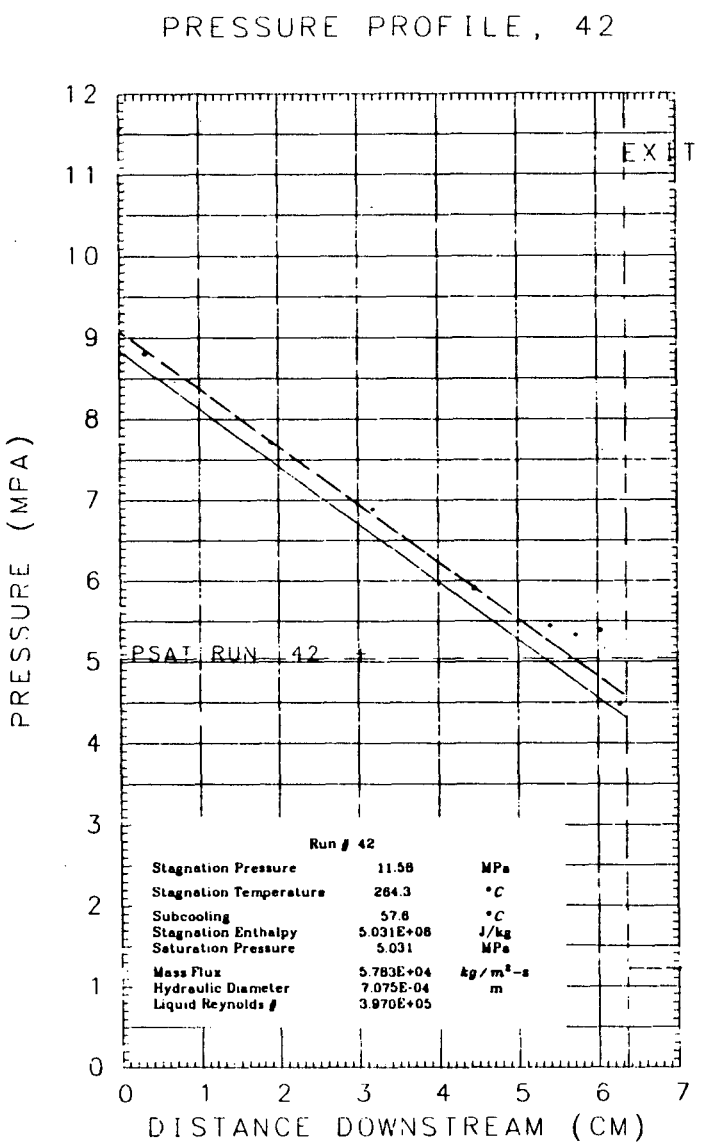

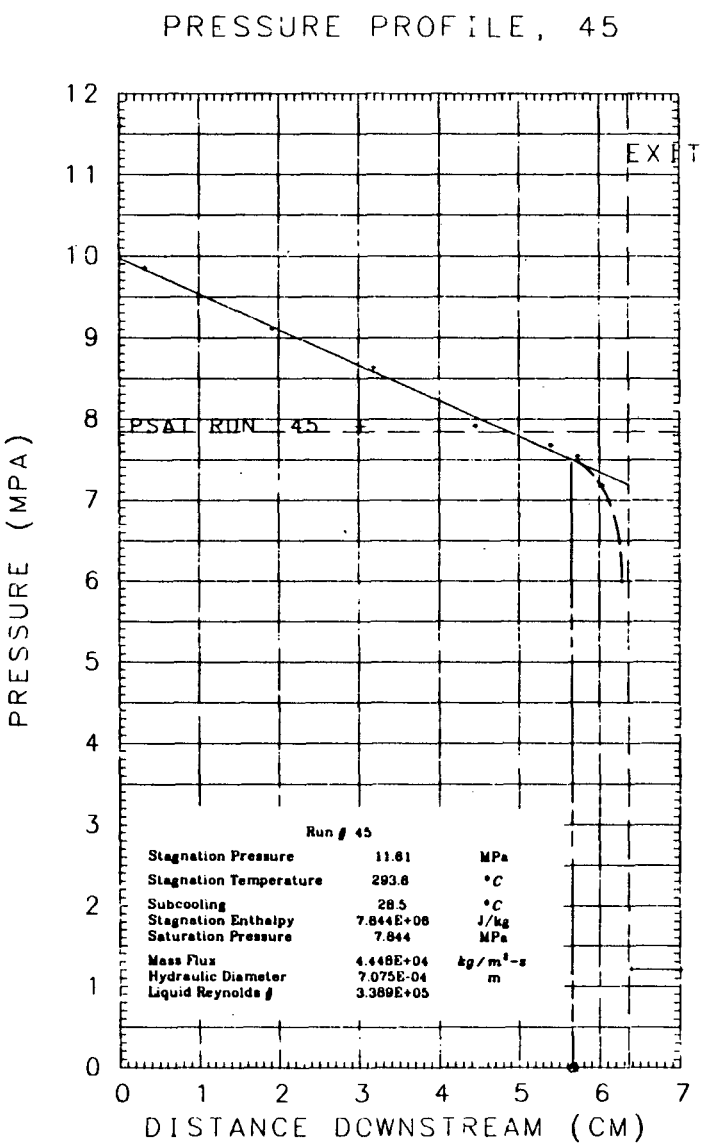

XBL 838-11048

PRESSURE PROFILE, 76

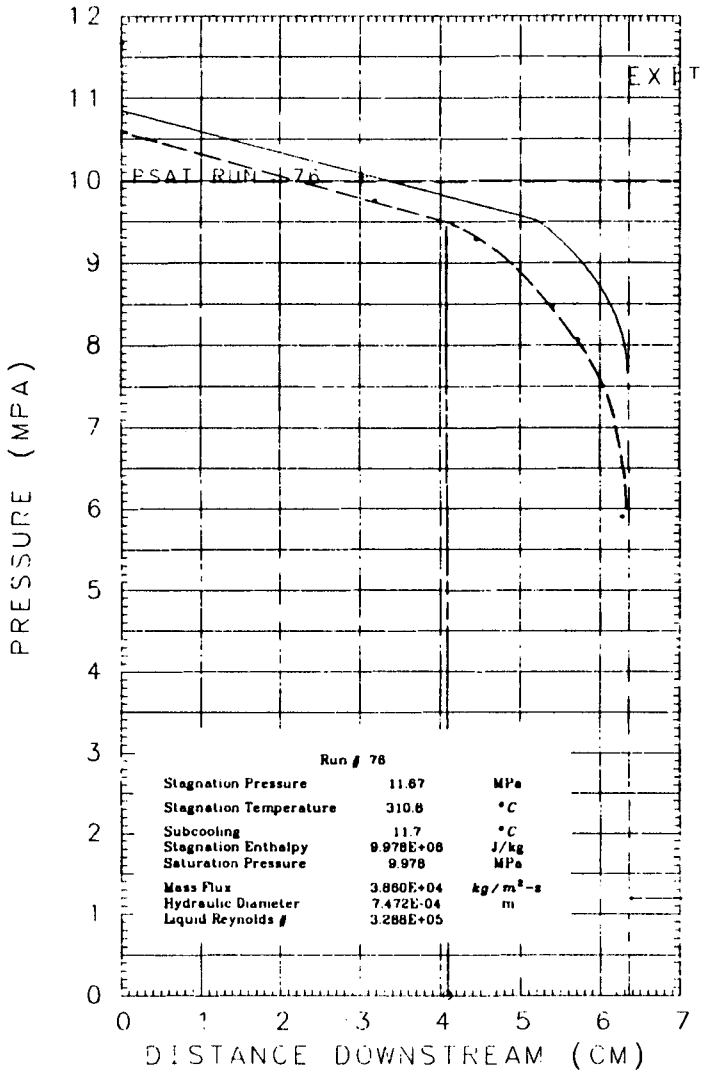

PRESSURE PROFILE, 79

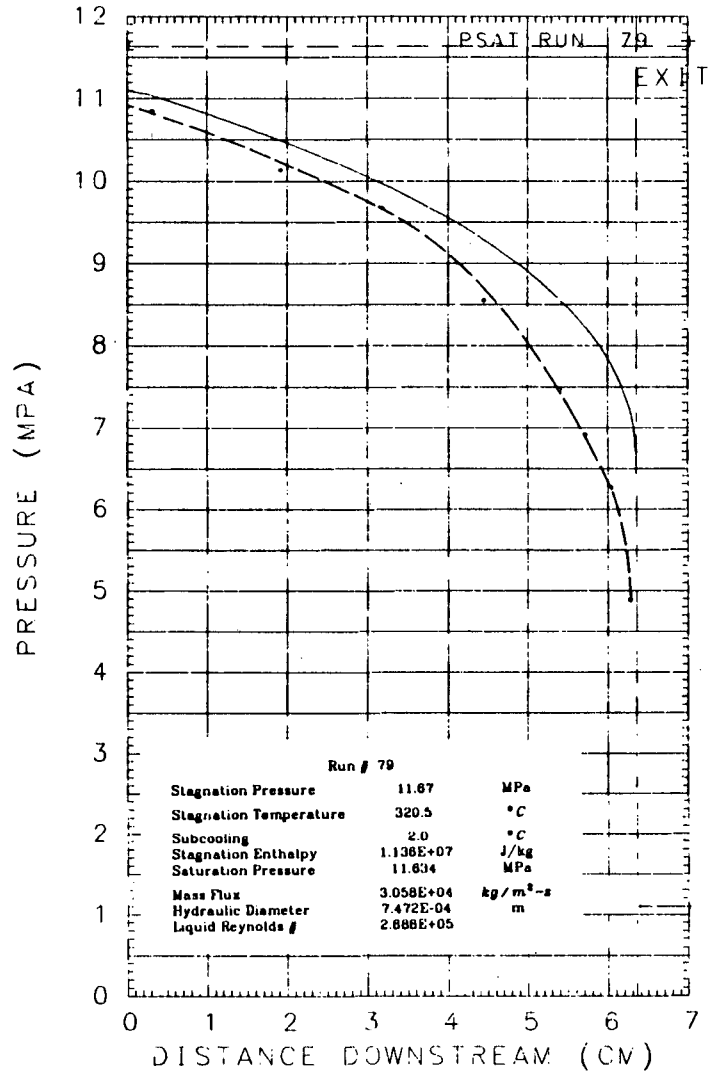

XBL 838-11059

PRESSURE PROFILE, 74

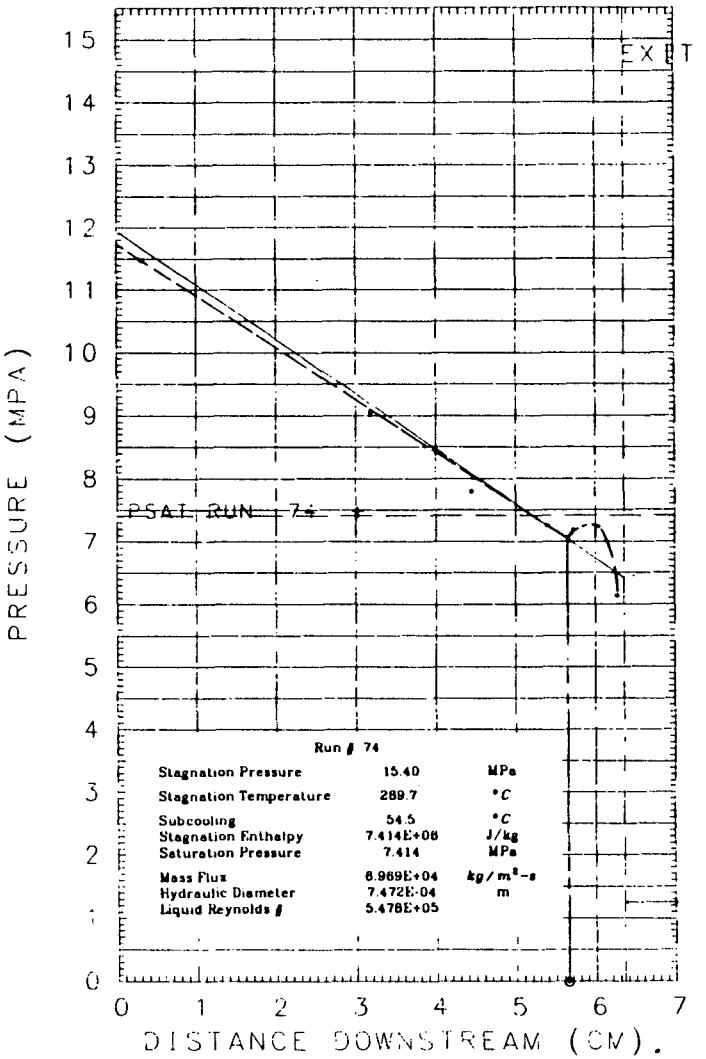

PRESSURE PROFILE, 78

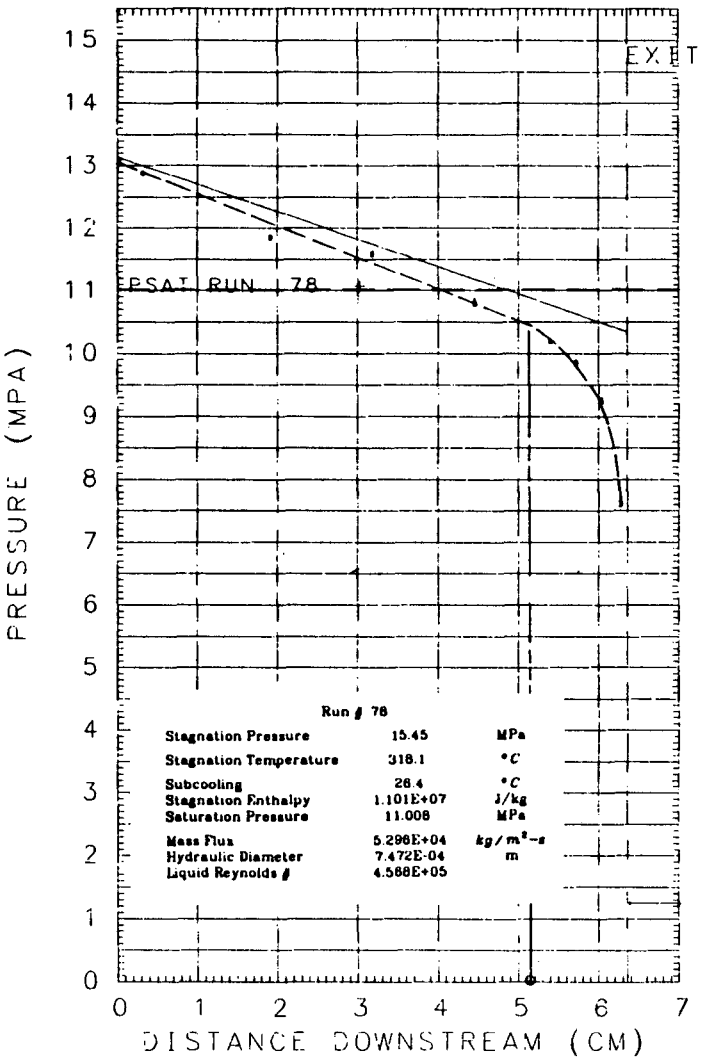

XBL 838-11058

SECTION II

0.254 mm Nominal Slit Opening

PRESSURE PROFILE, 68

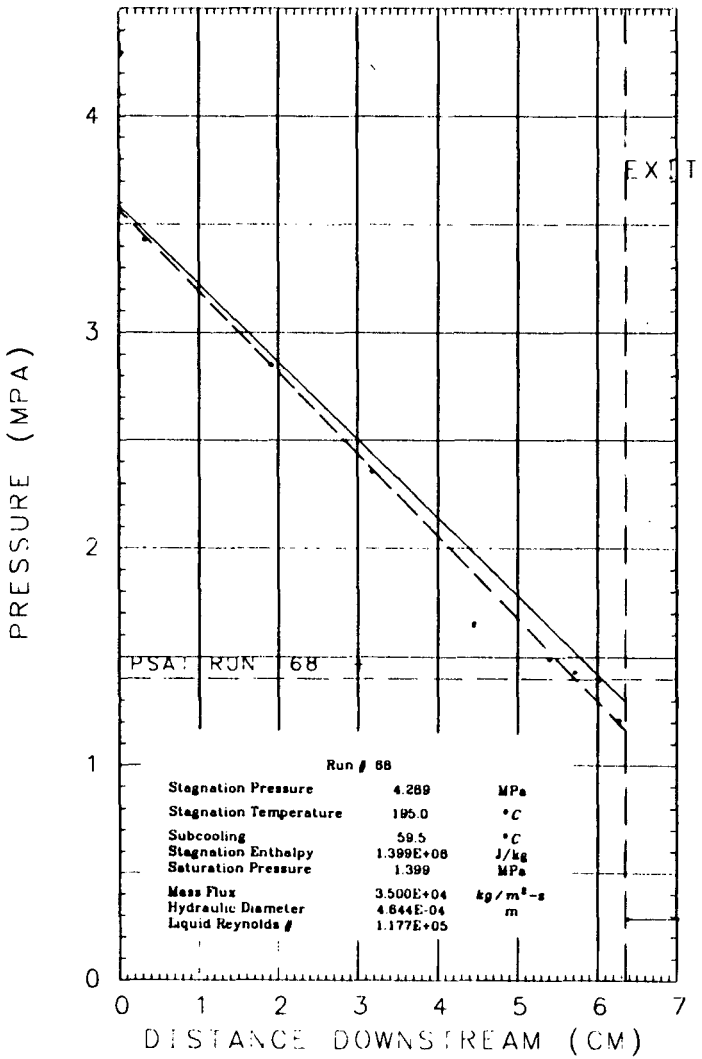

PRESSURE PROFILE, 70

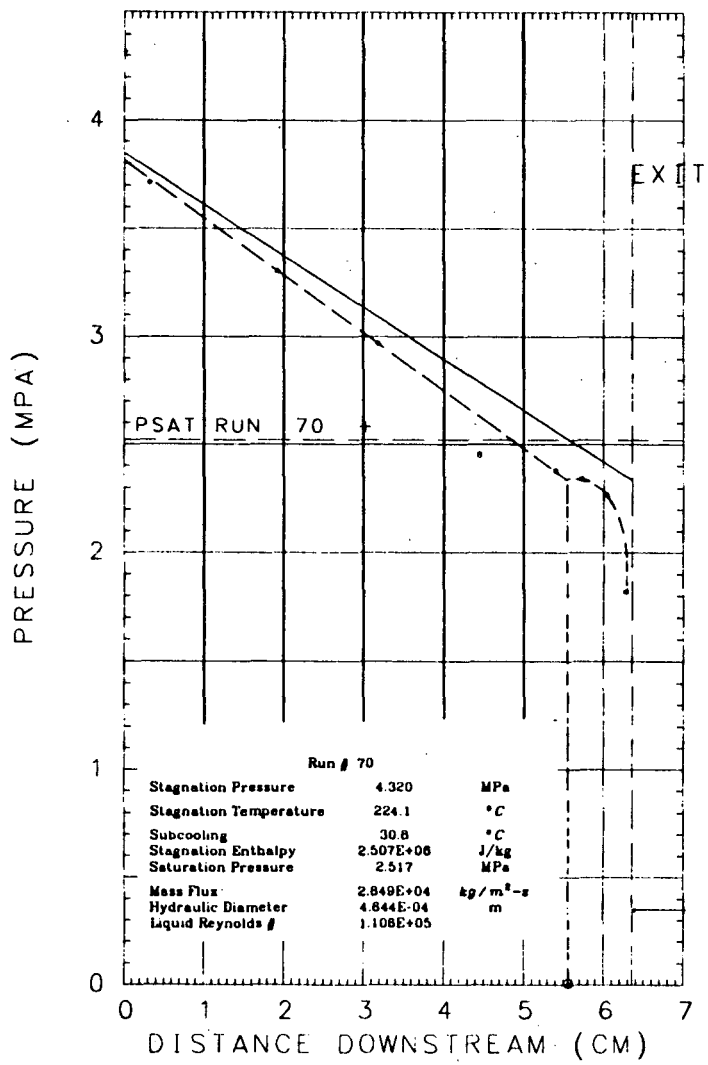

XBL 838-11056

PRESSURE PROFILE, 69

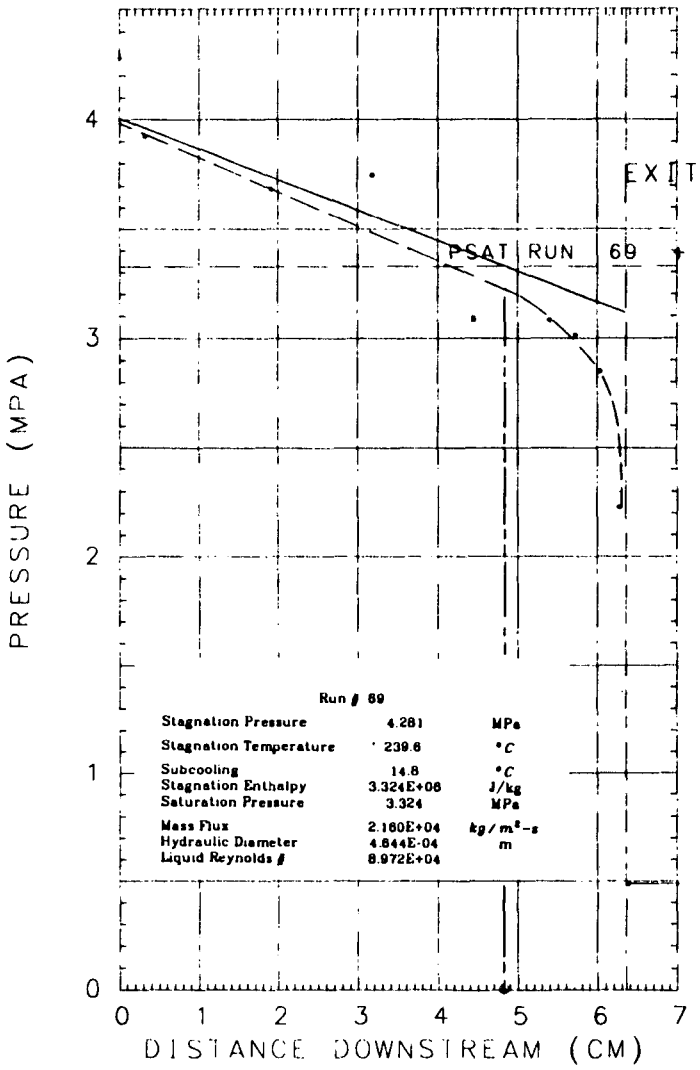

PRESSURE PROFILE, 71

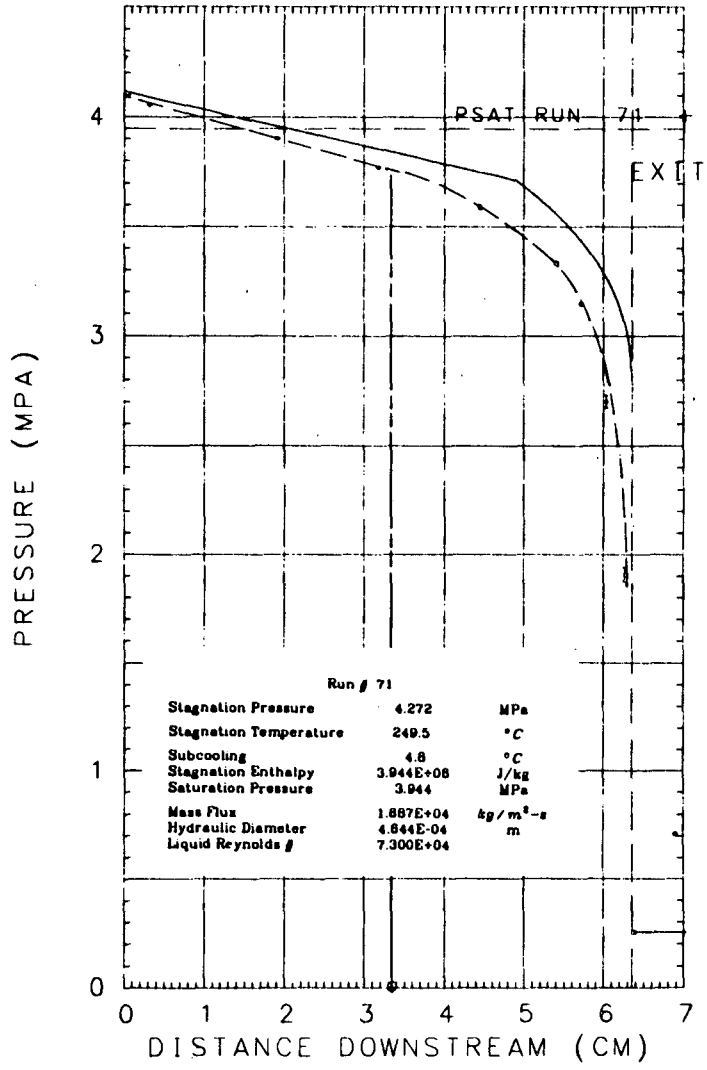

XBL 838-11057

PRESSURE PROFILE, 51

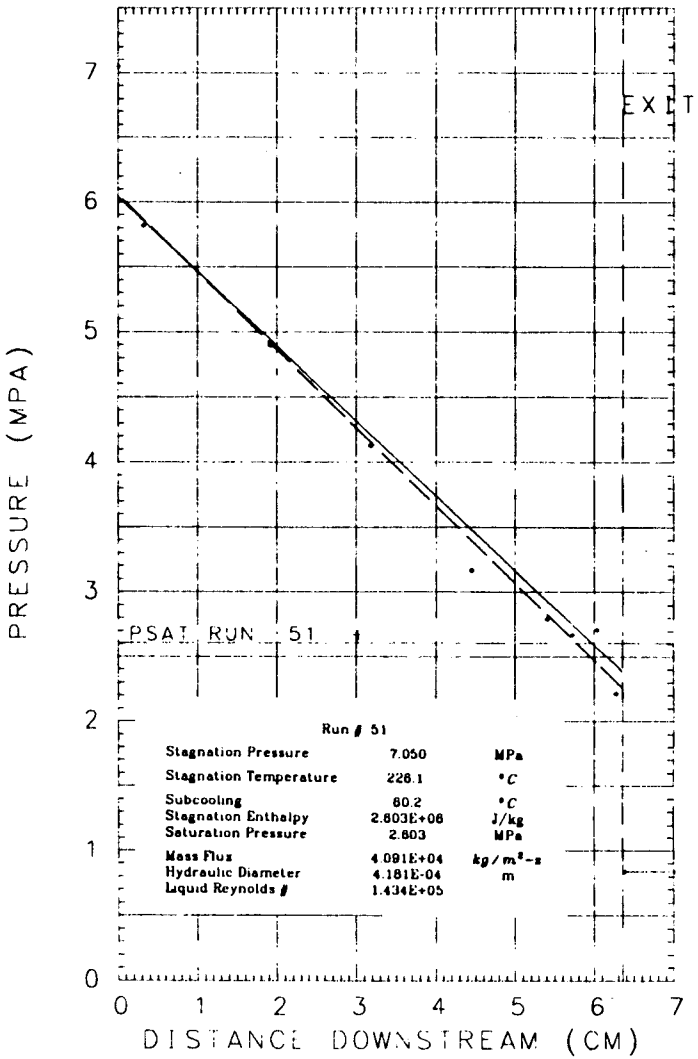

PRESSURE PROFILE, 24

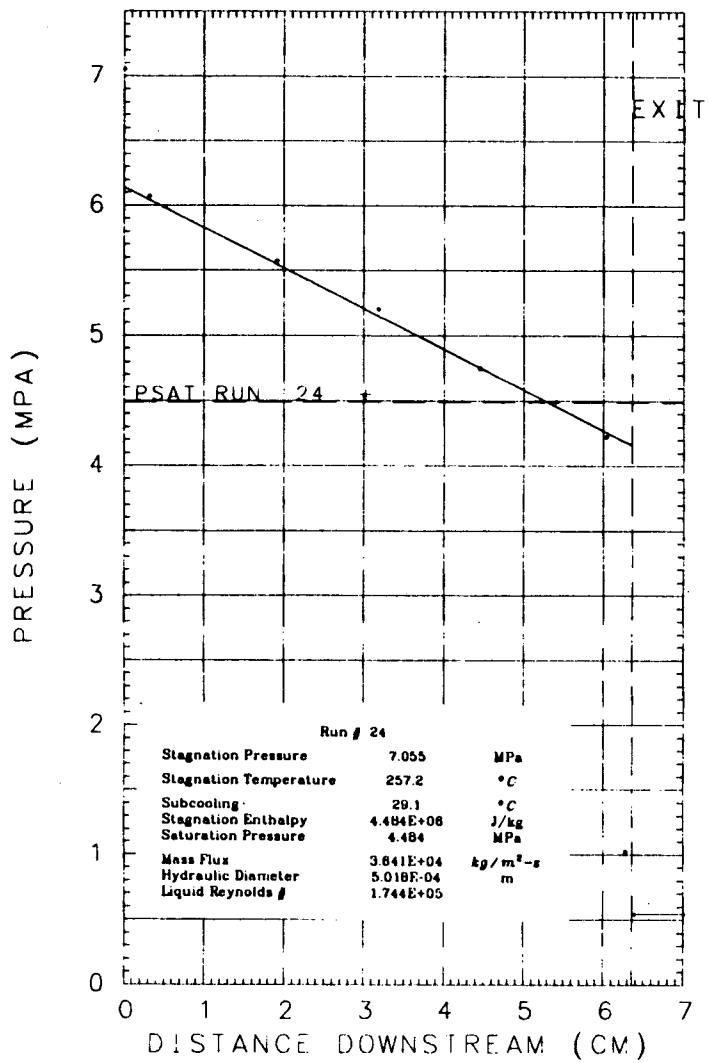

XBL 838-11050

PRESSURE PROFILE, 25

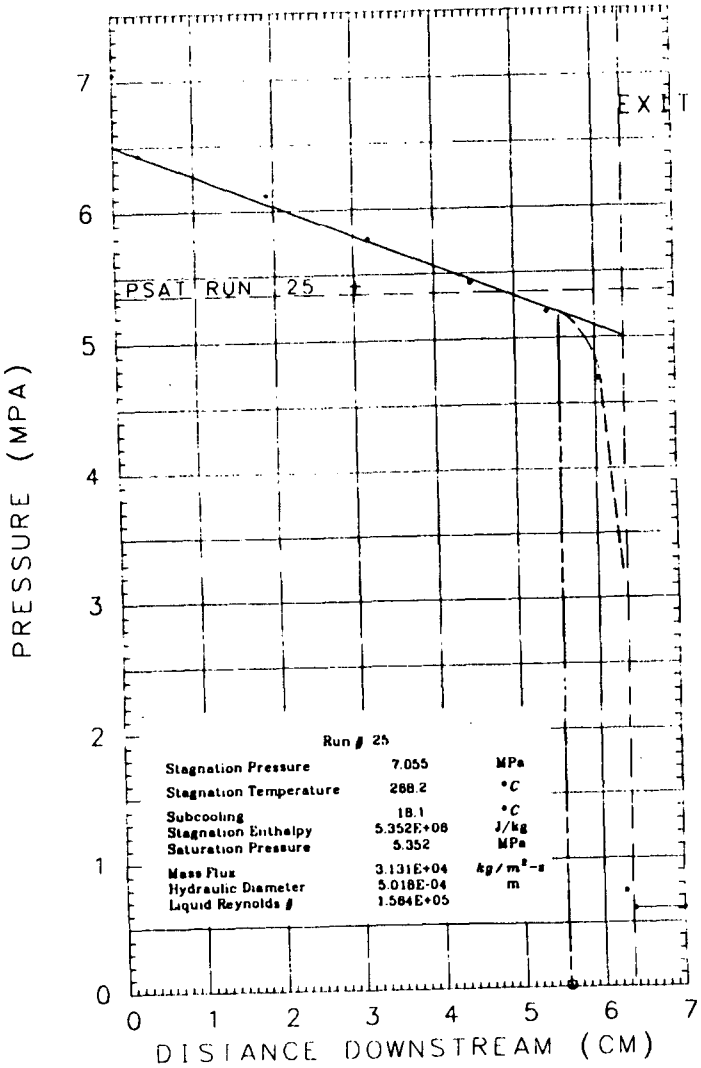

PRESSURE PROFILE, 26

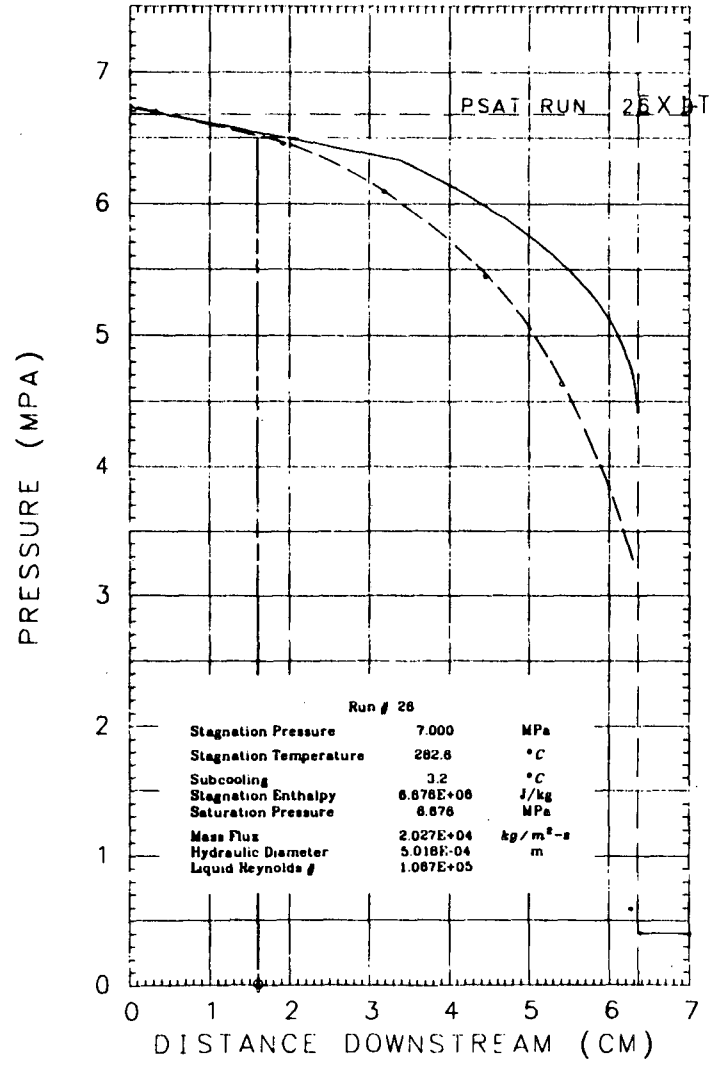

XBL 838-11041

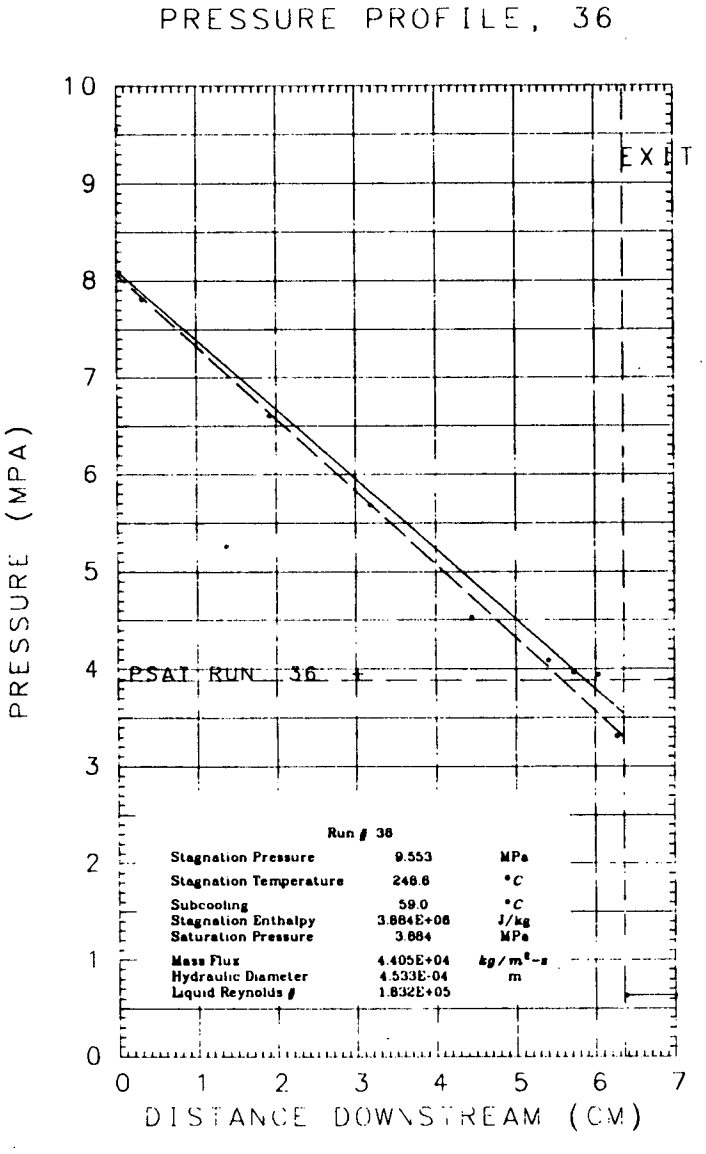

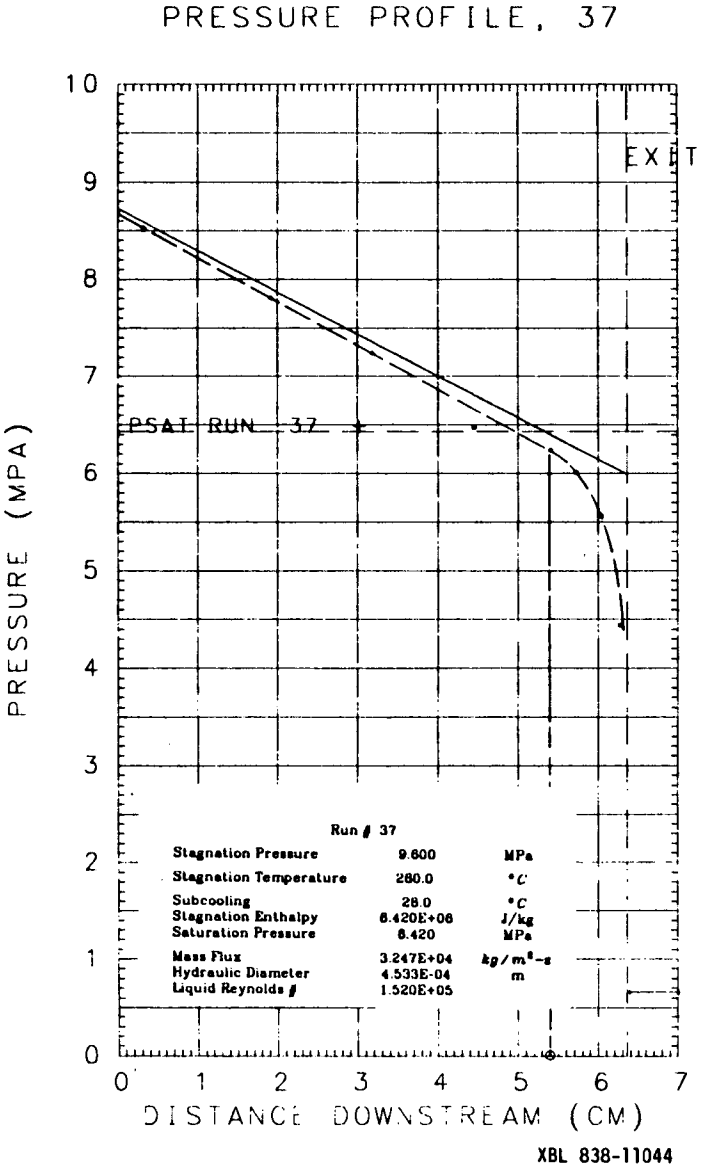

XBL 838-11044

PRESSURE PROFILE, 38

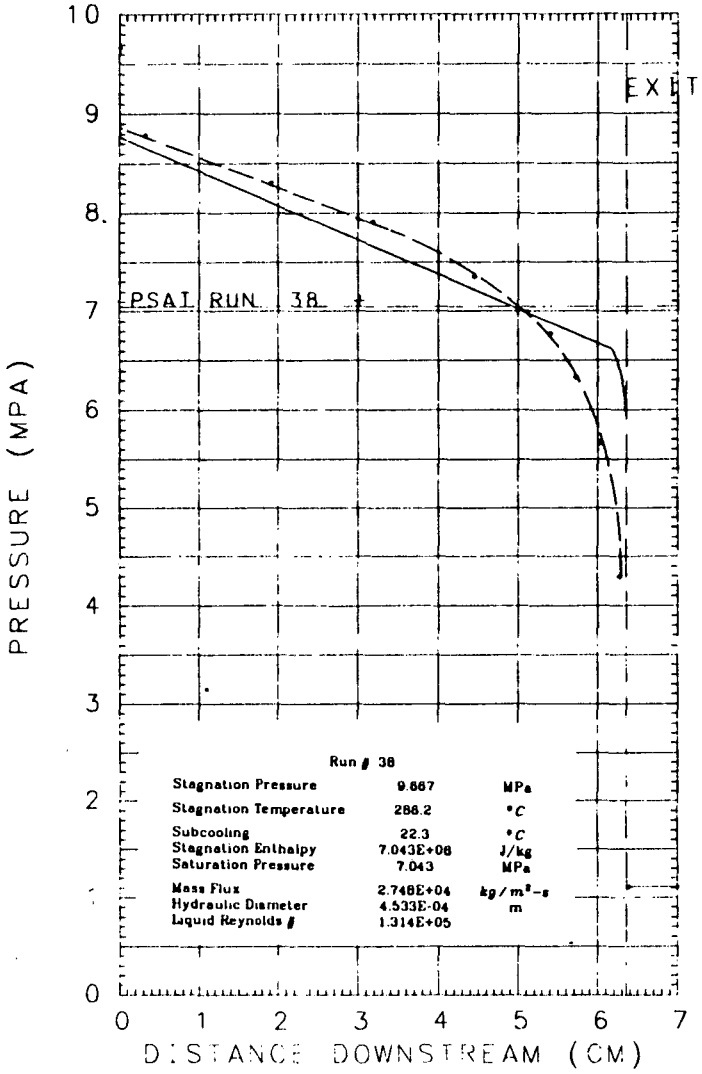

PRESSURE PROFILE, 55

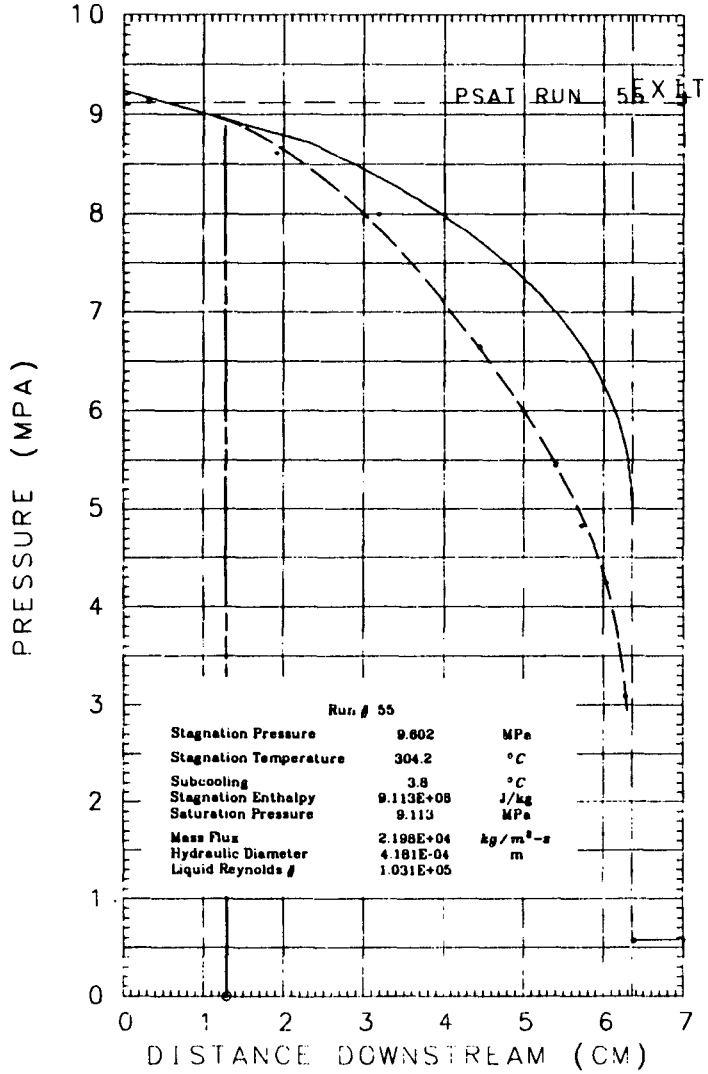

XBL 838-11045

PRESSURE PROFILE, 98

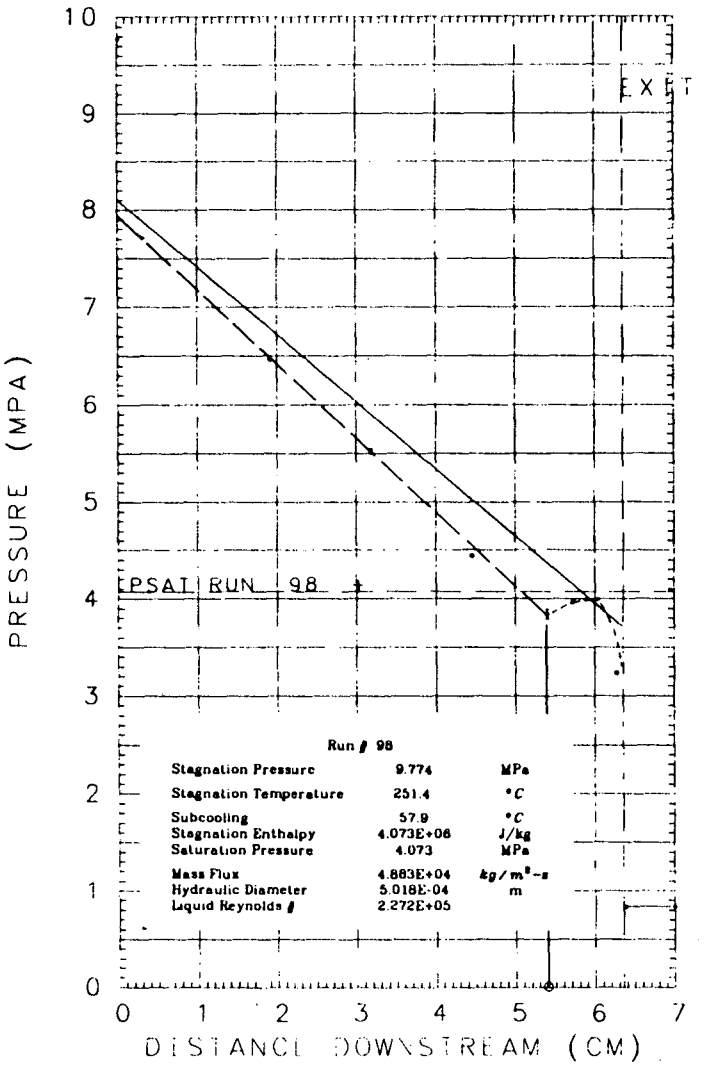

PRESSURE PROFILE, 99

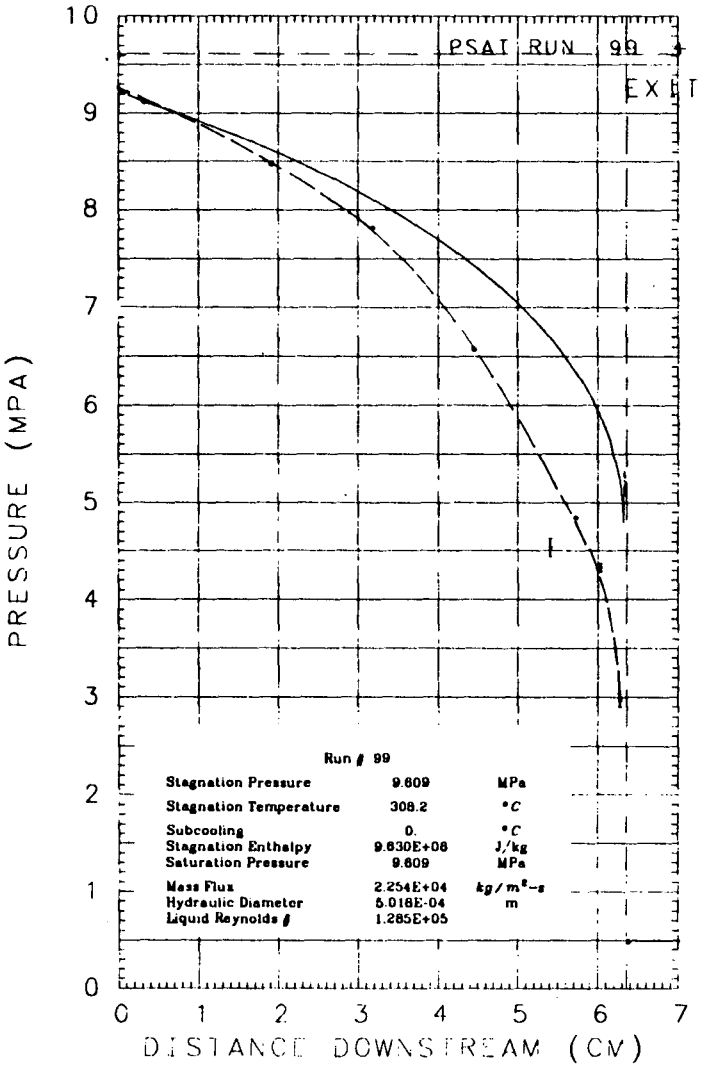

XBL 838-11063

PRESSURE PROFILE, 52

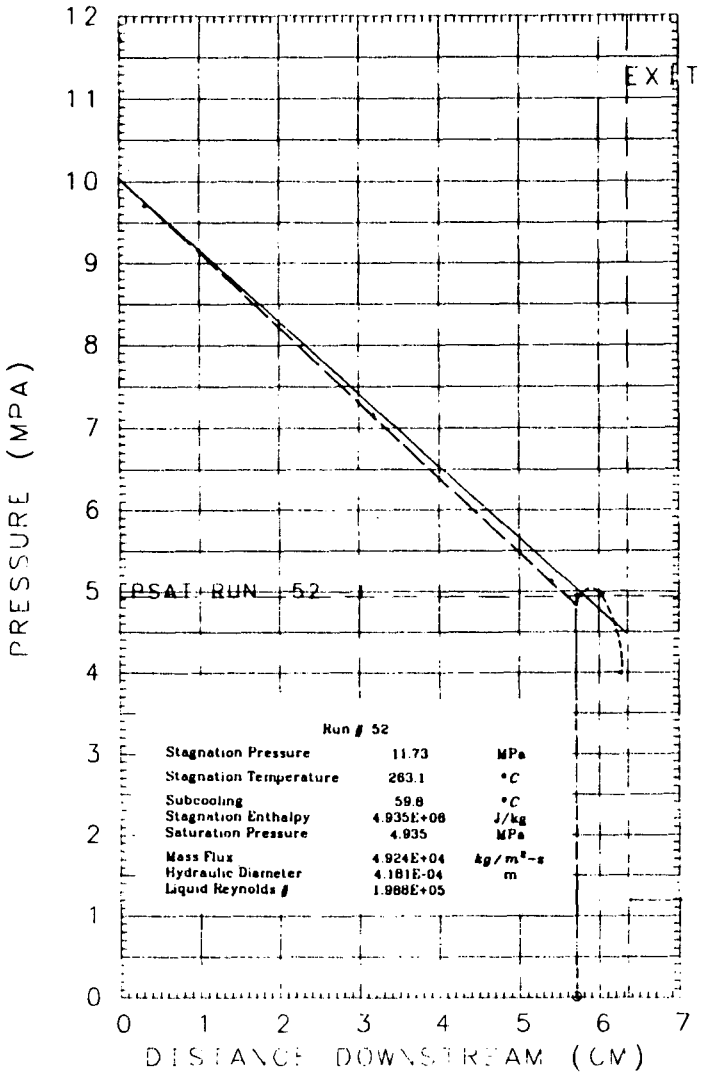

PRESSURE PROFILE, 39

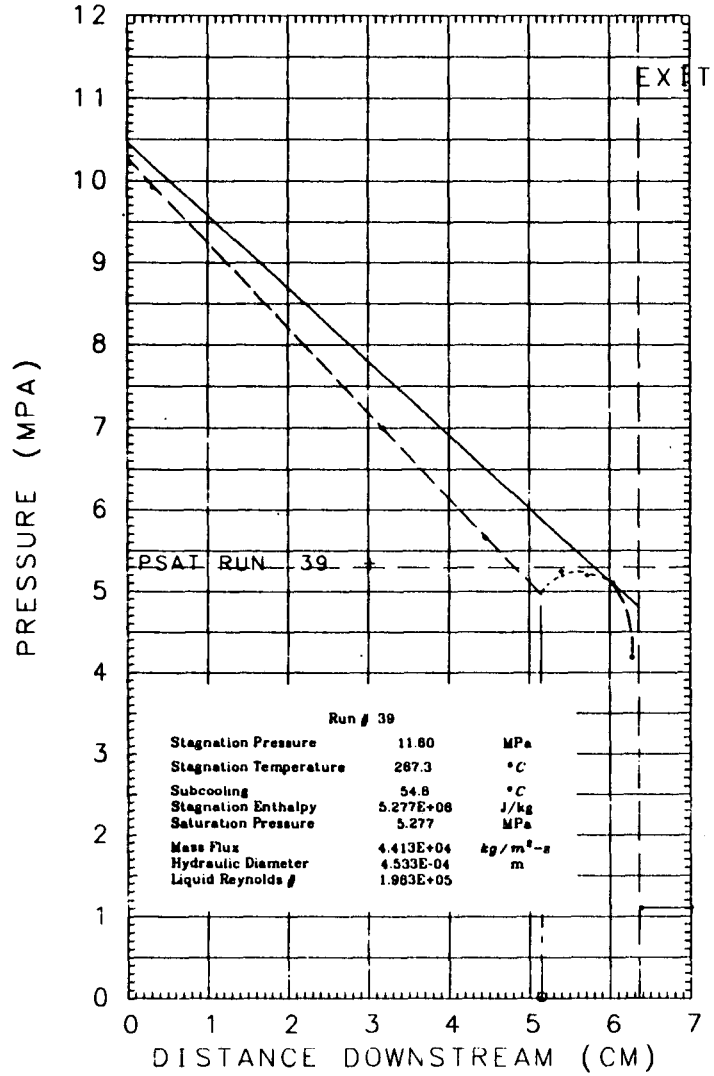

XBL 838-11051

PRESSURE PROFILE, 54

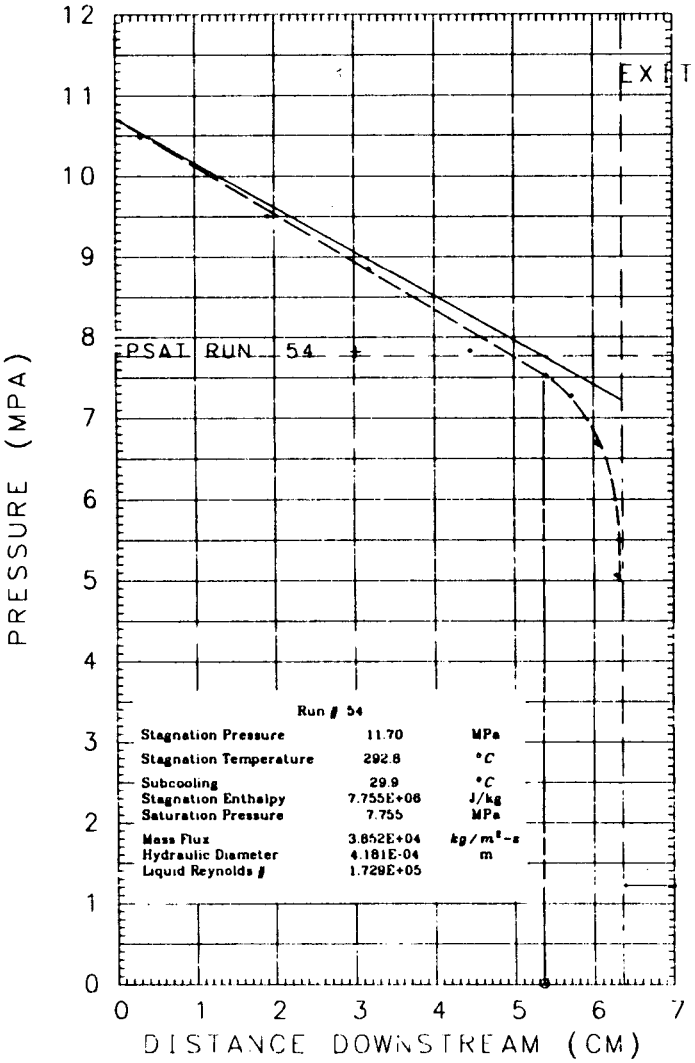

PRESSURE PROFILE, 95

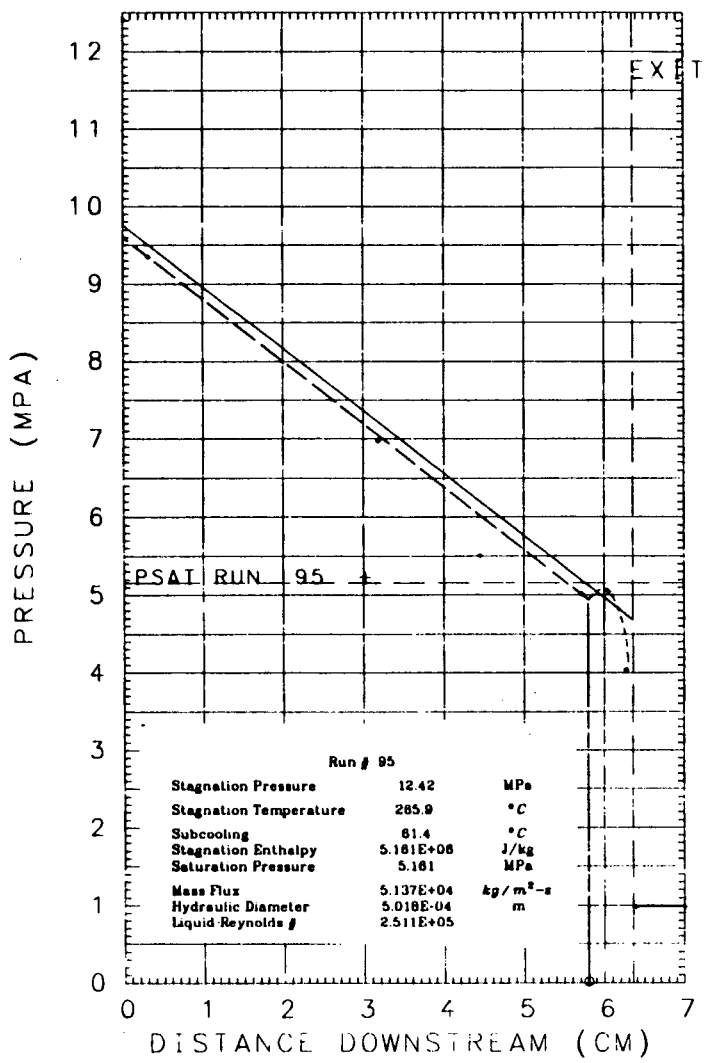

XBL 838-11039

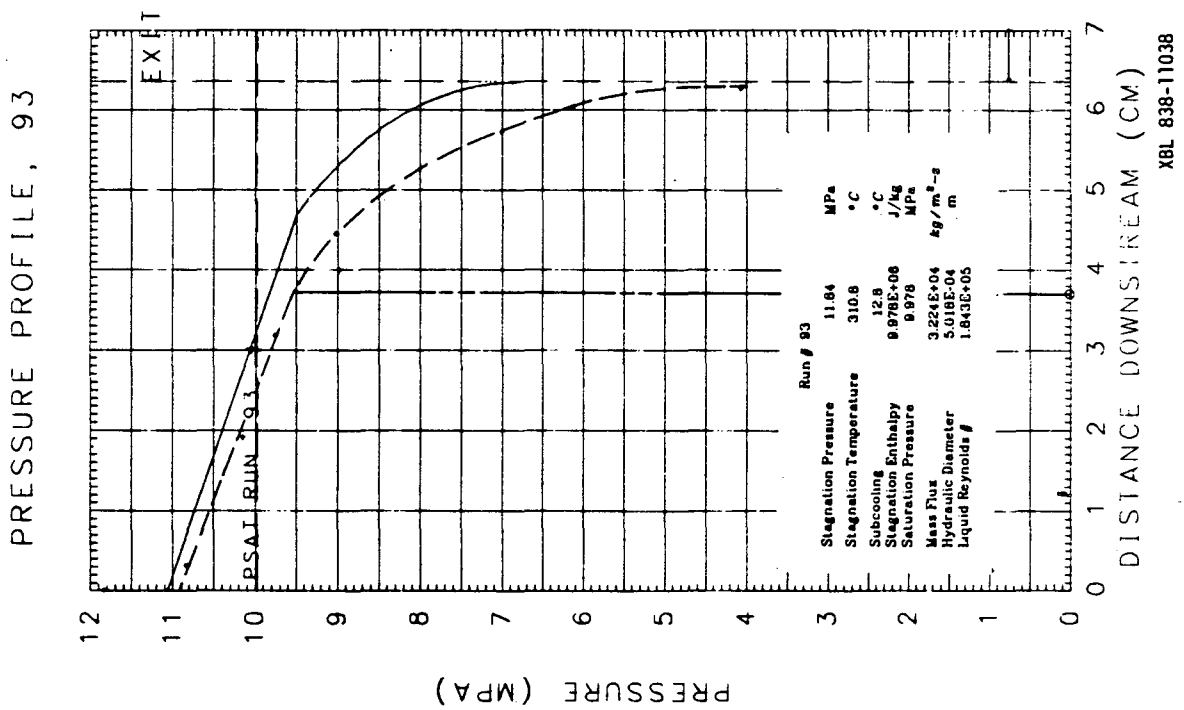
PRESSURE PROFILE, 93
EXIT
PSAT RUN 93
PRESSURE (MPA)
DISTANCE DOWNSTREAM (CM)
Run # 93
Stagnation Pressure 11.84 MPa
Stagnation Temperature 310.8 °C
Subcooling 12.8 °C
Stagnation Enthalpy 9.978E+06 J/kg
Saturation Pressure 9.978 MPa
Mass Flux 3.224E+04 kg/m²-s
Hydraulic Diameter 5.018E-04 m
Liquid Reynolds # 1.843E+05
XBL 838-11038

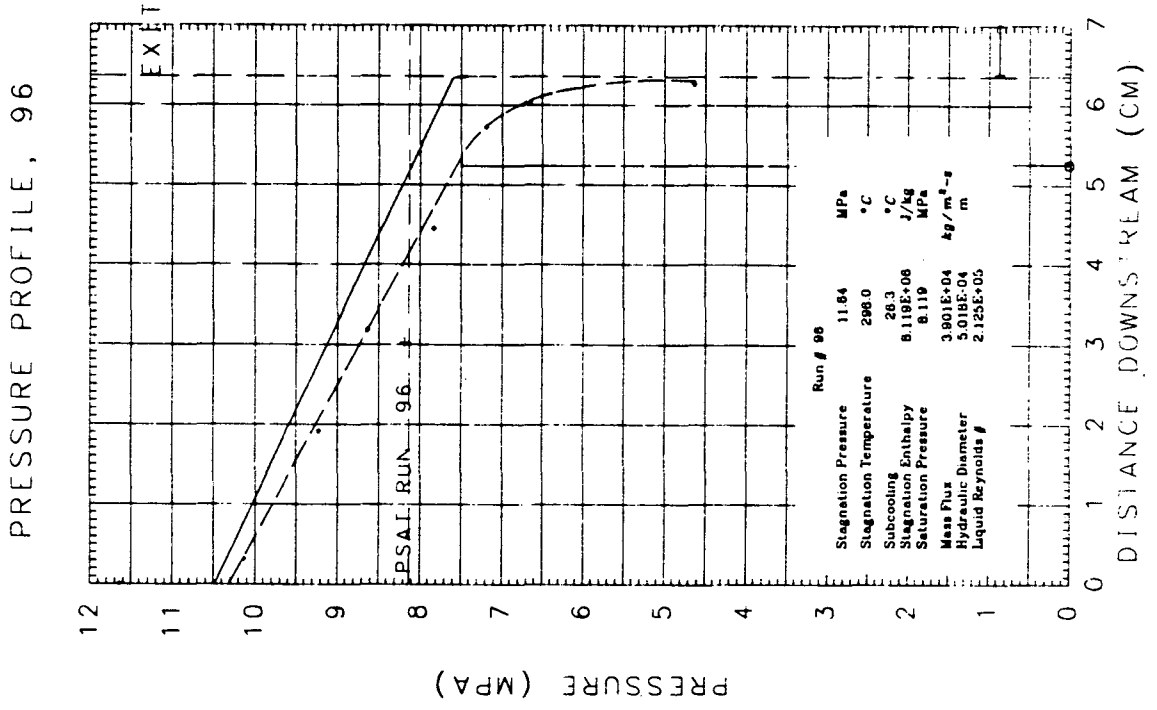
PRESSURE PROFILE, 96
EXIT
PSAT RUN 96
PRESSURE (MPA)
DISTANCE DOWNSTREAM (CM)
Run # 96
Stagnation Pressure 11.84 MPa
Stagnation Temperature 298.0 °C
Subcooling 26.3 °C
Stagnation Enthalpy 8.118E+06 J/kg
Saturation Pressure 8.119 MPa
Mass Flux 3.901E+04 kg/m²-s
Hydraulic Diameter 5.018E-04 m
Liquid Reynolds # 2.125E+05

PRESSURE PROFILE, 94

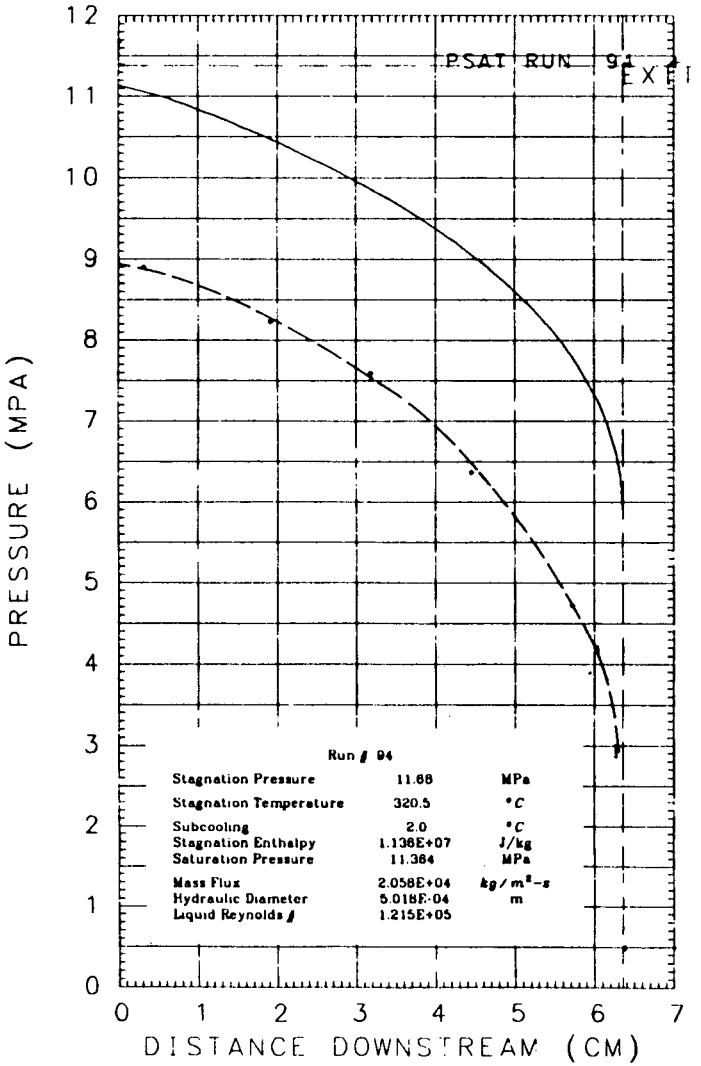

PRESSURE PROFILE, 72

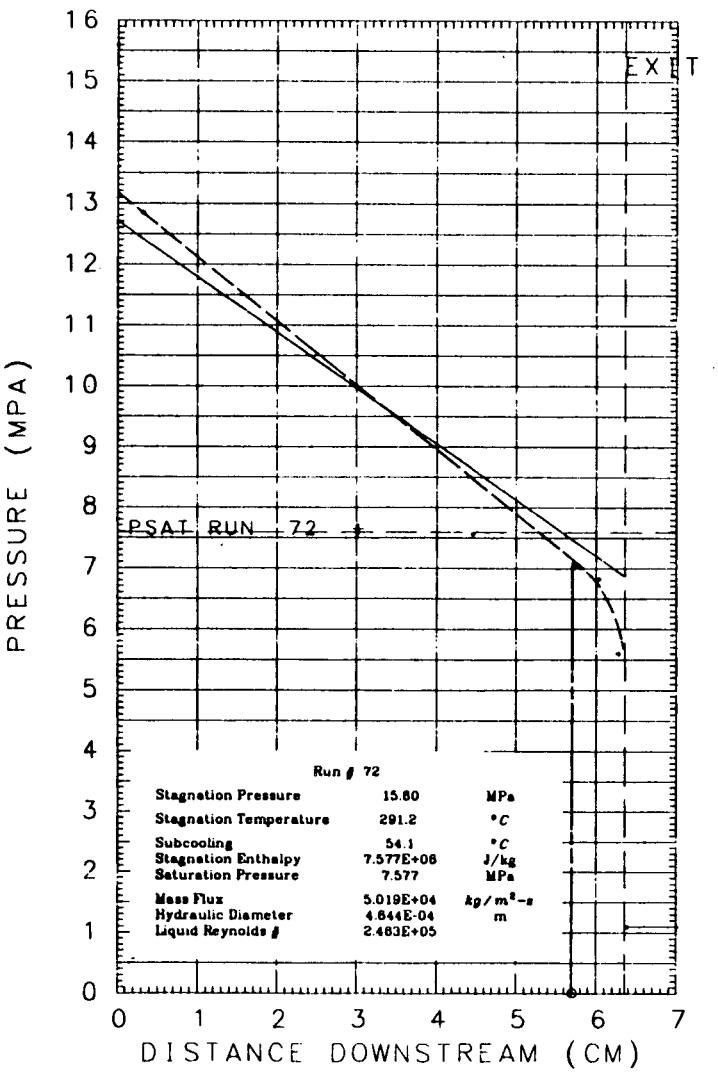

XBL 838-11037

PRESSURE PROFILE, 92

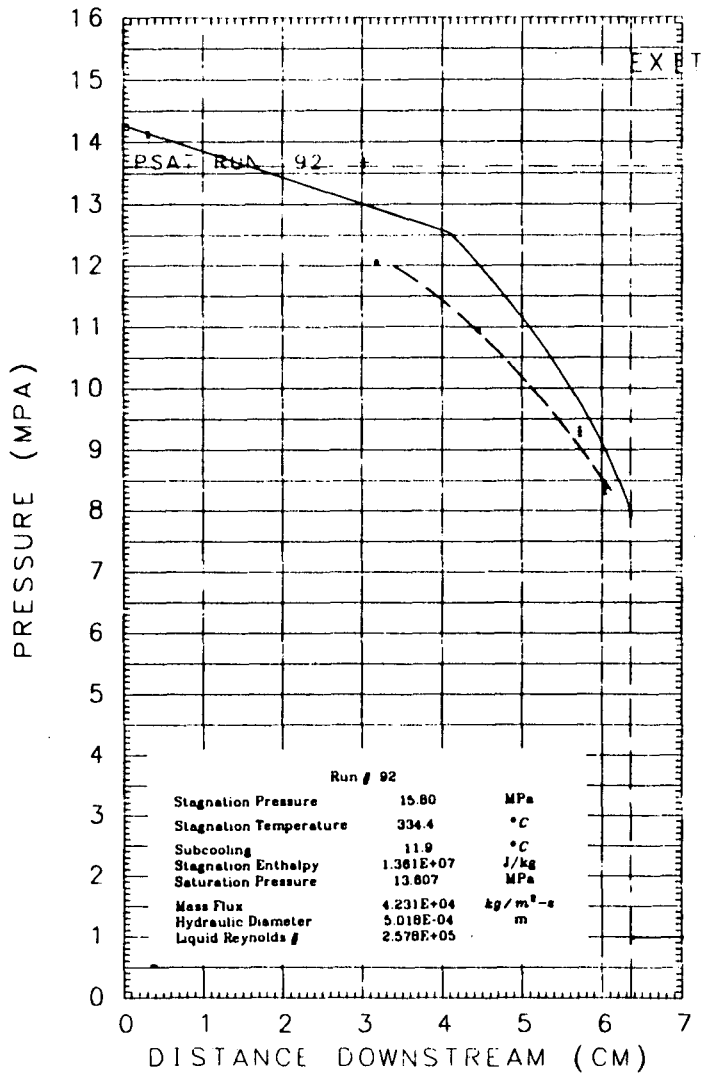

PRESSURE PROFILE, 97

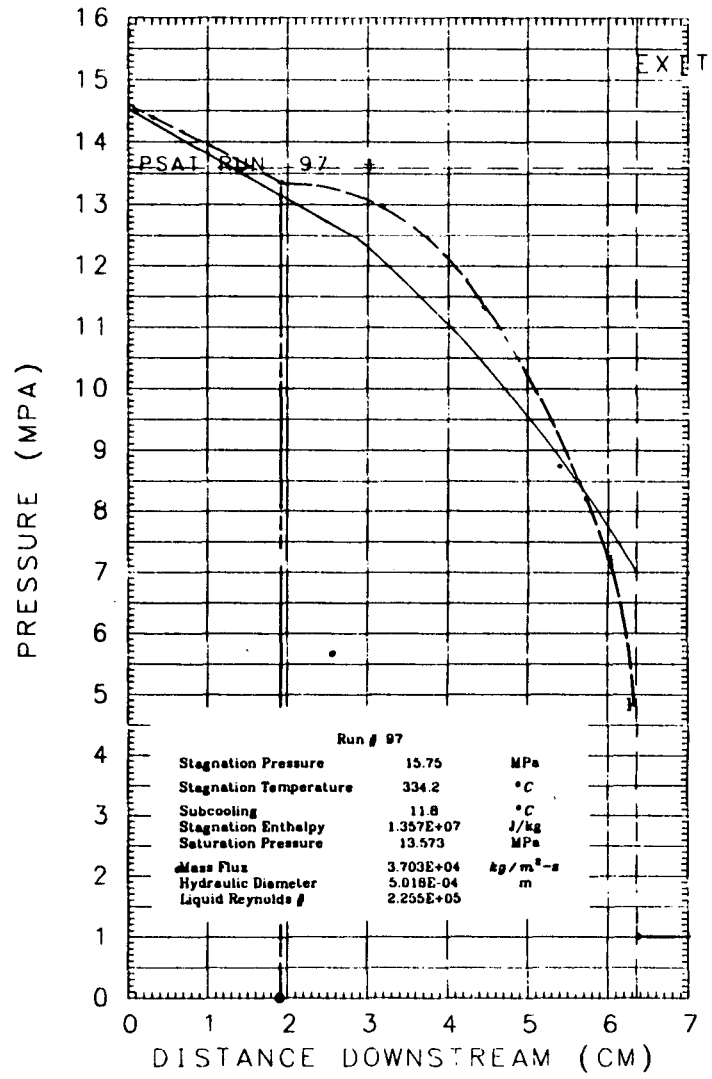

XBL 838-11036

PRESSURE PROFILE, 100

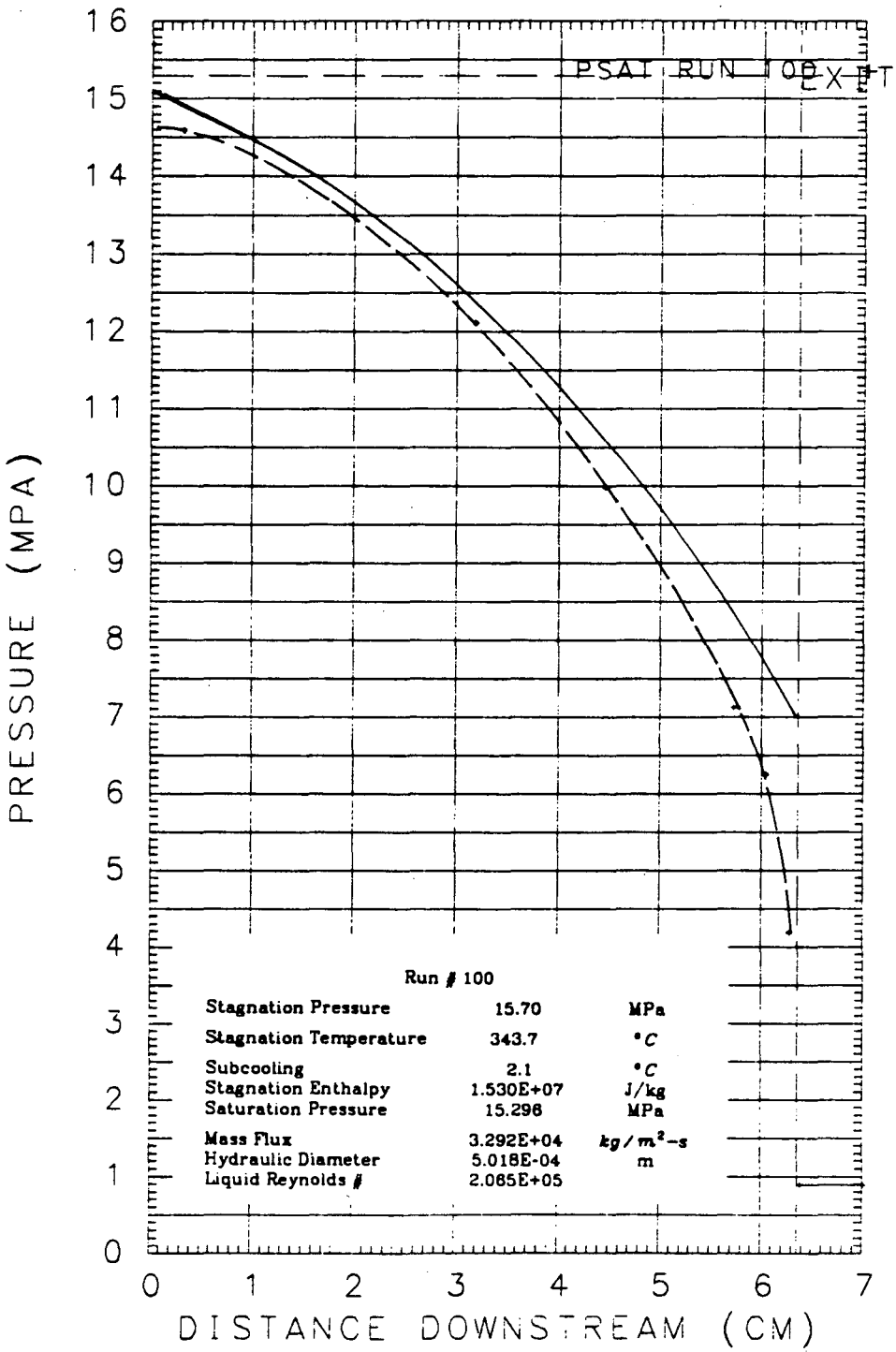

XBL 838-11064

SECTION III

0.127 mm Nominal Slit Opening

PRESSURE PROFILE, 15

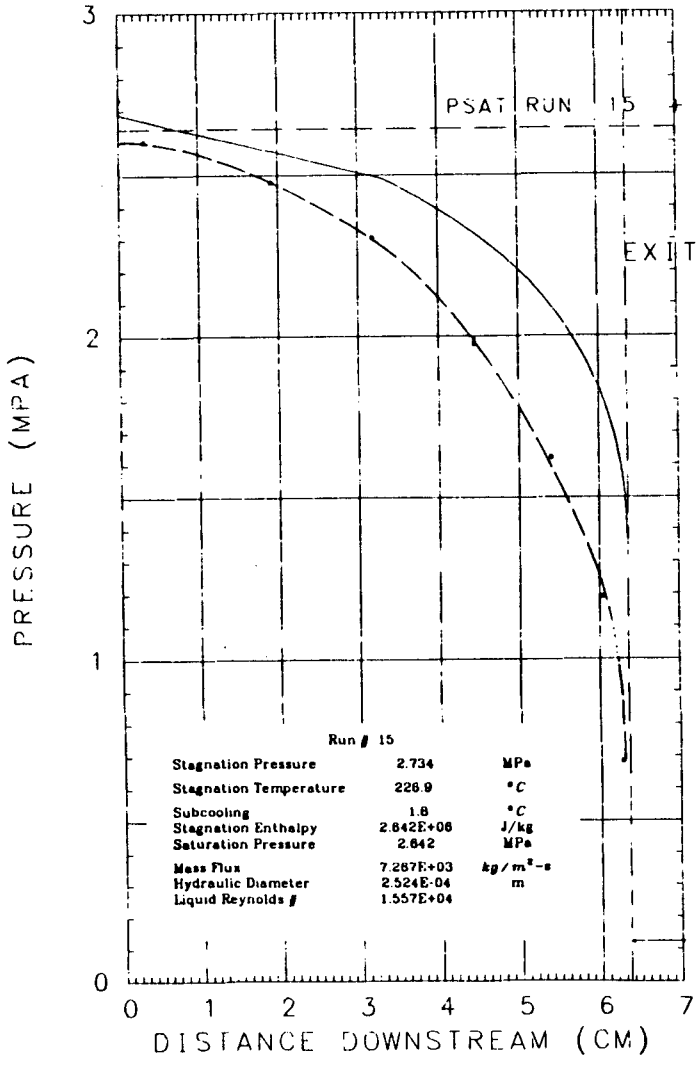

PRESSURE PROFILE, 61

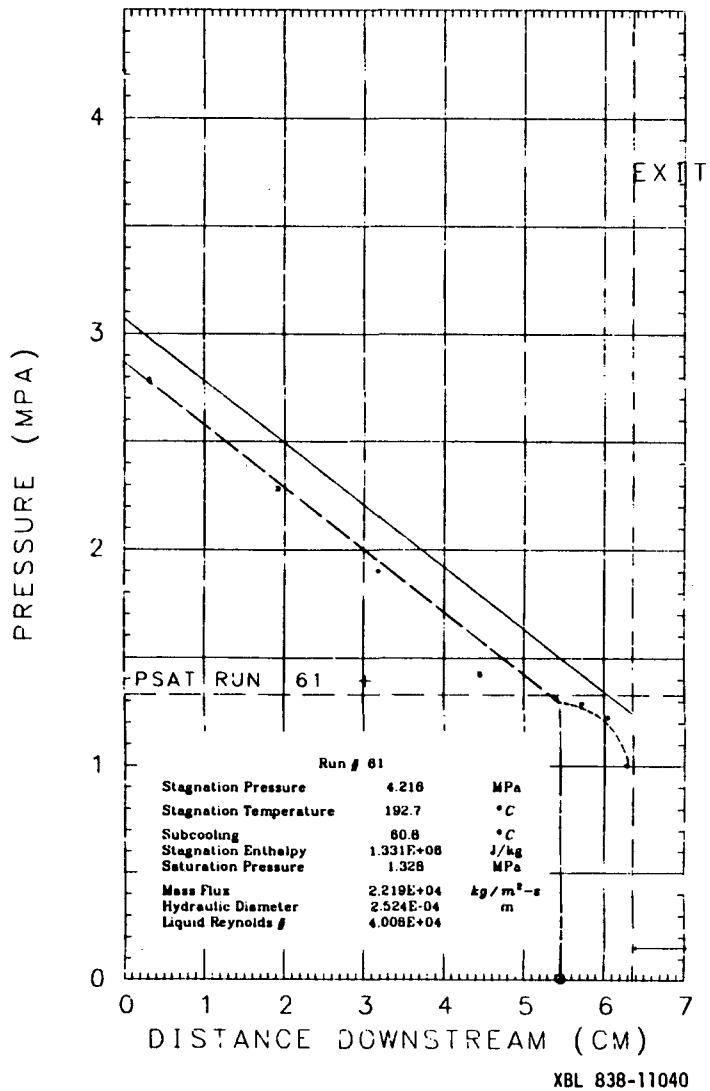

XBL 838-11040

PRESSURE PROFILE, 64

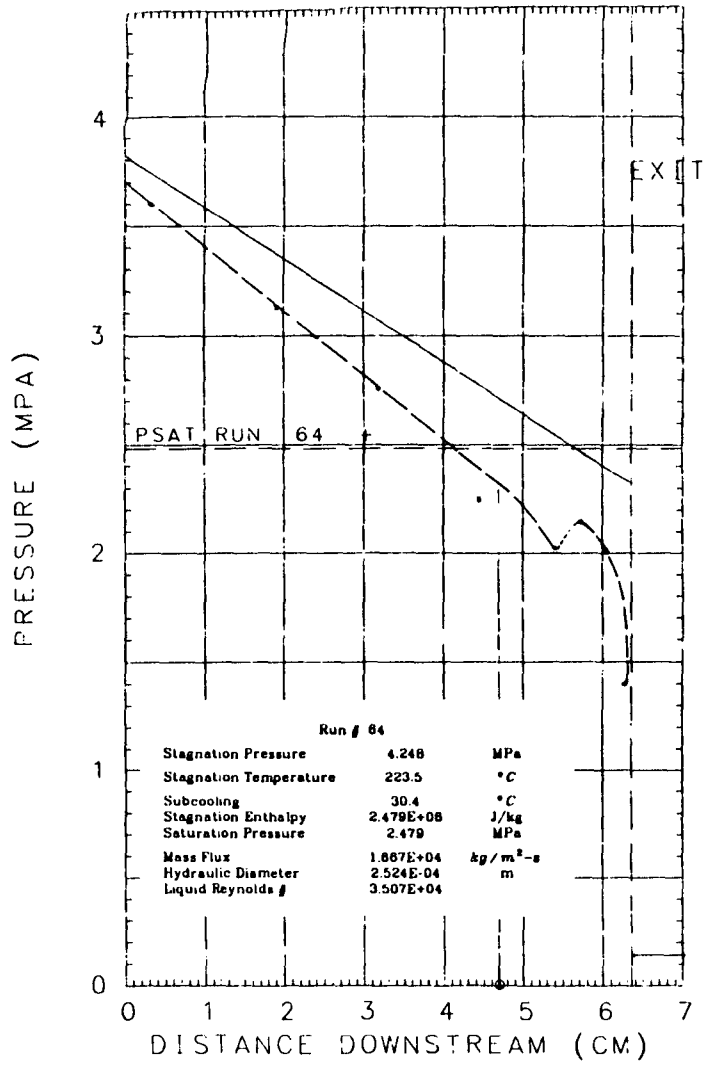

PRESSURE PROFILE, 63

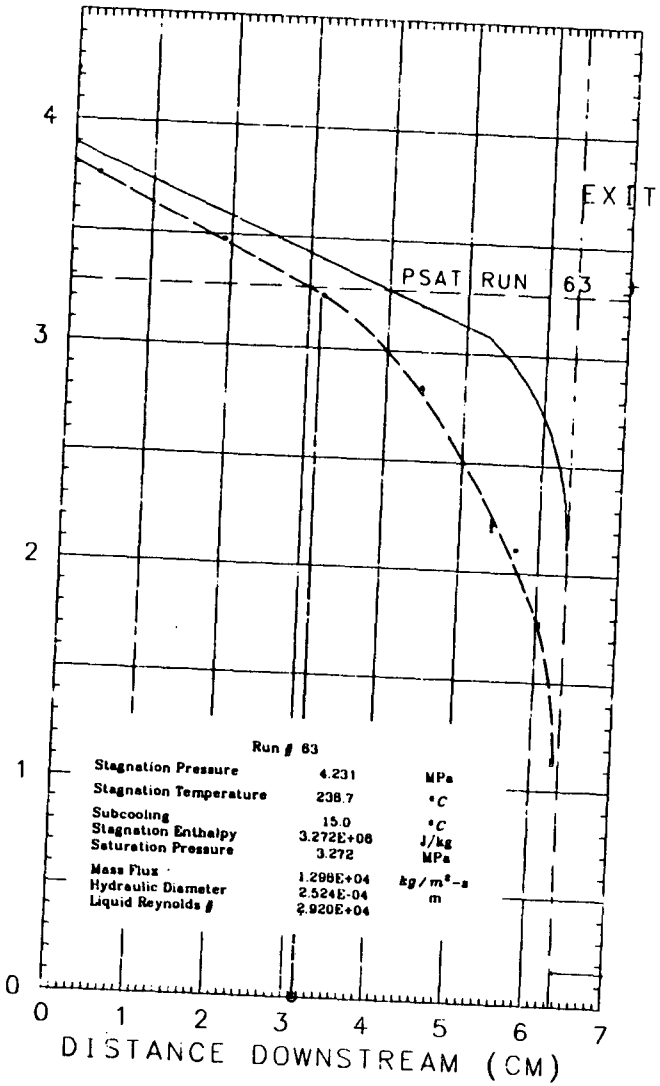

XBL 838-11033

PRESSURE PROFILE, 65

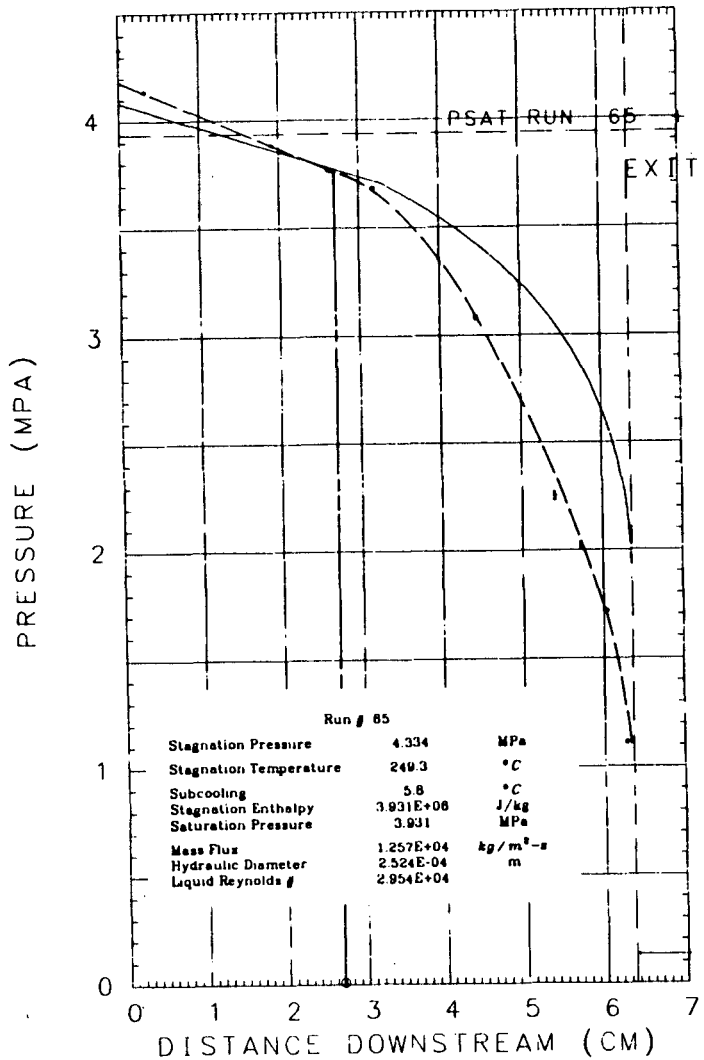

PRESSURE PROFILE, 17

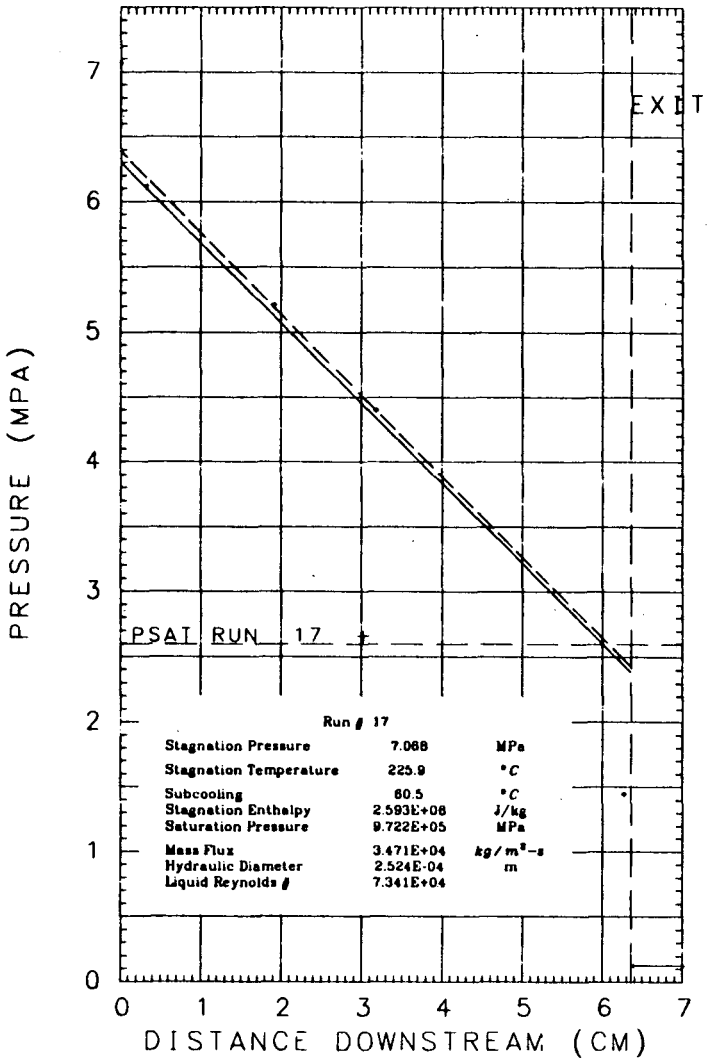

XBL 838-11054

PRESSURE PROFILE, 67

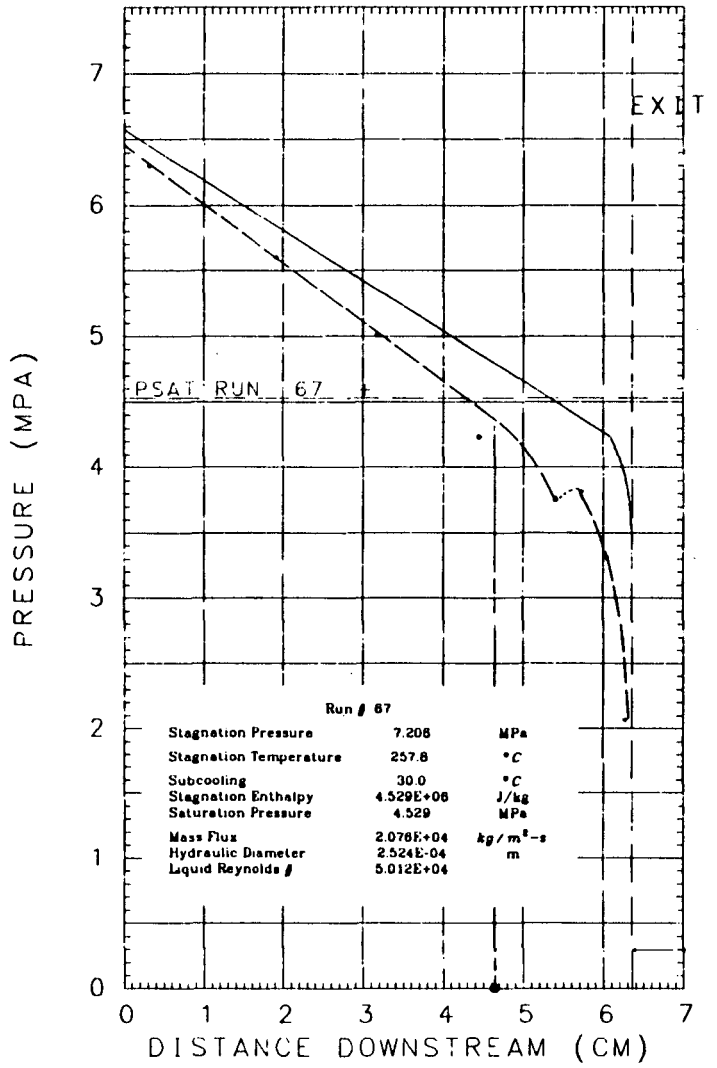

PRESSURE PROFILE, 22

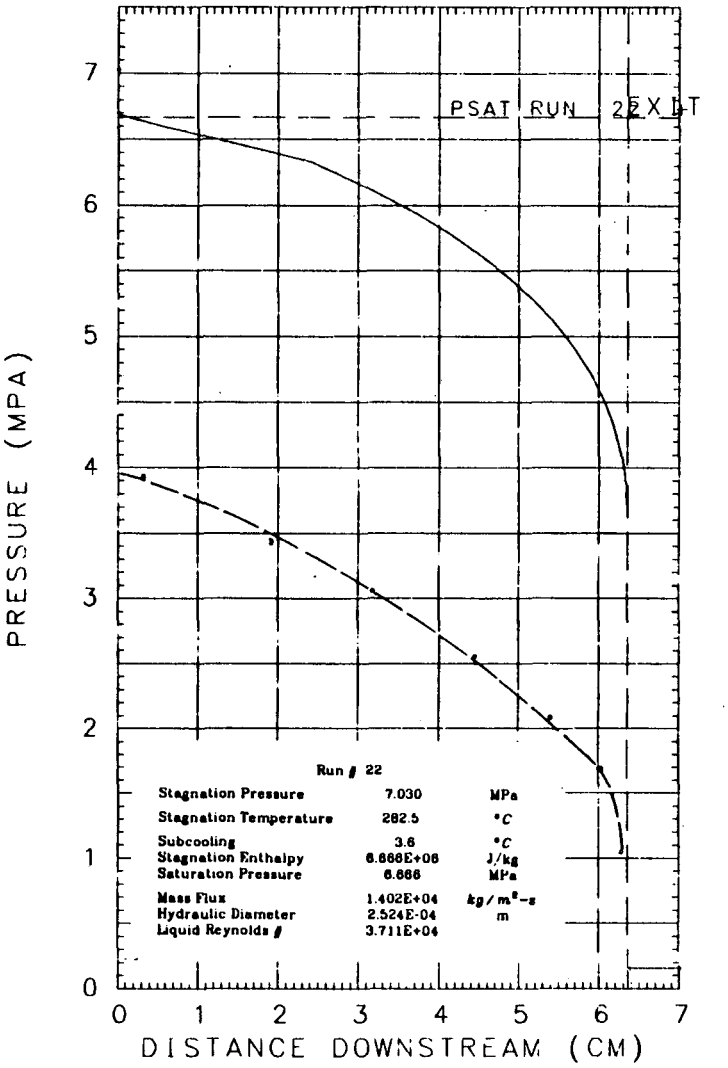

XBL 838-11055

PRESSURE PROFILE, 19

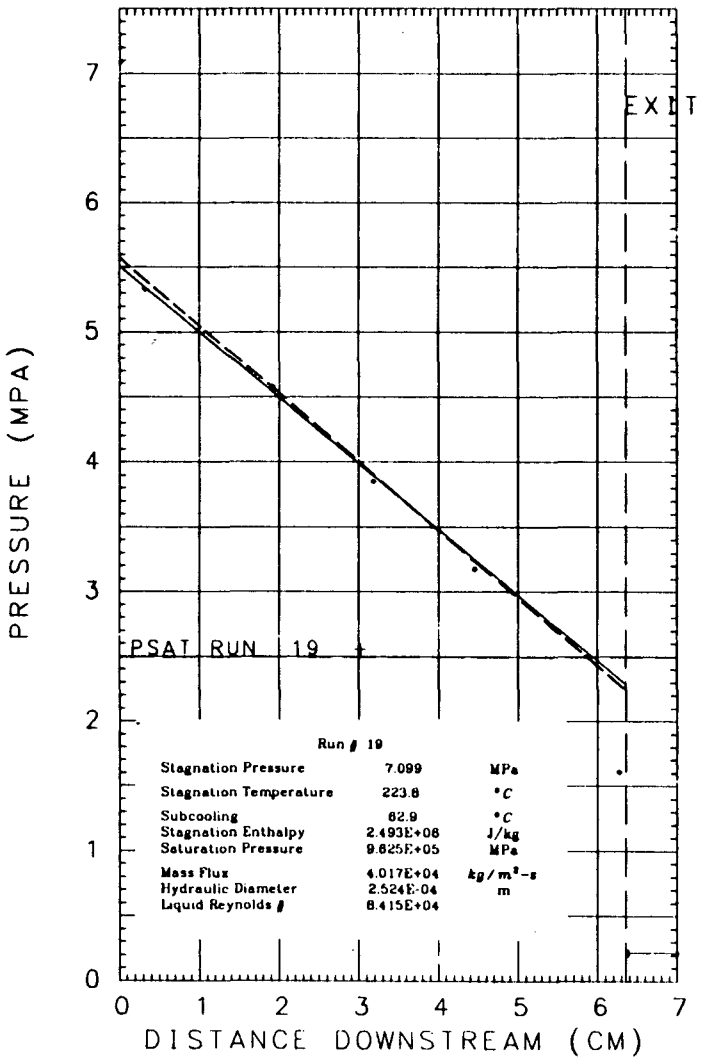

PRESSURE PROFILE, 50

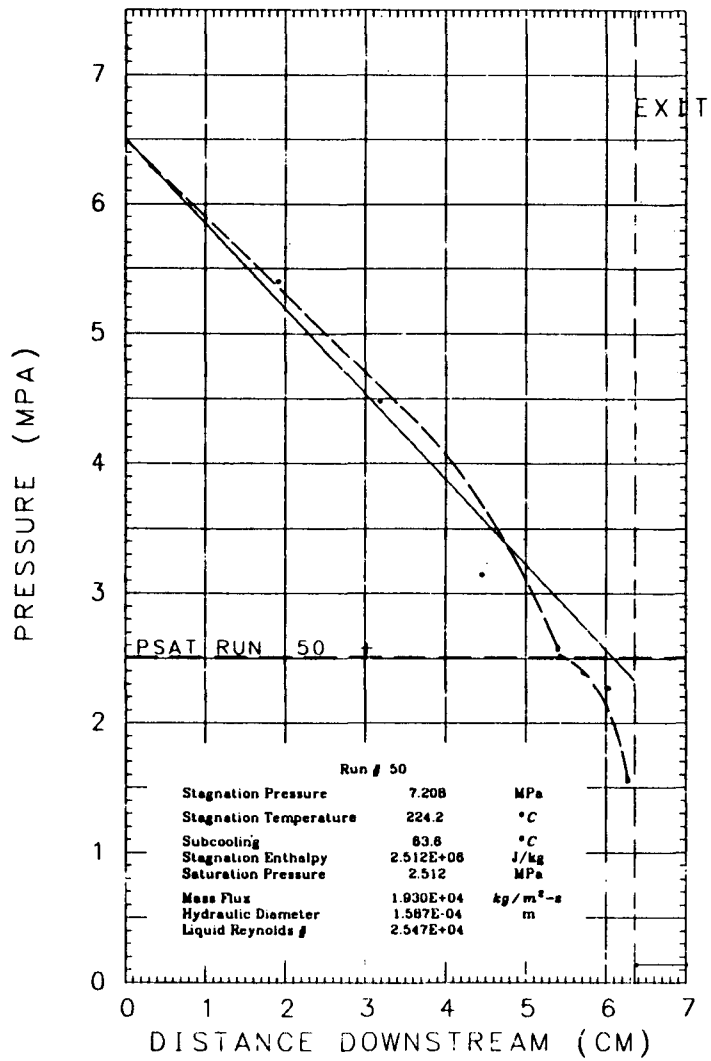

XBL 838-11030

PRESSURE PROFILE, 34

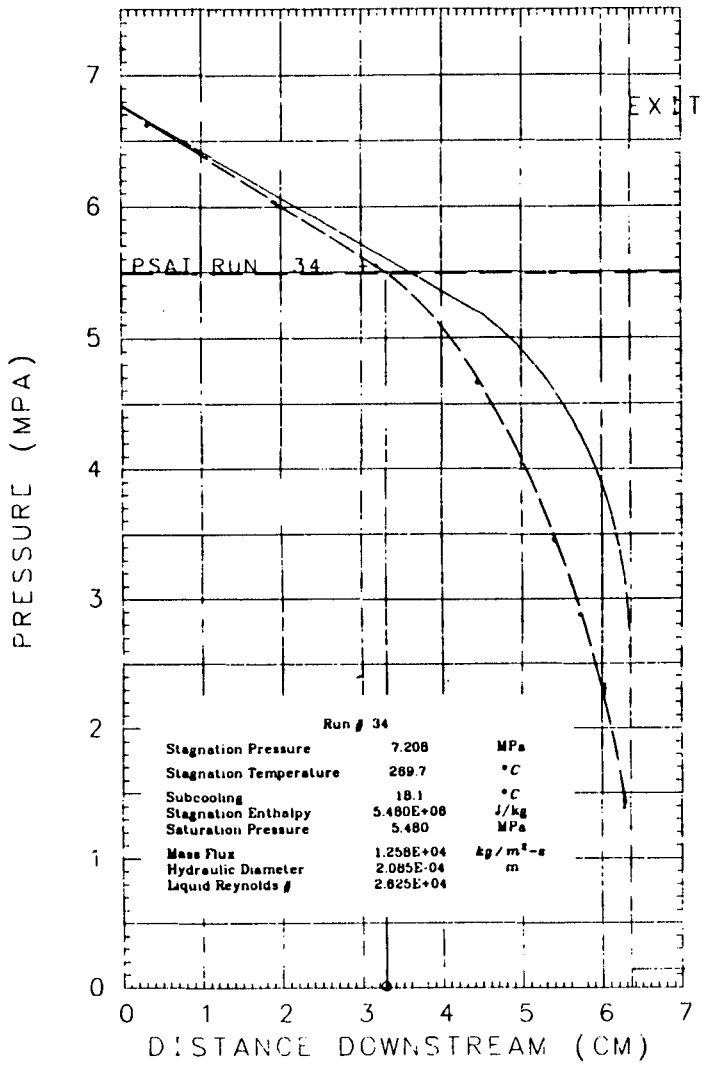

PRESSURE PROFILE, 33

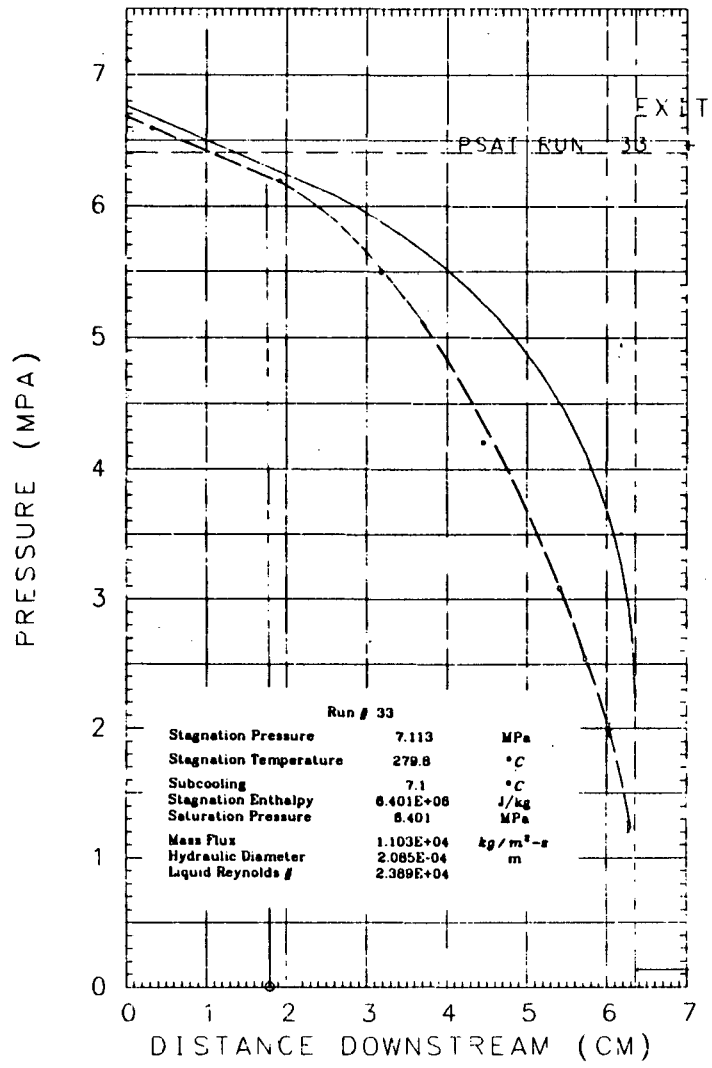

XBL 838-11043

PRESSURE PROFILE, 85

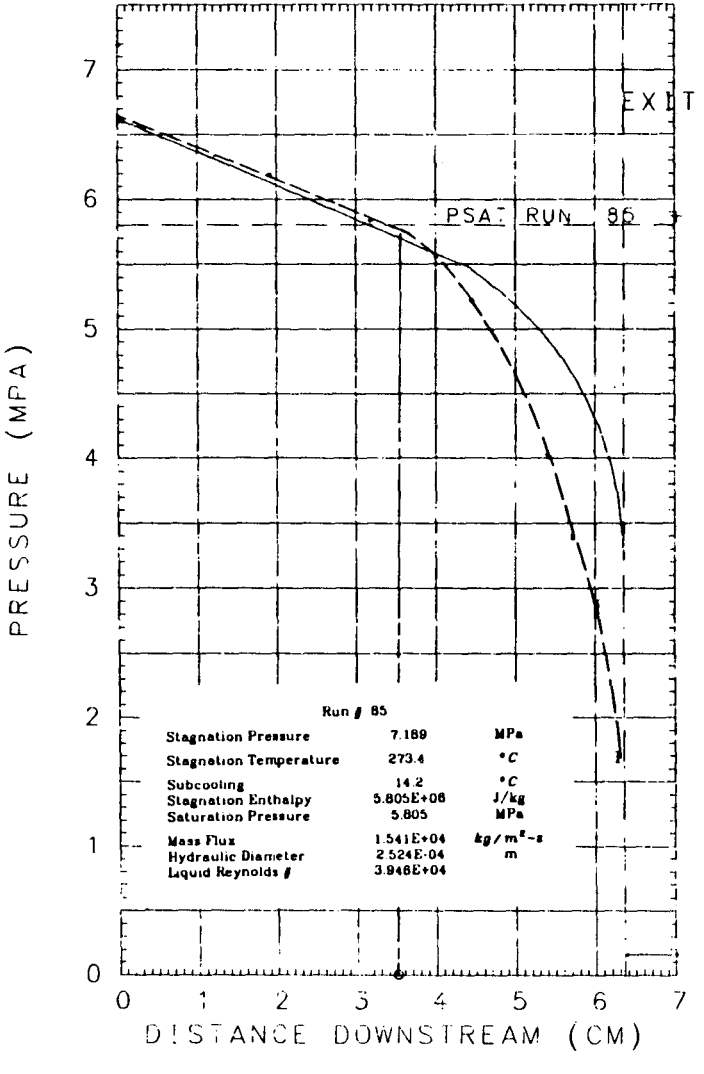

PRESSURE PROFILE, 86

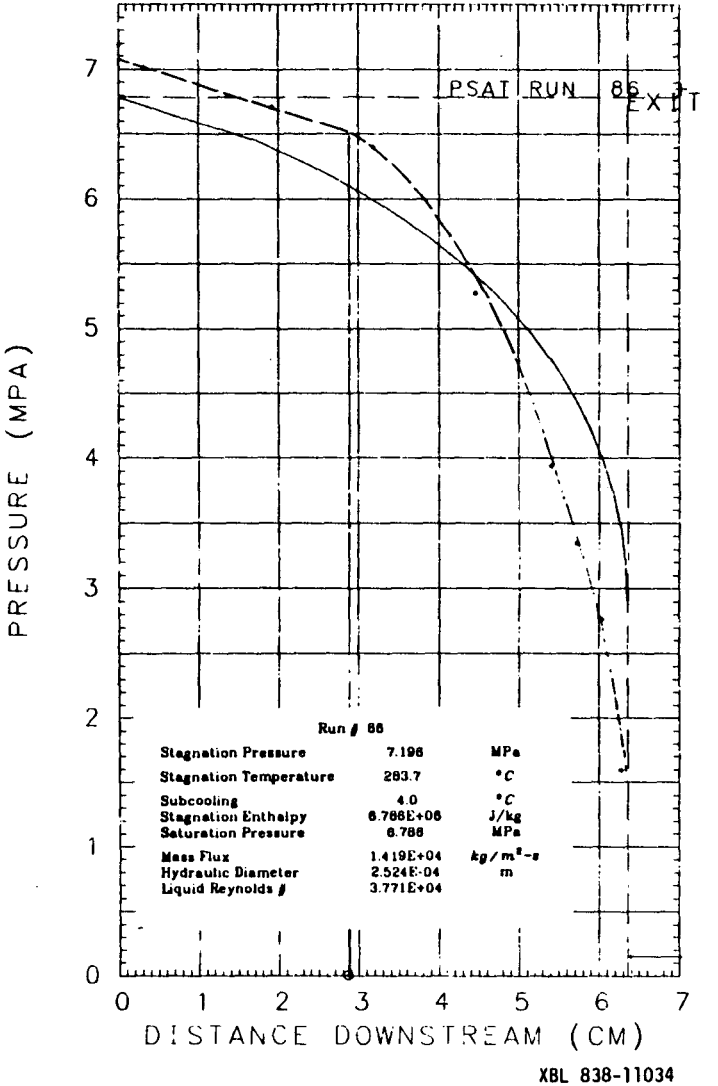

XBL 838-11034

PRESSURE PROFILE, 32

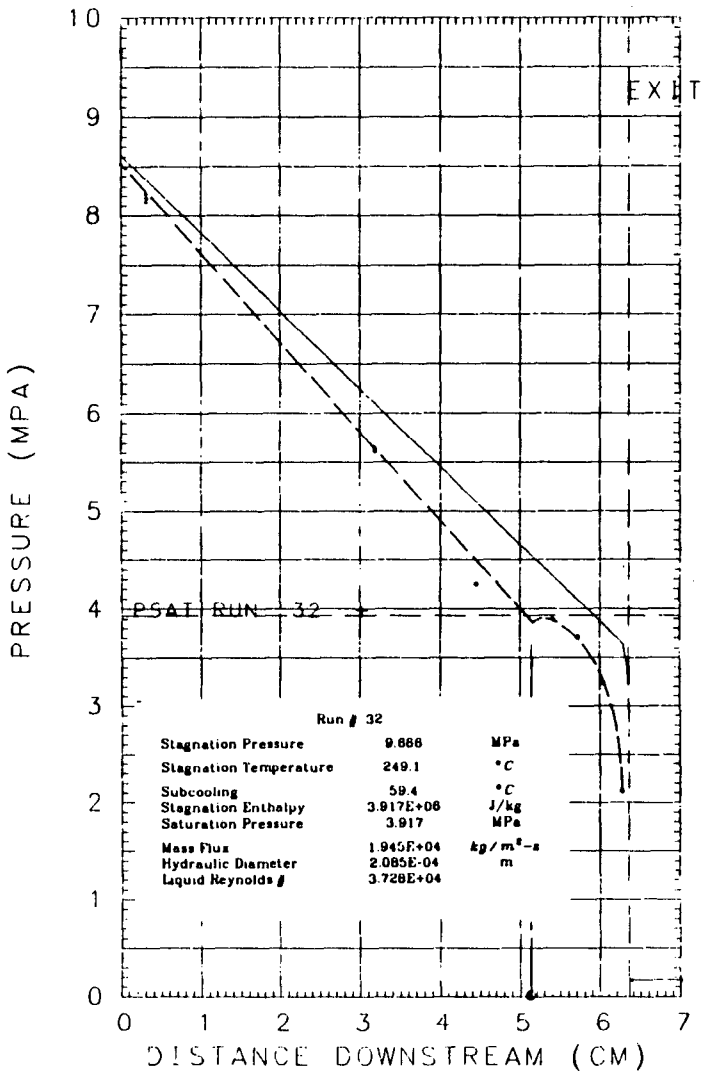

PRESSURE PROFILE, 82

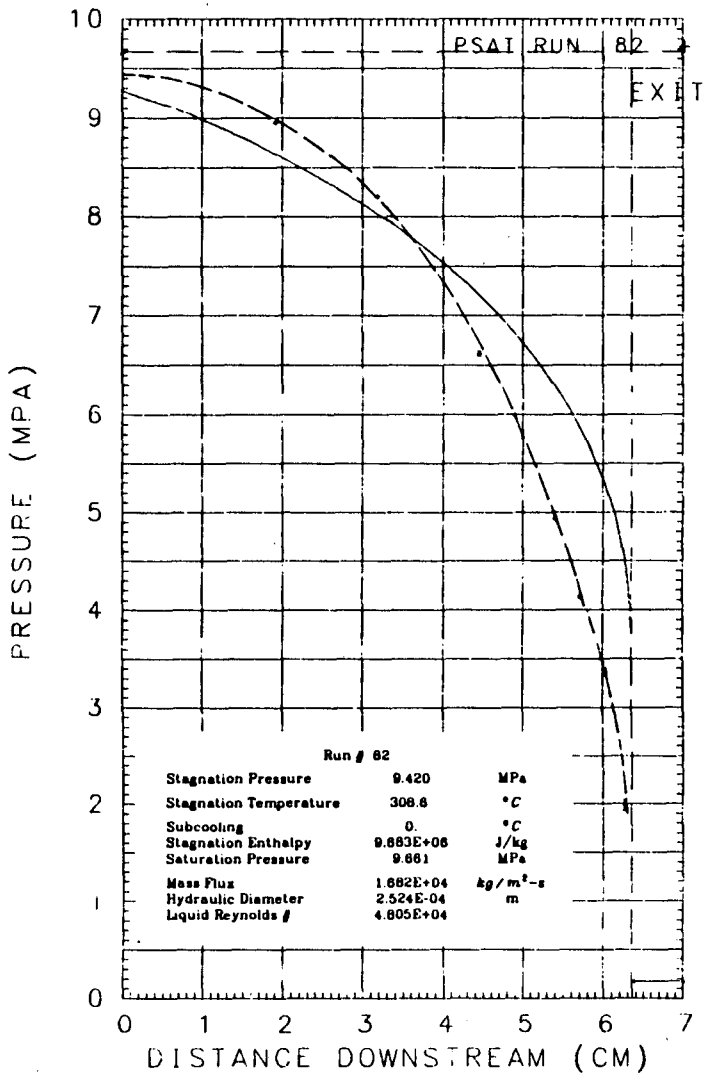

XBL 838-11042

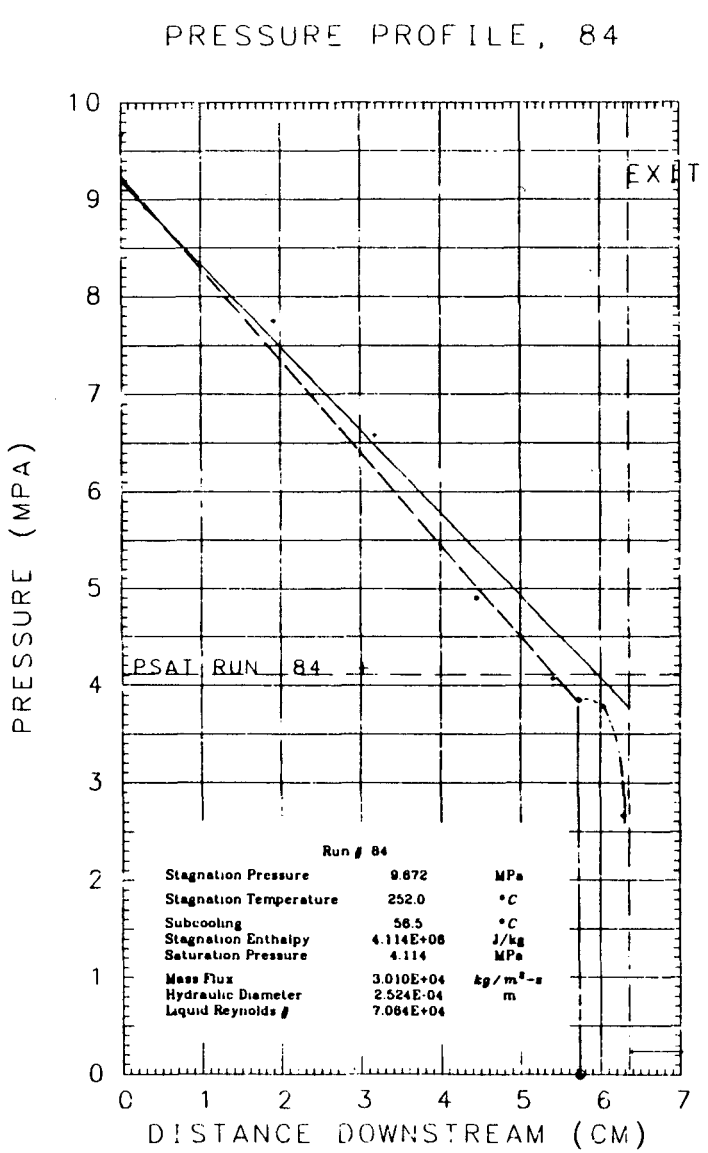

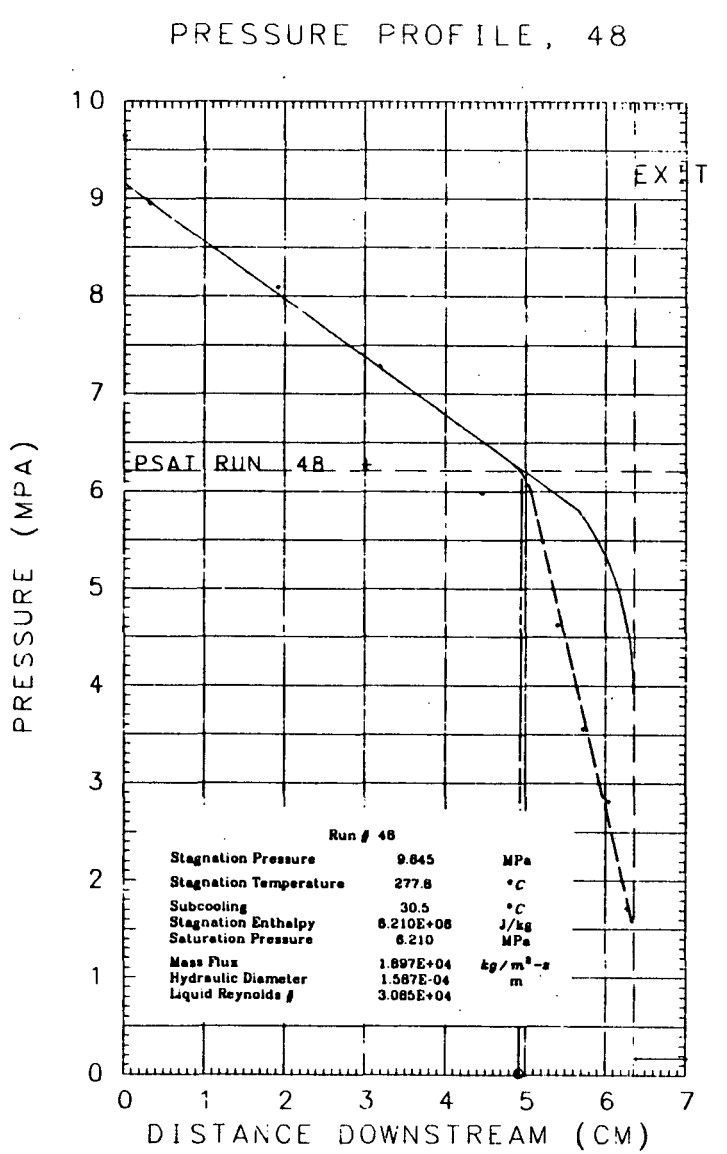

XBL 838-11061

PRESSURE PROFILE, 49

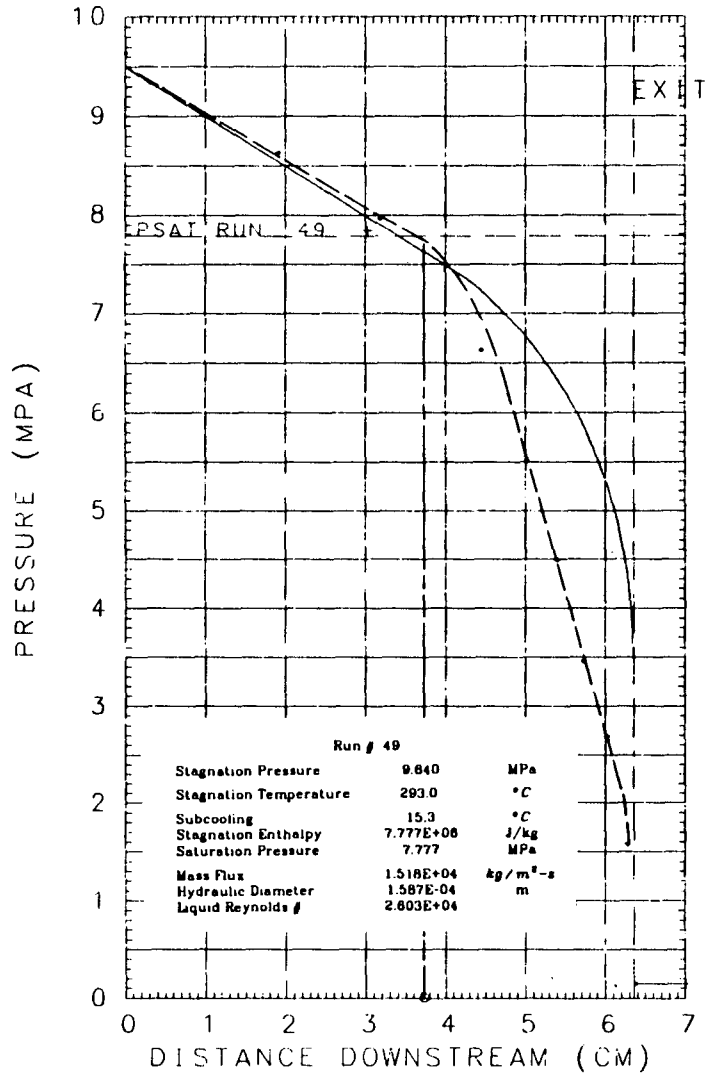

PRESSURE PROFILE, 47

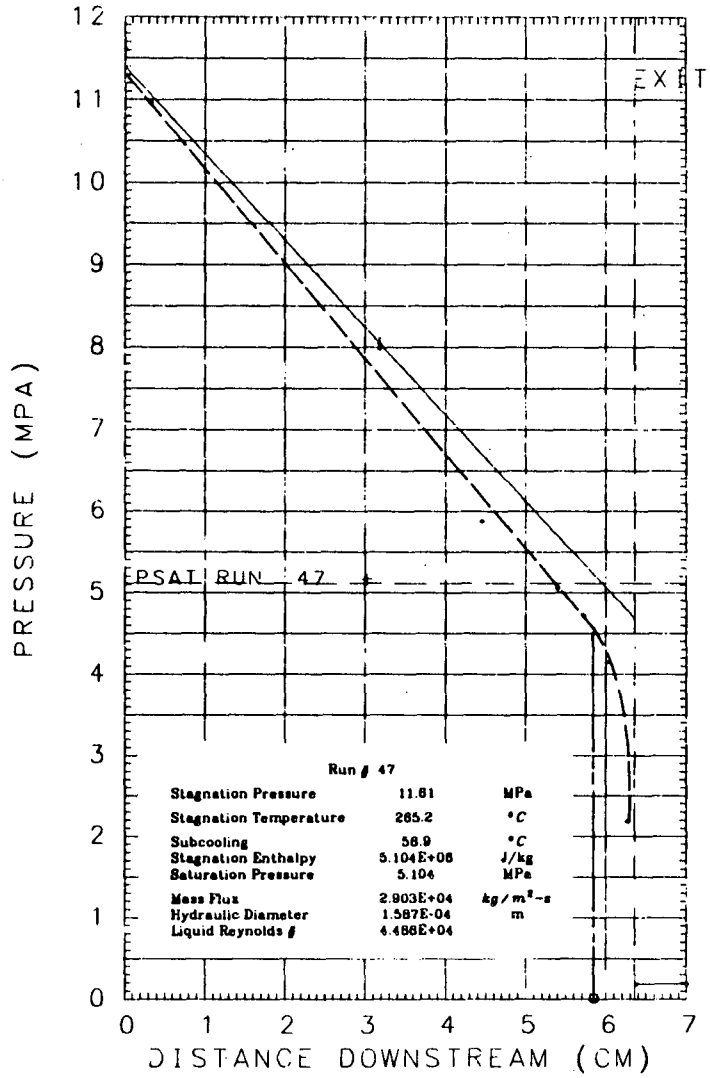

XBL 838-11049

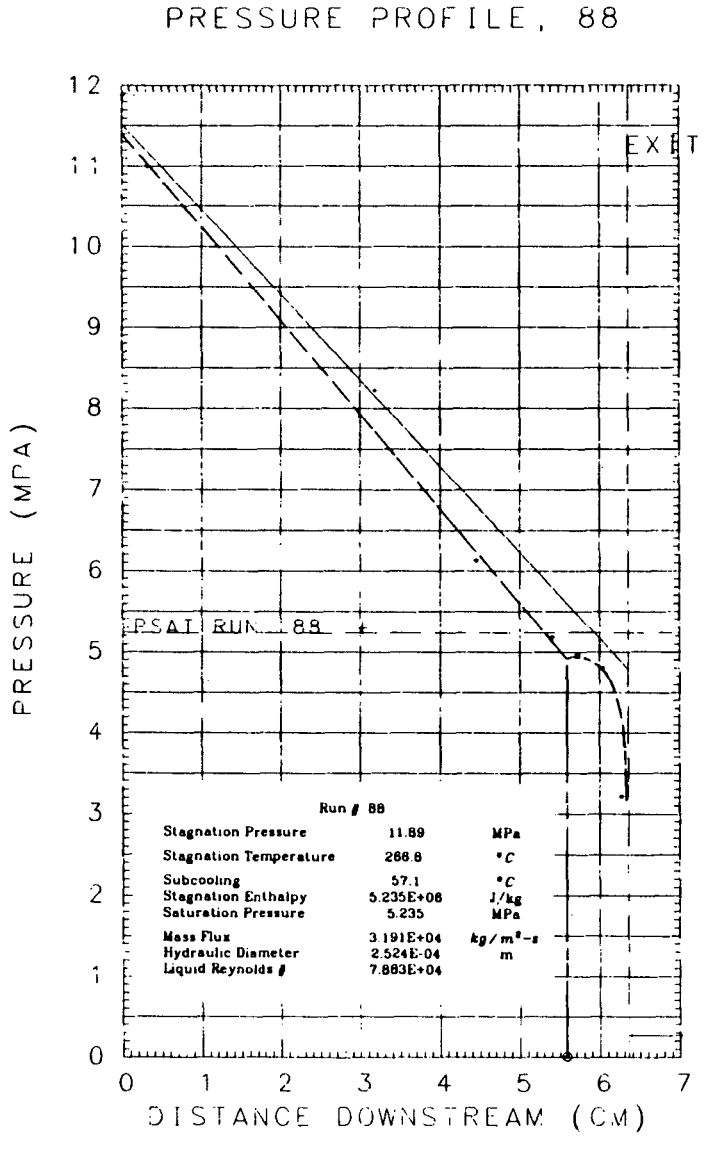

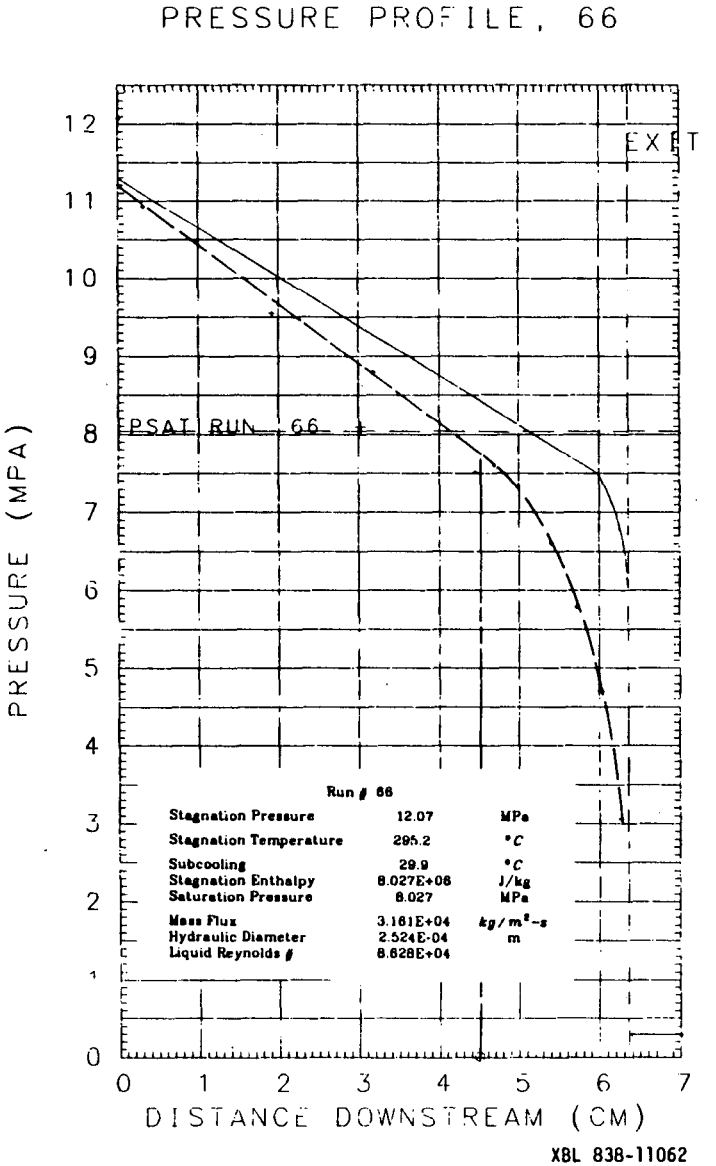

XBL 838-11062

PRESSURE PROFILE, 80

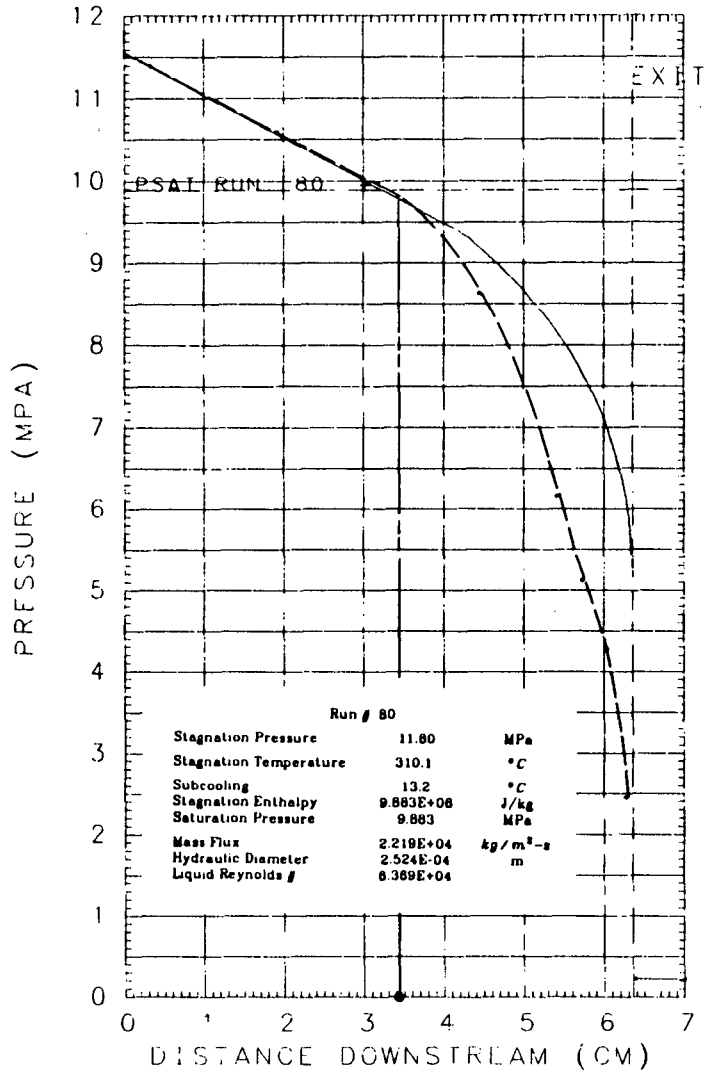

PRESSURE PROFILE, 81

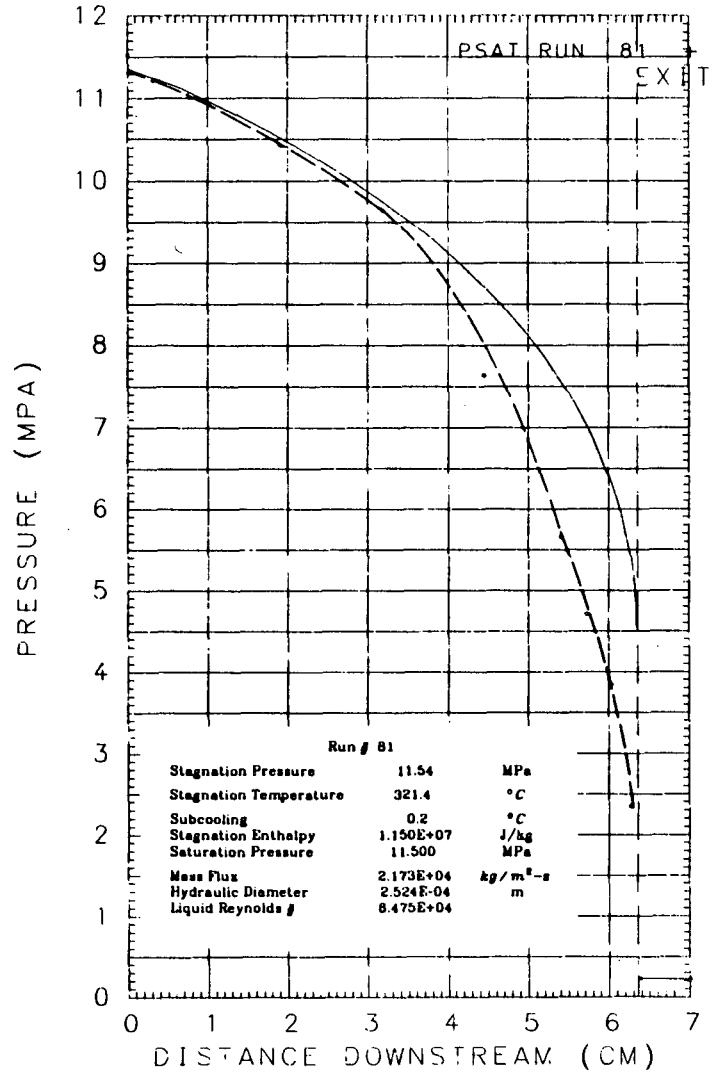

XBL 838-11060

PRESSURE PROFILE, 87

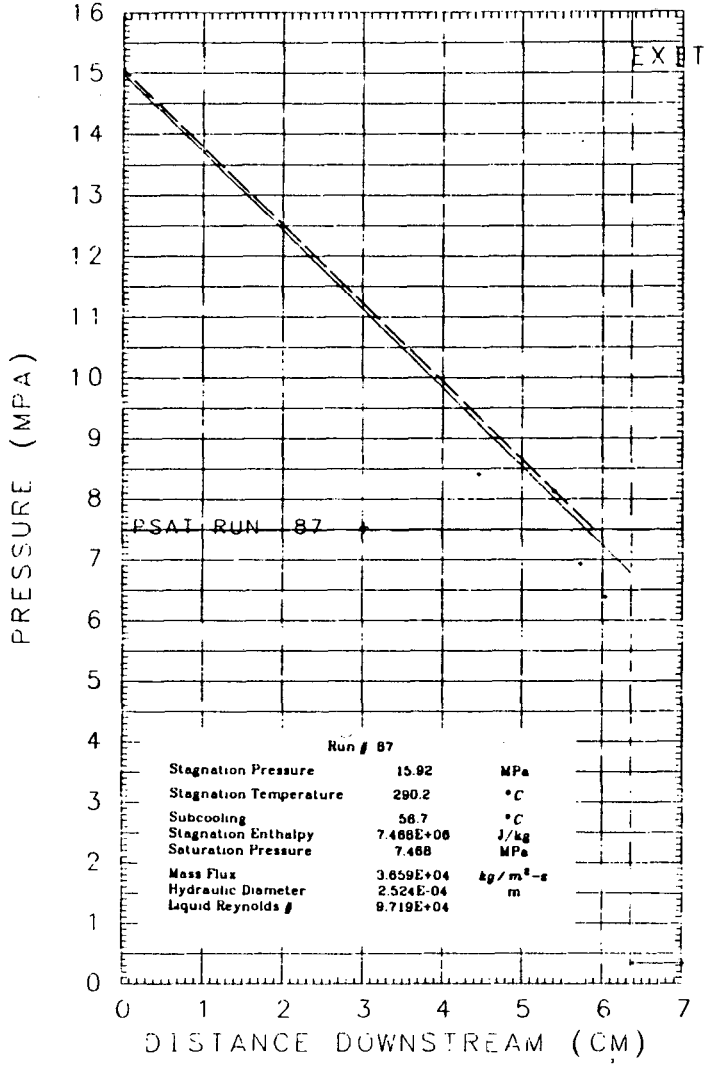

PRESSURE PROFILE, 89

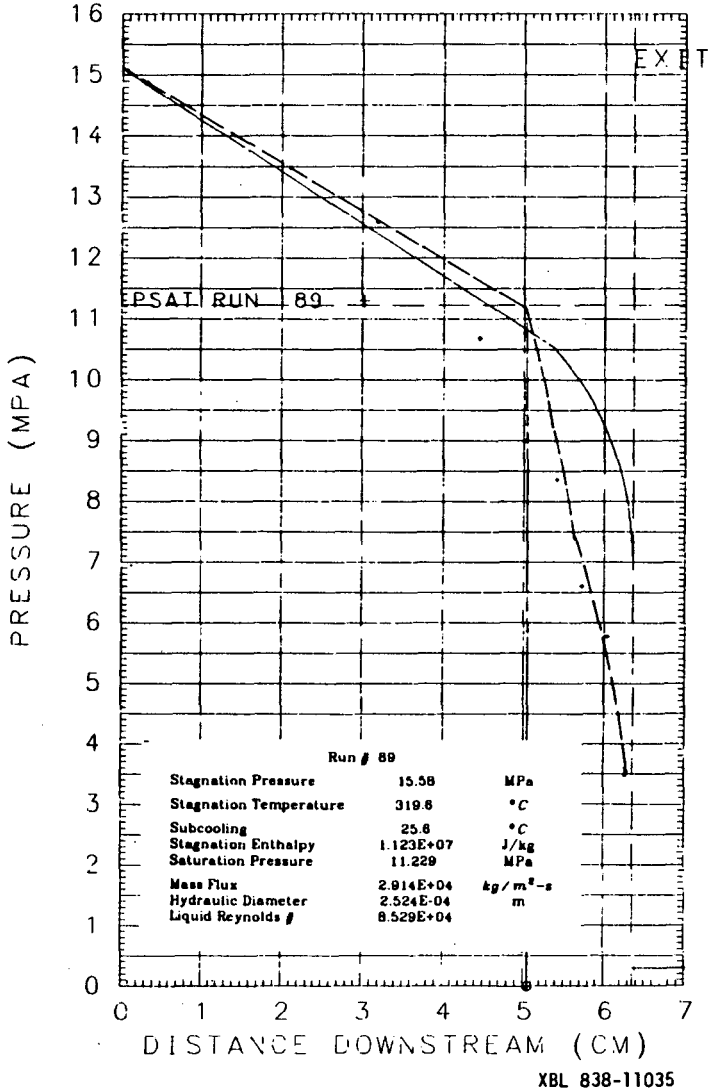

XBL 838-11035

SECTION IV

Cold Water Calibration

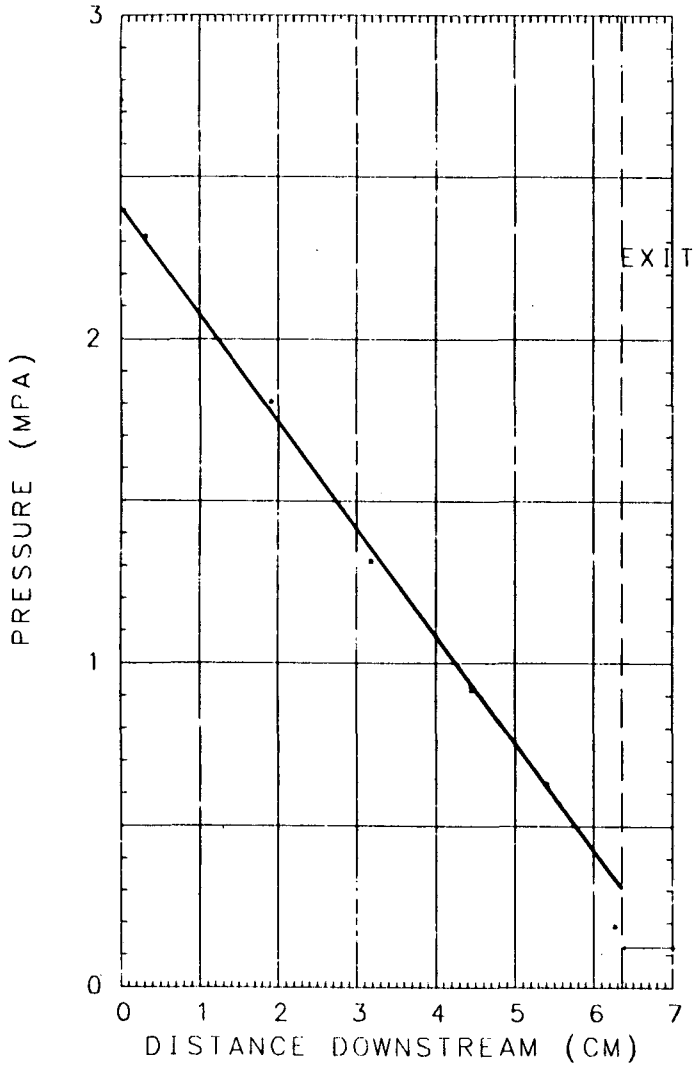

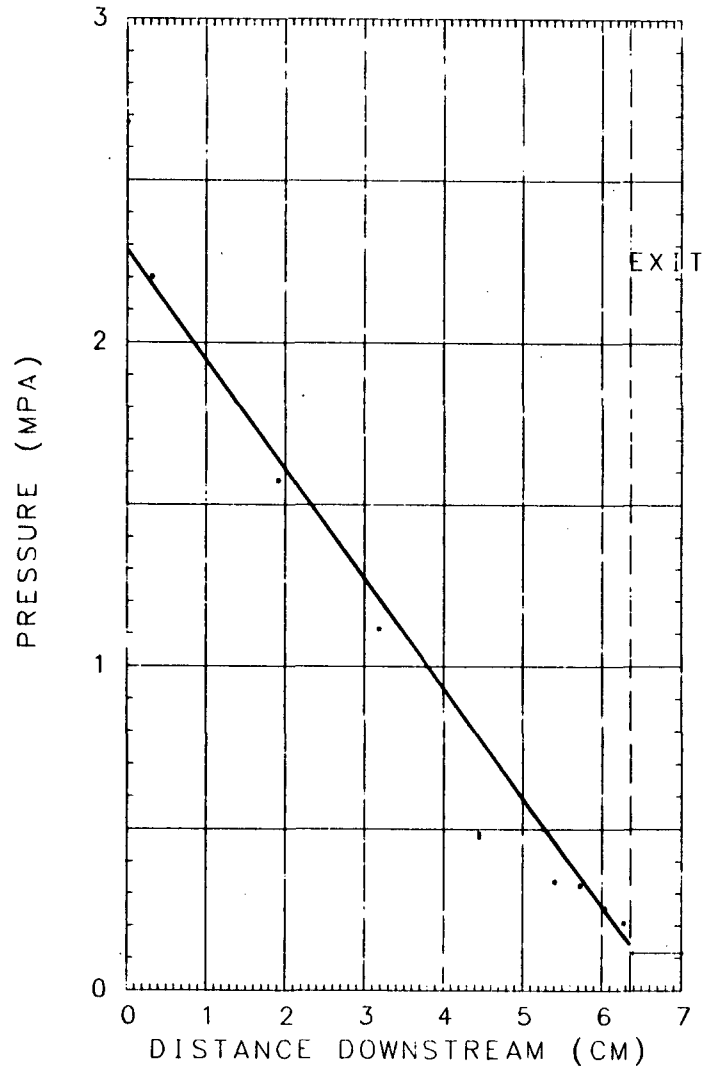

XBL 838-10984

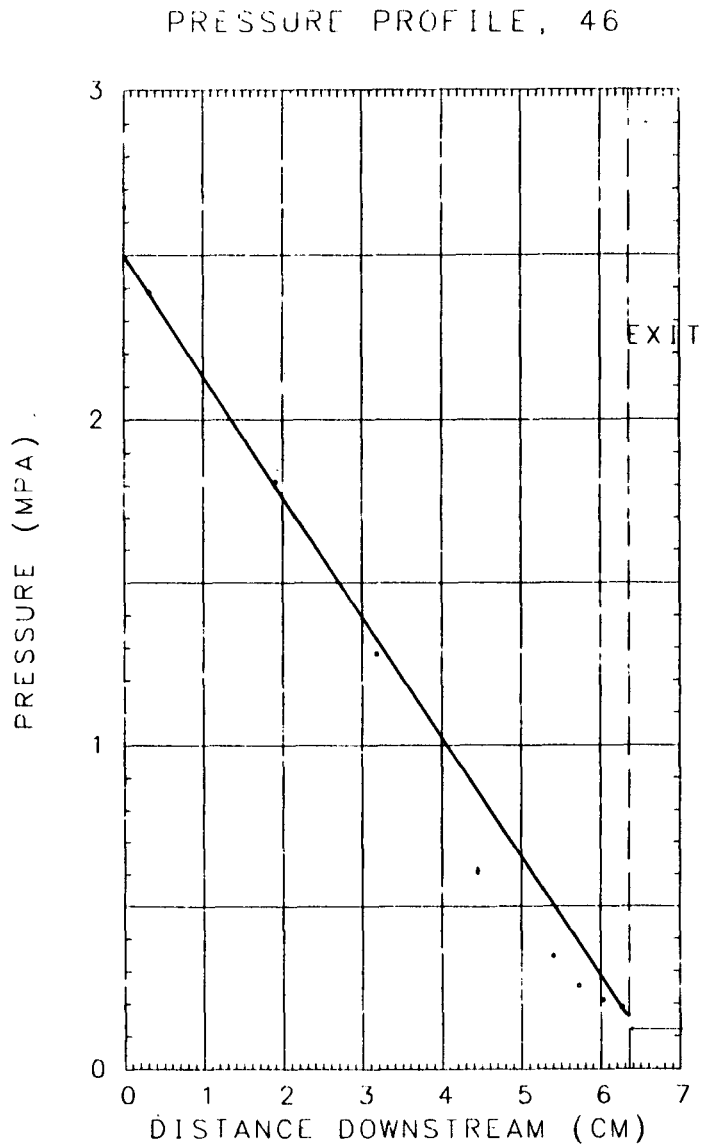

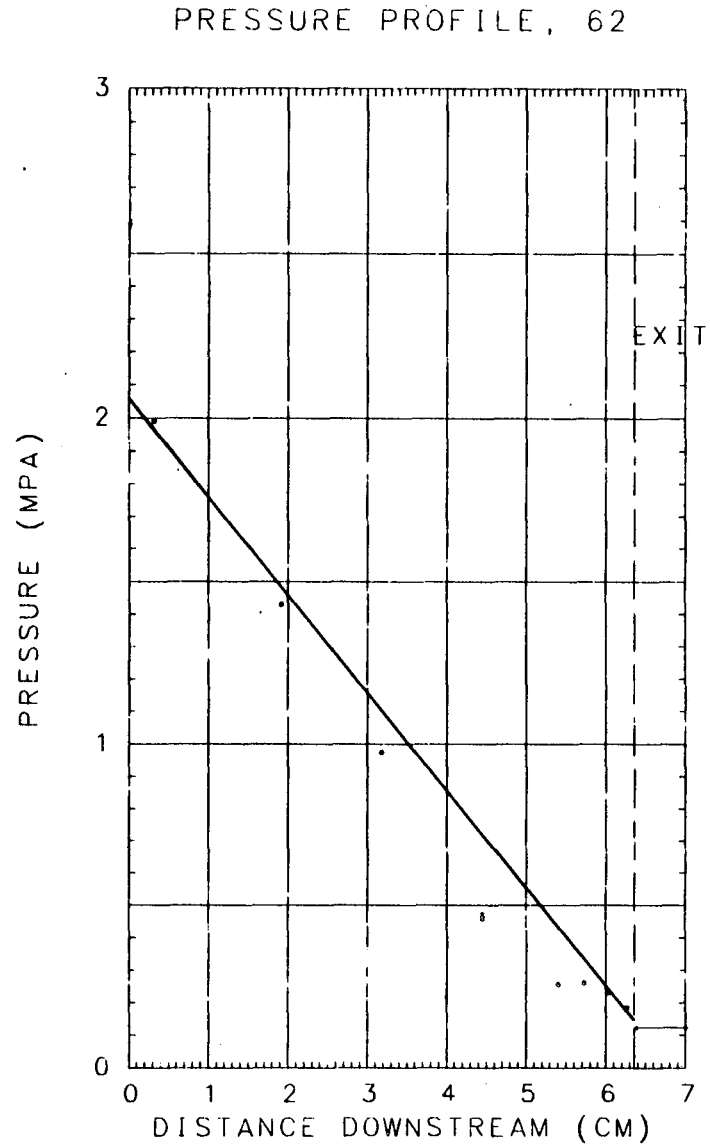

XBL 838-10985

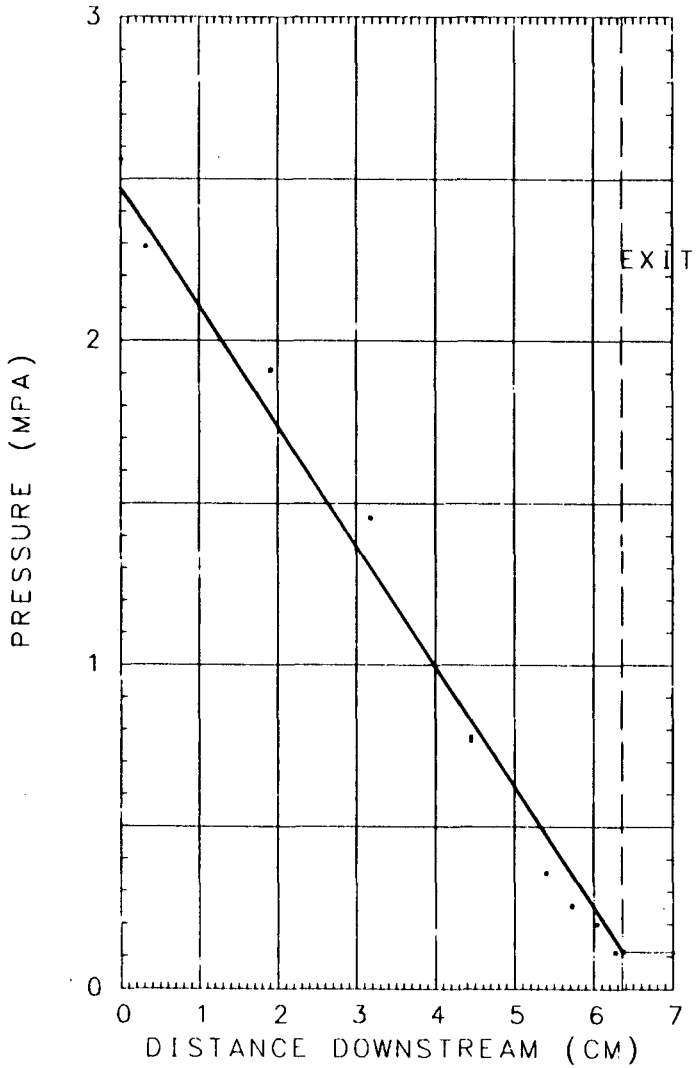

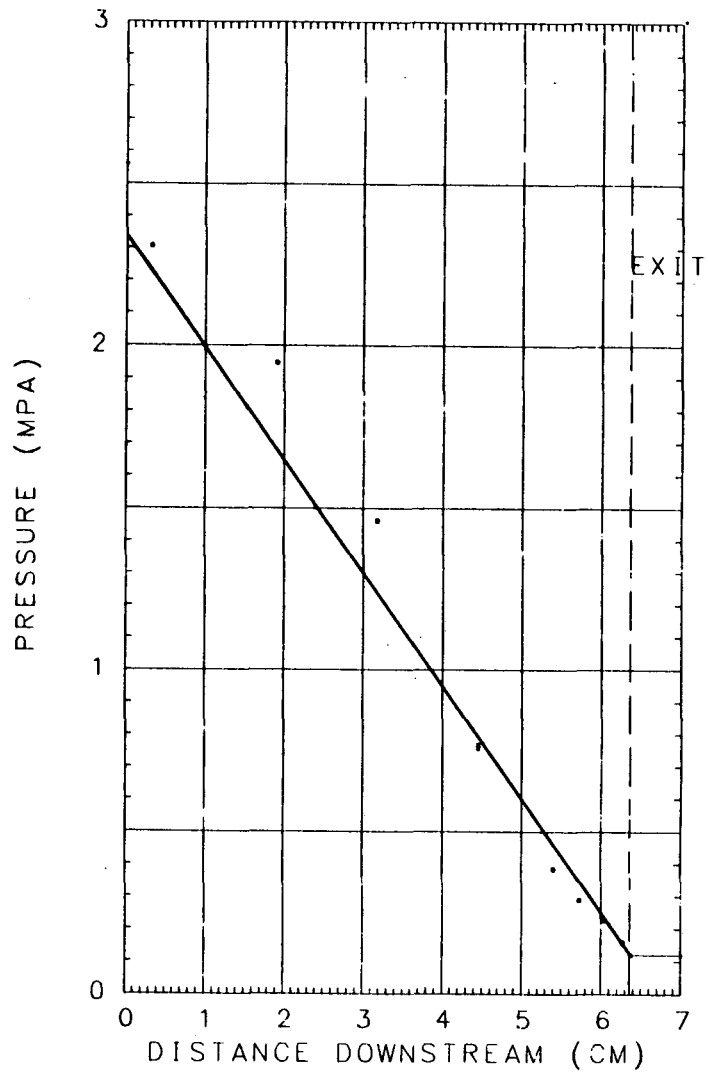

XBL 838-10986

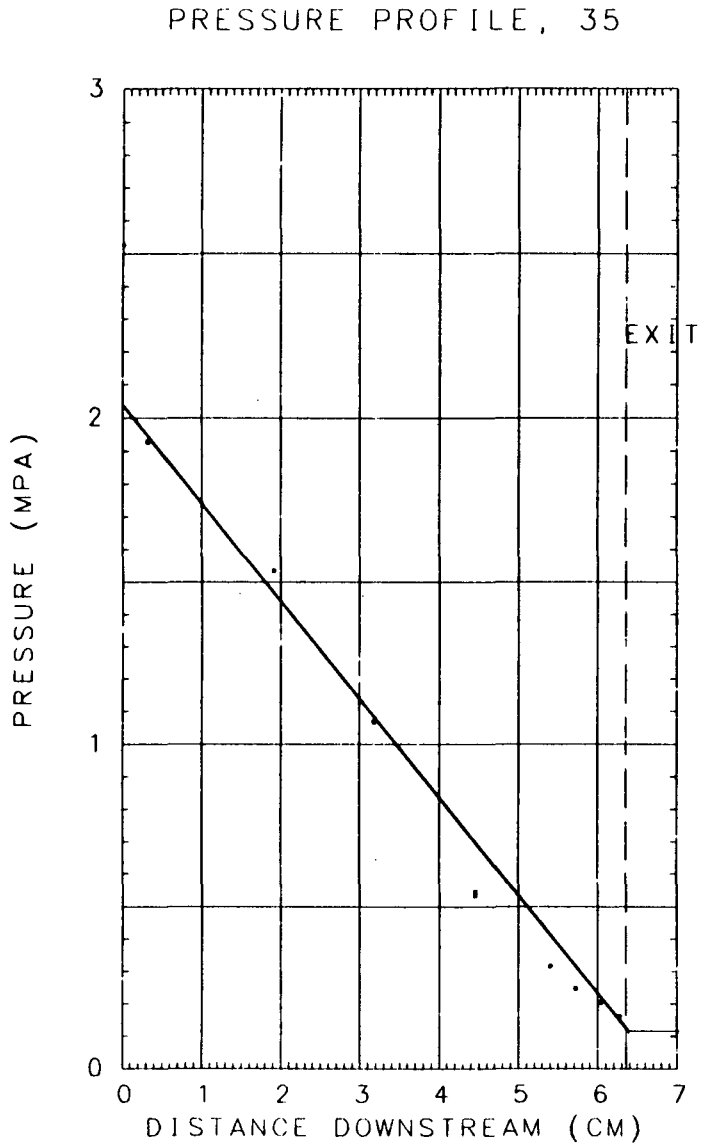

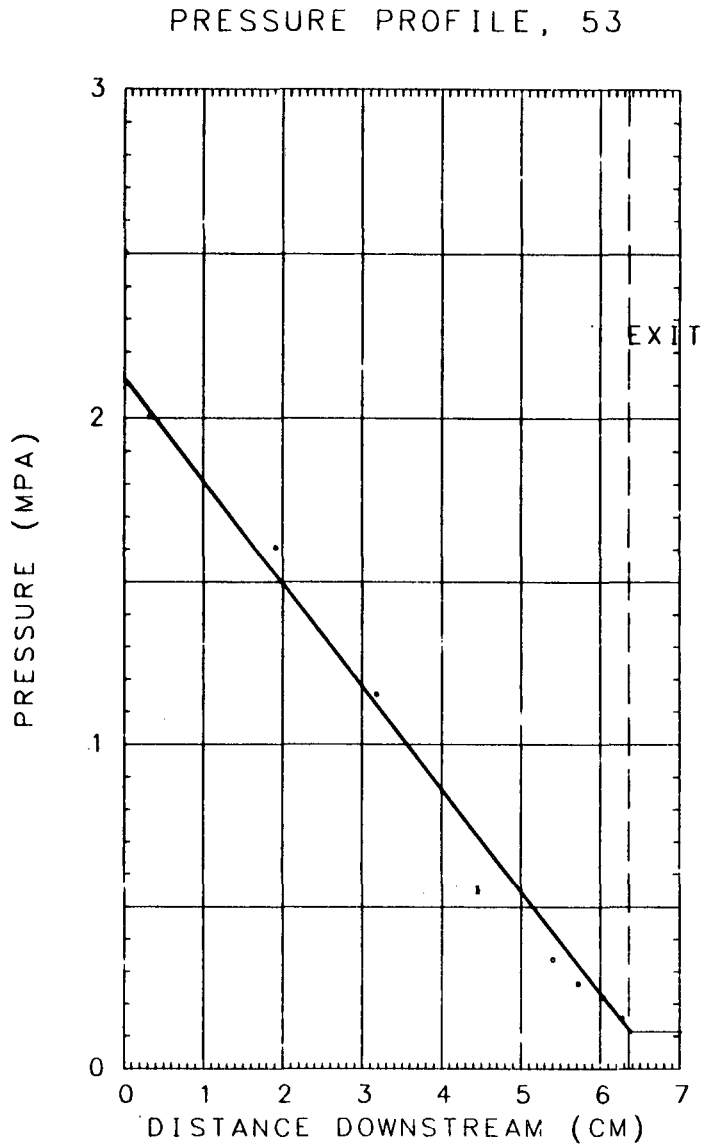

XBL 838-10987

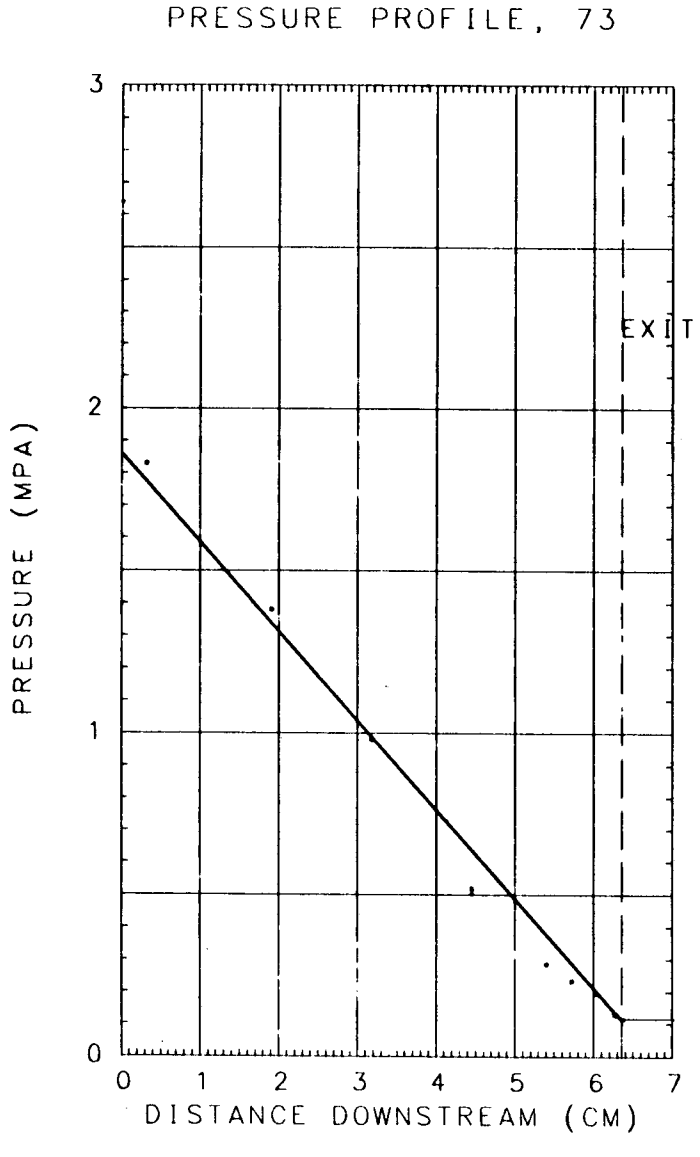

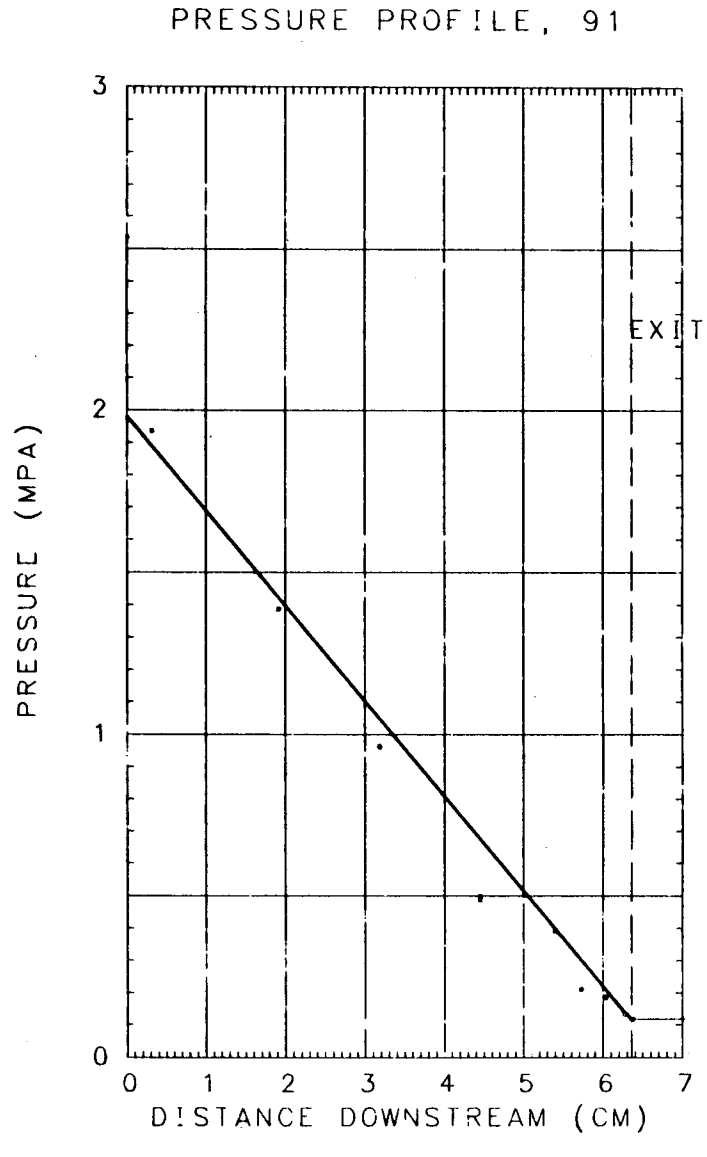

XBL 838-10988

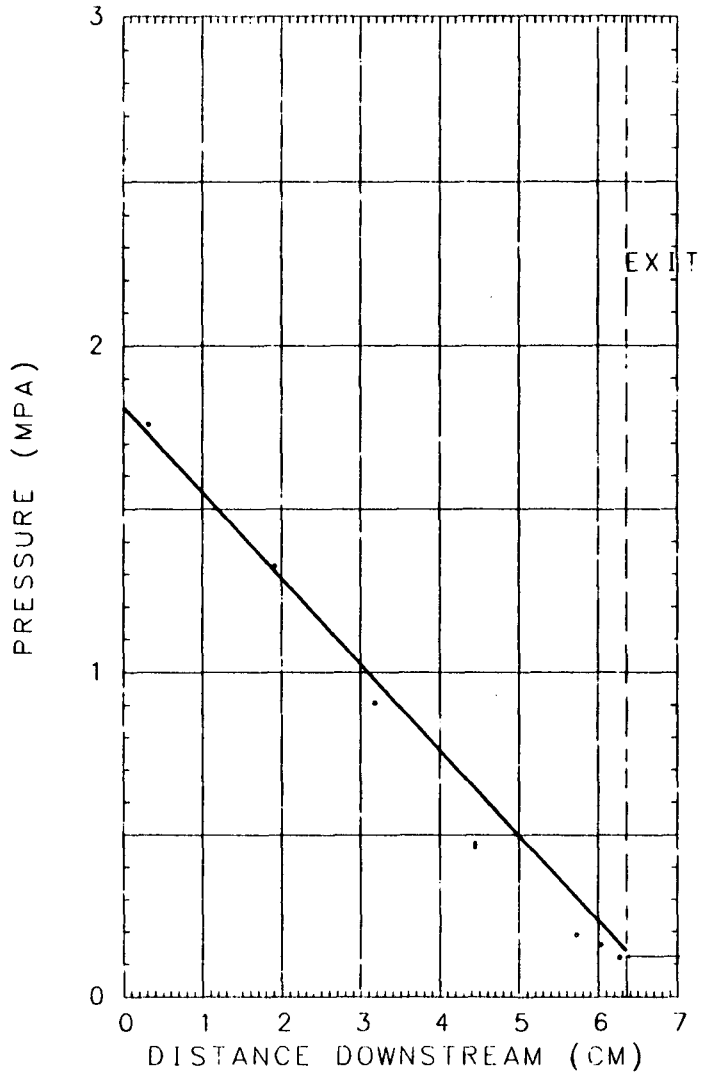

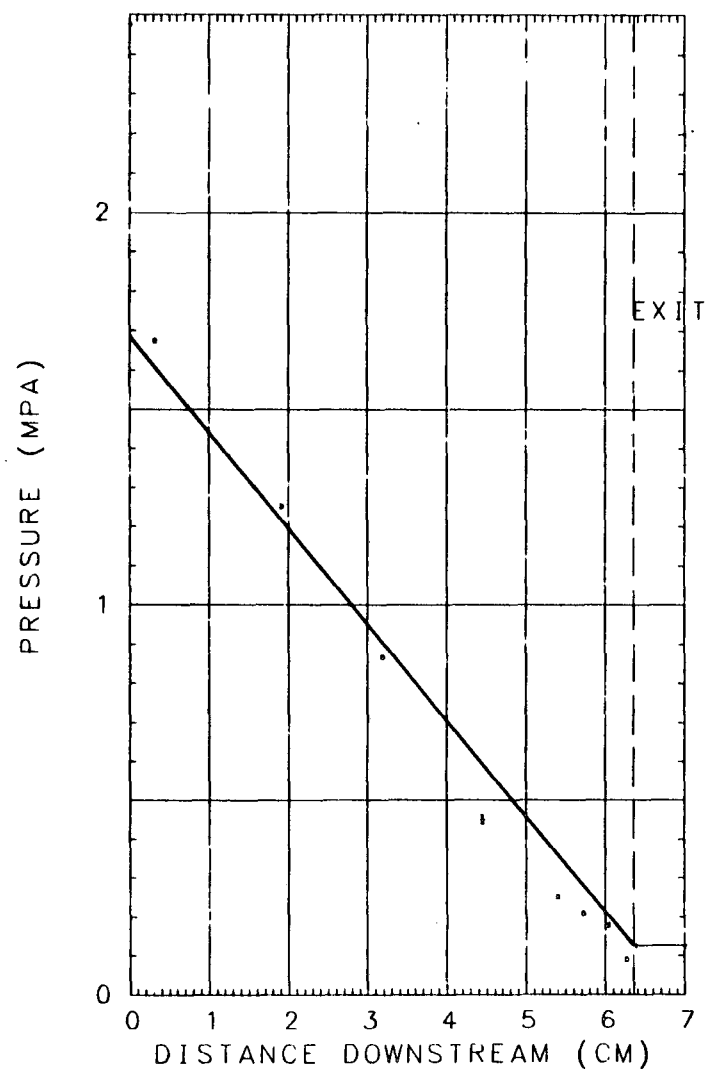

XBL 838-10989

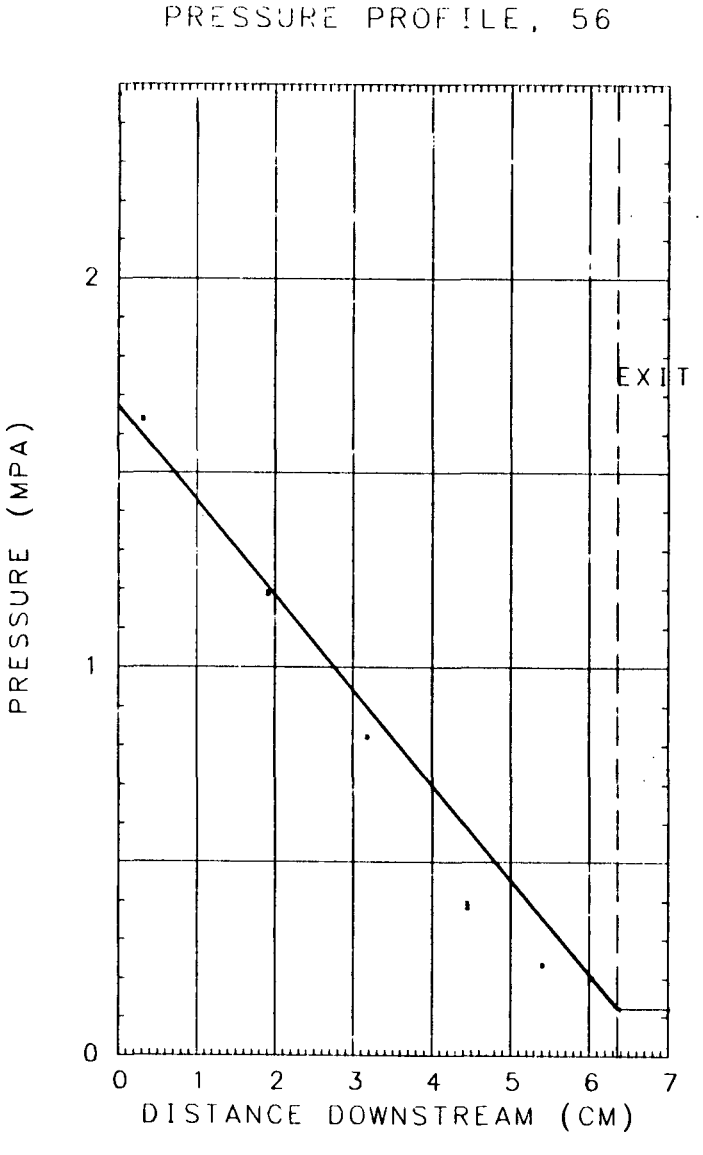

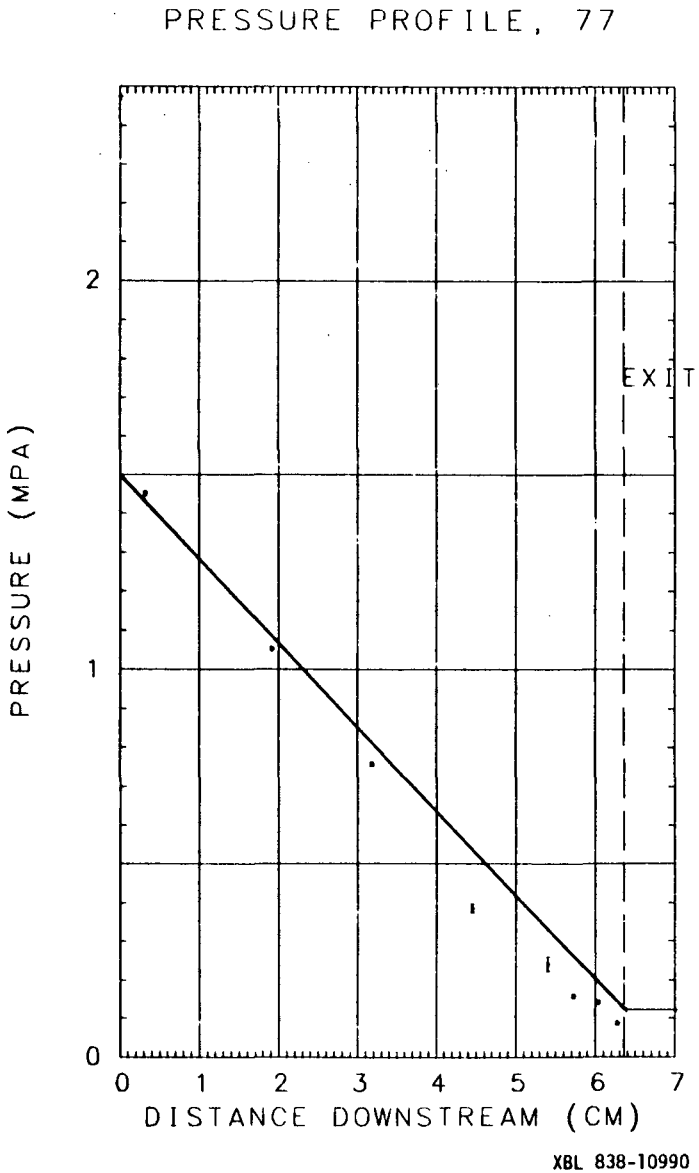

XBL 838-10990

APPENDIX C

Calibration of Instrumentation

C.1 Thermocouple Calibration

The vessel internal thermocouples and the thermocouple used to measure the stagnation temperature were all calibrated at three points. The three points used were: the freezing point of water, the boiling point of water, and the freezing point of lead (327.5°C).

For the calibration, the thermocouples were wired exactly as in the experiment. The ice junction, as in the experiment, was made by immersing a thermocouple made from standard extension wire in a glass vacuum bottle filled with crushed ice and distilled water. The thermocouple emf was measured by the Auto-Data Eight. Data was printed on paper tape so that appropriate averages of the data could be determined. When using the printer, the Auto-Data's scanning rate is reduced to 2.5 readings/sec. As described in Chapter III, the Auto-Data's resolution is 10 micro-volts. For the iron-constantan thermocouples this corresponds to an uncertainty in the measurement of between ± 0.18 and ± 0.19°C. Copper-constantan thermocouples have a more variable (with temperature) Seebeck coefficient and the uncertainty is between ± 0.17 and ± 0.24°C.

All the thermocouples showed a zero offset which was determined by immersing the thermocouple in the ice junction container. This reading was taken after a 5 minute immersion to a depth of approximately 10 cm. It only required about a minute for the reading to stabilize; five minutes was allowed to ensure that the probe was in equilibrium. An immersion depth of 10 cm assured a minimal fin effect on the junction from the exposed length of the probe.

Boiling water in a 400 ml beaker, open to the air at standard atmospheric pressure, supplies the 100°C reference point. During the reading, the thermocouple was held 3 to 4 cm away from the bottom of the beaker so that any superheat generated by heating the smooth bottom would not influence the reading. The water was boiled vigorously during the measurement. Readings were observed to remain stable.

To measure the lead freezing point, lead was melted in a brass container. The Auto-Data was then started and the thermocouple immersed approximately 3 cm into the lead. Allowing the lead to freeze slowly caused the thermocouple to trace a cooling curve, as shown in Figure C-1. That portion of the curve with zero slope corresponds to the freezing point. The average emf at this point was taken to correspond with the lead freezing temperature.

Since the copper-constantan thermocouples used within the test section had exposed junctions, the above procedures could not be used to calibrate them. Instead, a copper block was fabricated into which four of the thermocouples to be calibrated, plus a thermocouple calibrated by the above procedure, could be inserted. The block was immersed in linseed oil which was then heated. The exposed junction thermocouples were then calibrated using the fifth thermocouple as a standard. Making the block from copper, which has high thermal conductivity, reduced any possible temperature gradients within the block. Immersion in linseed oil ensured that the outer surfaces of the block (except the top, which was exposed to the air) were exposed to a uniform temperature. Linseed oil was particularly useful because it has a high boiling point (287°C). All fifteen exposed junction thermocouples were calibrated, four at a time, in this apparatus. It was found that the exposed junction probes agreed with the sheathed probe to within the uncertainty of the Auto-Data measurement.

Prior to run #31, five chromel-constantan thermocouples were installed in the test section. These thermocouples were not calibrated. However, comparison of data taken from these thermocouples with those from adjacent copper-constantan thermocouples during the heat-up phase of the experiment show agreement within ±1°C. This is adequate, since these data were only used for qualitative analysis.

Calibration data for the iron-constantan thermocouples used in the vessel showed agreement with standard calibration tables to within the Auto-Data resolution once the zero offset of +0.03mV had been subtracted. No correction to the tabulated calibration was made. For the copper-constantan thermocouples, a deviation from the calibration table which increased with temperature was revealed. After accounting for the zero offset, only two reference points remained. A linear correction to the standard calibration was used.

Calibration table data was implemented in the data reduction program with a cubic spline of the NBS (National Bureau of Standards) calibration tables. Splines covered the range from 0 to 350°C. A check of the spline accuracy was made on the computer by calculating the temperature corresponding to each emf list ed in the table. Agreement between table and spline was always within 0.03°C. Corrections for the copper-constantan thermocouples were made by first calculating the temperature from the spline and then adding to that temperature the correction predicted by the linear equation resulting from the calibration experiments.

C.2 Pressure Transducers

All the pressure transducers, with the exception of the vessel level transducer, were calibrated using a Crosby fluid pressure scale; model CD-1M. The scale applies a fluid pressure to the instrument to be calibrated. This pressure can be read directly from a balanced scale beam. The smallest division on the scale beam is 6.89 kPa.

Calibration of each transducer began by setting the zero on the pressure scale and recording the transducer emf as read by the Auto-Data. Fluid pressure was then increased in steps of a size suitable for making at least fifteen readings over the range of that transducer. Auto-Data reading and fluid pressure were recorded for each step. These results are shown for each transducer as Tables C-1 through C-9.

A least-squares fitting algorithm was used to obtain a correlation equation for each transducer. This equation was used in the data reduction program. Tables C-1 through C-9 also show the discrepancy between the pressure predicted by the calibration equation and that determined by the pressure scale. More is said about errors incurred by this procedure in Appendix D.

The vessel level transducer had a full scale range equal to 3.6 times the smallest division of the pressure scale balanced beam. It was therefore necessary to use other means for calibrating this transducer. In fact, two other techniques were employed.

The first calibration was with a water filled manometer. Again using the Auto-Data, the transducer output was recorded as a function of height of the water column in the manometer. These results are tabulated in Table C-10. A correlating equation was obtained in the same manner as described above.

The second calibration procedure proved superior to the first. Since the vessel was made from standard pipe, the inner surface is somewhat irregular. Calculation of the water mass in the vessel from a measurement of differential pressure requires knowledge of the inside diameter. Accurate determination of the inside diameter was hampered by the rough surface and the fact that only 15 cm of the nearly 290 cm of pipe were accessible for accurate measurement. At best, the measurement made of the inside diameter was only correct within about 2%. To avoid this potential source of error, the

second calibration was performed with the transducer installed on the vessel. Starting with the vessel full, water was drained in units of about 900 ml. The exact volume of water drained was measured in a graduated cylinder. Transducer emf was recorded as a function of the amount of water drained. This calibration is shown in Table C-11. A correlating equation was calculated which gives volume of water necessary to fill the vessel versus transducer emf. This calibration can be used directly to determine the mass of water in the vessel if the fluid density is known. The inside diameter of the pipe is not required.

C.3 Weigh Tank Load Cells

As with the calibration of the vessel level transducer, the load cells were best calibrated in place. Two methods for calibrating the load cells were employed. For the first the weigh tank was filled with water to the lowest level which would allow steam condensation; about 12 cm above the jet nozzles. Steel weights, of 4.214 kg each were then placed in the center of the tank. The output of both cells was recorded by the Auto-Data after the addition of each weight. A total of ten weights were added, covering a range of 150% of the capacity of the vessel. This method proved unsatisfactory since the reading would change by 1 to 2% depending upon how the weights were distributed in the bottom of the tank.

Greater accuracy was achieved by adding measured quantities of water to the tank rather than weights. This method was very similar to the second method used for calibrating the vessel level transducer which is described above. Readings of the output from each load cell were recorded after each addition. The average of the sum of the two readings was used as the datum for calibration. The calibration was repeated with a slightly different slant on the tank to ensure that transducers were sufficiently similar for the summation technique to be accurate. Using the sum of the load cell outputs avoided the problem of calibrating the load cells separately and then re-setting the mechanical bias for the tare weight when they were re-installed in the weigh tank frame.

During the experiment, the dynamic loading produced by the jet nozzles caused the tank to sway. This induced sway gives rise to oscillations in the tank mass reading on the order of 0.5 kg. Because of the feature, data from the weigh tank was used only to confirm flowrate calculations based on level transducer data. Thus it was deemed unnecessary to refine the calibration by doing each load cell separately. Calibration data is presented in Table C-12.

Table C-1

Calibration of Stagnation Pressure Transducer
Gould-Statham Model PA822-3M
Using Signal Conditioner/Amplifier

Pressure (MPa)	Amplifier Output (Volts)	Calibration Error (kPa)	Pressure (MPa)	Amplifier Output (Volts)	Calibration Error (kPa)
0.00	-3.872	16.7	1.034	-3.166	1.1
1.724	-2.688	2.4	2.068	-2.447	0.1
2.413	-2.212	6.6	2.431	-2.211	5.1
2.758	-1.973	7.2	3.447	-1.493	5.5
4.137	-1.013	3.9	4.482	-0.768	-4.1
4.826	-0.534	3.7	4.826	-0.529	-3.6
6.205	0.428	-2.6	6.205	0.432	-8.4
6.895	0.905	0.0	7.240	1.139	7.7
7.584	1.381	3.9	7.584	1.386	-3.2
8.619	2.102	-0.1	9.308	2.582	-1.9
9.653	2.818	3.0	9.653	9.653	-5.7
9.998	3.062	-3.7	10.342	3.299	-0.3
11.376	4.016	-0.1	11.721	4.255	1.7
11.721	4.258	-2.6	12.066	4.496	-0.6
12.411	4.736	-1.6	13.100	5.211	3.7
13.100	5.214	-0.6	13.790	5.696	-5.4
13.790	5.698	-8.3	14.479	6.167	5.7
15.169	6.648	2.3	15.169	6.650	-0.6
15.513	6.891	-3.0	15.858	7.125	4.7
16.203	7.367	0.8	16.548	7.605	2.7

Probable Error in Pressure Reading = 3.4kPa

Probable Error in Transducer Output Reading = 0.001 Volts
Equivalent to 1.4 kPa

Calibration Equation:

$$P_0 = X_2(V)^2 + X_1(V) + X_0$$

where,

$X_2 = 3.8554 \times 10^1$

$X_1 = 1.439968 \times 10^6$

$X_0 = 5.5916 \times 10^6$

The maximum error between the measured differential pressure in the above calibration and the prediction of the calibration equation was 8.4 kPa (= 0.04% *Full Scale*).

rms error = 4.8 kPa

Table C-2

Calibration of Differential Pressure Transducer
Gould-Statham Model PM8142±1000, s/n 649

Pressure (MPa)	Transducer Output (mV)	Calibration Error (kPa)	Pressure (MPa)	Transducer Output (mV)	Calibration Error (kPa)
0.000	0.00	0.0	0.689	3.97	4.8
1.379	7.92	5.8	2.068	11.87	6.6
2.758	15.85	-5.2	3.447	19.77	7.2
4.137	23.64	-6.8	4.826	27.58	-8.8
5.516	31.57	-3.2	6.205	35.35	3.6
6.895	39.54	7.6			

Probable Error in Pressure Reading = 3.4kPa

Probable Error in Transducer Output Reading = 0.01mV
Equivalent to 1.7 kPa

Calibration Equation:

$$P = X_2(mV)^2 + X_1(mV) + X_0$$

where,

$X_2 = -8.756 \times 10^{-6}$

$X_1 = 0.174693$

$X_0 = 0.0$

The maximum error between the measured differential pressure in the above calibration and the prediction of the calibration equation was 8.8 kPa (= 0.1% *Full Scale*).

rms error = 5.9 kPa

Table C-3

Calibration of Differential Pressure Transducer
Validyne Model DP-15, s/n 50141, ±862 kPa

Pressure (kPa)	Demodulator Output (Volts)	Calibration Error (kPa)	Pressure (kPa)	Demodulator Output (Volts)	Calibration Error (kPa)
0.0	-1.713	-1.6	68.9	-1.000	1.4
137.9	-0.238	0.4	206.8	0.516	0.5
275.8	1.281	0.1	344.7	2.045	0.2
413.7	2.816	0.2	482.6	3.608	-1.2
551.6	4.364	1.1	620.5	5.168	-0.4
689.5	5.966	-0.8	758.4	6.753	0.2
827.4	7.533	2.2	896.3	8.383	-1.1

Probable Error in Pressure Reading = 3.4kPa

Probable Error in Transducer Output Reading = 0.001 Volts
Equivalent to 0.1 kPa

Calibration Equation:

$$P(kPa) = X_2(V)^2 + X_1(V) + X_0$$

where,

$X_2 = -0.39638$

$X_1 = 91.372$

$X_0 = 159.31$

The maximum error between the measured differential pressure in the above calibration and the prediction of the calibration equation was 2.2 kPa (= 0.3% *Full Scale*).

rms error = 0.9 kPa

Table C-4

Calibration of Differential Pressure Transducer
Validyne Model DP-15, s/n 50139, ±2.2 MPa

Pressure (MPa)	Demodulator Output (Volts)	Calibration Error (kPa)	Pressure (MPa)	Demodulator Output (Volts)	Calibration Error (kPa)
0.000	-0.278	0.0	0.000	-0.278	0.0
0.000	-0.279	-0.2	0.069	0.015	-2.9
0.207	0.627	-3.3	0.345	1.245	-2.8
0.345	1.267	2.1	0.414	1.568	0.2
0.414	1.569	0.5	0.483	1.868	0.5
0.552	2.177	-2.3	0.552	2.190	-2.3
0.621	2.489	-1.9	0.690	2.817	1.7
0.758	3.117	-0.9	0.758	3.118	-0.7
0.827	3.431	-0.7	0.827	3.434	-0.1
0.896	3.742	-1.2	0.896	3.751	0.8
1.103	4.684	-1.8	1.103	4.685	-1.5
1.172	5.008	0.0	1.241	5.321	-0.9
1.241	5.328	0.7	1.300	5.637	8.9
1.300	5.647	11.7	1.379	5.948	-2.7
1.379	5.968	1.6	1.448	6.274	-1.1
1.448	6.284	1.1	1.517	6.583	-3.4
1.586	6.903	-3.4	1.655	7.232	-2.5
1.724	7.552	-1.9	1.724	7.555	-1.3
1.724	7.562	0.2	1.793	7.883	-1.7
1.862	8.197	-2.0	1.862	8.203	-0.7
2.000	8.844	-2.2	2.000	8.852	-0.5
2.000	8.863	1.9	2.068	9.173	-1.3
2.137	9.507	0.4	2.206	9.824	-1.6
2.206	9.832	0.1			

Probable Error in Pressure Reading = 3.4kPa

Probable Error in Transducer Output Reading = 0.001 Volts
Equivalent to 0.2 kPa

Calibration Equation:

$$P(MPa) = X_2(V)^2 + X_1(V) + X_0$$

where,

$X_2 = -7.2528 \times 10^{-4}$

$X_1 = 2.2517 \times 10^{-3}$

$X_0 = 6.8203 \times 10^{-4}$

The maximum error between the measured differential pressure in the above calibration and the prediction of the calibration equation was 11.7 kPa (= 0.5% *Full Scale*).

rms error = 2.1 kPa

Table C-5

Calibration of Absolute Pressure Transducer
Gould-Statham Model PA891-3M

Pressure (MPa)	Transducer Output (mV)	Calibration Error (kPa)	Pressure (MPa)	Transducer Output (mV)	Calibration Error (kPa)
0.000	-1.41	-11.2	0.345	-1.05	-8.3
0.689	-0.69	-5.4	1.034	-0.33	-2.4
1.379	0.03	0.6	1.724	0.40	5.9
2.068	0.76	3.0	2.413	1.12	0.0
2.758	1.48	3.0	3.103	1.84	5.9
3.447	2.21	-0.6	3.792	2.57	2.3
4.137	2.93	5.3	4.482	3.30	-1.2
4.826	3.66	1.7	5.171	4.02	4.7
5.516	4.39	-1.9	6.205	5.11	4.1
6.895	5.84	0.5	7.584	6.56	6.4
8.274	7.29	2.8	8.963	8.01	8.8
9.653	8.74	5.2	10.342	9.47	1.7
11.032	10.19	7.6	11.721	10.91	13.5
12.411	11.65	0.4	13.100	12.37	6.3
13.790	13.11	-6.7	14.479	13.84	-10.3
15.169	14.56	-4.3	15.858	15.29	-7.9
16.548	16.02	-11.5			

Probable Error in Pressure Reading = 3.4kPa

Probable Error in Transducer Output Reading = 0.01mV
Equivalent to 13.5 kPa

Calibration Equation:

$$P = X_1(mV) + X_0$$

where,

$X_1 = 9.493827 \times 10^5$

$X_0 = 1.349901 \times 10^6$

The maximum error between the measured differential pressure in the above calibration and the prediction of the calibration equation was 13.5 kPa (= 0.07% *Full Scale*).

rms error = 5.3 kPa

Table C-6

Calibration of Differential Pressure Transducer
Gould-Statham Model PM8142±1000, s/n 650

Pressure (MPa)	Transducer Output (mV)	Calibration Error (kPa)	Pressure (MPa)	Transducer Output (mV)	Calibration Error (kPa)
0.000	0.00	0.0	0.689	3.89	-5.1
0.689	3.93	2.0	1.379	7.82	-1.4
1.379	7.86	1.0	2.068	11.82	4.4
2.758	15.76	1.4	2.758	15.76	1.4
3.447	19.71	-0.8	3.447	19.74	4.4
4.137	23.66	-5.9	4.137	23.68	-2.5
4.826	27.67	-1.6	5.516	31.67	-2.0
6.205	35.68	-1.6	6.205	35.68	-1.6
6.895	39.72	1.0	6.895	39.72	1.0

Probable Error in Pressure Reading = 3.4kPa

Probable Error in Transducer Output Reading = 0.01mV
Equivalent to 1.8 kPa

Calibration Equation:

$$P = X_2(mV)^2 + X_1(mV) + X_0$$

where,

$X_2 = -6.14947 \times 10^{-5}$

$X_1 = 0.176057$

$X_0 = 0.0$

The maximum error between the measured differential pressure in the above calibration and the prediction of the calibration equation was 5.9 kPa (= 0.08% *Full Scale*).

rms error = 2.7 kPa

Table C-7

Calibration of Differential Pressure Transducer
Gould-Statham Model PM8142±1000, s/n 651

Pressure (MPa)	Transducer Output (mV)	Calibration Error (kPa)	Pressure (MPa)	Transducer Output (mV)	Calibration Error (kPa)
0.000	0.43	0.0	0.345	2.37	-2.9
0.689	4.35	-1.8	1.034	6.32	-3.5
1.379	8.31	-1.7	1.724	10.30	0.2
2.068	12.28	1.3	2.413	14.46	1.4
3.103	18.21	-0.1	3.447	20.18	-0.7
3.447	20.19	1.0	3.792	22.16	-0.6
4.137	24.13	-2.2	4.482	26.12	-0.3
4.826	28.10	0.8	5.171	30.05	-4.3
5.516	32.06	1.1	5.861	34.04	1.3
6.205	36.00	-1.0	6.550	37.99	0.1
6.895	39.95	-2.4			

Probable Error in Pressure Reading = 3.4kPa

Probable Error in Transducer Output Reading = 0.01mV
Equivalent to 1.7 kPa

Calibration Equation:

$$P = X_2(mV)^2 + X_1(mV) + X_0$$

where,

$X_2 = 7.8601 \times 10^{-7}$

$X_1 = 0.174278$

$X_0 = 7.494 \times 10^{-2}$

The maximum error between the measured differential pressure in the above calibration and the prediction of the calibration equation was 4.3 kPa (= 0.07% *Full Scale*).

rms error = 1.8 kPa

Table C-8

Calibration of Differential Pressure Transducer
Gould-Statham Model PM8142±1000, s/n 652

Pressure (MPa)	Transducer Output (mV)	Calibration Error (kPa)	Pressure (MPa)	Transducer Output (mV)	Calibration Error (kPa)
0.000	0.00	0.0	0.345	1.95	-6.1
0.689	3.95	-3.0	1.034	5.92	-6.4
1.379	7.95	0.1	1.724	9.96	2.8
2.068	11.96	4.4	2.413	13.96	4.6
2.758	15.96	4.4	3.103	17.97	5.5
3.447	19.93	-1.4	3.447	19.91	-4.8
3.447	19.90	-6.5	3.792	21.92	-4.5
3.792	21.90	-7.9	4.137	23.91	-7.9
4.482	25.98	1.9	4.826	28.01	5.4
5.171	30.00	0.7	5.516	32.02	0.8
5.861	34.04	-1.3	6.205	36.06	0.7
6.550	38.09	1.2	6.895	40.16	8.1
6.895	40.17	9.8			

Probable Error in Pressure Reading = 3.4kPa

Probable Error in Transducer Output Reading = 0.01mV
Equivalent to 1.7 kPa

Calibration Equation:

$$P = X_2(mV)^2 + X_1(mV) + X_0$$

where,

$X_2 = -4.926 \times 10^{-5}$

$X_1 = 0.173870$

$X_0 = 0.0$

The maximum error between the measured differential pressure in the above calibration and the prediction of the calibration equation was 9.8 kPa (= 0.14% *Full Scale*).

rms error = 5.1 kPa

Table C-9

Calibration of Differential Pressure Transducer
Validyne Model DP-15, s/n 50140, ±2.2 MPa

Pressure (MPa)	Demodulator Output (Volts)	Calibration Error (kPa)	Pressure (MPa)	Demodulator Output (Volts)	Calibration Error (kPa)
0.000	0.001	-1.4	0.207	0.979	2.7
0.345	1.645	3.4	0.482	2.329	1.1
0.621	3.004	1.4	0.689	3.355	-0.8
0.896	4.381	-1.1	1.034	5.066	-0.5
1.172	5.746	1.9	1.379	6.794	1.4
1.517	7.481	4.3	1.655	8.204	0.9
1.793	8.908	2.1	2.000	9.985	1.4
2.068	10.345	1.4	2.206	11.073	0.5
2.413	12.193	-4.4	1.379	6.820	-3.8
1.034	5.075	-2.3	1.724	8.564	-2.3
1.517	7.503	0.0	1.241	6.116	-2.6
1.103	5.431	-4.4	1.034	5.090	-5.3
1.034	5.075	2.3	0.689	3.364	-2.7

Probable Error in Pressure Reading = 3.4kPa

Probable Error in Transducer Output Reading = 0.001 Volts
Equivalent to 0.2 kPa

Calibration Equation:

$$P(MPa) = X_2(V)^2 + X_1(V) + X_0$$

where,

$X_2 = 8.170 \times 10^{-4}$

$X_1 = 2.0815 \times 10^{-3}$

$X_0 = 1.1856 \times 10^{-3}$

The maximum error between the measured differential pressure in the above calibration and the prediction of the calibration equation was 5.3 kPa (= 0.2% *Full Scale*).

rms error = 2.4 kPa

Table C-10

Calibration of Vessel Level Transducer
Gould-Statham Model PM8142±3.6
Differential Pressure Method

Reading #	mm H_2O at 23° C	ΔP (kPa)	Transducer Output (mV)	Calibration Error (Pa)
1	0.0	0.00	0.00	13.10
2	297.7	2.912	4.95	8.96
3	563.0	5.508	9.40	1.38
4	828.8	8.108	13.84	-0.69
5	1096.6	10.727	18.26	23.44
6	1361.9	13.322	22.69	13.10
7	1622.8	15.874	27.02	13.10
8	1708.8	16.715	28.45	10.34
9	1793.6	17.545	29.85	13.79
10	2282.4	22.326	37.94	8.96
11	2309.6	22.592	38.40	2.76
12	1925.1	18.831	32.07	-11.72
13	1897.1	18.557	31.61	-13.79
14	1819.2	17.795	30.31	-7.58
15	1615.9	15.806	26.97	-24.82
16	1400.0	13.694	23.39	-26.89
17	1091.5	10.677	18.20	8.96
18	1137.4	11.126	18.96	11.03
19	826.3	8.903	13.78	9.65
20	870.2	8.512	14.55	-12.41
21	607.5	5.943	10.16	-8.27
22	561.2	5.490	9.39	-10.34
23	340.9	3.334	5.70	-6.89
24	294.1	2.877	4.92	-8.27
25	112.7	1.103	1.84	15.86
26	12.1	0.119	0.17	6.21

Probable Error in Manometer Reading = 0.5mm
Equivalent to 4.9 Pa

Probable Error in Transducer Output Reading = 0.01mV
Equivalent to 5.8 Pa

Calibration Equation:

$$\Delta P = X_2(mV)^2 + X_1(mV) + X_0$$

where,

$X_2 = 1.2347 \times 10^{-1}$

$X_1 = 583.18$

$X_0 = 13.362$

The maximum error between the measured differential pressure in the above calibration and the prediction of the calibration equation was 26.89 Pa (= 0.11% *Full Scale*).

Table C-11

Calibration of Vessel Level Transducer
Gould-Statham Model PM8142±3.8
Discharged Volume Method

Reading #	Volume Discharged at 27° C (ml)	Transducer Output (mV)	Calibration Error (ml)
1	0.0	0.00	96.54
2	458.2	0.57	26.6
3	1,341.0	2.09	15.9
4	2,293.0	3.69	27.2
5	3,235.0	5.33	4.8
6	4,148.0	6.92	18.7
7	5,144.0	8.55	19.9
8	6,073.0	10.14	13.5
9	7,031.0	11.77	12.3
10	8,001.0	13.43	5.4
11	8,931.0	15.02	-0.5
12	9,922.0	16.70	1.4
13	10,863.0	18.31	-5.6
14	11,812.0	19.92	-4.8
15	12,773.0	21.55	-3.9
16	13,728.0	23.18	-9.2
17	14,697.0	24.82	-6.5
18	15,654.0	26.44	-4.2
19	16,585.0	28.05	-22.1
20	17,546.0	29.67	-16.2
21	18,466.0	31.23	-16.0
22	19,424.0	32.84	-7.4
23	20,336.0	34.38	-3.7
24	21,320.0	36.03	7.0
25	22,288.0	37.66	13.3
26	23,299.0	39.36	21.1
27	24,299.0	41.04	19.5
28	25,260.0	42.70	10.6
29	25,820.0	43.67	-2.1
30	26,330.0	44.53	-0.2
31	26,821.0	45.38	-10.8
32	27,367.0	46.30	-8.1

Probable Error in Volume Discharge Measurement (rms) = 10ml

Probable Error in Transducer Output Reading = 0.01mV
Equivalent to 5.9 ml

Calibration Equation

$$VD = X_2(mV)^2 + X_1(mV) + X_0$$

where,

$X_2 = 0.030468$

X_1 = 587.759

X_0 = 96.537

The maximum error between the measured volume of water discharged in the above calibration and the prediction of the calibration equation was 27.2ml (= 0.10% *Full Scale*). The error at zero of 96.5ml has been discounted since the zero point is arbitrary.

Table C-12

Calibration of Weigh Tank Load Cells
Gould-Statham Model UC3 with UC4 Adapters

Reading #	Mass Added (kg)	Sum of Load Cell Outputs (mV)	Calibration Error (kg)
1	0.00	35.08	0.10
2	0.91	34.77	0.10
3	1.80	34.45	0.04
4	2.71	34.13	0.01
5	3.60	33.81	-0.04
6	4.49	33.51	-0.04
7	5.37	33.21	-0.04
9	7.12	32.60	-0.09
10	7.99	32.30	-0.10
11	8.85	32.01	-0.09
12	9.72	31.71	-0.10
13	10.54	31.44	-0.08
14	11.37	31.16	-0.07
15	12.19	30.89	-0.04
16	13.01	30.62	-0.02
17	13.81	30.35	-0.02
18	14.61	30.09	0.02
19	15.40	29.82	0.01
20	16.36	29.50	0.03
21	17.34	29.16	0.01
22	18.34	28.83	0.04
23	19.23	28.52	0.02
24	20.14	28.22	0.04
25	21.06	27.91	0.05
26	22.05	27.57	0.04
27	23.01	27.25	0.06
28	23 99	26.92	0.06
29	24.96	26.58	0.04
30	25.96	24.24	0.04
31	26.95	25.90	0.03
32	27.92	25.57	0.02
33	28.90	25.24	0.03
34	29.86	24.91	0.02
35	30.84	24.58	0.03
36	31.80	24.26	0.05
37	32.78	23.92	0.02
38	33.73	23.59	0.01
39	34.70	23.27	0.04
40	35.69	22.93	0.02
41	36.67	22.60	0.03
42	37.65	22.26	0.01
43	38.62	21.93	0.01
44	39.61	21.59	0.00
45	40.59	21.27	0.02
46	41.53	20.95	0.04

Table C-12 (cont.)

Reading #	Mass Added (kg)	Sum of Load Cell Outputs (mV)	Calibration Error (kg)
47	42.51	20.61	0.02
48	43.47	20.28	0.00
49	44.46	19.94	0.00
50	45.30	19.66	0.00
51	46.29	19.32	-0.01
52	47.26	18.99	0.00
53	48.24	18.65	-0.03
54	49.21	18.32	-0.02
55	50.18	18.00	0.00
56	51.15	17.65	-0.05
57	52.10	17.33	-0.05
58	53.09	17.00	-0.03
59	54.05	16.67	-0.05
60	54.97	16.35	-0.07

Probable Error in Mass Added Measurement (rms) = 0.01kg

Root Mean Square Error in Transducer Output Reading = 0.014mV Equivalent to 0.04 kg. This could be determined from the data for this calibration and was required since two transducers were employed. For pressure transducer calibrations least significant bit error has been reported.

Calibration Equation

$$W = X_1(mV) + X_0$$

where,

X_1 = -2.94357

X_0 = 103.16

The maximum error between the measured volume of water discharged in the above calibration and the prediction of the calibration equation was 0.10kg (= 0.04% *Full Scale*).

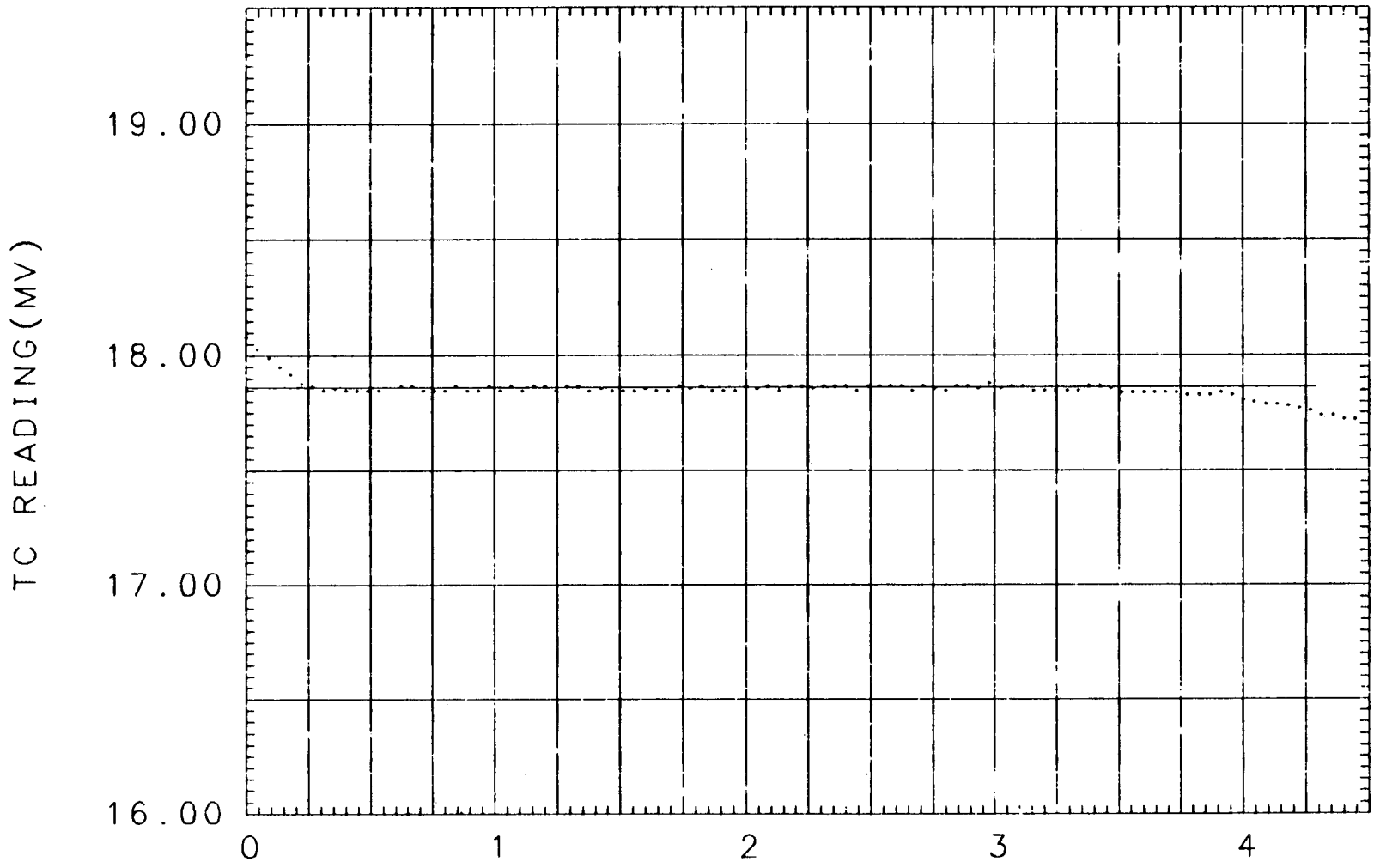

XBL 838-10991

APPENDIX D

Error Analysis

In this appendix, the experimental uncertainty in measurements and calculated parameters reported in this study are discussed. With the exception of the mass flowrate calculation, the error analysis is straightforward. This is true since the other results which have been reported herein are either directly measured quantities, or the algebraic sum of such quantities. Propagation of measurement error into the calculated mass flux results is discussed to the extent which is reasonable in light of the fact that the uncertainty in channel geometry is the largest contribution to the error and the least easy to quantify.

In this analysis it has been assumed that stagnation pressure and temperature measurements, as well as pressure measurements within the slit, can be treated as multiple-sample data. In other words, it has been assumed that the thermocouple and the pressure transducers were exposed to a constant pressure and temperature over the time period for which the data has been reported (11 scans of the Auto-Data Eight). This approach is consistent with the presumption that the stagnation state of the fluid, and the flow within the test section, were maintained in steady state for this period. The error in the measurements, calculated under this assumption, reflect the degree to which this was valid; in addition to actual error in the determination.

Vessel level and weigh tank mass measurements, in addition to measurements of temperature within the test section, cannot be treated by the same approach. In contrast to measurements of the stagnation state and the pressure profile within the slit, these quantities exhibited virtually continuous change over the course of each run. Consequently, these measurements are single-sample data. By this it is meant that the quantity measured has that value only at the instant which the measurement is made. (More precisely, the data represents an average value of the transducer signal over a short measuring period. For the Auto-Data the sample period is approximately 4 microseconds). As discussed by Kline and McClintock [106], errors in data from single-sample experiments are far less easy to quantify than errors from multiple-sample experiments. For multiple sample experiments, statistical analysis of the data gives a good indication of the error. Single-sample experiments require a certain amount of judgment in the determination of the error and the uncertainty interval.

D.1 Factors Contributing to the Error

In these experiments, there are essentially three factors which contribute to the error in a given measurement. These factors, in order of decreasing importance, are: 1) dynamic influence on the system on the instrument or probe, 2) calibration error, and 3) error in recording the measurement. Errors in the calculation of the mass flowrate from the vessel level measurement include these errors, but error in the determination of the density of nitrogen within the vessel must also be considered. All methods of determining the mass flux include error due to inaccuracies in the assumed slit dimensions. Because of these complications, the discussion of errors in the reported mass flux results is left to the last section of this appendix. Errors in the measured data are discussed below in reverse order of importance.

D.2 Recording and Calibration Errors

By recording error, it is meant the difference between the "actual" emf output of a transducer (or thermocouple) and the emf recorded by the Auto-Data. As stated in Chapter III, the manufacturer claims the Auto-Data Eight to have an accuracy of ± 1 in the last significant bit. The error in a

measurement corresponding to this uncertainty is given in Appendix C for each instrument. The confidence level for this uncertainty was checked as part of the process of determining the calibration of the Auto-Data. A standard cell was connected to one of the Auto-Data channels and 757 readings (approximately five minutes running time) of the emf were recorded. It was found that the distribution around the mean (1.018 Volts) was was narrower than would be expected for a Gaussian distribution. Only six readings (0.8%) were more than ± 0.001 V the value of the least significant bit) different from the mean. None of the readings were more than 0.002 V different. Thus the estimated uncertainty interval is ± 1 least significant bit at 99% confidence. This applies to all measurements. It should be noted that the error expressed as a percentage of the reading may be large if the signal measured is small.

By calibration error, it is meant the difference between the actual output of a transducer in response to an applied pressure or temperature, and the response predicted by the calibration equation. The data used to determine the calibration equations are given in Appendix C. In that appendix, the rms error between the data and the calibration curve, as well as the maximum error between the two, are given. In all cases the maximum error is less than three times the rms error. This suggests that the maximum error encountered would be a good choice for the magnitude of the calibration error, provided it is at least as great as the probable error in the standard quantity used for the calibration. Calibration error has thus been taken to be the larger of these two quantities with a confidence interval of 99%. Calibration error is not stochastic, but systematic. Thus, calibration error should be added directly to other errors, not summed statistically.

Determination of the calibration error for the thermocouple used to measure the stagnation temperature is critical to determining the uncertainty associated with the measurement of the fluid stagnation state. Unfortunately, there is no way of determining the accuracy with which the freezing point of pure lead was approximated by the calibration experiment. While reagent grade lead was used, which contained less than 0.5% Antimony, there was no method for ensuring that the thermocouple junction temperature was exactly 327.5°C while the lead froze. The temperature of the boiling water, used as the low temperature calibration point, was verified with a Mercury thermometer. Since the correspondence between the thermocouple indication and the theoretical freezing point of lead was 0.6°C, according to standard calibration tables, it seems probable that the calibration was fairly reliable. A similar correspondence was found in calibrating the iron-constantan thermocouples. A calibration error of ± 0.5°C, at 99% confidence, seems a reasonable estimate for the calibration for the thermocouples described in Appendix C. This is less than the maximum error, between the thermocouple reading and the standard tables, of 1.0% at 350°C, specified by the manufacturer.

D.3 Dynamic Error

For multiple-sample data, the dynamic error is best calculated as the rms error between the data and its' mean. Assuming that this error is stochastic, the calculated error, shown in Appendix A, should be approximately the standard deviation. The error corresponding to a 99.7% confidence level should be approximately three times this calculated value. This calculated value includes the reading error discussed in the previous section. Calibration error should be added.

Dynamic error for the mass flux data has been estimated in an analogous manner. For the thermocouples embedded in the slit wall, analysis of the dynamic error is not particularly important. This data has only been used qualitatively. For these probes, dynamic error is induced by conduction effects within the thermocouple in response to the developing temperature profile within the test section. These effects result in the thermocouple tending to read higher than the temperature of the test section at the location of the junction. The amount of this error may be 2 to 3 degrees Celsius early in the transient. At later times, error from this effect is negligible. For the majority of each run the main contribution to the error in thermocouple data is calibration and reading error.

For the vessel level and weigh tank mass data, the dynamic error can be estimated as the rms error between the data and the best fit line to the data. This procedure assumes the flowrate from the vessel to be constant during the period over which it is applied. Such an assumption is consistent with the approach used in analysis of other data uncertainties. The magnitude of the error calculated by this procedure is dependent on the flowrate. This error is shown in Appendix A and includes the reading error. Because of data aliasing, introduced by the flowrate averaging technique (discussed in Chapter IV), the results of this calculation for the weigh tank data are invalid. A better estimate is given by the difference in mass flux calculated by the two methods.

D.4 Error In The Mass Flux Calculation

Ideally, the integral of the mass flowrate calculated by the volume discharge method, over time, for the entire run, should be equal to the total mass gained by the weigh tank. This result was verified for a few runs (8) and agreement was within 3%. This application is probably the best use of weigh tank data. The error is attributable to the the error in estimating the nitrogen density. Comparison of the calculated total volume discharged and the measured mass gained by the weigh tank agree within 4.7% for all the runs. Only 6 of the 94 exceed 3% difference. Since the volume data exceeds the weigh tank data a combination of evaporation from the tank and an overestimate of the nitrogen temperature (or failure to account for water vapor present in the cover gas) account for the difference. It seems reasonable, therefore to claim a $\pm 5\%$ error in the mass flowrate, with 99% confidence.

Error in the calculated mass flux is most difficult to estimate. The error should be the 5% estimated in the previous paragraph, plus the percentage error in the cross-sectional area of the slit. In comparing results for the same test section assembly the $\pm 5\%$ error applies. Slit width was measured to with in ± 0.03 mm using a vernier micrometer. Thus, error in the slit width measurement is negligible; on the order of 0.1%.

Slit opening dimension was determined by the shim thickness provided the slit walls were flat. Shim thicknesses were measured, again with a vernier micrometer (a more accurate variety), and found to be 0.127 mm, 0.254 mm, and 0.381 mm ± 0.003 mm. The quoted error is the largest encountered over approximately 50 made on each shim thickness. The test section was originally ground flat to within ± 0.001 mm so this contribution is negligible. Thus, prior to the test section deforming, and probably subsequent to its' repair, The error in the cross-sectional area is $\pm 3\%$, $\pm 1.5\%$, and $\pm 1\%$ for the 0.127 mm, 0.254 mm, and 0.381 mm slits respectively. These are probably applicable with a lower confidence level for runs made subsequent to the repair of the test section.

Estimation of the error in the mass flux measurement due to deformation of the test section is difficult. Measurements of the depressions in the wall surfaces were at most 0.03 mm. These measurements are consistent with the correction factors shown in Table 4-4. To what extent the corrections made to the nominal slit dimensions (described in Chapter IV) were accurate cannot be ascertained. The reliability of the assumptions made about the characteristics of the frictional pressure loss is unknown.

The best available data which allows an estimate of the accuracy with which slit sizes were calculated are the model comparisons of Chapter V. Inconsistencies between trends predicted by a model and data obtained for test section assemblies for which a correction to the mass flux data was required, give an indication of the possible error. For 0.381 mm nominal assemblies, the runs involved were #41 through #45. No inconsistencies are apparent. For the 0.254 mm nominal assemblies, runs #35 through #39, #51 through #55, and #68 through #72 were affected. Again, no clear discrepancy is noted. Runs #31 through #34 and #46 through #50 were affected amoung the 0.127 mm nominal assemblies. It would appear that the former group have mass fluxes which are too high by approximately 5%. (Compare #34 with #85 and #32 with #84). On the other hand, results for the second group indicate that the correction was again quite adequate.

In conclusion, it would seem appropriate to include a 5% uncertainty in the calculated mass flux for the two larger slit sizes due to possible dimensional variations. The total uncertainty is thus ±10% with 99% confidence. A 10% dimensional uncertainty seems appropriate for the 0.127 mm nominal slit size results. The total error for these is then ±15% with 99% confidence. Calibration error, reading error, and dynamic error, recorded in Appendix A are negligible by comparison. When no correction was required, the ±5% error plus the 1 to 3% error in the slit opening dimension is appropriate. The 0.381 mm slit data, upon which most of the discussion has been based has an error of approximately 6% with a confidence of 99% for all by 5 runs. These 5 appear to be well corrected, based on model comparisons, so the 11% error calculated by the above procedure is probably an overestimate.

APPENDIX E

Installation of Instrument Probes in The Test Section

The construction of the test section was a fairly complicated procedure. Figure 3-7 identifies the test section components mentioned in the following description.

Pressure sense lines and sheathed thermocouples were mounted permanently in the test section. Holes were drilled into the face of the "U"-shaped block opposite the slit wall to accommodate the probes. Pressure sense line holes were 6.4 mm in diameter. (These holes are shown in the profile view of the test section in Figure 3-7.) Holes for the thermocouples were 6.4 mm over the first 3.0 cm. Thermocouple holes were completed by drilling to within 0.25 mm of the slit wall with a 1.6 mm drill. Pressure tap holes were terminated about 1 mm from the wall. Once the drilling was completed the holes were carefully cleared of chips by hand reaming. The block was then cleaned in an ultrasonic cleaner.

The lower support plate and the lower spacer block were prepared by drilling holes large enough to clear the instrumentation probes. Clearance was kept to a minimum since these holes would serve to guide the probes into the correct holes in the center block. Also, it was important not to weaken the lower support plate by making the holes too large. At this time holes for dowel pins in the support plates, spacer blocks, and center parts were drilled. These pins were used to align parts of the test section during assembly.

Drilling holes into the "U"-shaped block which came so close to the surface caused dimples to be raised in the surface. Since this was to form the slit wall the surface was ground flat before assembly continued. Less that 0.015 mm of material was removed in grinding. The lower face of the insert block was also ground; this surface formed the opposite wall of the slit. Ground surfaces had a mirror finish, flat to within 2.5×10^{-4} mm.

Before forming the pressure taps in the slit wall, the test section was used in shake down runs of the equipment. Runs #8 through #13 were made without pressure taps so that comparisons between runs with and without pressure taps could be made. For these runs, thermocouples were pressfit into the mounting holes.

Pressure taps were formed in the slit wall using a spark cutter. This machine cuts metal using a high voltage arc. It holds an advantage over drills for this application in that it does not raise a burr around the top of the hole. A template for the holes was made from a piece of Lucite which fit snugly into the bottom of the "U". A 0.508 mm tool was used on the spark cutter. The holes that were formed could be seen to have slightly turned down edges. All the taps that were cut aligned with the center of the sense line hole, which had been drilled from the opposite face, within 2 mm.

In order to locate the pressure tap at the exit of the test section as close to the exit plane as possible, it was placed in a different manner from the rest. A 0.8 mm square groove was cut in the downstream face of the "U"-shaped block, running from the slit wall to the lower face. The tap was formed by braising a 0.79 mm diameter tube into the groove. The end of the tube was cut square and mounted flush with the slit wall. Thus, the centerline of the tap was only 0.4 mm from the exit plane of the slit. The diameter of the tap was approximately 0.49 mm. Extending the sense line, which had been braised into the center block, through holes in the lower spacer and lower support plate, allowed attachment of fittings to connect this line to the standard 3.2 mm tubing used for all the sense lines in the equipment.

Sections of stainless steel tubing, approximately 30 cm long, were mounted in the holes drilled into the test section for the pressure sense lines. These sections were connected to the sense lines, after assembly and mounting of the test section, using compression fittings. Originally, the pressure sense lines were mounted using high temperature epoxy (M-Bond 610). This method prooved inadequate, and leakage through the taps began after a few runs. Prior to run #31, the taps were remounted by braising. The braising was done in a vacuum oven at 900°C. This temperature was held long enough for the braise, which melts at 840°C, to run down the sense line tubing to within 1 cm of the slit wall. The exit pressure sense line was braised in the same operation. Apparently, this method was successful since no major leaks were detected in the remaining runs. It is possible that some seepage was occurring by the end of the test program.

With the pressure sense lines thus mounted, the lower spacer block and lower support plate were threaded over the tubes. Both pieces were then tack welded together and then to the "U"-shaped block. All that remained was installing the two types of thermocouples. The entire assembly was heated in an oven to 700°C. A lower temperature braise, than was used for the pressure sense lines, was employed for mounting the 0.25 mm sheathed chromel-constantan thermocouples. The silver braise used improves the thermal contact between the thermocouple and the test section. This mounting technique could not be used for the copper-constantan thermocouples for two reasons. First, since the junction was exposed, the braise might have altered the Seebeck coefficient, degrading the measurement accuracy. Second, the copper lead would have undergone severe oxidation at the temperatures necessary to melt the braise. For these reasons the copper-constantan thermocouples were mounted using high temperature epoxy (M-Bond 610).

For mechanical protection, guide tubes, about 8 cm long, were used around the exposed portion of the thermocouple probes. These were made from 3.18 mm tubing and were braised into the top of the thermocouple mounting holes in the upper support plate. The guide tube provided support for the probes which, had little rigidity.

Fittings were provided on both the thermocouples and pressure sense lines so that the test section could be disconnected from the instrumentation. This was necessary when the test section was removed from the vessel for reassembly. As mentioned above, compression fittings were used on the pressure sense lines. Thermocouple probes were fitted with polarized isothermal plugs.

APPENDIX F

Techniques Employed For The Integration of Ordinary Differential Equations

It is the purpose of this appendix to provide an overview of the methods which have been used to integrate the ordinary differential equations which were presented in Chapter V. Many details of these methods have been omitted. In the case of the NAG library, specific details about step size and method order selection are not available since the source program is proprietary. References cited herein give detailed descriptions of most of the algorithms available for numerical integration of ODE's.

F.1 Error Control in the NAG Library

For the reasons discussed in Chapter V, the NAG library routines, which integrate the system of ODE's until the value of a user input function is zero, were employed to predict critical flowrates for the models. The zero point is located by extrapolation of the dependent variables from the derivatives available in the solving routine. A root finding routine is then used to locate the exact zero point. The error allowed in locating the zero point is controlled by the input value "TOL". Where "TOL" is the difference between the calculated function value and zero. "TOL" is primarily used in controling the integration error. Error control in the NAG routines is fairly primative. The local error e_n, defined by

$$\bar{e}_n \;=\; \bar{y}_n \;\textit{minus}\; \bar{y}(t_n) \tag{F-1}$$

is estimated by the particular solution method used. The solver adjusts step size and/or method order until the following criterion is met

$$E \;\leq\; TOL \times \max\{eps, \frac{1}{N}\sum_{I=1}^{N} y_n^2(I)\} \tag{F-2}$$

where eps is a small number proportional to the machine precision (approx. 10^{-14} for CDC 7600). $y_n(I)$ is the I^{th} element of $\bar{y}_n$ and E is the current estimate of $\sum_{I=1}^{N} e_n^2(I)$. If (F-2) is not satisfied for any allowable step size or method order, the integration is aborted.

In the discussion below we will consider a single equation of the form:

$$y'(t) = f(y,t) \tag{F-3}$$

The methods described are general to the case where y and f are vector-valued.

F.2 Single Phase Liquid Flow

The three equations used to model the compressible flow of single phase liquid are non-stiff and are amenable to solution by single-step methods. Economical integration was accomplished using the D02BHF subroutine, which employs the fourth order Runge-Kutta-Merson formulation. The recursion relation is given by:

$$y_{n+1} = y_n + \frac{1}{6}(k_0+4k_3+k_4) \qquad \text{(F-4)}$$

where,

$$\eta_0 = y_n, \; k_0 = hf(\eta_0) \qquad \text{(F-4a)}$$

$$\eta_1 = \eta_0 + \frac{1}{3} k_0, k_1 = hf(\eta_1) \qquad \text{(F-4b)}$$

$$\eta_2 = \eta_0 + \frac{1}{6} (k_0 + k_1), k_2 = hf(\eta_2) \qquad \text{(F-4c)}$$

$$\eta_3 = \eta_0 + \frac{1}{8} (k_0 + k_2), k_3 = hf(\eta_3) \qquad \text{(F-4d)}$$

$$\eta_4 = \eta_0 + \tfrac{1}{2} (k_0 - 3k_2 + 4k_3), k_4 = hf(\eta_4) \qquad \text{(F-4e)}$$

Local error is estimated as:

$$e_n = | y_{n+1} - \eta_4 | \qquad \text{(F-5)}$$

If the inequality, (F-2), is satisfied the step is accepted and integration continues; if not, the step size is reduced and the step repeated. Five function evaluations are required for each attempted step. A detailed discussion of this method is given by Gear [107].

F.3 Two-Phase Steam-Water Flow

When function evaluations are expensive, multi-step methods are generally preferred. These methods often require fewer function evaluations than single step methods such as Runge-Kutta. This saving is accomplished by making use of the computed solution at previous mesh points. Some extra work is incurred in the manipulation of these data. Since the evaluation of y' is fairly costly in two-phase flow, multi-step methods proved more economical.

In most cases, usually when the quality was small, the equations for the Modified Henry Model (MHM) and the Homogeneous Non-Equilibrium Model (HNEM), were not very stiff. In these cases, the D02CHF subroutine, which uses Adams multi-step methods, was successful. For the Homogeneous Equilibrium Model (HEM), and for the other two in the case that D02CHF failed, it was necessary to use D02EHF, which employs Gear's method for stiff equations.

F.4 Adams Methods

Adams methods [108] are based on numerical integration. One can write,

$$y_{n+1} = y_n + \int_{t_n}^{t_{n+1}} f(y(x),x)dx \tag{F-6}$$

Rather than directly apply a numerical integration routine, Adams methods approximate f (y,x) with a polynomial which interpolates previously calculated values of f.

$$f(y(t),x) \rightarrow P(t) = \sum_{m=0}^{k} (-1)^m \binom{-s}{m} \nabla^m f_n \tag{F-7}$$

where,

$$s = \frac{t - t_n}{h}$$

and we have made use of the short-hand notation,

$$\binom{i}{j} = \frac{i(i-1)\cdots(i-j+1)}{j!}$$

$$\nabla^m f_n = \sum_{i=0}^{m} (-1)^i \binom{m}{i} f_{n-i}$$

The number k is the number of steps (past values of y_n) used. We refer to this as a k-step method.

An explicit Adams method is referred to as the Adams-Bashford method [108]. The recursion formula is given by:

$$y_{n+1} = y_n + h \sum_{i=0}^{k} \beta_{ki} f_{n-i} \tag{F-8}$$

where the β_{ki} are calculated as implied by equations (F-6) and (F-7). Values of these coefficients are tabulated in Henrici [109].

The Adams-Moulton method [110] is an implicit form of Adams' method which requires the solution to k algebraic equations at each step. Implicit methods are generally more stable than explicit ones. In fact, purely explicit methods are rarely used. The Adams-Moulton recursion formula is:

$$y_n = y_{n-1} + h \sum_{i=0}^{k} \gamma_i \nabla^i f_n \tag{F-9}$$

Where γ_i can be found tabulated in Henrici [109] and are evaluated from:

$$\gamma_i = (-1)^m \int_{-1}^{0} \binom{-s}{m} ds \tag{F-9a}$$

The solution strategy used in D02CHF is a predictor-corrector scheme using an Adams-Bashford predictor and an Adams-Moulton corrector. Specifically, a $P_k EC_{k+1} E$ algorithm is used. In this convention, P denotes N applications of the predictor. N is calculated at each step by the routine and depends upon k and other factors. C denotes a single application of the corrector and E an evaluation of f. The subscripts refer to the method order for the current step. Using the notation

$f_n^p = f(t_n, y_n^p)$ we write the process as:

P: y_{n+1}^p is calculated using eqn (F-8)

E: f_{n+1} is evaluated

P and E are repeated for γ=0 to N

C: y_{n+1} is calculated using eqn (F-9)

E: f_{n+1} is evaluated

Local error is estimated from:

$$E_k = h\gamma_k \nabla^k f_{n-1} \tag{F-10}$$

If the inequality, (F-2) is satisfied, the step is accepted. If not, the step is repeated with h reduced. Since multi-step methods require k prior steps with h fixed, it is necessary at this juncture to interpolate the back values of f required to implement a new step size.

Variable order is possible in this routine as well as variable step size. After the completion of a successful step, the order may be changed by one, up or down, before the next step. This decision is made on the basis of estimates of the value of E_{k-1} and E_{k+1}. These estimates can be made using current and back values of f. An estimate of the necessary step size for each of the orders considered is also made. If, for the accuracy required (TOL), a change in the order is predicted to reduce the amount of work required, this change is made. Work required is proportional to the reciprocal of the maximum step size estimate. The highest order allowed is 6, beyond this, the stability of the methods is questionable. When the decision to change order is close, the routine selects the lower order to reduce the work involved.

Unlike single step methods, multi-step methods are not self-starting. Values of y and f prior to the starting value would be required to begin integration with a k-step method. Starting is accomplished by beginning with k=1 and building up the order as integration progresses. (Other solvers, which do not have variable order capability, obtain starting values from single step methods such as Runge-Kutta). A detailed discussion of variable order and step size techniques is given in Chapter 6 of the book by Hall and Watt [111].

F.5 Gear's Method

In the HEM, and the other models, when the quality is high, (at which instance MHM and HNEM approach the HEM), the system of equations becomes stiff, which was characterized by rapid steepening of gradients of the dependent variables. In the Adams method routine this caused a reduction in the step size to the point where no progress was made in the integration. When this problem was encountered D02CHF aborted. The model program then continues integration using D02EHF which implements Gear's method.

Rather than using numerical integration as a basis as do Adams methods, Gear's method employs numerical differentiation. As with Adams methods, a polynomial is used to interpolate back values of f. However, the polynomial is differentiated rather than integrated.

$$P'(t_{n-r}) = \frac{1}{h} \sum_{m=0}^{k} \delta_{r,m} \nabla^m y_n \tag{F-11}$$

where,

$$\delta_{r,m} = (-1)^m \frac{d}{ds}\binom{-s}{m}_{s=-r} \tag{F-11a}$$

Values of $\delta_{r,m}$ may be found in the book by Henrici [109].

Integration of the equation is accomplished by the solution of the following expression which is derived from (F-3) and (F-11).

$$\frac{-1}{h_{n+k}}\delta_k\, y_{n+k} - \frac{1}{h_{n+k}}\sum_{j=0}^{k-1}\delta_j y_{n+j} = f(t_{n+k},y_{n+k}) \tag{F-12}$$

Where h has been subscripted to emphasize the variable step size possibility and the dual subscripts on δ omitted with the understanding that values of δ are dependent on the interpolating point being considered.

To see how (F-12) may be solved, and an estimate made of the local error, the equation is re-cast as follows:

Let,

$$g = -\alpha_k \sum_{j=1}^{k-1}\delta_j y_{n+j} \tag{F-13}$$

$$\alpha_k = -\frac{1}{\delta k}$$

Since g depends only on back values of y ($j \leq k-1$) it is a constant during the evaluation of y_{n+k} (for h fixed). We write (F-12) using (F-13) as:

$$y_{n+k} - h\alpha_k f(t_{n+k},y_{n+k}) - g = 0 \tag{F-14}$$

A Newton-Raphson technique for non-linear equations is used which employs the following iteration,

$$\{ I - h\alpha_k J^{(m)} \}\times\{ y_{n+k}^{(m+1)} - y_{n+k}^{(m)} \} = h\alpha_k f(t_{n+k},y_{n+k}^{(m)}) - g \tag{F-15}$$

Where $J^{(m)}$ is the Jacobian of the system, (in general a 3rd rank tensor).

$$J^{(m)} = \frac{\partial f}{\partial y}(t_{n+k},y_{n+k}^{(m)}) \tag{F-15a}$$

Starting values for the iteration (F-15), $y_{n+k}^{(0)}$, are predicted by extrapolation of the interpolating polynomial; which is obtained by integration of (F-11). In many problems, the Jacobian of the system is not a strong function of y and need only to be evaluated at the first iteration. For this case $J^{(m)}$ in equation (F-15) is replaced by $J^{(0)}$. Re-evaluation is made should convergence not be achieved. Since the Jacobian cannot be given explicitly for the present equations a numerical estimate is made by the routine as:

$$\frac{\partial f_i}{\partial y_i} \approx \frac{f(x,y+\epsilon_j e_j)-f(x,y)}{\epsilon_j} \tag{F-15b}$$

where, e_j is the normalized jth coordinate vector, and ϵ_j is a small increment.

The local truncation error is estimated as the difference between $y_{n+k}^{(0)}$ and the solution y_{n+k}. Step size and method order selection are accomplished in a manner similar to that described above for Adams methods. Details of this procedure are, of course, different.

F.6 The LSODE Package

As a check on the accuracy of the NAG ODE solvers, and to calculate pressure profiles suitable for computer graphing, model equations were re-solved using LSODI. Details of LSODI, and a listing of the code, are available in the report by Hindmarsh [112].

LSODI solves the implicit system:

$$A(t,y)y' = B(t,y) \tag{F-16}$$

both stiff and non-stiff methods are available. The stiff method, which is just Gear's method described above, was used exclusively in this work. Due to the complexities involved only a brief outline of the theory of LSODE is presented here. A complete description is given in Gear's original paper [113].

Briefly, LSODI uses a variable transformation approach to avoid numerical errors which may be introduced by the matrix manipulation necessary to re-write the form (F-16) in the explicit form (F-3) required by conventional ODE solvers such as those in NAG. This transformation of dependent variables substitutes $\bar{a}_n$ for $\bar{y}$. Where,

$$\bar{a}_n = \left[y_n, hy'_n, \ldots, hy'^{(k-1)}_n/(k-1)! \right] \tag{F-17}$$

Evaluation of derivatives of order greater than two is costly and unnecessary in light of Gear's method. $\bar{a}_n$ can be approximated by a linear transformation of the Nordsiek history vector $\bar{N}_n$ (details are given in the book by Henrici [109]).

$$\bar{N}_n = \left[y_n, hy'_n, hy'_{n-k+2} \right]^T \tag{F-18}$$

The transformation takes the form $\bar{a}_n = T\,\bar{N}_n$. Evaluation of the constant matrix T is discussed by Gear [107]. Under the transformation we can write the system as:

$$F(\bar{a}_n, t) = 0 \tag{F-19}$$

Newton-Raphson iteration, described above (F-15), is used with $\bar{a}_n$ replacing y_n and F_n replacing f_n. This new equation is vector rather than scalar valued but the solution technique is unchanged.

REFERENCES

1. Ross, D.F., "Research Perspective For the Small Break LOCA," Proceedings of ANS Specialists Meeting On Small Break Loss-of-Coolant Accident Analyses in LWRs, Electric Power Research Institute, EPRI WS-81-201, August, 1981.

2. Sheron, B.W. and Themis, P.S., "Small Break LOCA Mitigation - A New Licensing Perspective," Proceedings of ANS Specialists Meeting On Small Break Loss-of-Coolant Accident Analyses in LWRs, Electric Power Research Institute, EPRI WS-81-201, August, 1981.

3. Simoneau, R.J., Pressure Distribution in a Converging-Diverging Nozzle During Two-Phase Choked Flow of Subcooled Nitrogen, National Aeronautics and Space Administration, NASA TMX-71762, 1975.

4. Sallet, D.W., "On the Sizing of Pressure Relief Valves for Pressure Vessels which are Used in the Transport of Liquefied Gases," ASME Winter Annual Meeting, Paper No. 78-WA/HT-39, San Francisco, December, 1978.

5. Lienhard, J.H., Alamgir, Md. and Trela, M., "Early Response of Hot Water to Sudden Release From High Pressures," J. Heat Transfer, Vol. 100, 1978, pp. 473–479.

6. Shapiro, A.S., *The Dynamics and Thermodynamics of Compressable Fluid Flow,* The Ronald Press Company, New York, 1953.

7. Hall, D.G., An Inventory of the Two-Phase Critical Flow Data Base, Idaho National Engineering Laboratory, EGG-CAAP-5140, June, 1980.

8. Abdollahian, D., Healzer, J., Janssen, E. and Amos, C., Critical Flow Data Review and Analysis, Part I, S. Levy Inc., SLI-7908-1, November, 1980.

9. Abdollahian, D., Healzer, J., Janssen, E. and Amos, C., Critical Flow Data Review and Analysis, Electric Power Research Institute, EPRI NP-2192, January, 1982.

10. Sozzi, G.L., and Sutherland, W.A., Critcal Flow of Saturated and Subcooled Water at High Pressure, General Electric Company, NEDO-13418, July, 1975.

11. Morrison, A.F., Blowdown Flow in a BWR BDHT Test Apparatus, General Electric Company, GEAP-21656, October, 1977.

12. Alleman, R.T., McElfresh, A.J., Neuls, A.S., Townsend, W.C., Wilburn, N.P. and Withes, High-Enthalpy-Water Blowdown Tests From a Simple Vessel Through a Side Outlet, Battelle Northwest Laboratories, BNWL-1470, February, 1971.

13. Starkman, E.S., Schrock, V.E., Neusen, K.F. and Maneely, D.J., "Expansion of a Very Low Quality Two-Pase Fluid Through a Convergent-Divergent Nozzle," J. Basic Engr., June, 1964, pp. 247–256.

14. James, R., "Steam-Water Critical Flow Through Pipes," Proc. Instn. Mech. Engrs., Vol. 176, No. 26, 1962, pp. 741–748.

15. Fauske, H.K., Contribution to the Theory of Two-Phase One-Component Critical Flow, Argonne National Laboratory, ANL-6633, October, 1962.

16. Marviken, The Marviken Full Scale Critical Flow Tests, Third Series, Summary Report, MXC-301, December, 1979.

17. Agostinelli, A., Salemann, V. and Harrison, N.J., "Prediction of Flashing Water Flow Through Fine Annular Clearances," Trans. ASME, Vol. 80, July, 1958, p. 1138.

18. Collier, R.P., "Second Status Report on a Study of Critical Two-Phase Flow Through Simulated Cracks," presented at, BWR Piping Integrity Analysis Program Review, Electric Power Research Institute, May, 1980.

19. Hendricks, R.C., Simoneau, R.J. and Hsu, Y.Y., "A Visual Study of Radial Inward Flow of Subcooled Nitrogen," in: *Advances in Cryogenic Engineering*, Vol. 20, K.D. Timmehaus, ed., Plenum Press, New York, 1975, p. 370.

20. Simoneau, R.J., Two-Phase Choked Flow of Subcooled Nitrogen Through a Slit, NASA Lewis Research Center, NASA TM-71516, 1974.

21. Henry, R.E., "The Two-Phase Critical Discharge of Initially Saturated or Subcooled Liquid," Nucl. Sci. Engr. Vol. 41, 1970, p. 336.

22. Henry, R.E., Fauske, H.K. and McComas, S.T., "Two-Pase Critical Flow at Low Qualities, Part I, Experimental," Nucl. Sci. Engr., Vol. 41, 1970, p. 79.

23. Travis, J.R., Hirt, C.W. and Rivard, W.C., "Multidimensional Effects in Critical Two-Phase Flow," Nucl. Sci. Engr., Vol. 68, 1978, pp. 338–348.

24. Uchida, H., and Nariai, H., "Discharge of Saturated Water Through Pipes and Orifices," Proc. of the Third Inter. Heat Trans. Conf., Vol. 5, Chicargo, Ill., 1966, pp. 1–12.

25. Benjamin, M.W., and Miller, J.G., "The Flow of a Flashing Mixture of Water and Steam Through Pipes," Trans. ASME, Vol. 64, 1942, pp. 657–669.

26. Burnell, J.G., "Flow of Boiling Water Through Nozzles Orifices and Pipes," Engineering, 12 December, 1947, pp. 572–576.

27. Flinta, J., Hernborg, G., Siden, L. and Skinstad, A., "Result From the Blowdown Test for the Excercise," European Two-Phase Flow Group Meeting, Denmark, 1971.

28. Isbin, H.S. and Fauske, H.K., Two-Phase Steam-Water Critical Flow, U.S. Atomic Energy Commission, TID-11061, November, 1960.

29. Ogasawa, E., "Discharge of Saturated Water From Long Ducts," Proc. Japan. Engr. Soc., No. 181, October, 1967, p. 121.

30. Borgartz, B.O., Goodman, R.M.E., O'Brien, T.P., Rawlington, M. and Edwards, A.R., Depressurization Studies, Phase 2, Results of Tests 127 and 128, AWRE Foulness Division, AWRE-44-86-151, June, 1978.

31. Haubenreich, P.N., The Flow of a Flashing Mixture of Water and Steam at High Pressures, U.S. Atomic Energy Commission, AEC-CF-55-5-200, May, 1955.

32. Seynhaeve, J.M., Giot, M.M. and Fritte, A.A., "Non-Equilibrium Effects of Critical Flow-Rates at Low Qualities," OECD Nuclear Energy Agency, Specialists' Meeting, Toronto, August, 1976.

33. Reocreux, M.L., "Experimental Study of Steam-Water Choked Flow," OECD Nuclear Energy Agency, Specialists' Meeting, Toronto, August, 1976.

34. Gallagher, E.V., Water Decompression Experiments and Analysis for Blowdown of Nuclear Reactors, IIT Research Institute, IITRI-578-P-21-39, July, 1970.

35. Necmi, S. and Hancox, W.T., "1An Experimental and Theoretical Investigation of Blowdown From a Horizontal Pipe," in: *Heat Transfer,* Vol. 5, Hemisphere Publishing Corporation, Washington, D.C., 1978, pp. 83–88.

36. Riebold, W. and Fritz, G., "Studies on Non-Steady Two-Phase Flow Phenomena in Ejection Experiments," Crest Meeting, Frankfurt, June, 1969.

37. Edwards, A.R. and O'Brien, T.P., "Studies of Phenomena Connected With the Depressurization of Water Reactors," J. British Nucl. Energy Soc., Vol. 9, No. 2, April, 1970, pp. 125–135.

38. Schrock, V.E., Starkman, E.S. and Brown, R.A., "Flashing Flow of Initially Subcooled Water in Convergent-Divergent Nozzles," J. Heat Transfer, Vol. 99, 1977, p. 647.

39. Powell, A.W., Flow of Subcooled Water Through Nozzles, Westinghouse Electric Corporation, WAPD-PT(V)-90, April, 1961.

40. Zimmer, G.A., Wu, B.J.C., Leonhardt, W.J., Abuaf, N. and Jones, O.C., Pressure and Void Distributions in a Converging-Diverging Nozzle With Nonequilibrium Vapor Generation, Brookhaven National Laboratory, BNL-NUREG-26003, April, 1979.

41. Keller, V.D., Mal'Tsev, B.K. and Khlestkin, D.A., "Critical Discharge of Superheated and Subcooled Water Through Cylindrical Passages at High Pressures," Heat Transfer - Soviet Research, Vol. 5, No. 5, September-October, 1973, pp. 53–56.

42. Shiba, M. and Curet, H.D., "Investigation of the Critical Flow Condition During a Loss-of-Coolant Accident," presented at The Winter Meeting of The American Nuclear Society, November-December, 1969.

43. Zaloudek, F.R., Steam-Water Critical Flow From High Pressure Systems, General Electric Company, HW-80535, January, 1964.

44. Gros D'Aillon, L. and Jeandey, Ch., "Two-Phase Flow Under Steep Pressure Gradients," CSNI Specialists' Meeting, Pasadena, CA, 1981.

45. Saha, P., A Review of Two-Phase Steam-Water Critical Flow Models With Emphasis on Thermal Nonequilibrium, Brookhaven National Lab., BNL-NUREG-50907, September, 1978.

46. Wallis, G.B., "Critical Two-Phase Flow," Int. J. Multiphase Flow, Vol. 6, 1980, pp. 97–112.

47. Henry, R.E., "Two-Phase Compressible Flow," presented at EPRI Workshop on Two-Phase Flow, Tampa, FL, 1979.

48. Boure, J.A., "The Critical Flow Phenomenon With Reference to Two-Phase Flow and Nuclear Reactor Systems," ASME Symposium on the Thermal and Hydraulic Aspects of Nuclear Reactor Safety, Vol. 1, 1977, pp. 195–216.

49. Rivard, W.C. and Torrey, M.D., KFIX: A Computer Program For Transient, Two-Dimensional, Two-Fluid Flow, Los Alamos Scientific Laboratory, LA-NUREG-6623, 1977.

50. Wallis, G.B., *One Dimensional Two-Phase Flow*, McGraw-Hill, New York, 1969.

51. Collins, R.L., "Choked Expansion of Subcooled Water and the I.H.E. Model," J. Heat Transfer, Vol. 100, No. 2, 1978. pp. 275–280.

52. Levy, S. and Abdollahian, D., "Homogeneous Non-Equilibrium Critical Flow Model," Int. J. Heat Mass Transfer, Vol. 25, No. 6, 1982, pp. 759–770.

53. Nicolette, V.F., A Parametric Analysis of Two-Phase Critical Fanno Flow Using the Homogeneous Equilibrium Model, M.S. Thesis, University of California, Berkeley, 1980.

54. Hancox, W.T., Mathers, W.G. and Kawa, D., "Analysis of Transient Flow Boiling: Application of the Method of Characteristics," AIChE Paper No. 42, 15th National Heat Transfer Conference, San Francisco, 1975.

55. Moody, F.J., "Maximum Flow Rate of a Single Component Two-Phase Mixture," J. Heat Transfer, Vol. 87, No. 1, 1965, pp. 134–142.

56. Levy, S., "Prediction of Two-Pase Critical Flow Rate," J. Heat Transfer, Vol. 87, No. 1, 1965, pp. 53–58.

57. Klingebiel, W.J., Critical Flow Slip Ratios of Steam-Water Mixtures, Ph.D. Thesis, University of Washington, Seattle, 1964.

58. Code of Federal Regulations, Title 10, Part 50, Appendix K, Acceptance Criteria For Emergency Core Cooling Systems for Light-Water Cooled Nuclear Power Reactors, 1976.

59. Moody, F.J., "Maximum Two-Phase Vessel Blowdown From Pipes," J. Heat Transfer, Vol. 88, No. 3, 1966, pp. 285–295.

60. Moody, F.J., "Maximum Discharge Rate of Liquid-Vapor Mixtures From Vessels," Symposium on Non-Equilibrium Two-Phase Flows, ASME Winter Annual Meeting, Houston, TX, 1975, pp. 27–36.

61. Zivi, S.M., "Estimation of Steady-State Void Fraction by Means of the Principle of Minimum Entropy Production," J. Heat Transfer, Vol. 86, 1964, pp. 247–252.

62. Tentner, A. and Weisman, J., "The Use of the Method of Characteristics For Examination of Two-Phase Flow Behavior," Nuclear Technology, Vol. 37, January, 1978, pp. 19–28.

63. Hughmark, G.A., "Holdup in Gas-Liquid Flow," Chem. Eng. Prog., Vol. 58, No. 4, 1962, pp. 62–65.

64. Henry, R.E., Fauske, H.K., and McComas, S.T., "Two-Phase Critical Flow at Low Qualities, Part II: Analysis," Nucl. Sci. Engr., Vol. 41, 1970, pp. 92–98.

65. Henry, R.E. and Fauske, H.K., "The Two-Phase, Critical Flow of One-Component Mixtures in Nozzles, Orifices, and Short Tubes," J. Heat Transfer, Vol. 93, No. 2, 1971, pp. 179–187.

66. Fauske, H.K., "Two-Phase Two- and One-Component Critical Flow," Proc. Symp. of Two-Phase Flow, Vol. 3, University of Exeter, Devon, England, 1965, p.101.

67. Tangren, R.F., Dudge, C.H. and Seifert, H.S., "Compressibility Effects in Two-Phase Flow," J. of Applied Physics, Vol. 20, No. 7, 1949, p. 637.

68. Alamgir, M.D. and Lienhard, J.H., "Correlation of Pressure Undershoot During Hot-Water Depressurization," J. Heat Transfer, Vol. 103, No. 1, 1981, pp. 52–55.

69. Simpson, H.C. and Silver, R.S., "Theory of One-Dimensional Two-Phase Homogeneous Flow," Proc. Inst. Mech. Engrs., Symposium on Two-Phase Flow, 1962, pp. 45–56.

70. Edwards, A.R., Conduction Controlled Flashing of a Fluid, and The Prediction of Critical Flow Rates in a One-Dimensional System, United Kingdom Atomic Energy Authority, ASHB(S) R.147, 1968.

71. Rohatgi, U.S. and Reshotko, E., "Non-Equilibrium One-Dimensional Two-Phase Flow in Variable Area Channels," Symposium on Non-Equilibrium Two-Phase Flows, ASME Winter Annual Meeting, Houston, TX, 1975, pp. 47–54.

72. Plesset, M.S. and Zwick, S.A., "The Growth of Bubbles in Superheated Liquids," J. Applied Physics, Vol. 25, pp. 493–500.

73. Theofanous, T.G., Biasi, L., Isbin, H.S. and Fauske, H.K., "A Theoretical Study oon Bubble Growth in Constant and Time-Dependent Pressure Fields," Chem. Engr. Sci., Vol. 24, 1969, pp. 885–897.

74. Jones, O.C. and Zuber, N., "Bubble Growth in Variable Pressure Fields," J. Heat Transfer, Vol. 100, 1978, pp. 453–459.

75. Cha, Y.S. and Henry, R.E., "Bubble Growth During Decompression of a Liquid," J. Heat Transfer, Vol. 103, February, 1981, pp. 56–60.

76. Ishii, M., *Thermo-Fluid Dynamic Theory of Two-Phase Flow,* Eyrolles, Paris, 1975.

77. Banerjee, S. and Chan, A.M.C., "Separated Flow Models - I: Analysis of the Averaged and Local Instantaneous Formulations," Int. J. Multiphase Flow, Vol. 6, 1980, pp. 1–24.

78. Boure, J.A., "On a Unified Presentation of the Non-Equilibrium Two-Phase Flow Models," Symposium on Non-Equilibrium Two-Phase Flows, ASME Winter Annual Meeting, Houston, TX, 1975, p. 1.

79. Moog, D., A State-Of-The-Art Assessment of Initially Subcooled Two-Phase Critical Flow, M.S. Thesis, University of California, Berkeley, 1983.

80. Ardron,K.H., "A Two-Fluid Model For Critical Vapor-Liquid Flow," Int. J. Multiphase Flow, Vol. 4, 1978, pp. 323–337.

81. Richter, H.J. and Minas, S.E., "Separated Flow Model for Critical Two-Phase Flow," ASME Symposium on Nonequilibrium Interfacial Transport Processes, San Diego, CA, 1979.

82. Malnes, D., "Critical Two-Phase Flow Based on Non-Equilibrium Effects," Symposium on Non-Equilibrium Two-Phase Flows, ASME Winter Annual Meeting, Houston, TX, 1975.

83. Giot, M. and Fritte, A., "Two-Phase and Two and One-Component Critical Flows With a Variable Slip Model," Progress in Heat and Mass Transfer, Vol. 6, 1972, pp. 651–670.

84. Zuber, N., "On The Problem of Hydrodynamic Diffusion in Two-Phase Flow Media," presented at All-Union Conference on Heat and Mass Transfer, Minsk, USSR, May, 1964.

85. Rowe, P.A. and Hernwood, C.A., "Drag Forces in a Hydraulic Model of a Fluidized Bed," Trans. Inst. Chem. Engrs., Vol. 39, 1961, pp. 43–54.

86. Bird, R.E., Stewart, W.E. and Lightfoot, E.N., *Transport Phenomena,* John Wiley & Sons, Inc., New York, 1960, p.409.

87. Kroeger, P.G., "Application of a Non-Equilibrium Drift Flux Model to Two-Phase Blowdown Experiments," Specialists' Meeting on Transient Two-Phase Flow, OECD Nuclear Energy Agency, Toronto, August, 1978.

88. Liles, D.R., et al, TRAC P1A An Advanced Best-Estmate Program for PWR LOCA Analysis, Los Alamos Scientific Laboratory, (Draft) March, 1979.

89. Zuber, N. and Findlay, J.A., "Average Volumetric Concentrations in Two-Phase Flow Systems," J. Heat Transfer, Vol. 87, 1965, p. 453.

90. Liles, D.R., et al, TRAC-PD2 An Advanced Best-Estimate Computer Program for Pressurized Water Reactor Loss-of-Coolant Accident Analysis, Los Alamos Scientific Laboratory, NUREG/CR-2054, LA-8709-MS, April, 1981.

91. Ransom, V., Wagner, R.J., Trapp, J.A., Carlson, K.E., Kiser, D.M., Kuo, H., Nelson, R.,and James, RELAP5/MOD1 Code Manual, Volume I: System Models and Numerical Methods, EG&G Idaho, Inc., NUREG/CR-1826, EGG-2070, November, 1980.

92. Reocreux, M.L., "Application of General Equations of Two-Phase Flows to the Study of Critical Flows," European Two-Phase Flow Group Meeting, Rome, Italy, June, 1972.

93. Raithby, G.D. and Hollands, K.T., "Laminar and Turbulent Free Convection," in *Advances in Heat Transfer,* Vol. 11, ed., T.F. Irvine and J.P. Hartnett, Academic Press, New York, 1975.

94. Carslaw, H.S. and Jaeger, J.C., *Conduction of Heat in Solids,* Clarendon Press, Oxford, 1959.

95. Alamgir, Md., Kan, C.Y. and Lienhard, J.H., "An Experimental Study of the Rapid Depressurization of Hot Water," J. Heat Transfer, Vol. 102, August, 1980.

96. Forest, T.W. and Ward, C.A., "Effect of a Dissolved Gas on the Homogeneous Nucleation Pressure of a Liquid," J. Chem Phys., Vol. 66, No. 6, March, 1977.

97. Jeandey, Ch., Gros D'Aillon, L., Bourgine, L. and Barriere, G., Auto Vaporization D'Ecoulements Eau/Vapeur, Commisariat a L'Energie Atomique, Report, T.T. No. 163, July, 1981.

98. Abuaf, N., Jones, O.C. and Wu, B.,J.,C., "Critical Flashing Flows in Nozzles With Subcooled Inlet Conditions," to be published in J. Heat Transfer, 1983.

99. Bauer, E.G., Houdayer, G.R. and Sureau, H.M., "A Non-Equilibrium Axial Flow Model and Application to Loss-of-Coolant Accident Analysis: The CLYSTERE System Code," presented at OECD/NEA Specialists' Meeting on Transient Two-Phase Flow, Toronto, August, 1976.

100. Owens, W.L., "Two-Phase Pressure Gradient," *International Developments in Heat Transfer, Part II,* ASME, 1961, pp. 363–368.

101. Levy, S., "Steam Slip - Theoretical Prediction From Momentum Model," J. Heat Transfer, Vol. 82, No. 1, 1960, pp. 113–124.

102. Lockhart, R.W. and Martinelli, R.C., "Proposed Correlation of Data for Isothermal Two-Phase Two-Component Flow in Pipes," Chem. Eng. Prog., Vol. 45, No. 1, 1949, pp. 39–48.

103. Martinelli, R.C. and Nelson, D.B., "Prediction of Pressure Drop During the Forced Ciculation of Boiling Water," Trans. ASME, Vol. 70, 1948, p.695.

104. Griffith, P. and Wallis, J.D., "The Role of Surface Conditions in Nucleate Boiling," Chem. Eng. Prog. Symp., Ser. 56, Vol. 30, 1960, pp. 49–63.

105. Wallis, G.B. and Richter, H.J., "An Isentropic Streamtube Model for Flashing Two-Phase Vapor-Liquid Flow," J. Heat Transfer, Vol. 100, November, 1978.

106. Kline, S.J. and McClintock, F.A., "Describing Uncertainties in Single-Sample Experiments," Mechanical Engineering, January, 1953, pp. 3–8.

107. Gear, C.W., *Numerical Initial Value Problems in Ordinary Differential Equations*, Prentice-Hall, Inc., Englewood Cliffs, NJ, 1971.

108. Bashford, F., and Adams, J.C., *Theories of Capillary Action*, Cambridge University Press, 1883.

109. Henrici, P., *Discrete Variable Methods in Ordinary Differential Equations*, John Wiley & Sons, Inc., New York, 1962.

110. Moulton, F.R., *New Methods in Exterior Ballistics*, Univ. Chicargo Press, 1926.

111. Hall, G. and Watt, J.M., *Modern Numerical Methods For Ordinary Differential Equations*, Clarendon Press, Oxford, 1976.

112. Hindmarsh, A.C., Gear...Ordinary Differential Equation System Solver, Lawrence Livermore Laboratory, UCID-30001, Rev. 3, 1974.

113. Gear, C.W., "Simultaneous Solution of Differential-Algebraic Equations," IEEE Transactions on Circuit Theory, Vol. CT-18, No. 1, January, 1971.

This report was done with support from the Department of Energy. Any conclusions or opinions expressed in this report represent solely those of the author(s) and not necessarily those of The Regents of the University of California, the Lawrence Berkeley Laboratory or the Department of Energy.

Reference to a company or product name does not imply approval or recommendation of the product by the University of California or the U.S. Department of Energy to the exclusion of others that may be suitable.

TECHNICAL INFORMATION DEPARTMENT
LAWRENCE BERKELEY LABORATORY
UNIVERSITY OF CALIFORNIA
BERKELEY, CALIFORNIA 94720